CORA Cork Open Research Archive
Cartlann Taighde Oscailte Chorcaí

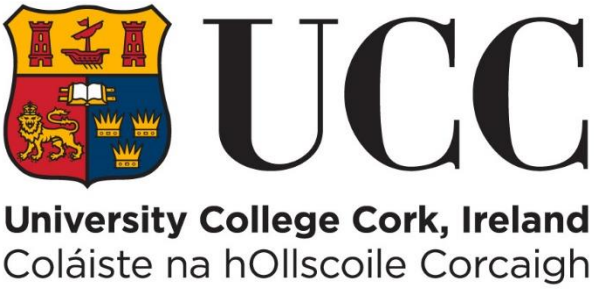
Title	Characterisation of atmospheric single particles in industrial and regional background environments using aerosol time of flight mass spectrometry
Authors	Arndt, Jovanna
Publication date	2015
Original Citation	Arndt, J. 2015. Characterisation of atmospheric single particles in industrial and regional background environments using aerosol time of flight mass spectrometry. PhD Thesis, University College Cork.
Type of publication	Doctoral thesis
Rights	© 2015, Jovanna Arndt. - http://creativecommons.org/licenses/by-nc-nd/3.0/
Download date	2026-10-31 05:23:26
Item downloaded from	https://hdl.handle.net/10468/2530

UCC
University College Cork, Ireland
Coláiste na hOllscoile Corcaigh

Characterisation of Atmospheric Single Particles in Industrial and Regional Background Environments using Aerosol Time of Flight Mass Spectrometry

A thesis submitted to

THE NATIONAL UNIVERSITY OF IRELAND, CORK



for the degree of

DOCTOR OF PHILOSOPHY

by

Jovanna Arndt

Based on research carried out at

Department of Chemistry

&

Environmental Research Institute

Supervisor

Professor John Wenger

Head of Department

Professor Martyn Pemble

University College Cork _____ December 2015

CONTENTS

Declaration vi

Quotation vii

Acknowledgements viii

Abstract x

List of abbreviations and acronyms xi

1. Introduction 1

1.1 Aerosols 2

1.2 Sources and Chemical Composition of Aerosols 2

1.3 Particle Size and Formation 6

1.4 Effects of Atmospheric Aerosols 9

1.4.1 Climate Effects 9

1.4.2 Health Effects 12

1.4.3 Air Quality Legislation 14

1.5 Measurements of Aerosol Particles 14

1.5.1 Aerosol Mass Spectrometers 16

1.5.2 Single Particle Mass Spectrometry Studies 17

1.6 Overview 29

1.6.1 Aims of Research 29

1.6.2 Overview of Thesis 29

2. Instrumentation and Methodology 30

2.1 Aerosol Time-of-Flight Mass Spectrometer (ATOFMS) 31

2.1.1 Particle Sampling 32

2.1.2 Particle Sizing 32

2.1.3 Particle Ionisation 33

2.2 Data Analysis 34

2.2.1 Scaling and Mass Reconstruction 37

2.3 Negative Ion Sensitivity 44

2.4 HYSPLIT Back Trajectories 45
3. Characterisation of airborne single particles during NANO-INDUS 46
3.1 Introduction 47
3.1.1 Particles from industrial activities 47
3.1.2 Dunkirk 57
3.1.3 Aims 62
3.2 Methodology 64
3.2.1 Sampling Site 64
3.2.2 Instrumentation 67
3.3 Results and Discussion 70
3.3.1 Meteorology 70
3.3.2 Particle Number and Mass Concentration 72
3.3.3 Particle Classes 74
3.3.4 Particle Sources 91
3.4 Conclusions 112
4. Characterisation of airborne single particles during ADRIMED and SAF-MED in Corsica, France 113
4.1 Introduction 114
4.1.1 Mediterranean Meteorology 114
4.1.2 Atmospheric Processing in the Mediterranean 116
4.1.3 Mediterranean PM Composition 119
4.1.4 Mediterranean Background Aerosol Studies 125
4.1.5 ChArMEx and Aims 127
4.2 Methodology 129
4.2.1 Sampling Site 129
4.2.2 Instrumentation 130
4.3 Results 134
4.3.1 Meteorology 134

4.3.2 Particle Number and Mass Concentrations 138
4.3.3 Particle Classes 141
4.3.4 Particle Sources 152
4.3.5 Processing Markers 169
4.4 Conclusions 175
5. Summary 176
5.1 NANO-INDUS 177
5.2 ADRIMED and SAF-MED 180
5.3 ATOFMS Comparison 183
5.4 Perspectives 184
6. References 187
7. Appendix I – Scaling 232
7.1 The Scaling Process 232
7.2 Scaling Factors 235
8. Appendix II – NANO-INDUS 237
8.1 Analysis of GMF Ores and Chimney Filters 237
8.2 Results: GMF Ores and Chimney Filters 238
8.2.1 Ores 238
8.2.2 Sintering unit – Firing Area (Chimney filter A) 239
8.2.3 Sintering unit – Cooling Area (Chimney filter B) 243
8.2.4 Smelting Unit (Chimney filter C) 243
8.2.5 Comparison of ores and industrial filter samples 243
8.2.6 Comparison of ATOFMS and SEM-EDX techniques 244
8.3 ATOFMS Data Capture 246
8.4 HYSPLIT 246
8.5 Size Distributions 248
9. Appendix III – ADRIMED/SAF-MED 251
9.1 ATOFMS Data Capture 251

9.2 OC Comparison 251
9.3 HYSPLIT 252
9.4 Size Distributions 263
9.5 Correlations 265

DECLARATION

The work presented in this thesis was performed at the Department of Chemistry and Environmental Research Institute, University College Cork during the academic years 2010 - 2015. Unless otherwise acknowledged, this thesis is the independent work of the author. This material has not been submitted to any institution, including University College Cork, for the purpose of obtaining any other degree or any other qualification.

_____

Jovanna Arndt

QUOTATION

“Everything is vague to a degree you do not realize till you have tried to make it precise.”

ACKNOWLEDGEMENTS

Human beings are social creatures and many of our greatest scientific achievements have only been possible through consistent and extensive collaborative effort. So, although I stubbornly refused to accept it on many occasions, this work would not have been possible without the guidance and support of a great number of other people. The man instrumental in encouraging me to apply for this PhD, ensuring our involvement in the field measurement campaigns and in attempting to make a legitimate atmospheric scientist out of me is Professor John Wenger. Thank you John, for the years of unrelenting patience, encouragement, support, optimism, cajoling, and calm thinking that have gotten me and our trusty ATOFMS this far. It's not on fire yet.

The man responsible for virtually all of my ATOFMS knowledge and data analysis skills is Dr. Robert Healy. I cannot appreciate enough the help he has given me over the years in making sense of this instrument and its data, and you will never find a more good-natured, patient and understanding mentor. There are still occasions, I'm sure, where we are lost without your expertise.

Dr. David Fergenson is the main reason the ATOFMS *isn't* on fire yet. Thank you, and your Livermore team, for the tremendous help you've given us in recent years and for returning the instrument to something of its former glory. Your enthusiasm and willingness to solve any of its problems, in any situation, at any time of day, has kept me sane and hopeful. You've got us covered. My hero!

Without this PhD, I could have spared myself a great deal of frustration and stress. I would also not have met some of my favourite people and would not have had some of the best times of my life. Memories of my time in Corsica with Allison Schwier will stay with me for as long as I live, in the best possible way. Miserable misanthrope that I am, meeting you reminded me that the world is full of great people I haven't met yet. You won't like me thanking you for your friendship, but here it is anyway. Allie, you are a fantastic scientist (policymaker, politician, musician, don't let us stop you!) and person, thank you for existing! My two other Eoins, Mac and Wilson: my time in CRAC was 135.8% worth it for getting to know you there (I can produce a graph of our friendship if required). You are sensational people, and many other people throughout your lives will be happier for knowing you. I *will* keep in touch (that's not a threat…). To the other, but of course not lesser, members of CRAC – Ian, Stig, Dave & Dave, Prof. Sodeau, Dean, Trevor, and now Paul – thank you for all of your kind words, witticisms and support throughout the

years. I have always felt part of the team. Thank you to everyone we worked with on the NANO-INDUS and ChArMEx campaigns –you helped make them memorable and enjoyable experiences, and no effort was too great in aid of good data.

To my parents: you are literally the foundations of my life. Some of the most compassionate, forgiving, patient, open-minded and kindest people I know, and I am aware every day of how lucky I am to be your daughter. You've always considered it your responsibility as parents to offer me unconditional love and support in everything I've done and that you require no thanks. Ridiculous! Thank you, ad infinitum. My little sister – practical, sensible and more grown-up than I am – has been on many an occasion a reminder of how to work hard in spite of your inner Schweinehund. I am frequently in awe of your backbone lady.

Someone very perceptive once said that "the good life is one inspired by love and guided by knowledge". So to Eoin, my despairing optimist: thank you for the last 11 years, 1 month and 12 days (approximately) of love, patience and support. Every day was a choice, and I appreciate all of them. You are the most conscientious, enthusiastic, determined, curious and sweetest scientist-man I know, and you have no equal in my eyes. Your love of science has been a constant source of inspiration, and your use of logic in almost every situation instructive, if frequently infuriating. You are always right! May you always have questions to answer love.

And I was worried I would run out of cheese.

ABSTRACT

The composition of atmospheric particles is an important factor in determining their impact on climate and health. In this study, an aerosol time-of-flight mass spectrometer (ATOFMS) was used to measure the chemical composition of ambient single particles at two contrasting locations – an industrial site in Dunkirk, France and a regional background site in Corsica. The ATOFMS data were combined with meteorological information and other particle measurements to determine the various sources of the particles observed at the sites.

The particle classes detected in Dunkirk included carbonaceous species from fossil fuel combustion and biomass burning, metal-containing types from local industries and sea-salt. Highest particle number concentrations and mass concentrations of $PM_{2.5}$, black carbon, organics, nitrate, ammonium and several metallic species (Fe, Mn, Pb, Zn) were found during periods heavily influenced by local industry. Particles from a ferromanganese alloy manufacturing facility were identified by comparing ambient ATOFMS data with single particle mass spectra from industrial chimney filters and ores. Particles from a steelworks were identified based on comparison of the ambient data with previous studies. Based on these comparisons, the steelworks was identified as the dominant emitter of Fe-rich particles, while the ferromanganese alloy facility emitted Mn-rich particles.

In Corsica, regional transport of carbonaceous particles from biomass burning and fossil fuel combustion was identified as the major source of particles in the Mediterranean background aerosol. Throughout the campaign the site was influenced by air masses altering the composition of particles detected. During North Atlantic air masses the site was heavily influenced by fresh sea salt. Regional stagnation was the most common type of air mass regime throughout the campaign and resulted in the accumulation of carbonaceous particles during certain periods. Mass concentrations were estimated for ATOFMS particle classes, and good agreement was found between the major carbonaceous classes and other quantitative measurements.

Overall the results of this work serve to highlight the excellent ability of the ATOFMS technique in providing source-specific composition and mixing state information on atmospheric particles at high time resolution.

LIST OF ABBREVIATIONS AND ACRONYMS

ADRIMED	Aerosol Direct Radiative Forcing on the Mediterranean Climate
AFL	Aerodynamic Focussing Lens
AGL	Above Ground Level
AMS	Aerosol Mass Spectrometer
APS	Aerodynamic Particle Sizer
AQEG	Air Quality Expert Group
ATOFMS	Aerosol Time of Flight Mass Spectrometer
BBOA	Biomass Burning Organic Aerosol
BC	Black Carbon
CAFE	Clean Air For Europe
CCN	Cloud Condensation Nuclei
CEST	Central European Summer Time
ChArMEx	Chemistry-Aerosol Mediterranean Experiment
CITEPA	Centre Interprofessionnel Technique d'Etudes de la Pollution Atmosphérique
CNRM-GAME	Centre National de Recherches Météorologiques - Groupe d'étude de l'Atmosphère Météorologique
COA	Cooking-related Organic Aerosol
CPC	Condensation Particle Counter
D/I	Desorption/Ionisation
DMA	Differential Mobility Analyser
DMS	Dimethyl Sulfide
D_m	Electrical Mobility Diameter
D_o	Optical Diameter
D_{va}	Vacuum Aerodynamic Diameter
D_{ve}	Volume Equivalent Diameter

EC	Elemental Carbon
EDX	Energy Dispersive X-ray spectrometry
EEA	European Environment Agency
EELS	Electron Energy Loss Spectroscopy
EMD-SAGE	Ecole des Mines de Douai, Département Sciences de l'Atmosphère et Génie de l'Environnement
ENCHILADA	Environmental Chemistry through Intelligent Atmospheric Data Analysis
EPA	Environmental Protection Agency
E-PRTR	European Pollutant Release and Transfer Register
GC	Gas Chromatography
GDAS	Global Data Assimilation System
GMF	Glencore Manganese France
HMS	Hydroxymethanesulfonate
HOA	Hydrocarbon-like Organic Aerosol
HPLC	High Performance Liquid Chromatography
HR-ToF-AMS	High-Resolution Time-of-Flight Aerosol Mass Spectrometer
HTDMA	Hygroscopicity Tandem Differential Mobility Analyser
HYSPLIT	Hybrid Single Particle Lagrangian Integrated Trajectory Model
IARC	International Agency for Research on Cancer
IC	Ion Chromatography
ICP-MS	Inductively Coupled Plasma Mass Spectrometry
IN	Ice Nuclei
IPCC	Intergovernmental Panel on Climate Change
LAMPAS	Laser Mass Analysis of Particles in the Airborne State
LCE	Laboratoire Chimie de l'Environnement
LIDAR	Light Detection And Ranging

LSCE	le Laboratoire des Sciences du Climat et de l'Environnement
LV-OOA	Low Volatility Oxidized Organic Aerosols
MAAP	Multi-Angle Absorption Photometer
MISR	Multi-Angle Imaging Spectroradiometer
MODIS	Moderate Resolution Imaging Spectroradiometer
MOUDI	Micro-Orifice Uniform-Deposit Impactor
MS	Mass Spectrometry
MSA	Methanesulfonate
NAMS	Nano-Aerosol Mass Spectrometer
Nd:YAG	Neodymium-doped Yttrium Aluminium Garnet
NOA	Nitrogen-enriched Organic Aerosol
OA	Organic Aerosol
OC	Organic Carbon
OM	Organic Matter
OOA	Oxidized Organic Aerosols
OPC/OPS	Optical Particle Counter/Sizer
PAH	Polycyclic Aromatic Hydrocarbon
PALMS	Particle Analysis by Laser Mass Spectrometer
PILS	Particle Into Liquid Sampler
PIXE	Particle-Induced X-ray Emission
PM	Particulate Matter
PMF	Positive Matrix Factorisation
PMT	Photomultiplier Tube
POA	Primary Organic Aerosol
PSL	Polystyrene Latex spheres
PTR-MS	Proton Transfer Reaction Mass Spectrometer
RF	Radiative Forcing

RH	Relative Humidity
ROS	Reactive Oxygen Species
RSMS-II	Rapid Single Particle Mass Spectrometer II
SAF-MED	Secondary Aerosol Formation in the Mediterranean
SEM	Scanning Electron Microscopy
SMPS	Scanning Mobility Particle Sizer
SOA	Secondary Organic Aerosol
SODAR	Sonic Detection And Ranging
SPAMS	Single Particle Aerosol Mass Spectrometer
SSA	Sea Salt Aerosol
St	Stokes number
SV-OOA	Semi-volatile Oxidized Organic Aerosols
TEOM	Tapering Element Oscillating Microbalance
TEM	Transmission Electron Microscopy
TMA	Trimethylamine
TOF	Time-of-Flight
TOMS	Total Ozone Mapping Spectrometer
UF	Ultra Fine
ULCO-LPCA	Université du Littoral Côte d'Opale, Laboratoire de Physico-Chimie de l'Atmosphère
UTC	Coordinated Universal Time
VOC	Volatile Organic Compounds
WHO	World Health Organization
WSOC	Water Soluble Organic Carbon
XRF	X-ray Fluorescence

1. INTRODUCTION

CONTENTS

1.1 Aerosols 2

1.2 Sources and Chemical Composition of Aerosols 2

1.3 Particle Size and Formation 6

1.4 Effects of Atmospheric Aerosols 9

1.4.1 Climate Effects 9

1.4.2 Health Effects 12

1.4.3 Air Quality Legislation 14

1.5 Measurements of Aerosol Particles 14

1.5.1 Aerosol Mass Spectrometers 16

1.5.2 Single Particle Mass Spectrometry Studies 17

1.6 Overview 29

1.6.1 Aims of Research 29

1.6.2 Overview of Thesis 29

1.1 AEROSOLS

Particles, or particulate matter, may be solid or liquid and when suspended in a gas are defined as aerosols (Finlayson-Pitts & Pitts, 2000). Particles are usually considered as such when their diameters fall between ~ 0.002-100 µm. The lower end of the size range represents the approximate diameter at which a cluster of molecules becomes a particle, while particles larger than 100 µm (e.g. fine sand) are subject to rapid gravitational settling and therefore do not remain suspended for significant periods of time. The critical characteristics of a particle for evaluating its lifetime, optical properties, and toxicity are assumed to be its size, surface area, phase (solid or liquid), volatility, hygroscopicity, chemical composition, morphology and density (Saxe & Larsen, 2004; Buseck & Adachi, 2008). The following chapter will present a brief introduction to the sources, composition and physical properties of atmospheric aerosols, as well their effect on global climate and human health.

1.2 SOURCES AND CHEMICAL COMPOSITION OF AEROSOLS

Particles have natural and anthropogenic origins and are released directly into the atmosphere, as primary emissions, or are formed in the atmosphere as secondary aerosols by chemical processing e.g. gas to particle conversion, nucleation or condensation of species onto existing particles (Finlayson-Pitts & Pitts, 2000; Pöschl, 2005; Monks et al., 2009; Calvo et al., 2013). Aerosol composition can vary hugely depending on whether the location is marine or coastal, urban, industrial, rural, desert or polar. Table 1.1 provides a brief list of the main chemical components and major sources of ambient particulate matter (AQEG, 2005). Primary and secondary components have both natural and anthropogenic origins. Natural sources of atmospheric aerosols include biogenic emissions, mineral dust, sea spray, volcanic eruptions and lightning (Calvo et al., 2013).

Primary biogenic particles take the form of seeds, pollen, spores, bacteria, protozoa, fungi, viruses, algae, and fragments of animals and plants (Hobbs, 2000). Secondary biogenic particles form from oxidation of biogenic VOCs (e.g. isoprene) to form secondary organic aerosol (SOA) (Claeys et al., 2004; Hallquist et al., 2009; Froyd et al., 2010). Global biogenic VOCs emissions are estimated to be ~10 times larger than anthropogenic emissions, thus an important source of SOA. Carbonaceous components (EC and OC) are released from biomass burning by naturally occurring wildfires.

Table 1.1. Main components and major sources of particulate matter (adapted from AQEG, 2005).

Primary components	Major sources
Sodium chloride	Sea salt
Elemental carbon (EC) or Black carbon (BC)	Formed during high temperature combustion of fossil fuel (coal, natural gas, diesel and petrol) and biomass fuel (wood pellets, forest fires, etc.).
Trace metals	Present at very low concentrations, includes Pb, Cd, Ni, Cr, Zn and Mn. Generated by metallurgical process (e.g. steel-making), impurities or additives in industrial fuels, and mechanical abrasion process (e.g. brake and tyre wear).
Mineral components	Includes Al, Si, Fe and Ca. Found mostly in coarse dusts from quarrying, construction and demolition, and in wind-driven dusts.
Secondary components	**Major sources**
Sulfate	Formed by oxidation of atmospheric sulphur dioxide (SO_2) to form sulfuric acid, which can react with ammonia (NH_3) to produce ammonium sulfate.
Nitrate	Formed by oxidation of nitrogen oxides (NO_X, which consists of nitric oxide, NO, and nitrogen dioxide, NO_2), which can react with NH_3 to produce ammonium nitrate. Also present as sodium nitrate through replacement of chloride on sea salt by NO_X.
Water	Components such as ammonium sulfates and ammonium nitrates take up water from atmosphere.
Primary and secondary components	**Major sources**
Organic carbon (OC) (radiation absorbing fraction referred to as brown carbon)	Primary OC comes from traffic or industrial combustion. Secondary OC comes from oxidation of volatile organic compounds (VOCs). There may be several thousand individual components and OC is the most difficult ambient particle component to accurately identify and measure in real time.

Mineral dust is one of the largest contributors to global aerosol mass and is generated mainly by wind action on deserts, dry lake beds, semi-arid surfaces and other soils, with the Sahara producing most of the world's mineral dust (Calvo et al., 2013). For wind-blown particles to be injected into the atmosphere the wind has to be above a frictional speed, which is dependent on the size and contents of the particle (Hobbs, 2000). While the majority of dust mass is accounted for by supermicron particles, an estimated 7-20%

of dust particles are less than 1 μm in diameter, a size range important for human health effects. The composition of mineral dust particles reflects its origin and includes components like aluminium, calcium, silicates and iron in the form of quartz, clays, calcite, gypsum and iron oxides (Seinfeld & Pandis, 2006).

Primary marine aerosols, containing sodium, chloride, calcium, magnesium, potassium, sulfate and OC, are produced at the ocean's surface by bursting of air bubbles which have been entrained in the water by wind-induced wave action (O'Dowd et al., 1997; Finlayson-Pitts & Pitts, 2000). Secondary marine aerosols, primarily as non-sea-salt (nss) sulfate and OC, form by gas-to-particle conversions such as homogeneous nucleation, heterogeneous nucleation and condensation (O'Dowd et al., 1997). Marine OC emissions (driven by biological activity) are comparable (or higher) to fossil fuel OC emissions and increase the global OC burden by at least 20% (O'Dowd et al., 2008; Roelofs, 2007). Oxidation of dimethyl sulfide (DMS), produced by marine organisms (particularly phytoplankton), is the dominant source of SO_2 and the exclusive source of methanesulfonic acid (MSA) in the marine atmosphere (Seinfeld & Pandis, 2006). Both of these are important components in the formation of new particles (Wyslouzil et al., 1991a, 1991b), which can then act as cloud condensation nuclei (CCN) (O'Dowd et al., 1997; Ayers & Gillett, 2000) and have associated climate effects.

Volcanic eruptions are an important source of natural primary and secondary aerosols, although emissions are extremely difficult to predict due to the wide range in eruptive styles and magnitudes. Primary particles are emitted as ash, generally fall into the 1-10 μm size range, and are comprised of many components, including S, Si, Cl, Pb, Cr, Cu, Fe, Ti, V, Al, Ba, Mn, Zn, Ca, K and Na (Allard et al., 2000; Mather et al., 2003). Secondary particles are comprised mainly of sulfate, formed by the oxidation of the large quantities of SO_2 released by eruptions. Various studies suggest 14-36% of tropospheric secondary sulfate aerosol mass may be of volcanic origin (Calvo et al., 2013). Volcanoes are also thought to contribute 2% of naturally emitted mercury (Mason, 2009).

Naturally occurring secondary nitrate particles are formed partly from NO and NO_2 produced from lightning (Schumann & Huntrieser, 2007), while aerosols, through their effects on clouds, have been correlated with an increase in lightning flashes (Yuan et al., 2011).

Traffic, especially in urban areas, is considered the main source of primary and secondary anthropogenic aerosols, and the main source of NO_X (Seinfeld and Pandis, 2006).

Emissions from vehicle exhaust depends on the engine type, age and maintenance, and contain carbon in the form of OC and EC with smaller amounts of trace metals and ions (Pant & Harrison, 2013). Gasoline engines are known to release a higher fraction of OC while diesel engines emit more EC. Elemental markers such as Cu, Mn, Fe, Zn, Ba, Sn, Ni, Mo and Sb have been used for vehicular emissions. Metals can be emitted from various exhaust-related sources including fuel and lubricant combustion, catalytic converters, particulate filters and engine corrosion (Lough et al., 2005). However, many of these also arise from non-exhaust sources, such as brake and tyre wear, road surface abrasion and resuspension by moving vehicles (Calvo et al., 2013). Other sources of anthropogenic aerosols include industrial activities (metallurgy, shipping, incineration, refineries, etc.) and solid fuel combustion for power generation and domestic heating (wildfires and combustion of agricultural crop residues are included in the biomass burning category). Carbonaceous materials (EC and OC) are a major component of aerosol released from these activities. EC is indicative of primary emissions while OC can be both primary and secondary, with the contribution to the aerosol depending on the location, time of year and meteorological conditions (Zhang et al., 2011b; Guzman-Morales et al., 2014). For example, in Barcelona it was found that ~47 % of the OC was primary whereas at a rural site, downwind of the city, the OC was predominantly of secondary origin (~85 %) (Minguillón et al., 2011).

Industrial activities are often important point-source emitters of metals, e.g., Fe, Mn and Zn from a ferromanganese alloy facility (Choël et al., 2010), Fe, Zn, Ni and Pb from steelworks (Dall'Osto et al., 2008), V and Ni from shipping (Ault et al., 2009; Healy et al., 2009) and Pb and Zn from waste incineration (Moffet et al., 2008a). Industries producing cement, bricks and ceramics, mining and quarrying also release large amounts of primary aerosols, either during production or manipulation and transport of raw materials (Sánchez de la Campa et al., 2010). Crustal elements such as Si, Al, K, Na, Ca, Fe and their oxides are used as markers for mineral dust from mining, quarrying and building activities (excavations, soil movement, demolitions) (Calvo et al., 2013). Dust from these activities and resuspended road dust are important contributors to PM_{10} in dry environments like the Mediterranean, where low precipitation rates prolong the lifetime of these particles in the atmosphere (Rodríguez et al., 2007; Pey et al., 2009; Amato et al., 2009; Reche et al., 2011).

Anthropogenic activities also emit large quantities of SO_2 (coal combustion and shipping), NO_X (traffic) and ammonia (farming, traffic and industrial activities), which can lead to formation of secondary particles (Finlayson-Pitts and Pitts, 2000). SO_2 can be oxidised to form H_2SO_4, while NO_X can undergo oxidation to form HNO_3. These acidic species can be neutralised by ammonia to form ammonium sulfate and ammonium nitrate particles respectively. In the atmosphere the production of ammonium sulfate is favoured and most of the sulfate must be neutralised prior to ammonium nitrate production (Bauer et al., 2007; Pathak et al., 2009). While ammonia is the major base present in the atmosphere, amines have also been observed in particles as aminium salts of nitrate and sulfate (Pratt et al., 2009c). Amines can be emitted by industrial activities, traffic, farming and sewage plants (Angelino et al., 2001; Rehbein et al., 2011). In addition to the production of secondary species through the homogeneous gaseous reactions mentioned above, heterogeneous reactions may occur between gaseous species and particles, e.g., the reaction of gaseous HNO_3 with sea salt particles (Finlayson-Pitts and Pitts, 2000).

$$NaCl_{(S)} + HNO_{3(g)} \rightarrow HCl_{(g)} + NaNO_{3(s)}$$

Secondary species may also be formed through aqueous phase reactions in fogs, clouds and on particle surfaces (Finlayson-Pitts and Pitts, 2000).

1.3 PARTICLE SIZE AND FORMATION

Of the several properties of particles important for their role in atmospheric processes, size is considered the most important (Finlayson-Pitts & Pitts, 2000), as it is related to the sources of the particles and their effects on health and climate. Particle size is measured and expressed as an effective diameter (McMurry, 2000), which depends on a physical property of the particle. The use of an effective diameter is a result of the variability in the shape of atmospheric particles – diameter implies that the particle is spherical, which some atmospheric particles are, but many also have irregular shapes. The most commonly used effective diameter is the aerodynamic diameter (D_a), defined as the diameter of a sphere of unit density (1 g/cm^3) that has the same settling velocity in air as the particle under consideration (Finlayson-Pitts & Pitts, 2000). This diameter is particularly useful as it reflects the behaviour of particles in moving air, e.g., in the respiratory system, and is measured by instruments that sample particles through an orifice or restricted channel. Other effective diameters include mass-normalised diameter (that of a sphere with the same mass as the actual particle but a density of 1 g/cm^3), electrical-mobility diameter

(that of a sphere with the same migration velocity through an electric field as the actual particle), volume-equivalent diameter (for particles with complex, irregular shapes), geometric or physical diameter (that of a particle observed by a microscope) and optical diameter (obtained by detecting light scattered by a particle) (Buseck and Adachi, 2008).

Based on their diameter, particles are generally grouped into the ultrafine (< ~100 nm), fine (< 2.5 µm, or $PM_{2.5}$) or coarse (> 2.5 µm, or PM_{10}) fraction. The fine fraction is further separated into the nucleation, Aitken and accumulation modes. The size distributions (a schematic is shown in Figure 1.1) each have distinctive chemical and optical properties, transformation mechanisms, and deposition pathways and reflect the origins of the atmospheric aerosols (Finlayson-Pitts & Pitts, 2000; Seinfeld & Pandis, 2006).

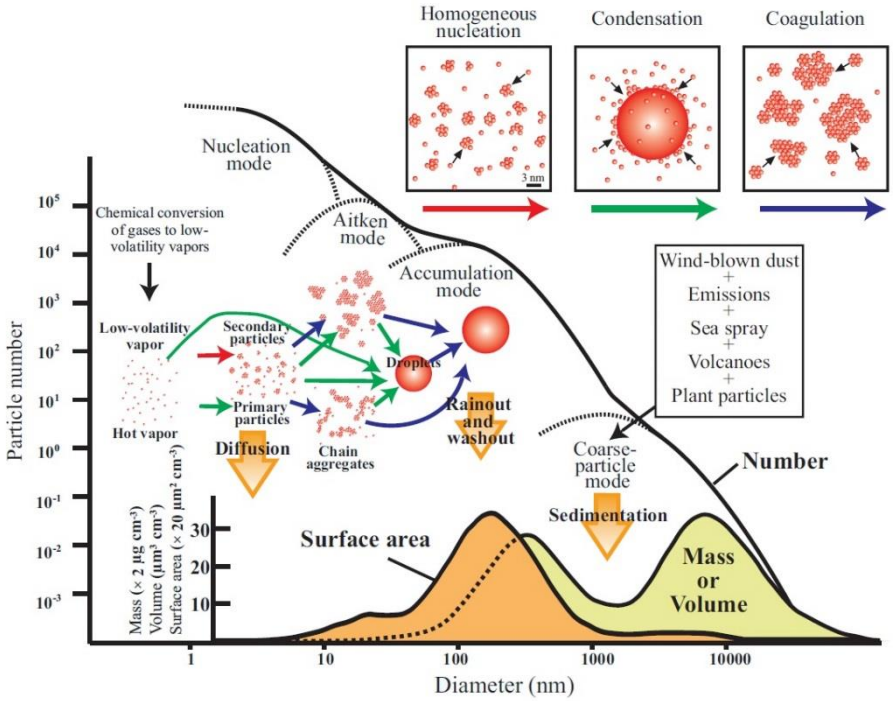


Figure 1.1. Schematic of the size distribution of atmospheric particles for various parameters (number, N; mass, M; volume, V; surface area, S) (Buseck & Adachi, 2008).

The fine fraction includes most of the total particle number and a large fraction of the mass, e.g., 30% in non-urban and 50% in urban areas (Finlayson-Pitts & Pitts, 2000; Seinfeld & Pandis, 2006). In comparison to the coarse fraction, fine particles have longer residence times in the atmosphere due to negligible dry deposition velocity, allowing them to be dispersed over greater distances (Kumar et al., 2010). They also have a larger surface to volume ratio, increasing their atmospheric reactivity (Nico et al., 2009) and their ability to absorb organic and inorganic compounds (Li et al., 2010), or bear free radicals on their surface (Samet et al., 2009). For legislative purposes, current particle

monitoring metrics are based on the mass-concentrations (mass/volume) of $PM_{2.5}$ or PM_{10}. However, emissions in terms of particle number are becoming more significant than those of particle mass (Rodríguez et al., 2007), particularly for vehicular traffic exhaust (Vu et al., 2015). Ultrafine particles do not contribute significantly to PM mass and are therefore not well accounted for by monitoring networks, despite their adverse effects on human health.

Nucleation mode particles are usually less than 10 nm in diameter and occur in the largest numbers of all the size modes. In the atmosphere, most nucleation-mode particles consist of sulfates, nitrates, and organic compounds (Buseck and Adachi, 2008). They form through gas-to-particle conversion of hot combustion vapour condensation and homogeneous nucleation of relatively non-volatile products of photochemically initiated atmospheric gas-phase reactions (Seinfeld & Pandis, 2006; Kulmala & Kerminen, 2008).

Formation of Aitken mode particles, in the range 10-80 nm, is similar to that of nucleation mode particles. Coagulation of the latter also contributes to formation of Aitken mode particles (Hobbs, 2000). Rapid coagulation of these particles with themselves (short lifetimes, sometimes only minutes), or more likely with larger particles, forms particles in the accumulation mode, in the range 100-2500 nm. The coagulation rates for particles in the nuclei range with the larger particles in the accumulation range are usually much larger than for self-coagulation of the small particles; this occurs because of the high mobility of the smaller particles combined with the larger target area of the bigger particles (Finlayson-Pitts & Pitts, 2000).

Accumulation mode particles include those produced from condensation of low-vapour-pressure gaseous species on Aitken nuclei (Seinfeld & Pandis, 2006), as well as particles remaining after cloud or fog droplets evaporate (Hobbs, 2000) This mode accounts for most of the aerosol surface area and a substantial fraction of the aerosol mass, and is so named because particle removal mechanisms are least efficient in this regime, causing particles to accumulate there (Seinfeld & Pandis, 2006).

Finally, coarse mode particles are usually produced by mechanical processes such as grinding, wind, or erosion and include sea salt and anthropogenic and natural dust. Particles in this mode have sufficiently large sedimentation velocities, so are removed from the atmosphere relatively quickly (residence time ~ 1 day) by gravitational settling, precipitation and impaction onto surfaces (depending on wind speed; Hussein et al.,

2006), although large scale transport mechanisms such as Saharan dust storms can transport them over long distances.

Figure 1.2 shows the size distribution of atmospheric aerosols from specific sources. Because of the nature of their sources, fine particles generally contain far more organics than the coarse particles (except biologically derived particles) as well as soluble inorganics such as NH_4^+, NO_3^-, and SO_4^{2-}.

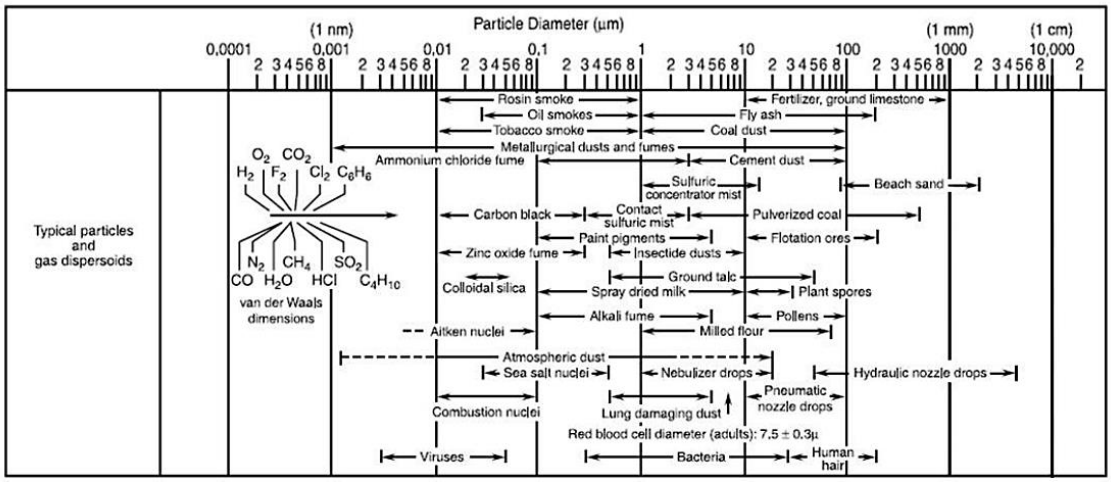


Figure 1.2. Size ranges of atmospheric aerosols from specific sources. Adapted from Finlayson-Pitts and Pitts (2000).

1.4 EFFECTS OF ATMOSPHERIC AEROSOLS

1.4.1 CLIMATE EFFECTS

The effects of aerosols on the Earth's climate are measured as radiative forcing, defined as "rate of energy change per unit area of the globe as measured at the top of the atmosphere". Radiative forcing due to aerosols can be positive or negative, depending on the chemical composition, physical and optical properties of the particles (Heald et al., 2014). Uncertainties for all of these are large, which is why aerosols are still the most uncertain drivers for global climate change (Myhre et al., 2013). Aerosols can have both direct and indirect effects on the climate, which the IPCC have estimated as -0.27 (-0.77 to 0.23) W/m^2 and -0.55 (-1.33 to -0.06) W/m^2 respectively (shown in Figure 1.3) (IPCC, 2013). Together these offset almost 50% of the positive radiative forcing due to CO_2, and 30% of that due to all greenhouse gases combined.

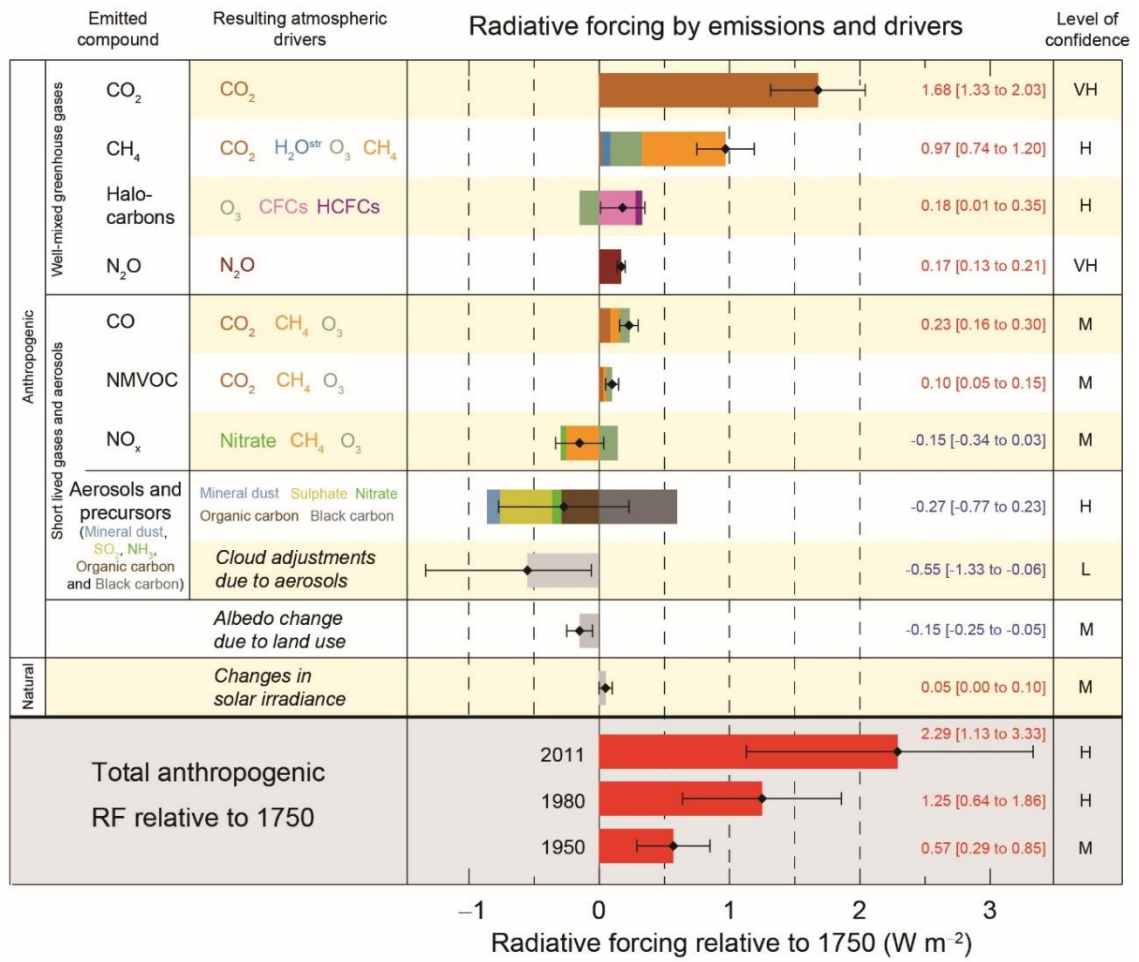


Figure 1.3. Radiative forcing estimates in 2011 relative to 1750 and aggregated uncertainties for the main drivers of climate change (IPCC, 2013).

Direct Effects

Figure 1.4 shows the radiative mechanisms associated with the direct and indirect effects of atmospheric aerosols on the climate. The direct effect refers to the ability of particles to scatter and absorb incoming solar radiation, as well as radiation emitted or reflected by the Earth's surface, thus affecting the planetary energy balance. Chemical composition, refractive indices of the components, size and shape all affect how much radiation particles scatter or absorb (Stier et al., 2007). Particles comprised of or containing sulfates and nitrates (particularly as a coating around a core) scatter incoming solar radiation, some of which returns to space, resulting in net cooling of the atmosphere. Sulfate, nitrate, dust, and primary and secondary organic aerosols are all estimated to contribute to negative radiative forcing of -0.4, -0.11, -0.1, -0.09 and -0.03 W/m^2 respectively (Myhre et al., 2013). BC aerosols absorb outgoing terrestrial radiation and have a positive radiative forcing effect (0.4 W/m^2), which is only slightly less than that of methane (0.48 W/m^2). Biomass burning emissions, where BC and organic aerosol offset each other, result in a negligible radiative forcing effect. Organic aerosol can also absorb radiation,

particularly that with ultraviolet wavelengths (Feng et al., 2013). This fraction of organic aerosol is often referred to as brown carbon and has been shown to directly absorb up to 50% of 405 nm solar radiation during periods associated with wildfire emissions (Healy et al., 2015).

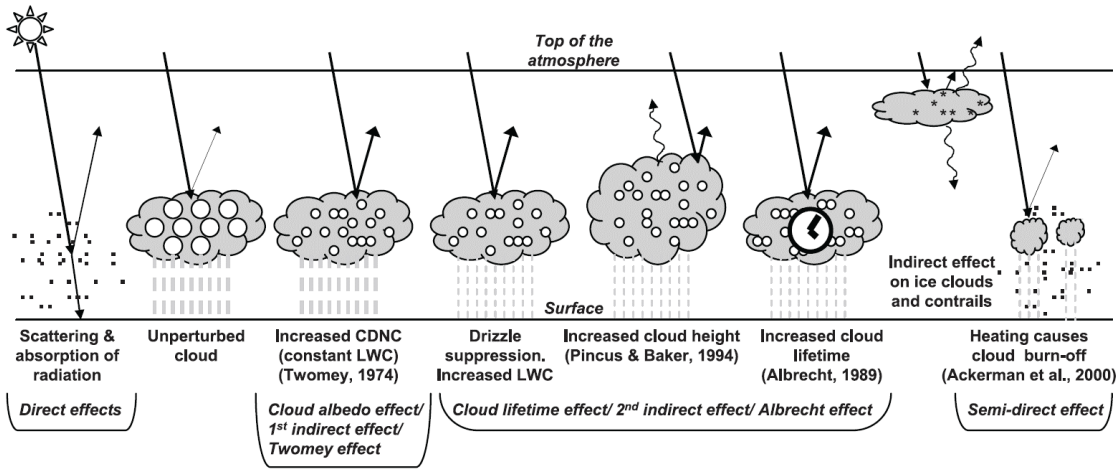


Figure 1.4. Schematic diagram showing various radiative mechanisms associated with direct and indirect effects of aerosols (IPCC, 2007). Small black dots represent aerosol particles, large circles represent cloud droplets and smaller circles represent cloud droplet number concentration (CDNC). Straight lines represent solar radiation, wavy lines represent terrestrial radiation and grey dashes represent rainfall. LWC refers to liquid water content.

Indirect effects

The indirect effect refers to the ability of particles to act as cloud condensation nuclei (CCN) or ice nuclei (IN) (Lohmann & Feichter, 2005), and is the largest uncertainty in global climate models (Figure 1.3). Part of this uncertainty stems from particle composition, which is highly variable and dependent on location, source and degree of atmospheric processing. Water can condense onto particles if they are hydrophilic enough, growing them into cloud droplets. Clouds can reflect or trap radiation depending on their altitude and type. Thick, low level clouds (stratus, cumulus or stratocumulus) reflect solar radiation whereas less dense high altitude clouds (cirrocumulus) transmit solar radiation and prevent radiation from the Earth's surface from leaving the atmosphere (Finlayson-Pitts and Pitts, 2000). Aerosols result in smaller, more numerous cloud particles which then reflect more solar radiation. Smaller cloud particles decrease precipitation efficiency, thus prolonging cloud lifetime, and delay the onset of freezing (Lohmann and Feichter, 2005). Absorption of solar radiation by particles (containing e.g. BC) may cause evaporation of cloud droplets (a semi-direct effect).

Aerosols can act as IN by coming into contact with supercooled cloud droplets (contact freezing) or by acting as deposition nuclei. Unlike CCN, ice nuclei are generally insoluble

particles; Murray et al. (2012) found that below -15 °C mineral dust and soot particles dominate ice nucleation. The most active IN (those nucleating ice at the highest sub-zero temperatures) discovered so far are of biological origin (bacteria, fungal spores, pollen, etc.) (Després et al., 2012).

1.4.2 Health Effects

The World Health Organization (WHO) considers clean air to be a basic requirement of human health and well-being. However, many epidemiological studies conducted around the world have demonstrated the role of atmospheric PM pollution in increased mortality and morbidity rates due to respiratory diseases such as asthma, chronic obstructive pulmonary disease, and bronchopulmonary cancers, as well as cardiovascular diseases (Dockery et al., 1993; Dockery & Pope III, 1994; Dockery, 2001; Pope III et al., 2002, 2004a, 2004b; Pöschl, 2005; Pope III & Dockery, 2006; Dockery, 2009). In addition, toxicological studies on human cells and animal models (Oberdörster et al., 2005) have provided solid evidence for the association of elevated atmospheric PM concentrations with both short-term and long-term health effects, including chronic respiratory and heart diseases, lung cancer, and damage to other organs (Ghio & Devlin, 2001; Schwarze et al., 2006). In 2013 the WHO International Agency for Research on Cancer (IARC) classified outdoor air pollution, and specifically particulate matter, as carcinogenic to humans (Loomis et al., 2013). An estimated 3.7 million premature deaths per year worldwide are thought to be due to PM_{10} exposure, with an estimated 223,000 deaths specifically from lung cancer (Loomis et al., 2013; Straif et al., 2013). Particle size and shape are critical factors controlling the extent to which airborne particles penetrate and interact with the human respiratory tract (Schwartz & Neas, 2000), while an increasing number of studies have found associations between particle number and adverse health effects (Zhang et al., 2009a; Atkinson et al., 2010; Niu et al., 2010; Oberdörster et al., 2010).

Figure 1.5 shows the extent to which particles in different size ranges penetrate the airways and lungs. Coarse fraction particles (> $PM_{2.5}$) generally deposit quickly in the mucus of the nose and upper respiratory tract, where cilia (small hair-like projections) move them into the gastrointestinal tract via swallowing (Finlayson-Pitts and Pitts, 2000). Particles less than 2.5 µm in diameter can reach the alveolar gas-exchange region of the lungs, where soluble components may be taken up into the bloodstream. This region does not have a protective mucus layer; instead macrophages (the immune system's scavengers) remove particles deposited on the lungs' surfaces. However, this removal

system is slower and can be overwhelmed by large particle numbers or by particle toxicity (Salvi & Holgate, 1999). Ultrafine particles are sufficiently small to undergo transfer across the epithelial cells and into the circulatory and lymphatic systems. Only ~20% of these particles are removed once deposited in the alveolar region, compared to 80% of particles larger than 500 nm (Oberdörster et al., 2005). Ultrafine particles induce more oxidative stress and a stronger pro-inflammatory response than larger particles, due to their large surface area. Composition also plays a role in particle toxicity, with acidic or toxic species, such as heavy metals or polycyclic aromatic compounds, thought to be the main sources of reactive oxygen species (ROS) and carcinogens (Harrison & Yin, 2000).

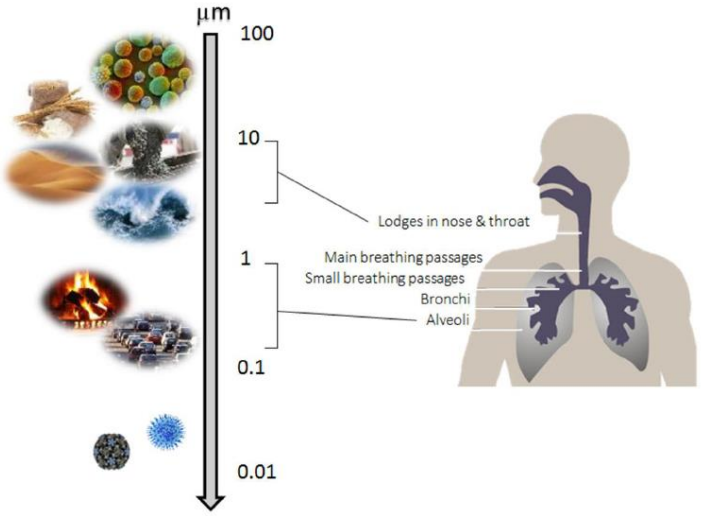


Figure 1.5. Extent to which particles in different size ranges penetrate into the airways and lungs.

ROS includes the superoxide radical anion ($\cdot O_2^-$), hydrogen peroxide (H_2O_2), and the hydroxyl radical ($\cdot OH$) (Halliwell & Cross, 1994; Halliwell & Whiteman, 2004). $\cdot OH$ is the most powerful and destructive ROS species in vivo, damaging DNA and cell membranes through lipid peroxidation (Halliwell & Cross, 1994). Among numerous particulate matter constituents, metals and quinoid compounds have been identified as major species that can catalyse the generation of ROS in cells (See et al., 2007; Shinyashiki et al., 2009). Most of the ROS activity in the organic fraction of diesel exhaust particles has been associated with quinone-like substances (Shinyashiki et al., 2009). Particles can form ROS in two ways after deposition into the lungs; through chemical reactions of redox-active components in the particles and through biological responses to the particles (Ma et al., 2015b). Ionisable metals mediate the formation of ROS through catalysing Fenton type reactions, whereas quinoid compounds can serve as catalysts to transport electrons from biological reducing equivalents like nicotinamide

adenine dinucleotide phosphate (NADPH) or ascorbate in cells to dissolved O_2 and lead to continuous production of $\cdot O_2^-$ and H_2O_2 (Tao et al., 2003).

1.4.3 Air Quality Legislation

The WHO has provided guideline targets for both PM_{10} and $PM_{2.5}$ mass. Annual mean and 24-hour mean mass values are included in order to take into account long term and short term exposure effects. For $PM_{2.5}$ the annual mean target is 10 $\mu g/m^3$, with a 24-hour mean of 25 $\mu g/m^3$. The PM_{10} targets are 20 $\mu g/m^3$ and 50 $\mu g/m^3$ for the annual and 24-hour mean respectively (WHO, 2006). In Europe the EU Clean Air for Europe directive (CAFE – Directive 2008/50/EC) sets limits for PM_{10} and $PM_{2.5}$ emissions; a 24-hour and annual mean of 50 $\mu g/m^3$ and 40 $\mu g/m^3$ for PM_{10} and an annual mean of 25 $\mu g/m^3$ for $PM_{2.5}$. Several studies have suggested that the exposure–response relationship between particulate pollution and mortality is essentially linear (WHO, 2006). In a linear relationship, increasing exposures are associated with increases in the frequency of effects. An important implication of this is the absence of a no-observable-effect level or limit value below which effects are not observed, meaning the effects of pollutants occur even at very low levels (WHO, 2006). Therefore, any standard or guideline value is unlikely to provide complete protection for every individual against all possible adverse health effects of particulate matter.

1.5 Measurements of Aerosol Particles

Reducing anthropogenic aerosol emissions is essential given that air pollution affects human health even at low levels. To facilitate this it is important to accurately identify and quantify the contribution from the many sources of aerosols, both natural and anthropogenic.

The chemical composition of atmospheric aerosols is classically analysed off-line, using particles collected on filters. The nature of this analysis depends on the species targeted. Elements can be identified using X-ray fluorescence (XRF), particle-induced X-ray emission (PIXE) and inductively coupled plasma mass spectrometry (ICP-MS) (Finlayson-Pitts and Pitts, 2000). Water soluble inorganic ions and organic carbon species (WSOC) can be quantified using ion chromatography (IC), infrared and Raman spectroscopy and also mass spectrometry (MS) (Finlayson-Pitts & Pitts, 2000; Heard, 2006). EC and OC can be measured and discriminated using thermal methods, digestion, extraction, and optical techniques (Watson et al., 2005). The large number of species

which constitute the OC fraction can be further distinguished by mass spectrometry, high-performance liquid chromatography (HPLC) and gas chromatography mass spectrometry (GC-MS) (Finlayson-Pitts & Pitts, 2000; Heard, 2006). Particles collected on filters using multi-stage impactors can be analysed gravimetrically, producing mass concentrations for different size ranges (depending on the number of impactor stages). The filters can also be analysed by scanning electron microscopy (SEM) or transmission electron microscopy (TEM) to investigate individual particle size and shape, while combination with energy dispersive X-ray (EDX) spectrometry can provide for identification of elements contained in the particles (Choël et al., 2006; Marris et al., 2012).

There are however several limitations to off-line measurements that catalysed the development of real-time on-line monitoring techniques. The trace nature of many analytes means a sufficient amount of material must be collected on the filters to pass the detection limits of the analytical techniques. This results in sampling times of several hours to days, therefore limiting the time resolution. High time resolution is particularly desirable when studying point sources such as ships or an industrial facility, which may emit large amounts of aerosol over hours or even minutes. Filter measurements are also subject to several sampling artefacts. Semi-volatile species may evaporate, collected particles may react with other particles or gases on the filter in the time between sampling and analysis and quartz filters can adsorb organic gases altering the OC fragments measured using GC-MS (Finlayson-Pitts & Pitts, 2000; Heard, 2006; Prather et al., 2008). Particle bouncing, interstage particle losses and deposition onto impaction walls are significant artefacts for multi-stage impactors (Sanderson et al., 2014). Some analytical methods also require time-consuming sample preparation and analysis steps (Riffault et al., 2015).

Online measurements of particle number and mass concentration can be made quickly and relatively simply with a scanning mobility particle sizer (SMPS) or optical particle sizer/counter (OPS/OPC) and a tapered element oscillating microbalance (TEOM). Several ionic species can be measured with an hourly resolution by coupling a Particle into Liquid Sampler (PILS) with ion chromatography (Heard, 2006), while EC can be monitored using optical instruments (EC is then referred to a Black Carbon, BC) such as multiangle absorption photometer (MAAP) or an aethalometer.

1.5.1 AEROSOL MASS SPECTROMETERS

The deployment of mass spectrometers in field measurements has become more common over the last decade, as they provide the average chemical composition or mixing state of individual particles in real time and have been instrumental in source identification and apportionment (Prather et al., 2008; Healy et al., 2010; Pratt & Prather, 2012). The fundamental principle of an aerosol mass spectrometer is to sample airborne particles, vaporize and ionize them, and then analyse them using mass spectrometry. A number of aerosol mass spectrometers have been developed including the Aerosol Time of Flight Mass Spectrometer (ATOFMS) (Prather et al., 1994; Gard et al., 1997), Aerosol Mass Spectrometer (Aerodyne AMS) (Jayne et al., 2000a, 2000b; Zhang et al., 2011b), Laser Mass Analysis of Particles in the Airborne State (LAMPAS) (Hinz et al., 1994), Particle Analysis by Laser Mass Spectrometer (PALMS) (Murphy & Thomson, 1995; Thomson et al., 2000), Rapid Single Particle Mass Spectrometer II (RSMS-II) (Phares et al., 2002) and Single Particle Aerosol Mass Spectrometer (SPAMS) (Fergenson et al., 2004; Martin et al., 2007a). Overviews of these instruments are provided elsewhere (Sullivan & Prather, 2005; Pratt & Prather, 2012) and the co-location of PALMS, ATOFMS, RSMS-II and AMS in Atlanta has been compared by (Middlebrook et al., 2003). The AMS and single particle mass spectrometers such as the ATOFMS operate using different principles. The AMS utilises thermal desorption, electron impact ionisation and quadrupole time-of-flight mass spectrometry to quantify nitrate, sulfate, ammonium, chloride and organics in the range 50-700 nm (D_a) but is unable to measure the refractory portion (EC, sea salt, metals) of atmospheric aerosol (Heard, 2006). The ATOFMS uses triggered laser desorption/ionisation and time-of-flight mass spectrometry to provide composition (EC, OC, metals, sea salt, inorganic species, etc.) of individual particles in the range 100-3000 nm (D_a, and size range varies for the type of single particle mass spectrometer used). Measurements of individual particle composition can determine the aerosol's internal mixing states (species in the same particle) and external mixing state (mixture of single particles comprising the bulk aerosol). However, inconsistent ionisation of a particle's components results in this information only being qualitative.

1.5.2 Single Particle Mass Spectrometry Studies

Single particle mass spectrometers have been deployed during many field measurement campaigns in various environments and also employed for lab-based measurements; the data has been reviewed in detail recently by Pratt and Prather (2012), Cai et al. (2015) and Li et al. (2015). A catalogue of "fingerprint" spectra for particles emitted from specific sources and subjected to different types of atmospheric processing has been established and is the basis for particle type and source identification in this work. An important application of single-particle data is source apportionment of ambient aerosol. If a unique particle composition signature can be linked with a specific particulate matter source, then a number concentration measurement of that particle composition will provide an estimate of the ambient mass concentration arising from the corresponding source. However, a single source may release a variety of types of particles, some of which may be common to a number of other sources, so independent apportionment of every single particle to a distinct source may not always be possible (Tan et al., 2002b). A list of key marker ions used to link single particle mass spectra to specific sources is given in Table 1.2.

A wide variety of particle sources have been identified and characterised by single particle mass spectrometers and include sea salt, mineral dust, vehicle exhaust, solid fuel combustion (coal and wood), shipping and various industrial emissions (Bhave et al., 2001, 2002b; Liu et al., 2003; Beddows et al., 2004; Spencer et al., 2008; Tao et al., 2011; Giorio et al., 2012; Harrison et al., 2012).

Table 1.2. Marker ions used to identify particle types by single particle mass spectrometry.

Source Category	Identifying Ions	References
Sea salt	$^{23}[Na]^+$, $^{46}[Na_2]^+$, $^{62}[Na_2O]^+$, $^{63}[Na_2OH]^+$, $^{81,83}[Na_2Cl]^+$, $^{108}[Na_2NO_3]^+$, $^{165}[Na_3SO_4]^+$, $^{24}[Mg]^+$, $^{39,41}[K]^+$, $^{35,37}[Cl]^-$, $^{58,60}[NaCl]^-$, $^{93,95}[NaCl_2]^-$, $^{16}[O]^-$,$^{17}[OH]^-$	(Noble & Prather, 1997; Gard et al., 1998a; Hughes et al., 1999; Dall'Osto et al., 2004)
Dust	$^{23}[Na]^+$, $^{24}[Mg]^+$, $^{27}[Al]^+$, $^{39,41}[K]^+$, $^{40}[Ca]^+$, $^{54,56}[Fe]^+$, $^{48}[Ti]^+$, $^{64}[TiO]^+$, $^{16}[O]^-$,$^{17}[OH]^-$, $^{43}[AlO]^-$, $^{59}[AlO_2]^-$, $^{60}[SiO_2]^-$, $^{76}[SiO_3]^-$, $^{77}[HSiO_3]^-$, $^{103}[AlSiO_3]^-$	(Silva et al., 2000; Guazzotti et al., 2001a; Dall'Osto et al., 2004; Creamean et al., 2014)
Traffic	$^{12,24,36,..}[C_n]^+$, $^{12,24,36,..}[C_n]^-$, $^{40}[Ca]^+$, $^{56}[CaO]^+$, $^{57}[CaOH]^+$, $^{96}[Ca_2O]^+$, $^{63}[PO_2]^-$, $^{79}[PO_3]^-$, $^{95}[PO_4]^-$	(Silva and Prather, 1997; Gross et al., 2000; Song et al., 2001; Suess and Prather, 2002; Gross et al., 2005; Sodeman, Toner and Prather, 2005; Toner, Sodeman and Prather, 2006; Toner et al., 2008; Jeong et al., 2015)
Coal combustion	$^{12,24,36,..}[C_n]^+$, $[^{12,24,36,..}C_n]^-$, $^{27}[C_2H_3]^+$, $^{39,41}[K]^+$, $^{97}[HSO_4]^-$	(Guazzotti et al., 2003; Healy et al., 2010; Furutani et al., 2011; Wang et al., 2013)
Biomass burning (wood, corn kernels, rice & corn straw)	$^{39,41}[K]^+$, $^{113,115}[K_2Cl]^+$, $^{213,215}[K_3SO_4]^+$, $^{26}[CN]^-$, $^{42}[CNO]^-$, $^{45}[CHO_2]^-$, $^{59}[C_2H_3O_2]^-$, $^{71}[C_3H_3O_2]^-$, $^{12,24,36,..}[C_n]^+$, $^{12,24,36,..}[C_n]^-$	(Silva et al., 1999; Qin & Prather, 2006; Pagels et al., 2013; Huo et al., 2015)
Organic carbon (primary & secondary)	$^{27}[C_2H_3]^+$, $^{43}[C_3H_7]^+$/$^{43}[C_2H_3O]^+$/ $^{43}[CHNO]^+$, $^{51}[C_4H_3]^+$, $^{63}[C_5H_3]^+$, $^{77}[C_6H_5]^+$	(Silva & Prather, 2000; McGuire et al., 2011; Healy et al., 2013)
Ship exhaust	$^{51}[V]^+$, $^{67}[VO]^+$, $^{56}[Fe]^+$, $^{58}[Ni]^+$, $^{97}[HSO_4]$, $^{12,24,36,..}[C_n]^+$, $[^{12,24,36,..}C_n]^-$	(Ault et al., 2009; Healy et al., 2009; Ault et al., 2010)
Industrial activities (steel-making, waste incineration, power generation, etc.)	$^{27}[Al]^+$, $^{39,41}[K]^+$, $^{40}[Ca]^+$, $^{51}[V]^+$, $^{52,53}[Cr]^+$, $^{54,56}[Fe]^+$, $^{55}[Mn]^+$, $^{63,65}[Cu]^+$, $^{64,66,68}[Zn]^+$, $^{208}[Pb]^+$, $^{35,37}[Cl]^-$	(Pekney et al., 2006; Murphy et al., 2007; Reinard et al., 2007; Dall'Osto et al., 2008; Snyder et al., 2009; Taiwo et al., 2014b),
Biological	$^{39,41}[K]^+$, $^{26}[CN]^-$, $^{42}[CNO]^-$, $^{63}[PO_2]^-$, $^{79}[PO_3]^-$, $^{95}[PO_4]^-$	(Sinha et al., 1984; Gieray et al., 1997; Steele et al., 2003; Fergenson et al., 2004; Tobias et al., 2005; Pratt et al., 2009a; Gaston et al., 2013)
Amines	$^{18}[NH_4]^+$, $^{30}[CH_4N]^+$, $^{46}[(CH_3)_2NH_2]^+$, $^{59}[C_3H_9N]^+$, $^{74}[(C_2H_5)_2NH_2]^+$, $^{86}[(C_2H_5)_2NCH_2]^+$/$[C_3H_7NHC_2H_4]^+$, $^{101}[(C_2H_5)_3N]^+$, $^{102}[(C_3H_7)_2NH_2]^+$, $^{114}[(C_3H_7)_2NCH_2]^+$, $^{143}[(C_3H_7)_3N]^+$	(Angelino et al., 2001; McGuire et al., 2011; Healy et al., 2014)
Cigarettes	Nicotine (*m/z* 84, 161, 163), $^{39,41}[K]^+$, $^{26}[CN]^-$, $^{42}[CNO]^-$, $^{35,37}[Cl]^-$, $^{59}[C_2H_3O_2]^-$	(Dall'Osto et al., 2007; Li et al., 2012)
Fireworks	$^{23}[Na]^+$, $^{24}[Mg]^+$, $^{27}[Al]^+$, $^{39,41}[K]^+$, $^{138}[Ba]^+$, $^{155}[BaOH]^+$, $^{147}[KNO_3NO_2]^-$, $^{163}[K(NO_3)_2]^-$, $^{208}[Pb]^+$	(Liu et al., 1997; McGuire et al., 2011)
Secondary inorganic (indicative of atmospheric processing/ageing)	$^{30}[NO]^+$, $^{46}[NO_2]^-$, $^{62}[NO_3]^-$, $^{89}[(COO)_2H]^-$, $^{97}[HSO_4]^-$, $^{125}[H(NO_3)_2]^-$, $^{195}[H(HSO_4)_2]^-$,	(Liu et al., 2000; Moffet et al., 2008b; Pratt et al., 2009c; Aggarwal & Kawamura, 2009; Yao et al., 2011)

Marine and Biological Aerosols

Atmospheric sea salt particles have been characterised by the presence of Na, Cl and NaCl adduct ions (Noble & Prather, 1997; Hughes et al., 1999; Dall'Osto et al., 2004; Freney et al., 2006); fresh emissions can be distinguished from those which have undergone chlorine loss through heterogeneous reactions between sea salt and nitrate by the lack of a sodium nitrate ion, $Na_2NO_3^+$ and by the presence of $NaCl_2^-$ ions (Gard et al., 1998a; Guazzotti et al., 2001a). The extent of this Cl replacement can be tracked by monitoring the relative signal intensities of Na_2Cl^+ and $NaCl_2^-$ ions (Gard et al., 1998a; Guazzotti et al., 2001a). Bromine and iodine have also been found internally mixed with sea salt (Murphy et al., 1997; Middlebrook et al., 1998) and to be depleted in particles with increasing sodium sulfate content and time spent in the marine atmosphere (Murphy et al., 1997).

Recently, Prather et al. (2013) and Collins et al. (2014) studied the size-resolved chemical composition of single particles produced by an enclosed ocean-atmosphere wave channel equipped with breaking waves and natural seawater. The sea salt aerosol production method was found to influence the chemical composition, size and shape of the particles. Examination of mass spectra of single sea salt particles reacted with nitric acid found a redistribution of Na^+, Mg^+, K^+ and Ca^+ in the core and on the surface of the particles and an enhanced organic coating, which has implications for modelling of how sea salt particles undergo reactions and take up water (Ault et al., 2013). A simulation of a phytoplankton bloom found that particles became enriched with organic species and the amount of organic residue around the inorganic cores of the particles increased as the bloom progressed (Lee et al., 2015). Analysis of single cyanobacteria and algal cells by an ATOFMS (Cahill et al., 2015a) equipped to transmit particles between 1 and 10 µm generated complex mass spectra, with many ion peaks unidentified by the authors. It was possible to measure the metabolic differences in the cells under environmental stress (varying nitrogen conditions) by monitoring the peak for a chloroplast membrane lipid.

A type of Mg-rich particle was found only in biologically productive seawater based on simultaneous single particle, dimethyl sulfide (DMS) and chlorophyll measurements in three different marine environments (Gaston et al., 2011), and was also found by (Dall'Osto et al., 2005) at a coastal Atlantic site. Biogenic marine emissions can also be identified based on the presence of methanesulfonate and elemental sulfur (Gaston et al., 2010, 2015).

Primary biological particles, such as bacterial spores, have been measured with single particle instruments (Sinha et al., 1984; Gieray et al., 1997; Steele et al., 2003; Fergenson et al., 2004; Tobias et al., 2005; Gaston et al., 2013) and can produce unique markers. However these instruments usually only measure the $PM_{2.5}$ fraction, while most primary biological particles are in the coarse fraction. An aerodynamic lens for transmission of particles up to 10 µm has recently been developed for the ATOFMS (Cahill et al., 2014) but has yet to be applied to biological particles outside the marine environment (Cahill et al., 2015a). Particles identified as biological in origin and characterised by calcium, sodium, organic carbon, organic nitrogen and phosphate were identified by ATOFMS in the 33% of residues of evaporated ice crystals sampled from an aircraft (Pratt et al., 2009b), but the types of biological particle could not be distinguished. Secondary biogenic aerosols, in the form of organosulfates from the reaction of isoprene (a significant source of SOA) photo-oxidation products with sulfate particles, have been studied using single particle mass spectrometers; organosulfates were found in at least 65% of submicron particles from a range of different sources (Hatch et al., 2011), and one organosulfate was determined as one of the most abundant single organic compounds in atmospheric aerosol (Froyd et al., 2010).

Dust

Mineral and soil dust particles observed by single particle mass spectrometers typically contain Al, Fe, Ca, K, Mg, Na, aluminium oxides, silicates, aluminosilicates and phosphates (Silva et al., 2000; Guazzotti et al., 2001b; Sullivan et al., 2007) and are usually larger than 1 µm, although submicron dust has also been detected (Bates et al., 2004; Dall'Osto & Harrison, 2006). Two dust particle types are often observed – one rich in calcium, the other rich in aluminium and silicon (Guazzotti et al., 2001a; Dall'Osto et al., 2004; Dall'Osto & Harrison, 2006; Moffet et al., 2008b; Furutani et al., 2011). Ca-rich dust was thought to be locally produced and Al/Si-rich dust identified as Saharan at a coastal Atlantic site (Dall'Osto et al., 2004). Freney et al. (2006) identified $CaSO_4$ (gypsum) particles as arising from construction which took place at their sampling site, as well as a Al/Fe/Li dust type which appeared to originate from nearby rock-salting and gritting of roads. Titanium, lead, manganese, lithium and zirconium have also been found in dust particles (Silva et al., 2000; Guazzotti et al., 2001a; Dall'Osto et al., 2004; Ma et al., 2015a). Particles identified as vegetative debris can appear similar to those from biomass burning due to a strong signal from potassium and the presence of organic

nitrogen ions, so size is a key element in distinguishing the two – vegetative debris particles should display a supermicron mode in their size distribution (Dall'Osto & Harrison, 2006). However, measurements of aerosol from grass mowing found plant debris particles containing potassium and organic nitrogen, with a peak aerodynamic diameter of 400 nm (Drewnick et al., 2008), similar to that of biomass burning particles. Potassium-rich particles have also been attributed to fly ash from coal combustion (Rijkenberg et al., 2008; Herich et al., 2008; Furutani et al., 2011) and were distinguished from biomass burning emissions by the presence of lithium and silicates. Dust can also be generated from tyre wear; particles generated in the laboratory were characterised by potassium, exo-sulfur aromatics and possible rubber copolymer components, but when compared with particles from road dust samples, only 4% could be identified as tyre wear (Dall'Osto et al., 2014). This suggested that a rotating tyre on a real road surface creates particles internally mixed with minerals from the road surface (Ca, Fe, Al, Ti). Dust particle occurrence is sensitive to wind speed, as it is an important factor is suspending and transporting crustal materials (Guazzotti et al., 2001b).

Ship-based ATOFMS measurements carried out during the ACE-Asia campaign found that the chemical composition of dust influences the uptake of secondary species with aluminosilicate and iron rich dust associated with sulfate while calcium rich dust was mixed with nitrate (Sullivan et al., 2007). A similar observation was made at Mace Head, Ireland (Dall'Osto et al., 2004) and in Athens (Dall'Osto & Harrison, 2006). Analysis of samples collected in the Sahara and ambient measurements performed in Cape Verde and Ireland showed that fresh particles contained no secondary species while ambient sample data obtained in Cape Verde included nitrate signals; particles sampled in Ireland contained nitrate, sulfate and methanesulfonate (Dall'Osto et al., 2010). Asian dust from the Gobi desert detected in Gosan, South Korea showed evidence of atmospheric aging by heterogeneous chemistry, as those particles were richer in nitrate, while Saharan dust detected in Puerto Rico was cloud processed, as the particles were richer in sulfate and oxalate (Fitzgerald et al., 2015).

Combustion Aerosols

Carbonaceous aerosol, comprised of EC and OC, has been detected in many single particle mass spectrometry measurements (Whiteaker et al., 2002; Dall'Osto et al., 2004; Ferge et al., 2006; Cozic et al., 2008; Eatough et al., 2008; Moffet & Prather, 2009; Bahadur et al., 2010; Dall'Osto & Harrison, 2012; Healy et al., 2012b; Qin et al., 2012;

Yang et al., 2012; Healy et al., 2013; Bi et al., 2015) and attributed to a variety of combustion sources such as traffic, domestic fuel combustion and industrial processes. Locally produced EC (mostly fossil fuel and biomass combustion) was found to contribute 79% of the total EC mass measured during winter in Paris (Healy et al., 2012b), while the remaining 21% originated from continental transport. While EC is found in primary emissions, OC has been attributed to both primary and secondary organic aerosol in single particle datasets. OC attributed to aged carbonaceous aerosol or SOA were measured in Mexico City (Moffet et al., 2008b), and California (Qin et al., 2012); it was also seen in fresh and aged combustion particles in ambient and laboratory measurements in Cork (Healy et al., 2010). Furthermore EC and OC have been found mixed in particles in a process which has been attributed to OC condensing on EC particle types (Liu et al., 2003; Moffet et al., 2008b; Qin et al., 2012).

Single particle mass spectrometers have identified markers capable of distinguishing emissions from combustion of different solid fuel types, from both ambient and controlled combustion experiments. Coal and wood are the most commonly combusted fuels for domestic space heating and readily distinguished by EC, sulfate and frequently lithium containing particles produced by coal burning (Guazzotti et al., 2003; Healy et al., 2010; Furutani et al., 2011; Wang et al., 2013) and potassium-rich particles produced by wood/biomass burning (Silva et al., 1999; Qin & Prather, 2006; Friedman et al., 2009; Bahadur et al., 2010; Pratt et al., 2010; Bi et al., 2011; Lea-Langton et al., 2015; Zhai et al., 2015). Wildfires, by their nature, are also an abundant source of biomass burning particles (Mühle et al., 2007). Controlled combustion experiments of wood have shown that combustion temperature, addition of fuel and air supply influence the prevalence of OC components, with low combustion temperatures and oxygen concentration resulting in the largest number of particles with strong OC markers (Pagels et al., 2013). Other biomass fuels have also been combusted; rice and corn straw (major source of biomass burning emissions in China) combustion particles were very similar in core composition to those from wood combustion (Huo et al., 2015), while particles from combustion of dried corn kernels could be distinguished from wood burning emissions by strong phosphate signals (Pagels et al., 2013). However this composition is similar to that of vegetative debris particles, so size and sampling location are key identifying factors.

Polycyclic aromatic hydrocarbons (PAHs) have been observed in several ATOFMS studies. PAHs present spectra with a broad number of signals associated with high

molecular weight carbonaceous fragments, and are of particular interest due to their often carcinogenic health effects. PAHs have been associated with traffic emissions in measurements undertaken in a road tunnel in California (Gross et al., 2000, 2005), in biodiesel and ethanol-gasoline combustion emissions (Dutcher et al., 2011a, 2011b), and as SOA formed from photochemical processing of VOCs emitted by traffic (Dall'Osto & Harrison, 2012). PAHs in ambient SOA have been found enhanced during the summer when aerosol was more photochemically aged and contained more sulfate (Denkenberger et al., 2007). The formation of PAHs through photolysis in SOA as well as their oxidation by chlorine or photolysis to form SOA has been studied in chamber experiments (Gross et al., 2006; Healy et al., 2012a; Riva et al., 2015). High molecular weight OC fragments have been associated with potassium and levoglucosan fragments; combined these were indicative of aged biomass burning emissions (Qin & Prather, 2006). PAHs have been measured at an industrial site and associated with steel-mill activity (Dall'Osto et al., 2012b) and also in soot samples from an incineration facility, where PAHs were enriched in soot sampled from an oxygen-lean part of the process and absent in soot sampled from a process with higher oxygen concentrations (Zimmermann et al., 2003).

Traffic Emissions

Traffic-related emissions present a unique combination calcium, phosphate and EC in single particles in the range 100-300 nm (Silva & Prather, 1997; Gross et al., 2000; Song et al., 2001; Suess & Prather, 2002; Gross et al., 2005; Sodeman et al., 2005; Toner et al., 2006; Shields et al., 2007; Toner et al., 2008; Jeong et al., 2015). Traffic particles have also been observed to contain OC fragments (Pastor et al., 2003; Spencer et al., 2006). These carbonaceous particle types are evident in many datasets due to the clear diurnal (rush hour) profile presented by the emissions. Vehicle exhaust of biodiesel and ethanol-gasoline combustion has also been studied (Dutcher et al., 2011a, 2011b). A systemic reduction in sulfate and EC and an increase in lubricating oil species (calcium, phosphate, zinc) was found as a function of gasoline dilution with ethanol; the latter was an indication of a proportional increase as the products of incomplete combustion were reduced. Concentrations of particle bound PAHs also decreased noticeably based on ATOFMS and supporting measurements. A similar reduction in sulfate signal was found for biodiesel content. Neither fuel mixtures produced markers unique enough to identify their emissions in atmospheric aerosol.

Industrial Aerosols

Single particle mass spectrometry characterisation of industrial particles is discussed in Chapter 3, as part of a review of fine and ultrafine particles in the vicinity of industrial activities (Riffault et al., 2015). Briefly, industrial particles are distinguished largely by metallic species, such as Fe, Pb, Zn, V and Mn. Particles containing vanadium, iron, nickel and sulfate have been attributed to heavy oil combustion by sources such as oil refineries or shipping (Lake et al., 2004; Ault et al., 2009; Healy et al., 2009; Ault et al., 2010; Furutani et al., 2011; de Foy et al., 2012; Gaston et al., 2013). Fe-rich particles, also containing Pb, K, Zn, V, Ca and Cr depending on the study, have been frequently associated with steel-making (Pekney et al., 2006; Murphy et al., 2007; Reinard et al., 2007; Dall'Osto et al., 2008; Herich et al., 2009; Snyder et al., 2009; Zhang et al., 2009b; Furutani et al., 2011; Corbin et al., 2012; Taiwo et al., 2014b), as well as coal-fired power generation when the particles also contained La and Ce (Reinard et al., 2007). Pb-rich particles have been associated with Pb and Zn smelters (Snyder et al., 2009),waste incineration when they also contain Zn and chloride (Moffet et al., 2008a) and welding or construction when they also contained Cr (Dall'Osto & Harrison, 2006). K-rich particles also rich in chloride can originate from steel-making (Dall'Osto et al., 2008; Taiwo et al., 2014b) or coal combustion (Bein et al., 2006, 2007; Zhang et al., 2009b; Furutani et al., 2011).

Amines

Laboratory studies have been carried out to generate mass spectra for several amine species (Angelino et al., 2001), including trimethylamine, di- and triethylamine, and di- and tripropylamine, which were found to react with nitric and sulfuric acid to form aminium salts. Markers for alkylamines and oxidised amines were found in aged OC-containing particles in Riverside, California (Pratt et al., 2009c); the amines were in the form of aminium salts of nitrate or sulfate in the summer, while during the autumn, nitrate and sulfate were preferentially associated with ammonium. A higher fraction of aminium sulfate was also found compared to aminium nitrate due to the fact that sulfuric acid is a stronger acid than nitric acid. Alkylamines have been detected in ambient air by single particle mass spectrometers in a variety of locations, including California, USA (Denkenberger et al., 2007; Pratt et al., 2009c; Qin et al., 2012; Gaston et al., 2013), Ontario, Canada (Tan et al., 2002a; McGuire et al., 2011; Rehbein et al., 2011), Shanghai and Guangzhou, China (Huang et al., 2012; Zhang et al., 2012), Mexico City, Mexico

(Moffet et al., 2008b), Mace Head, Ireland (Dall'Osto et al., 2012a), Cork, Ireland (Healy et al., 2014), Paris, France (also during NANO-INDUS and ADRIMED/SAF-MED) (Healy et al., 2014) and Zurich, Switzerland (Healy et al., 2014). Trimethylamine was found to be the most abundant alkylamine present at European sites (Healy et al., 2014), as well as in Ontario and Shanghai. This is in contrast to alkylamine-containing particles in California, where an ion indicative of triethylamine/dipropylamine or diethylamine is routinely observed as the highest intensity alkylamine peak in ambient aerosol. Alkylamines have been associated with agricultural emissions, vehicle emissions, waste treatment and industrial activities (Healy et al., 2014) and were enriched in particles during periods of high relative humidity or fog events, with uptake onto existing particles that increased with increasing aerosol acidity (Rehbein et al., 2011).

Atmospheric Processing

Aerosol mixing states determined by single particle mass spectrometry can also be used to determine particle acidity and hygroscopicity. Mineral dust of different origins has been observed to preferentially accumulate nitrate or sulfate depending on its chemical composition, which affects its pH and hygroscopicity and therefore its ability to act as CCN (Sullivan et al., 2007; Dall'Osto et al., 2010). Combination of ATOFMS and hygroscopicity tandem differential mobility analyser (HTDMA) data has shown that sea salt and particles containing amines and nitrate are hydrophilic, while the more OC particles contain the more hydrophobic they are (Herich et al., 2009; Wang et al., 2014). Dust or ash particles with strong aluminium and silicate signals fell into the hydrophobic category. Biomass burning particles hygroscopicity varies depending on potassium and OC content; a larger potassium salt content resulted in more hydrophilic particles while those with more OC were more hydrophobic. The distribution and type of sulfate, nitrate and ammonium ions can be used to study gas-to-particle partitioning of nitric and sulfuric acid and the extent of neutralisation of atmospheric aerosol (Wang et al., 2009; Yao et al., 2011). However, the ionisation efficiency of these ions is not consistent and varies with matrix effects (Yao et al., 2011), so aerosol acidity studies by single particle aerosol mass spectrometry should generally be considered qualitative.

Many of the afore-mentioned studies observed particles that contained secondary species such as nitrate, sulfate and ammonium ions. Such signals have been identified in many different particle types and are indicative of the processing of the particles after emission (Hughes et al., 1999, 2000; Liu et al., 2000; Bhave et al., 2002a; Pastor et al., 2003; Moffet

et al., 2008c; Dall'Osto et al., 2009b; Pratt & Prather, 2009; Wang et al., 2009). In many ATOFMS datasets, fresh particles are distinguished from aged ones by the presence of these secondary species (Liu et al., 2003; Healy et al., 2010) and can also be helpful in identifying particles from local or transported sources (Healy et al., 2012b). Enhancement of nitrate on particles has been shown to closely correlated with high relative humidity and lower temperatures (Wang et al., 2009), usually at night or early morning, while it can be removed during the day when the photolysis rate (to increase nitrate destruction) and temperature (for nitrate product evaporation) increases (Dall'Osto et al., 2009b). Through the use of an aircraft-ATOFMS, altitude was found to play a role in secondary inorganic ion content (Pratt & Prather, 2010); the number fraction of ammonium and nitrate containing particles decreased with increasing altitude (1-7 km), likely due to the majority of NH_3 and NO_X sources being at the Earth's surface, while those containing sulfate were found mainly at higher altitudes, due to cloud processing with SO_2. Particle coatings of secondary species such as ammonium nitrate and ammonium sulfate have been found to decrease the ionisation efficiency of the ATOFMS (Hatch et al., 2014),while ionisation efficiency of ammonium and nitrate was also found to decrease with increasing particle diameter (0.32-1.8 μm range) (Bhave et al., 2002a). The authors presumed this to be due to a greater volume of smaller particles ablated/ionised relative to larger particles and a lower probability of positive-negative charge recombination in the ablation plume of small particles. These are important considerations when analysing and reporting single particle data, as they may lead to under-detection of particles containing these species. Recent studies have shown that single particle instruments, if they produce mass spectra by laser ablation, are capable of creating a 'depth profile' of the major chemical constituents of a particle's core and shell (Cahill et al., 2015b). Applying this approach to ambient particle coatings is problematic however as there is a priori knowledge of the instrument's sensitivity as a function of laser power for a particular matrix composition, which varies considerably for atmospheric aerosols.

Aqueous-phase reactions in fog or cloud droplets play an important role in transforming aerosol and can be studied using the marker hydroxymethanesulfonate (HMS). HMS was associated with carbonaceous (EC, OC) and secondary inorganic components (ammonium, nitrate and sulfate) during fog events in California and London (Whiteaker & Prather, 2003b; Dall'Osto et al., 2009c). The percentage of particles containing HMS reached a maximum late in the lifetime of the fog and decreased at times of elevated ozone concentrations (Whiteaker & Prather, 2003b). The size distribution of these

particles indicated those larger than 700 nm were most affected by the fog and associated high relative humidity (Whiteaker & Prather, 2003b; Dall'Osto et al., 2009c). Examining the presence of HMS in real-time showed that this transient species remained in the aerosol for a limited time of less than 12 hours.

Ice and Cloud Condensation Nuclei

The ATOFMS has been used to study insoluble ice and cloud droplet residues, indicators for the composition of CCN and IN. Dust, biogenic material (bacteria or vegetative debris) and organic carbon from biomass burning are dominant components of cloud droplet residues (Holecek et al., 2007; Ault et al., 2011; Creamean et al., 2013, 2014, 2015). The latter was thought to be water soluble species dissolved in the precipitation solution and resuspended independent of the potassium cores. During one study, sea salt was found to be mixed with dust, either internally through cloud processing or as a salt coating on the dust particle after being in solution (Holecek et al., 2007). Sea salt was also found mixed with EC, hypothesised to have coagulated in clouds and then acted as CCN. EC inclusion in a material with a high refractive index, such as sulfate or sodium chloride, can result in strong absorption of solar radiation (Holecek et al., 2007). Furutani et al. (2008) found a distinct relationship between atmospheric ageing (represented by the presence of ammonium, sulfate and nitrate) and CCN activity, with the most aged air masses showing the highest CCN activity and smallest activation diameters. Oxalic acid, the most abundant low molecular weight dicarboxylic acid in atmospheric aerosols, has a high water solubility resulting in it being very CCN active. In Shanghai, biomass burning was the dominant primary source of oxalic acid (Yang et al., 2009). Pacific shipboard measurements found a preferential enrichment of oxalic acid in mineral dust over carbonaceous particles (Sullivan & Prather, 2007), resulting from oxalic acid produced through photochemical oxidation of VOCs partitioning to the alkaline calcium rich dust particles.

At a high-alpine research station in the Swiss Alps mineral dust was the dominant contributor to ice residue, while sulfate and nitrate dominated the cloud droplet residues (Kamphus et al., 2010). A second study at the same site found an enrichment of EC particles in ice residues, which were always associated with organic carbon and often with potassium (Cozic et al., 2008). The ability of EC and biomass burning particles to act as IN appear to depend on the relative humidity and temperature of the freezing regime (Corbin et al., 2012).

Ultrafine Particles

Although the most commonly used single particle mass spectrometers, such as the ATOFMS, typically only measure particles larger than 100 nm, smaller particles for the study of CCN, new particle formation and traffic emissions have been detected with these instruments (Kane & Johnston, 2000; Kane et al., 2002; Phares et al., 2002, 2003; Su et al., 2005, 2006; Shields et al., 2008; Creamean et al., 2011; Zauscher et al., 2011). This requires the aid of particle concentrators to grow ultrafine particles to a detectable size by concentration or an aerodynamic lens designed for transmission of particles less than ~ 300 nm in diameter.

Miscellaneous

Single particle mass spectrometry has also been used to characterise tobacco smoke (Hinz et al., 1994; Dall'Osto et al., 2007; Li et al., 2012), pesticide residues (Whiteaker & Prather, 2003a), chemical warfare agent simulants (Martin et al., 2007a), explosives (Martin et al., 2007b) inhaler-delivered drugs (Morrical et al., 2015), fireworks (Liu et al., 1997; McGuire et al., 2011) and particulate mercury (Hall et al., 2006).

1.6 OVERVIEW

1.6.1 AIMS OF RESEARCH

The overall aims of this study can be summarised as follows:

- To deploy an Aerosol Time of Flight Mass Spectrometer (ATOFMS, model 3800) at an industrial location in Dunkirk, France and at a regional background location in Corsica, France as part of the NANO-INDUS and ADRIMED/SAF-MED field measurement campaigns respectively.
- To use the ATOFMS datasets to determine the size-resolved chemical composition of atmospheric single particles in the size range 100 to 3000 nm in real-time.
- Interpretation of the ATOFMS data to determine:
  - (i) To investigate the types of particles produced by local industrial point sources;
  - (ii) The influence of regional transport on particle composition at a regional background location;
  - (iii) To obtain reconstructed mass concentrations for ATOFMS particles and compare these with coincident quantitative measurements at both measurement locations.

1.6.2 OVERVIEW OF THESIS

Chapter 1 presents a brief introduction to the sources, composition, physical properties and effects of atmospheric aerosols. A brief literature review of previous field studies undertaken using single particle mass spectrometers is also provided.

Chapter 2 provides an overview of the operating principles for the ATOFMS and data analysis techniques used during the work described within this thesis.

Chapter 3 provides details of the ATOFMS deployment in Dunkirk, France during the NANO-INDUS campaign. The ATOFMS identified the particle types present at the site during the sampling period in the range 100 to 3000 nm.

Chapter 4 describes the deployment of the ATOFMS during the ADRIMED/SAF-MED field measurement campaigns in Corsica, France.

Chapter 5 presents a short summary of the work performed in this thesis and perspectives.

2. INSTRUMENTATION AND METHODOLOGY

CONTENTS

2.1 Aerosol Time-of-Flight Mass Spectrometer (ATOFMS) 31

2.1.1 Particle Sampling 32

2.1.2 Particle Sizing 32

2.1.3 Particle Ionisation 33

2.2 Data Analysis 34

2.2.1 Scaling and Mass Reconstruction 37

2.3 Negative Ion Sensitivity 44

2.4 HYSPLIT Back Trajectories 45

2.1 AEROSOL TIME-OF-FLIGHT MASS SPECTROMETER (ATOFMS)

The data collected during the NANO-INDUS and ADRIMED/SAF-MED field measurement campaigns was obtained by an aerosol time-of-flight mass spectrometer (ATOFMS), TSI model 3800, supplied by TSI Inc. Shoreview, MN, USA. The instrument was originally developed by Dr. K.A. Prather and co-workers from University of California, Riverside, USA (Nordmeyer & Prather, 1994; Prather et al., 1994; Gard et al., 1997) to measure the size and chemical composition of single particles with aerodynamic diameters between 100-3000 nm. The core composition of single particles, in the form of EC, OC, transition metals or sodium chloride, as well as secondary species such as nitrate and sulfate, can be determined by the ATOFMS. Interpretation of particle composition, temporal profiles, size distributions and other data, such as meteorological information, effectively allows the user to perform source apportionment, assigning particles to natural and anthropogenic sources (Healy et al., 2010).

A schematic diagram of the ATOFMS is shown in Figure 2.1. It consists of three main operating regions described in detail in the following sections. Aerosol is drawn in through the inlet and into the sampling region where a particle beam is generated. The particles travel into the sizing region where they are detected by two lasers (λ=532 nm) to determine the particles aerodynamic diameter. The particle then enters the mass spectrometer region and is hit by a pulsed ultraviolet laser (λ=266 nm) to produce gaseous ions which enter the time-of-flight mass spectrometers to yield a positive and negative ion mass spectrum of the single particle.

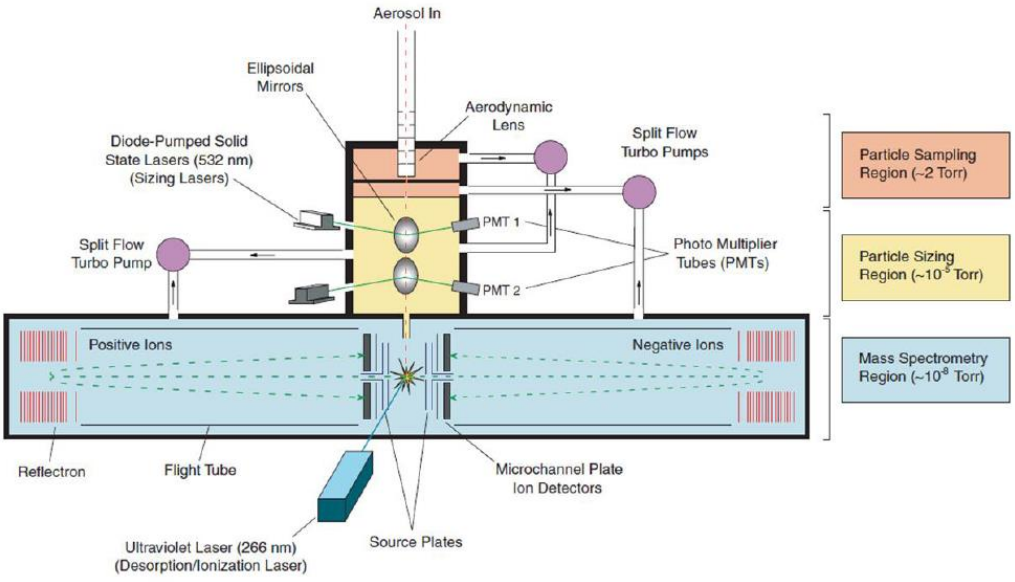


Figure 2.1. Schematic of the aerosol time-of-flight mass spectrometer (ATOFMS) (TSI, 2007).

2.1.1 Particle Sampling

This system consists of an initial flow-limiting orifice (which sets the gas flow rate to 0.1 L/min), a relaxation chamber (which forces the particles to decelerate, minimising wall losses), an aerodynamic focusing lens (TSI model AFL100) and an accelerating nozzle. A particle must travel along the centreline of the system in order to be drawn through the sizing region and into the mass spectrometer region. Because of the greater mass of particles compared to gas molecules, particles deviate from streamlines of expanding gas emerging from an orifice. The transit of the particle through the system is governed by the Stokes number (St), which is related to the particle density and size, along with the orifice diameter and the gas velocity. If St = 1 the particle will travel along the centreline while particles with St = 0 follow the gas streamline. Particles with St < 1 deviate from the streamlines while particles with St > 1 cross the centreline at the orifice and diverge from the centreline downstream (Johnston, 2000). The AFL consists of five successively smaller orifices; particles are transported closer to the centreline after passing each orifice and finally focused into a beam < 1 mm diameter. A schematic of this process is shown in Figure 2.2. Upon leaving the AFL, the accelerating nozzle controls supersonic gas expansion and acceleration of the particles to their terminal velocity, a factor that is based on aerodynamic diameter (Jayne et al., 2000; Johnston, 2000; Su et al., 2004).

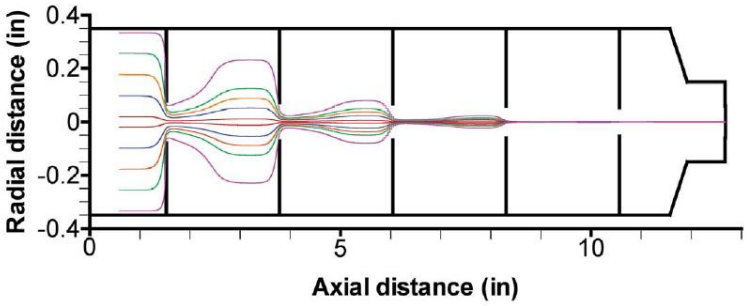


Figure 2.2. Schematic of the operation of an aerodynamic focusing lens (AFL) (TSI, 2007).

2.1.2 Particle Sizing

Having reached their terminal velocities, the particles travel between two continuous-wave, diode-pumped, solid state lasers (λ=532 nm, 50 mW) that are separated vertically by a distance of 6 cm and orientated perpendicularly to each other; this ensures that only particles that travel straight down the centre of the instrument are sized and counted. As the particle crosses the laser beam the scattered light is detected by a photomultiplier tube (PMT) and the signals from the two lasers are used to start and stop a clock registering the transit time (TSI, 2007). The transit time is then converted to aerodynamic diameter

using a calibration curve generated by performing separate measurements on polystyrene latex (PSL) spheres of known diameters. The wavelength of these lasers determines the lower size limit of the instrument; detection of smaller particles (< 150 nm) becomes increasingly difficult because they are unable to scatter enough light to be detected by the PMT (Su et al., 2004).

2.1.3 PARTICLE IONISATION

The transit time of the particles through the two laser velocimeter of the sizing region is used to trigger a pulsed desorption/ionisation (D/I) Nd:YAG (λ=266 nm) laser to hit the moving particle as it arrives at the centre of the mass spectrometry region. The D/I laser operates with a maximum output of 5 mJ/pulse with a pulse length of 5 ns and a maximum pulse rate of 20 Hz (TSI, 2007). The D/I laser ablates the particle, simultaneously generating positive and negative ions which then enter one of the two collinear time of flight (TOF) mass spectrometers (Prather et al., 1994; Gard et al., 1997; TSI, 2007). The time of flight of ions is measured from a starting point (here the ionisation event) until the ions arrive at the detector. Once generated, the ions are accelerated into a flight tube due to a potential generated by source plates. This acceleration (and therefore the velocity they reach at the end of the ion source) depends only on their mass-to-charge (m/z) ratio, so ions with a small m/z are accelerated to a higher terminal velocity than ions with a large m/z.

Ions can acquire additional kinetic energy in the D/I process which results in ions with the same m/z attaining different velocities and causes peak broadening in the mass spectrum. To reduce this effect, a reflectron is employed in each flight tube. In the reflectron (which is composed of a series of electrodes with a potential ramp applied) the ions slow down, stop, turn around and are accelerated back across the flight tube. Faster ions travel farther into the reflectron and have a longer residence time than slower ions with the same m/z, thus focusing ions of the same m/z to hit the detector at the same time, reducing the peak width. The ions therefore travel in a U shaped trajectory from the ion source through the flight tubes, into the reflectrons, and back through the flight tubes to the detectors (micro-channel plates) (Gard et al., 1997). The resolution of the ATOFMS mass spectrometer is 500 m/Δm. A schematic of this process is shown in Figure 2.3.

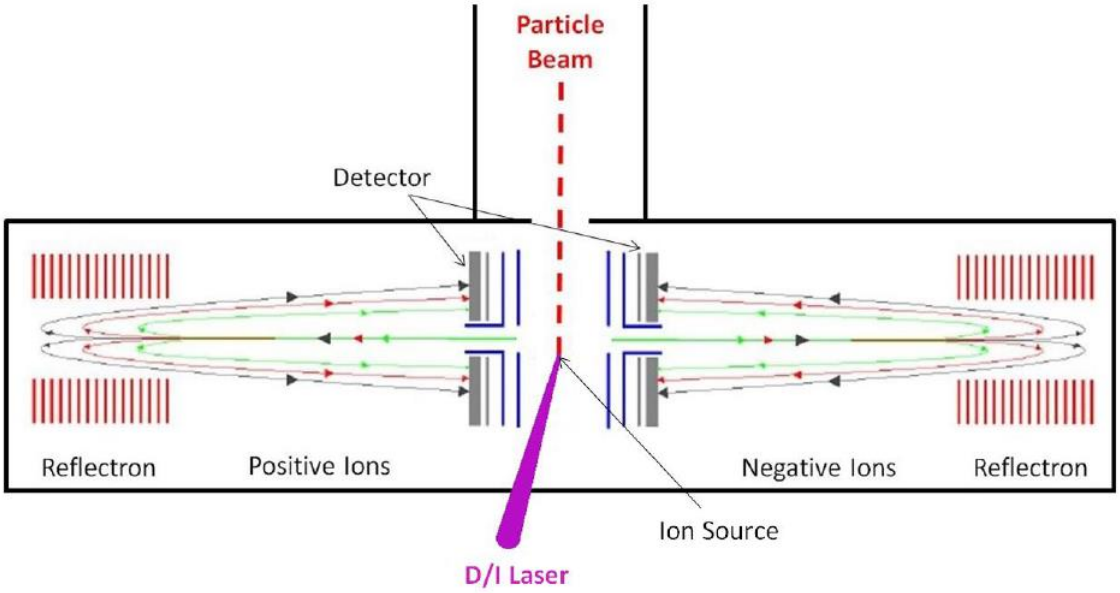


Figure 2.3. Schematic of the ATOFMS mass spectrometry region.

It should be noted that the ATOFMS does not "hit" all of the sized particles. This results in a detection efficiency for the instrument which is affected by several factors; (i) deviation from the particle beam after being sized, affected by particle shape and/or morphology such that the calculated "hit position" for the ionisation laser deviates from the actual one (there are no further focusing measures once the beam reaches the sizing region, and there is a 12 cm distance between the second sizing laser and the ionisation laser) (Hall et al., 2006), (ii) busy time during data acquisition (the instrument is only capable of calculating the time of flight and therefore D/I trigger time of a certain number of particles per second), (iii) charged particles that deviate from the ATOFMS source region due to the voltages applied at the source (Shields, 2008), and (iii) the composition of the particles - pure sulfuric acid, ammonium sulfate, and water have relatively high ionization thresholds at 266 nm (Thomson et al., 1997; Kane & Johnston, 2000) and hit rates as low as 5% were observed in Atlanta when sulfate concentrations were high (Wenzel, 2003). During the operation of the ATOFMS for both measurement campaigns performed in this work, 10 – 20% of the sized particles were successfully ionised.

2.2 DATA ANALYSIS

ATOFMS datasets require particle size calibrations and mass spectra calibrations prior to analysis. Size calibrations were performed prior to each measurement campaign using PSLs of known aerodynamic size (mean diameters of 240, 300, 400, 560, 700, 900 and 1300 nm). The PSLs were introduced into the instrument using a nebuliser and dryer and their transit time between the two sizing lasers was related to their aerodynamic diameter

using a calibration curve. Mass spectra calibrations are necessary to convert the measured time-of-flight into an *m/z* value and were performed daily using the ambient data collected during the measurement campaigns. Ions with readily identifiable signals and no isobaric interferences, such as EC fragments, nitrate, sulfate, K^+ and Pb^+ and their isotopes, were present in the ambient mass spectra and used in the calibrations. Daily calibrations using the ambient data minimises the effect of any changes in the TOF performance throughout the measurement periods, such as voltage fluctuations. Peaks in a wide range of ambient mass spectra collected per day were assigned *m/z* values, producing a calibration curve which was then applied to the full dataset.

Analysis of the calibrated ATOFMS data was performed using ENCHILADA (environmental chemistry through intelligent atmospheric data analysis), a freeware SQL-based program for analysing single particle data developed at Carlton College, Minnesota, USA by Gross et al. (2010). The *K*-means algorithm (MacQueen, 1967) was applied, involving clustering of the single particle mass spectra into a user defined number of clusters (*K*) based on their spectral similarity (square of Euclidean distance) (Anderson et al., 2005). The algorithm employed a refined centroid approach, where 50 subsets of the dataset were first clustered separately in order to find optimal starting centroids or "seeds" for clustering the entire dataset. Once these centroids were chosen, several passes of the dataset were performed until two successive iterations produced identical cluster assignments. The user-defined *K* value is then increased until further increases do not significantly affect the average distance of each particle from its assigned centroid in Euclidean space. At this point there are usually several clusters with a small population which indicates that the clustering is approaching the optimum *K* value. A *K* value of 80 was used for both the NANO-INDUS and ADRIMED/SAF-MED datasets. The user then inspects the resulting clusters for homogeneity. ENCHILADA produces a histogram for each cluster detailing the amount of particles each ion is present in; this information can be used to determine if the cluster is composed of two or more particle types, in which case it is sub-clustered to separate these types from each other. Particles with the same major ions can also be clustered differently if the signal intensities of those ions vary. Clusters exhibiting very similar average mass spectra (including those with the same major ions but varying relative signal intensities), comparable temporal trends and size distributions were merged. The final clusters were then identified as particle classes.

The particle class labelling scheme used herein is regularly used in the literature (Dall'Osto and Harrison, 2006; Spencer et al., 2006; Ault et al., 2010; Pratt and Prather, 2012) and indicates either the probable source (e.g. sea salt) or the dominant species in the positive mass spectra (e.g. K, EC, Fe etc.), with the order of the ions indicating their relative mass spectral intensities. For example, a particle class with high intensity mass spectral features for sodium and magnesium is labelled *Na-Mg*. In some cases this is followed by a secondary species detected in the negative mass spectra (e.g. *K-NO$_X$*), which usually provides insight into the atmospheric ageing the particles have undergone locally or during transport (Reinard et al., 2007). Common assignments for *m/z* generated by ATOFMS can be found in Table 2.1.

Table 2.1. Assignments for m/z found in average mass spectra of ATOFMS particle classes.

Positive Ions	*Ion/Fragment*	*Negative Ions*	*Ion/Fragment*
7	Li^+	-12, -24, -36,…	C_n^-
12, 24, 36,…	C_n^+	-16, -17	O^-, OH^-
18	NH_4^+	-19	F^-
23	Na^+	-26,-42	CN^-, CNO^-
24	Mg^+	-32	O_2^-
27	$Al^+/C_2H_3^+$	-35, -37	Cl^-
30	NO^+/CH_4N^+	-43, -59	AlO^-, AlO_2^-
32,64	S^+, S_2^+	-46, -62	NO_2^-, NO_3^-
39, 41	K^+	-60, -87	$CO_3/SiO_2/C_5^-$, $AlCO_3^-$
40, 56, 96	Ca^+, CaO^+, Ca_2O^+	-63, -79	PO_2^-, PO_3^-
43, 51, 63, 77	$C_3H_7^+/C_2H_3O^+$, $C_4H_3^+$, $C_5H_3^+$, $C_6H_5^+$	-76, -77	SiO_3^-, $HSiO_3^-$
46	Na_2^+	-88	FeO_2^-
48, 64	Ti^+, TiO^+	-89	$(COO)_2H^-$
51, 67	V^+, VO^+	-93,-95	$NaCl_2^-$
52,53	Cr^+	-95	$CH_3SO_3^-$
55	Mn^+	-97	HSO_4^-
56	Fe^+	-103, -120	$AlSiO_3^-$, $AlSiO_4^-/Si_2O_4^-$
58	Ni^+	-125	$H(NO_3)_2^-$
59	$CaF^+/ C_3H_9N^+$	-195	$H(HSO_4)_2^-$
63, 65	Cu^+		
64, 66, 68	Zn^+		
81, 83	Na_2Cl^+		
86	$(C_2H_5)_2NCH_2^+/C_3H_7NHC_2H_4^+$		
108	$Na_2NO_3^+$		
113,115	K_2Cl^+		
138, 155	Ba^+, $BaOH^+$		
208	Pb^+		
213, 215	$K_3SO_4^+$		

2.2.1 Scaling and Mass Reconstruction

Although single-particle mass spectrometers such as the ATOFMS are capable of identifying specific sources for unique particle classes (and general sources for less unique classes), they do not provide quantitative information in the form of particle number or mass concentrations. The transmission biases of the AFL, the number of particles the system can size and ionise at any given time, as well as the limits of the sizing lasers hinder full and accurate counting of particles over the ATOFMS size range. Allen et al. (2000) showed that particle detection efficiency conformed to a power law of diameter, decreasing by 2 orders of magnitude between 0.32 μm and 1.8 μm. Despite this, good agreement between ambient submicron ATOFMS and aerodynamic particle sizer (APS) counts has been observed (Rehbein et al., 2011), indicating that temporal variations in ATOFMS counts can directly correspond to changes in atmospheric concentrations (Qin et al., 2006; Spencer et al., 2008).

The D/I laser used by the ATOFMS complicates quantitative speciation. The effective laser power a particle experiences depends on shot-to-shot fluctuations in laser power density, variations in power density (Gaussian) across the laser beam, as well as the position of the particle in the beam (Wenzel & Prather, 2004; Steele et al., 2005). These factors create variance in the amount of a particle that is desorbed and can also lead to variations in resultant mass spectral peak height and area (Reinard & Johnston, 2008), although this phenomenon can be countered to some extent by using relative peak area for quantification instead (Gross et al., 2000). The sensitivity of a chemical species to laser ablation depends on its ionisation potential (Reilly et al., 2000); matrix effects result in different sensitivities depending upon the type of constituents also present in the same particle (Neubauer et al., 1996; Liu et al., 2000; Bhave et al., 2002a; Hinz & Spengler, 2007; Qin et al., 2006). Charge-transfer-induced neutralisation may suppress instrumental sensitivity for certain species (Reilly et al., 2000), while some particle matrices (e.g. ammonium sulfate) simply do not absorb efficiently at 266 nm (Wenzel, 2003). Detection of species by ATOFMS can also depend on particle size; sensitivities for nitrate and ammonium decline with increasing particle diameter between 0.32-1.8 μm (Bhave et al., 2002a). Lake et al. (2004) found that, for particles around 1 μm in diameter, over 70% produced detectable signals in the negative ion spectrum. As particle size decreased the fraction of particles that gave a detectable negative ion signal also decreased; for particles 100 nm in diameter and smaller only 10% gave a detectable signal.

Given these limitations, in order to produce meaningful particle number and mass concentrations for ATOFMS particle classes it is advisable to scale the total ATOFMS counts using a quantitative particle counting instrument, such as an optical particle counter (OPC) (Allen et al., 2000), scanning mobility particle sizer (SMPS) (Bein et al., 2006; Reinard et al., 2007; Pratt & Prather, 2009) or aerodynamic particle sizer (APS) (Qin et al., 2006).

Particle number concentrations can be derived from a SMPS and OPC/OPS. The SMPS operates on the physical principle that the ability of a particle to traverse an electric field (electrical mobility) is fundamentally related to particle size (McMurry, 2000). Particles entering the system are neutralised (using a radioactive source, Kr^{85}) such that they have a Fuchs equilibrium charge distribution. They then enter a differential mobility analyser (DMA) where an electric field is created and in which the particles drift according to their electrical mobility. The DMA consists of a cylinder, with a negatively charged rod at the centre. The main flow through this cylinder is laminar particle free sheath air. The particle flow is injected at the outside edge of the DMA; particles with a positive charge move across the sheath flow towards the central rod, at a rate determined by their electrical mobility. Particles of a given mobility exit through the sample slit at the top of the DMA, while all other particles exit with the exhaust flow. This monodisperse distribution then goes to a condensation particle counter (CPC) which determines the particle number concentration at that size. The operating principle of the CPC is that small particles grow to more easily measurable sizes if they are exposed to a saturated vapour of a fluid, e.g. n-butanol, which will readily condense if supersaturated. When passed into a cooling chamber, the vapour becomes supersaturated and condenses onto any particles that are present. The particles grow to micrometer size and are then passed through an optical detection cell where their number concentrations by size are obtained using an optical counter. Cut-off sizes are controlled by varying the supersaturation in the condensation chamber. The size of particle exiting the DMA is determined by the particle size and charge, as well as central rod voltage and flow within the DMA. By exponentially scanning the voltage on the central rod, a full particle size distribution is built up (Buseck & Adachi, 2008).

All optical particle counters or sizers work on the same principle; the aerosol crosses a perpendicular laser beam, creating a light pulse. A detector, set off-axis from the laser and particle beam, then records scattering intensity signals from individual particles.

These are then processed, using Mie theory and a calibration curve generated using calibration particles of known size, to give a total number concentration and a size-number distribution.

It is also possible to quantify specific chemical species in single particles based on their respective mass spectral ion intensities (Fergenson et al., 2001; Ferge et al., 2006; Spencer & Prather, 2006; Zelenyuk et al., 2008; Pratt et al., 2009c; Froyd et al., 2010; Jeong et al., 2011). However mass spectral peak intensities are qualitative and not directly proportional to the mass of the species, as they are also dependent on particle matrix, coupling between laser and particle and laser power variability (Smith et al., 2012). Quantitative determination of refractory and non-refractory chemical components of single particles therefore remains challenging.

In principle, quantitative number concentrations for individual ATOFMS particle classes can be determined by multiplying the fraction of total particles belonging to a given class by the total number concentration derived from a particle sizing instrument such as SMPS, OPS/OPC or APS for a selected size bin, for each hour of a measurement period. This assumes all particles were ionised with the same efficiency, which is known not to be the case, for the reasons discussed above.

The SMPS determines the number size distribution in the size range 20-500 nm (electrical mobility diameter, D_m) and the OPS/OPC in the range 0.3-10 μm (optical diameter, D_o), while the ATOFMS measures particles with vacuum aerodynamic diameter (D_{va}) in the range 0.1–3 μm. Reconciling SMPS, OPS and ATOFMS data requires conversion of D_m and D_o measured with the SMPS and OPS/OPC into the corresponding ATOFMS D_{va}. No correction factors were used to merge the SMPS and OPS/OPC data; D_m and D_o were assumed equivalent to geometric diameter. For spherical particles (most but not all submicron atmospheric particles are spherical), the electrical mobility diameter equals the geometric size (McMurry, 2000). However the calibration particles used for the OPS/OPC affects the ambient aerosol measurements; optical diameters are almost equivalent to geometric diameters if calibration particles were composed of oleic acid or dicotyl sebacate, but errors of 30-40% in scattered light signals have been found if PSLs were used (ambient particles which mostly contain water, inorganic salts and organics have a refractive index more similar to that of oleic acid than to PSLs) (Hering & McMurry, 1991; Stolzenburg et al., 1998).

The conversion involves first assuming that the particle is spherical and that no internal voids exist, and thus D_m and D_o equal the volume equivalent diameter, D_{ve}. The assumption of a unity shape factor (spherical geometry) does not take into account non-spherical particles such as fractal soot, which are more susceptible to divergence from the particle beam due to perpendicular drag forces, and thus may be detected less efficiently than spherical particle classes (Moffet & Prather, 2009). This could therefore lead to an over-prediction of the mass concentrations for combustion particle classes (Reinard et al., 2007).

Since D_{ve} (from D_m and D_o) is known, it can be converted to D_{va} by accounting for the density and shape factors:

$$d_{va} = \frac{\rho_p}{\rho_0}\frac{d_{ve}}{\chi}$$

where ρ_p is the particle density, ρ_0 is standard density (1 g cm^{-3}) and χ is the dynamic shape factor (assumed to be 1, for spheres). This is a highly simplified version of particle diameter, morphology and density relationships that are covered in much greater detail elsewhere (DeCarlo et al., 2004). Knowledge of the particle density is required for this conversion, and this can be estimated from mass concentration measurements made by an aerosol mass spectrometer (AMS) and aethalometer.

$$Average\ density = \frac{m_{BC} + m_{Org} + m_{Cl} + m_{SO_4} + m_{NO_3} + m_{NH_4}}{\frac{m_{BC}}{1.5} + \frac{m_{Org}}{1.2} + \frac{m_{Cl}}{1.52} + \frac{m_{SO_4}+m_{NO_3}+m_{NH_4}}{1.75}}$$

Where m is the average mass of BC from the aethalometer and the remaining species from the AMS. 1.5, 1.2, 1.52 and 1.75 (Allan et al., 2003) are material densities for BC, Organic Aerosol (Org), Cl and SO_4, NO_3 and NH_4 respectively.

Average estimated densities of 1.51 g/cm^3 and 1.4 g/cm^3 were observed for the NANO-INDUS and ADRIMED/SAF-MED campaigns respectively. From the density calculation it is clear that neither metal-rich nor sea salt particles (the AMS does not ionise sea salt so the Cl is nss-Cl) are taken into account. From the NANO-INDUS ATOFMS and ICP-MS measurements it was clear that metal-rich particles constituted a significant fraction of the aerosol, while the same was true for sea salt during ADRIMED/SAF-MED, as indicated by PILS measurements. The average density was therefore expected to be larger, thus a density of 1.7 (Reinard et al., 2007) was chosen to convert the diameters.

Mass concentrations can be obtained from the scaled number concentrations by (Reinard et al., 2007):

$$m = \frac{\pi}{6}\rho_p d_{ve}^3$$

The use of a single density for ATOFMS scaling has previously resulted in satisfactory PM mass reconstruction when compared to MOUDI and beta attenuation monitor data (Qin et al., 2006). The scaling factors were similar to those expected based on the shape of the particle transmission efficiency curve for the AFL-100 aerodynamic lens (Wang & McMurry, 2006; Jeong et al., 2011; Healy et al., 2012b). However, a single density assumption is known to be incorrect due to differing particle compositions, and fresh soot particles can exhibit several size-dependent effective densities (Maricq & Xu, 2004; Spencer & Prather, 2006). A precise transformation of number to mass concentration requires knowledge of χ and ρ_p for each class. As discussed above, χ is assumed to be 1. Different particle classes will exhibit different particle densities, particularly in the Dunkirk environment (NANO-INDUS), where the aerosol sources are numerous and diverse. A range of densities was therefore used to calculate mass concentrations for each particle class during NANO-INDUS and ADRIMED/SAF-MED and can be found in Table 2.2 and Table 2.3. The densities were estimated from the bulk densities of the chemical components indicated in the mass spectra as described by (Bein et al., 2006; Reinard et al., 2007) and from transmission electron microscopy coupled with an energy-dispersive X-ray detection (TEM-EDX) of single particles in the vicinity of a steelworks (Ebert et al., 2012).

Since both the assumed density and shape factor are subject to uncertainty, the ATOFMS number and mass concentration should also be considered to have a degree of uncertainty. Accurate and precise values for shape factor and density can be obtained only when single particle data are reconciled with size-resolved mass concentration data from a micro-orifice uniform deposit impactor (MOUDI) (Bein et al., 2006; Qin et al., 2006; Rehbein et al., 2011). Recently the refractive index and effective density of single particles was measured by a SPAMS fitted with a light scattering module, as well as effective density as a function of particle size by coupling a DMA to the SPAMS (Zhang et al., 2015).

Reconstructed ATOFMS mass concentrations were compared with other quantitative measurements such as mass concentrations of $PM_{2.5}$ (beta gauge), BC (MAAP, aethalometer), organics (AMS, ACSM), etc. Pearson's correlation coefficient, as R^2, was

used to evaluate the effectiveness of the ATOFMS mass reconstruction. This coefficient evaluates the relationship between two variables, considered linear when a change in one variable is associated with a proportional change in the other variable. This analysis was considered appropriate as the objective of ATOFMS mass reconstruction was to produce mass concentrations as similar as possible to other mass measurement techniques. R^2 values of 1 were unlikely due to the assumptions made during the mass reconstruction process, and are generally uncommon in comparisons of ambient aerosol measurements due to the complexity and highly variable nature of ambient aerosol. R^2 values of <0.5, ~0.5-0.7 and >0.7 are typically considered indicative of weak, moderate and strong linear (positive or negative) relationships respectively.

NANO-INDUS

Size distributions from an SMPS provided by UCC and an optical particle counter (OPC) provided by LPCA were used to scale the ATOFMS counts at a temporal resolution of 1 h. The ATOFMS counts represent particles that were both sized and successfully ionised to produce mass spectra. 3 SMPS size bins were used for the scaling procedure, created by merging bins in the ranges (D_m) 100-200 nm, 200-300 nm and 300-400 nm. 6 OPC size bins were used in the ranges (D_o) 400-500 nm, 500-650 nm, 650-800 nm, 800-1000 nm and 1000-1600 nm. Using a density of 1.7 the size range of the ATOFMS particles that could be scaled was 170–2720 nm, D_{va}.

Table 2.2. Densities assumed for each NANO-INDUS particle class for mass concentration reconstruction.

Particle Class	*Assumed Density (g/cm³)*	*Reference*
Sea salt	2.2	Bein et al., 2006, Reinard et al., 2007
Na-K	2.2	Bein et al., 2006, Reinard et al., 2007
Na-Mg	2.2	Bein et al., 2006, Reinard et al., 2007
Na-EC	2.2	Bein et al., 2006, Reinard et al., 2007
K	1.8	Bein et al., 2006, Reinard et al., 2007
K-Cl	2.2	Bein et al., 2006, Reinard et al., 2007
K-Aluminosilicate	2.6	Bein et al., 2006, Reinard et al., 2007
K-Al	2.6	Bein et al., 2006, Reinard et al., 2007
EC	1.5	Calculated *(from average density)*
EC-NO	1.5	Calculated *(from average density)*
EC-K	1.5	Calculated *(from average density)*
EC-K-NO	1.5	Calculated *(from average density)*
OC	1.8	Bein et al., 2006, Reinard et al., 2007
OC-PAH	1.8	Bein et al., 2006, Reinard et al., 2007
PAH	1.8	Bein et al., 2006, Reinard et al., 2007
Fe	3.6	Bein et al., 2006, Reinard et al., 2007
K-Fe	3.6	Bein et al., 2006, Reinard et al., 2007
Fe-Ca	3.5	Bein et al., 2006, Reinard et al., 2007
Fe-EC	3.6	Bein et al., 2006, Reinard et al., 2007
Ca	2.6	Ebert et al., 2012
Ca-K	2.6	Ebert et al., 2012
EC-Ca	1.5	Calculated *(from average density)*
V-Fe	3.1	Bein et al., 2006, Reinard et al., 2007
Na-V	3.1	Bein et al., 2006, Reinard et al., 2007
Mn	4	Ebert et al., 2012
K-Mn	4	Ebert et al., 2012
Al-Mn	4	Ebert et al., 2012
Mn-Fe	4	Ebert et al., 2012
Pb	4.3	Bein et al., 2006, Reinard et al., 2007
Li-Zn	3.8	Bein et al., 2006, Reinard et al., 2007
K-Amines	1.5	Bein et al., 2006, Reinard et al., 2007
EC-Amines	1.5	Bein et al., 2006, Reinard et al., 2007
Sulfur	1.7	Bein et al., 2006, Reinard et al., 2007
Poor positive spectra	1.5	Calculated *(from average density)*

ADRIMED/SAF-MED

Size distributions from a SMPS and OPS provided by CNRM-GAME were used to scale the ATOFMS counts at a temporal resolution of 1 h. One SMPS size bin was used for the scaling procedure, created by merging bins in the range (D_m) 172-300 nm. Two OPS size bins were used in the ranges (D_o) 300-579 nm and 579-1732 nm. OPS bins were merged because too many bins resulted in low ATOFMS particle numbers per bin and therefore large scaling factors. The ATOFMS effective lower size limit was 300 nm during ADRIMED and 500 nm during SAF-MED; using a density of 1.7, the size range of the ATOFMS particles that could be scaled was 292-3000 nm, D_{va}.

Table 2.3. Densities assumed for each ADRIMED/SAF-MED particle class for mass concentration reconstruction.

Particle Class	Assumed density (g/cm^3)	Reference
EC-SO_X	1.4	Calculated *(from average density)*
EC-Oxalate	1.4	Calculated *(from average density)*
EC-K	1.4	Calculated *(from average density)*
EC-K-SOx	1.4	Calculated *(from average density)*
EC-K-Oxalate	1.4	Calculated *(from average density)*
K-EC-SO_X	1.4	Calculated *(from average density)*
K-EC-NO_X	1.4	Calculated *(from average density)*
K-EC-Oxalate	1.4	Calculated *(from average density)*
K-CN	1.8	Bein et al., 2006, Reinard et al., 2007
K-NO_X	1.8	Bein et al., 2006, Reinard et al., 2007
K-SO_X	1.8	Bein et al., 2006, Reinard et al., 2007
K-SO_X-Oxalate	1.8	Bein et al., 2006, Reinard et al., 2007
OC	1.8	Bein et al., 2006, Reinard et al., 2007
OC-NO_X	1.8	Bein et al., 2006, Reinard et al., 2007
OC-SO_X	1.8	Bein et al., 2006, Reinard et al., 2007
K-TMA	1.5	Bein et al., 2006, Reinard et al., 2007
EC-TMA	1.5	Bein et al., 2006, Reinard et al., 2007
OC-TMA	1.5	Bein et al., 2006, Reinard et al., 2007
Sea salt-fresh	2.2	Bein et al., 2006, Reinard et al., 2007
Sea salt-aged	2.2	Bein et al., 2006, Reinard et al., 2007
Na-EC	2.2	Bein et al., 2006, Reinard et al., 2007
V	3.1	Bein et al., 2006, Reinard et al., 2007
EC-V	3.1	Bein et al., 2006, Reinard et al., 2007
K-Silicate	2	Bein et al., 2006, Reinard et al., 2007
K-Na	2	Bein et al., 2006, Reinard et al., 2007
Fe	3.6	Bein et al., 2006, Reinard et al., 2007
Ca	2.6	Ebert et al., 2012

2.3 NEGATIVE ION SENSITIVITY

For both the NANO-INDUS and ADRIMED/SAF-MED sampling campaigns, the ATOFMS negative ion detector was not functioning optimally. Many particles did not produce negative mass spectra and a number of those that were generated were of low intensity. Secondary species such as nitrate and sulfate are detected as anions, so information for atmospheric ageing of particles was limited. Aluminosilicate ions also

occur in negative spectra, and would have been useful for distinguishing potassium-rich mineral dust from biomass burning, particularly during ADRIMED/SAF-MED. The issue was most pronounced during NANO-INDUS, after which the mass spectrometer voltages were adjusted in the laboratory to recover some functionality. This voltage scheme and the resulting quality of mass spectra was stable for the analysis of industrial filters and ores (for NANO-INDUS) and the ADRIMED/SAF-MED campaigns. As a result, some difference in mass spectra between the ambient NANO-INDUS particles and the industrial filters and ores is possible.

Water has been shown to remain on particles which can suppress negative ion formation (Neubauer et al., 1997, 1998); in a port of Los Angeles study Ault et al. (2009) found between 30-80% of particles did not produce negative ion mass spectra. While this could have contributed to poor negative ion detection during the campaigns, recent service and repair with Livermore Instruments Inc. confirmed the negative ion detector was the main problem.

2.4 HYSPLIT BACK TRAJECTORIES

Back trajectory analysis was performed using the HYSPLIT model (Revision 631, July 2014) (Draxler & Hess, 1998) to identify air masses influencing the sampling site. The HYSPLIT model was run using the PC Windows-based software available online (http://www.ready.noaa.gov/HYSPLIT.php) and meteorological input from the Global Data Assimilation System (GDAS) archive. 120-hour back trajectories ending 500 m above ground level (AGL) at Grande-Synthe (Dunkirk) and Ersa (Corsica) were calculated for each hour between 15th May and 12th June 2012 (total: 691 trajectories) and 12th June and 6th August 2013 (total: 1344 trajectories). A cluster analysis was performed to categorise the trajectories, with those for ADRIMED/SAF-MED clustered for each period of the campaigns. Plots of total spatial variance as a function of the number of clusters was used to determine the number of clusters. These and plots of the individual trajectories for each cluster can be found in the Appendix I (Figure 8.7 and Figure 8.8) and Appendix II (Figure 9.3-Figure 9.13).

3. CHARACTERISATION OF AIRBORNE SINGLE PARTICLES DURING NANO-INDUS

CONTENTS

3.1 Introduction 47

3.1.1 Particles from industrial activities 47

3.1.2 Dunkirk 57

3.1.3 Aims 62

3.2 Methodology 64

3.2.1 Sampling Site 64

3.2.2 Instrumentation 67

3.3 Results and Discussion 70

3.3.1 Meteorology 70

3.3.2 Particle Number and Mass Concentration 72

3.3.3 Particle Classes 74

3.3.4 Particle Sources 91

3.1 INTRODUCTION

3.1.1 PARTICLES FROM INDUSTRIAL ACTIVITIES

Annual assessments of Europe's air quality have regularly concluded that, despite a number of past successes in reducing anthropogenic emissions, air quality still needs to improve in order to reduce harm to human health and the environment. In 2012 air pollution and greenhouse gases specifically from European industrial activities were estimated to cost Europe between €59 and €189 billion in the form of harmful impacts such as premature death, hospital costs, lost work days, health problems, damage to buildings and reduced agricultural yields (European Environment Agency, 2014). Over the period 2008-2012 the cost was at least €329 billion, more than Ireland's GDP in 2014 (~€230 billion). The majority of the quantified damage costs are caused by emissions of PM_{10}, ammonia (NH_3), nitrogen oxides (NO_X), sulphur oxides (SO_X), non-methane volatile organic compounds (NMVOCs) and CO_2, registered by facilities to the European Pollutant Release and Transfer Register (E-PRTR). While damage cost estimates associated with heavy metal and organic pollutant emissions are significantly lower, they still contribute hundreds of millions of euros worth of harm to human health and the environment, and at the local scale can cause significant adverse impacts. Recent studies (Vecchi et al., 2008; Hieu and Lee, 2010; Mbengue et al., 2014) have demonstrated that the current European daily mean limit of 25 µg/m^3 for $PM_{2.5}$ (WHO recommendations: 10 µg/m^3) is regularly exceeded in urban environments influenced by nearby industrial activities.

The European Environment Agency (EEA) report highlights that only those industrial facilities with an activity rate exceeding a defined threshold and emissions exceeding the pollutant-specific thresholds are required to report information to the E-PRTR register. As a result, the coverage of the E-PRTR varies significantly across the different pollutants and sectors, and many sources of industrial air pollution, particularly local ones, may be unaccounted for.

These costs due to industrial air pollution are incurred in parts of the world where stringent regulations on emissions are in place and where industrial activities represent only a minor contribution to the global burden of atmospheric particulate matter. In Europe, for instance, estimations based on 25 countries for the year 2000 showed that around 1.3×10^9 kg/y of $PM_{2.5}$ contributed to about 40% of the PM_{10} emissions, with two industrial sectors (manufacturing industry and industrial processes/solvent use)

accounting for 15.6% of $PM_{2.5}$ (Pulles et al., 2007). However the costs are certainly much higher in rapidly developing countries like China. The use of less clean energies, combined with a lack of enforcement of the emerging regulations, can lead to higher emissions, estimated to be as high as 1.3×10^{10} kg in 2007 for $PM_{2.5,}$ with industry contributing ~70% of the total (Cao et al., 2011). Major sources of primary industrial $PM_{2.5}$ have been identified as coal combustion, metal processing and refining, iron and steel manufacturing, waste and sludge incineration, and cement/lime production (Morishita et al., 2011a, 2011b). Fugitive emissions also arise from the suspension of raw materials from stockpiles and materials handling operations, which depend on both wind speed and atmospheric turbulence (Chalvatzaki et al., 2012) and thus poorly controlled.

The interest in industrial emissions lies in the fact that point sources can lead to greater human exposure to toxic air pollutants. Many studies suggested that particle concentration, size and composition may play important roles in adverse health effects (Donaldson et al., 1997; Pope III & Dockery, 2006). Properties like elemental composition and chemical speciation of PM are relevant to evaluate the toxicity of inhaled particles on lung cells and tissue (Voutsa & Samara, 2002; Majestic et al., 2007). Particulate matter may be the carrier of acidic or toxic species, such as heavy metals or polycyclic aromatic compounds, which are the main reason behind particle toxicity (Harrison & Yin, 2000). Studies performed in urban environments have shown that fine and ultrafine particles have a higher biological effect than their coarse counterparts in relation to their organic components (Ramgolam et al., 2008, 2009). For instance, the fine aerosol fraction contains high concentrations of mutagens (Ando et al., 1991, 1996) with 79–95% of PAHs concentrated in $PM_{2.5}$ (Sun et al., 1994). PAH toxicity is highly variable, the most important property related to human health being their carcinogenicity. Trace elements such as As, Cd, Cr, Cu, Fe, Hg, Mn, Ni, Pb, V, Zn, mainly from anthropogenic origins and potentially toxic or human carcinogens (Cr, As, Cd and Ni), are also often present in atmospheric particles (Davidson and Osborn, 1986; Nriagu and Pacyna, 1988; Hughes et al., 1998; Butler et al., 2008; Duan and Tan, 2013; Kolker et al., 2013). Some of them have been studied for their direct links to lung inflammation and damage (Claiborn et al., 2002; Osornio-Vargas, Bonner et al., 2003), and it has been found that the metal-soluble species in particles play an important role in lung injuries (Adamson et al., 2000; Kodavanti et al., 1998). Metals can generate reactive oxygen species (ROS), inducing a cellular pro-inflammatory response (Schaumann et al., 2004; Majestic et al., 2007) and are therefore considered to play a central role in the development of airway diseases like chronic obstructive pulmonary disease and asthma.

For example, oxidized forms of manganese (as Mn^{3+}) are involved in the formation of ROS and may compromise biological functions (Carter et al., 1997; Donaldson et al., 1997; Ghio et al., 1999; Lingard et al., 2005), such as the nervous system, in the form of manganism (Majestic et al., 2007). It is thus clearly essential to precisely characterise the physico-chemical composition of fine and ultrafine PM, not only to identify their origins and comprehend their fate in the atmosphere, but also in terms of health impact (Davidson et al., 2005).

Number Concentration and Size Distribution

Number concentration and size distributions of fine particles are very important for understanding particle generation mechanisms during industrial processes and enabling development of process and flue gas cleaning measures to reduce particle emissions (Chang et al., 2000; Maguhn et al., 2003). Number concentration depends on both the industrial activity and the material being processed. The type of filtration system (electrostatic precipitators, multi-cyclones, filters, etc.) has a great impact on both particle concentration and size distribution. Fine particles emitted by "high temperature" processes generally display a higher concentration than those emitted by colder processes. As an example, welding and smelting activities are responsible for higher particle concentrations ($\approx 10^6$ cm^{-3}) (Zimmer & Biswas, 2001; Zimmer, 2002; Evans et al., 2008) than grinding or concreting activities ($\approx 10^4$–10^5 cm^{-3}) (Thomassen et al., 2006; Evans et al., 2008). As emphasized in several studies, the industrial aerosol size distribution presents two major modes (Kauppinen & Pakkanen, 1990; Ohlström et al., 2000): a nucleation mode (below 10 nm) and an accumulation mode (between 100 and 1000 nm). Particles belonging to the accumulation mode can either be primary particles, or arise from the coagulation of smaller particles or from the condensation of semi-volatile compounds onto the surface of small particles. Particles belonging to the nucleation mode can be either directly emitted in the troposphere by high temperature processes or result from gas/particle conversion – primary and secondary particles, respectively (Brock et al., 2002; Maguhn et al., 2003; Buseck & Adachi, 2008). These particles can grow rapidly by coagulation and/or by gas condensation (Zimmer, 2002; Maguhn et al., 2003).

Air parcels that pass by industrial areas can pick up the particulate emissions from chimneys and stacks (Prati et al., 2000; Martley et al., 2004). However industrial plumes, particularly near the stack, tend to have a distinct signature compared to ambient air. Particle concentrations are maximized close to the source and gradually decrease as the plume disperses (Brock et al., 2003; Strawbridge, 2006). Coarse particles (D_a > 2.5 µm)

exhibit a stronger deposition rate than finer particles and will be deposited closer to plants, whereas finer particles have a longer lifetime in the atmosphere and will be transported over longer distances. One study showed that fine particles from a copper smelter were transported over more than 100 km (Daggupaty et al., 2006). Once emitted in the troposphere, the number size distribution of industrial particles will evolve very quickly inside the plume and be influenced by atmospheric dynamics (wind speeds, boundary layer height), concentrations of precursor gases (SO_2 and NO_X) and pre-existing particles (Brock et al., 2003; Marris et al., 2012; Stevens et al., 2012).

Chemical composition

Heavy Metals

In contrast with many organic compounds, most trace elements are only slightly influenced by atmospheric processes during their transport in the atmosphere and can therefore be considered conservative tracers (Morawska & Zhang, 2002; Wu et al., 2007; Dongarrà et al., 2009; Alleman et al., 2010; Lim et al., 2010; Zhang et al., 2011c) of urban and industrial sources. Among them, transition metals are largely emitted through anthropogenic activities (Figure 3.1), such as combustion processes in power plants and industrial facilities e.g., chemistry, petro-chemistry, metallurgy, cement production, waste incinerators, or vehicle emissions (Morawska & Zhang, 2002; Jang et al., 2007; Gugamsetty, 2012; Sánchez-Soberón et al., 2015).

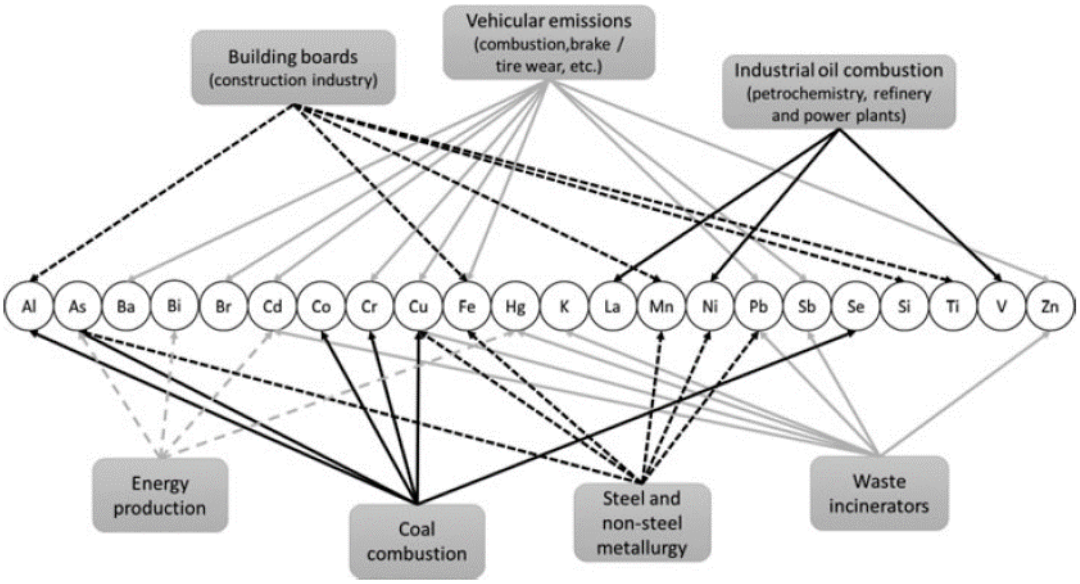


Figure 3.1. Main anthropogenic sources of metals in atmospheric particles (Riffault et al., 2015).

Generally, elements such as As, Cd, Cr, Cu, Hg, Mn, Ni, Pb, V, and Zn, derive primarily from high temperature anthropogenic activities including car exhaust (Cu and Zn being also emitted from brake and tyre wear), fuel combustion, steel smelting, welding, and oil

refining and tend to accumulate in the fine fraction (Fernández Espinosa et al., 2001; Manoli et al., 2002; Utsunomiya et al., 2004; Weitkamp et al., 2005; Hieu & Lee, 2010; Saffari et al., 2013). Other elements like Al, Ca, Fe, K, Mn, Mg, Si, and Ti, are mostly from crustal sources and industry, e.g., ceramic and glass manufacturing (Prati et al., 2000; Querol et al., 2001; Sternbeck et al., 2002; Sánchez de la Campa et al., 2010), and generally appear more concentrated in the supermicron size range (Fernández Espinosa et al., 2001; Birmili et al., 2006).

A number of studies have shown that the amount of toxic particulate metals is generally higher and more variable at locations directly influenced by industrial activities than at rural or urban sites (Osornio-Vargas et al., 2003; Schaumann et al., 2004; Lim et al., 2010; Mohiuddin et al., 2014). For example, $PM_{2.5}$ particles in an industrial zone (foundry) were found to be enriched in transition metals, notably Zn and Cu, compared to a rural sector (Schaumann et al., 2004), while La and to a lesser extent light rare earth elements (Ce, Pr, Nd, and Sm) were associated with a catalyst cracking process, and V and Ni attributed to oil combustion (Kulkarni et al., 2006). Chemical profiles have been reported for specific industrial emissions, sometimes based on long-term measurements. Elevated $PM_{2.5}$ concentrations were measured for Zn (38 ng/m^3), Cu (31 ng/m^3), Pb (16 ng/m^3), and As (5 ng/m^3) in the close environment (<4 km) of one of the largest Cu-smelters in the world (Sánchez de la Campa et al., 2011). The same authors (Sánchez de la Campa et al., 2010) have reported high concentrations in $PM_{2.5}$ for V (65 ng/m^3), Ti (30 ng/m^3), Cu (28 ng/m^3), Zn (28 ng/m^3), and Pb (22 ng/m^3) near ceramic factories in southern Spain. In Italy, downwind of a waste-to-energy plant, Mn and Zn concentrations greater than 60 ng/m^3 were determined in fine particles (Buonanno et al., 2010). In Australia, Fe and Zn were found to be leading metal contributors (up to 12% and 2%, respectively) to $PM_{2.5}$ and PM_1 mass fractions near iron and steel-making industries (Mohiuddin et al., 2014). For the same industrial sector, $PM_{2.5}$ released during the casting process of a steel mill contained a large proportion of metals (8–20% for the major elements Al, Ca, Fe, and Si; and 3–6% for the trace elements Cu, Mn, Pb, Ti, and Zn) (Chang et al., 2005).

However, the information provided by some of these studies is often limited by the relatively long sampling times (often 24 hr or more) which do not facilitate reliable monitoring of the high temporal variability of anthropogenic emissions and wind direction changes (Morishita et al., 2011a). A suitable method of following the high temporal variation of fine particle emission sources is to track industrial plume deposition areas. This strategy was implemented during intensive field campaigns to identify the

deposition areas in the industrial city of Huelva, Spain (Alastuey et al., 2006): for the fine fraction ($PM_{2.5}$), huge concentrations of Pb (466 ng/m^3), Zn (957 ng/m^3), and Cu (1461 ng/m^3) were reported downwind of a phosphate derivatives production plant; the µg/m^3 threshold was even exceeded for Pb (2.0), Cu (2.9), and Zn (4.9) in a Cu-metallurgy plume deposition area, and for Ti (1.2) close a TiO_2 production plant.

Inorganic Species

The role of sulfur and nitrogen containing species in the formation and growth of secondary particles is now well characterized and through aerosol nucleation (Kulmala & Kerminen, 2008) anthropogenic SO_2-containing plumes (especially from coal-fired power plants) can result in new particle formation in the 10–100 nm range (Stevens et al., 2012). However, inside industrial plumes the formation rate of new particles by nucleation is reduced, due to gaseous SO_2 and H_2SO_4 condensation onto pre-existing particles (Stevens et al., 2012).

Using the SEM-EDX technique coal-fired power plant emissions were shown to contain aluminosilicate spherules with a surface enrichment in Ba, Ca, and Fe (Goodarzi, 2006). Coal combustion is also a source of submicron spherical carbonaceous particles, the inorganic fraction of which was dominated by Al, Si, Fe, Ca, Na, and K) (Chen et al., 2004b). A TEM study showed that when worn tyres were fired in addition to coal, particles containing metals such as Pb, Zn, Fe, and K, in the form of sulfates, were detected in the $PM_{2.5}$ fraction (Gieré et al., 2006). This fraction has been also studied by TEM combined with electron energy loss spectroscopy (EELS) for residual oil fly ashes (Chen et al., 2004a). In addition to pure carbonaceous particles, the authors observed the presence of metal-coated carbon-rich particles in the form of sulfates, oxides, vanadates, and phosphates. Speciation of metallic and non-metallic elements can thus represent a useful tool to trace industrial emissions.

Carbonaceous Species

The carbonaceous fraction of particles emitted during industrial activities has been determined by many studies (Vega et al., 2004; Bencs et al., 2010; El Haddad et al., 2011; Morishita et al., 2011a; Zhang et al., 2011a; Joseph, 2012; Pateraki et al., 2012). These analyses mainly focused on two parameters: the measurement of OC and EC and the determination of particle-bound PAHs. OC can be emitted by fossil fuel combustion (i.e. primary emission) or formed by conversion of gaseous precursors, while the only source of EC is fuel combustion. Thus, the OC/EC ratio can be used to assess the contribution of primary and secondary organic aerosol to the carbonaceous fraction of aerosols.

OC/EC ratios measured at industrial sites are usually between those reported at urban sites and those at rural sites. The ratio depends highly on the type of industrial processes occurring in the vicinity of the sampling sites and on the sampling process, particle size, fuel type, combustion conditions, the reactivity of organic species with other atmospheric species (e.g., ozone, nitrogen oxides, hydroxyl radicals) and aging. The OC/EC ratio of particles generated from different industrial activities may vary from <0.5 (e.g., catalytic cracking, charcoal manufacturing, ferromanganese furnace) up to >20 (e.g., asphalt roofing, food and agriculture handling, secondary aluminium production, surface coating) (Chow et al., 2011).

One of the most important classes of organic compounds is PAHs, emitted by combustion processes associated with aluminium production, waste incineration, cement manufacturing, petrochemical and related industries, tyre manufacturing, and coke production as part of steel manufacturing (Yang et al., 2002; Tsai et al., 2007; Ravindra et al., 2006; Ciaparra et al., 2009; Baraniecka et al., 2010; Lin et al., 2011; Wei et al., 2012). Particle PAH content in particular was shown to be highly dependent on the combustion processes and fuel types. Industrial emissions of PAHs have also been shown to have an impact on air quality in nearby residential areas. For instance, the concentration of benzo(a)pyrene close to a medical waste incineration factory was 7 times higher than at a reference sampling site where no major sources of particles and PAHs were identified (Mao et al., 2007).

Single Particle Measurements

Valuable information on the size-resolved mixing state of various metal-containing particles emitted by industrial activities has been obtained using single particle mass spectrometry. A summary of previous studies that utilised this technique to characterise $PM_{2.5}$ in the vicinity of industrial activities is given in

Table 3.1.

The most detailed study in this area (Dall'Osto et al., 2008) involved investigation of the particulate emissions from an integrated iron and steelmaking site in Port Talbot (Wales, UK). Six different metal-rich particle types were identified and attributed to iron-making, steel/coke-making, and rolling mill processes occurring within the facility. Metals dominating the spectra included Fe, Pb, Zn, Ni, and K. All six types displayed unimodal size distributions, but peaked at different sizes in the range 300–600 nm.

Table 3.1. Metal-containing single particle types observed in the vicinity of industrial activities.

Metal	Associated species	Industrial activity	City (Country)	Reference
Cr	Mo, MoO, W	Steel-making	Pittsburgh, PA (USA)	(Pekney et al., 2006)
Cr	Pb	Welding/construction	Athens (Greece)	(Dall'Osto & Harrison, 2006)
Fe	Pb	Steel-making	Shanghai (China)	(Zhang et al., 2009b)
Fe	—	Steel-making	Pittsburgh, PA (USA)	(Pekney et al., 2006)
Fe	K, Na, P, NO_3^-	Iron and steel-making	Port Talbot (UK)	(Dall'Osto et al., 2008)
Fe	Co, Cr	Steel-making/vehicular brake wear	Okinawa Island (Japan)	(Furutani et al., 2011)
Fe	V, VO, Zn, ZnO, Pb, PO_4^{3-}	Steel-making/streetcar tracks	Toronto (Canada)	(Corbin et al., 2012)
Fe	Ag, Ba, Ca, Al, V	Smelters and metal production	Abisko-Stordalen (Sweden)	(Herich et al., 2009)
Fe	La, Ce	Coal-fired power generation	Wilmington, DE (USA)	(Reinard et al., 2007)
Fe	—	Welding/construction	Athens (Greece)	(Dall'Osto & Harrison, 2006)
K	Fe, Na, Li	Steel-making	Pittsburgh, PA (USA)	(Pekney et al., 2006)
K	Cl^-, EC	Steel/coke-making processes	Port Talbot (UK)	(Dall'Osto et al., 2008)
K	Al, Na, Li, Fe, OC, silicates, PO_4^{3-}	Coal combustion	Okinawa Island (Japan)	(Furutani et al., 2011)
K	Na, Cu, EC, OC, NO_3^-, SO_4^{2-}	Coal combustion	Shanghai (China)	(Zhang et al., 2009b)
K	Na, Si, Ca, Fe, Ga, Pb	Coal combustion	Pittsburgh, PA (USA)	(Pekney et al., 2006)
Ni	NO_3^-	Iron and steel-making	Port Talbot (UK)	(Dall'Osto et al., 2008)
Pb	K, Na, Zn, Fe, EC, OC	Steel-making	Wilmington, DE (USA)	(Reinard et al., 2007)
Pb	K, Cl^-, NO_3^-	Iron and steel-making	Port Talbot (UK)	(Dall'Osto et al., 2008)
Pb	K, Na, EC, OC, possibly amines	Steel-making/power generation/refining	Wilmington, DE (USA)	(Reinard et al., 2007)
Pb	SO_4^{2-}	Smelters	Airborne measurements over Canada	(Murphy et al., 2007)
Pb	—	Pb and Zn smelters/steel-making	St. Louis, IL (USA)	(Snyder et al., 2009)

The sampling site was ~2 km from the steelworks and particles were not sampled directly from the emission sources (e.g., stacks). However, such measurements were made where aerosol was sampled directly from the emission stack of a steel manufacturing and processing facility and compared with that sampled about 10 km from the facility (Reinard et al., 2007). A mixed-metal particle class observed in the ambient aerosol, containing Na, K, Zn, and Pb with smaller signals from Fe, EC, and OC, showed a clear wind dependence on the direction of the facility and ~ 4% of the stack particles produced

similar spectra. The other 96% of detected particles from the stack comprised an organic particle class, which was not observed in the ambient dataset. The authors suggested these particles were most likely composed of semi-volatile compounds that transferred to the particle phase upon sampling from the stack and cooling to ambient temperature; however, when emitted from the stack and diluted into ambient air, the semi-volatile components most likely evaporated and the particle class thus disappeared as the air mass was transported to the measurement site 10 km away. Also of note was the lack of iron signal in the particles emitted at the stack. It was suggested that, at the steel processing temperature, metals with lower vapour pressures, such as Zn and Pb, would be distributed more evenly on fine particles in the exhaust stream, while refractory metals such as Fe would segregate in coarse particles (Reinard et al., 2007).

Most single particle instruments that have detected industrially generated particles were in fact not located in close proximity to the activity. The instruments were deployed in a variety of locations, typically urban, and industrial particles were identified based on directional analysis, mass spectral markers, particle temporality, and size distributions. As such, source apportionment is generally tentative and formation and aging processes are infrequently addressed. Some studies do discuss these aspects: for instance, biomass burning plumes were followed on an aircraft and particles acquiring Pb (likely from smelters) as the plume traversed Canada were observed (Murphy et al., 2007); Zhang and co-workers (2009b) noted a sea salt particle type which appeared to have coagulated with Pb-rich particles emitted from industrial emissions.

The role of single particle mass spectrometry in source apportionment is due to its ability to provide internal mixing states for individual particles. For example, while particles containing Fe can originate from metallurgical facilities, they can also derive from crustal matter. Size is certainly a deciding factor, but so too are the associated elements; Fe is not a major component of crustal matter and is usually associated with other crustal elements such as Si and Al (Furutani et al., 2011),while Fe-containing particles of industrial origin are often dominated by Fe and are accompanied by metals such as Cr, Mn, Pb, and Cu. Waste incineration particles are distinctive for their combination of Pb, Zn, and Cl, while coal combustion is distinguishable from biomass burning by the frequent association of K with Li, as biomass burning aerosols produce a negligible Li ion peak (Guazzotti et al., 2003; Spencer et al., 2008); Ce is a recognized tracer for coal combustion (Laden et al., 2000; Pekney et al., 2006) but also Hg, As, and Se, as well as Na and K in particles below 500 nm (Linak et al., 2007). Moreover, elevated La/Ce ratios can be typical of the

dominant contribution of petrol refinery emissions to PM chemical composition (Moreno et al., 2010). In the same source apportionment study, these authors reported, in some specific situations, high V/Ni ratios (>4) typical of fuel-oil combustion sources.

Inorganic particles detected by the nano-aerosol mass spectrometer (NAMS) in Wilmington, DE, United States, contained substantial amounts of silicon, and were attributed to stack emissions from industrial facilities that utilize zeolite catalysts (Klems et al., 2012). The ATOFMS study performed at the Port Talbot steelworks also detailed the non-metallic particles associated with the works' activities (Dall'Osto et al., 2012). Sulfur was the only non-metallic particle type characterizing the iron-making sector (specifically from slag processing at the blast furnaces). Another particle type containing EC, OC, and sulfate was associated with the coke oven combustion processes while the mill sector was deemed to be the source of particles rich in aromatic and nitrogen-containing compounds. The authors suggested these signatures may be due to nitrogen-containing compounds (such as ammonia) used in treatment of the water widely used in the mill processes. Another inorganic particle type containing internally mixed chloride was attributed to hydrochloric acid pickling used in the tandem cold mill process.

The chemical characteristics of the organic fraction depend highly on the industrial process. For example results obtained with an ATOFMS situated close to a very large steelworks (Dall'Osto et al., 2008) showed that particles emitted by hot and cold mills were characterized by a high content of nitrogen-containing organic species and low molecular weight PAHs, while organics emitted by coke ovens included PAHs of higher molecular weight. Particles emitted by blast furnaces had an enhanced content of sulfur-containing organics. For the most part, organic species are internally mixed with metals and inorganic components such as nitrates and sulfates. Particles originating from industrial sources identified primarily by their organic content are usually PAH-containing. Such particles have been observed during the Port Talbot study (Dall'Osto et al., 2012b), where one cluster exhibited strong signals associated with the presence of benzopyrene and/or benzofluoranthene, and in re-aerosolized soot particles collected directly from a primary combustion chamber of an incineration pilot plant in Germany (Zimmermann et al., 2003). The latter were characterized by signals for K, Na, and a PAH signature in the *m/z* range 250–500.

3.1.2 DUNKIRK

Approximately 30% of PM_{10} emissions in France (CITEPA, 2014) are due to industrial activities. Nord–Pas de Calais in north-eastern France is one of the country's most industrialised regions. In 2001 it emitted an estimated 7000 metric tons of atmospheric particulate matter (Ledoux et al., 2009). 60% of these emissions originated from the highly-industrialised Dunkirk area. Dunkirk (210,000 inhabitants) is the third largest French harbour (freight transport: 58 million tons in 2008, (Alleman et al., 2010), servicing the busiest shipping lane in the world, the English Channel. The area is connected by high traffic density roads, which carry traffic between France, Belgium and England (A25: ~40,000 vehicles/day; A16: ~30,000 vehicles/day). The city outskirts are home to over 200 factories, including chemical and petrochemical plants, cement-making, fuel and lubricant refineries and one of Europe's major steelworks (Arcelor-Mittal), producing more than 6×10^9 kg of steel per year and emitting approx. 3×10^6 kg of airborne particulate matter per year (Flament et al., 2008). The numerous industrial plants generate polluted plumes which impact areas depending strongly on wind characteristics. Predominant wind directions are SW, N and NE. The frequent SW winds, which often reach speeds greater than 10 m/s (35 days in 2007, (Roukos et al., 2009)), tend to disperse the industrial emissions effectively toward the sea while NE winds have an opposite effect, increasing PM_{10} concentrations over the urban area (Rimetz-Planchon et al., 2008). Dunkirk is influenced by land-sea breezes associated with sudden wind direction inversions (Rimetz-Planchon et al., 2008), which may favour PM_{10} pollution episodes. Atmospheric sampling sites in the industrial zone, with its proximity to the coast, are likely to be located in the marine boundary layer (MBL) and previous work there did not seem to be affected by the eventual pollution of the atmospheric boundary layer above it (Koponen et al., 2002; Marris et al., 2012). The temperate oceanic climate of the region is relatively humid (annual average of 81%, with daily averages ranging from 51 to 96%), with a high frequency of rainfall (120 days/year) but a low average annual rainfall (676 mm) (Roukos et al., 2009). Monthly mean air temperatures ranging from 5 to 16 °C induce a long heating season (October-May), with natural gas dominating domestic heating (65% of heating energy). Coal, oil and wood are less common (10%) (Mbengue et al., 2014).

Mean PM_{10} mass concentrations of 23–30 $\mu g/m^3$ in Dunkirk have been reported by Mbengue et al. (2014) and Rimetz-Planchon et al. (2008). These concentrations agree with typical European urban background sites and are lower than the annual limit values

specified by the European Community (40 μg/m^3) but higher than the World Health Organization (WHO) reference value (20 μg/m^3). Mbengue et al. (2014) measured PM_{10}, PM_1 and $PM_{0.29}$ in industrial and urban-traffic locations in Dunkirk, and found mean mass concentrations were slightly lower for the industrial sector (23.6 ± 6.0, 10.1 ± 4.1 and 2.4 ± 1.1 μg/m^3, respectively) than for the urban–traffic sector (29.8 ± 4.1, 16.6 ± 3.9 and 5.8 ± 2.1 μg/m^3, respectively). However, less rain events during the urban-traffic sampling period was thought to have influenced this difference. A difference in mean mass size distributions was also observed, with higher mass concentrations for the coarse fraction ($PM_{1–10}$) in the industrial sector and higher values for submicron and ultrafine fractions in the urban sector. Higher wind speeds (~ 7 m/s) affected the industrial sector, and may have re-suspended soil, and road dust, whereas lower wind speeds in the urban sector could have favoured the suspension of submicron particles. Industrial dust, in the form of crude ore transport, storage (11.2 million tons in 2011) and resuspension from ore piles, as well as mechanical procedures related to the use of these materials in industrial processes (excavating, crushing, sintering and separation) likely contributed to the enhanced coarse fraction mass concentrations in the industrial sector.

A number of previous studies of particulate metal content have been performed in the Dunkirk area due to the importance of steelworks and metallurgy (Ledoux et al., 2006; Flament et al., 2008; Ledoux et al., 2009; Alleman et al., 2010; Marris et al., 2012; Hleis et al., 2013; Marris et al., 2013; Mbengue et al., 2014). Several elements or elemental ratios have been used as tracers for specific sources within the industrial area, for example Mn or Mn/Fe ratio for emissions from the ferromanganese alloy facility (Ledoux et al., 2006; Ledoux et al., 2009; Marris et al., 2012), Pb and Fe isotopic compositions for steelworks emissions (Veron et al., 1999; Flament et al., 2008) and V and Ni concentrations for petrochemistry (Alleman et al., 2010). Fe, Ca, Al and Mn have also been used as tracers for selected iron and steel processes, such as sintering, blast furnace, steelmaking and desulfurization slag processing (Hleis et al., 2013).

Measurements of metal and inorganic ion mass concentrations in 2001 at an urban location in Dunkirk and a rural site 15 km away found mean concentrations were all higher at the urban site (Ledoux et al., 2009). Concentrations for Mn (0.07 μg/m^3) and Fe (0.96 μg/m^3) in particular were 3.4 and 3.3 times larger than those at the rural site, highlighting the role of the ferromanganese production facility and the steelworks in particulate metal emissions in Dunkirk. At the urban site, NO_3, SO_4, and NH_4 were found to originate mainly from gas-particle conversion as they presented a unimodal distribution

in the fine mode. Urban background measurements of 42 elements by Alleman et al. (2010) found As and Mn volume-weighted mean concentrations very close to the European annual target value of 6 ng/m^3 for As (Directive 2004/107/EC) and the WHO annual guideline value of 150 ng/m^3 for Mn (WHO, 2000). Concentrations for other elements were in line with those in other urbano-industrialised areas in Europe (Querol et al., 2002; Voutsa et al., 2002). PCA and PMF produced eight factors which contributed to PM_{10}: crustal dust (Al, Fe, Si, Th, U) (11%), marine aerosols (K, Mg, Na, S, Sr) (12%), petrochemistry activities (Co, Eu, La, Ni, V) (9.2%), metallurgical sintering plant (Ag, Cs, Fe, Pb, Rb) (8.6%), metallurgical coke plant (Ag, Bi, Ce, Cs, La, Rb, Sm, Th, Ti) (12.6%), ferromanganese plant (As, Cd, Mn, Mo) (6.6%), road transport (Ag, Ba, Cd, Cu, Pb, S, Sb, Zn) (15%) and a less clearly interpretable profile probably associated to dust resuspension (Al, As, Ba, Ca, Co, Cr, Eu, Ni, Sc, Sr, U, Zr) (13%). These weighted contributions against wind direction frequencies demonstrated that industrial sources were the most important contributors to this site (37%), followed by natural sources (detrital and marine sources) (23%) and road transport (15%). These elements generally constitute only a small fraction (< 5%) of PM mass in Europe but are useful tracers for specific sources which is necessary in the Dunkirk area due to the unusually high number of industrial, natural and urban sources.

A similar, more recent study in the same area found enhanced crustal enrichment factors for Sb, Cd, As, Mo, Pb, Zn, Cu, Ni, Cr, Mn and V, indicating these were almost exclusively from anthropogenic origins (Mbengue et al., 2014). The highest trace metal concentrations were measured for Mn (60 ± 23 ng/m^3), Zn (50 ± 43 ng/m^3), Pb (17 ± 10 ng/m^3) and Cr (13 ± 5 ng/m^3) for downwind industrial emissions and Zn (25 ± 23 ng/m^3) and Mn (19 ±15 ng/m^3) for the urban sector. Concentrations of the remaining elements were always less than 10 ng/m^3. Analysis by wind sector showed higher concentrations of Na, Fe, Mg, Mn, Zn, Pb, Cr, Ni, As, Sr, Mo, Rb, Cd and Co for the industrial sector, while Cu, K, and V displayed slightly higher concentrations downwind of urban and traffic emissions. A comparison of the industrial and urban enrichment factors found no preferential enrichment in the $PM_{0.29}$ fraction for most of the elements. In contrast, $PM_{0.29\text{-}1}$ particles collected downwind of industrial emissions were enriched in metals in comparison with those from the urban sector, particularly As, Cd, Fe, Mn, Mo, Pb, Rb and Zn, which are commonly associated with metallurgical and refinery processes in the studied zone (Choël et al., 2006; Ledoux et al., 2009; Alleman et al., 2010). Manufacturing activities also contributed to metal enrichment in the $PM_{1\text{-}10}$ fraction (As,

Cd, Co, Cr, Fe, Mg, Mn, Mo, Na, Ni, Pb, Sr and Zn), either through direct emissions or by the coagulation of pre-existing particles in the accumulation mode.

Emissions from the processes of the two main metallurgical facilities in Dunkirk, the ferromanganese alloy plant and the steelworks, could be distinguished from each other based on Mn and Fe content but also contain several common components. Fe, Ca, Al and Mg are the major elements of the steelmaking process, with the individual stages producing relatively useful tracers (Hleis et al., 2013). The sintering stack produces relatively high amounts of KCl and Pb, while fugitive emissions from sinter screening contain higher amounts of Fe, Ca and Al and less K, Cl, Na and Pb. Spherical blast furnace particles are composed largely of Fe (in the form of hematite and magnetite), with lower levels of Ca, Zn and C (as graphite) compared to those from the steelmaking itself. Zn-rich, Fe-Zn and graphite particles, also spherical, were distinctive of this stage. Angular particles rich in Ca and Fe characterised the desulfurisation slag processing area. The Fe emissions of the steelworks are the dominant source of Fe in the Dunkirk air, estimated at 40 t/day (Flament et al., 2008). This may be equivalent to 1–2% of the annual atmospheric Fe deposition in the entire Mediterranean basin (Koçak et al., 2005) and also corresponds to the annual emission of heavy metals (As, Cd, Cr, Cu, Hg, Ni, Pb, Se and Zn) in France (1.1×10^3 t/y (CITEPA, 2014)).

Mn, Al and Fe are the main metallic constituents of particulate emissions from the ferromanganese alloy facility in Dunkirk (Marris et al., 2012), most of which come from the cooling chimney of the sintering process (32.3 t/y of PM emitted annually). Mean mass concentrations for these elements in this chimney were 380, 156 and 75 μg/m^3 for the $PM_{0.1–1}$ size fraction and 2110, 587 and 413 μg/m^3 for the $PM_{1–10}$ size fraction (Marris et al., 2012). Pb and Mg are also present in particles emitted from this chimney and represent minor metallic elements, while Ni, Cu, Zn, Cd and V are considered trace elements as the concentrations found by Marris et al. (2012) were generally less than 10 μg/m^3. All these elements come from the primary material (blend of manganese containing ores) used for the production of iron–manganese alloys and transformed during the smelting process. The relative abundance of Mn to other elements in the cooling chimney was found to be independent of size fraction and the element it was compared to, indicating that the bulk chemical composition of emitted particulate matter was almost constant in time for metallic elements, even if the emitted quantities were variable. Individual particles from the cooling chimney (analysed by SEM-EDX) were mostly constituted of internally mixed aluminosilicate and metallic compounds as major

components, whatever the size-class. An external mixing of metallic particles and aluminosilicate particles was also observed. The firing chimney of the sintering unit emits similar particles to the cooling chimney, but also a relatively high abundance of calcite particles and to a lesser extent carbonaceous particles (on average respectively 47% and 5% of analysed particles). Particles from the smelting chimney were essentially metallic (comprised 90% of Mn oxides, containing Al and Si as minor elements) for the $PM_{0.1–1}$ size fraction. Metal bearing particles were often nearly spherical for "pure" metallic particles (e.g. for a Fe oxide) or with an irregular shape for particles internally mixed (aluminosilicates-metals), with a heterogeneous distribution of metals inside them.

Ambient sampling 500 m downwind of the facility revealed large increases in Mn concentrations and moderate increases in Al and Fe concentrations in both $PM_{0.1-1}$ and PM_{1-10} fractions. Individual particle analysis of this plume found metallic particles (10–40%), Al–Si particles (9– 37%), calcite particles (5–10%), and to a lesser extent carbonaceous (3– 12%), gypsum (0–18%) and marine particles (0–4%). The main particle types observed inside the chimneys (metallic, Al–Si and metallic/Al–Si) were still present when the plume reached the edge of housing areas adjacent to the industrial zone, 1500 m away from the plant. Two types of particles were found in the plume that were not present in the chimneys. Metals (Fe, Mn) mixed with carbonaceous compounds, accounting for up to 14% of particles analysed, were thought to result from adsorption of VOCs on primary pure metallic particles or the coagulation of soot with these particles (Goss & Eisenreich, 1997). Mn-bearing particles containing sulfur (identified as metallic particles and accounting for 30% of this class) were thought to result from condensation of sulfuric acid on pre-existing metallic particles during the plume transport. This is consistent with a chemical evolution of emitted particles on a time scale of just a few minutes (Kulmala & Kerminen, 2008).

VOCs have also been measured at industrial, urban and rural locations around Dunkirk (Roukos et al., 2009) during winter and summer. Most VOC emissions in Dunkirk result from the industrial sector (75%); the largest emitters are a hydrocarbon cracking industry, a refinery and a steelworks with VOC emissions of 1124, 639 and 461 tons/year respectively. This corresponds to 37, 21 and 15% of the total VOCs emitted by the industrial sector, respectively. The residential sector accounts for 12%, followed by the transport sector with 10%. Biogenic emissions are considered unimportant in this area. Concentrations of benzene, toluene, ethylbenzene and xylenes were higher at industrial sites than in urban and rural areas (where they were characteristic of background

pollution), and were also higher in the winter. The latter trend was attributed to higher emissions (domestic heating and cold starting for vehicles), reduced dilution processes due to a lower mixing layer and reduced photochemical reactivity in winter. The winter sampling period was characterised by oceanic air masses known to be poorly loaded in VOC (Sauvage et al., 2009). Therefore, concentrations were dominated by local inputs during this period. The situation during the summer period was reversed, with long-range transported compounds in air masses which had undergone photochemical processes and were associated with continental air back trajectories.

3.1.3 AIMS

From these studies it is clear that the industrial activities in Dunkirk can significantly impact local air quality, particularly considering their proximity to large residential areas. However the precise impact of any of these activities is not well known. Facilities are required to limit and measure emissions of particles and gases and certain species, while air quality monitoring networks usually avoid performing measurements close to industrial areas because these locations are not considered as representative. The large number of industrial and urban sources produce complex aerosols, although similar elemental profiles (Alleman et al., 2010) make characterisation of specific particle sources very challenging. As a result there is little characterisation of emissions after they leave an industrial area and identification of their origins is therefore difficult, as the degree and speed of atmospheric processing is unknown. The two largest metallurgy facilities in Dunkirk have been studied to some degree, but with a focus on distinguishing emissions from different stages of the process from each other.

In this context, the NANO-INDUS field campaign was performed at the boundary of the ferromanganese alloy facility and attempted to characterise its emissions and distinguish them from other industrial sources in the area. More specifically, the project was motivated by four inter-related questions:

- How do the physico-chemical characteristics of fine particles at the boundary of an industrial area differ from those directly emitted at the chimneys?
- Is there a link between the presence of fine particles at the boundary of an industrial area and gases directly emitted at the chimneys?
- Do fine particles within an industrial plume have a homogeneous chemical composition, size distribution and morphology, or are they produced by condensation and/or agglomeration, leading to particles with heterogeneous compositions and morphology?

- What is the link between the bio-accessibility of these fine particles and their physico-chemical characteristics?

To address these questions measurements of particles and gases sampled or measured directly at the three chimneys of the facility were compared with those obtained during a four-week field measurement campaign ~800 m southwest of the chimneys. The ATOFMS was deployed during the field campaign to provide size-resolved measurements of the chemical composition of ambient particles with hourly time resolution. ATOFMS analysis was also performed on the raw materials (ores) and particulate matter collected on industrial filters located in the three chimneys of the facility. This information, contained in Appendix I, allowed for source attribution of the particle types observed during the field campaign, thus providing an improved understanding of the impact of the ferromanganese alloy manufacturing facility on local air quality.

3.2 METHODOLOGY

3.2.1 SAMPLING SITE

All sampling and measurements took place directly on the site of a ferromanganese alloy manufacturing facility, operated by Glencore Manganese France (GMF), located in the industrial area of Grande-Synthe, ~7 km west of Dunkirk (51° 01' 44" North, 2° 16' 10" East, 10 m above sea level). Figure 3.3 shows the location of the sampling site relative to industrial and residential areas of Dunkirk and Figure 3.4 shows a close-up of the sampling site on the grounds of the ferromanganese alloy facility, where it was ~800 m southeast of the emission chimneys. The site was also influenced by other urban, industrial, rural, biogenic and marine emissions (within 2 km of the North Sea), depending on the wind direction (Figure 3.2).



Figure 3.2. Location of Dunkirk relative to the UK and Belgium, and nearby potential biogenic (national park) and agricultural emissions.

To the east of the sampling site there is a nearby steelworks (< 1 km away) and the urban areas of Fort Mardyck (3,600 inhabitants, ~2 km) and Dunkirk (93,000 inhabitants, ~7 km). The presence of the steelworks close to the sampling site is an important factor because, under certain wind directions, emissions from the steelworks could potentially mix with those from the ferromanganese alloy factory before reaching the sampling site. To the north and northwest of the site, in the direction of the North Sea, emissions were very limited and associated mainly with marine or shipping sources. However, an outdoor store of manganese ores lies ~200 m to the north of the site and during windy periods, some dust could potentially be transported to the sampling site. Finally, petrochemistry and glass production facilities lie to the west of the site and refineries lie to the southwest.

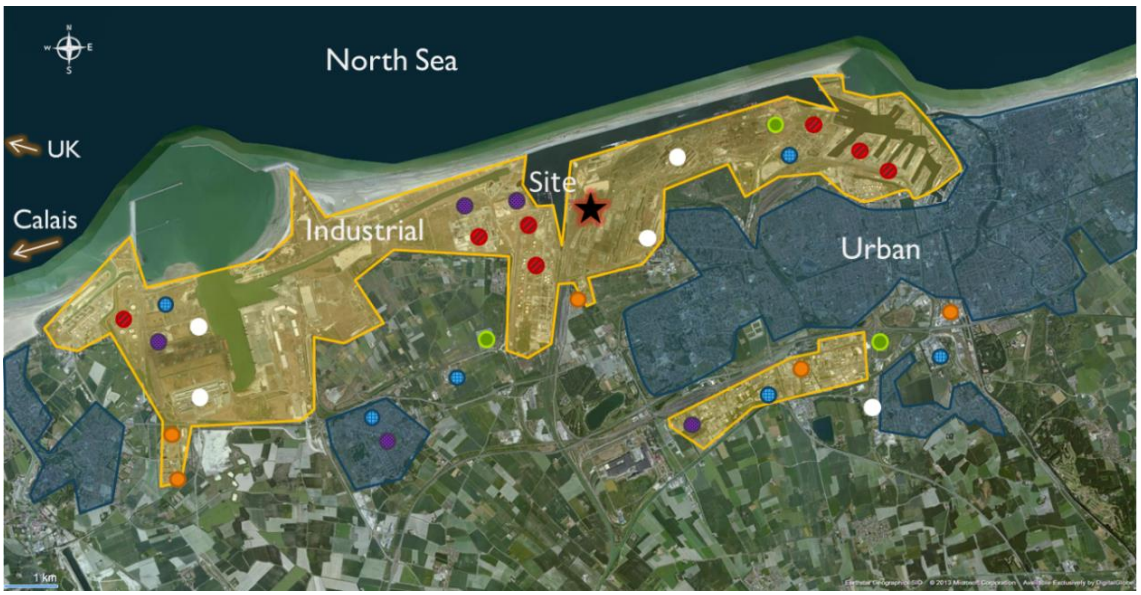


Figure 3.3. Overview of zones and industries in Dunkirk, France. Circles indicate type of industry: red=petrochemical industries, orange=other chemical facilities, white=metallurgy, green=energy production, blue=food & agricultural products, purple=others. Sampling site is marked with a star.



Figure 3.4. Close-up of sampling site location for NANO-INDUS on GMF grounds.

Ferromanganese alloy is made from iron-enriched manganese ores and is used in steelworks to improve the hardness and wear resistance of steel (European Commission, 2014). Production of the alloy at the Grande Synthe facility involves a number of processes, as indicated in Figure 3.5. The facility consists of a sinter unit, and an electric arc furnace. The industrial process can be described by three main steps.

In the first step, the manganese ores (naturally rich in iron) are sintered with anthracite and calcite ($CaCO_3$) in an oven. This involves heating of the sinter (~400 °C), an agglomeration technique of fine ores by melting the surface of smallest particles, followed by cooling, which forms larger agglomerates (Malan et al., 2004). This process produces a more suitable ore size and also reduces the natural ore to an intermediate metallurgical grade raw material, using anthracite as the reducing agent. The original ores are modified,

but their chemical compositions are not very different from the primary material composition. As a result, it is not surprising to identify in samples collected inside the sinter unit chimneys Mn and Fe oxides coming from the original ores, aluminosilicates from the gangue and calcite particles from the additive process (Marris et al., 2012). In the second step, the manganese ore, which is in the form of manganese dioxide (MnO_2), is reduced to metallic Mn using coke in an electric arc furnace (1400 °C), which provides the necessary energy for the redox reaction. The casting process (less emissive) operates at the liquid state and the obtained alloy is very different in composition from the original ores. As a result, collected particles are essentially metallic. Finally, the third step consists of crushing the alloy to obtain the final product.

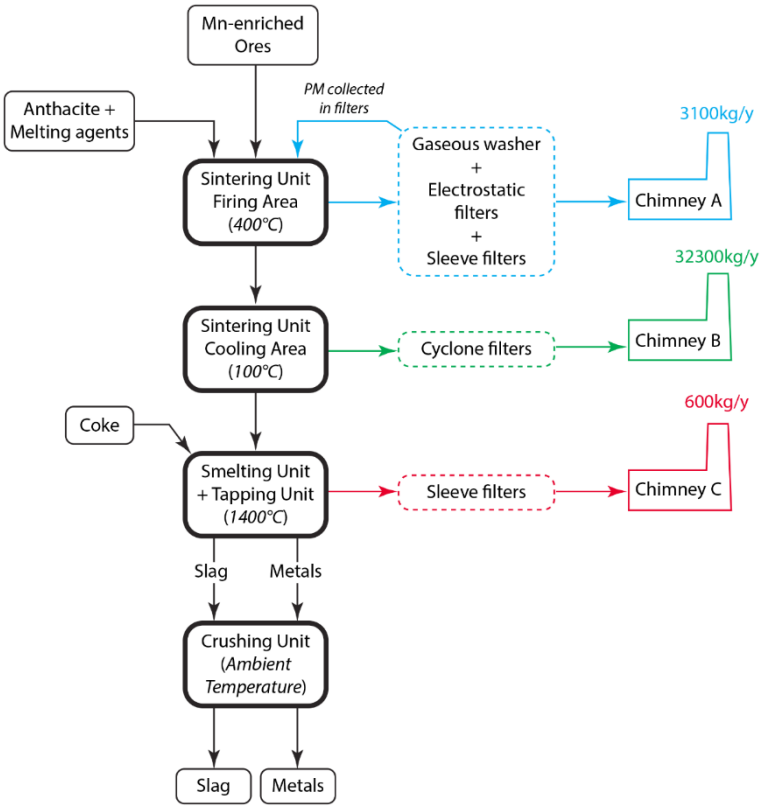


Figure 3.5. Schematic drawing of the Fe-Mn alloy manufacturing process and the industrial filtration system (outlined in dashed line). Atmospheric PM emissions (in kg/y) are reported for each main chimney (Marris et al., 2012, 2013).

Particles and gases emitted during these processes are driven into three different chimneys, where they are treated by filters before their release into the atmosphere. Two of these chimneys are located in the sintering unit, above the firing area and the cooling area, respectively, while the third chimney is in the smelting unit. The sintering unit works 24 hours a day, and thus particles and gases are continuously emitted from its two chimneys (Marris et al., 2012). Emissions from the smelting unit, where the electrochemical reduction of the manganese ore and subsequent casting of the final product takes place, occur continuously during 2 hours for a 6 hour cycle.

3.2.2 INSTRUMENTATION

The field campaign took place between May 15th and June 12th, 2012 and was a collaborative effort involving a number of research groups and institutes. A list of instruments deployed with the groups responsible for the measurements and data analysis is given in Table 3.2. Date and time are reported in Coordinated Universal Time (UTC). The local time during this study was Central European Summer Time (CEST), which corresponds to UTC +2:00. Local meteorological parameters were measured with a weather station and a sonic anemometer, while turbulence and vertical profiles of the wind components were assessed with a Doppler SODAR (Sonic Detection and Ranging). The exact position of the plumes emitted by the chimneys of the ferromanganese alloy plant and the periods during which the sampling site was under their direct influence was determined with an aerosol LIDAR (Light Detection and Ranging).

Particle number concentrations and size distributions were measured with a scanning mobility particle sizer (SMPS, 10 nm – 1 μm in mobility diameter) and optical particle counter (OPC, 300 nm – 20 μm in optical diameter). $PM_{2.5}$ mass concentrations were provided by a beta gauge PM monitor, which operates on the principle that particles on a filter tape absorb beta rays emitted by a C14 source, producing a mass proportional signal (Hauck et al., 2004). Black carbon concentrations were provided by an aethalometer, which collects particles onto a quartz filter fibre; the attenuation of a beam of light transmitted through the sample is linearly proportional to the amount of BC on the filter (Hansen et al., 1984; Magee Scientific Company, 2005).

A high-resolution time-of-flight aerosol mass spectrometer (HR-ToF-AMS) delivered quantitative mass concentrations of the major non-refractory chemical species (SO_4, NO_3, NH_4, non sea salt-Cl) present in submicron particles (Jayne et al., 2000b; DeCarlo et al., 2006). Non-refractory components of particles are vapourised by impaction on a resistively heated surface (~600 °C), ionized by electron ionization (70 eV) and detected by quadrupole or TOF mass spectrometry; the instrument is unable to vaporise black carbon, sea salt, potassium or mineral dust (Middlebrook et al., 2003). The capability to measure organics and secondary inorganic ions quantitatively in bulk aerosol using the AMS combined with the ability of the ATOFMS to qualitatively analyse refractory and non-refractory single particle components has produced complementary datasets when these instruments are deployed side by side (Healy et al., 2013).

Positive matrix factorisation (PMF) can be performed on AMS data to produce organic aerosol (OA) factors (Zhang et al., 2011b). Each individual factor typically corresponds

to a large group of OA constituents with similar chemical composition and temporal behaviour that are characteristic of different sources and/or atmospheric processes. Typical OA factors include hydrocarbon-like organic aerosol (HOA, representative of fossil fuel combustion), low-volatility oxygenated organic aerosol (LV-OOA), semi-volatile oxygenated organic aerosol (SV-OOA), biomass burning organic aerosol (BBOA), cooking-related organic aerosol (COA), and nitrogen-enriched organic aerosol (NOA). In environments in which chemical variation in the OOA is not significant, either because of lack of change in the meteorological conditions (e.g., ambient temperature), source effect, or photochemical age distribution, only one OOA is extracted. However, in environments where OOA is subject to continuous evolution, several OOA factors which represent the end points of a relatively continuous chemical variation arising from different levels of aging are observed. LV-OOA (previously known as OOA-1), the more oxidised OOA factor, correlates well with sulfate and is thought to be more aged and non-volatile. In contrast, the less oxidized SV-OOA (previously known as OOA-2) is thought to be typically semi-volatile because of its diurnal cycles and time trends that are similar to those of ammonium nitrate and chloride, both of which dynamically partition between gaseous and particulate phases depending on ambient temperature and humidity.

In addition to online particle measurements, several cascade impactors and a speciation sampler were employed to collect particles on filters for subsequent off-line analyses. These analyses included the determination of the elemental composition, mixing state and morphology by scanning electron microscopy coupled to energy-dispersive X-ray spectroscopy (SEM-EDX), the measurement of metals by inductively-coupled plasma mass spectrometry (ICP-MS), ions by ion chromatography (IC) with a conductivity detector, and organic carbon (OC) and elemental carbon (EC) by a thermal-optical method.

ATOFMS data analysis was carried out according to the procedures outlined in Chapter 2. ATOFMS particle numbers for each particle class were scaled using an SMPS and OPC and then converted to mass as described in Section 2.2.1. Reconstructed ATOFMS mass concentrations were compared with those obtained by the beta gauge, AMS and ICP-MS analysis of filters, in the form of regression analysis.

Table 3.2. List of instruments deployed during the NANO-INDUS field campaign.

Parameter	Instrument	Make & Model	Temporal resolution	Laboratory
Particle phase				
Chemical composition and size distribution of non-refractory particles (30-1000 nm, vacuum aerodynamic diameter)	HR-ToF-AMS	Aerodyne Research Inc.	4 min (continuous)	EMD-SAGE
Chemical composition and size distribution of non-refractory and refractory particles (100-3000 nm, vacuum aerodynamic diameter)	ATOFMS	TSI Instruments Ltd., model 3800-100	5 min (continuous)	UCC
Particle number size distribution (10-1000 nm, mobility diameter)	2 SMPS	Grimm Aerosol Technik, DMA model 55-900 and CPC model 5.403 TSI Instruments Ltd.	6 min (continuous)	ULCO-LPCA UCC
Particle mass size distribution (300 nm – 20 µm, optical diameter)	OPC	Grimm Aerosol Technik, model 1.108	5 min (continuous)	ULCO-LPCA
$PM_{2.5}$ mass concentration	Beta gauge		1 hr (continuous)	EMD-SAGE
Black carbon (BC)	Aethalometer	Magee Scientific, model AE42	5 min (continuous)	EMD-SAGE
Elemental (EC) and organic carbon (OC)	Partisol sampler (filters)	Sunset Laboratory or carbon aerosol analyser	24 hr (continuous)	EMD-SAGE
Trace metals concentration	3-stage cascade impactor (filters for ICP/MS and IC analysis)	Varian Inc., model 820-MS; or Perkin Elmer, model DRC Elan 6100	24 hr (continuous)	ULCO-LPCA
Morphology and elemental analysis of individual particles	3-stage cascade impactor (boron substrates for SEM/EDX analysis)	SEM: FEI Company, model Quanta 200. EDX: EDAX Inc.	20 min (punctual)	ULCO-LPCA
Atmospheric dynamics				
Detection of industrial plume, boundary layer height	Aerosol LIDAR	Raymetrics S.A.	15 min (continuous)	ULCO-LPCA
Turbulence, vertical profile of wind components	Doppler SODAR	Remtech, model PA2	15 min (continuous)	ULCO-LPCA
Turbulence, wind speed and direction	Sonic anemometer	METEK GmbH, model USA-1	15 min (continuous)	ULCO-LPCA
Pressure, temperature, relative humidity, solar radiation, rain, wind speed and direction	Weather station	Davis Instruments, model Vantage Pro 2	1 min (continuous)	ULCO-LPCA

EMD-SAGE: Ecole des Mines de Douai, Département Sciences de l'Atmosphère et Génie de l'Environnement
UCC: University College Cork
ULCO-LPCA: Université du Littoral Côte d'Opale, Laboratoire de Physico-Chimie de l'Atmosphère

3.3 RESULTS AND DISCUSSION

3.3.1 METEOROLOGY

Figure 3.6 shows time series of standard meteorological parameters: temperature, relative humidity, solar radiation, wind direction and speed. The temperature varied between 6 and 24°C, but for most of the field campaign was in the range 10-15°C and maximum solar radiation was in the range 750-850 W/m^2. The humidity was relatively high (mean ± 1 σ: 78.9 ± 14.3%) due to the coastal location of the receptor site.

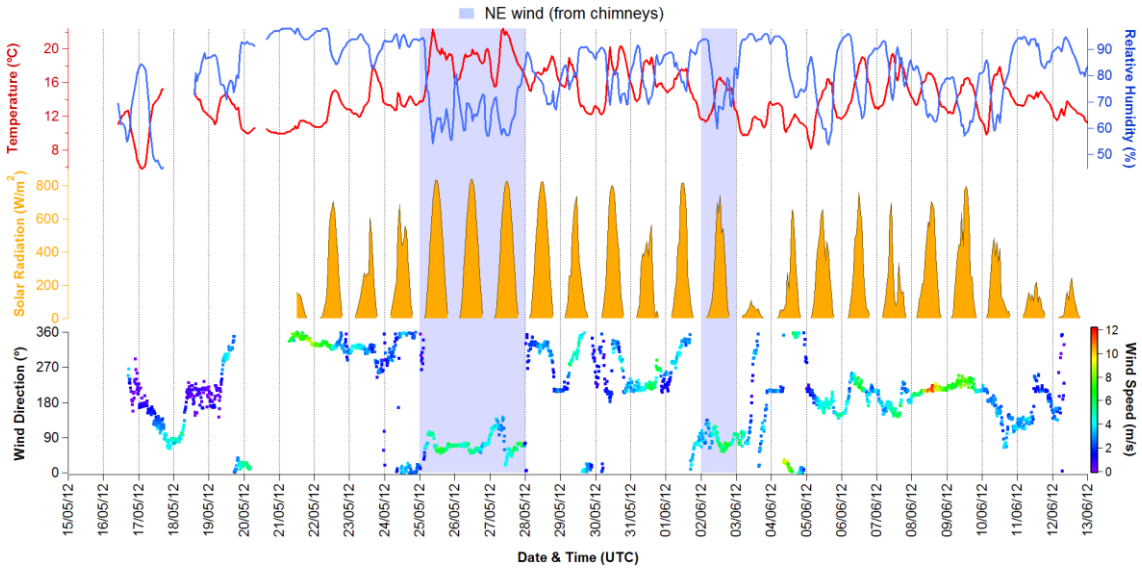


Figure 3.6. Time series of hourly averages of temperature, relative humidity, solar radiation and wind direction coloured by wind speed during NANO-INDUS. Shaded regions correspond to the main north-easterly wind periods which brought industrial plumes to the sampling site.

Wind direction was an important parameter used to identify periods during which north-easterly winds transported plumes from the emission chimneys to the receptor site. Wind direction was not regular during the field campaign, as shown by the wind rose plot (Figure 3.7). Prevailing, and strongest, winds during the campaign were south-westerly. Lowest wind speeds (0–2 m/s) also occurred mostly from the south-west. Winds with speeds >8 m/s were also observed from the north-west and the north, likely sea breezes. The wind was northeasterly for only 5% of the field campaign, and two periods were identified during which the emission plumes could be transported from the chimneys to the site: 25-27th May, and 2nd June, 2012. The period between 25th and 27th May is of particular interest, because it is the longest period with northeasterly wind and corresponds to the days of the campaign which received the most solar radiation, which could increase photo-oxidation and promote fast chemical transformations of particles and precursor gases between the emission chimneys and the sampling site. A high

temperature gradient could also promote sea breezes, and thus vertical mixing of the plumes.

ATOFMS particle numbers, BC and total AMS mass concentrations showed a strong dependence on north-easterly wind with moderate speeds (4-8 m/s), despite this wind sector being prevalent for only 5% of the campaign.

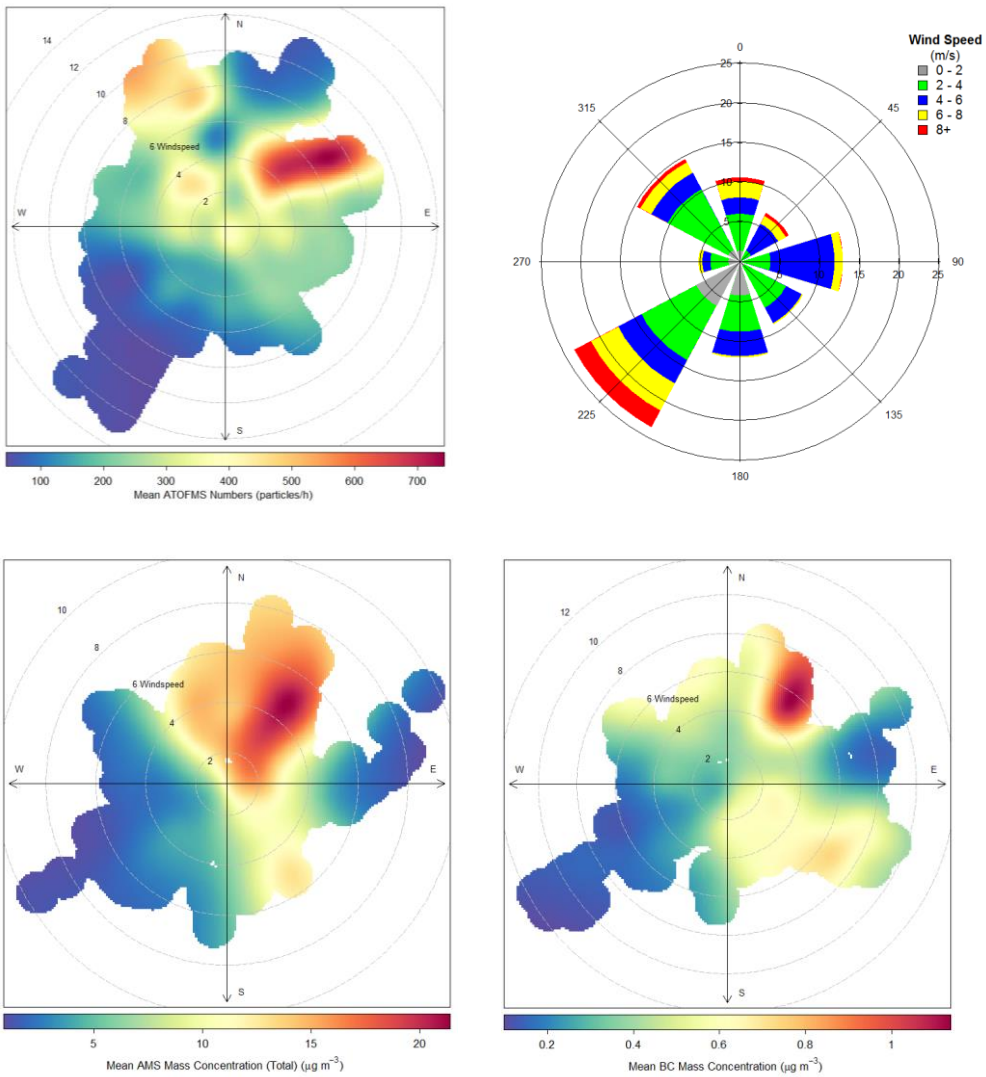


Figure 3.7. Wind rose of wind speed frequency (%) and wind dependences of ATOFMS particle numbers, total AMS and BC mass concentration during NANO-INDUS.

Figure 3.8 shows a map of Western Europe with the 9 clusters identified using HYSPLIT. Clusters 1, 4, 8 and 9 represent marine air masses from the North Atlantic, with the last 24 hours spent over the English Channel and northern France (including Paris). Clusters 2 and 3 also represent marine air masses but from over the Norwegian Sea and travelled over the UK and Ireland before reaching the site. The marine air masses accounted for 62% of trajectories and affected the site between 15-18th May and in the last two weeks of the campaign, likely bringing anthropogenic as well as marine emissions. Cluster 5 trajectories were slow moving over northern France in the last 48 hours of their transit,

again bringing a mix of marine and anthropogenic aerosol to the site from 18-20th May. Clusters 6 and 7 passed over northern and Eastern Europe from 21-28th May and probably carried anthropogenic emissions, as these regions are highly urbanized and industrialized, and contain some of the world's busiest harbours (Rotterdam, Antwerp, Hamburg, Amsterdam). These clusters are the only ones to correspond to a continental air mass, and were observed for 27% of the campaign duration. In summary, the back trajectory analysis suggests that the sampling site was influenced by long-range transport of anthropogenic and marine emissions as well as local pollutants, depending on air mass origin at the time.

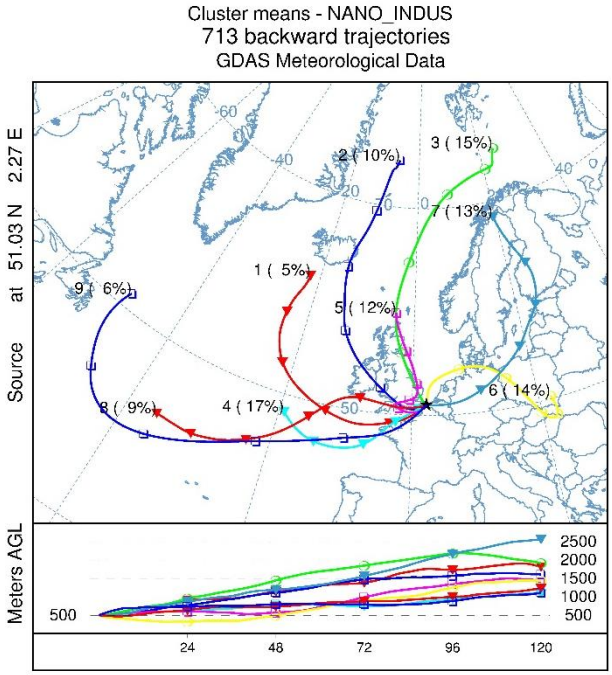


Figure 3.8. Cluster analysis of 120-hour back trajectories (calculated every hour during NANO-INDUS) ending at Grande-Synthe, Dunkirk at 500 m above ground level.

3.3.2 Particle Number and Mass Concentration

Hourly number concentrations measured by the SMPS and OPC are shown in Figure 3.9. Size bins with similar temporal profiles were grouped for clarity. The 10-50 nm SMPS bin accounts for most of the SMPS particle numbers (74%) and correlates well with the OPC bin 800 nm – 20 µm (R^2=0.6). The majority of particles in these bins were observed from 25-27th May, with a peak number concentration of ~2×10^5 particles/cm^3 for those in the 10-50 nm bin. Similar temporal profiles for these bins suggests that emissions during NE wind/industrial periods were a mixture of newly formed and large particles (possibly resuspended dust or raw material). A large concentration of 50-300 nm particles was also observed from 25-27th May, but not exclusively during this period. This bin correlates moderately with AMS organics (R^2=0.51) and ATOFMS K-rich and Fe-rich mass

concentrations (R^2=0.53, 0.52), indicating that a significant amount of particles in this size range originated from biomass burning and industrial emissions and were composed of oxidised organic compounds. The temporal profile for 300-800 nm particles is different again, and correlates well with ATOFMS EC and AMS NO_3 and NH_4 mass concentrations (R^2=0.75, 0.57 and 0.57 respectively). This suggests a strong association with fossil fuel combustion for particles in this size range, as well as some atmospheric processing.

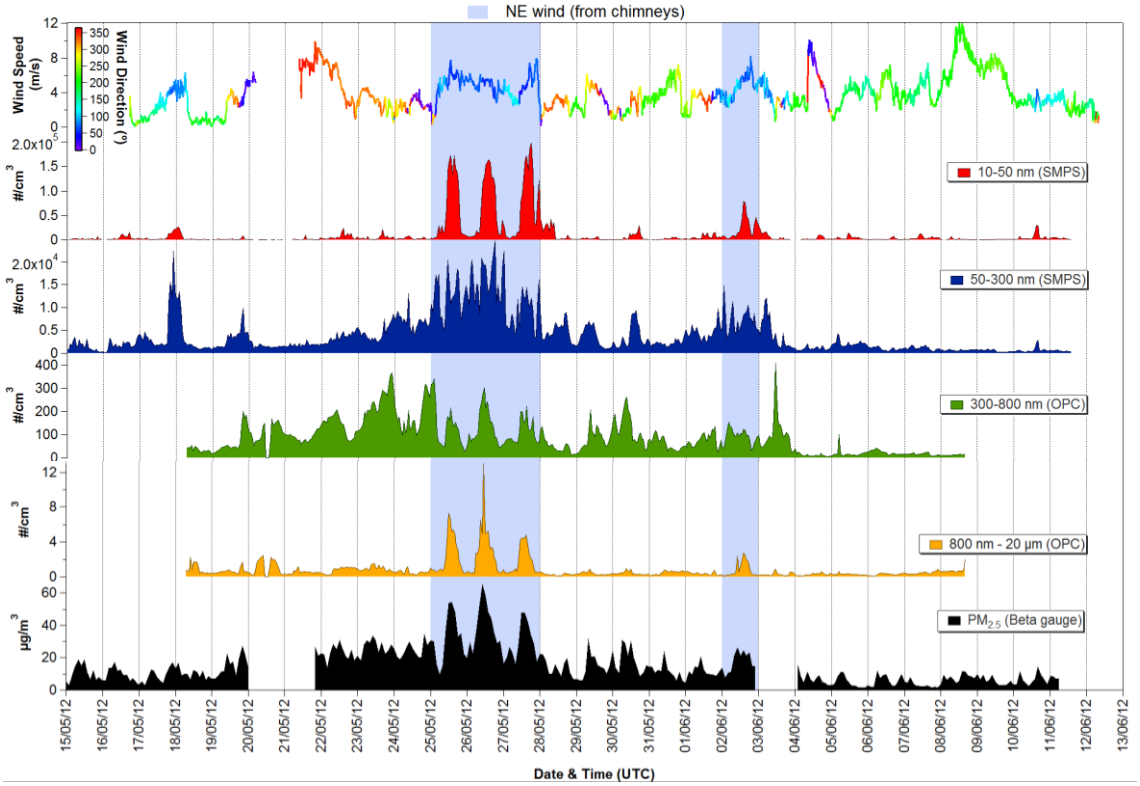


Figure 3.9. Time series for hourly number concentrations measured by the SMPS and OPS during NANO-INDUS.

Mass concentrations were highest with NE wind, corresponding to periods with the largest metallurgical industry influence. The average $PM_{2.5}$ concentration during these periods was 35.7 µg/m^3, twice as high as during periods dominated by marine emissions (N wind: 18.5 µg/m^3, NW wind: 18.7 µg/m^3), and 4-5 times higher than periods with predominantly urban influences. Examination of the wind speed during these periods indicates that high mass loadings occurred during periods of low wind speed, while the decrease of the particle mass loading during the last week occurred when the wind speed increased significantly. Thus, wind speed played an important role in the dilution and dispersion of pollutants.

3.3.3 Particle Classes

Approximately 800,000 single particle mass spectra were generated by the ATOFMS during the sampling period and clustered using the *K*-means algorithm (K = 80), as described in detail elsewhere (Healy et al., 2009, 2010; Gross et al., 2010). 32 distinct ATOFMS particle classes were identified and subsequently grouped into 9 general categories for clarity. The contribution to ATOFMS particle number and mass concentration of all particle classes can be found in Table 3.3. Detailed descriptions of the particle classes and their occurrence during the field campaign are provided in the following sections. Assignment of particle classes originating from the ferromanganese alloy manufacturing facility is based on comparison with single particle mass spectra obtained from the chimney filter samples and ores, presented in Appendix I.

Table 3.3. Detailed composition of ATOFMS dataset during NANO-INDUS, by particle classes.

Category	Particle Class	No. of Particles	% of Total Ionised	% Particles with negative spectra	% of Total ATOFMS Mass	Peak Aerodynamic Diameter (µm)
Na-rich	Sea salt	167093	21	17	6	1.54
	Na-K	12551	2	31	3	0.85
	Na-Mg	2299	0.3	42	0.3	2.89
	Na-EC	1583	0.2	12	0.2	0.89
K-rich	K	166290	21	23	23	0.57
	K-Cl	4718	1	100	0.7	0.51
	K-aluminosilicate	2058	0.3	100	0.2	1.00
	K-Al	1405	0.2	22	0.1	0.76
EC	EC	67346	8	13	9	0.74
	EC-amm-nit	15858	2	15	3	0.74
	EC-K	76148	9	22	9	0.74
	EC-K-amm-nit	14707	2	41	2	0.74
OC & PAH	OC	9073	1	79	3	0.48
	OC-PAH	3127	0.4	92	0.5	1.41
	PAH	1004	0.1	49	0.2	0.38
Fe-rich	Fe	21683	3	50	3	0.64
	K-Fe-Na	11020	1.4	55	6	0.76
	Fe-K-Ca	4064	0.5	67	1	0.93
	Fe-EC	955	0.1	19	0.2	0.81
Ca-rich	Ca	10760	1	55	2	0.79
	Ca-K	1618	0.2	42	0.6	0.81
	EC-Ca	1354	0.2	72	1	0.27
V-rich	V-Fe	8957	1	11	3	0.64
	Na-V	1414	0.2	62	1	0.45
Mn-rich	Mn	2563	0.3	5	0.9	0.74
	K-Mn	3287	0.4	62	0.9	0.82
	Al-K-Mn	2328	0.3	70	0.7	0.74
	Mn-K-Fe	1136	0.1	75	0.3	0.72
Others	K-Pb	8029	1	77	3	0.43
	Li-Zn	457	0.1	33	0.1	0.74
	K-Amines	1764	0.2	6	0.2	0.56
	EC-Amines	1048	0.1	10	0.1	0.53
	Sulfur	224	0.02	1	0.01	0.59
	Poor positive spectra	124848	15.5	7	17	0.53

Na-rich

Four Na-rich particle classes were observed during NANO-INDUS and together account for 23% of all ATOFMS particles ionised (of which the *Sea salt* class was the main contributor); average mass spectra are shown in Figure 3.10. *Sea salt* particles are typical of those observed in other coastal/marine environments (Gard et al., 1998a; Dall'Osto et al., 2004; Healy et al., 2010) and are characterised by $^{23}Na^+$, $^{39}K^+$ and low intensity $^{81,83}Na_2Cl^+$ adducts. The composition of *Na-K* particles is similar, with $^{26}CN^-$, $^{79}PO_3^-$, $^{12,24,36,\cdots}C_n^-$ fragments and sulfate ($^{97}HSO_4^-$) in the negative mode, but without the $^{81,83}Na_2Cl^+$ adducts. *Na-K* particles have been previously observed in Mexico City where they were attributed to a combination of industrial emissions as well as salt particles from a nearby dry lake bed (Moffet et al., 2008b). *Na-Mg* particles have an additional signal for $^{24}Mg^+$. $^{35}Cl^-$ is present in *Sea salt*, *Na-K* and *Na-Mg* particles but not in *Na-EC*. The latter are characterised by $^{12,24,36,\cdots}C_n$ peaks in both positive and negative mass spectra. *Na-EC* particles were also been seen in Mexico, where they were thought to have been produced by industrial emissions and incineration or refuse burning (Moffet et al., 2008b). *Na-EC* particles, described as internally mixed sea salt and EC, were found in ambient aerosol and aerosolised rainwater samples from California and the Indian Ocean, where they were most likely formed by cloud processing occurring during long-range transport (Holecek et al., 2007). The authors anticipated that this composition, an absorbing particle (EC) mixed with a high refractive index material (sea salt) would strongly absorb radiation and have important climate ramifications.

Nitrate ($^{46}NO_2^-$, $^{62}NO_3^-$) signals dominate the average negative mass spectra of all four Na-rich classes. The lack of NaCl adducts in the negative mode of the *Sea salt* class indicates replacement of Cl by nitrate to form sodium nitrate particles (Noble & Prather, 1997; Gard et al., 1998b). However it should be noted that only 17%, 35%, 42% and 12% of *Sea salt*, *Na-K*, *Na-Mg* and *Na-EC* particles produced negative mass spectra. It is possible that fresh sea salt particles were detected and included in the *Sea salt* class but did not produce any negative mass spectra.

Mg-rich particles similar to the *Na-Mg* class have been observed at a North Atlantic coastal site (Dall'Osto et al., 2005), on the Californian coast and over the Indian Ocean (Gaston et al., 2011). They were associated with fresh sea salt emissions at all three locations, particluarly during episodes of heavy rain (Dall'Osto et al., 2005) or when wind speeds were above 10 m/s (Gaston et al., 2011), as well as with atmospheric and seawater dimethylsulfide (DMS) during the Indian Ocean study. The latter suggests that the Mg-

rich particles were detected due to changes in ocean chemistry associated with biological activity. Chlorophyll, which is an essential component of marine phytoplankton, is comprised of a cyclic organic structure co-ordinated to a central atom of magnesium. Gaston et al. suggest the Mg-rich particles, which also contained OC markers ($^{27}C_2H_3^+$, $^{43}C_2H_3O^+$), could result from extracellular polymeric substances excreted by microorganisms, cell debris or fragments, viruses, bacteria or the seawater bubble bursting process lysing cells, releasing organics and/or chlorophyll *a* into the water column. The *Na-Mg* particles could therefore reflect an organic-rich particle coating when water insoluble organic material is present in sea spray aerosols.

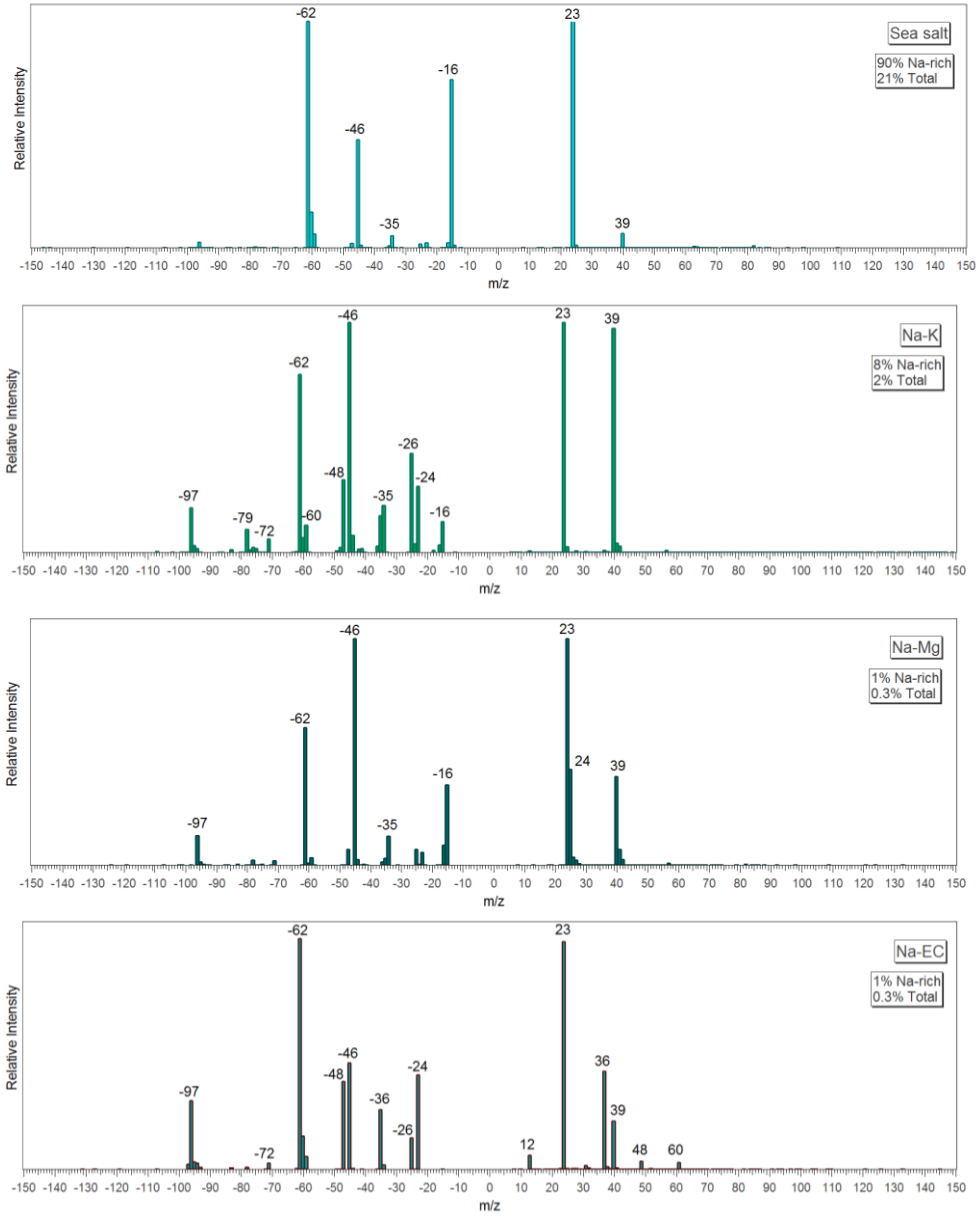


Figure 3.10. Average mass spectra for Na-rich particle classes observed during NANO-INDUS.

Many of the Mg-rich particles detailed by Gaston et al. lacked negative ion spectra even though a heated inlet was used to control relative humidity (RH) at 55%, an indicator of

particle-phase water (Neubauer et al., 1997, 1998). In contrast, sea salt particles produced both positive and negative ion spectra at the same RH, indicating that Mg-rich particles have hygroscopic properties that differ from pure sea salt. Many of the *Na-Mg* particles detected during NANO-INDUS also lacked negative ion spectra (58%), but so too did the sea salt particles (83%), suggesting that non-optimal performance of the negative ion detector was responsible, as outlined in Section 2.3.

Mg has previously been found in dust particles (Silva et al., 2000) but these usually also present $^{27}Al^+$ and $^{56}Fe^+$ signals, which was not the case for the *Na-Mg* particles seen during NANO-INDUS or in the afore-mentioned Mg-rich particles, which were also found to be anti-correlated with dust particles supporting their marine rather than continental origin (Gaston et al., 2011).

Iodine and bromine are important components of marine aerosol (Mahajan et al., 2010), particularly in coastal regions (O'Dowd et al., 2002). They can increase the production of both NO_2 and OH and iodine compounds are an accepted source of new tropospheric particles (Roscoe et al., 2015). Iodine and bromine have been previously detected by single particle mass spectrometers in marine environments (Murphy et al., 1997; Middlebrook et al., 1998) and at a remote rural location in the UK (Beddows et al., 2004), where iodine was found in 0.7% and 1.2% and bromine in 4.5% and 6.6% of fine and coarse particles respectively. Iodine presents as an anion with *m/z* -127 and bromine as anions with *m/z* -79 and -81 (*m/z* -79 can also be assigned to PO_3^- so the combination of peaks at *m/z* -79 and -81 is important for bromine detection). Detection of both was expected to be limited due to the negative ion detector issue; neither were found in any average mass spectra so queries for both were undertaken. Only a few particles were found to contain either element; 93 conatined iodine and 181 contained bromine.

EC

Four EC particle classes were identified, together accounting for 22% of total ATOFMS particles ionised (of which the *EC* and *EC-K* classes were the main contributors); average mass spectra are shown in Figure 3.11. All four classes are characterised by $^{23}Na^+$ and by $^{12,24,36,\cdots}C_n$ peaks in both positive and negative mass spectra, with *EC-K* and *EC-K-amm-nit* presenting a signal for $^{39}K^+$ (weaker relative to $^{36}C_3^+$). The peak at *m/z* 30 has been assigned to NO^+ for *EC-amm-nit* and *EC-K-amm-nit* particles and has been previously used as a marker for ammonium nitrate (Song et al., 1999; Kane & Johnston, 2000; Bhave et al., 2002a). This *m/z* could also be assigned to methylamine but this is more often associated with the presence of other amine fragments so it seems unlikely it would be

the only amine fragment in these EC particles. $^{18}NH_4^+$ is also present in *EC-amm-nit* and *EC-K-amm-nit* particles, supporting the assignment of *m/z* 30 to NO^+. While K is often used as a marker for biomass combustion, internally mixed EC and K has also been observed in particles from coal combustion (Healy et al., 2010). EC particles without K are more difficult to source apportion, lacking any unique markers, and could be assigned to various fossil fuel combustion sources (traffic, fuel oil, etc.).

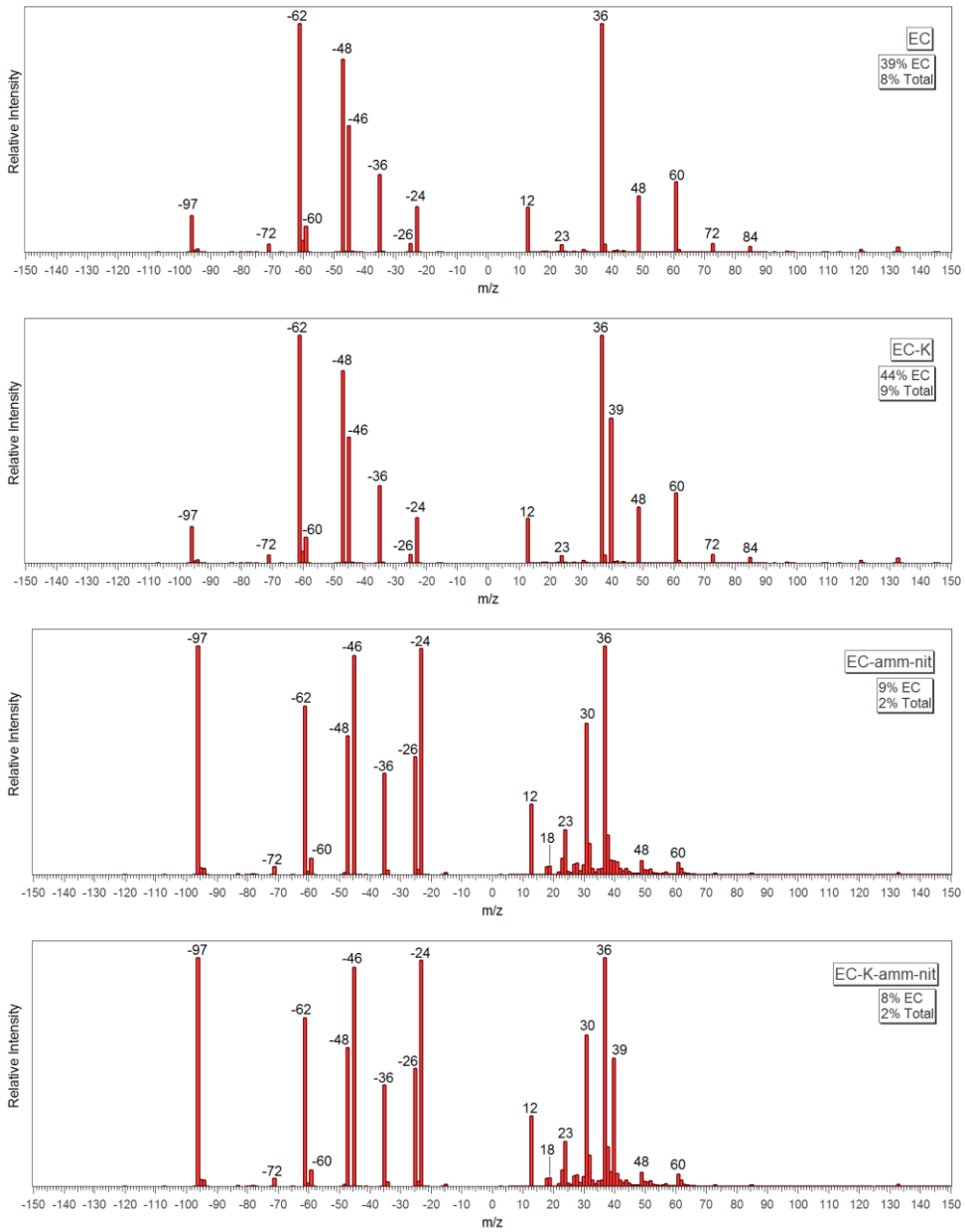


Figure 3.11. Average mass spectra for EC particle classes observed during NANO-INDUS.

Strong signals for sulfate ($^{97}HSO_4^-$) relative to nitrate ($^{46}NO_2^-$, $^{62}NO_3^-$) can be seen in the negative mass spectra of *EC-amm-nit* and *EC-K-amm-nit* particles, while the opposite is the case for *EC* and *EC-K* particles. However, only 13%, 22%, 15% and 41% of *EC*, *EC-K*, *EC-amm-nit* and *EC-K-amm-nit* particles produced negative mass spectra so the average mass spectra do not represent the negative ion population of all EC particles.

OC and PAH

Three OC or PAH-containing particle classes were identified, together accounting for 2% of total ATOFMS particles ionised (of which the *OC* class was the main contributor); average mass spectra are shown in Figure 3.12. All three classes produced hydrocarbon fragments in the positive mass spectra ($^{27}C_2H_3^+$, $^{37}C_3H^+$, $^{43}C_2H_3O^+$, $^{51}C_4H_3^+$, $^{63}C_5H_3^+$, $^{74}C_6H_2^+$, $^{84}C_7H^+$) as well as $^{39}K^+$ and $^{23}Na^+$. Some $^{12,24,36,\cdots}C_n^-$ fragments, $^{26}CN^-$ and sulfate ($^{97}HSO_4^-$) are evident in the negative mass spectra, while nitrate ($^{46}NO_2^-$, $^{62}NO_3^-$) dominates those of the *OC* and *PAH* classes.

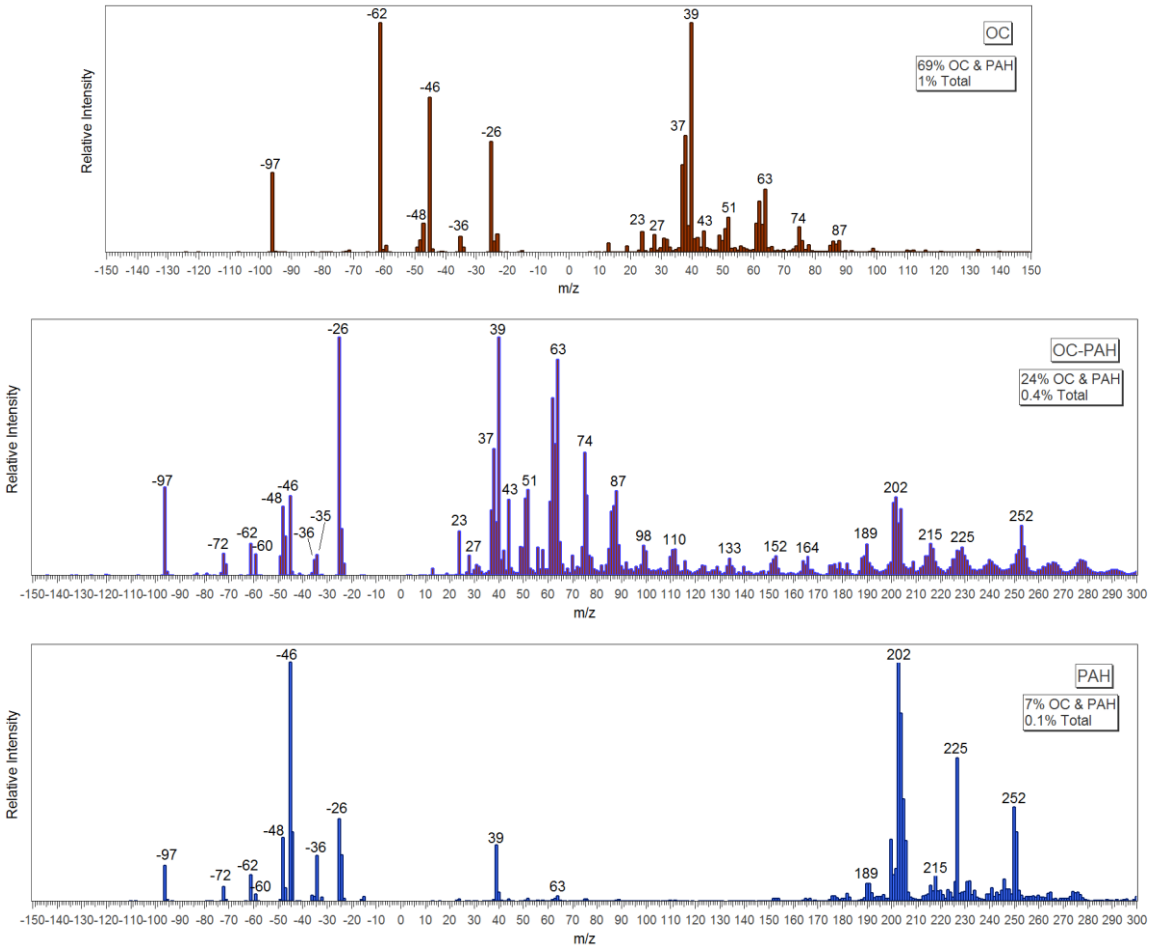


Figure 3.12. Average mass spectra for OC and PAH-containing particle classes observed during NANO-INDUS.

Mass spectra similar to the *OC*, *OC-PAH* and *PAH* classes were also observed in the Port Talbot steelworks study (Dall'Osto et al., 2012) and correspond to the particle classes labelled EC-OC-Sul, PAH-low and PAH-high respectively. Dall'Osto et al. proposed that signals at m/z 189, 202, 216, and 226 were likely due to low molecular weight PAHs, with *m/z* 202 assigned to pyrene and/or fluoranthene. PAH-low particles were attributed to emissions from the hot and cold mills sector of the steelworks. EC-OC-Sul and PAH-high particles were related to steel/coke-making sector, with the latter displayed signals

for high molecular weight PAHs, which could be associated with the presence of benzopyrene and/or benzofluoranthene in the particles (Dall'Osto et al., 2012).

The distribution of low and high molecular weight hydrocarbon fragments in the *OC-PAH* and *PAH* classes could also be considered similar to that found when the laser fluence is reduced from 1 mJ (typically used by ATOFMS in ambient studies) to 0.2 mJ, as seen during photolysis experiments of 1-nitronapthalene (Healy et al., 2012a). In these experiments the intensity of peaks for high molecular weight hydrcarbon fragments such as *m/z* 225 increased as laser fluence was decreased.

K-rich

Four K-rich particle classes were identified, accounting for 23% of total ATOFMS particles ionised (of which the *K* class was the main contributor); average mass spectra are shown in Figure 3.13. *K* particles were dominated by $^{39}K^+$ in the positive mass spectra and produced strong signals for nitrate ($^{46}NO_2^-$, $^{62}NO_3^-$), as well as weaker signals for $^{26}CN^-$, $^{12,24,36,\cdots}C_n^-$ fragments, $^{79}PO_3^-$ and sulfate ($^{97}HSO_{4-}^-$). ATOFMS K-rich particles are usually associated with biomass burning emissions, however the AMS did not produce a fresh biomass burning organic aerosol (BBOA) factor and one of the largest steelworks in Europe is located ~ 1 km NE of the site; this facility uses potassium chloride as an additive during the sintering process. The majority of particles from this process contain C, O, Cl and K which correspond to pure KCl particles and KCl particles associated with carbon and oxygen from enriched ores (Flament et al., 2008). KCl particles represent ~40% of sintering emissions from this steelworks in Dunkirk (Hleis et al., 2013), while the sintering process is also the main contributor to steelworks emissions (PM_{10} emission factor ~100 g/t sinter). K-Cl particles have also been observed in the vicinity of the Port Talbot steelworks (Dall'Osto et al., 2008). An industrial source of the K-rich particles observed during NANO-INDUS is therefore considerably more likely than biomass burning. A strong signal for Cl would be a good marker for sintering emissions, however only 24% of K particles produced a negative mass spectrum and of these only 3% yielded $^{35}Cl^-$ ions. Those K particles containing Cl were separated into their own class, *K-Cl*. It is likely that particle numbers for this class were a lower limit and more likely remained in the *K* class, a lack of negative mass spectra making identification and source apportionment difficult. K-rich particles were queried for silicate peaks (relative peak area 0.1-1000) and the resulting particles separated into their own cluster *K-aluminosilicate*. This class is characterised by signals for $^{43}AlO^-$,$^{60}AlO(OH)^-/SiO_2^-/CO_3^-$, $^{76}SiO_3^-$ and $^{103}AlSiO_3^-$. Nitrate ($^{46}NO_2^-$, $^{62}NO_3^-$), phosphate ($^{79}PO_3^-$), chloride ($^{35,37}Cl^-$) and

oxygen ($^{16}O^-$) were also present in the negative mode, while $^{39}K^+$, $^{23}Na^+$ and $^{56}Fe^+$ were present in the positive mode. Despite signals for aluminosilicate fragments, no aluminium was found in *K-aluminosilicate* positive mass spectra.

Neither *K*, *K-Cl* nor *K-aluminosilicate* particles were found in the GMF industrial chimney filters or ores. However *K-Al* particles appear to originate from the firing chimney. Ambient *K-Al* particles produced stronger signals for $^{27}Al^+$, nitrate ($^{46}NO_2^-$, $^{62}NO_3^-$) and sulfate ($^{97}HSO_4^-$) while the industrial filter *K-Al* particles produced stronger signals for $^{16}O^-$, $^{26}CN^-$ and $^{12,24,36,\cdots}C_n^-$. Both classes produced similar signals for $^{35}Cl^-$ and $^{19}F^-$. Fluoride was identified as a unique marker for firing chimney emissions.

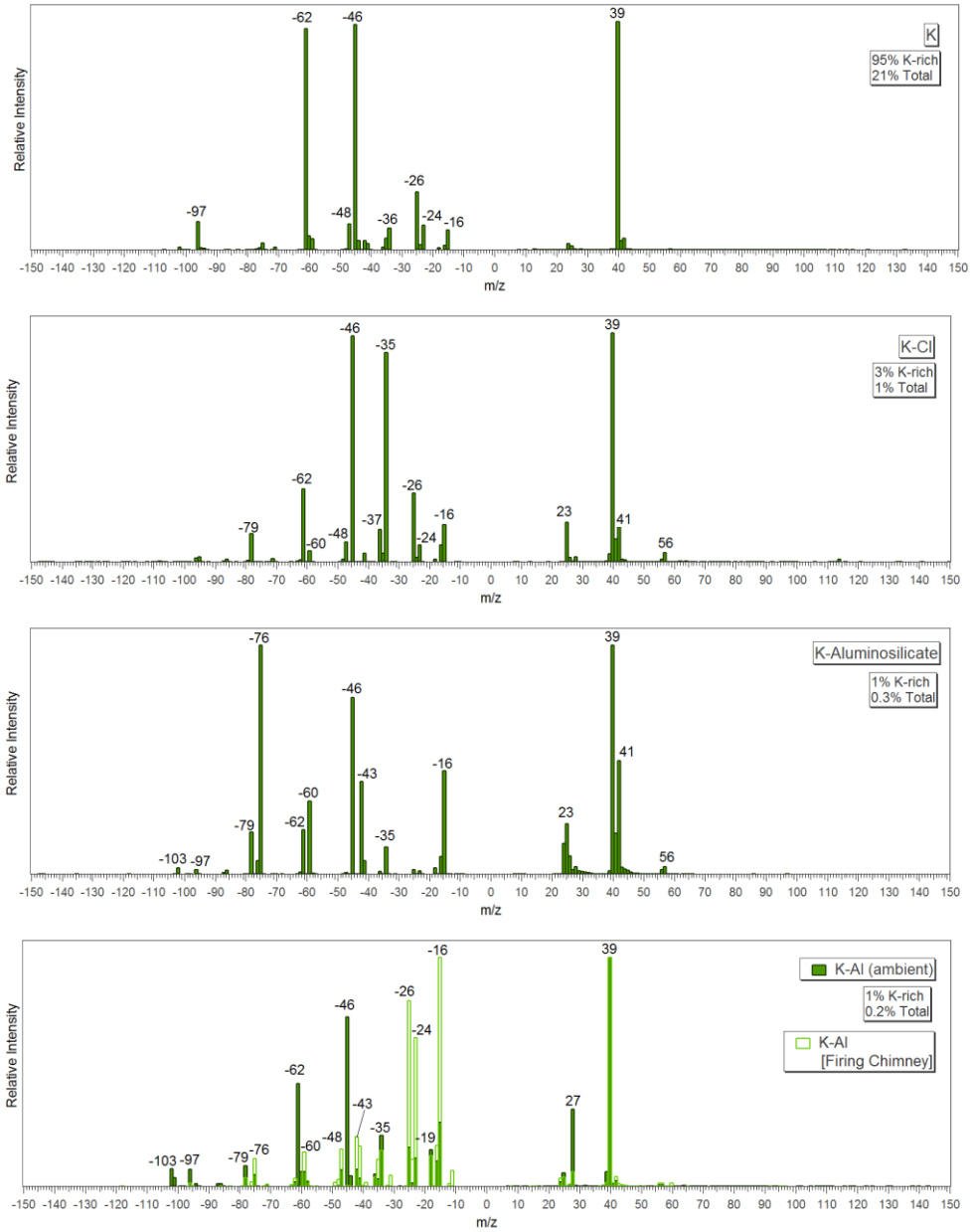


Figure 3.13. Average mass spectra of K-rich particles observed during NANO-INDUS, and average mass spectra for similar particle classes produced from industrial filter samples.

Internal mixtures of $^{39}K^+$, $^{26}CN^-$ and phosphate ($^{63}PO_2^-$, $^{79}PO_3^-$) have been previously associated with primary biological particles (Sinha et al., 1984; Gieray et al., 1997; Steele et al., 2003; Fergenson et al., 2004; Tobias et al., 2005) or particles of biogenic origins (Pratt et al., 2009a; Gaston et al., 2013). However all of these components are also seen mixed with industrial activity markers, such as $^{27}Al^+$, $^{56}Fe^+$, $^{35}Cl^-$ and aluminosilicates in Figure 3.13. No particles matching the composition of biogenically derived particles seen in previous single particle mass spectrometry studies were found during this campaign. However, the poor quality of negative mass spectra obtained limited detection of markers indicative of biological particles ($^{26}CN^-$, $^{63}PO_2^-$, $^{79}PO_3^-$) and therefore restricted assignment of particles to this source. The extensive surrounding agricultural areas and large national park to the southwest were potential sources of such particles so their occurrence during the campaign is a possibility, although not confirmable by the ATOFMS data.

Ca-rich

Three Ca-rich particle classes were identified, accounting for 2% of total ATOFMS particles ionised (of which the *Ca* class was the main contributor); average mass spectra are shown in Figure 3.14. Both *Ca* and *Ca-K* particles appear to originate from the firing chimney. Ambient *Ca* particles were similar in composition to the *Ca-aluminosilicate* class found in the firing chimney; both are characterised by a strong signal for $^{40}Ca^+$, with weaker signals for $^{23}Na^+$ and $^{56}CaO^+$. In the negative mass spectra, ambient *Ca* particles produced stronger signals for nitrate, phosphate and sulfate, while the firing chimney particles produced stronger signals for $^{16}O^-$, $^{26}CN^-$, $^{43}AlO^-$ and $^{76}SiO_3^-$. A similar observation can be made for the firing chimney *Ca* particles relative to the ambient *Ca-K* class. In the positive mode, ambient *Ca-K* particles appeared to contain more sodium, while the chimney *Ca* particles contained fluoride ($^{19}F^-$, $^{59}CaF^+$). Flament et al. (2008) observed that calcium salts (calcite, lime, calcium carbide) are also added in the steelworks sintering process, but the Ca-containing particles produced are formed from aggregation of Fe_2O_3, $CaCO_3$ and KCl particles. These constituted 8% of the sample analysed from the sintering process, while Ca-rich particles accounted for ~80% of the particles from the firing chimney filter, although the steelworks produced 2.72×10^6 kg of total suspended particles in 2008 (Hleis et al., 2013) while the GMF chimneys produce ~ 3.6×10^5 kg/y (emissions for other parts of the process are not available). Fe was also not a prominent component of the firing chimney Ca-rich particles. Ca-containing particles have been assigned to the blast furnace unit of the Port Talbot steelworks by

Taiwo et al. (2014), but these particles were also internally mixed with EC and OC and no Ca particles were found in the previous Port Talbot studies by Dall'Osto et al. (2008, 2012). Thus, there remains a small possibility that some of the Ca-rich particles could have originated from the steelworks.

The third Ca-rich class, *EC-Ca*, is typical of traffic emissions (Spencer et al. 2006; Shields et al. 2007; Toner et al. 2008; Healy et al. 2010). Dominated by C_n fragments in both positive and negative mass spectra, the size of these particles also falls into the range typical of traffic emissions detected by ATOFMS (peak d_a 270 nm, Table 3.3). Particles from vehicle exhaust similar to ambient *Ca* particles have been previously observed (Spencer et al. 2006; Shields et al. 2007; Healy et al. 2010), but without aluminosilicate fragments. The temporal profile and size distribution of the ambient *Ca* particles in this study were also more consistent with industrial emissions than traffic (Section 0).

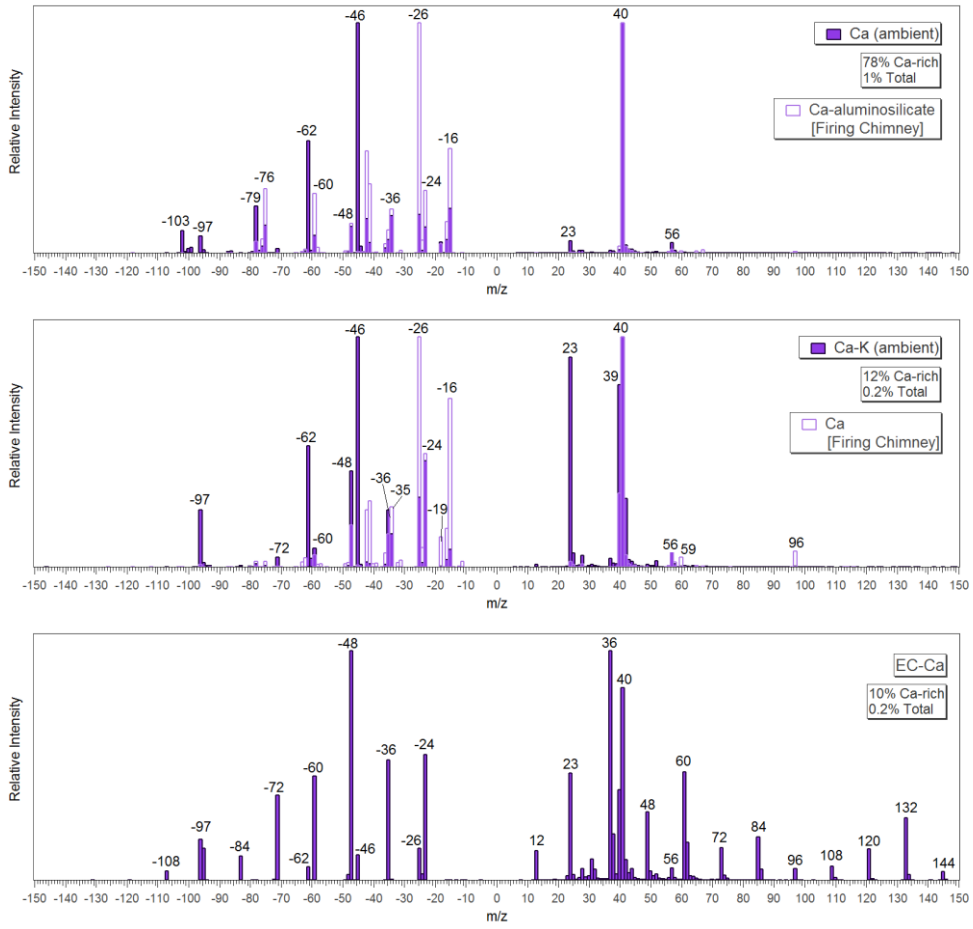


Figure 3.14. Average mass spectra of Ca-rich particle classes observed during NANO-INDUS, and average mass spectra for similar particle classes produced from industrial filter samples.

Fe-rich

Four Fe-rich particle classes were identified, together accounting for 5% of total ATOFMS particles ionised (of which the *Fe* and *K-Fe-Na* classes were the main contributors); average mass spectra are shown in Figure 3.15.

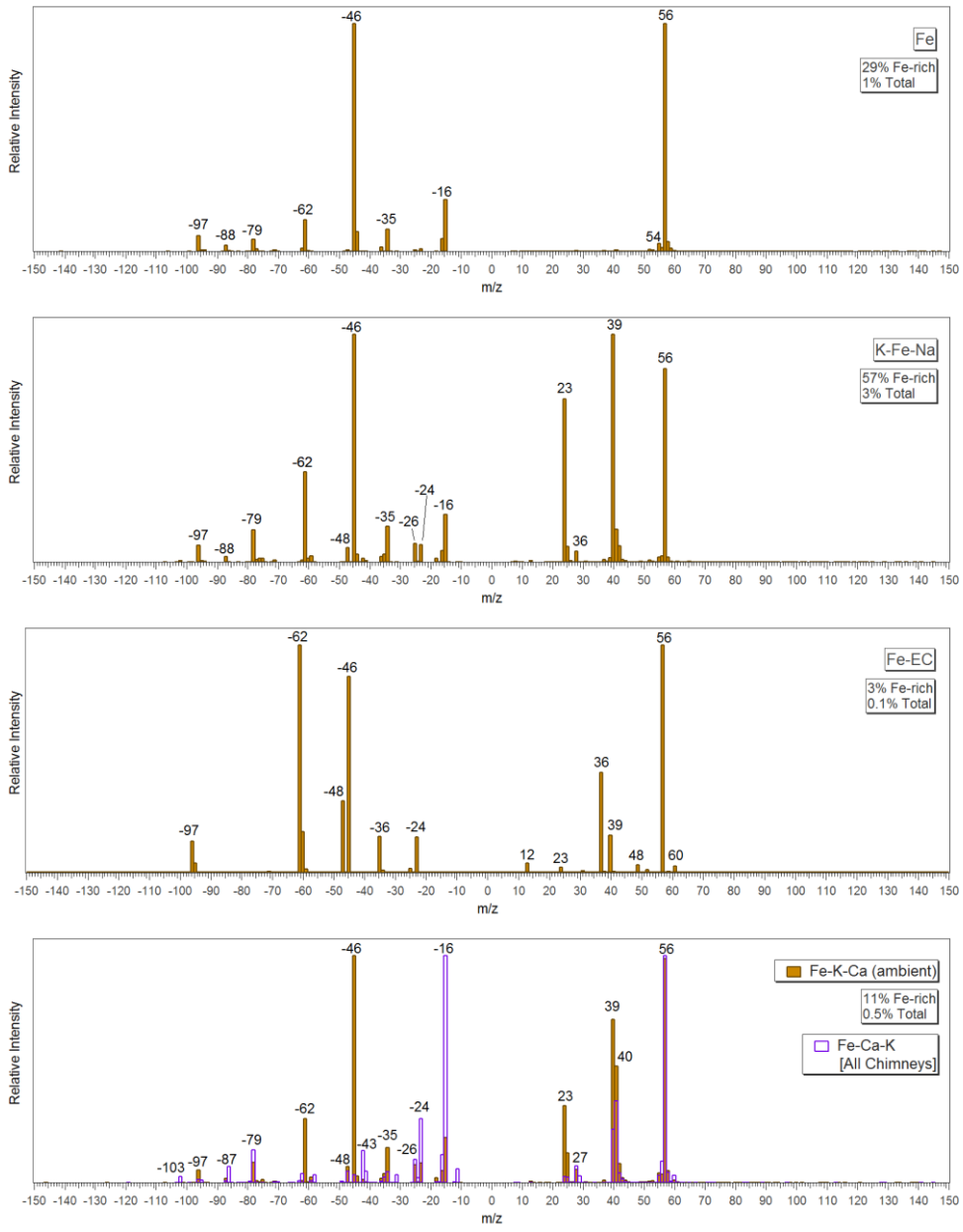


Figure 3.15. Average mass spectra of Fe-rich particles observed during NANO-INDUS, and average mass spectra for similar particle classes produced from industrial filter samples.

Fe particles are distinguished by the dominance of $^{56}Fe^+$ in the positive mode and nitrate ($^{46}NO_2^-$,$^{62}NO_3^-$) in the negative mode. $^{16}O^-$, $^{35}Cl^-$, $^{79}PO_3^-$, $^{88}FeO_2^-$ and $^{97}HSO_4^-$ were also present. *K-Fe-Na* particles produced signals (in relatively equal proportions) for $^{56}Fe^+$, $^{39}K^+$ and $^{23}Na^+$ in the positive mass spectra and for $^{46}NO_2^-$, $^{62}NO_3^-$, $^{16}O^-$, $^{26}CN^-$, $^{35}Cl^-$, $^{79}PO_3^-$, $^{88}FeO_2^-$, $^{97}HSO_4^-$, as well as EC (both positive and negative $^{12,24,36,\cdots}C_n$ fragments).

Fe-EC particles were also dominated by $^{56}Fe^+$ but also produced stronger signals for $^{12,24,36,..}C_n$ relative to *K-Fe-Na* particles.

Fe-K-Ca particles found during the sampling campaign were similar to *Fe-Ca-K* particles found in all three chimney filter samples. *Fe-K-Ca* particles are characterised by a dominant signal for $^{56}Fe^+$, followed by $^{39}K^+$, $^{40}Ca^+$, $^{23}Na^+$ and $^{27}Al^+$; *Fe-Ca-K* particles differ in the relative intensities of $^{39}K^+$ and $^{40}Ca^+$. As is the case for the other ambient particle classes with matches in the chimney filters or ores, ambient *Fe-K-Ca* particles were dominated by nitrate in their negative mass spectra, while the chimney filter particles produced stronger signals for $^{16}O^-$ and aluminosilicates.

While a match between ambient and GMF emissions was found for Fe-containing particles it should be noted again that the steelworks is the single biggest source of particulate Fe in Dunkirk. A study of the steelworks emissions showed that the majority of particles consisted of either Fe_2O_3, $CaCO_3$, KCl or as graphite flakes (Flament et al., 2008). Fe-rich particles similar to the *Fe-K-Ca* class (named FeP) were detected in the vicinity of the Port Talbot steelworks (Dall'Osto et al., 2008), where they accounted for 2.5% of all particles ionised and were associated with the use of phosphate-containing corrosion inhibitors in the hot and cold mills of the facility. There are no unique markers to distinguish steelworks Fe and Ca-containing particles from those emitted by GMF, and given that the *Fe-K-Ca* class only contributed a small fraction of particles from each chimney filter sample it seems likely that the majority of *Fe-K-Ca* particles originated from the steelworks.

Particles similar to those in the *K-Fe-Na* class were also found in the vicinity of the Port Talbot steelworks (Dall'Osto et al., 2008), where they accounted for 0.8% of all particles ionised and were associated with the iron and steel-making processes. *K-Fe-Na* particles accounted for more of the NANO-INDUS ATOFMS dataset, at 3%, likely a reflection of meteorological conditions. No particles similar to the *Fe* class were found near the steelworks; Fe was always mixed with other inorganic or metallic elements.

Mn-rich

Four Mn-rich particle classes were identified, together accounting for 1% of total ATOFMS particles ionised (of which the *K-Mn* class is the main contributor); average mass spectra are shown in Figure 3.16. All four classes are characterised by the presence of $^{55}Mn^+$, while $^{39}K^+$ was found in *Al-K-Mn*, *K-Mn* and *Mn-K-Fe* particles and $^{56}Fe^+$ was found in the *Al-K-Mn* and *Mn-K-Fe* classes. The strongest signal for $^{27}Al^+$ was seen in *Al-*

K-Mn particles. Three of the four ambient Mn-rich classes clearly originate from the ferromanganese alloy facility.

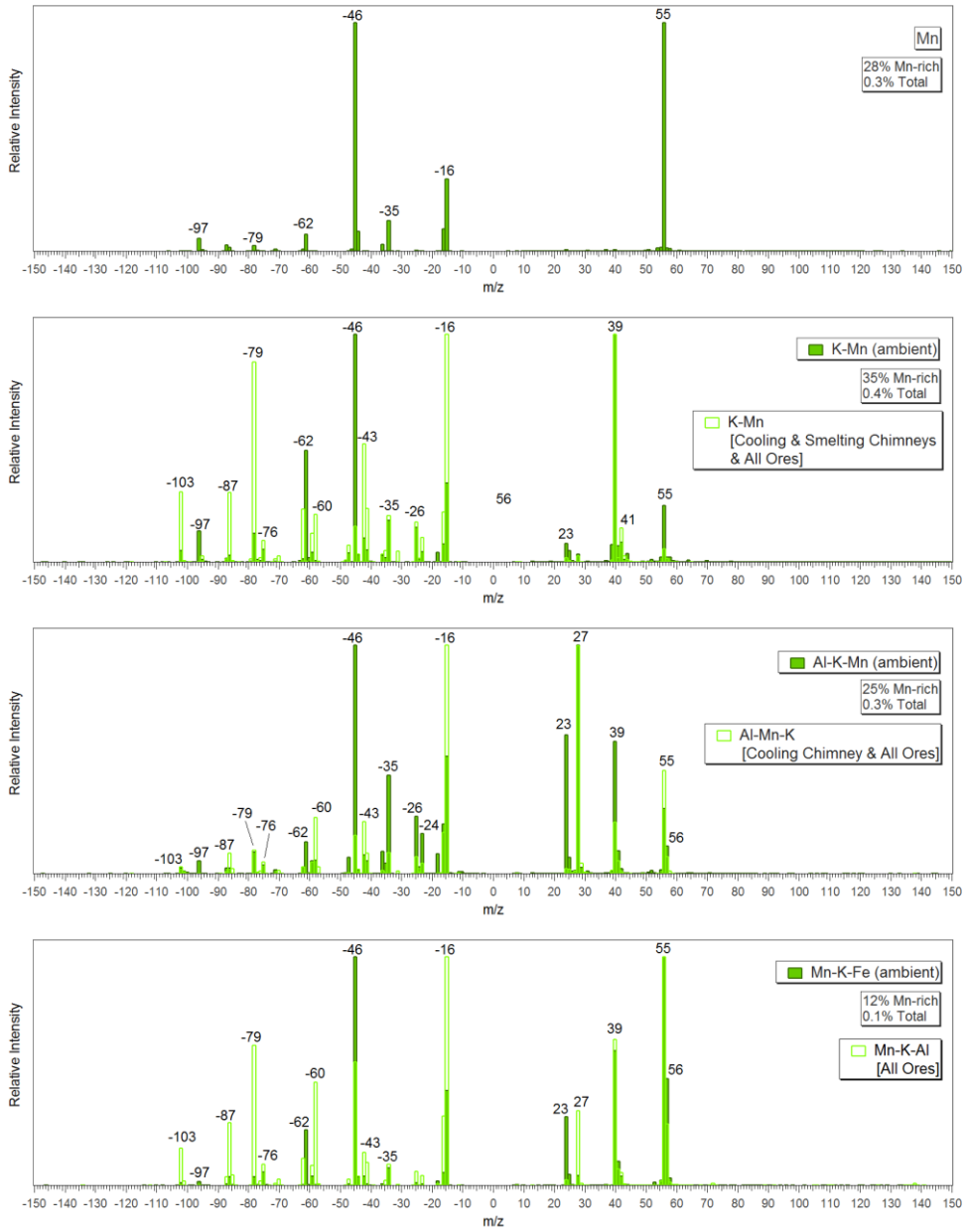


Figure 3.16. Average mass spectra of Mn-rich particles observed during NANO-INDUS, and average mass spectra for similar particle classes produced from industrial filter and ore samples.

Ambient *K-Mn* particles could have originated from either the cooling or smelting chimneys or the ores. Analysis of the cooling and smelting chimneys produced two *K-Mn* classes, with different intensities for $^{39}K^+$ and $^{55}Mn^+$. The signal intensities for these ions was considered too variable in the ambient data to merit separate particle classes, so only a single class is shown here. The core composition of the two classes is very similar, with some difference in signal intensities and the addition of nitrate and sulfate in the ambient particles. Chimney and ore samples produced stronger signals for $^{43}AlO^-$, $^{60}AlO(OH)$, $^{79}PO_3^-$, $^{87}AlCO_3^-$ and $^{103}AlSiO_3^-$. While the smelting chimney sample was dominated by

K-Mn (or *Mn-K*) particles, it is likely that most of these particles come from the cooling chimney, as its particulate emissions are considerably higher than for the smelting chimney. Particles dominated by $^{39}K^{+}$ and $^{55}Mn^{+}$ have been observed in the vicinity of the Port Talbot steelworks by Taiwo et al. (2014), where their wind dependence indicated a diffuse local low-level source, but a more precise origin was not identified.

Ambient *Al-K-Mn* particles are similar to those found in the cooling chimney and samples of the three ores. Stronger signals for $^{23}Na^{+}$ and $^{39}K^{+}$ were found in the ambient particles, while the chimney and ore particles produced a stronger signal for $^{55}Mn^{+}$. In the negative mode, ambient *Al-K-Mn* particles appear to contain more nitrate and chloride, while the chimney and ores samples produced stronger signals for aluminium oxides $^{43}AlO^{-}$ and $^{60}AlO(OH)$ (or SiO_2^{-}/CO_3^{-}) and oxygen. Ambient *Al-K-Mn* particles contained fluoride ($^{19}F^{-}$), which was only found in the firing chimney samples.

Ambient *Mn-K-Fe* particles are similar to *Mn-K-Al* particles which were unique to the ore samples. *Mn-K-Fe* are dominated by $^{55}Mn^{+}$ and also produce a strong signal for $^{56}Fe^{+}$. Ambient *Mn-K-Fe* particles show a larger peak for sodium, while ore sample particles appear to contain more Al. Variability in ATOFMS signal intensity may account for this difference as the ambient particles are unlikely to have undergone much processing beyond resuspension (certainly no exposure to high temperatures as for the chimney particles).

Despite being dominated by $^{55}Mn^{+}$, *Mn* particles did not match any found in the industrial filter or ore samples. It is possible that matrix effects suppressed the signals of K, Na, Al or Fe (though unlikely as K and Na in particular are usually the suppressors) but the temporal profile, discussed later, was very different to the other three Mn classes. A second source of Mn may thus have influenced the site. Manganese is essential to photosynthesis (Gavalas & Clark, 1971; Johnson et al., 2013), and while particles with biological origins have been identified by single particle mass spectrometry none of these appeared to contain manganese. Manganese has to date been identified by this technique as a component of soil (Silva et al., 2000) or industrial emissions (Snyder et al., 2009; Taiwo et al., 2014b; Zhai et al., 2015). Markers for biological particles include internally mixed $^{39}K^{+}$, $^{26}CN^{-}$ and $^{79}PO_3^{-}$; due to the poor quality of the negative mass spectra obtained during this campaign detection of these markers was limited and the presence of biological particles could not be confidently confirmed. However, their occurrence during the campaign remains a possibility, given the surrounding agricultural areas and large national park to the southwest.

V-rich

Two V-rich particle classes were identified, together accounting for 1% of total ATOFMS particles ionised (of which the *V-Fe* class was the main contributor); average mass spectra are shown in Figure 3.17. $^{51}V^+$, $^{67}VO^+$, $^{56}Fe^+$, $^{58}Ni^+$ and sulfate ($^{97}HSO_4^-$) are typical markers for particles emitted by ships or oil refineries (Ault et al., 2009; Healy et al., 2009) and are present in both V-rich classes. Both classes are dominated by sulfate in the negative mass spectra, while *V-Fe* particles also produced strong signals for nitrate. Weak signals for C_n are evident in both negative and positive mass spectra. *Na-V* particles are distinctive for the dominant $^{23}Na^+$ signal.

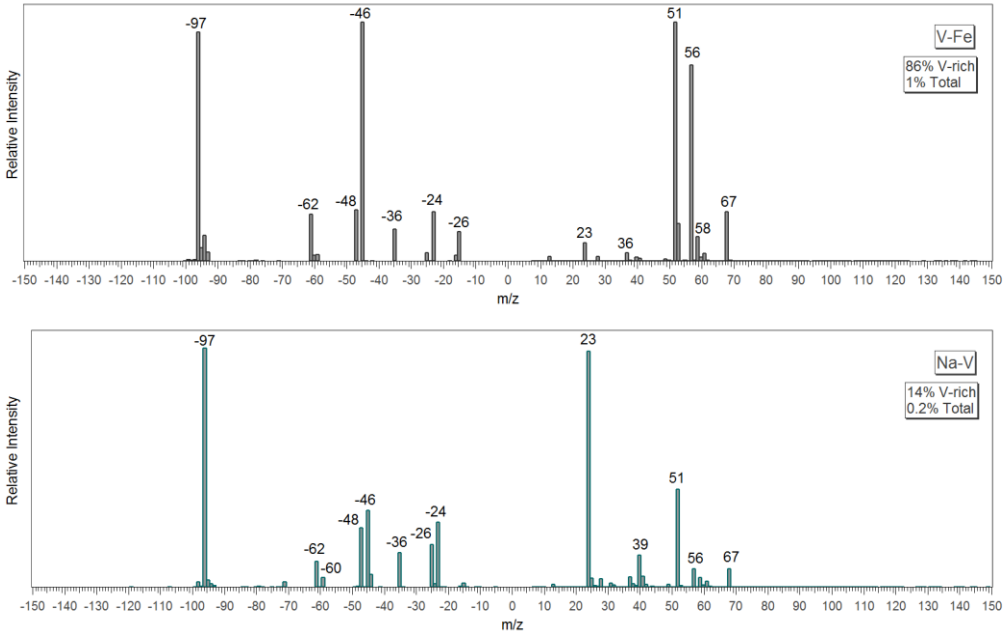


Figure 3.17. Average mass spectra for V-rich particles observed during NANO-INDUS.

The ratio of V to Ni in residual fuel oil is ~2.5 (Murphy et al., 2009), however only small signals for Ni have been seen in shipping/oil combustion single particles (Ault et al., 2009; Healy et al., 2009) indicating low sensitivity of the ATOFMS for this species. Internally mixed sodium, potassium, calcium, vanadium, nickel and iron particles have also been observed in ship exhaust particles using off-line TEM-EDS and two-step laser mass spectrometry (Moldanová et al., 2009).

Others

Pb and *Li-Zn* particles accounted for 1% and 0.1% of total ATOFMS particle ionised and based on SEM-EDX analysis of the chimney filter samples, which showed that ~33% and 3% of particles contained Zn and Pb respectively, these two particle classes could originate from the smelting chimney. However, the ATOFMS only detected Pb in the firing chimney samples. Average mass spectra for these classes are shown in Figure 3.18.

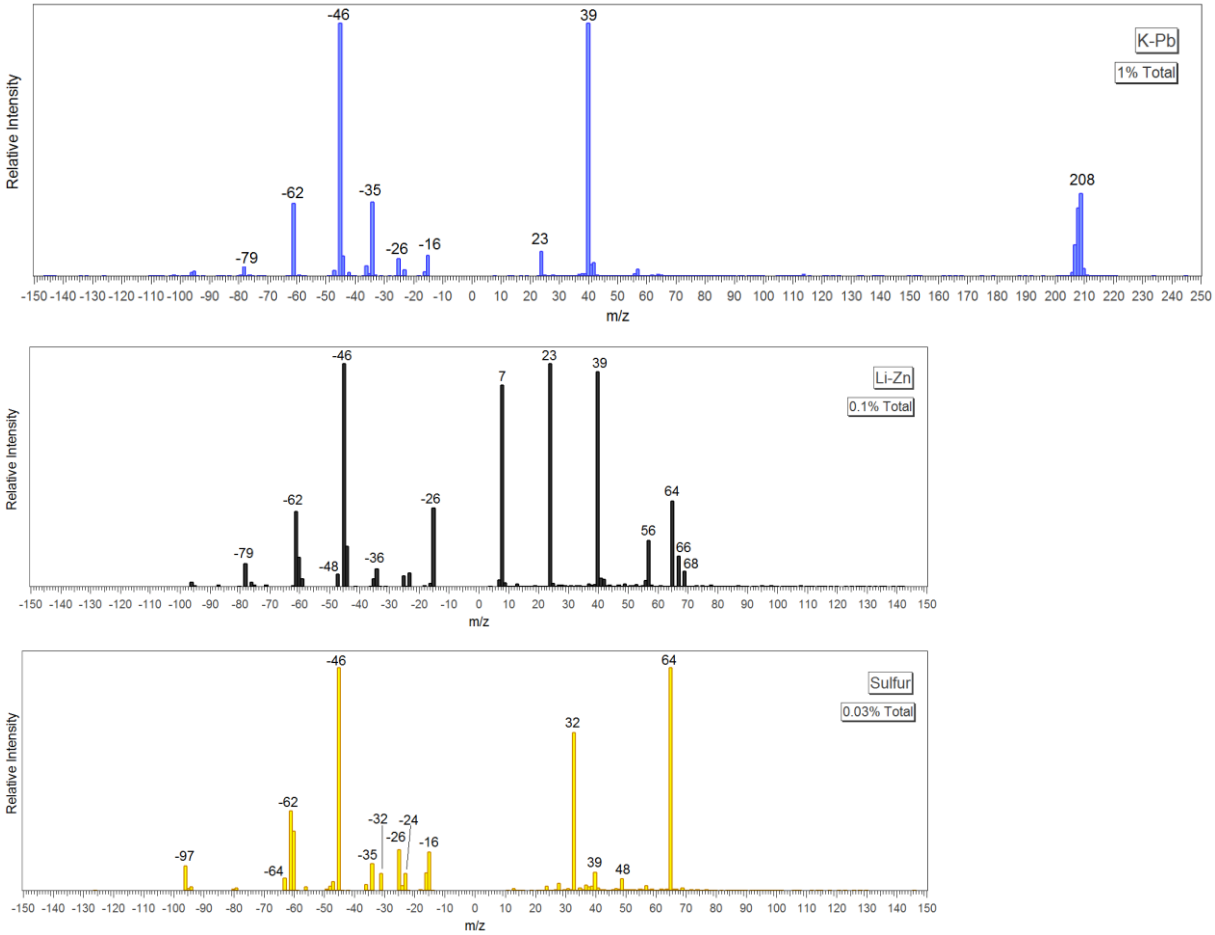


Figure 3.18. Average mass spectra of K-Pb, Li-Zn and Sulfur particles observed during NANO-INDUS.

Ambient *Pb* particles are characterised by $^{39}K^+$, $^{23}Na^+$, $^{208}Pb^+$, $^{35}Cl^-$ and nitrate. Pb-containing particles similar to the *Pb* class found during NANO-INDUS were observed in the vicinity of the Port Talbot steelworks, where they accounted for 0.6% of all particles ionised and were associated with the hot and cold mills (Dall'Osto et al., 2008). Those Pb-containing particles were also found mixed with KCl, which was the case for ~9% of NANO-INDUS *Pb* particles. A very small proportion of firing chimney filter particles contained Pb (0.8%); the same particles also contained Mn and Ca, thus it is likely that most of the ambient *Pb* particles originated from the steelworks.

Li-Zn particles contain $^{7}Li^+$, $^{64,66,68}Zn^+$, $^{56}Fe^+$, potassium, sodium, nitrate, phosphate and some EC. Particles containing lithium have been previously associated with coal combustion (Guazzotti et al., 2003; Furutani et al., 2011), but these contained more EC. Zn particles were also associated with the Port Talbot steelworks, but these particles did not contain Li. No Zn particles were found in single particle mass spectra of the chimney filter or ore samples, despite SEM-EDX analysis confirming its presence.

Sulfur particles are characterised by peaks for positive and negative elemental sulfur ions, ^{32}S and $^{64}S_2$, as well as weaker signals for $^{39}K^+$ and positive and negative EC ion

fragments. Nitrate ($^{46}NO_2^-$, $^{62}NO_3^-$) dominates the negative mass spectrum, with smaller signals for sulfate ($^{97}HSO_4^-$), organic nitrogen ($^{26}CN^-$), chloride ($^{35}Cl^-$) and oxygen ($^{16}O^-$) also present. Similar particles were found associated with either a slag granulation or an open-pit slag process carried out at the Port Talbot steelworks by Dall'Osto et al. (2012). Elemental sulfur-containing particles have also been detected in several marine environments (Gaston et al., 2015), where they were seen as indicators of reduced sulfur compounds, such as hydrogen sulfide, products of the biogenic marine sulfur cycle which also produces DMS. However these particles also contained inorganic ($^{23}Na^+$, $^{24}Mg^+$, $^{39}K^+$, $^{40}Ca^+$) and organic markers ($^{27}C_2H_3^+$, $^{43}C_2H_3O^+$), most of which were not present in the *Sulfur* particles. Another unique feature of the majority of the marine sulfur particles was a lack of negative ion spectra, indicating the presence of particle-phase water which suppresses negative ion formation. Only 1% of *Sulfur* particles produced negative mass spectra and while the negative ion detector was likely responsible for most of this issue it is not unusual to observe negative ion suppression in ambient single particle measurements.

Two amine-containing particle classes were identified; *K-Amines*, characterised by $^{39,41}K^+$ and indicative of biomass burning or possibly industrial emissions given the detection of *K-Cl* particles, and *EC-Amines*, characterised by $^{12,36}C_n^+$ fragments and indicative of fossil fuel combustion sources. Both classes produced marker ions for trimethylamine (TMA, $^{59}(CH_3)_3N^+$,), protonated dimethylamine (DMA, $^{46}(CH_3)_2NH_2^+$), and $^{86}C_3H_7NHC_2H_4^+/(C_2H_5)_2NCH_2^+$, associated with triethylamine (TEA) and dipropylamine (DPA) or an adduct ion in diethylamine (DEA).

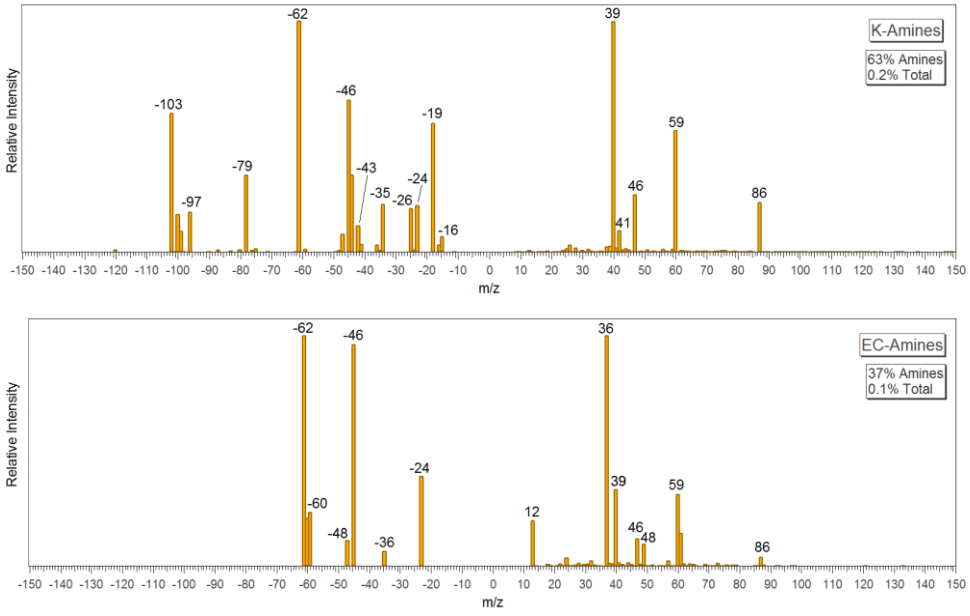


Figure 3.19. Average mass spectra for Amines particle classes observed during NANO-INDUS.

TMA was the most abundant alkylamine marker ion, while DMA has been unidentified in other ATOFMS datasets to the best of this author's knowledge. A comparison of ATOFMS datasets obtained in Cork, Paris, Zurich, and those obtained for NANO-INDUS and ADRIMED/SAF-MED found this ion only in the latter two datasets (Healy et al., 2014).

This study queried several European ATOFMS datasets for alkylamines, including those mentioned above. For Dunkirk, four types of amine-containing particles were identified which contributed 1.3% to total ATOFMS particles ionised, considerably more than the two amine-containing classes identified here from the general clustering approach. As well as TMA, DMA and DEA/TEA and DPA, other characteristic ions for TEA (*m/z* 101), DPA (*m/z* 102), DPA and tripropylamine (TPA) (*m/z* 114) and a photo-oxidation product of TEA (*m/z* 118) were observed. Close inspection of the mass spectra in these clusters revealed many to be of poor quality, where the afore-mentioned ions were the only peak in the mass spectrum. This was also observed for almost every *m/z* from 100-300, and most of these spectra were grouped into the "poor positive spectra" particle class. The only particles with mass spectra of sufficient quality to allow confident identification of alkylamines resulted in the *K-Amines* and *EC-Amines* classes.

Sulfate ($^{97}HSO_4^-$), nitrate ($^{46}NO_2^-$, $^{62}NO_3^-$), phosphate ($^{79}PO_3^-$), fluoride ($^{19}F^-$), chloride ($^{35}Cl^-$), aluminium oxide ($^{43}AlO^-$) and aluminosilicate ($^{103}AlSiO_3^-$) ions were found in the negative mass spectra of *K-Amines* and nitrate and EC fragments in *EC-Amines*, however only 6% and 10% of these particles actually produced negative mass spectra. The average negative mass spectra should therefore not be considered representative of all particles in these classes.

3.3.4 Particle Sources

Figure 3.20 shows the temporal trends for the general ATOFMS particle categories observed during the campaign. Sea salt particles dominated (23% of total particles with mass spectra), followed by K-rich and EC particles (22% each). Sea salt particles contributed more to particle number during certain periods than K-rich or EC, suggesting influence from marine air masses. Particles with poor positive spectra (16%), and therefore no markers for source identification, have been included in this analysis as their temporal profile is distinctive and coincides with that of other particle classes (e.g. amines) at certain times. Most Fe-rich (5%), OC and PAH particles (2%), Ca-rich (2%), Mn-rich (1%) and Pb (1%) particles were observed between 25-27th May and on 2nd June, and are associated with specific industrial sources. K-rich, EC and poor positive spectra

particles also peaked noticeably on the 25th, 26th and 27th May, also suggesting some industrial sources. However at other times their temporal profile is more indicative of transported particles. V-rich (1%) and Zn, Sulfur and Amines (0.4% combined) particles are discussed in further sections. Wind speed appeared to have an effect on ATOFMS particle numbers, with the period of highest wind speed (8-10th June) associated with lowest particle numbers. North-easterly winds were strongly associated with industrial emissions (ferromanganese facility and steelworks), while the longest period of north-westerly winds (21-23rd May) coincided with a prolonged increase in EC particle numbers.

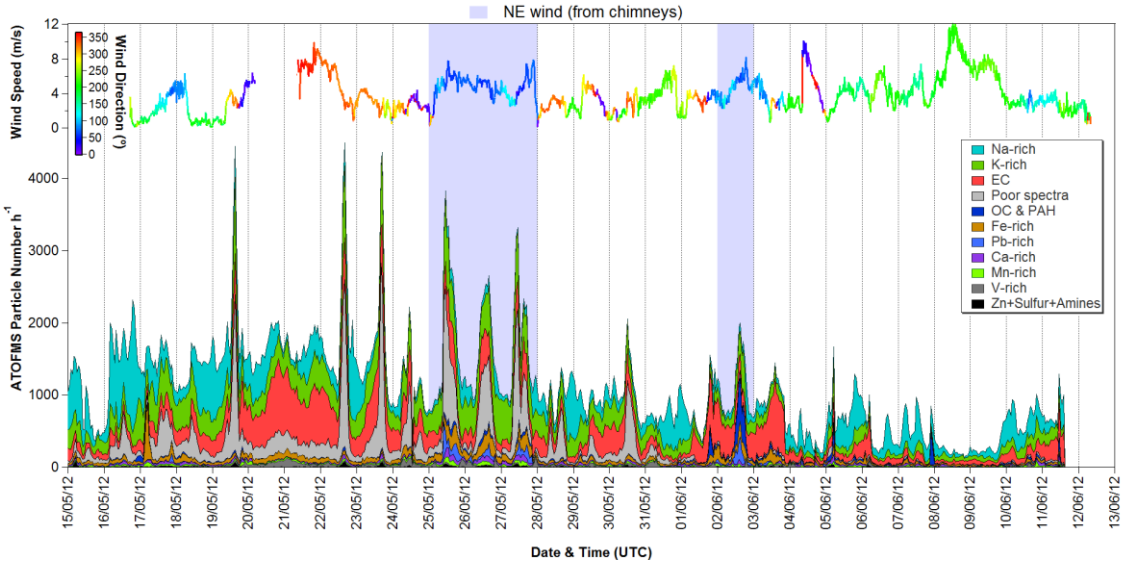


Figure 3.20. Time series (stacked) of hourly unscaled particle numbers for ATOFMS particle categories and wind speed coloured with wind direction during NANO-INDUS.

Hourly size distributions for all ATOFMS particles with mass spectra are shown in Figure 3.21. Highest particle numbers were found between 300-500 nm on 19th, 22nd, 25th, 26th and 27th May. The latter three days and the 2nd June were identified as periods most likely to transport ferromanganese facility and steelworks emissions to the site; most ATOFMS particles were less than 1 μm in diameter on these days. A bimodal distribution is apparent on several days and is a result of an external mixture of sea salt and urban/industrial emissions. Days where mostly submicron particles were observed coincide with days where sea salt was detected, as well as a small fraction of large industrial particles.

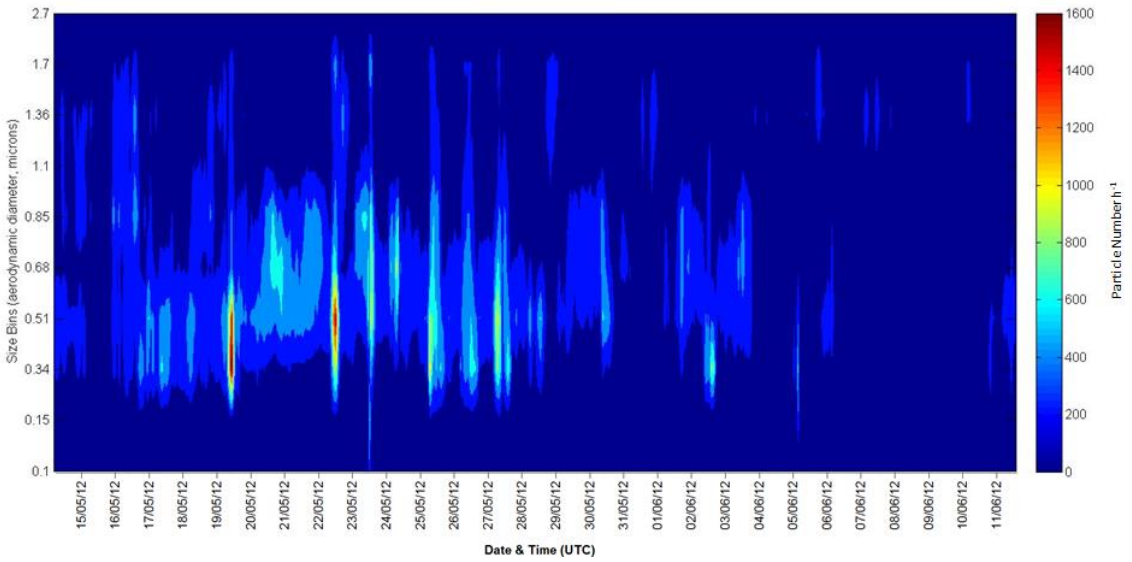


Figure 3.21. Hourly size distribution for all ATOFMS particles observed during NANO-INDUS.

Size distributions for the ATOFMS particle categories can be found in Figure 3.22. The majority of ATOFMS particles were found in the 400-900 nm size range, consistent with the transmission efficiency of the aerodynamic focusing lens. Sea salt particles were noticeably larger, with most found in the supermicron range. Most of the metal-rich industrial particles were also found in the 400-900 nm range.

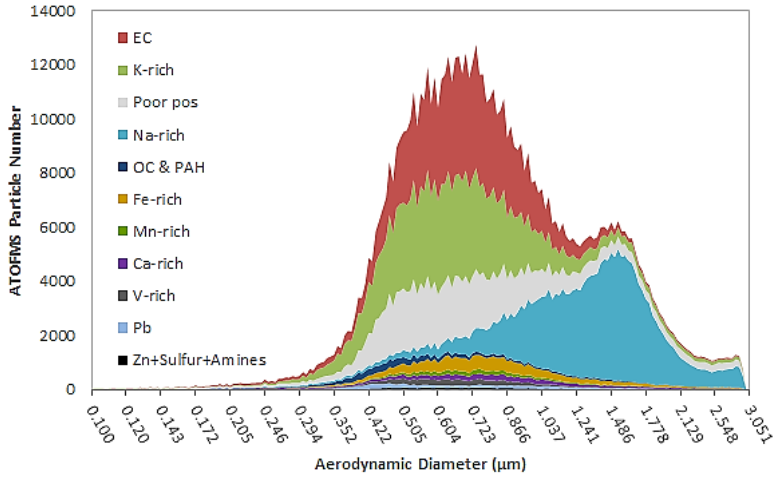


Figure 3.22. Size distributions (stacked) of ATOFMS particle categories observed during NANO-INDUS.

Figure 3.23 shows hourly mass concentrations for $PM_{2.5}$, AMS species, BC and total ATOFMS particles (AMS and aethalometer data was analysed by Ari Setyan, ULCO-LPCA). Inorganic species accounted for ~2/3 of the total submicron mass detected by the AMS, while the organic fraction accounted for the remaining ~1/3. Sulfate (SO_4), nitrate (NO_3), ammonium (NH_4) and organics account for most of the $PM_{2.5}$ mass as measured by the beta gauge. During NE wind periods, the contribution of nitrate increased, while that of sulfate decreased. BC and non-refractory chloride (Cl) concentrations also increased during these periods (up to ~5 $\mu g/m^3$ each).

ATOFMS total mass concentrations were in good agreement with $PM_{2.5}$ (R^2=0.6) and total AMS (R^2=0.7) mass concentrations for most of sampling period. Organics and NH_4 in particular correlated well with ATOFMS mass; R^2 of 0.67 and 0.61 respectively.

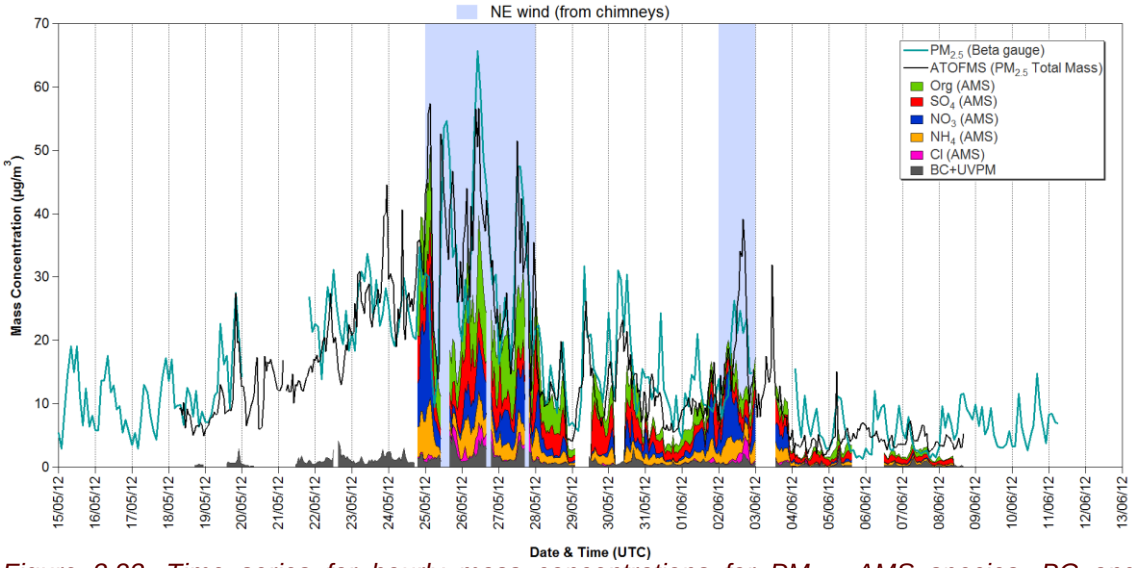


Figure 3.23. Time series for hourly mass concentrations for $PM_{2.5}$, AMS species, BC and ATOFMS during NANO-INDUS.

Figure 3.24 shows hourly reconstructed ATOFMS mass concentrations for the particle categories. Most of the ATOFMS mass was accounted for by K-rich (24%) and EC (23%) particles. Na-rich classes contributed 10% of ATOFMS mass, Fe-rich 10%, Ca-rich 4%, V-rich 4%, Mn-rich 3%, OC and PAH 3%, Pb-rich 3% and Zn, Sulfur and Amines combined 0.4%. K^+ is readily ionised by the ATOFMS desorption/ionisation laser so its prevalence in these particles is not representative of its mass concentration. Considering the AMS data it is likely that these particles are composed of more organics, SO_4, NO_3 and NH_4 than the ATOFMS mass spectra indicated. While the AMS provides quantitative composition of the particles, the ATOFMS yields marker ions that can be used for source identification.

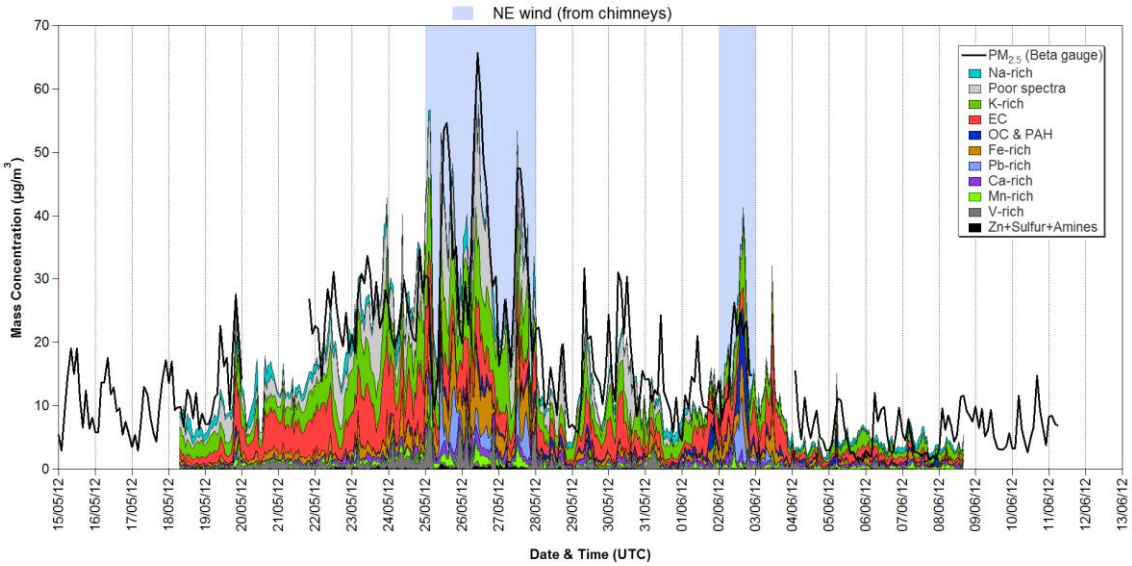


Figure 3.24. Time series for hourly reconstructed ATOFMS mass concentrations for the particle categories during NANO-INDUS.

Figure 3.25 shows the comparison of ATOFMS mass concentrations with PM_1, $PM_{2.5}$ and PM_{10} mass obtained from the 13-stage impactor (impactor data was analysed by Saliou Mbengue and Laurent Alleman, ULCO-LPCA). ATOFMS mass concentrations correlated strongly with all impactor fractions (R^2 = 0.81, 0.82 and 0.84 for PM_1, $PM_{2.5}$ and PM_{10} respectively). ATOFMS mass was consistently less than that of the $PM_{2.5}$ - fraction, and frequently less than that of PM_1. Removal of periods without data when calculating the average for ATOFMS and AMS mass concentrations, as well as being unable to calculate that average for precisely the same sampling period as the impactor may account for the difference in concentrations.

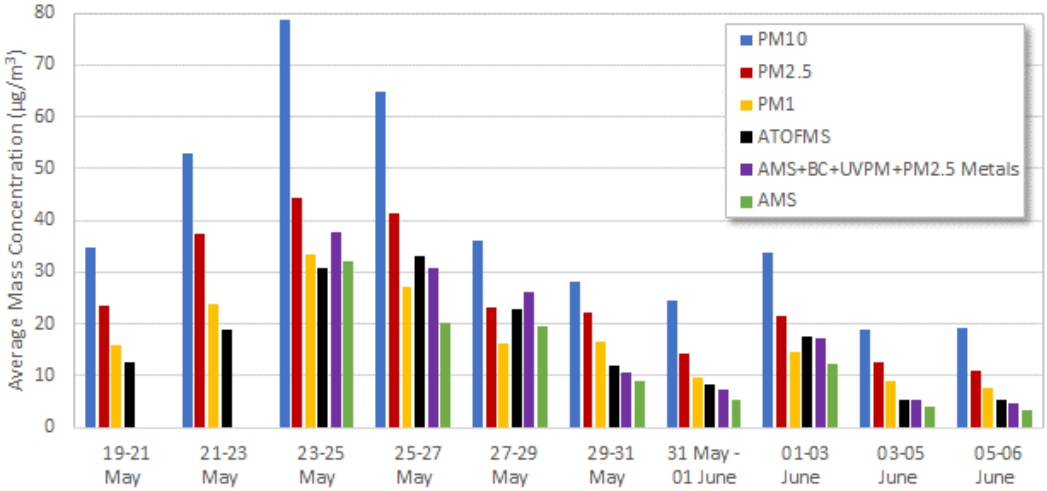


Figure 3.25. Comparison of average mass concentrations for PM_{10}, $PM_{2.5}$, PM_1, ATOFMS, AMS, BC and metals during NANO-INDUS.

Elemental composition of the $PM_{2.5}$ fraction, determined by ICP-MS (analysed by Saliou Mbengue and Laurent Alleman, ULCO-LPCA)., can be found in Figure 3.26. Fe, Mn, Ca, Al, K, Na, Mg and Zn account for most of the elemental mass in this fraction (97%). Their mass concentrations (also Pb, Cu, Ti, Ba, Rb, and Sr) increased significantly

between 25-27th May and 1-3rd June, the periods with largest metallurgical industry influence.

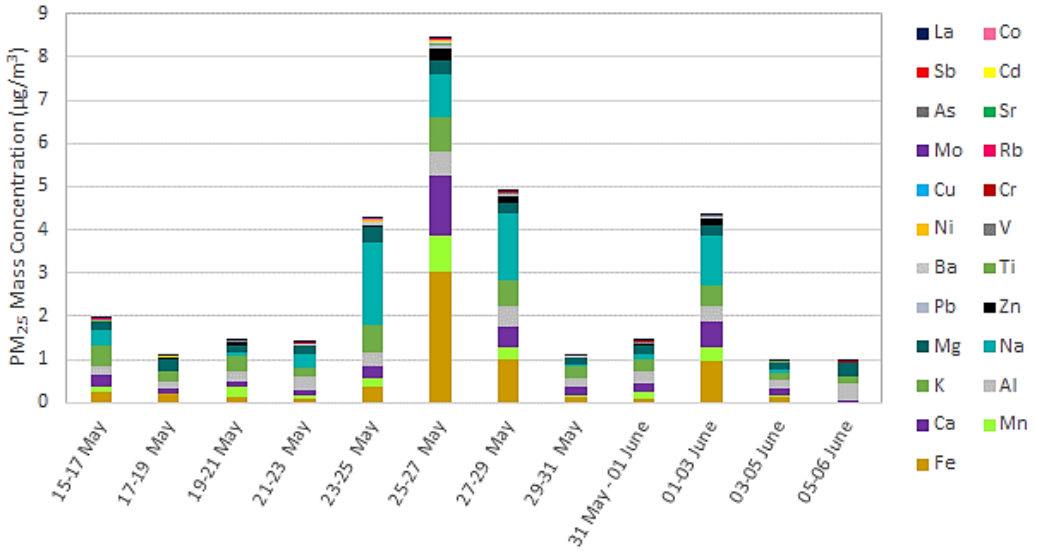


Figure 3.26. Mass concentrations of metals in $PM_{2.5}$ analysed by ICP-MS during NANO-INDUS.

Marine

Time series of particle numbers for classes from marine emissions (*Sea salt*, *Na-Mg*, *Na-EC*) are shown in Figure 3.27. Maximum *Sea salt* particle numbers were observed during a period of air masses from the North Atlantic (15-18th May). Numbers for this class generally increased when K-rich or EC particle numbers decreased and vice versa; this was particularly apparent when compared with the *EC-K* class which increased noticeably in number from 1-4th June (Figure 3.30).

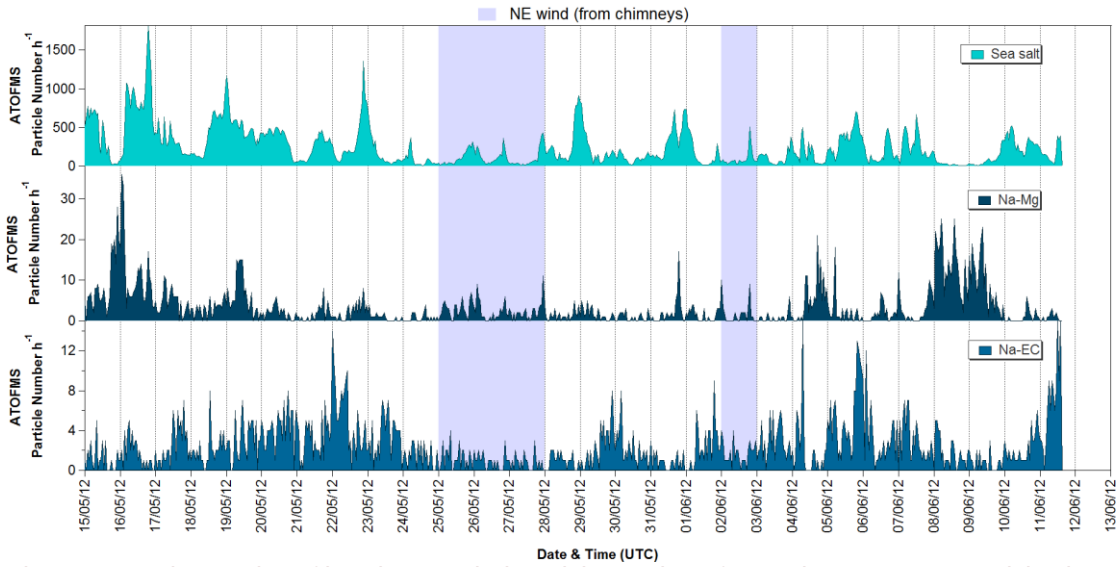


Figure 3.27. Time series of hourly unscaled particle numbers for marine ATOFMS particle classes during NANO-INDUS.

Na-Mg particles, although much less in number than *Sea salt* particles, appeared to increase during lows in *Sea salt* numbers (16th May, 8-10th June). This was also the only

particle class whose numbers noticeably increased during the period of highest wind speed (8-10th June). Wind speed and direction dependences for the Na-rich classes are shown in Figure 3.28. *Na-Mg* particles exhibit a clear dependence on south-westerly winds with speeds of 10-14 m/s. Highest numbers for *Sea salt* particles were found at low wind speeds (< 2 m/s), with lower numbers also seen from the north and north west (direct marine source) and the south and east (mixing of marine air masses with those influenced by local anthropogenic emissions). Numbers for *Na-EC* particles were low, but a strong north-westerly dependence was found, with a weaker dependence on the south-east sector (urban).

Na-EC particles were few and generally tracked the temporal profile of sea salt particles. Their wind dependence also coincides with the moderate (4-6 m/s) north-westerly and south-easterly wind dependence of *Sea salt* particles. This suggests two different sources, which their size distribution supports (Appendix II, Figure 8.11).

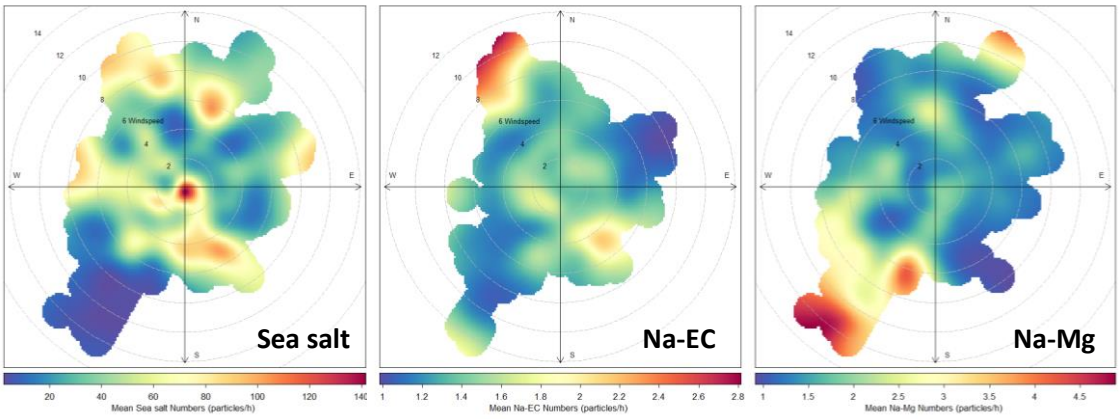


Figure 3.28. Wind speed and direction dependences of mean particle numbers for marine ATOFMS particle classes during NANO-INDUS.

Particle size for *Na-EC* particles varied considerably throughout the campaign, with the smallest particles seen around 150 nm on 5th June, while a few hours later an accumulation of supermicron particles was detected. Previous studies have associated *Na-EC* particles with incineration emissions (Moffet et al., 2008b) or identified them internally mixed sea salt and EC (Holecek et al., 2007); both a combustion and processed marine source seem possible given the distribution here. A typical size distribution for sea salt particles analysed by ATOFMS was found (Figure 8.9), with a peak aerodynamic diameter of 1.5 µm, while *Na-Mg* particles were larger with a peak aerodynamic diameter of 2 µm. Some Mg-containing particles were found by both ATOFMS and SEM-EDX in the industrial filters and the ores. However, the fraction of particles analysed by ATOFMS which contained Mg was small and they also contained Ca and Al, which the ambient *Na-Mg* particles did not. An industrial source could have been possible though on the 5th June,

where a concentration of *Na-Mg* particles around 300 nm was seen. Mg-rich particles of marine biological origins similar to *Na-Mg* particles were found to peak around 1.6 µm (Dall'Osto et al., 2005) and less than 500 nm (Gaston et al., 2011). They were also found to contribute to 60% of submicron ATOFMS particle number during the "clean" periods when they were detected (Dall'Osto et al., 2005). *Na-Mg* particles made no such contribution to particle number at any point in the campaign, indicating that at least for this sampling period marine biological emissions did not heavily impact the site. The enhancement of Mg-rich particles in smaller sizes depends on conditions that affect the formation of this class such as wind speed (Gaston et al. 2011).

Mass concentrations for *Na-Mg* particles were compared with those for Mg in the $PM_{2.5}$ fraction analysed by ICP-MS (from 48 hour filters, ATOFMS data binned and averaged to best match the sampling times), shown in Figure 3.29. Mass concentrations for ATOFMS *Na-Mg* particles were consistently lower than the average Mg mass in $PM_{2.5}$, indicating that either the density used for mass conversion was too low or that *Na-Mg* particles were under-detected. The latter seems more likely as the ATOFMS transmission efficiency for supermicron particles is significantly poorer than for 500-700 nm particles, and from the observed size distribution of this particle class, it is clear that they were at the edge of the ATOFMS size range.

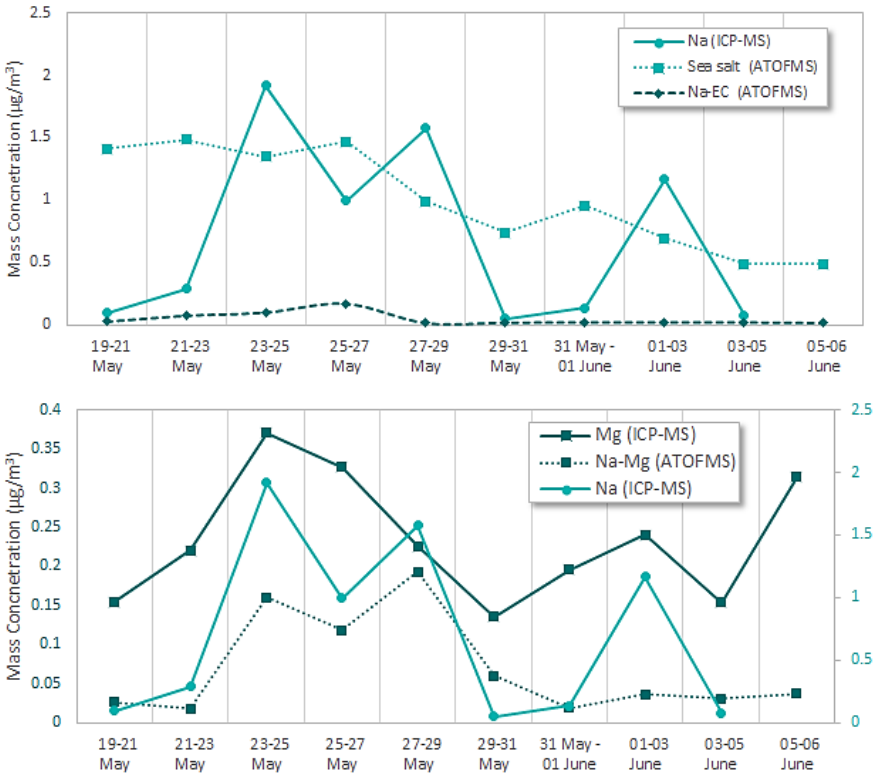


Figure 3.29. Time series of average mass concentrations for $PM_{2.5}$ Mg and Na (ICP-MS) and ATOFMS Na-rich particles during NANO-INDUS.

Correlation between Mg and ATOFMS *Na-Mg* particles is poor ($R^2 = 0.25$), but a stronger correlation was found between ATOFMS *Na-Mg* particles and $PM_{2.5}$ Na ($R^2 = 0.7$) measured by ICP-MS. $PM_{2.5}$ Na and Mg also correlate moderately ($R^2 = 0.55$). It is possible that *Na-Mg* particles detected by ATOFMS contain more Na and less Mg in terms of mass than the signal intensities indicate. Average mass concentrations for the *Sea salt* and *Na-EC* classes were also compared with $PM_{2.5}$ Na concentrations. Correlations were poor, with R^2 of 0.11 and 0.17 for *Sea salt* and *Na-EC* compared to Na concentrations. The correlation did not improve when Na concentrations were compared with ATOFMS Na-rich particles. Given this observation, and that 17% of sea salt particles produced negative ion signals for nitrate (this was likely a minimum and that there was more that was not detected), it seems likely that Na was a smaller component by mass of sea salt particles detected by ATOFMS than the ion signal intensities suggested.

Transported/Urban

Time series of particle numbers for classes (*K, EC-K, EC-K-amm-nit, EC-amm-nit, EC-Ca*) attributed to urban emissions is shown in Figure 3.30. These classes did not display any clear peaks during the 3-day event. K is usually a marker for biomass burning, however the steelworks neighbouring the sampling site is known to produce significant amounts of KCl particles (Hleis et al., 2013). *K-Cl* particles were identified in the ATOFMS dataset but this relied on negative ions ($^{35}Cl^-$) which were not generated for every particle due to the negative ion detector issue. It is therefore likely that more of the *K* class should be apportioned to an industrial source.

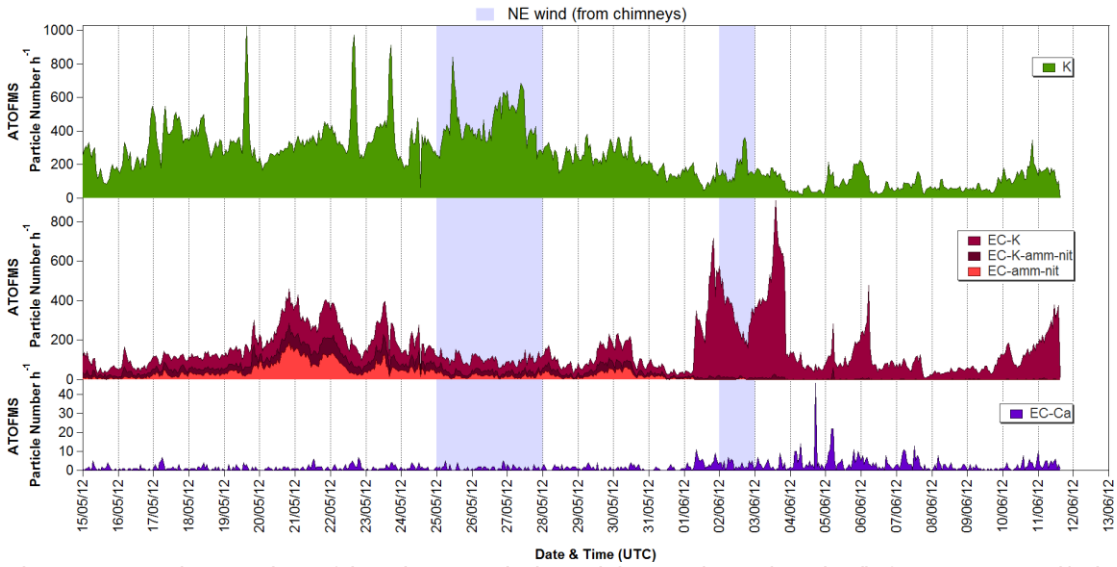


Figure 3.30. Time series of hourly unscaled particle numbers (stacked) for transported/urban ATOFMS particle classes during NANO-INDUS.

The *K* class displayed a diffuse wind direction dependence (Figure 3.31); highest numbers were seen from the north-west with 8-12 m/s winds, with only slightly fewer numbers detected from the north-east.

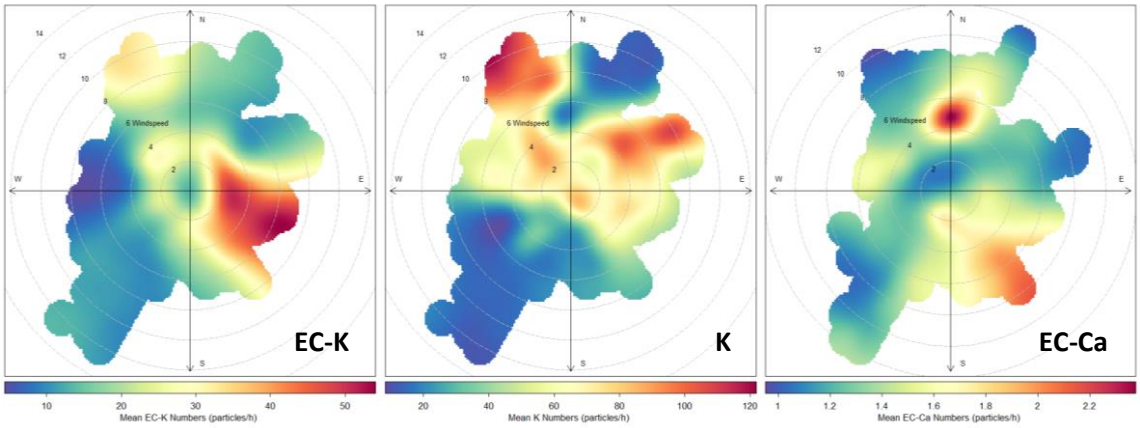


Figure 3.31. Wind speed and direction dependences of mean particle numbers for major transported/urban ATOFMS particle classes during NANO-INDUS.

In terms of size (Appendix II, Figure 8.10), highest particle numbers were found in the range 300-600 nm. The largest *K* particles were between 1-2.5 µm and observed during brief periods (a few hours on 22nd, 23rd and 25th May), but only accounted for a small fraction of all *K* particles. *K* particles in the range 300-600 nm probably originated from biomass burning, as particles with clear industrial sources (discussed in the next section) were slightly larger. However fresh local emissions were thought to be negligible in Dunkirk at this time of year and no biomass burning organic aerosol (BBOA) factor was resolved by the AMS.

Transport of regional aged biomass emissions then seems a more likely source of some of the *K* particles observed. Aged or oxidised OC is typically resolved as OOA (oxidised organic aerosol), SV-OOA (semi-volatile OOA) or LV-OOA (low volatility OOA). Aged biomass burning emissions would be likely to produce one of these factors. Mass concentrations for the *K* class, as well as the *EC* class, are compared with those of the AMS OOA-II factor in Figure 3.32. A strong correlation between the *K* class and the OOA-II factor ($R^2 = 0.69$), as well as a moderate correlation with AMS NH_4 ($R^2 = 0.53$) supports this conclusion. The *EC* class correlates moderately with both OOA-I ($R^2 = 0.48$) and OOA-II ($R^2 = 0.48$) factors, and strongly with all organics measured by the AMS ($R^2 = 0.67$), suggesting multiple sources of OA contributed to the ATOFMS *EC* particle class.

It is evident from Figure 3.32 that organics were a major component of *K* and *EC* particles, and that the EC ions functioned more as source markers than providing information on mass composition; correlation between *EC* particles and BC was poor ($R^2 = 0.22$). Correlations were poorer when AMS organics mass concentrations were compared with

those for all EC classes combined (R^2 = 0.47) but stronger correlations were found with the combined EC classes and AMS NO_3 (R^2 = 0.63) and NH_4 (R^2 = 0.72), indicating distribution of these species across all ATOFMS EC particles, as well as some atmospheric processing.

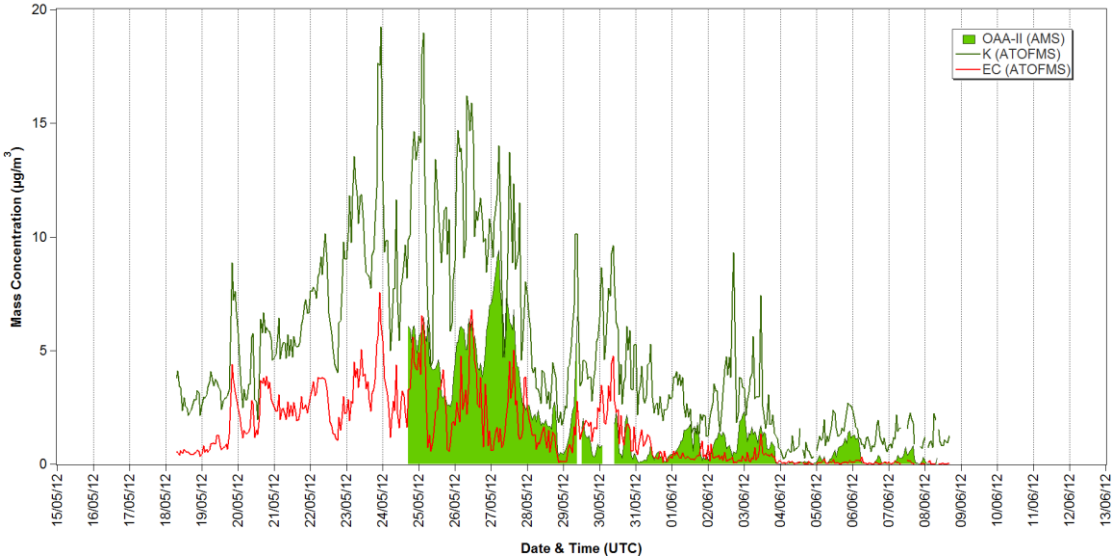


Figure 3.32. Time series of hourly mass concentrations for the AMS OOA-II factor and ATOFMS K and EC particle classes (stacked to compare possible mass contribution of OC).

Average $PM_{2.5}$ K mass concentrations, as analysed by ICP-MS, peaked during the 3-day event (Figure 3.33), indicating industrial sources. Average mass concentrations for the K-rich particles were in good agreement with those for $PM_{2.5}$ K, with R^2 of 0.64, 0.7 and 0.69 for *K*, *Na-K* and *K-Al* particles respectively. From Figure 3.32 it is apparent that ATOFMS *K* particles contain an aged OA component, probably associated with biomass burning. The average mass concentration for ATOFMS *K* particles is a factor of ~9 larger than that of $PM_{2.5}$, so while the strong correlation suggests an industrial contribution, the difference in mass concentrations supports a larger contribution to mass from a component such as OA.

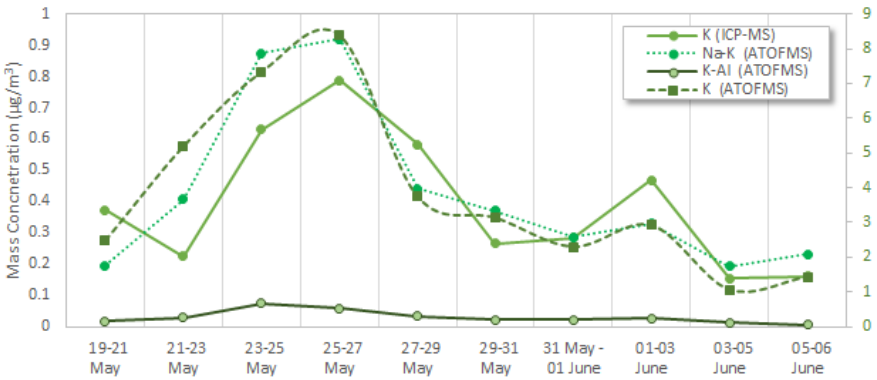


Figure 3.33. Time series of average mass concentrations for $PM_{2.5}$ K (ICP-MS) and ATOFMS K-rich particles during NANO-INDUS.

For *Na-K* particles a stronger correlation with $PM_{2.5}$ K rather than Na ($R^2 = 0.5$) suggests that, despite relatively similar signal intensities for the two ions in the mass spectra, K is a more significant component of these particles than Na. Also the correlation between $PM_{2.5}$ K and Na indicates that they have similar industrial sources, so any poor correlation between ATOFMS particles and these species should not be a result of different sources (marine versus industrial) but rather a function of composition.

Temporal profiles for *EC* particles which produced signals for $^{30}NO^+$ (indicative of ammonium nitrate) were noticeably different to that of *EC-K* particles. Profiles for *EC-amm-nit* and *EC-K-amm-nit* are similar to that of the *EC* class, with particle numbers accumulating from 19-23rd May, a period characterised by local 8-10 m/s north-westerly winds class (Figure 3.35) and influenced by relatively slow moving air masses over northern France and the English Channel. No clear peaks were seen during the 3-day industrial event, possibly indicating more ammonium nitrate had partitioned to particles regionally transported during periods of north-westerly winds. *EC-amm-nit* and *EC-K-amm-nit* particles virtually disappeared after the 1st June, at which point *EC-K* particles dominated. Wind dependences for *EC-amm-nit* and *EC-K-amm-nit* particles were identical to those for the *EC* class (Figure 3.35), but in contrast *EC-K* particles depended strongly on south-easterly winds (ranging from 2-8 m/s) (Figure 3.31), indicating urban emission sources. *EC-amm-nit*, *EC-K-amm-nit* and *EC-K* particles were found in similar size ranges to *EC* particles, with a peak diameter of 740 nm, indicative of aged particles.

Particles attributed to traffic emissions, *EC-Ca*, only constituted a small fraction of the ATOFMS dataset (0.2% of total numbers, 1% of total mass). This is partly due to the lower transmission efficiency for particles less than 200 nm in diameter, the range where most traffic particles are detected. However, traffic particles contributed ~50% of the mass between 150-300 nm, as analysed by the same ATOFMS in Paris (Healy et al., 2012b), so significant quantities of traffic particles can be detected by this instrument. The *EC-Ca* particle size distribution was typical of that for traffic emissions detected by ATOFMS, with most particles in the range 100-300 nm and a peak aerodynamic diameter of 270 nm (Figure 8.9). No diurnal variation in particle number typical of local traffic emissions was seen and the highest number of particles was found with northerly winds of moderate speeds (4-6 m/s) (Figure 3.31), suggesting the sampling site was mostly influenced by very local industrial vehicular traffic. The wind rose also shows a weaker contribution from the urban sector (south-east), so urban traffic made a small contribution at the site.

Transported/Local Industrial

Time series of particle numbers for classes (*EC, Poor positive spectra, K-Amines, EC-Amines, Na-K*) with a mixture of urban and industrial sources are shown in Figure 3.34. Possible industrial sources for these classes were likely based on the distinctive peak in particle number on the 25th, 26th and 27th May, previously identified as the period most strongly influenced by industrial emissions (followed by the 2nd June). The *EC* class was the only one dominated by EC which displayed an industrial influence, and the lack of potassium indicates a fossil fuel combustion origin. Graphite flakes were observed in emissions from the steelworks (Flament et al., 2008) and given the detection of *EC* particles during the industrially influenced period it is possible that this facility contributed to their emission. Particle numbers also accumulated from 19-23rd May, a period characterised by local 8-10 m/s north-westerly winds and influenced by relatively slow moving air masses over northern France and the English Channel. Transported regional aerosol therefore seems likely; this extended peak in *EC* numbers coincides with a peak in *V-Fe* particles, indicative of heavy fuel oil combustion from shipping or refineries. The wind dependence for *EC* particles, as shown in Figure 3.35, confirms the strong north-westerly sector influence, as well as the weaker north-easterly one. The size distribution (Appendix II, Figure 8.12) shows *EC* particles were relatively large, ranging from 300-1000 nm, with peak particle numbers around 700 nm. This further supports attribution of this particle class to transported aged aerosol. Lower numbers of supermicron *EC* particles were detected during the 3 day event, in an almost separate mode to the particles between 300-700 nm.

16% of all ATOFMS particles ionised produced poor quality positive mass spectra. These are usually excluded from data analysis, as no source markers can be identified. However, their temporal profile is very similar to that of *EC-Amines* and *K-Amines* (Figure 3.34), as well as coinciding with *EC* and *K* particles on 19th, 22nd and 23rd May, periods influenced by north-westerly wind. It is therefore likely that these particles represent more *EC-Amines, K-Amines, EC* and *K* particles, but without good mass spectra it is impossible to tell how many. Amines and particles with poor positive spectra were also present during the 3-day industrial event, suggesting they have industrial sources in common with *EC, K* and various metal-rich particles. Amines displayed a similar wind dependence to that of particles with poor positive spectra, with a strong influence from the north-east industrial sector and a weaker north-westerly influence as previously stated. The majority of particles with poor positive spectra were found in the 300-500 nm size range (Appendix II, Figure 8.11), with low numbers in the 1.3-2.5 µm range during short periods (22nd,

23rd, 25th, 27th May). Size distributions for *EC-Amines* and *K-Amines* have not been shown as they are virtually identical to that of poor positive spectra particles.

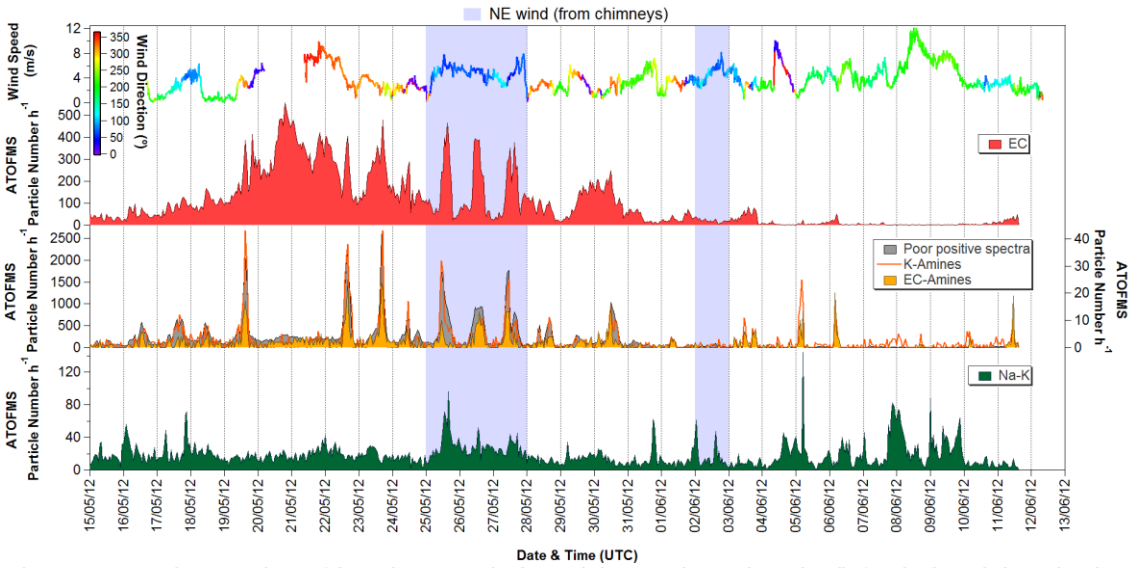


Figure 3.34. Time series of hourly unscaled particle numbers (stacked) for industrial and urban ATOFMS particle classes during NANO-INDUS.

Na-K particles were also present during the 3-day industrial event, but with less clearly defined peaks in particle number (Figure 3.34). Highest numbers were seen during periods of westerly winds (5-12th June), with lower numbers detected with north-easterly wind (3-day industrial event), as shown in Figure 3.35. Based on their composition these particles could have both marine and industrial sources.

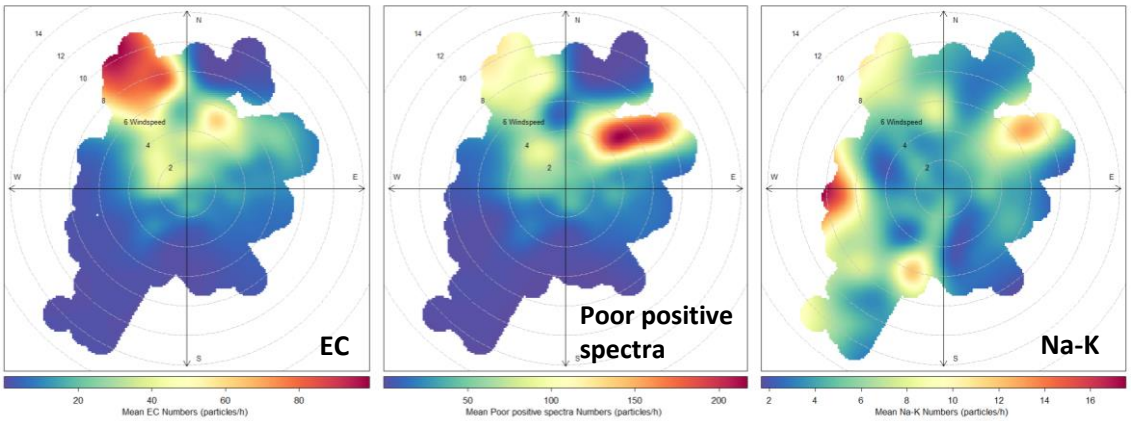


Figure 3.35. Wind speed and direction dependences of mean particle numbers for transported/local industrial ATOFMS particle classes during NANO-INDUS.

Their size distribution (Appendix II, Figure 8.11) indicates emissions from both. During the 3-day industrial event, particles ranged from 500-1000 nm in size, with numbers peaking around 700 nm. From 5-12th June, particles were clearly larger, ranging from 1-2.5 µm. Another much smaller mode was seen on the 5th June, at the same time as *Na-EC* particles, between 100-350 nm. While the composition of these classes is often indicative of marine emissions, their size suggests high temperature combustion sources.

Transported Industrial

Time series of particle numbers for classes (*Fe*, *Sulfur*, *Mn*, *Fe-EC*, *V-Fe*, *Na-V*) with industrial sources that do not peak during the 3-day industrial event are shown in Figure 3.36. The composition of these particles indicates industrial or non-urban origins, but their number did not peak during either of the two periods strongly influenced by industrial emissions. A large concentration of *Fe* particles was seen on the 17th May; the steelworks is the largest emitter of Fe in Dunkirk, however considering that *Fe* particles did not peak during periods where emissions from this facility were impacting the site a second source of Fe during this short period is more likely. A study of the Port Talbot steelworks (Dall'Osto et al., 2008) did not find any particles similar in composition to the *Fe* class, supporting the idea that another source was responsible for emitting these particles. However, it is surprising that with such a large Fe emitter close to the site, 30% of Fe-rich particles (represented by the *Fe* class) were not accounted for by this source. Other than this large peak, the temporal profile for the *Fe* class is very similar to that of *Mn*, *Fe-EC* and *V-Fe*, particularly from 19-23rd May.

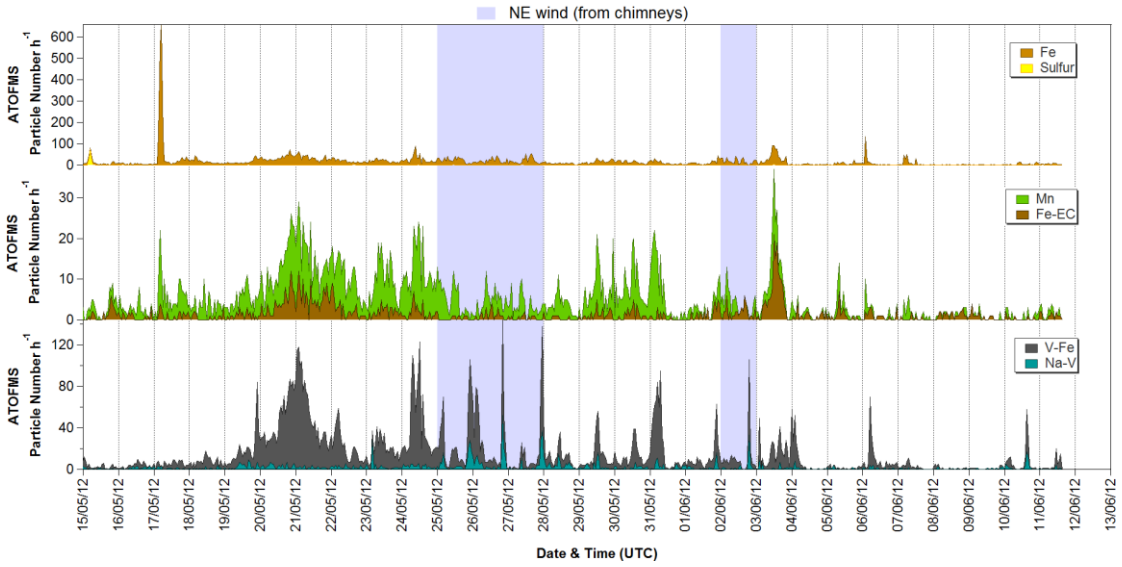


Figure 3.36. Hourly unscaled particle numbers (stacked) for transported industrial ATOFMS particle classes during NANO-INDUS.

As previously mentioned, *EC* particles accumulated during this period, and the north-westerly wind dependence observed for that class was also evident for *Fe*, *Mn*, *Fe-EC* and *V-Fe* particles (Figure 3.39). Transport of these particles from over northern France and the English Channel seems the most likely source. Long-range transport of submicron Fe-rich particles internally mixed with sodium, nitrate, sulfate and EC was recently found in London (Harrison et al., 2012). The *V-Fe* class should also have local marine traffic sources, as the site was only a few hundred metres from a berth which saw occasional

use; a large ship docked there for several hours on the 24th May, which appears to be represented by a peak in *V-Fe* numbers during this time.

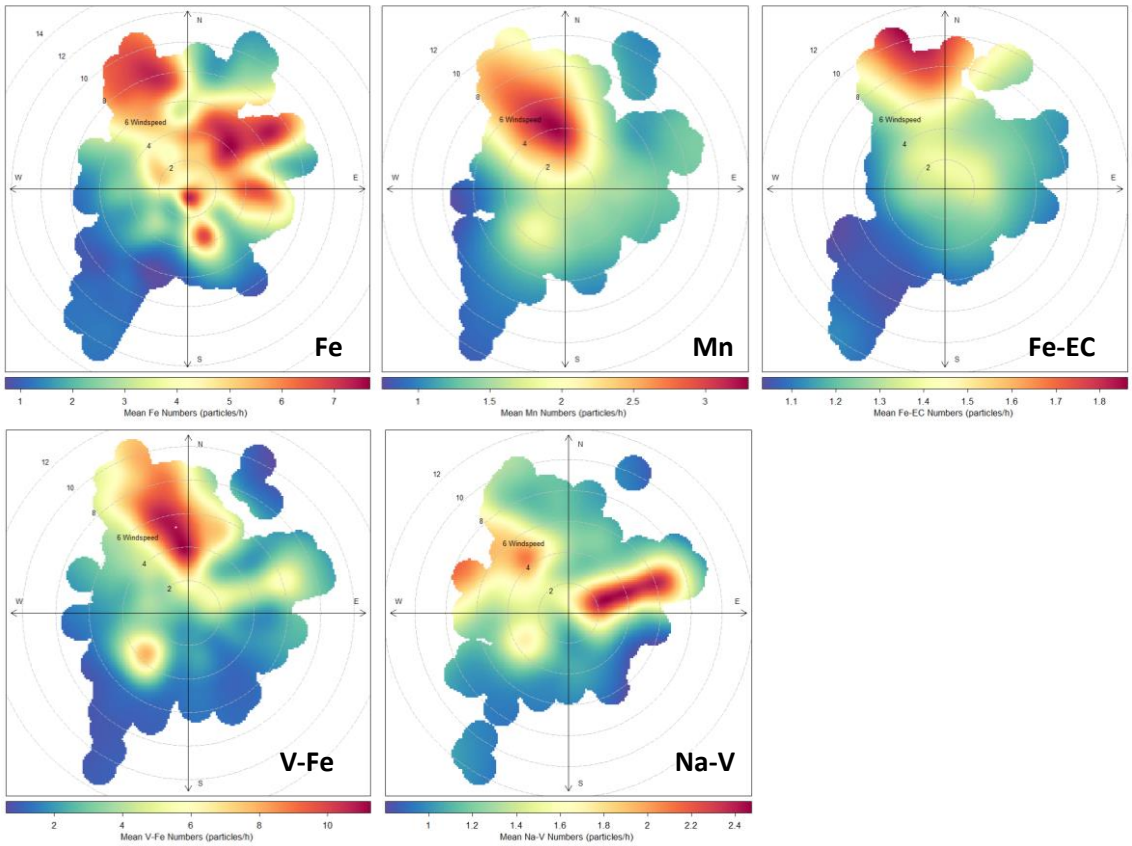


Figure 3.37. Wind speed and direction dependences of mean particle numbers for transported industrial ATOFMS particle classes during NANO-INDUS.

Most of the *V-Fe*, *Fe*, *Mn*, *Fe-EC* and *Na-V* particles were found in the range 400-900 nm during the transport event (19th-23rd May) (Appendix II, Figure 8.10), and were noticeably smaller for the rest of the campaign (400-700 nm), possibly indicative of fresher local emissions.

Very few sulfur particles were detected by the ATOFMS and only during one short period on 15th May. A sulfur class, with both positive and negative ions indicative of sulfur, was detected in the vicinity of the Port Talbot steelworks by Dall'Osto et al. (2012), but only a brief period of a few hours (over the course of a two week campaign) and was assigned to either a slag granulation or open-pit slag process. Given the seemingly infrequent nature of these emissions, it seems likely that meteorological conditions limited the detection of more sulfur particles from the steelworks during the NANO-INDUS campaign.

Local Industrial

Time series of particle numbers for classes with industrial sources (*K-Fe-Na*, *Fe-K-Ca*, *K-Mn*, *Al-K-Mn*, *Mn-K-Fe*, *K-Cl*, *K-aluminosilicate*, *K-Al*, *OC*, *OC-PAH*, *PAH*, *Ca* and *Ca-K*), that peak on 25th, 26th and 27th May, are shown in Figure 3.38. The *K-Fe-Na*, *K-Pb*, *Ca*, *OC*, *K-Cl* and *Fe-K-Ca* classes contribute most to the particle number during the 3-day industrial event, while on 2nd June (the other period strongly influenced by industrial emissions) *OC* and *OC-PAH* particles dominate. Peaks particle numbers occurred between 17:00-18:00 UTC on each of these days.

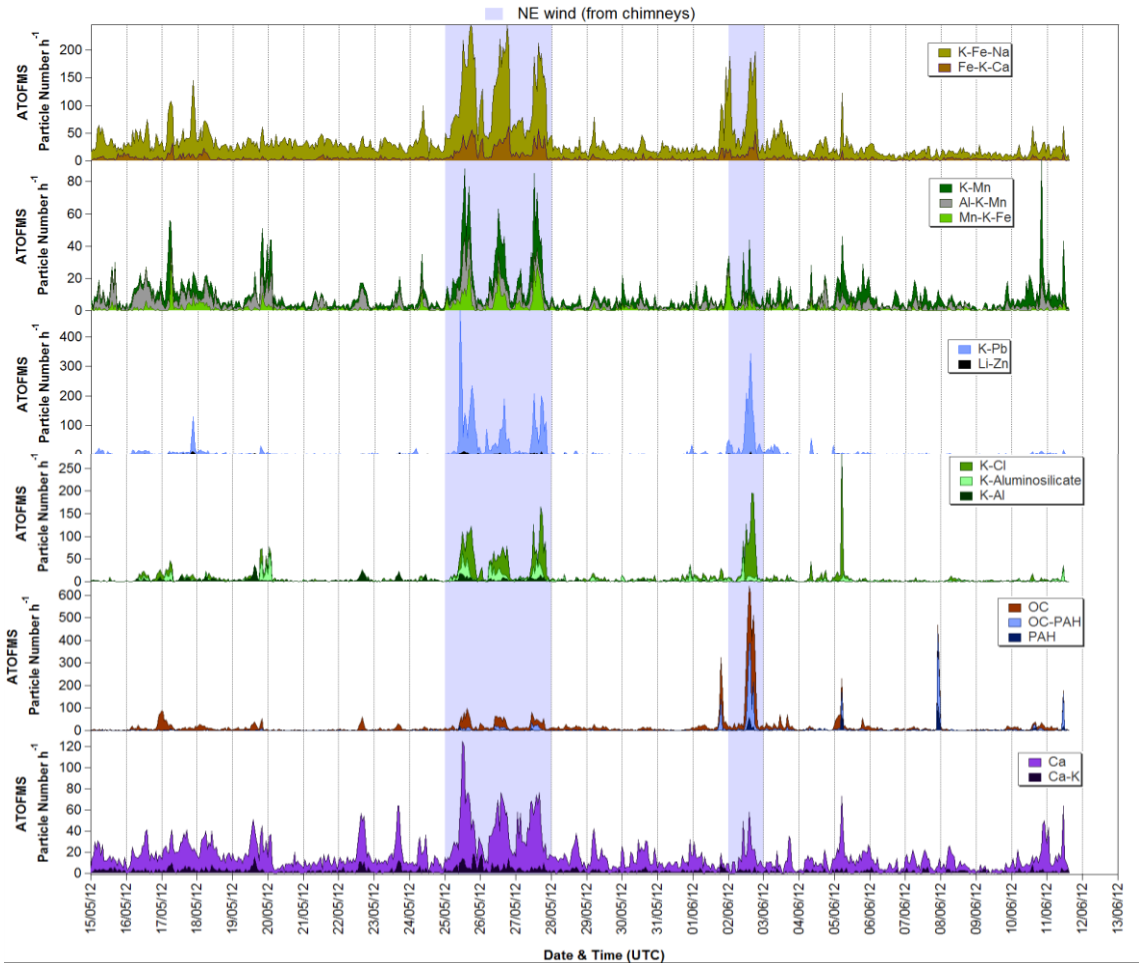


Figure 3.38. Hourly unscaled particle numbers (stacked) for local industrial ATOFMS particle classes that peaked during the 3-day industrial event.

K-Pb, *Ca* and *Fe-K-Ca* particles were found in the industrial filters of the ferromanganese alloy facility, however elemental Pb, Ca and Fe have also been detected in emissions from the steelworks (Hleis et al., 2013). Zn was found in the smelting chimney filters by SEM-EDX but not by ATOFMS, and has also been found in steelworks emissions (Dall'Osto et al., 2008; Hleis et al., 2013). Given that *Fe-K-Ca*, Pb-containing and Zn-containing particles only contributed a small fraction of particles from the industrial filters, it is likely that most of these were from the steelworks. The same can be said of *K-Fe-Na*, *K-Cl*, *OC*,

OC-PAH and *PAH*, as no similar particles were found in any of the industrial filter or ore samples.

K-Mn, Al-K-Mn, Mn-K-Fe, K-Al, Ca and *Ca-K* were found in the industrial filter or ore samples, and apart from *Ca* and *Ca-K* (Ca is a major component of steelworks sintering emissions) can be considered reliable tracers for emissions from the ferromanganese facility. The combined contribution of the *K-Mn, Al-K-Mn, Mn-K-Fe* and *K-Al* classes was 1% of total ATOFMS particle number and 2% of total reconstructed ATOFMS mass. The combined contribution of the *K-Fe-Na*, *K-Cl*, *OC*, *OC-PAH* and *PAH* classes, likely to be from the steelworks, was 5% to total ATOFMS number and 9.5% to total ATOFMS mass. This considers only classes which can be confidently attributed to the ferromanganese alloy facility or the steelworks and is therefore a conservative estimate but from this it is apparent that the steelworks contributed significantly more than the ferromanganese alloy facility to particle number and mass concentrations as analysed by ATOFMS.

Of the local industrial classes all but the *OC* class depended strongly on north-easterly winds, shown in Figure 3.39. *OC* particles depended more on easterly winds, and a second southerly sector influence (an oil refinery lies ~ 2km to the south-west) with low wind speeds (2-4 m/s) was apparent for *PAH* particles.

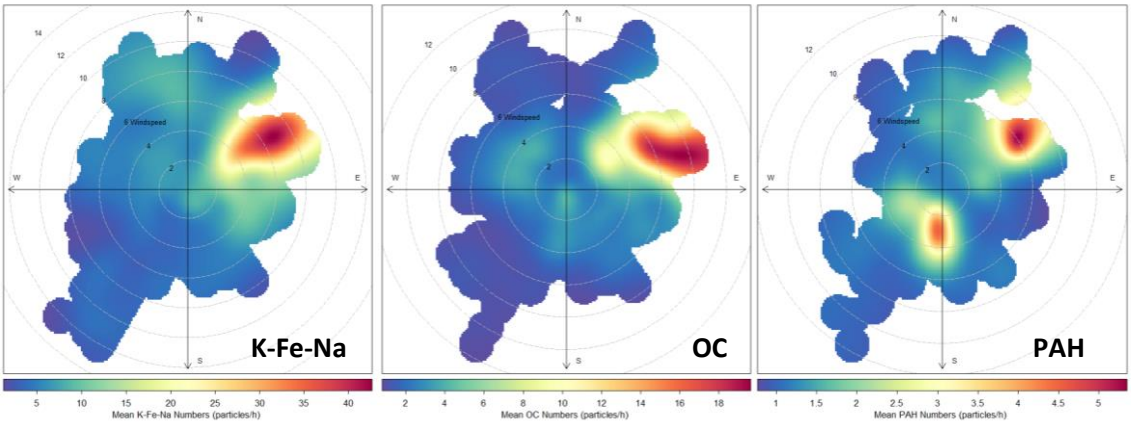


Figure 3.39. Wind speed and direction dependences of mean particle numbers for local industrial ATOFMS particles classes. Wind rose for K-Fe-Na is representative of Fe-K-Ca, K-Mn, Al-K-Mn, Mn-K-Fe, K-Cl, K-aluminosilicate, K-Al, Ca, Ca-K and OC-PAH.

Most of the 3-day industrial event particles were found in the 300-1000 nm range (represented by the *K-Fe-Na* distribution, Appendix II, Figure 8.12), with a second larger mode between 1-2.5 µm during those three industrial days. This observation is also true of *Mn-K-Fe* particles, which were found in the ferromanganese ore samples and were therefore indicative of resuspended ore dust. Differences were seen in the distributions for *K-aluminosilicate*, *OC-PAH* and *PAH* particles, also peaking during the 3-day industrial event. Most *K-aluminosilicate* particles, possibly fine dust, were found in the

range 700-2500 nm, with peak numbers around 850 nm. *PAH* particles were found in different size ranges during different periods – 300-500 nm on 5th June and from 800-1500 nm on 7th June, indicating different formation mechanisms were involved. *OC-PAH* particles were of a similar size to *PAH* particles on the 7th June, but were considerably larger (peak numbers around 1 µm) than *OC* particles (peak aerodynamic diameter of 490 nm, Appendix II, Figure 8.9) also seen on the 2nd June.

Mass concentrations for industrial particle classes were compared with those for Fe, Mn, Ca, Pb, V, Zn and Al in the $PM_{2.5}$ fraction analysed by ICP-MS, as shown in Figure 3.41. Fe, Mn, Ca, Pb, Zn and Al concentrations peaked between 25-27th May and mass concentrations for most of the particle classes containing these elements are thus in good agreement as they peak during the same period. $PM_{2.5}$ Fe correlates best with Mn, Ca, Zn and Pb (R^2=0.94, 0.98, 0.92, 0.92 respectively), suggesting similar sources or meteorological influences, with weaker correlations between Al and V (R^2=0.7, 0.32), indicating different sources for these two elements.

$PM_{2.5}$ Fe mass concentrations correlate best with those of *K-Fe-Na* and *Fe-K-Ca* particles (R^2=0.87 for both), with the *K-Fe-Na* class contributing most of the mass, at similar concentrations to $PM_{2.5}$ Fe. Considering that these particle classes contain more than just Fe, $PM_{2.5}$ Fe should have less mass than the Fe-rich classes combined; comparing these shows this is the case, Fe-rich concentrations ~ 1 µg/m^3 higher than $PM_{2.5}$ Fe from 25-27th May. The *Fe* and *Fe-EC* classes, which had very different temporal profiles to the other clearly local Fe-rich classes, correlate moderately (R^2=0.51) and weakly (R^2=0.26) with $PM_{2.5}$ Fe concentrations, indicating that they may contain less Fe than their mass spectra suggest and that they were minor contributors to Fe mass during the sampling period.

$PM_{2.5}$ Mn mass correlated well with that of the *K-Mn* and *Mn-K-Fe* classes (R^2=0.81, 0.76), but poorly with *Mn* (R^2=0.05) and *Al-K-Mn* (R^2=0.04) as these peaked from 23-25th May, possibly indicating they did not contain as much Mn as their mass spectra suggested. The lack of agreement between $PM_{2.5}$ Mn and the *Al-K-Mn* class is surprising considering that chimney filter analysis by both ATOFMS and SEM-EDX showed Al and Mn containing particles dominated the cooling chimney filter sample and this chimney is by far the most emissive in the facility. The temporal profile for this class (Figure 3.38) showed these particles were also frequently observed during periods other than the 3-day event, suggesting more sources. It is also possible that these particles were underdetected during the 3-day event, or that the wrong density was applied during mass reconstruction,

which would affect which size bins the particles were scaled to and their final mass. *Al-K-Mn* and *K-Al*, the two classes which contained Al, also did not correlate well with $PM_{2.5}$ Al concentrations, likely for the same reasons.

$PM_{2.5}$ Ca mass concentrations correlated well with those of the major Ca-containing particles combined (shown as Ca-rich, R^2=0.75), but only moderately with individual classes (R^2=0.55 for *Ca*, R^2=0.57 for *Ca-K*), indicating that no one particle class was the main contributor to $PM_{2.5}$ Ca mass. *Fe-K-Ca* particles also contain Ca, which were not included in the Ca-rich category, and this class produced a good correlation with $PM_{2.5}$ Ca (R^2=0.88). Dall'Osto et al. (2008, 2012) did not find any particles similar to *Ca* or *Ca-K* near the Port Talbot steelworks, however Flament et al. (2008) indicated that Ca was found as $CaCO_3$ or mixed with Fe in the Dunkirk steelworks emissions. This combined with the likelihood that the steelworks is the major source of *Fe-K-Ca* particles suggests that the steelworks produced most of the Ca-rich particles, with a smaller contribution from GMF, detected by ATOFMS during the NANO-INDUS campaign.

Based on the emissions rates of the three chimneys (Firing: 3100 kg/y, Cooling: 32300 kg/y, Smelting: 600 kg/y, Figure 3.5), average *Al-K-Mn* and *K-Mn* mass concentrations should outweigh those of *Ca* and *Ca-K* particles. From Figure 3.40 it is apparent that this is not the case, as *Ca* and *Ca-K* particles generally contributed more mass than *Al-K-Mn* and *K-Mn* particles. This further supports a dominant steelworks source of *Ca* and *Ca-K* particles.

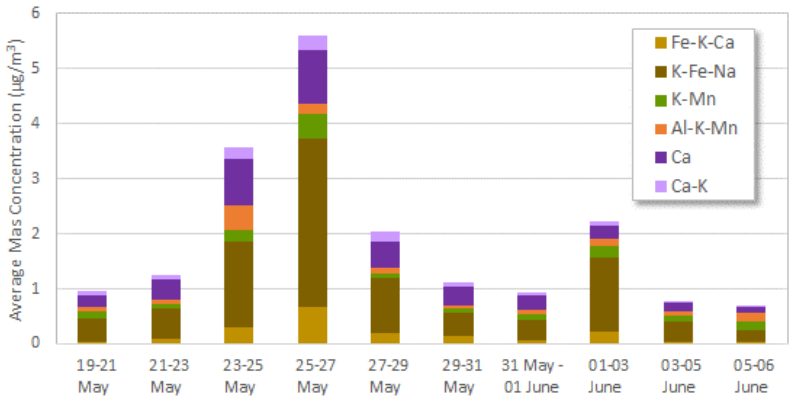


Figure 3.40. Comparison of average mass concentrations of GMF and steelworks particle classes observed during NANO-INDUS.

$PM_{2.5}$ Pb mass concentrations correlated well with those of the *K-Pb* class (R^2=0.81), although the average mass of *K-Pb* particles is considerably larger (Figure 3.41) than that of $PM_{2.5}$ Pb (factor of 23). This indicates that Pb is a minor component of these particles or that too large a density was used for reconstructing the mass.

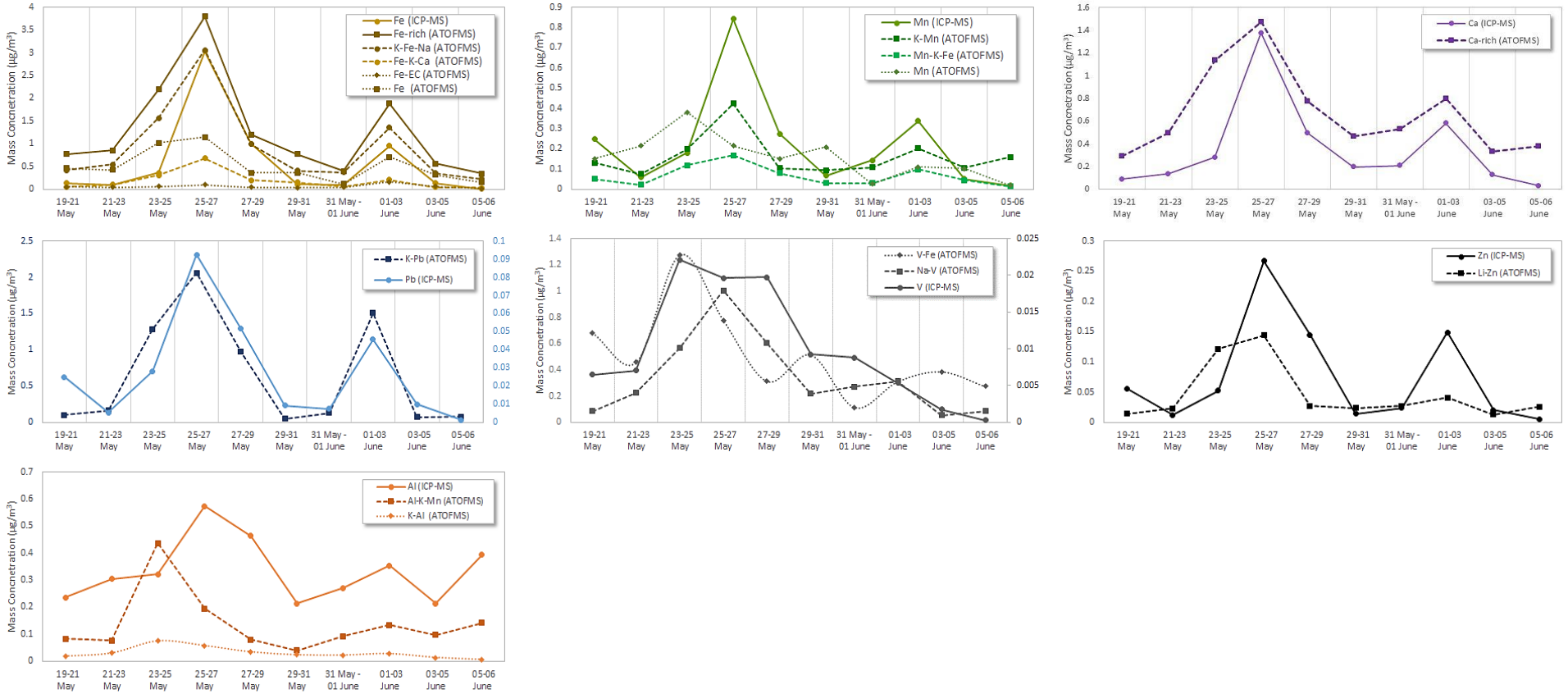


Figure 3.41. Time series of average mass concentrations for $PM_{2.5}$ Fe, Mn, Ca, Pb, V, Zn and Al (ICP-MS) and ATOFMS particle classes containing these species observed during NANO-INDUS.

$PM_{2.5}$ V mass concentrations correlated well with those of *Na-V* particles (R^2=0.75) but weakly with *V-Fe* concentrations (R^2=0.37), suggesting that *Na-V* particles contained more V than *V-Fe* particles. However average *Na-V* mass concentrations are ~ 33 times larger (Figure 3.41) than $PM_{2.5}$ V, so V was a small component of these particles.

$PM_{2.5}$ Zn mass concentrations correlated only moderately with those of *Li-Zn* particles (R^2=0.41). Zn was found in smelting chimney particles by SEM-EDX but found by ATOFMS, indicating that under-detection of Zn in ambient particles was likely.

3.4 CONCLUSIONS

34 distinct ATOFMS particle classes were identified from single particle mass spectra which were grouped into 9 general categories: Na-rich, K-rich, EC, Fe-rich, OC and PAH, Ca-rich, V-rich, Mn-rich and Others. Mass concentrations were reconstructed for the ATOFMS particle classes and were in good agreement with other quantitative measurements (beta gauge $PM_{2.5}$, AMS species, ICP-MS elemental mass). Some underestimation and overestimation of $PM_{2.5}$ mass was observed and likely originated from the use of multiple densities for mass conversion, a result of the complexity of the mixing states, particularly those of the metal-rich particles.

Five general sources of $PM_{2.5}$ particles were identified during NANO-INDUS: local industrial, transported industrial, transported/local industrial, urban/transported and marine. Marine emissions were dominated by sea salt and urban/transported emissions by aged biomass burning and fossil fuel combustion particles. Transported/local industrial emissions included carbonaceous particles with both transported and local industrial origins and alkylamine-containing particles likely from local industrial origins. Transported industrial emissions included Fe-rich and Mn-rich particles likely transported across the English Channel. Local industrial emissions were characterised by metal-rich particles with a variety of mixing states, observed during specific periods heavily influenced by local industry. During these periods particle number concentrations and mass concentrations of $PM_{2.5}$, BC, nitrate, non-refractory chloride, Fe, Mn, Ca, Al, K, and Zn were at their highest.

Assignment of particle classes originating from the ferromanganese alloy manufacturing facility was based on comparison with single particle mass spectra obtained from chimney filter samples and ores from the facility. Emissions from a Steelworks were also identified and contributed significantly more to $PM_{2.5}$ than the ferromanganese alloy facility.

4. CHARACTERISATION OF AIRBORNE SINGLE PARTICLES DURING ADRIMED AND SAF-MED IN CORSICA, FRANCE

CONTENTS

4.1 Introduction 114

4.1.1 Mediterranean Meteorology 114

4.1.2 Atmospheric Processing in the Mediterranean 116

4.1.3 Mediterranean PM Composition 119

4.1.4 Mediterranean Background Aerosol Studies 125

4.1.5 ChArMEx and Aims 127

4.2 Methodology 129

4.2.1 Sampling Site 129

4.2.2 Instrumentation 130

4.3 Results 134

4.3.1 Meteorology 134

4.3.2 Particle Number and Mass Concentrations 138

4.3.3 Particle Classes 141

4.3.4 Particle Sources 152

4.3.5 Processing Markers 169

4.4 Conclusions 175

4.1 INTRODUCTION

4.1.1 MEDITERRANEAN METEOROLOGY

The Mediterranean is a region with unique characteristics. Three continents converge around a large interior sea that is relatively deep and warm (abyssal temperatures of ~13°C vs. 4°C for the oceans, (United Nations Environment Programme/Mediterranean Action Plan (UNEP/MAP), 2012) to form a basin with extensive coastal areas mostly surrounded by high mountains. The Iberian Peninsula on the western coast of the basin, the Alps to the north, the Apennines and Balkans to the east and the Atlas Mountains to the south act as physical barriers between the frontal weather systems of northern Europe and the Sahara, and the Inter Tropical Fronts in the south. Owing to its relatively small dimensions (2.5×10^6 km^2, 1% of the world's oceanic surface) and the fact that its open waters are never further than 300 km off the coasts (Heimbürger et al., 2010), the Mediterranean Sea is strongly subjected to numerous and various land-based emissions from anthropogenic activities.

This geography and the anthropogenic emissions of heavily industrialised parts of Europe (Genoa and Milan, Italy), the megacities of Istanbul and Cairo and smaller population centres such as Barcelona and Marseille, and dense maritime transport traffic render the Mediterranean basin one of the most sensitive zones on the planet to air pollution (de la Paz et al., 2013; Karanasiou et al., 2014). Natural sources such as Saharan dust, sea-spray and frequent forest fires exert further considerable stress on regional air quality (Kanakidou et al., 2011). Transport of air pollution from outside the Mediterranean region is one cause for increased concentrations of primary and secondary pollutants (Lelieveld et al., 2002). In the summertime upper troposphere, Asian monsoon outflow transports pollution across northern Africa and the Mediterranean (Scheeren et al., 2003). In the middle troposphere, westerly winds prevail, transporting polluted air masses from western Europe and North America (Marmer & Langmann, 2005). In the surface layer, land emissions from south and central Europe are transported to the Western Mediterranean by northerly winds (Sciare et al., 2003).

The geography and regional meteorological processes in the Western Mediterranean also favours the accumulation and ageing of these polluted air masses (Millán & Salvador, 1997; Salvador et al., 1999; Millán et al., 2000; Gangoiti et al., 2001; Soriano et al., 2001; Lelieveld et al., 2002; Millán et al., 2002; Rodríguez et al., 2002). In summer the

Mediterranean meteorological situation is characterised by two high-pressure ridges – one over central Europe and one over the western Mediterranean basin – and a deep trough extending from the Persian Gulf to the eastern Mediterranean basin (Figure 4.1).

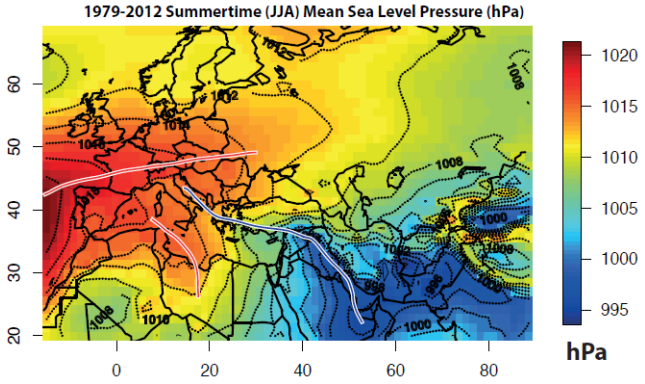


Figure 4.1. 1979–2012 summertime (June, July and August) averages of meteorological variables taken from 12 h ERA-Interim reanalysis; the red lines represent the high-pressure ridges and the blue line the deep trough (Doche et al., 2014).

The central Europe ridge results from an extension of the Azores anticyclone, while the western ridge results from an extension of the North African anticyclone. These systems lead to low winds, persistent clear-sky conditions, high solar irradiation, anticyclonic subsidence and stratification (Service & Prezerakos, 1984; Tyrlis & Lelieveld, 2013; Anagnostopoulou et al., 2014; Doche et al., 2014). The Western Mediterranean Basin (WMB) becomes isolated from the "classic" frontal systems approaching from the Atlantic which affect the weather in central and northern Europe. The east and south-facing slopes of high coastal mountains (Atlas Mountains and eastern Iberian mountain ranges) surrounding the basin become strongly heated during the day, favouring the formation of upslope winds. These combine with sea breezes, which transport pollutants inland during the day and seaward at night, and the compensatory subsidence of air masses associated with the mountain and sea breezes, creating closed-loop circulations. These processes form stacked layers along the coasts (Millán et al., 1996, 2002), with the most recently formed layers at the top (vertically injected by the mountain breezes), and the older ones closer to the sea (returned by subsidence). Layering has been documented to reach 2–3 km in depth and extend out over the sea to more than 300 km (Millán et al., 1996; Millán & Salvador, 1997). At night, the winds generated by land-surface heating die down, and the layers formed on the previous day(s) can drift up to 150 km along the coast (Millán et al., 2002), acting as reservoir layers of aged pollutants. The next day the sea breeze brings the lowest layers inland and the circulation continues. Tracer experiments on the Spanish east coast have shown that turnover times for these re-circulations range from 2 to 3 days (Gangoiti et al., 2001). Similar processes involving either vertical re-circulations and/or oscillations of aged air masses have also been

documented in the central Mediterranean (Ciccioli et al., 1987; Fortezza et al., 1993; Kallos et al., 1993; Georgiadis et al., 1994; Ferretti et al., 2003; Caccia et al., 2004; Federico et al., 2010). These circulations typically dominate during periods of weak gradient conditions over the western Mediterranean, often associated with the Iberian thermal low (Hoinka & De Castro, 2003); daily cycles have been observed for wind speed, with maximum values during daylight, and wind direction, with SE winds blowing during the day and NW winds blowing at night (Rodríguez et al., 2002). Wind speed and direction do not undergo diurnal cycles during periods dominated by synoptic scale meteorological processes, such as advection of African air masses from the south or North Atlantic air masses from the north.

4.1.2 Atmospheric Processing in the Mediterranean

The circulations act as "large natural photochemical reactors," where most of the NO_X emissions and other precursors are transformed into oxidants, acidic compounds, aerosols and O_3 (Millán & Salvador, 1997; Millán et al., 2000; Gangoiti et al., 2001; Rodríguez et al., 2002; Doche et al., 2014) and inhibited from dispersing (Sandroni & Migon, 1997). Concentrations of trace gases such as nitric oxide (NO), formaldehyde (HCHO), acetone (CH_3COCH_3) and methanol (CH_3OH) have been found to be 2-10 times larger over the Mediterranean than in the background troposphere, indicating large *in situ* production of peroxy radicals (Lelieveld et al., 2002). This contributes to the Mediterranean basin being the European region at highest risk of O_3 pollution (Sicard et al., 2013) and to aerosol radiative forcing, which is among the highest in the world during summertime (Haywood & Boucher, 2000; Formenti et al., 2001; Andreae et al., 2002). Climate change is expected to be more pronounced in the Mediterranean Basin than in most other regions of the world (IPCC, 2001). Climate models predict that Mediterranean summers will be increasingly characterized by warm, dry weather with calm winds (IPCC, 2007) and the Mediterranean Basin will be one of the areas subject to the most drastic reductions in precipitation and therefore increases in atmospheric aerosol lifetimes (IPCC, 2001). Thus it seems that the conditions that favour high ozone levels over the sea and along the coasts are likely to become more frequent in the coming years and the conditions that favour the build-up of ozone will presumably also promote the build-up of other air pollutants (Velchev et al., 2011).

As the Mediterranean basin is a crossroad of different aerosol types it is an ideal natural laboratory to study the effect of different types of absorbing aerosol on the regional and local radiation budget and the consequences for atmosphere dynamics in the region

(Mishra et al., 2014). So far, most global and regional climate simulations have investigated the impact of global warming on the Mediterranean climate without detailed considerations of the possible radiative influence and climatic feedback from the different Mediterranean aerosols (anthropogenic, marine, biomass burning, secondary biogenic and mineral dust particles). There are significant differences in aerosol loading between the eastern, central, and western sub-basins and between the North and the South of the Mediterranean as shown by long-term aerosol satellite products (Figure 4.2). The atmospheric aerosol content can be represented by the aerosol optical depth (AOD), which is the vertical integral over an atmospheric column of the fraction of incident light scattered and absorbed by aerosols. This optical parameter is often used as input for calculations of aerosol direct and semi-direct radiative forcing in regional climate models (RCMs). The AOD displays moderate (0.2 to 0.5 in the visible wavelengths) values (Figure 4.2), depending on the aerosol types observed over the Euro-Mediterranean region (Nabat et al., 2013).

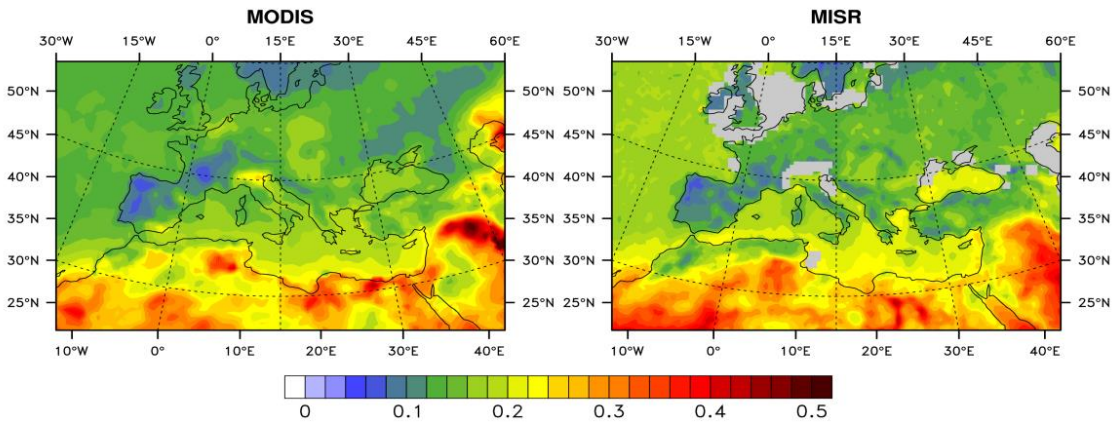


Figure 4.2. Aerosol Optical Depth (at 550 nm) derived from MODIS and MISR satellites for the 2003 to 2012 period (Mallet et al., 2015).

Numerous studies have documented the AOD for polluted-anthropogenic Mediterranean aerosols at local scale over south-eastern France (Mallet et al., 2006; Roger et al., 2006), Spain (Horvath et al., 2002), Greece (Chazette & Liousse, 2001; Gerasopoulos et al., 2003), Crete (Fotiadi et al., 2006), and Italy (Tafuro et al., 2007; Ciardini et al., 2012). Under polluted conditions, they report moderate values ranging from 0.1 to 0.5 (at visible wavelengths). In parallel, multi-year TOMS and MODIS observations over the eastern Mediterranean (Hatzianastassiou et al., 2009) or the Po Valley (Royer et al., 2010) indicate the occurrence of high AOD values (up to more than 0.8 at 500 nm) over large urban areas surrounding megacities.

Such atmospheric aerosol loadings are known to significantly change the radiative budget of the Mediterranean region through direct radiative forcing by (1) decreasing the sea-surface incoming shortwave radiations, (2) increasing/decreasing outgoing shortwave

fluxes depending on the surface albedo and (3) possibly heating turbid atmospheric layers when particles absorb solar light. Absorbing aerosols were shown to increase the absorption of solar radiation in the atmospheric column (+11.1 W/m^2) and reduce the surface radiation (−16.5 W/m^2), inducing significant atmospheric warming and surface cooling over the region (Papadimas et al., 2012). Markowicz et al. (2002) found that the daily averaged atmospheric warming (+11.3 W/m^2) and surface cooling (−17.9 W/m^2) by summertime absorbing aerosol over the Mediterranean are similar to the highly absorbing south Asian haze observed over the Arabian Sea. Significant negative radiative forcing at the surface has also been reported in dust dominant (−70.8 W/m^2) and pollution dominant (−39.1 W/m^2) case studies (Meloni et al., 2003).

Secondary inorganic components of aerosol, such as ammonium, nitrate and sulfate, exhibit seasonal spatial and temporal profiles (Rodríguez et al., 2002, 2007), shown in Figure 4.3. The contribution of ammonium nitrate to PM is enhanced during the winter (owing to its greater thermodynamic stability at low temperatures), particularly in urban regions. In contrast, ammonium sulfate contributions to PM are enhanced during summer due to the prevailing low dispersive conditions, high photochemical oxidation and the possible higher summer contribution of marine secondary sulfate from DMS oxidation (Querol et al., 2009a).

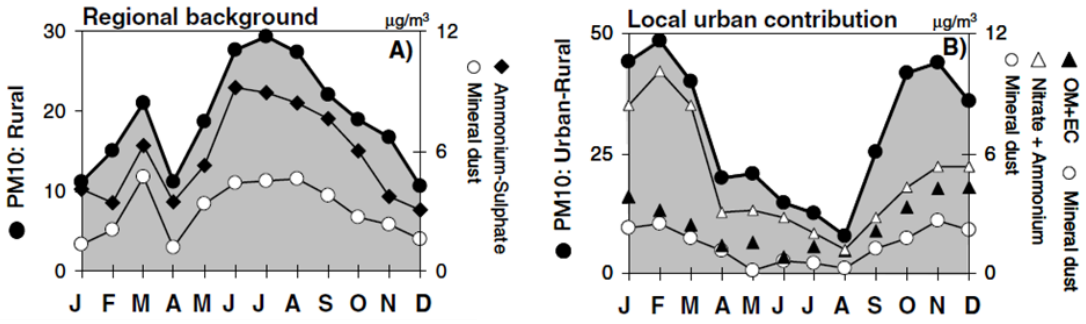


Figure 4.3. Monthly mean concentrations of regional and urban contributions to PM_{10} and the most important contributors in eastern Spain (deduced from two rural sites and two urban sites) (Rodríguez et al., 2007).

Enhanced sulfate levels (5– 6 µg/m^3), among the highest in Europe, have been measured in the eastern Mediterranean relative to the western basin (3 µg/m^3) (Querol et al., 2009a), as a result of air masses from eastern Europe, SO_2 emissions from coal power generation in Greece and Black Sea countries and high insolation favouring H_2SO_4 production via homogenous reactions. This results in depletion of gas-phase NH_3 over the eastern basin, so that little ammonium nitrate is formed and coarse mode nitrate is instead prevalent.

Previous size fractionated aerosol measurements conducted in the Mediterranean have indicated low levels of submicron nitrate (Bardouki et al., 2003; Querol et al., 2009a); concentrations of 1.7 to 1.9 µg/m^3 were lower than those in central Europe and UK (2–4

µg/m^3). During summer, high hydroxyl radical (OH) levels (up to about 2·× 10^7 molecule/cm^3), relatively high NO_X ($NO+NO_2$) concentrations (Cyrys et al., 2012) and the lack of precipitation promote the build-up of HNO_3 from gas phase reactions (Berresheim et al., 2003). Once HNO_3 is formed, it is most likely captured by coarse mode (D≥1.2 µm) sea-salt and mineral dust particles, leading to a depletion of aerosol nitrate in the fine mode (D<1.2 µm) (Metzger et al., 2005). When ammonia is present in excess, ammonium nitrate can be formed during night, however this salt can evaporate during the day and the aerosol precursor gases NH_3 and HNO_3 are therefore likely to condense on pre-existing and larger aerosol particles (Wexler & Seinfeld, 1990).

4.1.3 MEDITERRANEAN PM COMPOSITION

Long term measurements (2006/2007-2010) of $PM_{2.5}$, PM_{10}, and gaseous pollutants (CO, SO_2, NO_2 and O_3) at traffic and urban background sites in four Southern European countries (Spain, France, Italy and Greece) have been used to show that the origin of air pollution in Southern Europe seems to be local rather than regional, with the highest levels registered under low wind speeds (Karanasiou et al., 2014). This implies that the background Mediterranean aerosol should be influenced mostly by southern European emissions, with occasional African dust and Atlantic marine aerosol intrusions. Arid conditions, combined with high radiation and photochemical conversion rates significantly enhance air pollution in the form of PM_{10}, $PM_{2.5}$ and NO_2, with the highest concentrations generally found in southern and eastern Europe and attributed to diverse emission sources such as industry, traffic, resuspended dust, shipping emissions and African dust intrusions (Karanasiou et al., 2007, 2009; Querol et al., 2004; Lelieveld et al., 2002; Rodríguez et al., 2007; Karanasiou et al., 2011, 2014)(Lelieveld et al., 2002; Querol et al., 2004; Rodríguez et al., 2007; Karanasiou et al., 2007, 2009, 2011, 2014). A number of studies have reported that in rural environments in the Mediterranean, airborne particulate matter (PM) concentrations undergo a seasonal cycle characterised by a summer maximum (Bergametti et al., 1989; Kubilay & Saydam, 1995; Querol et al., 1998a, 1998b; Rodríguez et al., 2001, 2002). This seasonal cycle has not been reported at rural sites in central and northern Europe, where high PM events are mostly recorded in winter during stagnant episodes caused by cold temperature inversions and low wind speed (Monn et al., 1995; Turnbull & Harrison, 2000; Röösli et al., 2001). During summer 2000 the highest PM episodes (daily concentrations 40– 60 µg/m^3) were observed during African dust outbreak events (Rodríguez et al., 2002). The second highest PM levels (daily concentrations 20–45 µg/m^3) were reported during regional pollution episodes

associated with ozone events, induced by Mediterranean meteorology. The lowest PM_{10} levels (daily concentrations <20 μg/m^3) occurred during abrupt entries of Atlantic air masses into the western Mediterranean basin. (Querol et al., 2009a) reported mean maximum hourly values of 23, 16 and 13 μg/m^3 in summer for PM_{10}, $PM_{2.5}$ and PM_1 in the Montseny National Park, Barcelona, from long term (2001-2007) PM_{10} and $PM_{2.5}$ speciation measurements. These were also conducted in Finokalia (Crete) and Erdemli (Turkey) and showed that mineral matter is the major component of PM_{10} (22-38%) in both western and eastern Mediterranean basins, with relatively high proportions in $PM_{2.5}$ (8-14%), followed by sulfate, organic matter (OM), nitrate and ammonium. 10-14% of PM_{10} mass (and 2-16% of $PM_{2.5}$) was unaccounted and mainly attributed to moisture not eliminated during filter conditioning, as well as a small fraction of inorganic hetero-atoms (F, O, H), not analysed during those studies.

Carbonaceous aerosol

EC and OM levels were homogenous across the regional background of the Mediterranean (0.2–0.4 and 5–6 μg/m^3 respectively) and lower compared to most background sites of central Europe (Putaud et al., 2004; Pio et al., 2007). Mean OC/EC ratios of ~11 were found in the western basin, which was attributed to significant SOA formation from biogenic and anthropogenic volatile organic compounds (VOCs) emitted from a range of sources, including biomass burning (Reid et al., 2005; Hallquist et al., 2009). SOA formation is enhanced by the low regional atmospheric renovation in spring-summer and higher photochemical activity. Long term measurements (2001-2006) of EC and OC in Crete (Sciare et al., 2008) showed long-range transport of agricultural waste (post-harvest wheat residual) burning in countries surrounding the Black Sea were important contributors to these species from March-April and July-September; 34% and 32% of EC and OC mass concentrations during August (20% and 14% on a yearly basis). Ukraine has the largest agricultural land area in Europe (FAO, 2015) and it has been suggested wheat yields there have the potential to double long term (Rabbinge & Van Diepen, 2000); agricultural waste burning in this region will likely represent an important source of combustion aerosols in the future and their influence on radiative forcing over the source region and the downwind Mediterranean could be significant.

In the eastern Mediterranean high insolation and high levels of O_3 (up to 87 ppbv) prevailing during summer, as well as increased traffic owing to greater tourism and the burning of vegetation and forest, contribute to high mean concentrations of oxalate; 170-255 ng/m^3 in Finokalia, Crete, among the highest reported for rural areas (Bardouki et al.,

2003; Koçak et al., 2004). Oxalate was found to be the main organic ionic species in both coarse and fine modes, contributing 50% of coarse and 40% of fine organic ionic mass. Together with acetate and formate, it accounted for up to 90% of total organic ionic mass (0.58 μg/m^3) (Bardouki et al., 2003). Koçak et al. (2004) found seasonal cycles of oxalate, with a maximum in the summer. Oxalate formation is likely from photochemical breakdown of gas- or aerosol-phase higher dicarboxylic acids and unsaturated fatty acids after reaction with O_3 or partly due to marine biogenic emissions (Kawamura and Sakaguchi, 1999). Koulouri et al. (2008) found 59% of oxalate mass was in the fine fraction, with an average concentration of 117 ng/m^3 and a range of 29-258 ng/m^3. After nss-SO_4^{2-} and NH_4^+, oxalate and nss-K^+ were the second most important contributors to anionic and cationic mass. The authors found correlations between oxalate and NH_4^+, nss-SO_4^{2-}, K^+ and MSA. The association with the latter implies at least some of the oxalate mass originated from marine biogenic activity as MSA arises only from precursor marine DMS through gas to particle conversions, while the association with K^+ indicated biomass burning sources. The average concentration in the coarse mode was 78 ng/m^3, with a range of 8-301 ng/m^3. Similar to the proposed coarse mode nitrate formation pathway, oxalic acid, SO_2 and sulfuric acid can react with alkaline sea salt and mineral dust particles, in the coarse size range (Mamane & Gottlieb, 1992; Aymoz et al., 2004; Falkovich, 2004; Sullivan & Prather, 2007). In summer 2003 Portugal lost ~400,000 ha of forest to wildfires, more than any other European country that year; measurements by (Pio et al., 2008) found mean oxalate mass concentrations of 359 ng/m^3 and a range of 180-789 ng/m^3 and clear increases in oxalate mass during periods strongly impacted by wildfires from background levels indicated that this species, as well as other diacids, were either emitted by the fires or subsequently produced during plume ageing.

Marine emissions

Marine aerosol in the Mediterranean basin takes the form of sea salt and biogenic emissions. Sea salt varies strongly across the region, with lower levels found in the western basin compared to the eastern, and higher levels in coastal areas (annual average ~4 μg/m^3 in PM_{10} at the Balearic Islands) compared to the mountainous areas surrounding the Mediterranean (0.5 and 0.2 μg/m^3 for PM_{10} and $PM_{2.5}$ at Montseny, Barcelona) (Querol et al., 2009a). These levels are all lower however than those found at Atlantic sites in Europe (4 to 12 μg/m^3: Querol et al., 2004; Sillanpää et al., 2006; Jaeglé et al., 2011). Querol et al. (2009) found highest sea salt concentrations in the western basin (Montseny, Barcelona) during the summer, related to the intensified coastal sea breeze

circulation, and an association of sea salt with wind speed variation in both basins. Low chlorine/sodium ratios were found across the Mediterranean in the summer, attributed to chlorine replacement by nitrate.

Methanesulfonate (MSA) is a well-established tracer for marine phytoplankton activity (Andreae and Crutzen, 1997; Hallquist et al., 2009; Gaston et al., 2010), formed from OH (day) and NO_3 (night) oxidation of DMS, the enzymatic cleavage product of dimethylsulfoniopropionate (DMSP), a compound produced by oceanic phytoplankton. It is therefore a good indicator of biogenic (marine) sulfate and its presence in aerosols typically indicates that they have undergone some oceanic transport, rather than being produced locally (Gaston et al., 2010). While MSA has been proposed to primarily contribute to particle growth in the atmosphere (Kreidenweis et al., 1989; Wyslouzil et al., 1991a, 1991b), there is evidence that MSA can also contribute to new particle formation (Dawson et al., 2012). Both MSA and sulfate strongly influence particle hygroscopicity, meaning that the enhanced production of either of these species by anthropogenic particle types could have significant implications for cloud droplet formation in both marine and inland environments (O'Dowd et al., 2004; Lee et al., 2010). Measurements of DMS oxidation products, primarily sulfate and MSA, typically use off-line bulk analysis techniques. These measurements revealed that particle mass concentrations of both sulfate and MSA peak during the summer, and the ratio of the two species depends on factors such as temperature, cloudiness, NOx concentrations, and contributions from anthropogenic sulfate (Ganor et al., 2000; Kouvarakis & Mihalopoulos, 2002; Hopkins et al., 2008). MSA has been quantified at sea using an aerosol mass spectrometer (AMS), showing diurnal trends in particulate MSA concentrations and correlations with oceanic biological activity (Phinney et al., 2006; Zorn et al., 2008). Mean MSA concentrations of 35 ng/m^3(range 5.9-121 ng/m^3) have been measured in the Gulf of Lion by Sellegri et al. (2001) and 40-60 ng/m^3 on Lampedusa (Becagli et al., 2013), while in the eastern Mediterranean (Finokalia, Crete) similar mean concentrations of 26 ng/m^3 (Kubilay et al., 2002), 27 ng/m^3 (range 4-99 ng/m^3) (Kouvarakis & Mihalopoulos, 2002) and 32 ng/m^3 (Bardouki et al., 2003) were observed. Mean concentrations of 50 ng/m^3 (range 0.1-552 ng/m^3) have been measured at Mace Head, Ireland and 45 ng/m^3 at Erdemli, Turkey, both areas influenced by elevated marine biological productivity (Kubilay et al., 2002). On board the cruise ship Costa Pacifica during summer 2010 around the western Mediterranean, Schembari et al. (2014) estimated that 26% of sulfate mass was of marine biogenic origin, with the remainder assigned to anthropogenic emissions. The majority of MSA mass has been found in fine

aerosols; Koulouri et al. (2008) detected 85% of MSA in the fine mode (mean of 35 ng/m^3 with range 3-145 ng/m^3 as compared to 6 ng/m^3 in the coarse mode, with range 0-27 ng/m^3), Bardouki et al. (2003) found maximum concentrations in 0.26-0.46 μm impactor stages and Sellegri et al. (2001) found highest concentrations in 0.3-0.5 μm range and no MSA on particles <0.1 μm. MSA has been observed enhanced relative to sulfuric acid in particles <0.1 μm in Finland (Kerminen et al., 1997; Mäkelä et al., 2001) and Mace Head (Facchini et al., 2008); that this has not been the case so far in the Mediterranean suggests condensation on pre-existing particles rather than new particle formation.

Shipping emissions

The Mediterranean Sea is among the world's busiest waterways, accounting for 15 % of global shipping activity by number of port calls (UNEP/MAP, 2012); passenger ships and dry cargo ships make up the majority of ships calling at Mediterranean ports (34% and 31% respectively). Container ships and tankers also transit through the region. Ship emissions contribute to sulfate aerosol concentration mainly in the western Mediterranean; 54% of the mean sulfate aerosol burden during summer and over 50% of direct sulfate radiative forcing, according to modelling by (Marmer & Langmann, 2005). Without ship emissions, the mean summertime direct forcing over the Mediterranean is no longer outstanding and has the same values as the European mean.

Ambient measurements on board the Costa Pacifica as it visited five Mediterranean harbours (Savona, Barcelona, Palma, Tunis and Civitavecchia) in 2009 and 2010 found an average decrease of 66% of the daily SO_2 means in three of the four EU harbours (Schembari et al., 2012), in connection with the impact of the EU directive 2005/33/EC that regulated the SO_2 emissions from ships in EU harbours from January 2010. A 75% decrease in ambient SO_2 concentration was also seen in the measurements at a monitoring station in the harbour area of Barcelona and downwind of the harbour of Palma de Mallorca. Notably, the SO_2 concentration in the only non-EU harbour, Tunis, did not change significantly. Neither the concentrations of NO_X nor BC changed significantly in any of the harbours from 2009 to 2010. Measurements were also carried out on the ship as it travelled from port to port (Schembari et al., 2014); a combustion factor identified by PMF, which showed evidence of contribution from ship emissions (sulfur predominantly found in the fine fraction and V/Ni ratios consistent with shipping emissions) contributed 55%, 63% and 80% to PM_{10}, BC and sulfate concentrations. A second set of measurements in 2011, this time on the Costa Concordia (Bove et al., 2015),

resolved this combustion factor into two separate factors, secondary sulfate and heavy oil combustion, which contributed 35% and 12% to PM_{10}.

Becagli et al. (2012) estimated the average mass of SO_4^{2-} emitted by heavy fuel oil combustion around the island of Lampedusa during the summer (long term measurements from 2004-2008) to be 1.2 µg/m^3, about 30% of the total $nssSO_4^{2-}$, 3.9% of PM_{10}, 8% $PM_{2.5}$, and 11% PM_1. A peak value of 6.1 µg/m^3 was reached on 26 June 2008, corresponding to 47% of $nssSO_4^{2-}$ and 15% of PM_{10}. In Marseille the petrochemical activities, industrial emissions and shipping are believed to cause elevated levels of SO_2 (Karanasiou et al., 2014). Studies in Barcelona, the Balearic islands, Crete and South Turkey (Querol et al., 2009a; Pey et al., 2010) found a strong presence of the fuel-oil combustion aerosols over the Mediterranean, from power plants and shipping traffic, as levels of V and Ni were factors of 3-9 higher in these areas than at most sites in central Europe.

The Mediterranean basin is characterized by atmospheric stagnation for most of the year, and consequently, shipping emissions accumulate on a regional scale. This is especially relevant along the Gibraltar Strait, as at this point ship traffic from the Mediterranean basin converges toward the Atlantic Ocean. Viana et al. (2009) estimated the mean annual contribution of shipping emissions to ambient PM_{10} in Melilla, on the African coast, was 0.8 µg/m^3 (2%) as primary particles and 1.7 µg/m^3 (4%) as secondary particles (mainly sulfate aerosols from the oxidation of co-emitted SO_2). For $PM_{2.5}$ the sum of primary and secondary particles from shipping accounted for 2.6 µg/m^3 (14%). Pandolfi et al. (2011) characterised shipping emissions in this area (Bay of Algeciras) by La/Ce ratios between 0.6 and 0.8 and V/Ni ratios around 3 for both PM_{10} and $PM_{2.5}$, and distinguished them from refinery emissions (elevated La/Ce ratios of 1-5) and stainless steel plant emissions (low average V/Ni ratio of ~1). The authors assessed the direct contribution from shipping at 1.4-2.6 µgPM_{10}/m^3 (3-7%) and 1.2-2.3 µg$PM_{2.5}$/m^3 (5-10%). Harbours are particularly influenced by emissions from ships (Pandolfi et al., 2011; Reche et al., 2011); an apportionment study performed in Barcelona (Amato et al., 2009) revealed a mean annual contribution from heavy fuel oil combustion (mainly shipping emissions) of 5, 6 and 8% of PM_{10}, $PM_{2.5}$ and PM_1.

Dust

In addition to regional circulations, synoptic scale meteorology induces frequent outbreaks of African dust in summer. North African deserts emit most of the dust particles released to the atmosphere worldwide (Salvador et al., 2014). Saharan dust outbreaks

influence the Mediterranean through anticyclonic flow from western Africa, reaching the area from the west in the lower free troposphere (Moulin et al., 1998; Ganor et al., 2000; Lelieveld et al., 2002), as southerly winds are uncommon in summer. Such African dust outbreaks (ADO) occur only occasionally, around 10 reported annually in eastern Spain (Rodríguez et al., 2001) and/or following seasonal patterns (Querol et al., 2009b; Pey et al., 2013; Salvador et al., 2014), but can represent a significant fraction of daily PM_{10} levels at both rural and urban monitoring sites in the Mediterranean basin (Querol et al., 1998a, 2004, 2008, 2009b; Rodríguez et al., 2002; Gerasopoulos et al., 2006; Escudero et al., 2007a; Bouchlaghem et al., 2009; Pey et al., 2013; Karanasiou et al., 2014). A considerable percentage of the exceedances of the PM_{10} daily limit value (50 µg/m^3 after the 2008/50/EC European Directive) registered at these sites was exclusively attributed to the mineral dust transported during ADOs (Escudero et al., 2007b; Viana et al., 2010; Salvador et al., 2013).

Ti, Li, Al_2O_3, Rb, Mg, La, Ca and Fe (typical soil constituents) have been associated with mineral dust from Saharan dust transport, construction, demolition and road dust (Rodríguez et al., 2007; Pey et al., 2009) associated, with Ca, Fe, Sb, Sn, Cu and Zn identified as specific tracers for urban road dust (Pey et al., 2010). Low precipitation rates in the western Mediterranean result in poor vegetal coverage of soils, from which natural resuspension processes increase the mineral dust contributions to ambient PM levels, and enhance mineral dust accumulation on and resuspension from roads; resuspended road dust accounted for 17% of PM_{10} registered in Barcelona (Amato et al., 2009). Further measurements in Barcelona during winter (Reche et al., 2011) revealed construction and demolitions works increased $PM_{2.5\text{-}10}$ levels up to 63% with respect to the daily mean (an increase of 7.5 µg/m^3). The impact of these sources was strongly dependent on meteorological processes, as the emissions were transported to the study site via the Mediterranean sea breeze circulations.

4.1.4 Mediterranean Background Aerosol Studies

Continent based coastal sites are subjected to the proximity of urban or industrial emission areas (Sandroni & Migon, 1997). The background composition of the western Mediterranean atmospheric aerosol is therefore best represented on the shore line of industry-free or poorly industrialized islands such as Corsica, Sardinia or Balearic Islands, and studies in these locations have so far been limited.

On Lampedusa (an island between Sicily and Tunisia), Saharan dust has been measured in terms of its optical properties and radiative effects (di Sarra et al., 2001; Di Sarra et al.,

2002; Meloni et al., 2004; Meloni et al., 2008; di Sarra et al., 2011). Biomass burning/urban-industrial particles, 65% of which originated from central-eastern Europe (from 2001-2003), were also identified based on their average aerosol optical depth Ångström exponent and were found to absorb visible radiation whereas scattering is prevalent for desert dust (Meloni et al., 2008; Di Biagio et al., 2010). Artuso et al. (2009, 2010) found growth rates of greenhouse gases such as CO_2 (1.9 ppm yr^{-1}) and N_2O (0.78 ppb y^{-1}) from 1992-2008. Becagli et al. (2012) estimated the contribution of heavy fuel oil emissions (V, Ni, nss-SO_4^{2-}) to PM_{10} (4%), $PM_{2.5}$ (8%) and PM_1 (11%) between 2004 and 2008.

Studies on Corsica are considerably fewer and focus on trace metals. Bergametti et al. (1989) studied the temporal variability of markers for major aerosol sources (soil erosion: Al, Si; pollution: S, Pb; sea-salt: Na) and concluded mean travel time of about two days to be a good estimate of the duration of the long-range transport between continental source-regions, primarily Spain and north-Africa, and the Corsican atmosphere. Similar peak Al concentrations have been found in NE Spain (Rodríguez et al., 2002), during African dust events, indicating the extent this dust affects the western-central Mediterranean. Concentrations of Pb, Zn and Mn have been found to be ~3 times lower at background Mediterranean (e.g. Vignola, west Corsican coast) sites than at coastal continental sites (e.g. Camargue, south France), which were influenced more by industrial/continental regions of northern and central Europe (Sandroni & Migon, 1997). Concentrations of Cu, Al and Fe were factors between 2.2 and 2.6 larger, while Ni and Cd were factors between 1.2 and 1.8 larger. The authors emphasised that the background values represented the natural contribution mixed with the medium-range transported component of the anthropogenic inputs. Loye-Pilot and Morelli (1988) analysed rainwater from south Corsica for pH and major ions (Na^+, K^+, Ca^{2+}, Mg^{2+}, Cl^-, SO_4^{2-}, NO_3^- and NH_4^+) and observed episodes of acid rain when incoming air masses passed over various European industrial regions (lowest pH values ~4). On the contrary, air masses arriving from North Africa coincided with the highest pH values (6-7) and corresponded to red rain episodes with high content in PM containing up to 30% of calcite. When Saharan and European air masses mixed, intermediate pH values were observed, possibly as a consequence of a neutralising effect of the incoming desert aerosol on atmospheric acidity, suggesting that Saharan dust may counterbalance the effects of acidic rain in the Mediterranean.

4.1.5 ChArMEx and Aims

In this context, the Chemistry-Aerosol Mediterranean Experiment (ChArMEx; http:charmex.lsce.ipsl.fr) initiative aims to scientifically assess the impacts of present and future anthropogenic and climatic pressures on the Mediterranean atmosphere. ChArMEx is a coordinated experimental and modelling international effort to assess the regional budgets of short-lived (< 1 month) particulate and gaseous tropospheric trace species, their trends, and their impacts on air quality, marine biogeochemistry, and regional climate. It comprises a number of interlinked projects. The work presented in this Chapter is related to results obtained from field measurements performed on Corsica during summer 2013 as part of two ChArMEx projects: ADRIMED and SAF-MED.

The objectives of the Aerosol Direct Radiative Impact on the Regional Climate in the Mediterranean region (ADRIMED) project are the following:

- to conduct an experimental campaign, based on surface and aircraft observations, for creating an innovative database gathering the physical, chemical, optical properties as well as the vertical distribution of the main Mediterranean aerosols;
- to use experimental surface-aircraft observations to estimate the 1D-local direct radiative forcing of aerosols over the two instrumented super sites at the sea-surface, Top of the Atmosphere (TOA) and within the atmospheric layer (ATM);
- to investigate how the modifications of the radiative budget due to aerosols affect the sea-surface evaporation fluxes, relative humidity profiles, cloud-cover, precipitation and more largely the Mediterranean hydrological cycle.

The Secondary Aerosol Formation in the Mediterranean (SAF-MED) project aims to develop a better understanding of the origins of the high secondary organic aerosol (SOA) concentrations observed in the western Mediterranean in summer with a focus on the role of atmospheric chemical processing and particle properties in SOA formation. Most SOA at the continental scale over Europe is of biogenic origin but because the oxidation of biogenic VOCs is enhanced by anthropogenic emissions, reducing the oxidant levels and absorbing carbon mass associated with these emissions may actually reduce the biogenic SOA concentration. (Sartelet et al., 2012) estimated 15-16% less SOA formation if all anthropogenic emissions were eliminated, with as much as 50% less SOA locally over large urban centres. Correctly estimating organic aerosol (OA) concentrations, their properties and origins is desirable in order to find out the most efficient way to reduce them. The main objectives are as follows:

- To estimate the concentrations and properties of SOA and photo-oxidants in the western Mediterranean;
- To investigate the origin of SOA and the influence of photochemical aging on SOA properties;
- Improvement of operational air quality models.

Aerosol physical and chemical properties will be measured close to real-time. The concentrations of photo-oxidants will also be measured, because they impact on the formation of SOA and will provide an estimate of the age of the air mass. Hygroscopicity, mixing state of particles, and the volatility of organic aerosol (OA) which appears to be a key feature to discriminate between fresh and processed aerosol sources, will be measured. The determination of major organic and other aerosol sources in the western Mediterranean will be obtained from the model-based analysis and from the specific source apportionment analysis from campaign observations.

The ATOFMS provided real-time single particle mixing state and thereby emission source information during two ChArMEx projects: ADRIMED and SAF-MED. Single particle mass spectrometry measurements in the Mediterranean are scarce and restricted to urban environments (Dall'Osto & Harrison, 2006; Dall'Osto et al., 2013; McGillicuddy, 2014). The dataset obtained by the ATOFMS in Corsica during ADRIMED and SAF-MED therefore represents only the third of its kind in the Mediterranean and the first to characterise the Mediterranean background aerosol.

4.2 METHODOLOGY

4.2.1 SAMPLING SITE

The UCC ATOFMS was deployed at the air quality monitoring station in Ersa (coordinates: 42°58'10''N, 09°22'49''E), Cape Corsica, near the North tip of Corsica Island (Figure 4.4). This station is well positioned to investigate polluted air masses transported over the Mediterranean basin from the highly industrialized regions of the Po Valley (Royer et al., 2010) and/or the Marseille/Fos-Berre (Cachier et al., 2005) zones, and is fully equipped for documenting the aerosol chemical, physical and optical properties as well as their possible mixing and their vertical structure at local scales. This ground-based remote station is located at an altitude of 530 m and has unobstructed views to the sea over ~270° (Figure 4.4). The Cape Corsica peninsula is a remote site excluding important anthropogenic sources that could affect the in-situ measurements (Lambert et al., 2011).



Figure 4.4. Ersa sampling site at the start of the ADRIMED campaign (mid-June, 2013).

4.2.2 INSTRUMENTATION

The ADRIMED and SAF-MED field campaigns took place from 11th June to 5th July and from 12th July to 6th August 2013 respectively, during the Mediterranean dry season over the western and central Mediterranean basins. A list of key instruments deployed during the campaigns by the various participating research institutes is given in Table 3.2. A full list of instruments deployed during ADRIMED can be found in the overview for this campaign by Mallet et al. (2015), while an overview of the SAF-MED measurements is still in progress. Date and time are reported in Coordinated Universal Time (UTC). The local time during this study was Central European Summer Time (CEST), which corresponds to UTC +2:00. The experimental set-up involved several ground-based measurement sites including two ground-based reference sites on islands (Corsica and Lampedusa) and different secondary sites, details of which can be found in (Mallet et al., 2015).

At the Ersa supersite local meteorological parameters were measured with an automated weather station. Particle number concentrations and size distributions were measured with a scanning mobility particle sizer (SMPS, 10-1000 nm in mobility diameter) and optical particle counter (OPC, 300 nm to 20 μm in optical diameter). PM_{10} and PM_1 mass concentrations were measured with tapered element oscillating microbalance (TEOM) analysers. The TEOM measures the accumulation of mass on a heated filter attached to the tip of a hollow, tapered, oscillating glass rod (Patashnick & Rupprecht, 1991; Allen et al., 1997). The change in the oscillation frequency is used to make a direct measurement of the accumulation of mass on the filter over time. Dividing the mass rate by the flow rate through the filter provides a continuous output of the particle mass concentration.

An aerosol chemical speciation monitor (ACSM) and a high-resolution time-of-flight aerosol mass spectrometer (HR-ToF-AMS) delivered quantitative mass concentrations of the major non-refractory chemical species (SO_4, NO_3, NH_4, non-sea-salt Cl) present in submicron particles (Jayne et al., 2000b; DeCarlo et al., 2006) throughout the ADRIMED/SAF-MED and during SAF-MED only, respectively. The ACSM was recently developed for long-term autonomous field measurements by modifying the AMS design (Ng et al., 2011): (i) the electron impact ion source is smaller but otherwise identical; (ii) a lower cost residual gas analyser (RGA) type quadrupole mass analyser instead of high-performance quadrupole and time-of-flight spectrometers; (iii) and removal of the fast data acquisition and particle beam chopper system for measuring particle time-of-flight to obtain particle size information. These modifications result in a

more compact and less costly instrument compared to the AMS at the expense of lower sensitivity and time resolution.

Black carbon concentrations were provided by a multi-angle absorption photometer (MAAP). The operating principle is described in detail elsewhere, (Petzold & Schönlinner, 2004) but briefly the optical absorption and scattering of light (light source, LED, $\lambda = 670$ nm) by particles collected on the filter tape are simultaneously measured at multiple angles and corrections for filter and aerosol scattering are made using a radiative transfer model (Petzold & Schönlinner, 2004). When the MAAP technique was compared with a thermal reference method for various types of test and ambient aerosol, a constant specific absorption was found that can be used to convert optical absorption coefficient to black carbon mass.

Quantification of bulk aerosol water-soluble ionic components such as chloride, nitrate, sulfate, ammonium, sodium, magnesium, calcium, potassium, oxalate and methanesulfonate was achieved using a particle into liquid sampler (PILS) coupled with ion chromatography (IC) (Orsini et al., 2003). Aerosol particles are sampled from an airstream (15-17 l/min) and mixed with a smaller turbulent flow of 100 °C steam (1.5 l/min). Rapid adiabatic cooling of the warmer turbulent steam by the cooler ambient sample gives a high supersaturation of water vapour. In this supersaturated environment, the aerosol particles grow into droplets ($D_p > 1$ μm) large enough to be collected by an single jet inertial impactor onto a vertical quartz plate, which is washed with water to produce a continuous liquid flow for online analysis by IC.

ATOFMS data analysis was carried out according to the procedures outlined in Chapter 2. ATOFMS particle numbers for each particle class were scaled using an SMPS and OPC and then converted to mass as described in Section 2.2.1. Reconstructed ATOFMS mass concentrations were compared with those obtained by the TEOM, PILS, ACSM and MAAP.

The ATOFMS size range was limited to 300-3000 nm instead of the usual 100 nm lower limit, due to degrading sizing lasers (Figure 4.5). From the 12th – 18th July, the ATOFMS did not detect particles effectively. Originally it was thought one of the sizing lasers had malfunctioned and it was therefore exchanged. However, it later emerged that the substitute laser had a lower power output and as a result smaller particles were no longer sized. From 18th July, the effective operating range of the instrument was therefore restricted to 500-3000 nm. This was not immediately apparent as particle numbers were

no lower than they had been prior to the technical difficulties, but was noticeable in later data analysis and following comparison with other measurements.

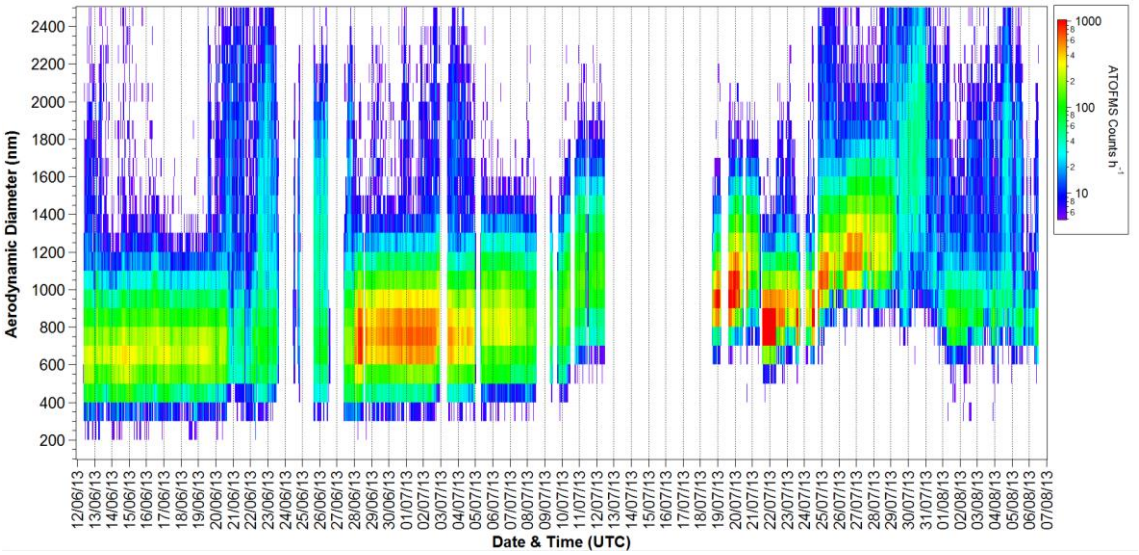


Figure 4.5. Hourly size resolved ATOFMS particle numbers during ADRIMED/SAF-MED.

As shown in Figure 4.6, this technical issue impacted the number of particles observed during SAF-MED, which is to be expected given that smaller particles were no longer detected (laser power was too weak to scatter light effectively from small particles, which is an issue already with this sizing system). The issue would not have affected sea salt detection, as the sea salt particles were above the 500 nm cut-off and marine emissions influenced the site at times during SAF-MED. The higher sizing limit would have affected detection of combustion particles; classes from such sources were found throughout ADRIMED and SAF-MED and a shift to larger peak diameters during SAF-MED confirms that these were affected. Scaling of the ATOFMS particle numbers allowed for correction of some of this drop in detection efficiency, but even so some underestimation of reconstructed mass concentrations.

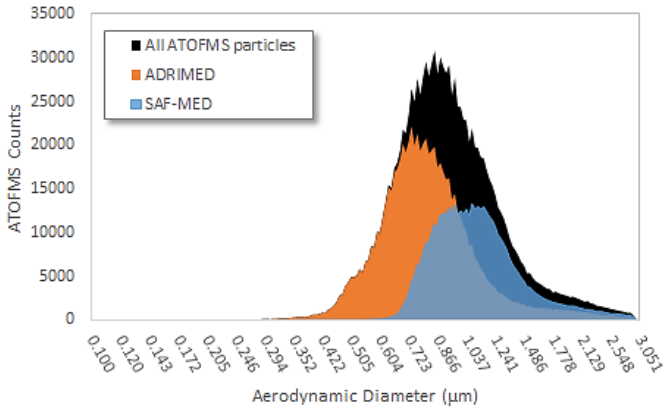


Figure 4.6. Comparison of ATOFMS particle size distributions during ADRIMED and SAF-MED.

Table 4.1. List of instruments deployed during the ADRIMED and SAF-MED field campaigns.

Parameter	Instrument	Make & Model	Temporal resolution	Laboratory
		Particle phase		
Particle number size distribution (10-500 nm, mobility diameter and 300 nm – 20 µm, optical diameter)	SMPS	TSI Instruments Ltd., DMA model 3080 and CPC model 3010	5 min (continuous)	CNRM GAME
	OPC	TSI Instruments Ltd., model 3300	5 min (continuous)	CNRM GAME
PM_{10} and PM_1 mass concentration	TEOM		continuous	LSCE
Chemical composition and size distribution of non-refractory and refractory particles (100-3000 nm, vacuum aerodynamic diameter)	ATOFMS	TSI Instruments Ltd., model 3800-100	continuous	UCC
Chemical composition of non-refractory particles (30-1000 nm, vacuum aerodynamic diameter)	ACSM	Aerodyne Research Inc.	25 min (continuous)	LSCE
Chemical composition and size distribution of non-refractory particles (30-1000 nm, vacuum aerodynamic diameter)	HR-ToF-AMS (SAF-MED only)	Aerodyne Research Inc.	4 min (continuous)	LCE
Black carbon (BC)	MAAP	Thermo-Scientific, model 5012	5 min (continuous)	LSCE
PM_{10} chemical composition (Na^+, Mg^+, Cl^-, Ca^{2+}, K^+, NH_4^+, NO_2^-, SO_4^{2-}, MSA, Oxalate)	PILS		12/18 min (continuous)	LSCE
Pressure, temperature, relative humidity, solar radiation, rain, wind speed and direction	Weather station	Campbell Scientific, Model CR1000	5 min (continuous)	LSCE

UCC: University College Cork
LSCE: Le Laboratoire des Sciences du Climat et de l'Environnement
LCE: Laboratoire Chimie de l'Environnement, Aix-Marseille Université
CNRM-GAME : Centre National de Recherches Météorologiques - Groupe d'étude de l'Atmosphère Météorologique

4.3 RESULTS

4.3.1 METEOROLOGY

Figure 4.7 shows time series of standard meteorological parameters (temperature, relative humidity, solar radiation, wind speed and atmospheric pressure. The temperature varied between 12 and 32°C, with an average ± 1 std. dev of 20.9 ± 3.8°C. Solar radiation maxima ranged from ~499 – 713 W/m^2, with clear consistency. Humidity ranged from 26 – 100%, with an average ± 1 std. dev of 69.7 ± 19.1%, and was >90% for 18% of the whole sampling period. Pressure averaged at 956.3 ± 2.3 mBar, and the average wind speed was 4.2 ± 2.6 m/s.

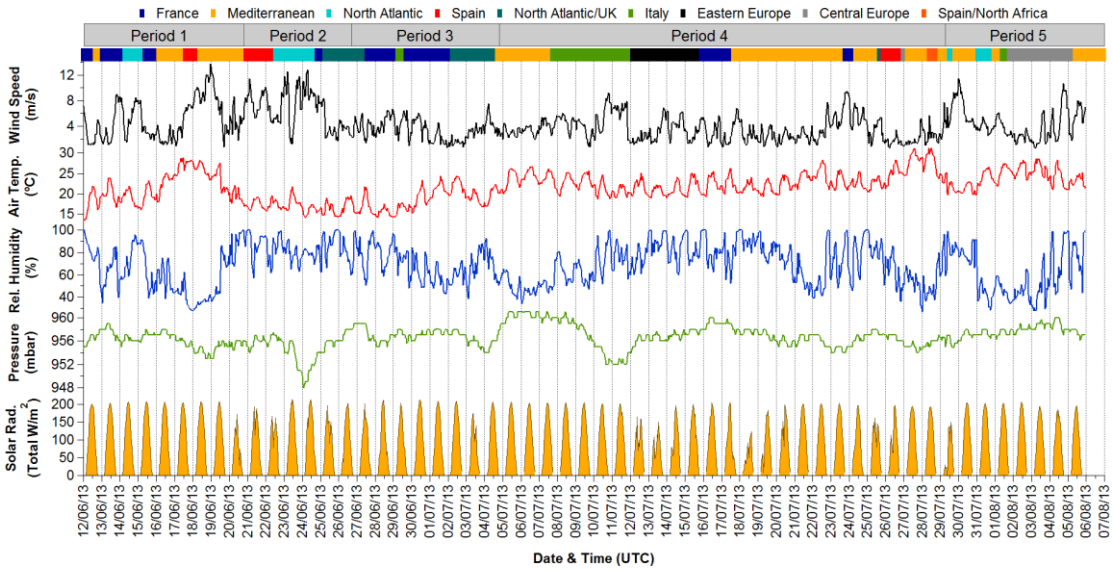


Figure 4.7. Hourly wind speed, air temperature, relative humidity, atmospheric pressure and solar radiation during ADRIMED/SAF-MED.

Figure 4.8 shows wind speed and mean ATOFMS particle number dependences on wind speed and direction. South-westerly winds prevailed, both in terms of low and high wind speeds. North-westerly winds with speeds greater than 10 ms^{-1} occurred with less frequency. Highest ATOFMS particle numbers were associated with gentle breezes from the east, with lower numbers also from the north-east and south-east under more moderate wind speeds. However, since the site was mainly influenced by regional sources, air mass trajectories were of more importance for particle source identification.

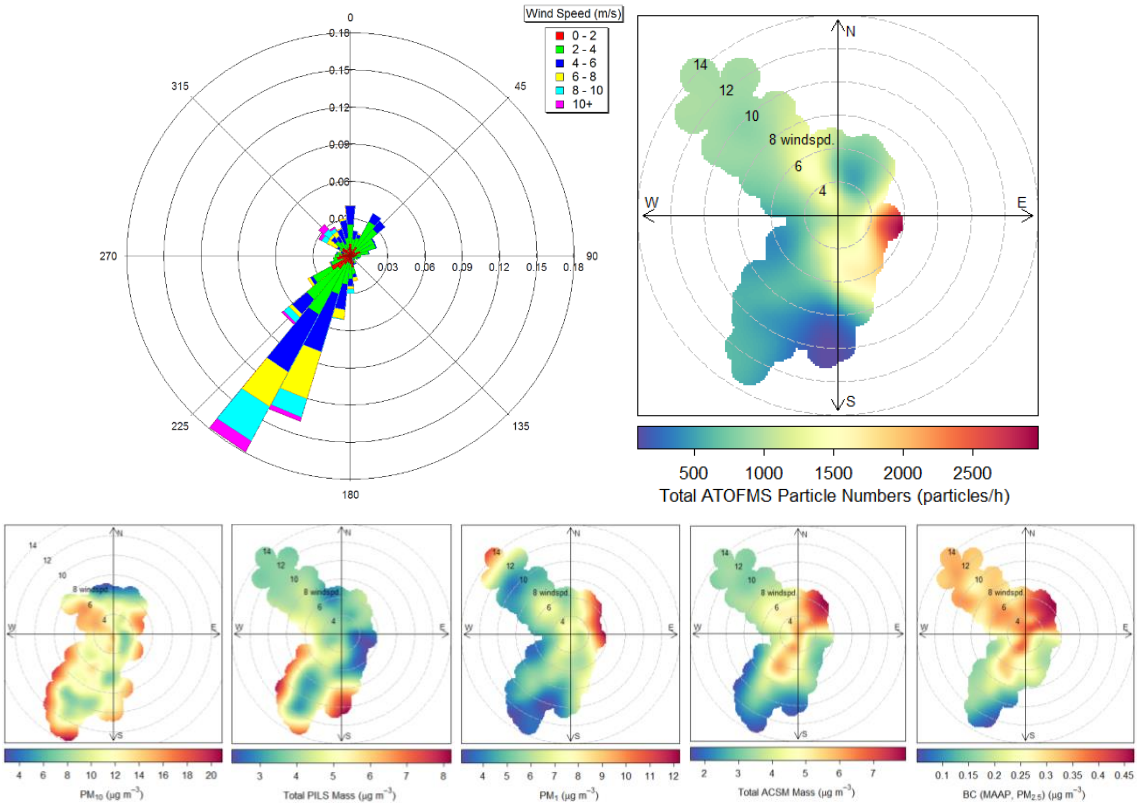


Figure 4.8. Wind speed rose and wind speed and direction dependences for mean total ATOFMS particle numbers and PM_{10}, PM_1, BC and total ACSM and PILS mass concentrations during ADRIUMED/SAF-MED.

Five broad periods were identified based on the OPS, ACSM, PM_1 and PM_{10} temporal profiles (Figure 4.21); clustered HYSPLIT 120 hr back-trajectories for each period (Figure 4.9) were used to determine which air masses influenced the ATOFMS measurements, and temporal profiles for particle numbers and mass concentrations have been labelled with these air mass origins.

Period 1 displayed a variety of air mass pathways, most of these short-range regional. 48% of trajectories during this period resided over the Mediterranean Sea for more than half of their travel time to the site. This is indicative of air mass stagnation and the recirculations typical of the Mediterranean in the summer. 29% of trajectories resided over France, 12% over the North Atlantic and the remaining 9% over Spain prior to reaching the site.

Period 2 was dominated by North Atlantic air masses; 35% arrived at the site via the north of Spain/south of France, while another 35% passed over the UK and France. 24% of trajectories resided over Spain and the remaining 6% resided over France.

Period 3 was dominated by air masses which resided over France (60%), while a further 34% originated over the North Atlantic and the UK, but also passed over most of France before reaching the site. The remaining 6% resided over northern Italy and Croatia.

Period 4 was characterised by a variety of air masses; 49% (~12 days of sampling) circulated over the Mediterranean Sea, as for Period 1. 18% of trajectories resided over northern Italy and Croatia, 15% over eastern Europe (Hungary, Ukraine, Romania), 9% over France, 4% over Spain, 2% over Spain and northern Africa, 1 % over central Europe (Germany, Switzerland) and 1 % over the North Atlantic and the UK. The trajectories over Spain and northern Africa are the only set to potentially carry Saharan dust to the site at an altitude of 500 m AGL. The trajectories end near the Strait of Gibraltar and the north coast of Africa, but it is well documented that much of the Saharan dust is delivered to the Mediterranean from the west, in a loop from the desert to the south.

Period 5 was characterised by air masses influenced by central Europe (43%: France, Germany, Switzerland, northern Italy) and circulations over the Mediterranean Sea (39%). 13% of trajectories resided over the North Atlantic and the UK and the remaining 4% over northern Italy.

In summary, Period 1 was dominated by recirculating air masses over the Mediterranean Sea, Period 2 by North Atlantic air masses, Period 3 by trajectories residing largely over France, Period 4 mostly by Mediterranean recirculations and a variety of other trajectories, and Period 5 by Mediterranean recirculations and by continental Europe air masses. The sampling site was therefore influenced by long-range North Atlantic marine emissions and European emissions which were then recirculated over the Mediterranean Sea, with relatively infrequent input from the Sahara.

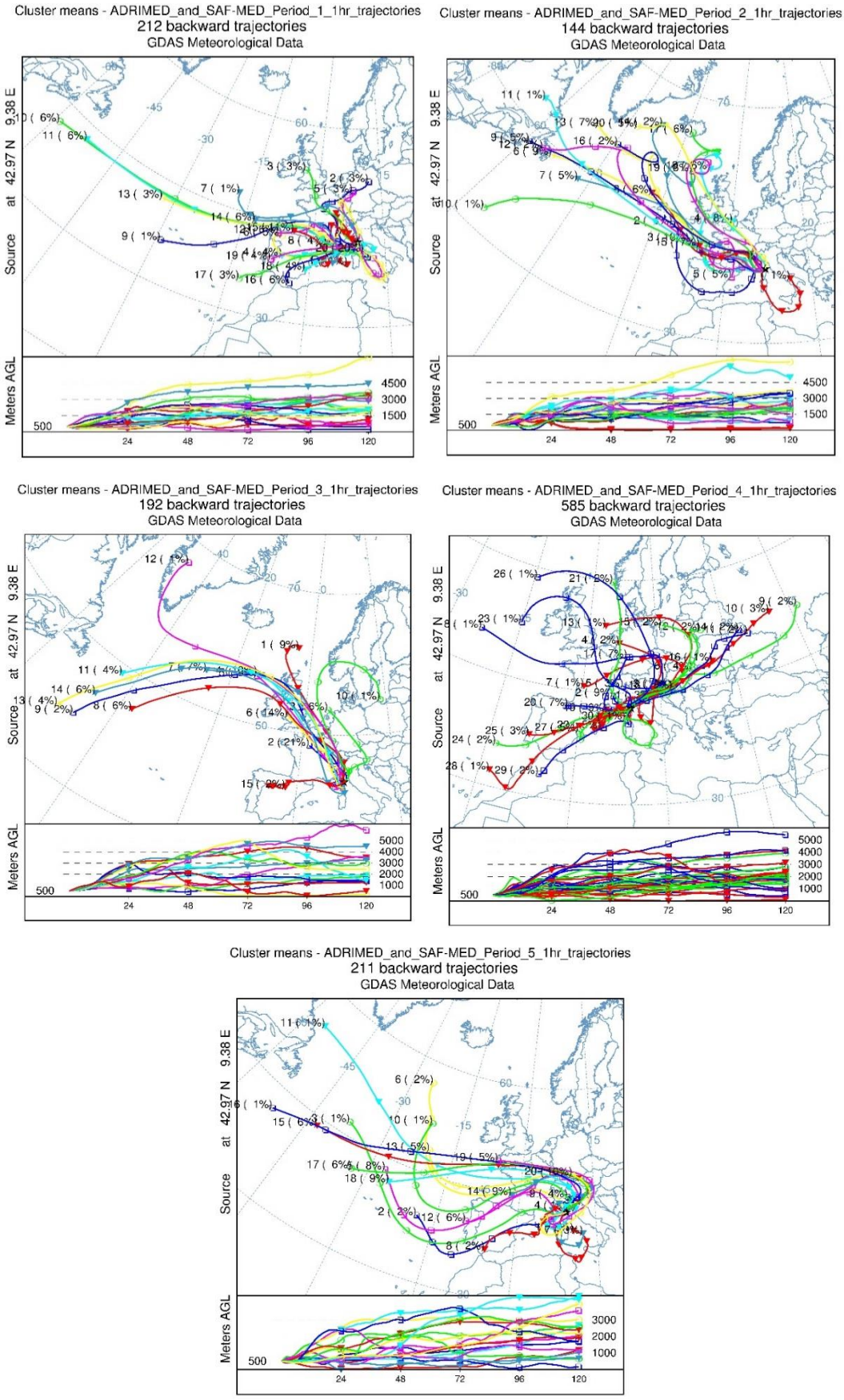


Figure 4.9. Cluster analysis of 120-hour back trajectories ending at Cap Corse sampling site, at 500 meters above ground level, every 1 hour, for the five periods identified during ADRIMED/ SAF-MED.

4.3.2 Particle Number and Mass Concentrations

Ground-based measurements show PM_1 (average ~7 µg/m^3) mass accounted for 86% of the total PM_{10} mass (average ~13 µg/m^3) at the Ersa site between 12th June and 7th August 2013. The bulk of the PM_1 mass fraction can be described by relatively few chemical components: combined, the ACSM species and BC from the MAAP account for most of the PM_1 mass (68%). Despite the fact that the PILS measures PM_{10}, the combined mass of PILS species was not dissimilar from that of the total ACSM mass (Figure 4.10). PILS mass concentrations only exceeded those of the ACSM during periods of elevated sea salt concentration (ACSM, BC, PILS, PM_{10} and PM_1 data analysed by Jean Sciare, LSCE). The total reconstructed ATOFMS mass correlated moderately with PM_1 mass (R^2=0.44) and well with the total ACSM mass (R^2=0.71), despite not detecting particles <300 nm during ADRIMED and <500 nm during SAF-MED.

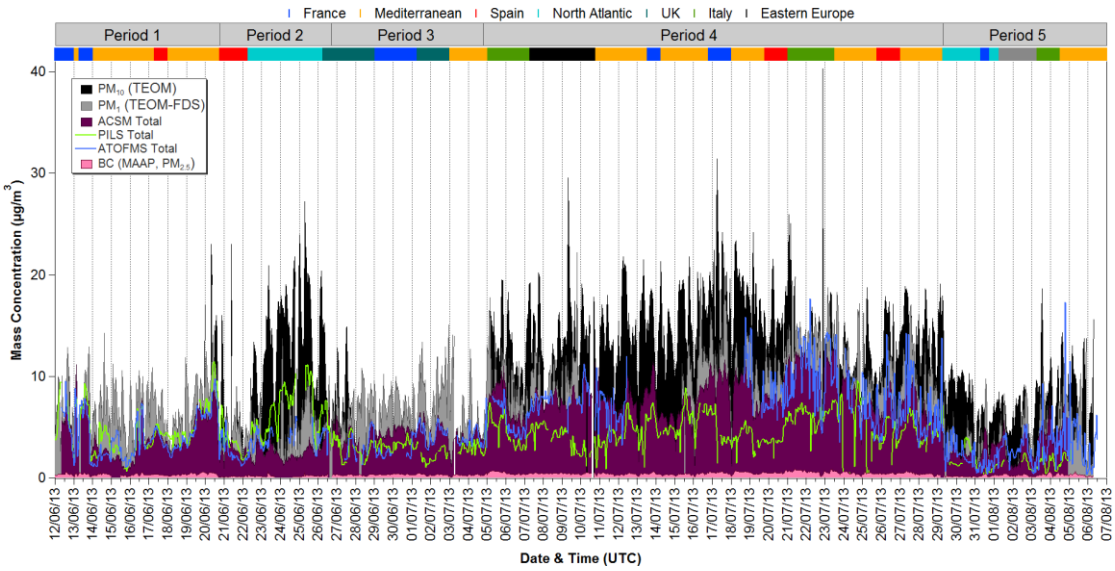


Figure 4.10. Hourly mass concentrations of PM_{10}, PM_1, ACSM, PILS, ATOFMS and BC.

A breakdown of PM_{10} mass can be found in Figure 4.11. For the majority of the sampling period, organics (36%), sulfate (16%) and ammonium (10%) constitute most of the PM_{10} mass. Calcium makes a smaller (7%) but consistent contribution throughout, while sodium, chloride and magnesium (together 9%) dominate during a clear sea salt event between 23rd and 26th June and to a lesser extent on the 30th July. BC (4%), nitrate (5%), potassium (0.4%), methanesulfonate (MSA) (0.2%) and oxalate (0.1%) contribute relatively little mass. Fossil fuel emissions, transported from population centres around the Mediterranean, therefore appear to have a much smaller contribution to PM_{10} mass than secondary aerosols in the form of organics and ammonium sulfate. 13% of PM_{10} mass remains unattributed.

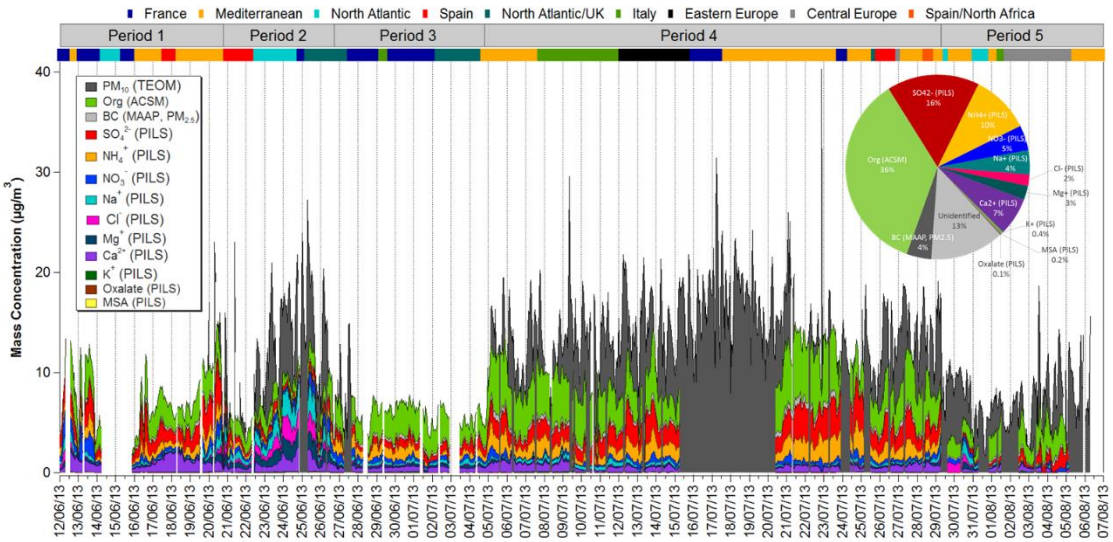


Figure 4.11. Breakdown of PM_{10} mass using BC (MAAP), PILS species and Org (ACSM).

Hourly particle number concentrations measured by SMPS and OPS are shown in Figure 4.12. Hourly average SMPS and OPS number concentrations for ADRIMED/SAF-MED.. For clarity, size bins have been grouped into larger size ranges based on similar profiles. SMPS number concentrations averaged ~1900 cm^{-3}, with a range of 470-7700 cm^{-3}; the 15 nm – 0.175 µm bin accounted for most of these numbers (79%). Peak numbers of 15 nm - 0.175 µm particles coincided with an extended period of North Atlantic marine air masses, while 0.175-0.3 µm particles decreased during this period. Maximum number concentrations for this bin were found during Period 4, a period of extended alternating regional transport and stagnation over the Mediterranean which appears to have allowed both particle number and mass concentrations to accumulate.

OPS number concentrations averaged 45 cm^{-3}, with a range of 3-137 cm^{-3}; the 0.3-0.579 µm bin accounted for most of these numbers (98%). Peak number concentrations in the 0.3-0.579 µm range occurred during Period 4; almost all of July was characterised by higher concentrations of these size particles relative to other size ranges. Concentrations then decreased sharply on the 29th July, indicating a change in air mass regime, and remained relatively low for the remainder of the sampling period. The trends between 0.3 and 8.032 µm were similar throughout July, however peak number concentrations in 0.579-2.156 µm and 2.156-8.032 µm particles did not occur during this period. Peaks were instead observed between 22nd and 25th June for 0.579-2.156 µm, with similar profiles during this period for 2.156-8.032 µm; number concentrations in this range peaked during a 6 hour event on the 29th July. Two short (a few hours) dust events on the 25th of June and 25th July characterised the profile of 8.032-10 µm particles.

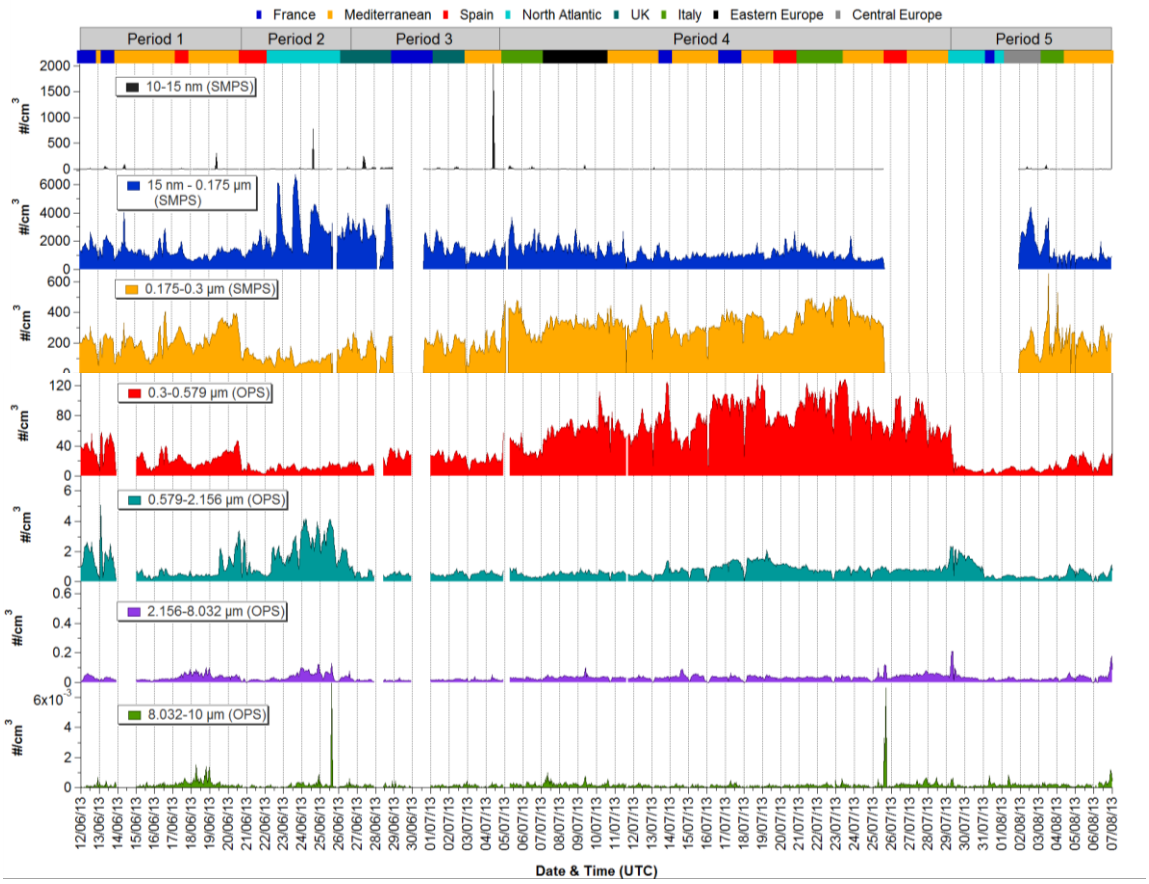


Figure 4.12. Hourly average SMPS and OPS number concentrations for ADRIMED/SAF-MED.

Effective reconstruction of ATOFMS mass concentration relies on number concentration data that reflects and agrees reasonably with mass measurements from other instruments e.g. TEOM or AMS/ACSM. Good correlations were found between the temporal trends of 0.3-0.579 µm number concentrations (which accounted for most of the total OPS particles) and several other measurements (Table 4.2): PM_1 (R^2=0.54), total ACSM mass (R^2=0.82), MAAP BC (R^2=0.57) and PILS sulfate (R^2=0.6), suggesting that the OPS was measuring the same particles from the same sources as the mass-based instruments.

Table 4.2. Correlations (R^2) between particle number concentrations and mass concentrations.

	Mass Concentrations (µg/m³)										
SMPS & OPS *(#/cm³)*	***PM_1 (TEOM)***	***BC (MAAP)***	***Total ACSM***	***Org (ACSM)***	***SO_4 (ACSM)***	***NH_4 (ACSM)***	***SO_4^{2-} (PILS)***	***NH_4^+ (PILS)***	***Na^+ (PILS)***	***Cl^- (PILS)***	***Mg^{2+} (PILS)***
0.175-0.3 µm	*0.41*	*0.63*	*0.81*	*0.67*	*0.72*	*0.69*	*0.59*	*0.42*	*0.13*	*0.15*	*0.18*
0.3-0.579 µm	*0.54*	*0.57*	*0.82*	*0.68*	*0.71*	*0.70*	*0.60*	*0.46*	*0.10*	*0.11*	*0.14*
0.579-2.156 µm	*0*	0	0	0	0	0	0	0	*0.68*	*0.68*	*0.66*

4.3.3 PARTICLE CLASSES

Over 1.2 million single particle mass spectra were generated by the ATOFMS during the sampling period and clustered using the *K*-means algorithm (*K*=80), as described in detail elsewhere (Healy et al., 2009, 2010; Gross et al., 2010). 27 distinct ATOFMS particle classes were identified and subsequently grouped into 8 general categories for clarity. The contribution to total particle number and mass concentration of all particle classes can be found in Table 3.3.

While the aerosol mixing state is varied, only a few particle classes make up the bulk of particle numbers. The Na-rich category is dominated by Sea salt-aged particles, the EC category by EC-SO_X particles, the K-rich category by K-SO_X particles, the Amines category by K-TMA and EC-TMA particles, the OC-containing category by OC particles and the V-rich category by V particles.

Table 4.3. Detailed composition of ATOFMS dataset during ADRIMED/SAF-MED, by particle classes.

Category	*Particle Class*	*No. of Particles*	*% of Total Ionised*	*% Particles with negative spectra*	*% of Total ATOFMS Mass*	*Peak Aerodynamic Diameter (µm)*
EC	EC-SO_X	329555	28	3	22	0.74
	EC-Oxalate	15462	1	0.5	1	0.72
	EC-K	40666	3	16	4	0.76
	EC-K-SO_X	13627	1	76	5	0.74
	EC-K-Oxalate	23399	2	0.3	1	0.74
	K-EC-NO_X	1391	0.1	100	7	0.74
	K-EC-SO_X	57553	5	100	4	0.85
	K-EC-Oxalate	161225	13	0.3	7	0.74
K-rich	K-CN	41740	3	35	17	0.76
	K-NO_X	12078	1	100	1	0.91
	K-SO_X	296512	25	9	3	0.85
	K-SO_X-Oxalate	28754	2	100	2	0.97
	K-Aluminosilicate	3797	0.3	21	2	0.91
	K-Na	2500	0.2	14	1	0.79
Na-rich	Sea salt-fresh	26175	2	68	6	1.54
	Sea salt-aged	69566	6	59	3	1.81
	Na-EC	1415	0.1	100	3	0.59
Amines	K-TMA	25603	2	0	1	0.74
	EC-TMA	19688	2	0.3	1	0.78
	OC-TMA	3734	0.3	18	0.5	0.70
OC-rich	OC	13323	1	2	2	0.74
	OC-NO_X	1368	0.1	100	0.2	0.66
	OC-SO_X	7435	1	95	1	0.64
V-rich	V	9810	1	9	2	0.70
	EC-V	3827	0.3	43	1	0.69
Fe-rich	Fe	2199	0.2	71	0.5	0.88
Ca-rich	Ca	2400	0.2	82	1	1.08

EC

Eight EC particle classes were identified during ADRIMED and SAF-MED, together comprising ~53% of the total ATOFMS counts. *EC-SO$_X$* and *K-EC-Oxalate* classes dominated, contributing 52% and 25% respectively to the EC category and 27% and 13% to the total particle counts (Figure 4.13). Average mass spectra are shown in Figure 4.13. All of the EC classes were characterised by elemental carbon fragments ions $^{12,24,36,..}C_n^+$ in the positive mass spectra. *EC-SO$_X$* and *EC-Oxalate* did not contain $^{39}K^+$, indicating they are most likely from fossil fuel combustion (coal/oil burning or traffic). *EC-K*, *EC-K-SO$_X$* and *EC-K-Oxalate* were characterised by a stronger signal for $^{36}C_3^+$ relative to $^{39}K^+$; similar particles have previously been attributed to coal combustion (Healy et al., 2010). *K-EC-NO$_X$*, *K-EC-SO$_X$* and *K-EC-Oxalate* produced stronger signals for $^{39}K^+$ relative to $^{36}C_3^+$, which is usually associated with biomass burning emissions.

Sulfate ($^{97}HSO_4^-$) dominated the SO$_X$ classes, but was also present to a lesser extent in the other six classes. Despite the average spectra for the EC classes showing large signals for sulfate and nitrate ($^{46}NO_2^-$, $^{62}NO_3^-$) most of the particles in these classes produced no negative ion spectra or only weak negative ion signals (due to the detector issues described in Section 2.3). It is therefore not possible to definitively describe their mixing state; however certain conclusions can still be drawn from their temporal profiles. Even with a fully functioning detector, less nitrate, or weaker signals for these species, relative to sulfate was expected given the high temperatures; nitrate mixed with EC is usually in the form of ammonium nitrate, which is more volatile than ammonium sulfate (Sciare et al., 2008; Querol et al., 2009a).

A smaller signal for MSA, $^{95}CH_3SO_3^-$ (Neubauer et al., 1997), relative to sulfate was found in the *K-EC-SO$_X$* class, indicating processing with marine emissions (Gaston et al., 2010). The oxalate classes are characterised by their signal at *m/z* -89, a marker for deprotonated oxalic acid (Yang et al., 2009) and aged aerosol. Very small signals for ammonium ($^{18}NH_3^+$), not marked in the mass spectra, were found in all but the *EC-Oxalate* class.

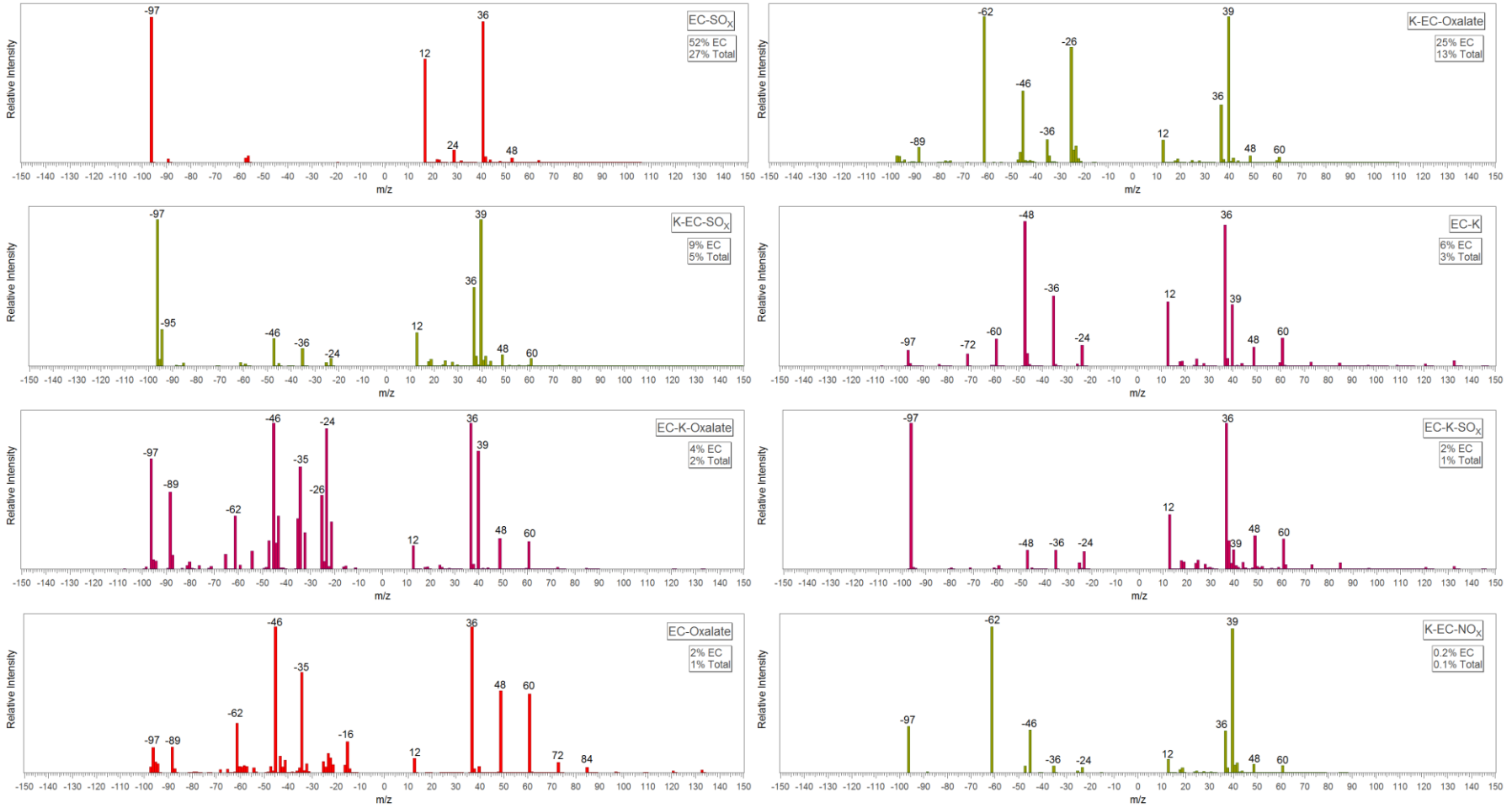


Figure 4.13. Average mass spectra for EC particle classes observed during ADRIMED/SAF-MED.

OC-rich

Three OC-containing particle classes were observed during ADRIMED and SAF-MED; *OC* and *OC-SO$_X$* particles constitute most of this category, contributing 60% and 29% respectively. Average mass spectra are shown in Figure 4.14. *OC, OC-NO$_X$* and *OC-SO$_X$* are characterised by a large signal for $^{39}K^+$ (confirmed by prominent signal for the $^{41}K^+$ isotope), hydrocarbon fragments ($^{27}C_2H_3^+$, $^{29}C_2H_5^+$, $^{51}C_4H_3^+$, $^{63}C_5H_3^+$) in the positive mode and strong signals for $^{43}C_2H_3O^+$, a marker for oxidised organic aerosol (Silva & Prather, 2000). The dominance of $^{39}K^+$ in the *OC* classes suggests a biomass burning origin (Silva et al., 1999; Pagels et al., 2013).

Sulfate was found in all three OC-containing classes, but dominated the negative mass spectra of *OC-SO$_X$* particles. *OC-SO$_X$* particles also exhibited a small MSA ($^{95}CH_3SO_3^-$) signal. Nitrate dominated the *OC-NO$_X$* class and was also present to a lesser extent in the *OC* and *OC-SO$_X$* classes. *OC* particles, which produced the strongest signal for $^{43}C_2H_3O^+$, exhibited further signs of ageing as oxalate ($^{89}(COO)_2H^-$) was found in their negative ion mass spectra.

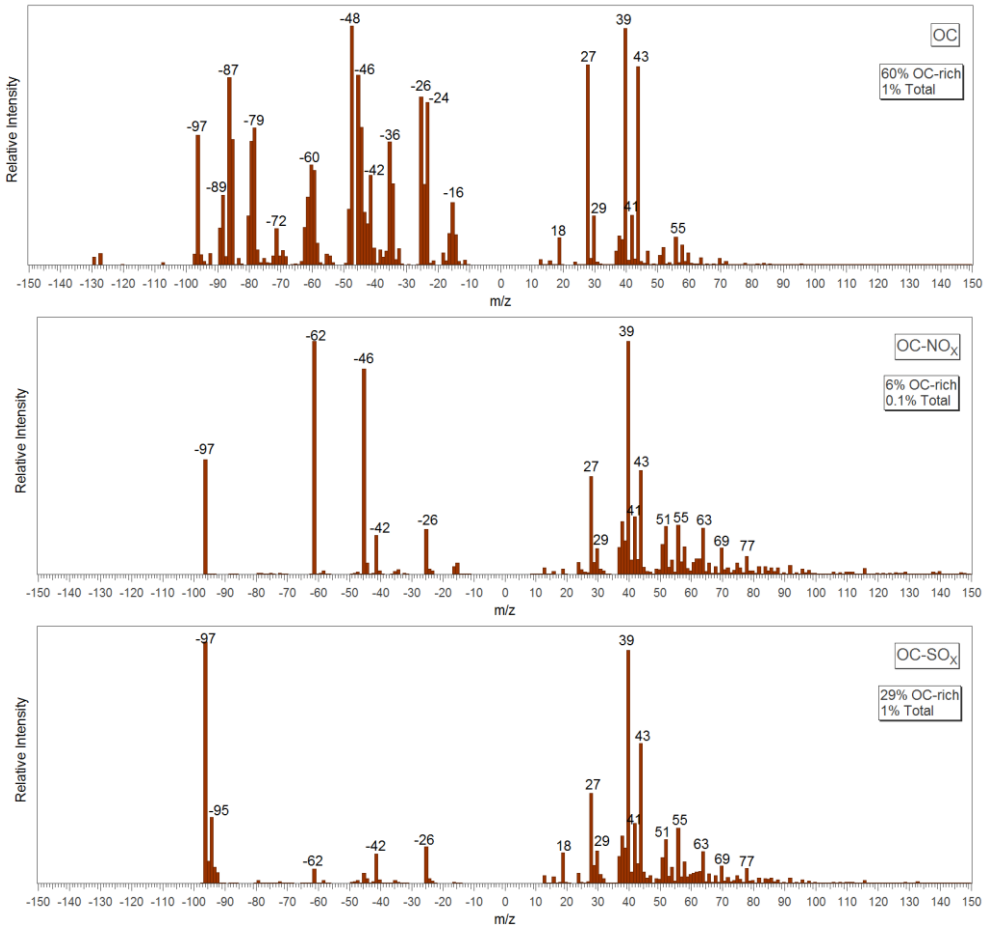


Figure 4.14. Average mass spectra for OC-containing particle classes observed during ADRIMED/SAF-MED.

K-rich

Six K-rich particle classes were identified during the sampling period; average mass spectra are shown in Figure 4.15. The positive ion mass spectra *for K-CN, K-NO_X, K-SO_X, K-SO_X-Oxalate* and *K-Aluminosilicate* classes are exclusively dominated by $^{39}K^+$, typical of biomass burning particles detected by ATOFMS (Silva et al., 1999; Qin & Prather, 2006; Pratt et al., 2010; Lea-Langton et al., 2015), while *K-Na* also produced signals for $^{23}Na^+$ and $^{56}Fe^+$.

Sulfate ($^{97}HSO_4^-$) dominates the negative ion mass spectra of the *K-SO_X* and *K-SO_X-Oxalate* classes, with additional MSA ($^{95}CH_3SO_3^-$) and oxalate ($^{89}(COO)_2H^-$) signals in *K-SO_X* and *K-SO_X-Oxalate* particles respectively. $^{26}CN^-$, internally mixed carbon and nitrogen, probably in the form of nitrogen-containing organic compounds (Silva et al., 1999), dominates the negative ion mass spectra of *K-CN* particles and is present with less intensity in the other K-rich classes. The same can be said of nitrate ($^{46}NO_2^-$, $^{62}NO_3^-$), which characterises *K-NO_X* particles. A strong signal for $^{43}AlO^-$ and $^{76}SiO_3^-$, typical components of mineral dust (Silva et al., 2000; Guazzotti et al., 2001b; Sullivan et al., 2007), characterised the *K-Aluminosilicate* class, though EC fragments were also present in the negative ion mass spectrum. EC fragments were found in all K-rich negative ion mass spectra, indicating either biomass combustion emissions or mixing with these emissions in the case of *K-Aluminosilicate*.

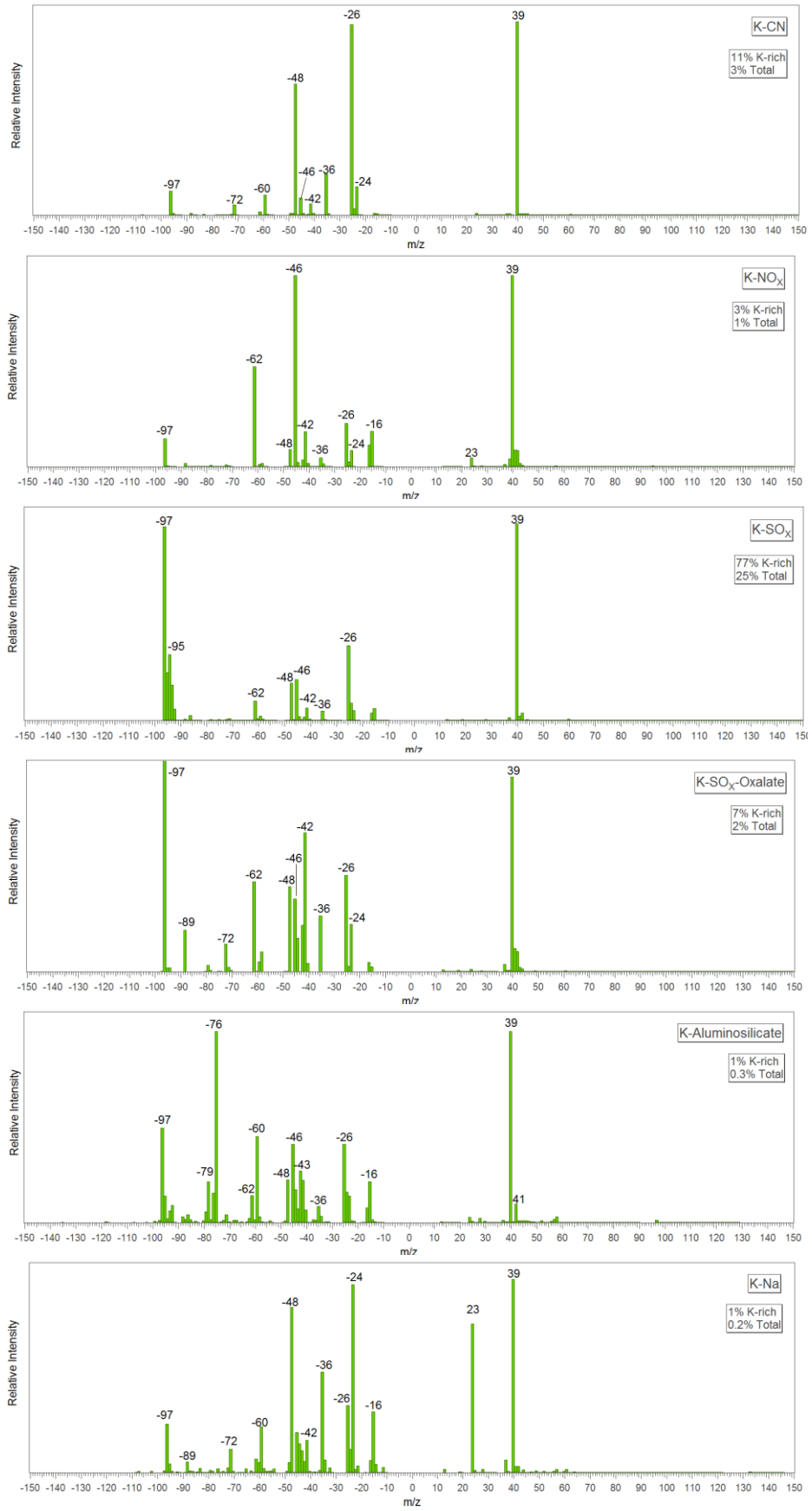


Figure 4.15. Average mass spectra for K-rich particle classes observed during ADRIMED/SAF-MED.

Na-Rich

Two sea salt particle classes were identified during the ADRIMED and SAF-MED sampling periods; fresh sea salt and an aged class. Together, these two classes account for ~ 8% of all ionised particles, and were distinguished from each other based on their composition (Figure 4.16). Fresh sea salt was characterised by the presence of $^{81,83}Na_2Cl^+$, $^{58}NaCl^-$ and $^{93,95}NaCl_2^-$ (Gard et al., 1998a), though some chloride replacement with nitrate occurred before detection as evidenced by signals at $^{46}NO_2^-$ and $^{62}NO_3^-$. However the aged particles contained less chloride as they produced no signals for NaCl adducts. Two further classes dominated by $^{23}Na^+$ were classified but each only contributed 1% to the Na-rich category. *Na-EC* particles were characterised by EC fragments in the positive and negative ion mass spectra, along with a strong signal for sulfate. Soot mixed with sea salt has been observed in previous studies during long-range transport episodes and likely forms by coagulation processes occurring during transport (Holecek, Spencer and Prather, 2007; Spencer et al., 2008; Ault et al., 2009).

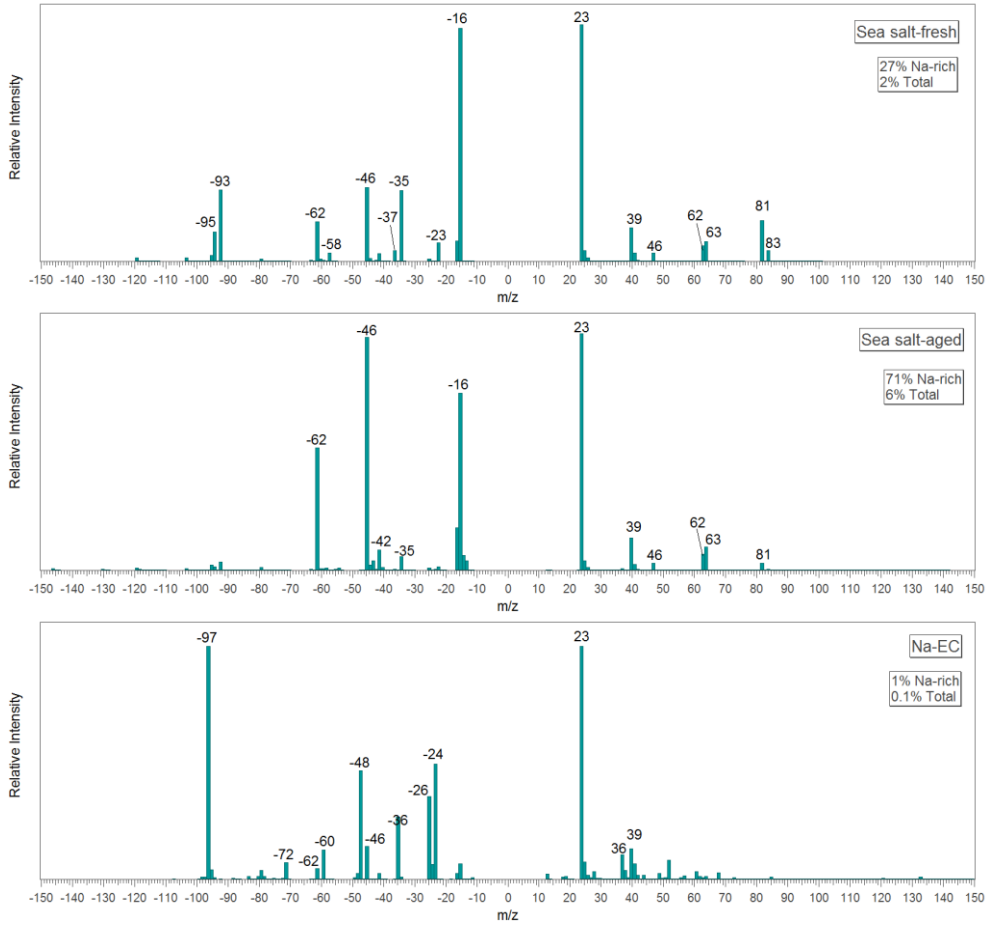


Figure 4.16. Average mass spectra for Na-rich particle classes observed during ADRIMED/SAF-MED.

The ATOFMS dataset was also queried for iodine and bromine with a relative peak area of > 0.001; only 25 particles were found to contain iodine and 53 contained bromine.

Amines

Three amine-containing particle classes were identified from the general *K*-means clustering approach. The most abundant classes were *K-TMA* and *EC-TMA*, which each accounted for 2% of all ATOFMS particles ionised, and 52% and 40% respectively of all Amine particles. Trimethylamine (TMA, $^{59}(CH_3)_3N^+$,) was the most abundant alkylamine marker ion. Also present in all three classes was a marker ion for protonated dimethylamine (DMA, $^{46}(CH_3)_2NH_2^+$), previously unidentified in other ATOFMS datasets to the best of this author's knowledge. A comparison of ATOFMS datasets obtained in Cork, Paris, Zurich, and those obtained for NANO-INDUS and ADRIMED/SAF-MED found this ion only in the latter two datasets. Ammonium ($^{18}NH_4^+$) was also found in all three Amine classes.

The *K-TMA* class was dominated by $^{39}K^+$, indicative of biomass burning, while *EC-TMA* particles produced $^{12,\ 36}C_n^+$ signals, indicating fossil fuel combustion origins. OC-TMA particles are characterised by strong $^{39,41}K^+$, OC ($^{27}C_2H_3^+$) and oxidised OC ($^{43}C_2H_3O^+$) signals, suggesting biomass burning sources and atmospheric processing during transport to the site.

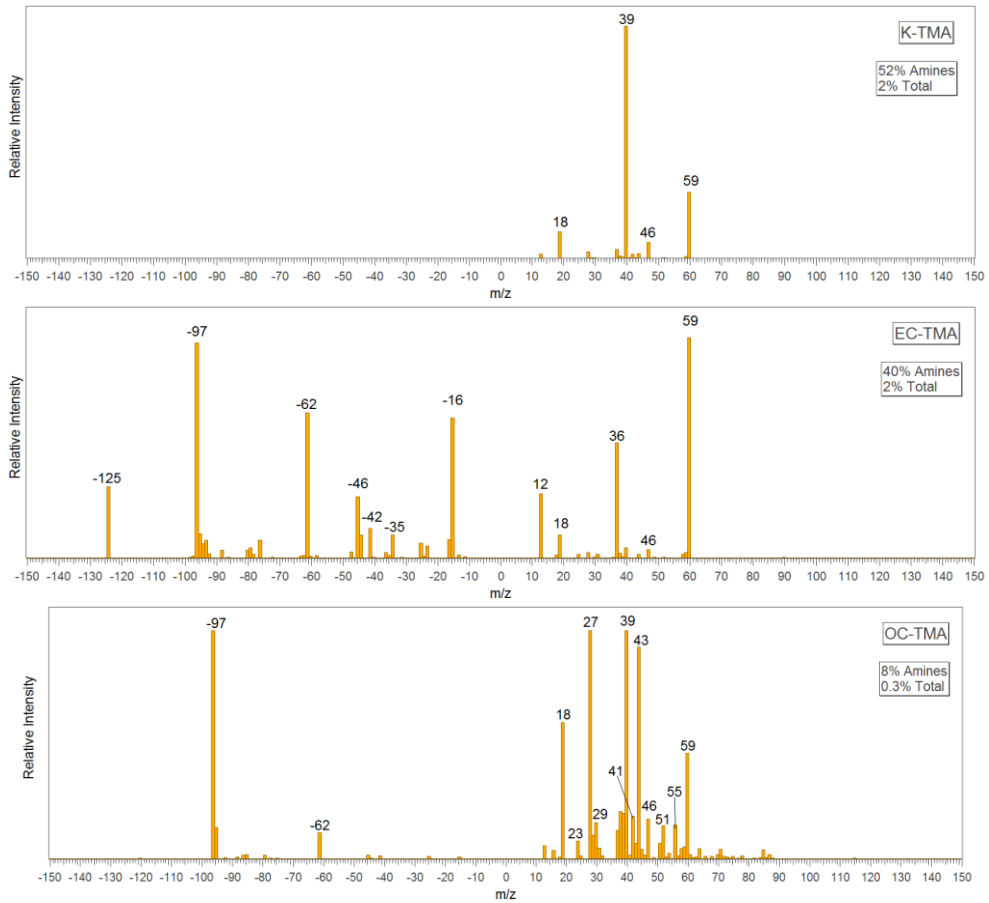


Figure 4.17. Average mass spectra for Amine particle classes observed during ADRIMED/SAF-MED.

Sulfate ($^{97}HSO_4^-$) and nitrate ($^{46}NO_2$, $^{62}NO_3$, $^{125}H(NO_3)_2^-$) were found in the negative mass spectra of *EC-TMA* and *OC-TMA*, however only 0.3% and 18% of these particles actually produced negative mass spectra and *K-TMA* particles produced none. Alkylaminium sulfate particles have been shown to readily absorb water at low relative humidities (< 45%) (Chan & Chan, 2013; Hu et al., 2014), while particle-bound water has been shown to suppress negative ion formation in mass spectrometers (Neubauer et al., 1997, 1998). The proportion of Amine particles with negative mass spectra is low, even considering the negative ion detection issue, 100% of particles in other classes (K-EC-SO_X, K-SO_X-Oxalate) produced negative mass spectra. This suggests particle-bound water could have had a significant effect on negative ion formation for these particles.

The average negative mass spectra should therefore not be considered representative of all particles in these classes. Healy et al. (2014) found MSA internally mixed with *EC-TMA* and *K-TMA* particles. However, on close inspection of their mass spectra the majority of these were found to be poor quality, with *m/z* -97 frequently miscalibrated as *m/z* -95. The resulting average mass spectrum of these particles would contain peaks for both *m/z* -97 and -95, which initially suggests the particles contain both HSO_4 and MSA. The presence of MSA in TMA and other amine-containing particles is however possible, as indicated by laboratory studies of particle formation and growth from reactions between MSA, TMA (or methylamine and DMA) and water (Chen et al., 2015b, 2015a).

V-rich

Two particle classes rich in vanadium were observed during ADRIMED and SAF-MED sampling periods; *V* and *EC-V* particles accounted for 61% and 39% of the V-rich category and 1% and 0.3% of total ATOFMS particles ionised. Average mass spectra for these classes are shown in Figure 4.19. $^{51}V^+$, $^{67}VO^+$, $^{56}Fe^+$, $^{58}Ni^+$ and sulfate ($^{97}HSO_4^-$) are typical markers for particles emitted by ships or oil refineries (Ault et al., 2009; Healy et al., 2009) and are present in both V-rich classes. The ratio of V to Ni in residual fuel oil is ~2.5 (Murphy et al., 2009), however only small signals for Ni have been seen in shipping/oil combustion particles (Ault et al., 2009; Healy et al., 2009) indicating low sensitivity of the ATOFMS for this species. Nebulising a standard solution containing both V and Ni at equal concentrations confirms this, as ATOFMS mass spectra with a strong signal for $^{51}V^+$ but only a weak signal for $^{58}Ni^+$ are produced (Healy et al., 2009). *V* particles were dominated by nitrate relative to sulfate and also contained oxalate ($^{89}(COO)_2H^-$), indicating aged emissions. A small signal for MSA ($^{95}CH_3SO_3^-$) was present in *EC-V* particles. Internally mixed sodium, potassium, calcium, vanadium, nickel

and iron particles have also been observed in ship exhaust particles using off-line TEM-EDX and two-step laser mass spectrometry (L2MS) (Moldanová et al., 2009). Small signals for $^{39}K^+$ and $^{23}Na^+$ were found in the Corsica V-rich particles, but none for $^{40}Ca^+$.

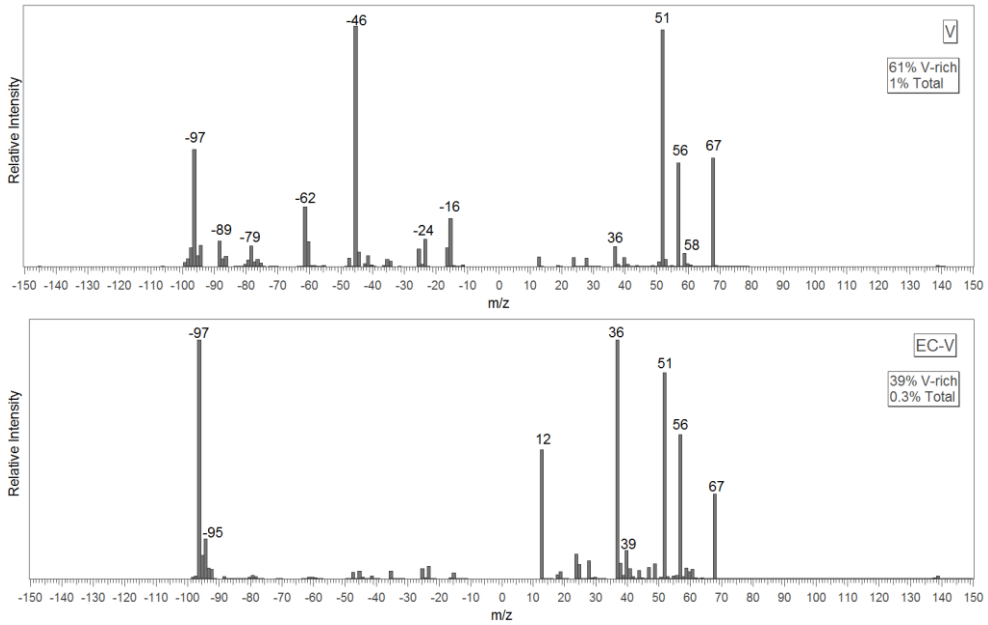


Figure 4.18. Average mass spectra of V-rich particle classes observed during ADRIMED/SAF-MED.

The mass spectra of the *EC-V* and *V* classes were also similar to those of regionally transported shipping particles (labelled V-Ni-Fe) found by Ault et al. (2009), and which were strongly associated with an ECOC class. These were the only two classes attributed to shipping or refinery emissions in this region at the time of sampling. A large number of these did not produce negative spectra; the authors suggested this was a result of significant chemical aging during transport where the particles accumulated water, which can suppress negative ion formation (Neubauer et al., 1997, 1998). The larger size (0.5 – 1 µm) and the presence of sulfate and nitrate in the limited number of particles with negative spectra supported this aging. Despite transport from the LA port over ~125 km along the California coast to the sampling site, these V-Ni-Fe particles did not appear to contain MSA, a significant difference to the Corsican V-rich classes, as both of these displayed small signals for MSA (MSA is discussed in more detail in Section 4.3.5).

Fe-rich and Ca-rich

Fe and Ca, along with Al and aluminosilicates are typical dust tracers which produce ions detectable by ATOFMS (Silva et al., 2000; Guazzotti et al., 2001b; Sullivan et al., 2007). K-rich dust is also a possibility. The *Fe* particles detected in Corsica were internally mixed with $^{39}K^+$, $^{23}Na^+$, $^{27}Al^+$, sulfate ($^{97}HSO_4^-$) and nitrate, although only a weak signal for $^{27}Al^+$ and no aluminosilicate signals (e.g. $^{43}AlO^-$, $^{59}AlO_2^-$, $^{60}SiO_2^-$, $^{76}SiO_3^-$, $^{77}HSiO_3^-$,

$^{103}AlSiO_3^-$) were found, which could also suggest industrial origins (Dall'Osto et al., 2008; Zhang et al., 2009b; Corbin et al., 2012).

Ca particles are dominated by $^{40}Ca^+$, with weaker signals for $^{56}CaO^+$ and $^{96}Ca_2O^+$. 34% of all Ca particles produced positive EC ions, which probably represents vehicular traffic (Silva & Prather, 1997; Gross et al., 2000; Song et al., 2001) to and from the site and from a few local villages whose tourist population increases during the summer. The remainder are then likely to be mineral dust.

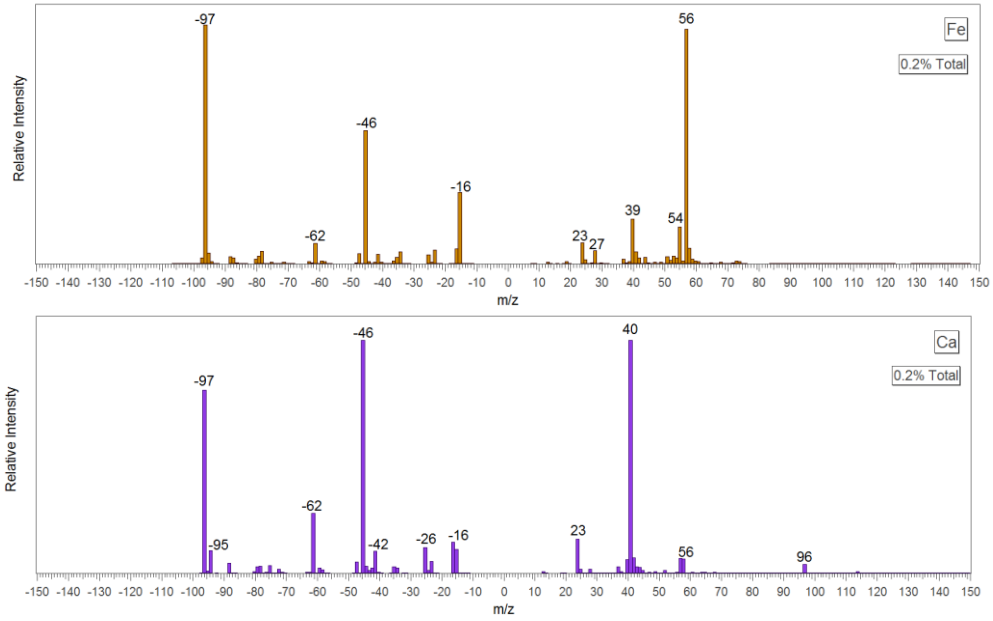


Figure 4.19. Average mass spectra of Fe and Ca-rich particle classes observed during ADRIMED/SAF-MED.

4.3.4 PARTICLE SOURCES

Temporal profiles for the 8 ATOFMS particle categories are shown in Figure 4.20. Elemental carbon (EC) dominated the dataset (53% of total spectra), followed by K-rich particles (32%) and Na-rich (mostly sea salt) (8%). The remaining particle categories include Amines (4%), OC-rich (2%), V-rich (1%), Fe-rich (0.2%) and Ca-rich (0.2%). A temporal profile for all ATOFMS particle numbers, which highlights the down-time of the instrument, is shown in Appendix III (Figure 9.1).

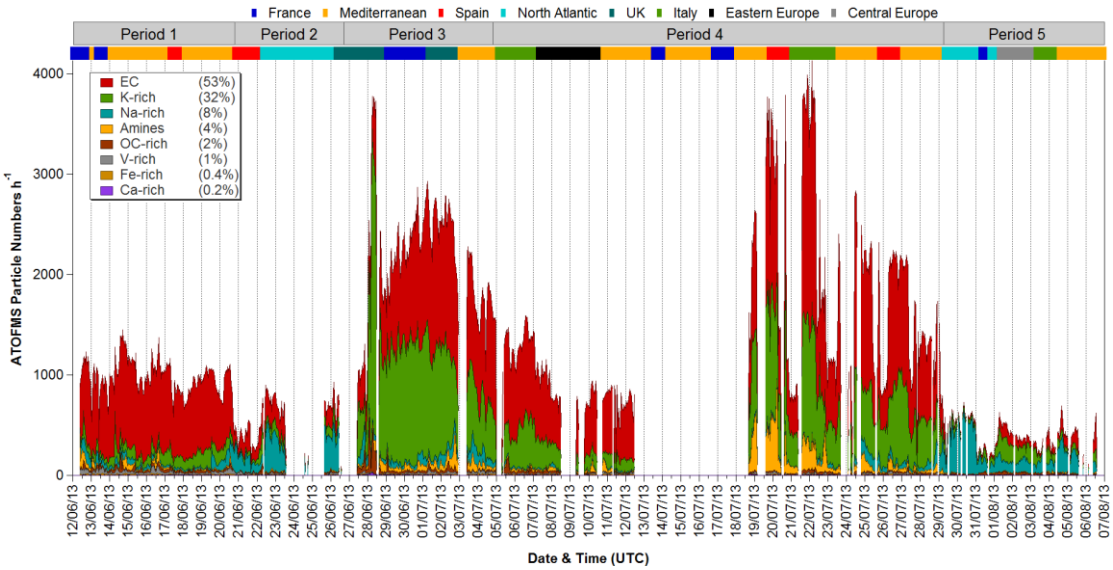


Figure 4.20. Time series of hourly unscaled particle numbers for the general ATOFMS particle categories observed during ADRIMED/SAF-MED.

The temporal profiles for the particle categories vary with the five meteorological periods described above. EC particle numbers were most abundant during Periods 1, 3 & 4 and dominated over K-rich particles (associated with biomass burning and dust) initially (Period 1); during later periods (3 & 4) their profiles are more similar, with K-rich particles peaking from 27 – 28th June. The profiles of both these categories suggest transport from regional sources, and a moderate overall correlation between them was found (R^2 = 0.42 overall, 0.80 for Period 4). Sea salt particle numbers were at their highest during periods where EC particles were at their lowest (Periods 2 & 5), and were generally low when EC particle numbers were high. OC-rich particles were present during the same period K-rich numbers peaked, suggesting an association with the transport of biomass burning particles. Aside from this event, the profile is not similar to any of the others and counts for this category were low, suggesting a less regional source, independent of the air masses influencing EC and sea salt particle occurrence. Amine particles were concentrated during the latter half of Period 4 (SAF-MED) and exhibited a similar profile to EC particles at this time (R^2 = 0.69). V, Fe and Ca-rich particles contribute very little to the total ATOFMS particle numbers, but were present throughout the two campaigns,

with Ca-rich numbers peaking during the same K-rich and OC-containing event. V-rich particles are typically associated with shipping emissions, while Fe and Ca are common components of mineral dust.

Reconstructed mass concentrations for the 8 ATOFMS particle categories are shown in Figure 4.21. Total ATOFMS mass correlates strongly over the full sampling period with SMPS number concentrations from 174.7-495.8 nm (R^2=0.72), OPS number concentrations from 300-579 nm (R^2=0.71), total ACSM mass concentrations (R^2=0.71), and moderately with mass concentrations of PILS SO_4^{2-} and NH_4^+ (R^2=0.58, 0.44), the ACSM factor SV-OOA (R^2=0.58), BC (MAAP) (R^2=0.55) and PM_1 (R^2=0.44).

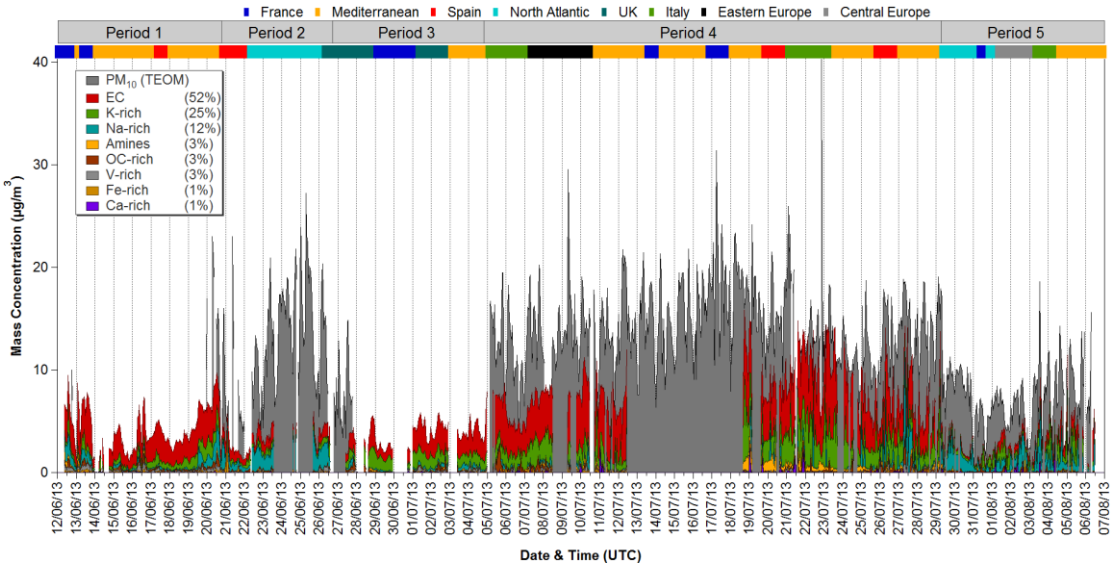


Figure 4.21. Time series of hourly reconstructed ATOFMS mass concentrations of major particle categories observed during ADRIMED/SAF-MED.

ATOFMS species account for a reasonable proportion of PM_{10} mass, particularly during Period 4 (70-90%), despite the aerosol composition being dominated by organics, sulfate and ammonium, species which the ATOFMS often underestimates (Thomson et al., 1997; Kane & Johnston, 2000; Silva & Prather, 2000). This suggests the mixing state and sources of these species can be explained to some degree by the ATOFMS particle classes. ATOFMS particles account for relatively little of the PM_{10} mass during periods when sea salt is abundant, which is expected given the upper size limit (3 µm) of the instrument and the drop in detection efficiency for supermicron particles (Cahill et al., 2014). Much of PM_{10} mass during the first sea salt event (20-26th June, 30th July) was unaccounted for by any of the PILS or ACSM species. Given the prevalence of Na, Cl, Mg and Ca during this period, it is likely that iron and aluminosilicates represent some of this unidentified mass. The ATOFMS is capable of detecting these species, but as components of mineral dust, they are also largely out of the instrument's size range.

Similar to particle number contributions, EC (52%), K-rich (23%) and Na-rich (12%) particles constitute most of the reconstructed ATOFMS mass.

Regionally Transported Combustion

Temporal profiles for hourly summed counts for EC and major K-rich classes are shown in Figure 4.22. There are two main types of profile; that of *EC-SO_X*, *EC-K* and *EC-Oxalate*, and that of *K-SO_X*, *K-EC-Oxalate*, *K-EC-SO_X*, *K-CN* and *EC-K-Oxalate*. The former dominated Period 1 and were considered markers for fossil fuel combustion as most of these did not contain $^{39}K^+$. Their particle numbers remained at relatively constant levels throughout the campaigns. For the first half of Period 1 regional air masses passed over France (including Marseille's heavy industries) and northern Italy (including the industrialised Po Valley) before reaching the site, while during the latter half of this period these air masses were then recirculated over the western Mediterranean (Appendix III, Figure 9.5).

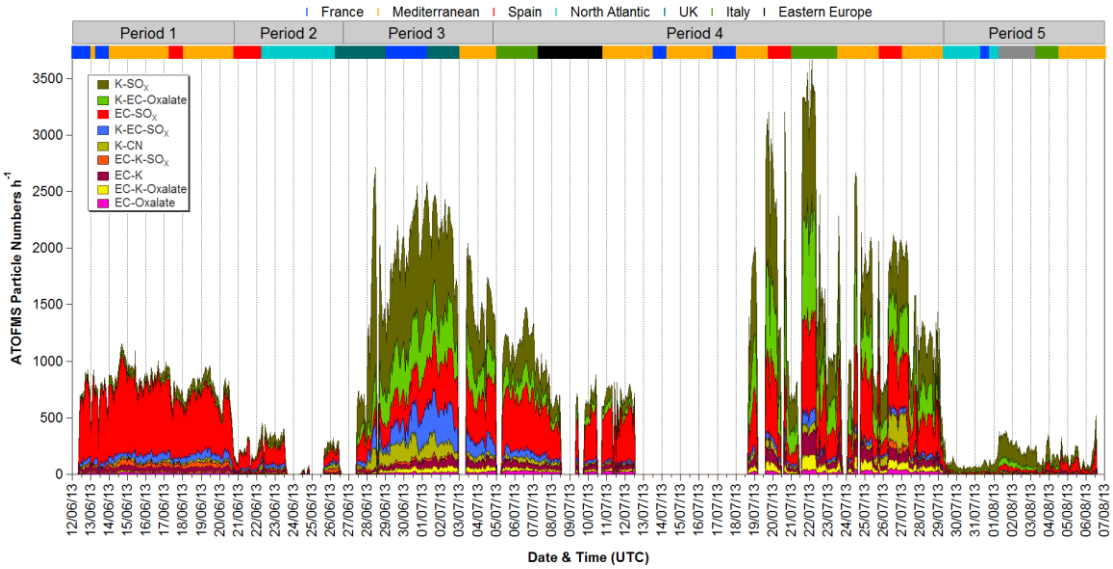


Figure 4.22. Time series of hourly unscaled particle numbers for ATOFMS EC and major K-rich particle classes observed during ADRIMED/SAF-MED. Temporal profiles have been stacked so relative contributions can be compared.

On the other hand K-rich particles, markers for biomass combustion, dominated Periods 3 and 4. Particle numbers for all EC and major K-rich classes decreased noticeably during Periods 2 and 5, which were influenced by synoptic scale air masses from the North Atlantic, effectively cleaning out the aerosols accumulated during the previous periods. Fires were detected by MODIS (Figure 4.24) over northern Italy throughout the sampling period and the site was heavily influenced by air masses passing over this region (Figure 4.9), which could explain the constant presence of K-rich particles in the background aerosol. The increase in these particles during Period 3 may be explained by longer residence times of air masses over southern France and northern Italy relative to Period

1, and particle numbers then began to decrease when trajectories from the North Atlantic and UK arrived at the end of Period 3.

The three Amine particles classes, *K-TMA*, *EC-TMA* and *OC-TMA*, presented similar temporal profiles (Figure 4.23) to those of major EC and K-rich particles classes shown in Figure 4.22. Numbers of *K-TMA* and *EC-TMA* particles peaked during Period 4, while *K-TMA* particles dominated over *EC-TMA* particles during Period 3, as was the case for the major K-rich and EC classes. The dominant Amine class, *K-TMA*, correlated well with two major classes, *K-SO_X* and *K-EC-Oxalate*, particularly during Period 4 (R^2=0.76, 0.7 respectively). Alkylamines have been found enriched in particles during periods of high relative humidity or fog events, with uptake onto existing particles that increased with increasing aerosol acidity (Rehbein et al., 2011). No association between any of the Amine classes and relative humidity was found, suggesting that if this had an effect it did so during transport of the Amine particles to the site. It also indicates that the Amine particles were not formed locally at the site.

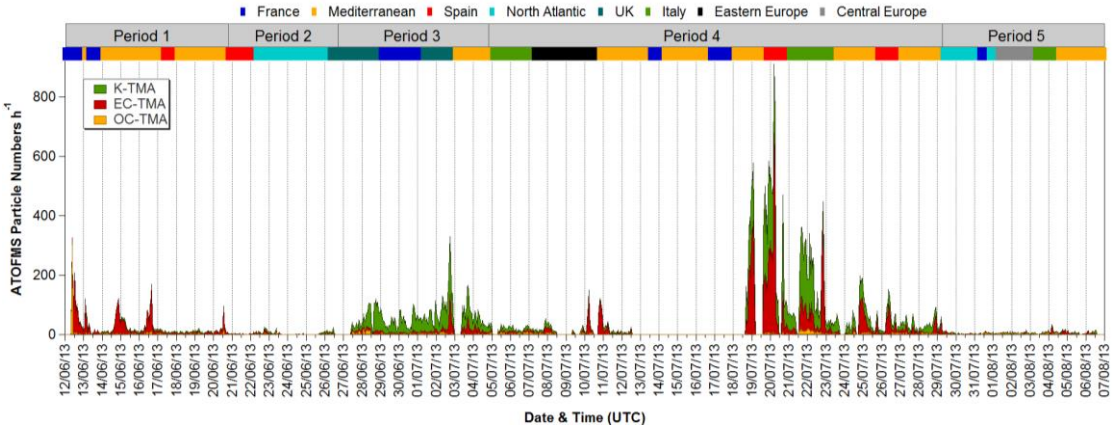


Figure 4.23. Time series of hourly unscaled particle numbers (stacked) for Amine particle classes observed during ADRIMED/SAF-MED.

A significant increase in fires was detected around the Black Sea from 10th July until the end of the sampling period (Figure 4.24). The burning of wheat residuals has been previously documented in this area and contributed at least 30% of EC and OC measured during similar time periods between 2001-2006 (Sciare et al., 2008). For ~4 days during Period 4, air masses from over the Black Sea and eastern Europe influenced the site, followed by extensive stagnation and recirculation of that air over the western Mediterranean. These observations coincided with a further increase in K-rich particle numbers relative to Period 3, levels which likely would have been higher had the ATOFMS not been limited to detecting particles >500 nm aerodynamic diameter.

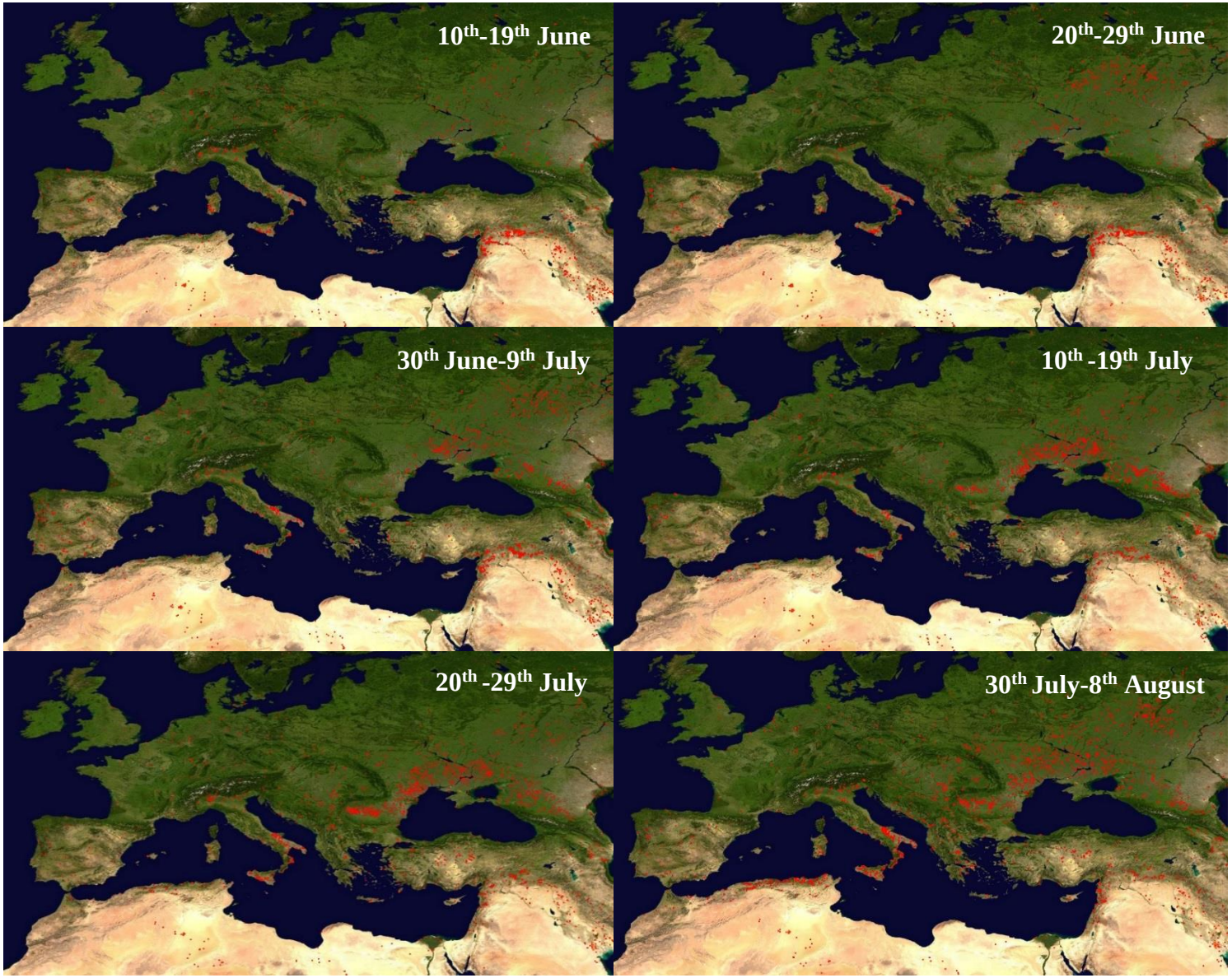


Figure 4.24. Locations of fires detected by MODIS on board the Terra and Aqua satellites over 10-day periods. Each coloured dot indicates a location where at least one fire was detected. (http://lance-modis.eosdis.nasa.gov/cgi-bin/imagery/firemaps.cgi)

Ageing of these biomass burning emissions was supported by elevated numbers of oxalate-containing particles, relative to Period 1, and occurred under low wind speed and diffuse wind direction conditions (Figure 4.25). In general, most EC and major K-rich particle classes were associated with low wind speeds, and dependences on speed and direction were similar for most of these classes.

Size-resolved particle number distributions for major EC and K-rich classes (*EC-SO_X* and *K-SO_X* were representative of other smaller classes) were consistent with aged combustion particles (Appendix III, Figure 9.14). The majority of *EC-SO_X* particles were between 400-800 nm, with particle numbers peaking around 500 nm for the first half of the campaign. The *K-SO_X* class displayed a peak aerodynamic diameter of 850 nm. *K-EC-Oxalate* particle numbers also peaked around 700 nm for the same period, while *EC-SO_X* particles of a similar size were seen after numbers of *K-SO_X* and *K-EC-Oxalate* began to decrease (5-7th July). A further shift in *EC-SO_X* size to around 900 nm was evident at the end of the campaign.

For the full sampling period reconstructed mass concentrations of all ATOFMS EC particle classes correlated well with ACSM SO_4^{2} (R^2=0.61), NH_4^{+} (R^2=0.62) and the SV-OOA factor (R^2=0.63) mass concentrations (which accounted for most of the organics mass), OPS 0.3-0.579 μm number concentrations (R^2=0.69) and moderately with PM_1 (R^2=0.46), BC (MAAP) (R^2=0.5), and AMS SO_4^{2} (R^2=0.56) and NH_4^{+} (R^2=0.6) (only present during SAF-MED) mass concentrations. Reconstructed mass concentrations for all K-rich classes (including local combustion) correlated with the same species but only moderately (R^2 ranged from 0.3-0.5). Individual particle classes did not produce stronger correlations, suggesting no one class was representative of the majority of $PM_{2.5}$ composition.

The average mass spectra of the ATOFMS classes showed sulfate, nitrate, oxalate and MSA were present. However many of these particles did not actually produce negative mass spectra and the frequency of spectra that contained those species was low. It is therefore not possible to describe with confidence the internal mixing state of EC and K-rich particles with secondary species.

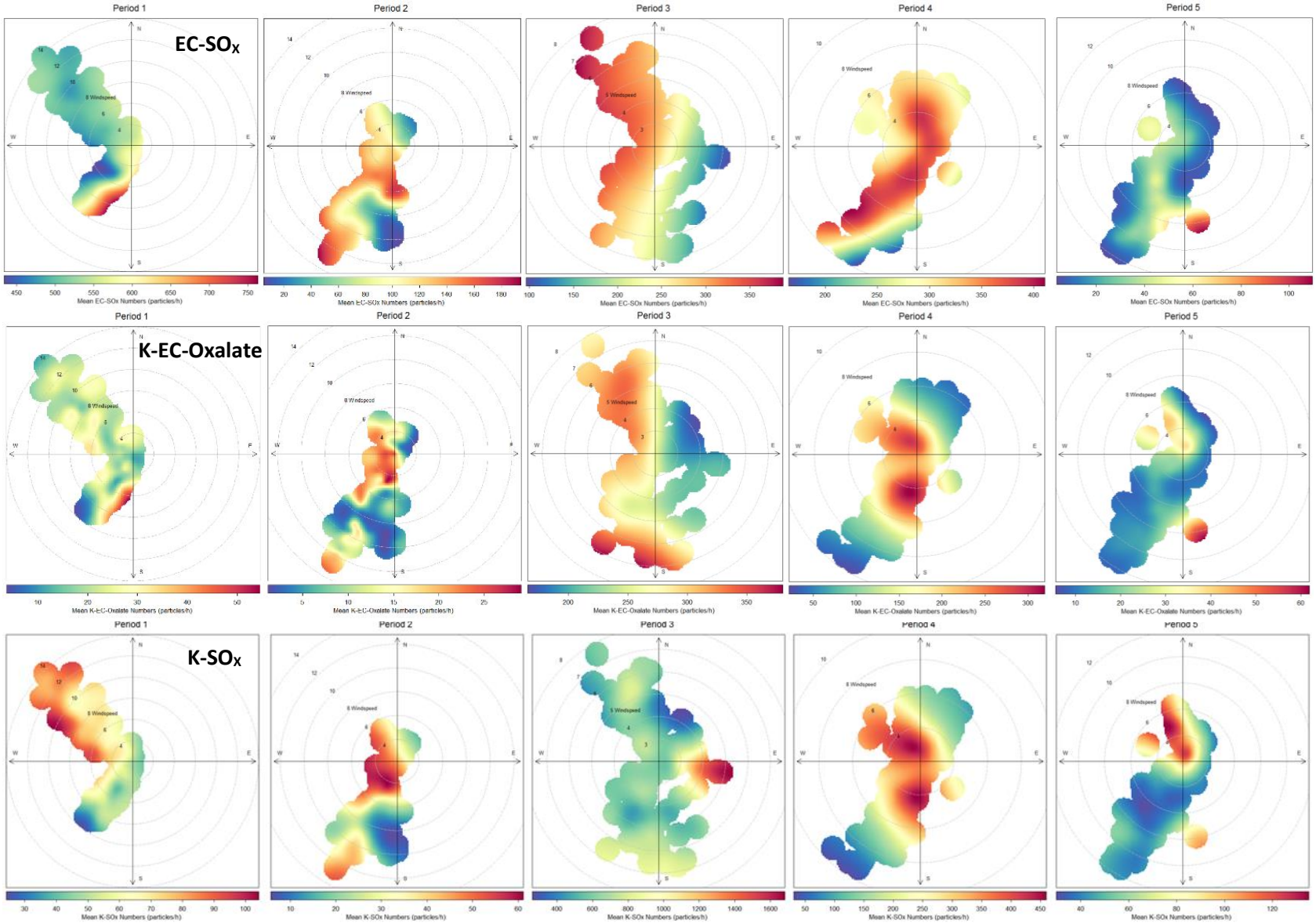


Figure 4.25. Wind speed and direction dependences of mean particle numbers for major EC and K-rich ATOFMS particle classes for each period during ADRIMED/SAF-MED.

From the PILS and ACSM measurements it was clear that ammonium and sulfate were the dominant secondary inorganic ions, with nitrate contributing relatively little to both PM_1 and PM_{10} mass. K^+, oxalate and MSA contributed considerably less to PM_{10} than nitrate, indicating that even if all EC and K-rich MSA and oxalate classes actually contained these species (which could not be concluded from the mass spectra) they would not have contributed substantially to the mass. PILS measurements indicate that K^+ mass concentrations were also not an important component of PM_{10}, which initially seems at odds with the ATOFMS EC and K-rich particle composition. However, K^+ is readily ionised by the ATOFMS desorption/ionisation laser so its prevalence in these particles is not representative of its mass concentration. The high level of agreement between EC and K-rich particles, BC and major ACSM species suggests those particles were comprised to a considerable degree of SV-OOA, as is apparent from Figure 4.26.

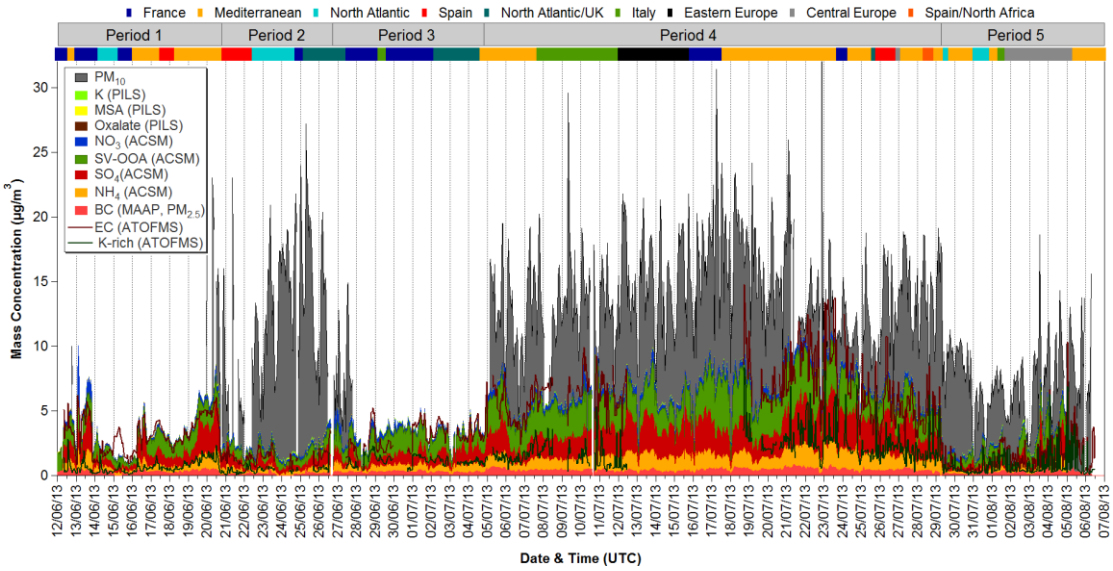


Figure 4.26. Hourly mass concentrations of PM_{10}, BC, ACSM Org, SO4 and NH4 and reconstructed ATOFMS EC and K-rich categories. BC and ACSM species profiles are stacked, as are both ATOFMS categories, but separately. This compares the ATOFMS mass concentrations with the total of BC and ACSM species.

However, no significant OC signals were found in any of the EC or K-rich classes, and particles with strong signals for OC in their positive mass spectra resolved themselves into classes which contributed relatively little to total ATOFMS particle numbers. Similarly to $^{39}K^+$, the ATOFMS favours ionisation of EC over OC (Silva & Prather, 2000; Ferge et al., 2006), which may account for the under-representation of organic aerosol in the ATOFMS measurements. The ATOFMS dataset was queried for particles containing OC fragments $C_2H_3^+$ and $C_2H_3O^+$, which then accounted for 28% of all ATOFMS particles. After clustering these results the classes *K-EC-Oxalate*, *K-SO_X*, *EC-SO_X* and *K-EC-SO_X* were found to contribute most of these OC-containing particles (22%, 19%, 14% and 13% respectively), with the remainder belonging to the other EC and K-rich classes

and OC-rich, V-rich and *EC-TMA*, *K-TMA*, *OC-TMA* classes. SV-OOA accounted for ~62% of the ACSM organics, and correlated well with the LV-OOA factor (33%); correlations of EC (R^2=0.42) and K-rich (R^2=0.32) particles with LV-OOA were weaker compared to those with SV-OOA.

In general, atmospheric SV-OOA corresponds to fresh SOA that evolves into LV-OOA with additional photochemical processing (Jimenez et al., 2009). LV-OOA and SV-OOA accounted for 85% of the total OA observed by (Minguillón et al., 2015) in Montseny, Barcelona; large increases in SV-OOA concentrations relative to BC at midday were found, which were attributed to local SOA formation. LV-OOA concentrations did not increase to the same degree, indicating a more regional and well-oxidised aerosol, and were considered representative of regional background SOA.

Also observed by Minguillón et al. (2015) was an underestimation of the relative ionisation efficiency of OA measured by the ACSM when this was compared with OC collected on filter samples, which resulted in an overestimation of OA by the ACSM. This is currently being investigated by the instrument's manufacturer but does not appears to be an issue for the ACSM deployed during ADRIMED/SAF-MED, shown in Appendix III (Figure 9.2). OA mass concentrations from the ACSM and AMS are similar for most of the period when both instruments were deployed, and both reported higher OA concentrations than the thermo-optical analysis of filters.

A large concentration of ATOFMS particle numbers, specifically the *K-SO$_X$*, *K-SO$_X$-Oxalate*, *OC*, *OC-TMA* and *Ca* classes, was observed from 17:00 on 27th June to 10:00 on 28th June (Figure 4.27).

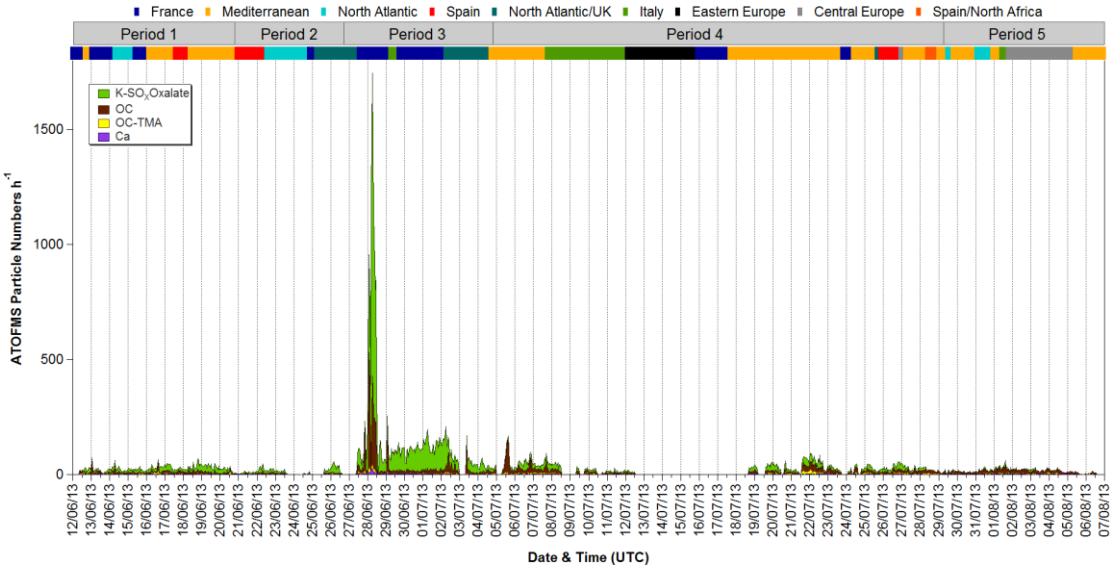


Figure 4.27. Time series of hourly unscaled particle numbers for particle classes observed on the 28th June during ADRIMED/SAF-MED.

K-SO$_X$ particles were seen throughout the sampling period (Figure 4.22) but the other four classes were confined largely to this event. $^{39}K^+$ is a common marker for biomass combustion, which typically also produces organic aerosols (Silva et al., 1999; Qin & Prather, 2006; Pratt et al., 2010; Lea-Langton et al., 2015).

It is likely that these classes represent a regionally transported biomass burning event; HYSPLIT trajectories for these two days show air masses residing over northern Italy (Appendix III, Figure 9.8) and all four classes displayed a strong dependence on easterly winds (Figure 4.28) consistent with the direction of those trajectories. Local combustion events produced less particles and during shorter periods than this regional event. Local particles were also mostly smaller than these regional ones; *K-SO$_X$-Oxalate* particle numbers peaked around 880 nm, *Ca* around 1 µm, *OC-TMA* around 790 nm and *OC* between 740 nm (Appendix III, Figure 9.15).

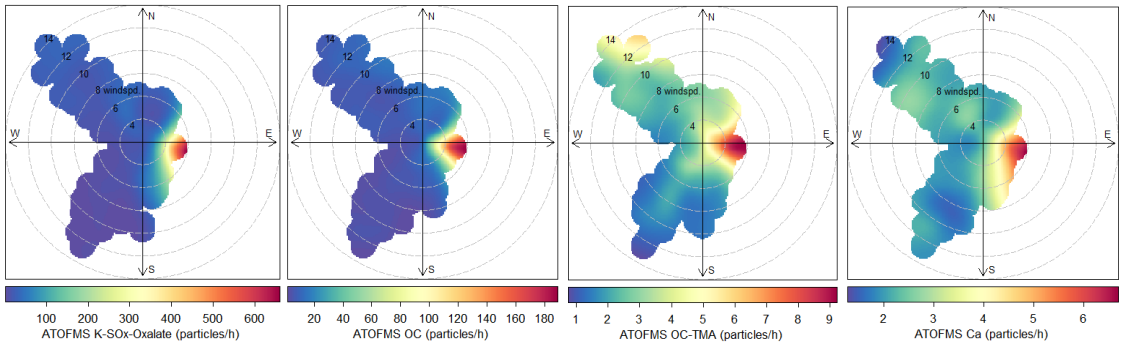


Figure 4.28. Wind speed and direction dependences for regional combustion particle classes observed on the 28th June (ADRIMED).

Satellite monitoring of wildfire activity from the 26th June and a mean transport time of ~ 2 days from FLEXPART simulations (Figure 4.29, analysed by Marine Claeys, CNRM-GAME) suggest particles from a forest fire in northern Italy were transported to the site and detected.

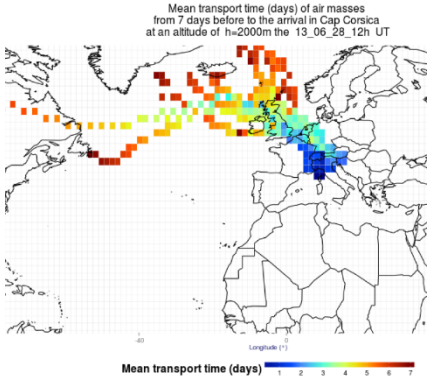


Figure 4.29. Flexpart simulations of transport time for air masses arriving at Cap Corse on 28th June (Marine Claeys, CNRM-GAME).

Local Combustion

The sampling site on Corsica was chosen for its negligible local sources relative to the regional background. However, some local sources did influence the site, though these did not contribute significantly to particle number or mass concentrations. Local combustion events were detected in the form of *K-NO_X*, *OC-NO_X*, *OC-SO_X* and *Na-EC* particles, and distinguished themselves from the dominating regional aerosol by occurring mostly during Periods 1 and 2 over 5-7 hours (Figure 4.30). The first event was observed on the 12th June from 13:00-18:00 UTC and its source as biomass burning (in the form of vegetation trimmings) visually confirmed on the slopes north-east of the site. The composition of these particles is consistent with this observation; K^+ is a common marker for biomass combustion, which typically also produces organic aerosols. Further events were detected on 14th June (05:00-10:00 UTC, 12:00-19:00 UTC), 15th June (05:00-10:00 UTC, 13:00-19:00 UTC), 16th June (05:00-11:00 UTC, 15:00-19:00 UTC), 17th June (05:00-10:00 UTC), 22nd June (02:00-09:00 UTC) and 1st July (05:00-09:00 UTC), but were not visible from the site. Garden waste biomass was frequently burned in the surrounding villages during June; such combustion was prohibited from July onwards which explains the lack of similar local events. No local wildfires or controlled agricultural burning was noted during the sampling period. Between 27th June and 1st July, *K-NO_X*, *K-EC-NO_X* and possibly *OC-SO_X* were of regional biomass burning origins, as their temporality was noticeably different to the preceding short local events; this period was influenced by short-range air masses residing over southern France and northern Italy. *K-NO_X* and *OC-SO_X* particles were also present throughout both campaigns, in low numbers outside of events, indicating persistent regional sources.

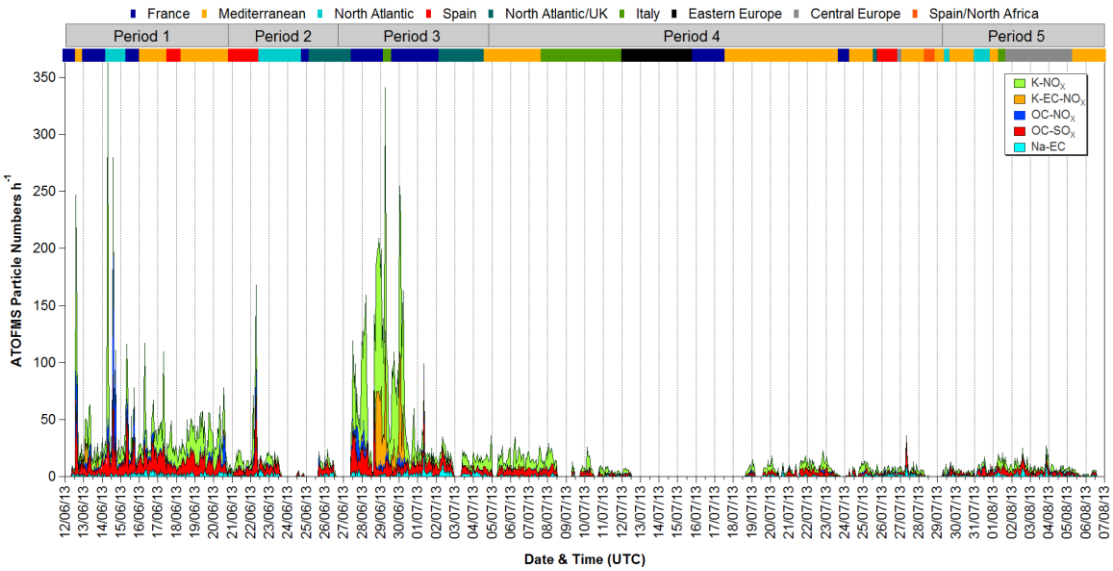


Figure 4.30. Time series of hourly unscaled particle numbers for particles associated with local biomass burning observed during ADRIMED & SAF-MED.

Size distributions (Appendix III, Figure 9.14) for *K-NO_X*, *OC-SO_X* and *OC-NO_X* were similar and typical for particles produced from inefficient, low temperature combustion, with numbers peaking between 300 and 500 nm for most of the local events. Regionally transported *K-NO_X* and *K-EC-NO_X* were noticeably larger, peaking between 700 and 900 nm; this represents a significant amount of growth through ageing, assuming these particles were of a similar size at their source to those burned locally in Corsica. *Na-EC* particles can form from combustion processes or through soot mixing with sea salt (Holecek et al., 2007; Spencer et al., 2008; Ault et al., 2009); these two distinct sources are represented in the size distribution for this class (Appendix III, Figure 9.15). The majority of particles were between 300 and 700 nm in diameter, representing local combustion, but during certain periods (e.g. 22nd June) a separate mode around 1.5 µm was evident, consistent with sea salt coagulation.

Marine and Dust

The two ATOFMS sea salt classes presented noticeably different temporal profiles (Figure 4.31). Fresh sea salt was detected mostly during short periods (20-26th June, 30th July) which coincided with increases in OPS number concentrations in the 0.579-2.156 µm range and PILS sea salt aerosol (SSA), calculated using SSA=$[Cl^-]+[Na^+]\times1.47$ (Bates et al., 2012), and Mg^{2+} mass concentrations. Correlations between these measurements can be found in Table 9.1. Association between ATOFMS fresh sea salt numbers and the OPS and PILS sea salt components is weak to moderate (R^2=0.3-0.5) throughout the whole sampling period, but this strengthened when reconstructed ATOFMS mass was compared (R^2=0.5-0.8). Correlation between ATOFMS fresh sea salt mass and SSA is particularly strong (R^2=0.81) for the sea salt event during Period 2, with an identical R^2 with 0.579-2.156 µm at this time.

Moderate correlations with Ca^{2+} and K^+ were also observed during this period; from Figure 4.31 it is apparent that temporal profiles of these species are similar to those of 0.579-2.156 µm, with Ca^{2+} also correlating moderately with 2.156-8.032 µm particles (R^2=0.54) during Period 1. SSA, Mg^{2+}, Ca^{2+} and K^+ combined constituteed at least 50% of PM_{10} for the majority of the Period 2 sea salt event, with contributions of >80% for some hours of the event. ATOFMS fresh sea salt mass accounted for 50-80% of the SSA mass during this period, suggesting that a significant amount of sea salt was in the $PM_{2.5}$ fraction.

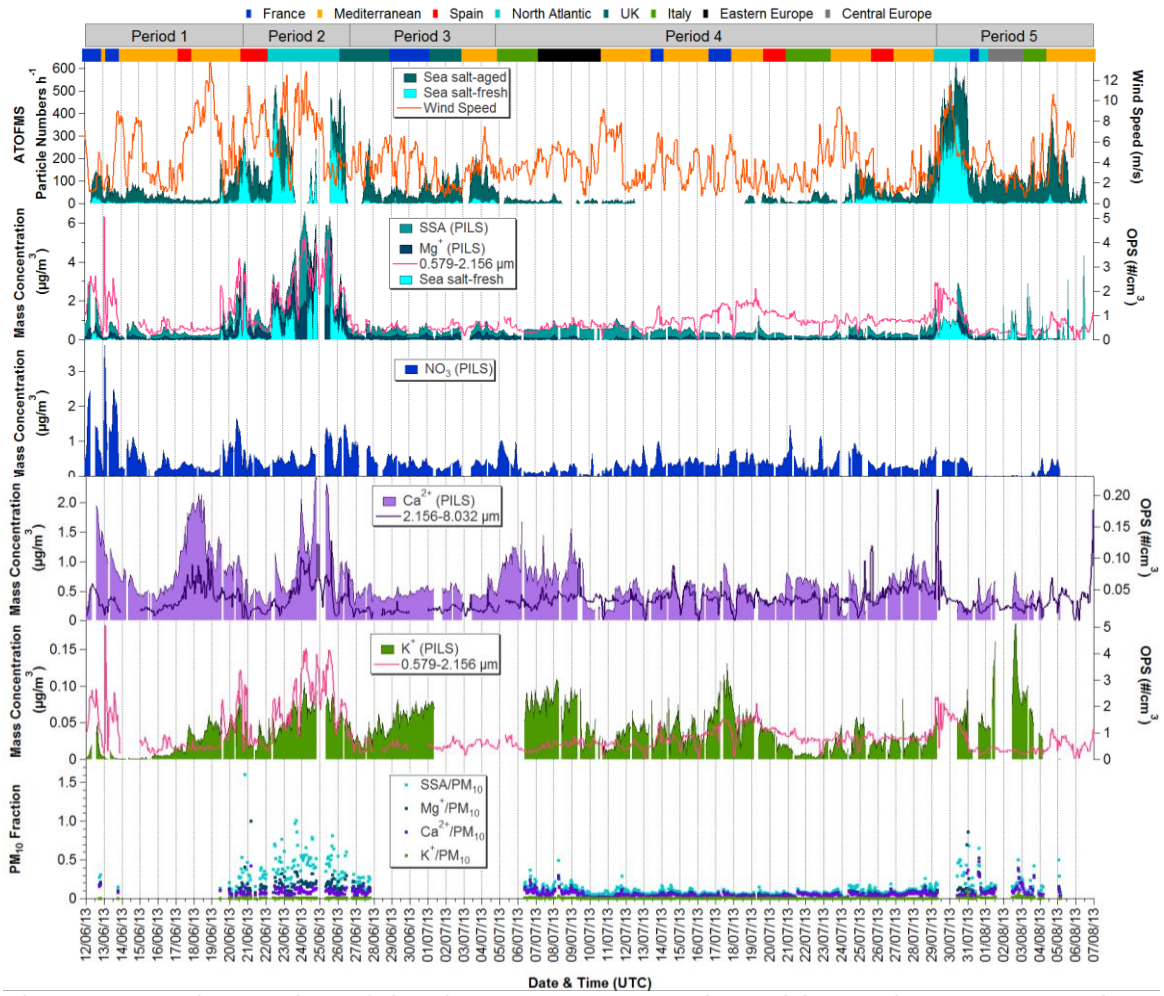


Figure 4.31. Time series of hourly ATOFMS sea salt particle numbers, OPS number concentrations, PILS SSA, Mg^{+}, NO_3^{-}, Ca^{+} and K^{+} mass concentrations, and PM_{10} fractions observed during ADRIMED/SAF-MED.

The majority of ATOFMS aged sea salt particles were detected outside of the fresh sea salt events. Neither particle numbers nor mass concentrations of this class correlated with any other sea salt markers for the whole sampling campaign. However, some associations were found for individual periods (Appendix III, Table 9.1). During Period 1 particle numbers and mass concentrations for ATOFMS aged sea salt correlated moderately to strongly with SSA and 0.579-2.156 µm particles, while moderate correlations were also observed with ACSM SO_4^{2-}, NH_4^{+} and Cl^{-}. These species were measured in PM_1 and ammonium sulfate in particular has been shown to contribute significantly to PM levels in the Mediterranean during the summer (Rodríguez et al., 2002, 2007; Querol et al., 2009a). The conditions which favoured the production and accumulation of these species during this period also enhanced the replacement of Cl in sea salt to form sodium nitrate particles. PILS NO_3^{-} correlated well with ACSM NO_3^{-} (R^2=0.65) and NH_4^{+} (R^2=0.51) (but not SO_4^{2-}) during Period 1, indicating that ammonium nitrate formation was favoured, and strongly with 0.579-2.156 µm particles and SSA during Period 5, suggesting aged sea salt/sodium nitrate was being formed. Both fresh and aged ATOFMS

particle numbers correlated moderately with PILS NO_3^- during this period; it is probable that the "fresh" sea salt contained more nitrate at this point than during the Period 2 event.

Peak SSA mass concentrations were found under high wind speed conditions (Figure 4.32), with a strong south-westerly dependence. The number of marine particles over the ocean is directly proportional to the wind speed (Calvo et al., 2013), and an increase sea salt mass concentrations with high wind speed has also been observed around the Mediterranean (Querol et al., 2009a). Both ATOFMS fresh and aged sea salt particle numbers also displayed strong dependencies on south-westerly winds, while some aged sea salt was also associated with low winds speeds, from multiple directions. The majority of trajectories produced with HYSPLIT originated over the North Atlantic during Period 2, consistent with the dominance of fresh sea salt, while the event during Period 5 was influenced by air masses alternating between the North Atlantic origins and recirculations over the Mediterranean, consistent with the mixture of fresh and aged sea salt observed.

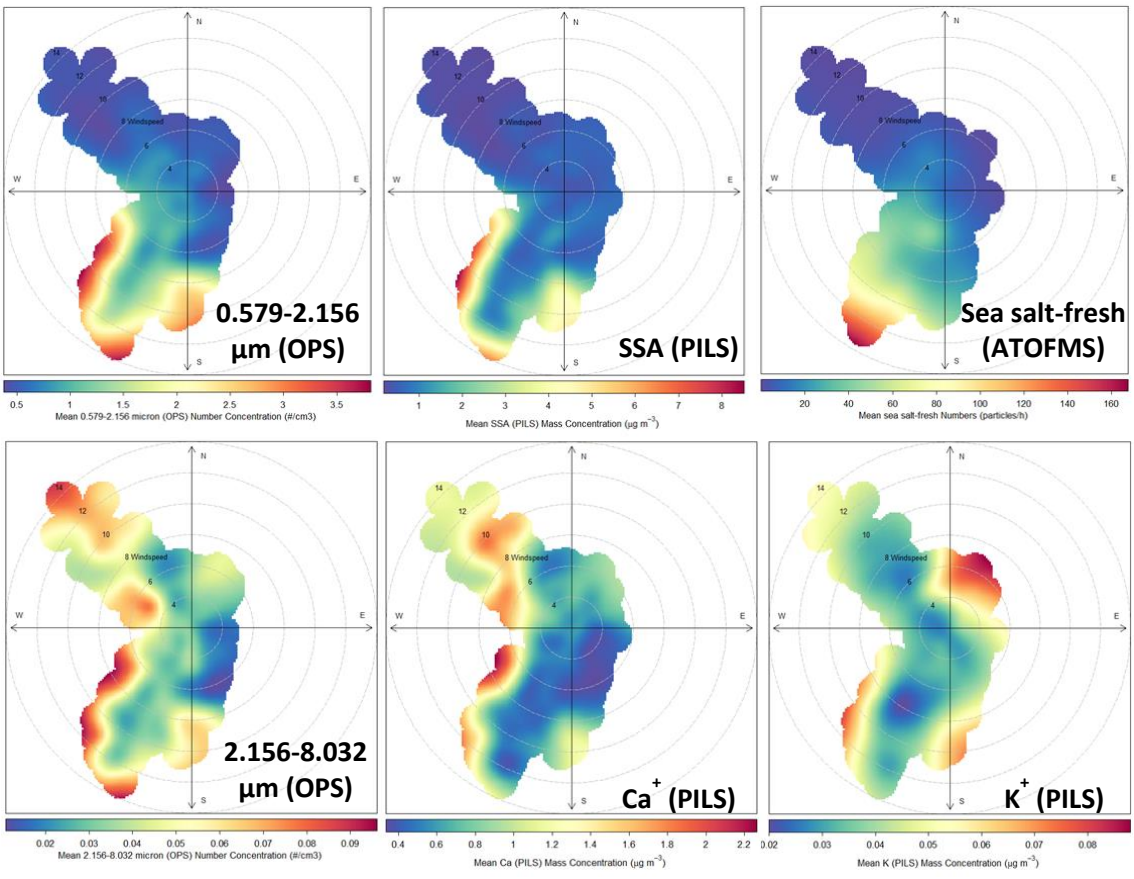


Figure 4.32. Wind speed and direction dependence for mean PILS SSA, Ca^+ and K^+ mass concentrations, OPS number concentrations and mean ATOFMS sea salt particle numbers (fresh and aged sea salt dependence identical) observed during ADRIMED and SAF-MED.

Coinciding with the sea salt event during Period 2 were increased concentrations of K^+ and Ca^{2+} (PILS) mass and 2.156-8.032 µm particle numbers. The association between K^+ and 0.579-2.156 µm and 2.156-8.032 µm particles (R^2=0.68, 0.51), and between Ca^{2+} and 0.579-2.156 µm and 2.156-8.032 µm particles (R^2=0.53, 0.59) during this period indicates

an influence of mineral dust as well as marine emissions. Using Ca^{2+} and 2.156-8.032 μm particles as dust tracers, a mineral dust event was evident from 17th-19th June, prior to the sea salt event and not influenced by marine emissions (no increase in SSA or 0.579-2.156 μm particles). This dust event also coincided with an increase in wind speed, similar to that which influenced sea salt levels, and air masses which originated over the south east coast of Spain and the north coast of Africa. No increase in K^+ concentrations was seen during this time; the use of K^+ as a dust tracer is complicated by contributions from biomass burning, but a lack of association between the two also implies different mineral dust sources, as these produce different Ca^{2+} and K^+ content.

Ca^{2+} does not correlate with 2.156-8.032 μm particles throughout the sampling period, indicating that mineral dust is not the only source. Ca mixed with EC is used as an ATOFMS tracer for traffic emissions. Although Ca-EC particles were detected during the sampling period, they were not present in statistically relevant numbers. It is likely that since traffic emissions are an important component of anthropogenic aerosol in the Mediterranean that there were more traffic particles impacting the site than detected, as these are usually <300 nm in diameter and that the sizing laser power issues prevented effective detection in that range.

Dust particles detected with an ATOFMS are typically comprised of Fe, Ca and aluminosilicates. *Ca* particle numbers peaked on 28th June around 1 μm, with low numbers (~5 particles h^{-1}) outside of this event, even considering the poor AFL transmission efficiency for larger particles. This suggests very little of the Ca^{2+} detected by PILS was in $PM_{2.5}$, and as a result neither ATOFMS Ca particle numbers or mass concentrations correlate with any other dust tracers. Similar observations can be made for *Fe* particles, most of which were between 500-900 nm in diameter and very few were larger than 1 μm (Appendix III, Figure 9.15). Both were absent during the mixed sea salt/mineral dust of Period 2. It is therefore likely that most Fe particles detected by the ATOFMS were of regional industrial origin, particularly from the start of the sampling period to the beginning of July. Possible K-rich dust classes include *K-Aluminosilicate* and *K-Na* but the size distributions for *K-Na* show (Appendix III, Figure 9.15) that not all of these particles were likely to be mineral dust. As for the *Ca* and *Fe* particles, these classes contribute very little to particle numbers, and no correlations with any dust tracers were found.

Shipping

Heavy fuel oil combustion aerosols, from power plants and shipping, have a strong presence in the Mediterranean (Querol et al., 2009a; Pey et al., 2010). There are more than 15 passenger ferry lanes incurring shipping traffic around the northern tip of the island; the closest pass is ~16.5 km north and ~12.5 km east of the site (Figure 4.33). Ferries travelling around the northern tip and to the east of the site, take approx. one hour to reach Bastia and between the ferry companies SNCM, La Méridionale, Moby, Corsica Ferries and Sardinia Ferries ~ 50 sailings take place per week.

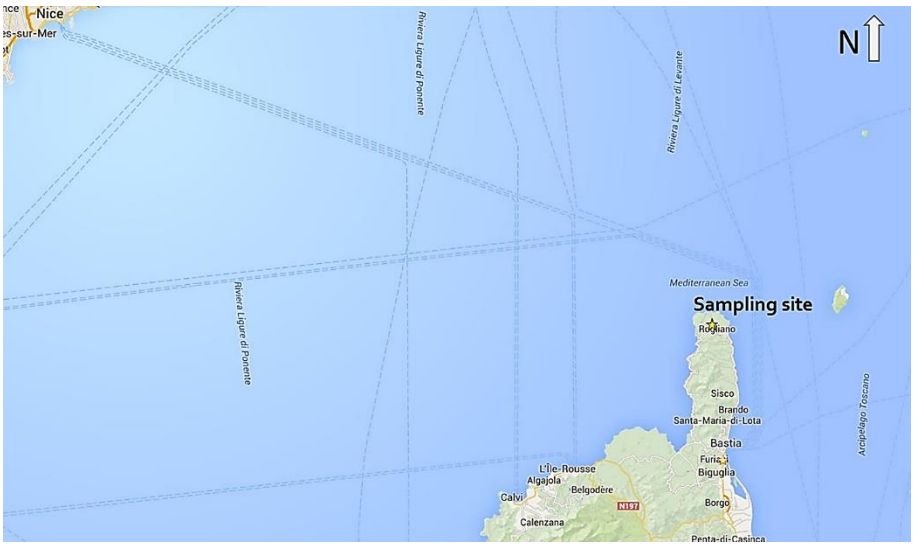


Figure 4.33. Passenger ferry lanes around the sampling site on Corsica.

V and *EC-V* ATOFMS particles both contain tracers for heavy fuel oil combustion. Particle numbers for these two classes correlate moderately (R^2=0.47) over the whole sampling period, suggesting similar sources, and exhibited temporal profiles (Figure 4.34) typical of the regional emissions characterised thus far.

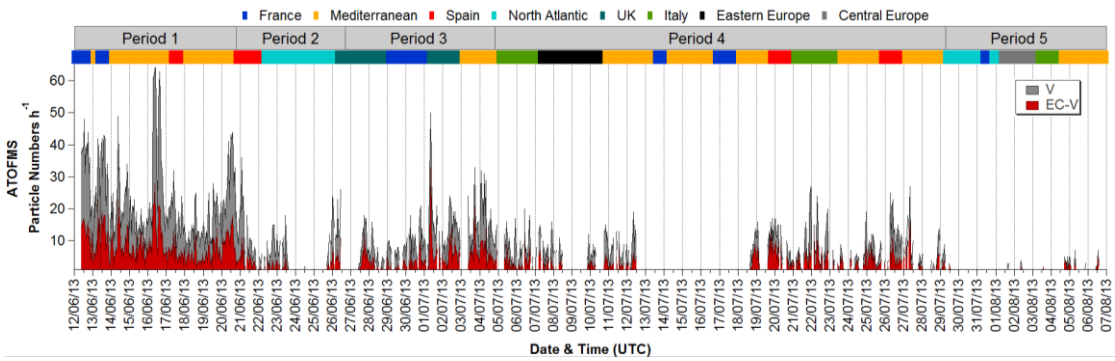


Figure 4.34. Hourly summed particle numbers for V-rich particles observed during ADRIMED/ SAF-MED.

Both classes displayed strong north-westerly and south-westerly wind dependences (Figure 4.35), consistent with the distribution of most ferry lanes (Figure 4.33), under the full range of wind speed conditions.

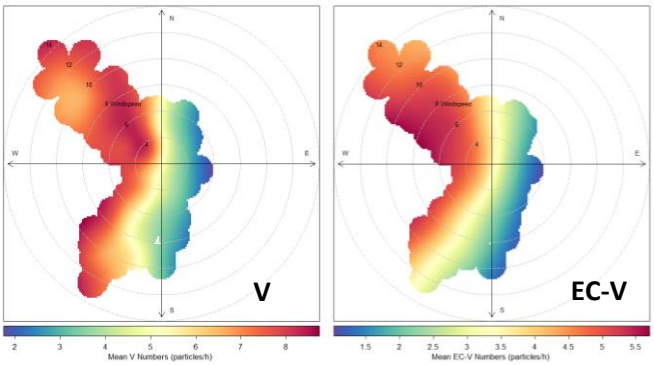


Figure 4.35. Wind speed and direction dependences for V-rich particles observed during ADRIMED and SAF-MED.

It was unlikely that any fresh heavy oil combustion emissions were observed with the ATOFMS as most freshly emitted shipping particles are between 200-300 nm aerodynamic diameter (Healy et al., 2009), and the closest shipping lane is at 12.5 km from the site. *EC-V* and *V* particle numbers consistently peaked around 740 nm aerodynamic diameter (Appendix III, Figure 9.15) indicating that the observed particles were aged to some degree. However, no particles smaller than 300 nm were measured by the ATOFMS, so the presence of fresh shipping particles at the site cannot be completely ruled out.

Fresh shipping particles were also found by Ault et al. (2010) in the Port of Los Angeles; an OC-V-sulfate class was attributed to residual fuel plumes, and a fresh soot class was attributed to distillate fuel plumes. Neither class contained nitrate and both were in the 100-500 nm aerodynamic diameter size range, consistent with fresh fuel combustion emissions. No V-rich particles dominated by OC were found during ADRIMED or SAF-MED; however using the querying approach outlined in Section 4.3.5. 50% of *EC-V* and 30% of *V* particles produced low intensity signals for $^{27}C_2H_3^+$ and $^{43}C_2H_3O^+$. Also accompanying soot particles in the distillate fuel plumes were Ca-ECOC particles, typically associated with distillate fuel used by light and heavy duty road vehicles (Sodeman et al., 2005; Toner et al., 2006), but also agreeing with enhanced calcium mass fractions from ships burning distillate fuels compared to residual fuel (Agrawal et al., 2008a, 2008b). No associations between any EC or Ca classes and V-rich particles was found, suggesting distillate fuel is not prevalent in the Mediterranean.

The mass spectra of the *EC-V* and *V* classes were also similar to those of regionally transported shipping particles (labelled V-Ni-Fe) found by Ault et al. (2009), and which were strongly associated with an ECOC class. No association between V-rich particles and any EC or OC-rich classes was found during ADRIMED or SAF-MED. V-rich particles contributed 3% to the total reconstructed ATOFMS mass concentrations

(effectively $PM_{2.5}$), whereas primary shipping particles contributed 2% of mean annual PM_{10} at the north African coast opposite Spain (Viana et al., 2009), 3-7% of PM_{10} and 5-10% of $PM_{2.5}$ around the Straits of Gibraltar (Pandolfi et al., 2011) and 5, 6 and 8% to PM_{10}, $PM_{2.5}$ and PM_1 in Barcelona (Amato et al., 2009).

4.3.5 PROCESSING MARKERS

As a substantial number of ionised ATOFMS particles produced low intensity signals in their negative ion mass spectra, or none at all, the average mass spectra favoured those species that ionised most efficiently i.e. nitrate and sulfate. Ions that usually produce small signals under optimum detector conditions, such as oxalate or $^{125}H(NO_3)_2^-$, were expected to be under-represented in the average mass spectra so an additional querying approach was taken to examine the mixing state of these species. The dataset was also queried for sulfate, nitrate and MSA to determine how many particles actually contained these species, which is not usually necessary under optimum detector conditions. Ions were queried for peak height between 1 and 5000, to include all mass spectra containing these species. Table 4.4 shows the negative ions queried for and the number of particles containing them. These particles were then clustered using the *K*-means algorithm to produce particle classes.

Table 4.4. Negative ions indicative of atmospheric processing queried for in ADRIMED/SAF-MED ATOFMS dataset.

Ion	$^{46}NO_2^-/^{62}NO_3^-$	$^{89}(COO)_2H^-$	$^{95}CH_3SO_3^-$	$^{97}HSO_4^-$	$^{111}HOCH_2SO_3^-$	$^{125}H(NO_3)_2^-$	$^{195}[H(HSO_4)_2]^-$
No. of particles	87,238	9627	2779	106,732	136	66	23
% of total particles	7	0.8	0.2	9	0.01	0.005	0.002

Oxalate

Oxalate (*m/z* -89) was found in ~9600 particles, 0.8% of total particles ionised. The mixing states derived from this query are similar to those produced from general clustering and are varied, suggesting that the detector issue did not prevent oxalate from being detected in certain types of particles. Despite this consistency, it should not be assumed that all particles in a class from the general clustering approach which produced oxalate signals actually contained this species, as indicated by the querying results.

From the querying approach it was apparent that oxalate preferentially partitioned to K-rich particles rather than the more abundant carbonaceous particles. 52% of the queried oxalate particles were dominated by $^{39}K^+$ and sulfate (~90% of all the queried particles contained sulfate), coinciding with the *K-SO$_X$-Oxalate* class from the general approach;

the temporality of the queried particles confirms this, as numbers also peaked on the 28th June. Particles most similar to *K-NO$_X$* accounted for a further 33% and produced signals for nitrate, EC, CN, CNO and sulfate. In contrast only 2% of queried oxalate particles produced EC-rich positive mass spectra. Particles with typical dust tracers (Fe, Ca, Al, aluminosilicates) accounted for 7%; this fraction applies to $PM_{2.5}$ but would be larger for PM_{10}. The remaining queried oxalate particles were classified as aged sea salt (3%), *OC* (2%), *V* (0.7%) and *Cu-Pb* (0.4%). Assuming these fractions hold if the queried oxalate particle numbers could be scaled up to real ambient levels, then biomass burning emissions play a large role in the fate of particle phase oxalate in the western Mediterranean.

The average mass concentration of oxalate as measured by the PILS was 10±0.63 ng/m^3, with a range of 0.2-37 ng/m^3. Moderate correlation between oxalate and SV-OOA (R^2=0.56), WSOC (R^2=0.55), BC (R^2=0.55) and ATOFMS EC+K-rich mass concentrations (R^2=0.55) were obtained for the period 21st June-4th August; hourly mass concentrations for these species can be found in Figure 4.36.

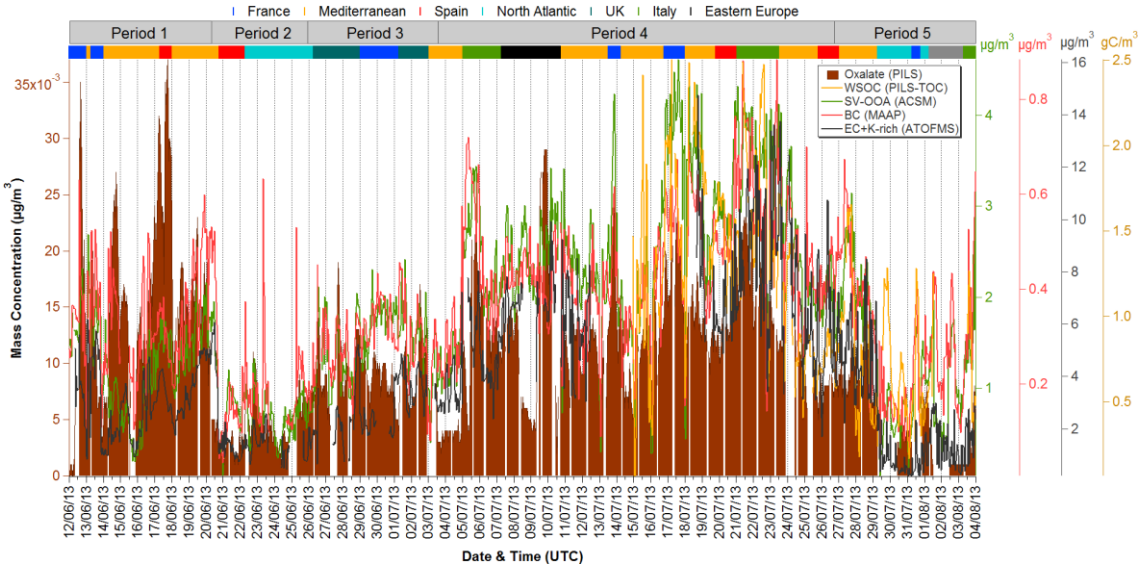


Figure 4.36. Hourly mass concentrations of SV-OOA ACSM factor, BC (MAAP), WSOC (PILS-TOC) and ATOFMS EC+K-rich particles.

Oxalic acid is often the single most abundant water-soluble organic compound identified in ambient aerosols (Yu et al., 2005), which explains the agreement between oxalate and WSOC mass concentrations. A moderate association with OPS 0.3-0.579 µm particles concurs with the findings of Koulouri et al. (2008) who found 59% of oxalate mass in the fine fraction (< 1.3 µm). The same study also found a moderate correlation between nitrate and oxalate (R^2=0.56), which was attributed to heterogeneous processes on alkaline cation surfaces originating from sea salt and mineral dust; no such agreement was observed during either ADRIMED or SAF-MED. The ATOFMS querying approach

indicated a prevalence for oxalate mixed with K-rich particles, however correlations between PILS oxalate and K-rich mass were poor; better correlations were found with EC and K-rich mass combined, suggesting more EC particles actually contained oxalate than was detected.

The mixing states of particles containing oxalate as identified by single particle techniques is varied, and indicates oxalate formation either in fog/cloud processing or photochemical oxidation of biogenic and anthropogenic VOCs. Oxalate has been found in biomass burning particles (Yang et al., 2009; Healy et al., 2010), mixed with industrial combustion particles containing Pb and Zn (Moffet et al., 2008a, 2008b), in aged sea salt (Yang et al., 2009) and in aged carbonaceous particles containing highly oxidised organics, non-oxygenated organics and amines (Qin et al., 2012; Pratt et al., 2009c). Oxalic acid has been found preferentially enriched on Asian mineral dust over carbonaceous particles (Sullivan & Prather, 2007), while Fitzgerald et al. (2015) characterised Asian dust as rich in nitrate and aged through heterogeneous chemistry and African dust as cloud processed and rich in sulfate and oxalate. Yang et al. (2009) found enrichment of oxalate in dust and sea salt particles and night-time peaks in diurnal profiles of both these and relative humidity, indicating heterogeneous reactions in hydrated/deliquesced aerosols contributed to oxalate formation. The authors also observed correlations between oxalate and sulfate, suggesting that in-cloud processing also played a role. Cloud processing has also been observed in orographic clouds by an ATOFMS on board an aircraft for biomass burning particles internally mixed with oxalate and enriched in homogenously nucleated ice and cloud droplets (Pratt & Prather, 2010). Yao et al. (2002), through MOUDI and IC measurements found higher concentrations of oxalate in a droplet mode of 0.32-1 µm than in a condensation mode of 0.097-0.32 µm and concluded that aqueous reactions could be more important than gas phase photochemical reactions in oxalate formation. While the humidity was relatively high throughout the two campaigns, so too was the solar radiation, with few instances of cloud or fog formation at the site. The association with SV-OOA also supports a preference for photo-chemical oxidation as the oxalate formation mechanism.

MSA

MSA, *m/z* -95, was identified in ~2700 particles (0.2% of total particles ionised). Sulfate was found in all of these. The mixing states derived from the querying approach largely agrees with those from the general approach. Similar to oxalate, MSA clearly favoured partitioning to biomass combustion particles. Particles similar to the *K-SO$_X$*, *EC-K-SO$_X$*

and *K-EC-SO$_X$* classes accounted for 45%, 25% and 11% of the MSA queried particles. *EC-V, V* and *Cu-Pb* classes contributed 11%, 4% and 1% respectively.

The preference for partitioning to combustion particles is in contrast to findings from Riverside, USA (Gaston et al., 2010) where only small fractions of carbonaceous ATOFMS particle types contained MSA, and Tivoli, Ireland (Healy et al., 2010), where only one ATOFMS particle class of several carbonaceous classes identified was internally mixed with MSA. The authors suggest accumulation of secondary species during transport from the LA coast to Riverside potentially masked the detection of MSA in their carbonaceous particles (Pratt & Prather, 2009).

In addition, they demonstrated that biogenically emitted sulfur species, such as MSA, can condense onto anthropogenic aerosols catalysed by vanadium, which has also been shown to enhance the conversion of anthropogenically produced SO_2 to sulfate (Ault et al., 2010). ~40% of OC-V-sulfate (residual fuel combustion primarily from ships) particles and 33% of aged sea salt particles in Riverside contained MSA; these were both coastally emitted along with DMS, which suggests that DMS oxidation products primarily partitioned onto coastal particle types that then underwent aging as they were transported inland. No MSA was found on aged sea salt particles in Corsica; *m/z* -95 was only found in fresh sea salt particles and was likely a result of $NaCl_2$ as it was present in the typical isotopic ratio i.e. its signal was smaller than *m/z* -93. A similar fraction of V-rich particles found in Corsica could have contained MSA had the negative detector been fully functioning. This is again in contrast to (Healy et al., 2010), where none of the V-rich shipping classes were associated with MSA. However, the authors note that the sampling site was very close to shipping berths, so most shipping particles detected were expected to be freshly emitted.

OC-SO$_X$ particles, identified with the general clustering approach, produced average mass spectra with MSA signals. This was not supported by the querying approach; no OC-rich particles were found to contain MSA, or at least so few as to not resolve into their own clusters. No Amine particles were identified in the MSA query. This is contrast to results of an amine query of the Corsica dataset (Healy et al., 2014), which found MSA mixed with both *EC-TMA* and *K-TMA* particles. This was determined from the average mass spectra of the queried amine particles, which was based on positive mass spectra and therefore suffered from the same inclusion of poor quality or blank negative spectra as the general clustering approach used here. As discussed earlier, the presence of MSA in TMA and other amine-containing particles is possible, as indicated by laboratory studies

of particle formation and growth from reactions between MSA, TMA (or methylamine and DMA) and water (Chen et al., 2015b, 2015a). Amines have been frequently observed in marine aerosol (Facchini et al., 2008; Müller et al., 2009; Sorooshian et al., 2009; Gaston et al., 2010), and particulate amine levels have been found to correlate with particulate MSA levels (Sorooshian et al., 2009). Facchini et al. (2008) observed that MSA, DMA, and diethylamine were the most abundant organic species detected in fine particles in the North Atlantic during periods of high biological activity. The lack of sufficient good quality negative mass spectra unfortunately limited investigation of particles influenced by MSA and marine amines, however the above shows that these are possible.

The remaining 3% of MSA queried particles was accounted for by particles containing dust tracers (Fe, Ca, Al). The Riverside study found no MSA was found on submicron dust and only 3% of supermicron dust contained MSA (Gaston et al., 2010). The authors expected this since the dust they observed was locally produced unlike MSA. In contrast, internally mixed OC, sea salt, sulfate, Ti (dust) and MSA formed particles 1 – 2 µm in size at Mace Head during the EUCAARI project (Dall'Osto et al., 2009a) and were associated with a period of sub-tropical maritime air originating from the Azores high-pressure region. The number of dust particles identified with the MSA query in this work were statistically too few to consider submicron/supermicron ratios; from these previous studies it is not unusual to detect MSA on dust particles, however it is unlikely that they represent significant surfaces for MSA to condense onto as most of the MSA mass measured in the Mediterranean to date has been found in the submicron fraction. This observation is also echoed by Gaston et al. (2010); 67% of the submicron particles in Riverside contained MSA.

In Riverside MSA-containing particles were also associated with fog processing markers $^{81}HSO_3^-$ and hydroxymethanesulfonate (HMS, $^{-111}HOCH_2SO_3^-$), highlighting aqueous phase chemistry as important in MSA formation (Bardouki & Rosa, 2002), as well as the hygroscopic nature of MSA (Barnes et al., 2006). Other studies correlated HMS with relative humidity (RH) during stagnant fog events (Whiteaker & Prather, 2003b), however in Riverside the HMS correlation with MSA suggested HMS formation was not due to local increases in RH; rather MSA-particles had undergone aqueous phase processing either coastally or during transport. Unfortunately queries for *m/z* -81 and -111 did not return a statistically useful number of particles, and the summed signal for

both of these was too low to produce a statistically useful time series (it follows on from this that it didn't appear in any average mass spectra).

PILS mass concentrations of MSA did not correlate with any ATOFMS particle numbers or mass concentrations, or with any other measurements over the whole sampling period. However, some correlations were found for certain periods; from 7-15th July MSA mass agreed well with that of PILS NO_3^-, while from 23rd July – 3rd August moderate correlations were found with PILS NO_3^- (R^2=0.53), SO_4^{2-} (R^2=0.48) and NH_4^+ (R^2=0.54), and ACSM NO_3^- (R^2=0.46). Increases in MSA mass coincided with sea salt events during Period 2 (Figure 4.37), although there were no good correlations with SSA concentration, suggesting MSA was not present on sea salt particles but formation was enhanced by the influx of marine air masses.

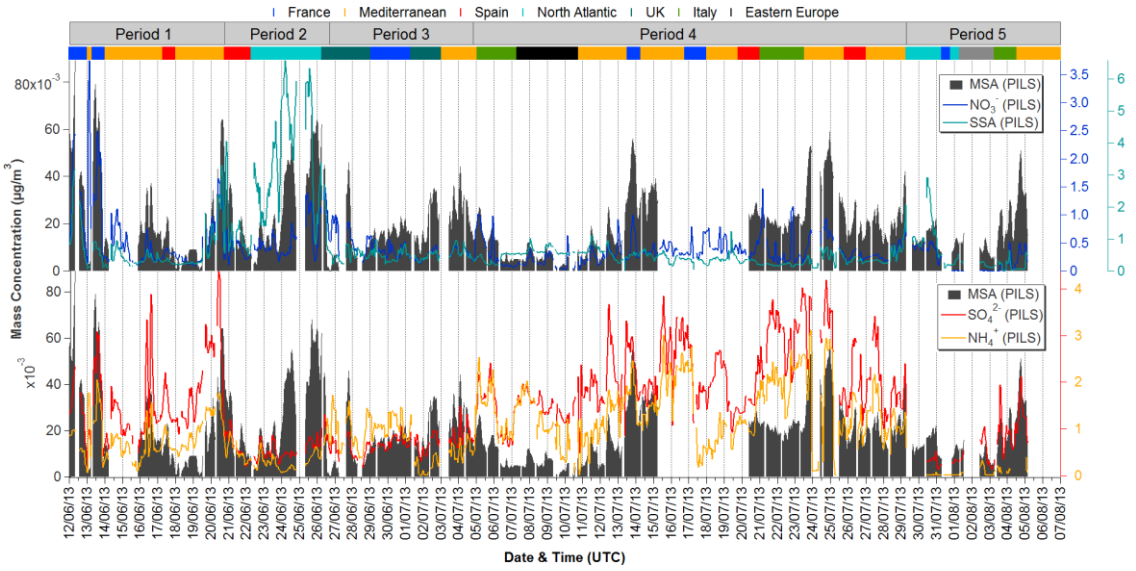


Figure 4.37. Hourly mass concentrations of PILS MSA, NO_3^-, SSA, SO_4^{2-} and NH_4^+ during ADRIMED/SAF-MED.

4.4 CONCLUSIONS

27 distinct ATOFMS particle classes were identified from single particle mass spectra which were grouped into 8 general categories: EC, K-rich, Na-rich, Amines, OC-rich, V-rich, Fe-rich and Ca-rich. Mass concentrations were reconstructed for the ATOFMS particle classes and were in good agreement with other quantitative measurements (PM_1, ACSM species, BC). Total ATOFMS mass ($PM_{2.5}$) accounted for 70-90% of PM_{10} mass, most of which was comprised of regionally transported fossil fuel combustion particles, and particles from biomass burning in northern Italy and eastern Europe, the accumulation of which was favoured by repeated and extended periods of air mass stagnation over the western Mediterranean.

Three other sources were also identified: local biomass burning, marine and shipping. Local combustion particles contributed little to $PM_{2.5}$ particle numbers and mass concentrations but were easily distinguished from regional combustion particles. Marine emissions comprised fresh and aged sea salt, the former detected mostly during one 5 day event and the latter detected throughout the sampling period. Dust was not efficiently detected by the ATOFMS, as other measurements showed that it was mainly in the $PM_{2.5-10}$ fraction. Shipping particles, indicative of heavy fuel oil combustion, were identified as aged regional emissions which made only a small contribution to $PM_{2.5}$ particle numbers and mass concentrations.

The mixing states of oxalate, a photochemically aged aerosol marker, and MSA, a marine emissions marker, were described but limited by poor negative ion detection. The majority of particles containing oxalate contained K and sulfate, indicative of aged biomass burning emissions, while MSA was also strongly associated with biomass burning particles and to a lesser extent with Shipping particles.

5. SUMMARY

CONTENTS

5.1 NANO-INDUS 177

5.2 ADRIMED and SAF-MED 180

5.3 ATOFMS Comparison 183

5.4 Perspectives 184

During this work an Aerosol Time of Flight Mass Spectrometer (ATOFMS) was deployed at an industrial location and a regional background location during the NANO-INDUS and ADRIMED/SAF-MED field measurement campaigns. The ATOFMS provided the size-resolved chemical composition of atmospheric single particles in the size range 100 to 3000 nm in real-time. The single particle information collected was then analysed by application of the *K*-means algorithm in order to generate a list of particle types influencing the monitoring sites during sampling. The particle types identified during these campaigns were used to determine the composition and origins of particles at both locations. This information, along with meteorological data and measurements made by co-deployed instruments, was used to investigate local point sources of industrial particles and the influence of regional transport on PM composition in Mediterranean background aerosol.

5.1 NANO-INDUS

In Dunkirk the ATOFMS collected approximately 800,000 single particle mass spectra, which were classified into 34 distinct ATOFMS particle classes: *Sea salt, Na-K, Na-Mg, Na-EC, K, K-Cl, K-Aluminosilicate, K-Al, EC, EC-amm-nit, EC-K, EC-K-amm-nit, OC, OC-PAH, PAH, Fe, K-Fe-Na, Fe-K-Ca, Fe-EC, Ca, Ca-K, EC-Ca, V-Fe, Na-V, Mn, K-Mn, Al-K-Mn, Mn-K-Fe, K-Pb, Li-Zn, Sulfur, K-Amines, EC-Amines* and particles with poor positive spectra. These were grouped into 9 general categories: Na-rich (23% of total spectra), K-rich (22%), EC (22%), Fe-rich (0.4%), OC and PAH (2%), Ca-rich (0.2%), V-rich (1%), Mn-rich (1%) and Others (17%).

Maximum particle number and $PM_{2.5}$ mass concentrations were observed during an extended period strongly influenced by local industrial emissions. The contribution of nitrate, non-refractory chloride and BC increased during this period. $PM_{2.5}$ elemental mass concentrations determined by ICP-MS were also at their highest, with Fe, Mn, Ca, Al, K, Na, Mg and Zn accounting for most of (97%) this elemental mass.

Mass concentrations for the ATOFMS particle classes were reconstructed, and total ATOFMS mass was found to correlate well with SMPS (50-300 nm) and OPS (300-800 nm) number concentrations, as well as $PM_{2.5}$, total AMS and organics and ammonium mass concentrations. ATOFMS mass concentrations also correlated well with average PM_1, $PM_{2.5}$ and PM_{10} mass fractions obtained from 48 hour filters. Particles detected by ATOFMS accounted for 40-90% of $PM_{2.5}$ mass for most of the sampling period. Some underestimation and overestimation of $PM_{2.5}$ mass was observed and likely originated

from the complexity of the mixing states, particularly those of the metal-rich particles. Several different densities were used in converting the number of these particles to mass, which may not have been appropriate or which may have varied for each class throughout the sampling period. Most of the ATOFMS mass concentrations were accounted for by K-rich particles (24%) and EC particles (23%), followed by Na-rich (10%), Fe-rich (10%), Ca-rich (4%), V-rich (4%), Mn-rich (3%), OC and PAH (3%) and Zn, Sulfur and Amines combined (0.4%).

Five general sources of $PM_{2.5}$ particles were identified during NANO-INDUS; local industrial, transported industrial, transported/local industrial, transported/urban and marine. Assignment of particle classes originating from the ferromanganese alloy manufacturing facility was based on comparison with single particle mass spectra obtained from chimney filter samples and ores from the facility.

Marine emissions, primarily in the form of Sea salt particles, were influenced by North Atlantic air masses and generally increased when carbonaceous combustion particle numbers decreased and vice versa. Particles with a marine biological origin (*Na-Mg*) were detected, although they did not have a significant impact on aerosol at the site as they contributed very little to either particle number or mass. Particles with both marine and local combustion sources were also identified (*Na-EC*), representing internally mixed sea salt and EC and possibly industrial combustion emissions. These too did not heavily impact the site.

Transported/urban emissions represented those without a clear industrial influence and which may have been produced in the local urban environment or transported from other urban locations. Particles categorised as urban/transported accounted for most of the ATOFMS particles with mass spectra and include the *K, EC-K, EC-K-amm-nit* and *EC-amm-nit* classes. The lack of sufficient negative mass spectra limited the evidence for aged transported emissions, however the presence of ammonium nitrate, as $^{30}NO^{+}$, in the *EC-K-amm-nit* and *EC-amm-nit* classes indicated ageing of these particles. K is usually a marker for biomass burning, however the steelworks neighbouring the sampling site is known to produce significant amounts of KCl particles (Hleis et al., 2013). *K-Cl* particles were identified through querying of the *K* class, but it likely that more of the *K* class should be apportioned to an industrial source due to the negative ion detector issue.

Transported/local industrial emissions represented those detected during the clear industrial period but which were also present at similar or higher levels at other times during the campaign. These included EC and amine-containing particles; the majority of

the former occurred during a 4-day period associated with air masses over the English Channel and northern France, while those detected during the industrial period may have originated from the steelworks in the form of graphite flakes (Flament et al., 2008).

Transported industrial emissions included particle classes whose composition indicated industrial sources but which did not peak during the industrial period. These accumulated during the same 4-day event that transported *EC* particles to the site. This transport represented a second non-local source of *Fe*, *Fe-EC*, *Mn* and *V-Fe* particles.

Local industrial emissions include those for which maximum levels occurred during the period most strongly influenced by industry and which were observed at low levels or virtually absent for the rest of the campaign. These emissions produced the largest variety in particle mixing state and included K-rich, Fe-rich, Mn-rich, Ca-rich, Pb, OC and PAH classes. Some particle classes could be confidently assigned to either the ferromanganese alloy manufacturing facility, based on comparison of the ambient data with ATOFMS data for the chimney filters and ores from the facility, or to the steelworks, by comparing the ambient data with those obtained in previous ATOFMS studies at the Port Talbot steelworks (Dall'Osto et al., 2008; Taiwo et al., 2014b).

K-Mn, *Al-K-Mn*, *Mn-K-Fe*, *K-Al*, *Ca* and *Ca-K* were found in the industrial filter or ore samples, and apart from *Ca* and *Ca-K* (Ca is a major component of steelworks sintering emissions) can be considered reliable tracers for emissions from the ferromanganese facility. The combined contribution of the *K-Mn*, *Al-K-Mn*, *Mn-K-Fe* and *K-Al* classes was 1% of total ATOFMS particle number and 2% of total reconstructed ATOFMS mass. The combined contribution of the *K-Fe-Na*, *K-Cl*, *OC*, *OC-PAH*, *PAH* and *Sulfur* classes, likely to be from the steelworks, was 5% to total ATOFMS number and 9.5% to total ATOFMS mass. This considers only classes which can be confidently attributed to the ferromanganese alloy facility or the steelworks (*K-Pb*, *Ca*, *Ca-K*, *Fe-K-Ca*, *Li-Zn*) and is therefore a conservative estimate but from this it is apparent that the steelworks contributed significantly more than the ferromanganese alloy facility to particle number and mass concentrations as analysed by ATOFMS.

5.2 ADRIMED AND SAF-MED

In Corsica, the ATOFMS collected approximately 1.2 million single particle mass spectra, which were classified into 27 distinct ATOFMS particle classes: *EC-SO_X*, *EC-Oxalate*, *EC-K*, *EC-K-SO_X*, *EC-K-Oxalate*, *K-EC-NO_X*, *K-EC-SO_X*, *K-EC-Oxalate*, *K-CN*, *K-NO_X*, *K-SO_X*, *K-SO_X-Oxalate*, *K-Na*, *K-Silicate*, *sea salt-fresh*, *sea salt-aged*, *Na-EC*, *OC*, *OC-NO_X*, *OC-SO_X*, *EC-TMA*, *K-TMA*, *OC-TMA*, *V*, *V-EC*, *Fe*, and *Ca*. These were grouped into 8 general categories: EC (53% of total spectra), K-rich (32%), Na-rich (8%), Amines (4%), OC-rich (2%), V-rich (1%), Fe-rich (0.2%) and Ca-rich (0.2%).

Mass concentrations for the ATOFMS particle classes were reconstructed, and total ATOFMS mass was found to correlate well with SMPS and OPS number concentrations and total ACSM mass concentrations, and moderately with mass concentrations of PILS SO_4^{2-} and NH_4^+, the ACSM factor SV-OOA, BC and PM_1. Particles detected by ATOFMS accounted for 70-90% of PM_{10} mass for most of the sampling period, though considerably less during periods dominated by sea salt and dust. These findings indicate that adequate mass concentrations can be derived from ATOFMS particle numbers in an environment where the aerosol is dominated by biomass burning and fossil fuel combustion emissions and SOA. ATOFMS mass concentrations were dominated by EC particles (52%), followed by K-rich (25%), Na-rich (12%), Amines (3%), OC-rich (3%), V-rich (3%), Ca-rich (1%) and Fe-rich (1%).

Four general sources of $PM_{2.5}$ particles were identified during ADRIMED and SAF-MED; regionally transported combustion, local biomass burning, marine and shipping. EC particles were assigned to regionally transported fossil fuel combustion sources, with no local sources evident and clear decreases in particle numbers during periods where synoptic marine air masses influenced the site. However, no particle composition markers unique to different air masses were observed, so based on ATOFMS data alone it would not be possible to distinguish emissions originating in one country from another.

K-rich and OC-rich particles originated from both regionally transported and local biomass burning aerosol. Regionally transported biomass burning particles considerably outnumbered local emissions, which were identified by brief peaks in particle number and visually confirmed in situ. Fires were detected by MODIS over northern Italy throughout the sampling period and the site was heavily influenced by air masses passing over this region. The largest concentration of fires in all of Europe or North Africa was in eastern Europe, around the Black Sea and in the form of wheat residuals burning, from the end of June until the end of the sampling period. The site was clearly influenced by

air masses from this region for ~ 4 days in July, followed by extensive stagnation and recirculation of that air over the western Mediterranean.

Amine-containing particles were also assigned to regionally transported combustion sources, both fossil fuel and biomass burning. Previous studies of amine-containing particles found a strong dependence on relative humidity; this was not the case during these two campaigns, suggesting these particles were not formed locally.

Quantitative measurements by TEOM showed PM_1 particles accounted for most of PM_{10} mass concentrations over the whole sampling period. ACSM (PM_1) and PILS (PM_{10}) sulfate and ammonium mass concentrations were very similar, indicating most of the mass of these species was in the PM_1 fraction. Accordingly, organics (36%), sulfate (16%) and ammonium (10%) constituted most of the PM_{10} mass. Mass concentrations of EC and K-rich particles were in good agreement with those of ACSM sulfate, ammonium and the SV-OOA factor (which accounted for 62% of the organics), and BC. This comparison provided complementary information; EC and K-rich particles did not produce strong signals for OC fragment ions, which the ACSM data indicated were a significant component of both PM_1 and PM_{10} particles. From the ATOFMS average mass spectra of EC and K-rich particles it appeared EC and K were major components, but BC and K only contributed 4% and 0.4% to PM_{10} mass concentrations. However, ATOFMS mass spectra provided valuable source markers, allowing the identification of fossil fuel and biomass burning combustion sources. Combined, this information shows these sources provided the primary particles, containing EC and OC, which then accumulated ammonium, sulfate and alkylamines during regional transport. Oxidation of the OC components also likely occurred during transport.

Sea salt particles were separated into fresh and aged emissions; fresh sea salt dominated during two events (5 day and 1 day), while aged sea salt was present consistently in the background throughout both campaigns. Reconstructed mass concentrations for fresh sea salt particles accounted for 50-80% of SSA, derived from PILS Na and Cl concentrations, during the main event, with Mg^{2+} constituting most of the remaining mass. This and a strong correlation with 0.579-2.156 μm particles suggests a significant amount of fresh sea salt was in the $PM_{2.5}$ fraction.

Two prominent mineral dust events were characterised by increases in Ca^{2+} mass concentrations and 2.156-8.032 μm particle number concentrations; the second event coincided with the main sea salt event and was also distinguished by contributions of K^+. However, no agreement between potential ATOFMS dust particles and these

measurements was found indicating that mineral dust was not characterised well by the ATOFMS, as most of the dust particles were in the >$PM_{2.5}$ fraction.

V-rich particles, markers for heavy fuel oil combustion, were identified as aged regional emissions, as most fresh shipping particles would have been too small for the ATOFMS to have detected during the sampling period and there are no local power plants or refineries that could generate similar particles.

One of the aims was to investigate the photochemical ageing of particles in the western Mediterranean, and given the location marine emissions were also of interest. To address this, the mixing state of particles containing oxalate and MSA was examined. A querying approach of the ATOFMS dataset was required, as most particles either produced poor quality negative mass spectra or none at all, resulting in unrepresentative average negative mass spectra for some particle classes. Despite these limitations, this work represents the first characterisation of oxalate and MSA mixing states in $PM_{2.5}$ in the Mediterranean.

The majority of particles (85%) queried for oxalate contained K and sulfate, indicative of aged biomass burning emissions, consistent with previous studies in both the eastern and western Mediterranean. In contrast, only 2% of oxalate-queried particles could be classified as EC. However, good correlations were found between PILS oxalate and combined ATOFMS EC and K-rich mass concentrations, indicating more EC particles contained oxalate than could be determined by the limited number of negative mass spectra.

MSA was also strongly associated with biomass burning particles (81% of MSA queried particles), with Shipping particles contributing most of the remaining queried particles. No MSA was found in sea salt particles, though this has been the case in previous studies (Ault et al., 2010). Increases in MSA mass concentrations, determined by PILS, coincided with the main sea salt event, although there were no good correlations with SSA concentration, suggesting MSA was not present on sea salt particles but formation was enhanced by the influx of marine air masses. A small fraction (3%) of the queried MSA particles contained dust tracers (Fe, Ca, Al); MSA has been previously found internally mixed with supermicron dust (Dall'Osto et al., 2009a; Gaston et al., 2010). These observations are consistent with MSA measurements in the Mediterranean to date, which found most MSA mass in the submicrometer fraction. Previous ATOFMS studies of MSA-containing particles have found associations with the fog processing marker hydroxymethanesulfonate (HMS) and indications that the particles had undergone aqueous phase processing during transport (Gaston et al., 2010). HMS was not found in

the MSA-containing particles queried here, and a separate query for HMS did not return a statistically useful number of particles. No association was found between MSA mass concentrations or the MSA-containing particles and relative humidity, also indicating that MSA had not partitioned to the particles locally.

5.3 ATOFMS COMPARISON

A comparison of the NANO-INDUS and ADRIMED/SAF-MED ATOFMS datasets with other ATOFMS datasets from the MEGAPOLI and SAPUSS measurements campaigns (McGillicuddy, 2014) is shown in Figure 5.1. Particles in the Na-rich, K-rich and EC categories constitute the majority of each dataset, reflecting both the instrument's sensitivity to these species and also the size range it operates in, which favours combustion particles (K-rich and EC). The smallest fraction of Na-rich (mostly sea salt) particles was found in Paris, which was the furthest sampling site from a coast. The largest fraction of combustion-related particles was found in Paris (K-rich, EC and OC & PAH), as this was the largest urban site. Barcelona, also a large urban environment, displayed the largest proportion of dust particles (Ca-rich), reflecting the frequent incursions of Saharan dust observed there. The very small proportion of Ca-rich particles found in Corsica reflects the lack of sustained meteorological conditions required for Saharan dust to the island during the sampling period. Negligible local anthropogenic emissions means the majority of particles sampled at the site were regionally transported there, this may explain the large fraction of amine-containing particles relative to the other datasets as these were likely to form during extended atmospheric transport. It is also likely that the larger number of local sources at the other sampling sites could dominate the dataset. Particles from industrial activities were clearly identified in Dunkirk (Fe-rich, Mn-rich, Pb-rich, Ca-rich and V-rich), while similar particles were also observed in Barcelona, which is also home to several heavy industries as well as a busy harbour.

Such comparison of ATOFMS datasets is heavily influenced by sampling location, time of year and meteorological conditions; MEGAPOLI data was collected in January in a north European megacity, NANO-INDUS in May-June in a heavily industrialised small north European city, ADRIMED/SAF-MED in a remote location on a Mediterranean island and SAPUSS in a large coastal Mediterranean city. As such, large variation in sources and particle types is to be expected. The design of the instrument is more suited to short term measurements than long term data collection in one location, so the objective is to employ it in as many different environments as possible. Repeated measurements in one location and comparison of ATOFMS datasets from similar environments are

therefore rare. Also, a full account of ATOFMS dataset composition, in the form of particle types or categories as shown in Figure 5.1, is only occasionally reported in the literature which further restricts comparisons. A collection of raw ATOFMS data would be highly desirable, but would require an administrator and a considerable amount of data storage space, among other difficulties.

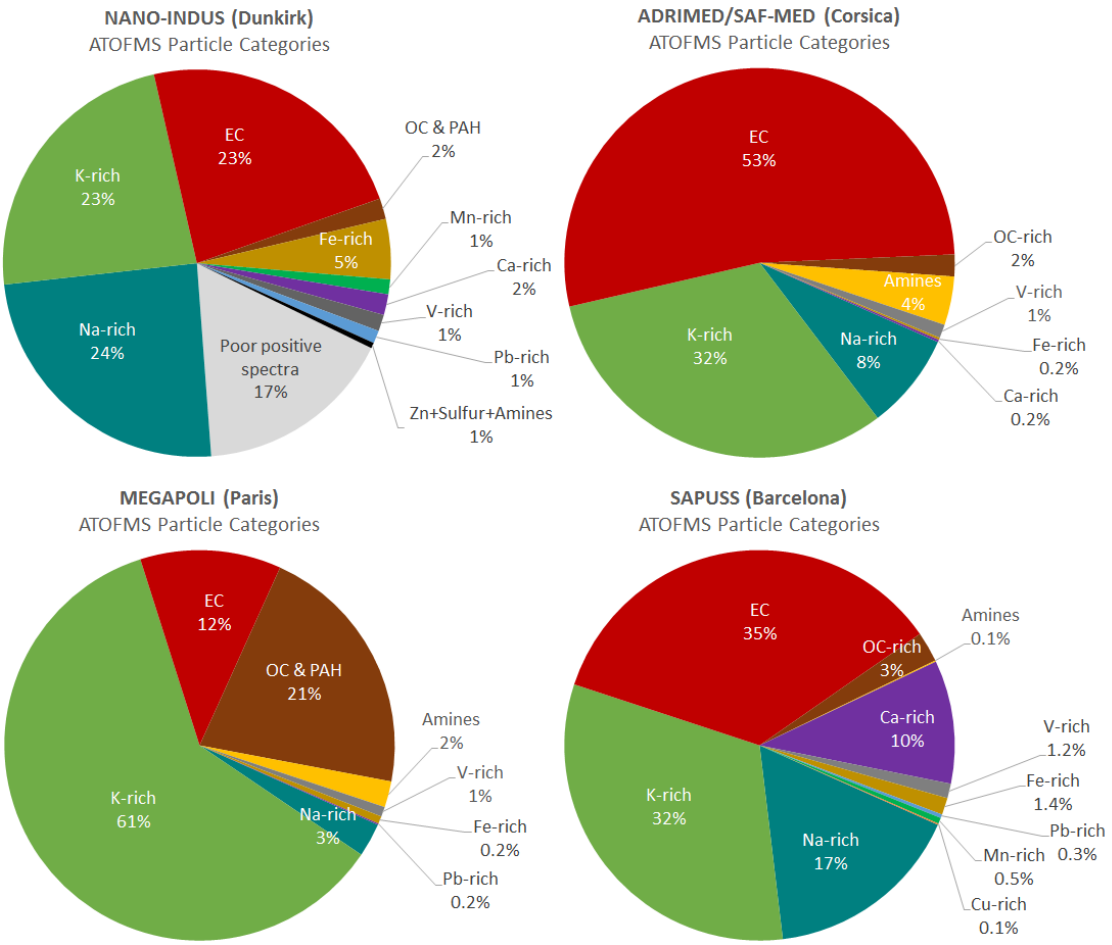


Figure 5.1. Comparison of ATOFMS datasets in terms of % particle numbers of particle categories.

5.4 PERSPECTIVES

Overall this work demonstrates that the ATOFMS is a very useful technique in the determination of the size resolved chemical composition of single particles in real time. In fact the ATOFMS remains one of the few instruments capable of providing this information. While the data provided by the ATOFMS is not quantitative, the benefit of the technique is that it enables identification of the different particle types influencing the measurement site and also the mixing state of the particle – information not provided by other techniques in real time. However, this work has shown that semi-quantitative information can be produced by scaling ATOFMS particle numbers to unbiased sizing measurements, thereby adequately accounting for $PM_{2.5}$ mass concentrations in both

industrial and regional background locations.

A great deal of work by the many researchers involved in both measurement campaigns remains to be done to achieve the objectives of those projects. NANO-INDUS aimed to characterise fine industrial particles as both their size and composition are of concern for human health. To assess if the physico-chemical characteristics of these fine particles change upon exiting a facility (this will improve their identification at different locations and any future sampling campaigns or monitoring), measurements of gases and particles made at the chimneys of the ferromanganese alloy facility will be compared with those made at the a downwind location. The comparison of ATOFMS and SEM-EDX analysis of samples from the facility (Arndt et al., 2016) is the first step in answering this question. Some work on the bioaccessibility of particles collected during NANO-INDUS has been published by Mbengue et al. (2015), and the cytotoxicity, oxidative stress and inflammation in human lung cells caused by particles previously collected in Dunkirk has been studied (Garçon et al., 2006), but to date no epidemiological studies have been carried out in Dunkirk to assess the impact of the considerable industrial activities in the city. While assessing this impact may have been outside the scope of the NANO-INDUS project, the possible health effects for people living in the vicinity of Dunkirk industries should be assessed in the future. We study the atmosphere to determine how we affect it and how it affects us. If the data collected here and in the many other studies carried out in Dunkirk are not used to determine how the cities' anthropogenic activities affect its population then it will only have been collected for its own sake.

The ADRIMED/SAF-MED campaigns were carried out as part of the ChArMEx project, under the MISTRALS initiative. This initiative represents a major collaborative effort to comprehensively study the Mediterranean's atmosphere, hydrosphere, biosphere and lithosphere in a context of climate change and increasing anthropogenic pressure. As such it will be many years before the hundreds of researchers involved have compiled the vast amount of data collected and are able answer any questions; even then it is very likely more research will be needed. Regarding the ADRIMED/SAF-MED specific objectives, work is being published in a special issue of Atmospheric Chemistry and Physics (http://www.atmos-chem-phys.net/special_issue334.html) and will continue to be for years to come. The optical, microphysical and radiative properties of mineral dust have been studied (Denjean et al., 2016; Sicard et al., 2016), as well as how that dust deposits (Vincent et al., 2015). Observations have been made by LIDAR of the long range transport and aerosol types during a North American biomass burning episode (Ancellet

et al., 2015) and also how biomass burning influences CCN number and hygroscopicity (Bougiatioti et al., 2015). Atmospheric vertical profile measurements on board balloons, aerial vehicles and ships (Di Biagio et al., 2015; Renard et al., 2015; Gheusi et al., 2016) will improve our understanding of by aerosol properties throughout the troposphere, not just at ground level. Long term measurements have also been made of the elemental composition of PM_{10} (Calzolai et al., 2015), among many other studies which can be found by following the above link. The ATOFMS was the only instrument deployed capable of determining the composition of single particles and therefore the most accurate means of source identification. The ATOFMS data will be discussed in relation to aerosol optical and radiative properties to address how particle composition influences these and therefore Mediterranean aerosol's effect on climate. ATOFMS data is currently difficult to incorporate effectively into models but as these are necessary to characterise current radiative forcing and estimate that of the future, improved ways of utilising ATOFMS data in models should be found. The ATOFMS data will be compared more thoroughly with ACSM, AMS and potentially off-line VOC data to determine the origin of SOA in the Mediterranean and also with hygroscopicity and volatility measurements as these properties can influence how the particles affect climate; analysis of data from these instruments is still ongoing.

This works also highlights the complexity of atmospheric aerosol. The task of resolving this complexity is complicated by the fact that no single instrument exists that is capable of completely characterising the physico-chemical properties of aerosols. Complementary in situ measurements performed by numerous instruments operating at high time resolution, combined with meteorological data, modelling, satellite, airborne and other mobile measurements currently provide the best means for quantifying contributions of different aerosol sources and for determining effects of atmospheric aerosol on climate and human health.

6. REFERENCES

Adamson, I.Y.R.Y., Prieditis, H., Hedgecock, C. & Vincent, R. (2000). Zinc Is the Toxic Factor in the Lung Response to an Atmospheric Particulate Sample. *Toxicology and Applied Pharmacology*. 166 (2). p.pp. 111–119.

Aggarwal, S.G. & Kawamura, K. (2009). Carbonaceous and inorganic composition in long-range transported aerosols over northern Japan: Implication for aging of water-soluble organic fraction. *Atmospheric Environment*. 43 (16). p.pp. 2532–2540.

Agrawal, H., Malloy, Q.G.J., Welch, W.A., Wayne Miller, J. & Cocker III, D.R. (2008a). In-use gaseous and particulate matter emissions from a modern ocean going container vessel. *Atmospheric Environment*. 42 (21). p.pp. 5504–5510.

Agrawal, H., Welch, W.A., Miller, J.W., Cocker, D.R., Wayne Miller, J. & Cocker, D.R. (2008b). Emission measurements from a crude oil tanker at sea. *Environmental Science & Technology*. 42 (19). p.pp. 7098–103.

Alastuey, A., Querol, X., Plana, F., Viana, M., Ruiz, C.R., Campa, A.S.D. La, Rosa, J.D. La, Mantilla, E. & Santos, S.G. Dos (2006). Identification and Chemical Characterization of Industrial Particulate Matter Sources in Southwest Spain. *Journal of the Air & Waste Management Association*. 56 (7). p.pp. 993–1006.

Allan, J.D., Jimenez, J.L., Williams, P.I., Alfarra, M.R., Bower, K.N., Jayne, J.T., Coe, H. & Worsnop, D.R. (2003). Quantitative sampling using an Aerodyne aerosol mass spectrometer 1. Techniques of data interpretation and error analysis. *Journal of Geophysical Research*. 108 (D3). p.pp. 1–10.

Allard, P., Aiuppa, A., Loyer, H., Carrot, F., Gaudry, A., Pinte, G., Michel, A. & Dongarrà, G. (2000). Acid gas and metal emission rates during long-lived basalt degassing at Stromboli volcano. *Geophysical Research Letters*. 27 (8). p.pp. 1207–1210.

Alleman, L.Y., Lamaison, L., Perdrix, E., Robache, A. & Galloo, J.C. (2010). PM10 metal concentrations and source identification using positive matrix factorization and wind sectoring in a French industrial zone. *Atmospheric Research*. 96 (4). p.pp. 612–625.

Allen, G., Sioutas, C., Koutrakis, P., Reiss, R., Lurmann, F.W. & Roberts, P.T. (1997). Evaluation of the TEOM method for measurement of ambient particulate mass in urban areas. *Journal of the Air & Waste Management Association (1995)*. 47 (June). p.pp. 682–689.

Allen, J.O., Fergenson, D.P., Gard, E.E., Hughes, L.S., Morrical, B.D., Kleeman, M.J., Gross, D.S., Gälli, M.E., Prather, K.A. & Cass, G.R. (2000). Particle Detection Efficiencies of Aerosol Time of Flight Mass Spectrometers under Ambient Sampling Conditions. *Environmental Science & Technology*. 34 (1). p.pp. 211–217.

Amato, F., Pandolfi, M., Escrig, A., Querol, X., Alastuey, A., Pey, J., Perez, N. & Hopke, P.K. (2009). Quantifying road dust resuspension in urban environment by Multilinear Engine: A comparison with PMF2. *Atmospheric Environment*. 43 (17). p.pp. 2770–2780.

Anagnostopoulou, C., Zanis, P., Katragkou, E., Tegoulias, I. & Tolika, K. (2014). Recent past and future patterns of the Etesian winds based on regional scale climate model simulations. *Climate Dynamics*. 42 (7-8). p.pp. 1819–1836.

Ancellet, G., Pelon, J., Totems, J., Chazette, P., Bazureau, A., Sicard, M., Di Iorio, T., Dulac, F. & Mallet, M. (2015). Long range transport and mixing of aerosol sources

during the 2013 North American biomass burning episode: analysis of multiple lidar observations in the Western Mediterranean basin. *Atmos. Chem. Phys. Discuss.* 2015 (22). p.pp. 32323–32365.

Anderson, B.J., Musicant, D.R., Ritz, A.M., Ault, A., Gross, D.S., Yuen, M. & Galli, M.E. (2005). *User-friendly clustering for atmospheric data analysis*. Northfield, Mn.

Ando, M., Katagiri, K., Tamura, K., Yamamoto, S., Matsumoto, M., Li, Y.F., Cao, S.R., Ji, R.D. & Liang, C.K. (1996). Indoor and outdoor air pollution in Tokyo and Beijing supercities. *Atmospheric Environment*. 30 (5). p.pp. 695–702.

Ando, M., Tamura, K. & Katagiri, K. (1991). Study on suspended particulate matter and polycyclic aromatic hydrocarbons in indoor and outdoor air. *International archives of occupational and environmental health*. 63 (4). p.pp. 297–301.

Andreae, T.W., Andreae, M.O., Ichoku, C., Maenhaut, W., Cafmeyer, J., Karnieli, A. & Orlovsky, L. (2002). Light scattering by dust and anthropogenic aerosol at a remote site in the Negev desert, Israel. *Journal of Geophysical Research*. 107. p.p. 4008.

Angelino, S., Suess, D.T. & Prather, K.A. (2001). Formation of aerosol particles from reactions of secondary and tertiary alkylamines: characterization by aerosol time-of-flight mass spectrometry. *Environmental Science & Technology*. 35 (15). p.pp. 3130–8.

AQEG (2005). *Particulate Matter in the United Kingdom: Summary*. Defra, London.

Arndt, J., Deboudt, K., Anderson, A., Blondel, A., Eliet, S., Flament, P., Fourmentin, M., Healy, R.M., Savary, V., Setyan, A. & Wenger, J.C. (2016). Scanning electron microscopy-energy dispersive X-ray spectrometry (SEM-EDX) and aerosol time-of-flight mass spectrometry (ATOFMS) single particle analysis of metallurgy plant emissions. *Environmental Pollution*. 210. p.pp. 9–17.

Artuso, F., Chamard, P., Chiavarini, S., di Sarra, A., Meloni, D., Piacentino, S. & Sferlazzo, M.D. (2010). Tropospheric halocompounds and nitrous oxide monitored at a remote site in the Mediterranean. *Atmospheric Environment*. 44 (38). p.pp. 4944–4953.

Artuso, F., Chamard, P., Piacentino, S., Sferlazzo, D.M., De Silvestri, L., di Sarra, A., Meloni, D. & Monteleone, F. (2009). Influence of transport and trends in atmospheric CO2 at Lampedusa. *Atmospheric Environment*. 43 (19). p.pp. 3044–3051.

Atkinson, R.W., Fuller, G.W., Anderson, H.R., Harrison, R.M. & Armstrong, B. (2010). Urban ambient particle metrics and health: a time-series analysis. *Epidemiology (Cambridge, Mass.)*. 21 (4). p.pp. 501–11.

Ault, A.P., Gaston, C.J., Wang, Y., Dominguez, G., Thiemens, M.H. & Prather, K.A. (2010). Characterization of the Single Particle Mixing State of Individual Ship Plume Events Measured at the Port of Los Angeles. *Environmental Science & Technology*. 44 (6). p.pp. 1954–1061.

Ault, A.P., Guasco, T.L., Ryder, O.S., Baltrusaitis, J., Cuadra-Rodriguez, L. a., Collins, D.B., Ruppel, M.J., Bertram, T.H., Prather, K.A. & Grassian, V.H. (2013). Inside versus outside: Ion redistribution in nitric acid reacted sea spray aerosol particles as determined by single particle analysis. *Journal of the American Chemical Society*. 135 (39). p.pp. 14528–14531.

Ault, A.P., Moore, M.J., Furutani, H. & Prather, K.A. (2009). Impact of emissions from

the Los Angeles Port region on San Diego air quality during regional transport events. *Environmental Science & Technology*. 43 (10). p.pp. 3500–3506.

Ault, A.P., Williams, C.R., White, A.B., Neiman, P.J., Creamean, J.M., Gaston, C.J., Ralph, F.M. & Prather, K.A. (2011). Detection of Asian dust in California orographic precipitation. *Journal of Geophysical Research*. 116 (D16). p.p. D16205.

Ayers, G.P. & Gillett, R.W. (2000). DMS and its oxidation products in the remote marine atmosphere: Implications for climate and atmospheric chemistry. *Journal of Sea Research*. 43 (3-4). p.pp. 275–286.

Aymoz, G., Jaffrezo, J.-L., Jacob, V., Colomb, a. & George, C. (2004). Evolution of organic and inorganic components of aerosol during a Saharan dust episode observed in the French Alps. *Atmospheric Chemistry and Physics Discussions*. 4 (4). p.pp. 3875–3909.

Bahadur, R., Russell, L.M. & Prather, K.A. (2010). Composition and Morphology of Individual Combustion, Biomass Burning, and Secondary Organic Particle Types Obtained Using Urban and Coastal ATOFMS and STXM-NEXAFS Measurements. *Aerosol Science and Technology*. 44 (7). p.pp. 551–562.

Baraniecka, J., Pyrzyńska, K., Szewczyńska, M., Pośniak, M. & Dobrzyńska, E. (2010). Emission of polycyclic aromatic hydrocarbons from selected processes in steelworks. *Journal of Hazardous Materials*. 183 (1-3). p.pp. 111–115.

Bardouki, H., Liakakou, H., Economou, C., Sciare, J., Smolík, J., Ždímal, V., Eleftheriadis, K., Lazaridis, M., Dye, C. & Mihalopoulos, N. (2003). Chemical composition of size-resolved atmospheric aerosols in the eastern Mediterranean during summer and winter. *Atmospheric Environment*. 37 (2). p.pp. 195–208.

Bardouki, H. & Rosa, M. Da (2002). Kinetics and mechanism of the oxidation of dimethylsulfoxide (DMSO) and methanesulfinate (MSI−) by OH radicals in aqueous medium. *Atmospheric Environment*. 36. p.pp. 4627–4634.

Barnes, I., Hjorth, J. & Mihalopoulos, N. (2006). Dimethyl sulfide and dimethyl sulfoxide and their oxidation in the atmosphere. *Chemical Reviews*. 106 (3). p.pp. 940–75.

Bates, T.S., Quinn, P.K., Coffman, D.J., Covert, D.S., Miller, T.L., Johnson, J.E., Carmichael, G.R., Uno, I., Guazzotti, S.A., Sodeman, D.A., Prather, K.A., Rivera, M., Russell, L.M. & Merrill, J.T. (2004). Marine boundary layer dust and pollutant transport associated with the passage of a frontal system over eastern Asia. *Journal of Geophysical Research*. 109 (D19). p.p. D19S19.

Bates, T.S., Quinn, P.K., Frossard, A.A., Russell, L.M., Hakala, J., Petäjä, T., Kulmala, M., Covert, D.S., Cappa, C.D., Li, S.-M., Hayden, K.L., Nuaaman, I., McLaren, R., Massoli, P., Canagaratna, M.R., Onasch, T.B., Sueper, D., Worsnop, D.R. & Keene, W.C. (2012). Measurements of ocean derived aerosol off the coast of California. *Journal of Geophysical Research: Atmospheres*. 117 (D21). p.p. n/a–n/a.

Bauer, S.E., Koch, D., Unger, N., Metzger, S.M., Shindell, D.T. & Streets, D.G. (2007). Nitrate aerosols today and in 2030: a global simulation including aerosols and tropospheric ozone. *Atmospheric Chemistry and Physics*. 7 (19). p.pp. 5043–5059.

Becagli, S., Lazzara, L., Fani, F., Marchese, C., Traversi, R., Severi, M., di Sarra, a., Sferlazzo, D., Piacentino, S., Bommarito, C., Dayan, U. & Udisti, R. (2013). Relationship between methanesulfonate (MS−) in atmospheric particulate and remotely sensed phytoplankton activity in oligo-mesotrophic central Mediterranean Sea. *Atmospheric Environment*. 79. p.pp. 681–688.

Becagli, S., Sferlazzo, D.M., Pace, G., di Sarra, a., Bommarito, C., Calzolai, G., Ghedini, C., Lucarelli, F., Meloni, D., Monteleone, F., Severi, M., Traversi, R. & Udisti, R. (2012). Evidence for heavy fuel oil combustion aerosols from chemical analyses at the island of Lampedusa: a possible large role of ships emissions in the Mediterranean. *Atmospheric Chemistry and Physics*. 12 (7). p.pp. 3479–3492.

Beddows, D.C.S., Donovan, R.J., Harrison, R.M., Heal, M.R., Kinnersley, R.P., King, M.D., Nicholson, D.H. & Thompson, K.C. (2004). Correlations in the chemical composition of rural background atmospheric aerosol in the UK determined in real time using time-of-flight mass spectrometry. *Journal of Environmental Monitoring*. 6 (2). p.p. 124.

Bein, K.J., Zhao, Y., Johnston, M.V. & Wexler, A.S. (2007). Identification of sources of atmospheric PM at the Pittsburgh Supersite—Part III: Source characterization. *Atmospheric Environment*. 41 (19). p.pp. 3974–3992.

Bein, K.J., Zhao, Y., Pekney, N.J., Davidson, C.I., Johnston, M.V. & Wexler, A.S. (2006). Identification of sources of atmospheric PM at the Pittsburgh Supersite—Part II: Quantitative comparisons of single particle, particle number, and particle mass measurements. *Atmospheric Environment*. 40. p.pp. 424–444.

Bencs, L., Ravindra, K., de Hoog, J., Spolnik, Z., Bleux, N., Berghmans, P., Deutsch, F., Roekens, E. & Van Grieken, R. (2010). Appraisal of measurement methods, chemical composition and sources of fine atmospheric particles over six different areas of Northern Belgium. *Environmental Pollution*. 158 (11). p.pp. 3421–3430.

Bergametti, G., Dutot, A.-L., Buat-Ménard, P., Losno, R. & Remoudaki, E. (1989). Seasonal variability of the elemental composition of atmospheric aerosol particles over the northwestern Mediterranean. *Tellus*. 41B. p.pp. 353–361.

Berresheim, H., Plass-Dülmer, C., Elste, T., Mihalopoulos, N. & Rohrer, F. (2003). OH in the coastal boundary layer of Crete during MINOS: Measurements and relationship with ozone photolysis. *Atmos. Chem. Phys.* 3 (3). p.pp. 639–649.

Bhave, P.V., Allen, J.O., Morrical, B.D., Fergenson, D.P., Cass, G.R. & Prather, K.A. (2002a). A Field-Based Approach for Determining ATOFMS Instrument Sensitivities to Ammonium and Nitrate. *Environmental Science & Technology*. 36 (22). p.pp. 4868–4879.

Bhave, P.V., Fergenson, D.P., Prather, K.A. & Cass, G.R. (2001). Source apportionment of fine particulate matter by clustering single-particle data: tests of receptor model accuracy. *Environmental Science & Technology*. 35 (10). p.pp. 2060–72.

Bhave, P.V., Kleeman, M.J., Allen, J.O., Hughes, L.S., Prather, K.A. & Cass, G.R. (2002b). Evaluation of an Air Quality Model for the Size and Composition of Source-Oriented Particle Classes. *Environmental Science & Technology*. 36 (10). p.pp. 2154–2163.

Bi, X., Dai, S., Zhang, G., Qiu, N., Li, M., Wang, X., Chen, D., Peng, P., Sheng, G., Fu, J. & Zhou, Z. (2015). Real-time and single-particle volatility of elemental carbon-containing particles in the urban area of Pearl River Delta region, China. *Atmospheric Environment*. 118. p.pp. 194–202.

Bi, X., Zhang, G., Li, L., Wang, X., Li, M., Sheng, G., Fu, J. & Zhou, Z. (2011). Mixing state of biomass burning particles by single particle aerosol mass spectrometer in the urban area of PRD, China. *Atmospheric Environment*. 45 (20). p.pp. 3447–3453.

Di Biagio, C., Doppler, L., Gaimoz, C., Grand, N., Ancellet, G., Raut, J.-C., Beekmann,

M., Borbon, a., Sartelet, K., Attié, J.-L., Ravetta, F. & Formenti, P. (2015). Continental pollution in the western Mediterranean basin: vertical profiles of aerosol and trace gases measured over the sea during TRAQA 2012 and SAFMED 2013. *Atmos. Chem. Phys.* 15 (16). p.pp. 9611–9630.

Di Biagio, C., Di Sarra, A. & Meloni, D. (2010). Large atmospheric shortwave radiative forcing by Mediterranean aerosols derived from simultaneous ground-based and spaceborne observations and dependence on the aerosol type and single scattering albedo. *Journal of Geophysical Research: Atmospheres*. 115 (10). p.pp. 1–11.

Birmili, W., Allen, A.G., Bary, F. & Harrison, R.M. (2006). Trace metal concentrations and water solubility in size-fractionated atmospheric particles and influence of road traffic. *Environmental science & technology*. 40 (4). p.pp. 1144–1153.

Bouchlaghem, K., Nsom, B., Latrache, N. & Haj Kacem, H. (2009). Impact of Saharan dust on PM10 concentration in the Mediterranean Tunisian coasts. *Atmospheric Research*. 92 (4). p.pp. 531–539.

Bougiatioti, A., Bezantakos, S., Stavroulas, I., Kalivitis, N., Kokkalis, P., Biskos, G., Mihalopoulos, N., Papayannis, A. & Nenes, A. (2015). Influence of biomass burning on CCN number and hygroscopicity during summertime in the eastern Mediterranean. *Atmos. Chem. Phys. Discuss.* 2015. p.pp. 21539–21582.

Bove, M.C., Brotto, P., Calzolai, G., Cassola, F., Cavalli, F., Fermo, P., Hjorth, J., Massabò, D., Nava, S., Piazzalunga, A., Schembari, C. & Prati, P. (2015). PM10 source apportionment applying PMF and chemical tracer analysis to ship-borne measurements in the Western Mediterranean. *Atmospheric Environment*.

Brock, C. a., Trainer, M., Ryerson, T.B., Neuman, J.A., Parrish, D.D., Holloway, J.S., Jr., D.K.N., Frost, G.J., Hübler, G., Fehsenfeld, F.C., Wilson, J.C., Reeves, J.M., Lafleur, B.G., Hilbert, H., Atlas, E.L., Donnelly, S.G., Schauffler, S.M., Stroud, V.R. & Wiedinmyer, C. (2003). Particle growth in urban and industrial plumes in Texas. *Journal of Geophysical Research*. 108 (D3). p.p. 4111.

Brock, C.A., Washenfelder, R.A., Trainer, M., Ryerson, T.B., Wilson, J.C., Reeves, J.M., Huey, L.G., Holloway, J.S., Parrish, D.D., Hübler, G. & Fehsenfeld, F.C. (2002). Particle growth in the plumes of coal-fired power plants. *Journal of Geophysical Research*. 107 (D12). p.p. 4155.

Buonanno, G., Stabile, L., Avino, P. & Vanoli, R. (2010). Dimensional and chemical characterization of particles at a downwind receptor site of a waste-to-energy plant. *Waste Management*. 30 (7). p.pp. 1325–1333.

Buseck, P.R. & Adachi, K. (2008). Nanoparticles in the Atmosphere. *Elements*. 4 (6). p.pp. 389–394.

Caccia, J.L., Guénard, V., Benech, B., Campistron, B. & Drobinski, P. (2004). Vertical velocity and turbulence aspects during Mistral events as observed by UHF wind profilers. *Annales Geophysicae*. 22. p.pp. 3927–3936.

Cachier, H., Aulagnier, F., Sarda, R., Gautier, F., Masclet, P., Besombes, J.L., Marchand, N., Despiau, S., Croci, D., Mallet, M., Laj, P., Marinoni, A., Deveau, P.A., Roger, J.C., Putaud, J.P., Van Dingenen, R., Dell'Acqua, A., Viidanoja, J., Martins-Dos Santos, S., Liousse, C., Cousin, F., Rosset, R., Gardrat, E. & Galy-Lacaux, C. (2005). Aerosol studies during the ESCOMPTE experiment: An overview. *Atmospheric Research*. 74 (1-4). p.pp. 547–563.

Cahill, J.F., Darlington, T.K., Fitzgerald, C., Schoepp, N.G., Beld, J., Burkart, M.D. &

Prather, K.A. (2015a). Online Analysis of Single Cyanobacteria and Algae Cells under Nitrogen-Limited Conditions Using Aerosol Time-of-Flight Mass Spectrometry. *Analytical Chemistry*. 87 (16). p.pp. 8039–8046.

Cahill, J.F., Darlington, T.K., Wang, X., Mayer, J., Spencer, M.T., Holecek, J.C., Reed, B.E. & Prather, K.A. (2014). Development of a High-Pressure Aerodynamic Lens for Focusing Large Particles (4–10 μm) into the Aerosol Time-of-Flight Mass Spectrometer. *Aerosol Science and Technology*. 48 (9). p.pp. 948–956.

Cahill, J.F., Fei, H., Cohen, S.M. & Prather, K.A. (2015b). Characterization of core–shell MOF particles by depth profiling experiments using on-line single particle mass spectrometry. *The Analyst*. 140 (5). p.pp. 1510–1515.

Cai, J., Zheng, M., Yan, C.-Q., Fu, H.-Y., Zhang, Y.-J., Li, M., Zhou, Z. & Zhang, Y.-H. (2015). Application and Progress of Single Particle Aerosol Time-of-Flight Mass Spectrometry in Fine Particulate Matter Research. *Chinese Journal of Analytical Chemistry*. 43 (5). p.pp. 765–774.

Calvo, A.I., Alves, C., Castro, A., Pont, V., Vicente, A.M. & Fraile, R. (2013). Research on aerosol sources and chemical composition: Past, current and emerging issues. *Atmospheric Research*. 120-121. p.pp. 1–28.

Calzolai, G., Nava, S., Lucarelli, F., Chiari, M., Giannoni, M., Becagli, S., Traversi, R., Marconi, M., Frosini, D., Severi, M., Udisti, R., di Sarra, A., Pace, G., Meloni, D., Bommarito, C., Monteleone, F., Anello, F. & Sferlazzo, D.M. (2015). Characterization of PM_{10} sources in the central Mediterranean. *Atmos. Chem. Phys.* 15 (24). p.pp. 13939–13955.

Carter, J.D., Ghio, A.J., Samet, J.M. & Devlin, R.B. (1997). Cytokine Production by Human Airway Epithelial Cells after Exposure to an Air Pollution Particle Is Metal-Dependent. *Toxicology and Applied Pharmacology*. 146 (2). p.pp. 180–188.

Chalvatzaki, E., Aleksandropoulou, V., Glytsos, T. & Lazaridis, M. (2012). The effect of dust emissions from open storage piles to particle ambient concentration and human exposure. *Waste Management*. 32 (12). p.pp. 2456–2468.

Chan, L.P. & Chan, C.K. (2013). Role of the aerosol phase state in ammonia/amines exchange reactions. *Environmental science & technology*. 47 (11). p.pp. 5755–62.

Chang, M.B., Huang, C.K., Wu, H.T., Lin, J.J. & Chang, S.H. (2000). Characteristics of heavy metals on particles with different sizes from municipal solid waste incineration. *Journal of Hazardous Materials*. 79 (3). p.pp. 229–39.

Chazette, P. & Liousse, C. (2001). A case study of optical and chemical ground apportionment for urban aerosols in Thessaloniki. *Atmospheric Environment*. 35 (14). p.pp. 2497–2506.

Chen, H., Ezell, M.J., Arquero, K.D., Varner, M.E., Dawson, M.L., Gerber, R.B. & Finlayson-Pitts, B.J. (2015a). New particle formation and growth from methanesulfonic acid, trimethylamine and water. *Phys. Chem. Chem. Phys.* 17 (20). p.pp. 13699–13709.

Chen, H., Varner, M.E., Gerber, R.B. & Finlayson-Pitts, B.J. (2015b). Reactions of Methanesulfonic Acid with Amines and Ammonia as a Source of New Particles in Air. *The Journal of Physical Chemistry B*. p.p. 151005113722003.

Chen, Y., Shah, N., Huggins, F.E. & Huffman, G.P. (2004a). Investigation of the microcharacteristics of PM2.5 in residual oil fly ash by analytical transmission electron microscopy. *Environmental Science and Technology*. 38 (859). p.pp. 6553–

6560.

Chen, Y., Shah, N., Huggins, F.E., Huffman, G.P., Linak, W.P. & Miller, C.A. (2004b). Investigation of primary fine particulate matter from coal combustion by computer-controlled scanning electron microscopy. *Fuel Processing Technology*. 85 (6-7). p.pp. 743–761.

Choël, M., Deboudt, K. & Flament, P. (2010). Development of Time-Resolved Description of Aerosol Properties at the Particle Scale During an Episode of Industrial Pollution Plume. *Water, Air, & Soil Pollution*. 209 (1-4). p.pp. 93–107.

Choël, M., Deboudt, K., Flament, P., Lecornet, G., Perdrix, E. & Sobanska, S. (2006). Fast evolution of tropospheric Pb- and Zn-rich particles in the vicinity of a lead smelter. *Atmospheric Environment*. 40 (24). p.pp. 4439–4449.

Choël, M., Deboudt, K., Osán, J., Flament, P. & Van Grieken, R. (2005). Quantitative Determination of Low-Z Elements in Single Atmospheric Particles on Boron Substrates by Automated Scanning Electron Microscopy-Energy-Dispersive X-ray Spectrometry. *Analytical Chemistry*. 77 (17). p.pp. 5686–5692.

Chow, J.C., Watson, J.G., Lowenthal, D.H., Antony Chen, L.-W. & Motallebi, N. (2011). PM2.5 source profiles for black and organic carbon emission inventories. *Atmospheric Environment*. 45 (31). p.pp. 5407–5414.

Ciaparra, D., Aries, E., Booth, M.-J., Anderson, D.R., Almeida, S.M. & Harrad, S. (2009). Characterisation of volatile organic compounds and polycyclic aromatic hydrocarbons in the ambient air of steelworks. *Atmospheric Environment*. 43 (12). p.pp. 2070–2079.

Ciardini, V., Di Iorio, T., Di Liberto, L., Tirelli, C., Casasanta, G., di Sarra, A., Fiocco, G., Fuà, D. & Cacciani, M. (2012). Seasonal variability of tropospheric aerosols in Rome. *Atmospheric Research*. 118. p.pp. 205–214.

Ciccioli, P., Brancaleoni, E., Di Palo, C., Brachetti, A. & Cecinato, A. (1987). Daily Trends of Photochemical Oxidants and Their Precursors in a Suburban Forested Area. A Useful Approach for Evaluating the Relative Contributions of Natural and Anthropogenic Hydrocarbons to the Photochemical Smog Formation in Rural Areas in Italy. In: G. Angeletti & G. Restelli (eds.). *Physico-Chemical Behaviour of Atmospheric Pollutants*. Dordrecht: Springer Netherlands, pp. 551–559.

CITEPA (2014). *Inventaire des émissions de polluants atmosphériques et de gaz à effet de serre en France – Format SECTEN*.

Claeys, M., Graham, B., Vas, G., Wang, W., Vermeylen, R., Pashynska, V., Cafmeyer, J., Guyon, P., Andreae, M.O., Artaxo, P. & Maenhaut, W. (2004). Formation of secondary organic aerosols through photooxidation of isoprene. *Science*. 303 (5661). p.pp. 1173–6.

Collins, D.B., Zhao, D.F., Ruppel, M.J., Laskina, O., Grandquist, J.R., Modini, R.L., Stokes, M.D., Russell, L.M., Bertram, T.H., Grassian, V.H., Deane, G.B. & Prather, K.A. (2014). Direct aerosol chemical composition measurements to evaluate the physicochemical differences between controlled sea spray aerosol generation schemes. *Atmospheric Measurement Techniques*. 7. p.pp. 3667–3683.

Corbin, J.C., Rehbein, P.J.G., Evans, G.J. & Abbatt, J.P.D. (2012). Combustion particles as ice nuclei in an urban environment: Evidence from single-particle mass spectrometry. *Atmospheric Environment*. 51. p.pp. 286–292.

Cozic, J., Mertes, S., Verheggen, B., Cziczo, D.J., Gallavardin, S.J., Walter, S.,

Baltensperger, U. & Weingartner, E. (2008). Black carbon enrichment in atmospheric ice particle residuals observed in lower tropospheric mixed phase clouds. *Journal of Geophysical Research*. 113 (D15). p.p. D15209.

Creamean, J.M., Ault, a. P., White, a. B., Neiman, P.J., Ralph, F.M., Minnis, P. & Prather, K. a. (2015). Impact of interannual variations in sources of insoluble aerosol species on orographic precipitation over California's central Sierra Nevada. *Atmospheric Chemistry and Physics*. 15 (11). p.pp. 6535–6548.

Creamean, J.M., Ault, A.P., Ten Hoeve, J.E., Jacobson, M.Z., Roberts, G.C. & Prather, K.A. (2011). Measurements of Aerosol Chemistry during New Particle Formation Events at a Remote Rural Mountain Site. *Environmental Science & Technology*. 45 (19). p.pp. 8208–8216.

Creamean, J.M., Lee, C., Hill, T.C., Ault, A.P., DeMott, P.J., White, A.B., Ralph, F.M. & Prather, K.A. (2014). Chemical properties of insoluble precipitation residue particles. *Journal of Aerosol Science*. 76. p.pp. 13–27.

Creamean, J.M., Suski, K.J., Rosenfeld, D., Cazorla, A., DeMott, P.J., Sullivan, R.C., White, a. B., Ralph, F.M., Minnis, P., Comstock, J.M., Tomlinson, J.M. & Prather, K. a. (2013). Dust and Biological Aerosols from the Sahara and Asia Influence Precipitation in the Western U.S. *Science*. 339 (6127). p.pp. 1572–1578.

Cyrys, J., Eeftens, M., Heinrich, J., Ampe, C., Armengaud, A., Beelen, R., Bellander, T., Beregszaszi, T., Birk, M., Cesaroni, G., Cirach, M., de Hoogh, K., De Nazelle, A., de Vocht, F., Declercq, C., Dedele, A., Dimakopoulou, K., Eriksen, K., Galassi, C., Graulevičiene, R., Grivas, G., Gruzieva, O., Gustafsson, A.H., Hoffmann, B., Iakovides, M., Ineichen, A., Krämer, U., Lanki, T., Lozano, P., Madsen, C., Meliefste, K., Modig, L., Mölter, A., Mosler, G., Nieuwenhuijsen, M., Nonnemacher, M., Oldenwening, M., Peters, A., Pontet, S., Probst-Hensch, N., Quass, U., Raaschou-Nielsen, O., Ranzi, A., Sugiri, D., Stephanou, E.G., Taimisto, P., Tsai, M.Y., Vaskövi, É., Villani, S., Wang, M., Brunekreef, B. & Hoek, G. (2012). Variation of NO2 and NOx concentrations between and within 36 European study areas: Results from the ESCAPE study. *Atmospheric Environment*. 62 (2). p.pp. 374–390.

Daggupaty, S.M., Banic, C.M., Cheung, P. & Ma, J. (2006). Numerical simulation of air concentration and deposition of particulate metals around a copper smelter in northern Quebec, Canada. *Geochemistry-Exploration Environment Analysis*. 6 (Part 2-3). p.pp. 139–146.

Dall'Osto, M., Beddows, D.C.S., Gietl, J.K., Olatunbosun, O. a., Yang, X. & Harrison, R.M. (2014). Characteristics of tyre dust in polluted air: Studies by single particle mass spectrometry (ATOFMS). *Atmospheric Environment*. 94 (SEPTEMBER). p.pp. 224–230.

Dall'Osto, M., Beddows, D.C.S., Kinnersley, R.P., Harrison, R.M., Donovan, R.J. & Heal, M.R. (2004). Characterization of individual airborne particles by using aerosol time-of-flight mass spectrometry at Mace Head, Ireland. *Journal of Geophysical Research*. 109 (D21).

Dall'Osto, M., Booth, M.J., Smith, W., Fisher, R. & Harrison, R.M. (2008). A Study of the Size Distributions and the Chemical Characterization of Airborne Particles in the Vicinity of a Large Integrated Steelworks. *Science*. (2003). p.pp. 981–991.

Dall'Osto, M., Ceburnis, D., Martucci, G., Bialek, J., Dupuy, R., Jennings, S.G.G., Berresheim, H., Wenger, J.C.C., Healy, R.M.M., Facchini, M.C.C., Rinaldi, M.,

Giulianelli, L., Finessi, E., Worsnop, D., Ehn, M., Mikkilä, J., Kulmala, M., O'Dowd, C.D.D., Sodeau, J.R.R., Healy, R.M.M., Facchini, M.C.C., Rinaldi, M., Giulianelli, L., Finessi, E., Worsnop, D. & O'Dowd, C.D.D. (2009a). Aerosol properties associated with air masses arriving into the North East Atlantic during the 2008 Mace Head EUCAARI intensive observing period: an overview. *Atmospheric Chemistry and Physics Discussions*. 9 (6). p.pp. 26265–26328.

Dall'Osto, M., Ceburnis, D., Monahan, C., Worsnop, D.R., Kulmala, M., Kurtén, T., Ehn, M., Wenger, J., Sodeau, J., Bialek, J., Kulmala, M., Kurtén, T., Ehn, M., Wenger, J., Sodeau, J., Healy, R. & O'Dowd, C. (2012a). Nitrogenated and aliphatic organic vapours as possible drivers for Marine Secondary Organic Aerosol growth. *Journal of Geophysical Research: Atmospheres*. 117 (D12). p.pp. 1–52.

Dall'Osto, M., Drewnick, F., Fisher, R. & Harrison, R.M. (2012b). Real-Time Measurements of Nonmetallic Fine Particulate Matter Adjacent to a Major Integrated Steelworks. *Aerosol Science and Technology*. 46 (6). p.pp. 639–653.

Dall'Osto, M. & Harrison, R.M. (2006). Chemical characterisation of single airborne particles in Athens (Greece) by ATOFMS. *Atmospheric Environment*. 40 (39). p.pp. 7614–7631.

Dall'Osto, M. & Harrison, R.M. (2012). Urban organic aerosols measured by single particle mass spectrometry in the megacity of London. *Atmospheric Chemistry and Physics*. 12 (9). p.pp. 4127–4142.

Dall'Osto, M., Harrison, R.M., Coe, H., Williams, P.I. & Allan, J.D. (2009b). Real time chemical characterization of local and regional nitrate aerosols. *Atmospheric Chemistry and Physics*. 9 (11). p.pp. 3709–3720.

Dall'Osto, M., Harrison, R.M., Furutani, H., Prather, K.A., Coe, H. & Allan, J.D. (2005). Studies of aerosol at a coastal site using two aerosol mass spectrometry instruments and identification of biogenic particle types. *Atmospheric Chemistry and Physics Discussions*. 5 (5). p.pp. 10799–10838.

Dall'Osto, M., Harrison, R.M., Highwood, E.J., O'Dowd, C., Ceburnis, D., Querol, X. & Achterberg, E.P. (2010). Variation of the mixing state of Saharan dust particles with atmospheric transport. *Atmospheric Environment*. 44 (26). p.pp. 3135–3146.

Dall'Osto, M., Harrison, R.M.M., Coe, H. & Williams, P. (2009c). Real-time secondary aerosol formation during a fog event in London. *Atmospheric Chemistry and Physics*. 9 (7). p.pp. 2459–2469.

Dall'Osto, M., Harrison, R.M.R.M., Charpantidou, E., Loupa, G. & Rapsomanikis, S. (2007). Characterisation of indoor airborne particles by using real-time aerosol mass spectrometry. *The Science of the Total Environment*. 384 (1-3). p.pp. 120–33.

Dall'Osto, M., Querol, X., Alastuey, A., Minguillon, M.C., Alier, M., Amato, F., Brines, M., Cusack, M., Grimalt, J.O., Karanasiou, A., Moreno, T., Pandolfi, M., Pey, J., Reche, C., Ripoll, A., Tauler, R., Van Drooge, B.L., Viana, M., Harrison, R.M., Gietl, J., Beddows, D., Bloss, W., O'Dowd, C., Ceburnis, D., Martucci, G., Ng, N.L., Worsnop, D., Wenger, J., Mc Gillicuddy, E., Sodeau, J., Healy, R., Lucarelli, F., Nava, S., Jimenez, J.L., Gomez Moreno, F., Artinano, B., Prévôt, A.S.H., Pfaffenberger, L., Frey, S., Wilsenack, F., Casabona, D., Jiménez-Guerrero, P., Gross, D. & Cots, N. (2013). Presenting SAPUSS: Solving Aerosol Problem by Using Synergistic Strategies in Barcelona, Spain. *Atmospheric Chemistry and Physics*. 13 (17). p.pp. 8991–9019.

Davidson, C.I., Phalen, R.F. & Solomon, P. a. (2005). Airborne Particulate Matter and

Human Health: A Review. *Aerosol Science and Technology*. 39 (8). p.pp. 737–749.

Dawson, M.L., Varner, M.E., Perraud, V., Ezell, M.J., Gerber, R.B. & Finlayson-Pitts, B.J. (2012). Simplified mechanism for new particle formation from methanesulfonic acid, amines, and water via experiments and ab initio calculations. *Proceedings of the National Academy of Sciences of the United States of America*. 109 (46). p.pp. 18719–24.

DeCarlo, P., Slowik, J., Worsnop, D., Davidovits, P. & Jimenez, J. (2004). Particle Morphology and Density Characterization by Combined Mobility and Aerodynamic Diameter Measurements. Part 1: Theory. *Aerosol Science and Technology*. 38 (12). p.pp. 1185–1205.

DeCarlo, P.F., Kimmel, J.R., Trimborn, A., Northway, M.J., Jayne, J.T., Aiken, A.C., Gonin, M., Fuhrer, K., Horvath, T., Docherty, K.S., Worsnop, D.R. & Jimenez, J.L. (2006). Field-Deployable, High-Resolution, Time-of-Flight Aerosol Mass Spectrometer. *Analytical Chemistry*. 78 (24). p.pp. 8281–8289.

Denjean, C., Cassola, F., Mazzino, A., Triquet, S., Chevaillier, S., Grand, N., Bourrianne, T., Momboisse, G., Sellegri, K., Schwarzenbock, A., Freney, E., Mallet, M. & Formenti, P. (2016). Size distribution and optical properties of mineral dust aerosols transported in the western Mediterranean. *Atmos. Chem. Phys.* 16 (2). p.pp. 1081–1104.

Denkenberger, K.A., Moffet, R.C., Holecek, J.C., Rebotier, T.P. & Prather, K.A. (2007). Real-Time, Single-Particle Measurements of Oligomers in Aged Ambient Aerosol Particles. *Environmental Science & Technology*. 41 (15). p.pp. 5439–5446.

Després, V.R., Alex Huffman, J., Burrows, S.M., Hoose, C., Safatov, A.S., Buryak, G., Fröhlich-Nowoisky, J., Elbert, W., Andreae, M.O., Pöschl, U. & Jaenicke, R. (2012). Primary biological aerosol particles in the atmosphere: a review. *Tellus B*. 64 (0).

Doche, C., Dufour, G., Foret, G., Eremenko, M., Cuesta, J., Beekmann, M. & Kalabokas, P. (2014). Summertime tropospheric-ozone variability over the Mediterranean basin observed with IASI. *Atmospheric Chemistry and Physics*. 14 (19). p.pp. 10589–10600.

Dockery, D.W. (2001). Epidemiologic evidence of cardiovascular effects of particulate air pollution. *Environmental health perspectives*. 109 Suppl (March). p.pp. 483–6.

Dockery, D.W. (2009). Health Effects of Particulate Air Pollution. *Annals of Epidemiology*. 19 (4). p.pp. 257–263.

Dockery, D.W. & Pope III, C.A. (1994). Acute respiratory effects of particulate air pollution. *Annual review of public health*. 15. p.pp. 107–32.

Dockery, D.W., Pope III, C.A., Xu, X., Spengler, J.D., Ware, J.H., Fay, M.E., Ferris, B.G. & Speizer, F.E. (1993). An Association between Air Pollution and Mortality in Six U.S. Cities. *New England Journal of Medicine*. 329 (24). p.pp. 1753–1759.

Donaldson, K., Brown, D.M., Mitchell, C., Dineva, M., Beswick, P.H., Gilmour, P. & MacNee, W. (1997). Free radical activity of PM10: iron-mediated generation of hydroxyl radicals. *Environmental health perspectives*. 105 Suppl (September). p.pp. 1285–1289.

Dongarrà, G., Manno, E. & Varrica, D. (2009). Possible markers of traffic-related emissions. *Environmental Monitoring and Assessment*. 154 (1-4). p.pp. 117–125.

Draxler, R.R. & Hess, G.D. (1998). An Overview of the HYSPLIT_4 Modelling System

for Trajectories, Dispersion, and Deposition. *Australian Meteorological Magazine*. 47 (June 1997). p.pp. 295–308.

Drewnick, F., Dall'Osto, M. & Harrison, R. (2008). Characterization of aerosol particles from grass mowing by joint deployment of ToF-AMS and ATOFMS instruments. *Atmospheric Environment*. 42 (13). p.pp. 3006–3017.

Dutcher, D.D., Pagels, J., Bika, A., Franklin, L., Stolzenburg, M., Thompson, S., Medrano, J., Brown, N., Gross, D.S., Kittelson, D. & McMurry, P.H. (2011a). Emissions from soy biodiesel blends: A single particle perspective. *Atmospheric Environment*. 45 (20). p.pp. 3406–3413.

Dutcher, D.D., Stolzenburg, M.R., Thomspon, S.L., Medrano, J.M., Gross, D.S., Kittelson, D.B. & McMurry, P.H. (2011b). Emissions from Ethanol-Gasoline Blends: A Single Particle Perspective. *Atmosphere*. 2 (2). p.pp. 182–200.

Eatough, D., Grover, B., Woolwine, W., Eatough, N., Long, R. & Farber, R. (2008). Source apportionment of 1h semi-continuous data during the 2005 Study of Organic Aerosols in Riverside (SOAR) using positive matrix factorization. *Atmospheric Environment*. 42 (11). p.pp. 2706–2719.

Ebert, M., Müller-Ebert, D., Benker, N. & Weinbruch, S. (2012). Source apportionment of aerosol particles near a steel plant by electron microscopy. *Journal of environmental monitoring : JEM*. 14 (12). p.pp. 3257–66.

EIPPCB (2014). *Best Available Techniques (BAT) Reference Document for the Non-Ferrous Metals Industries*.

Escudero, M., Querol, X., Ávila, A. & Cuevas, E. (2007a). Origin of the exceedances of the European daily PM limit value in regional background areas of Spain. *Atmospheric Environment*. 41. p.pp. 730–744.

Escudero, M., Querol, X., Pey, J., Alastuey, a., Pérez, N., Ferreira, F., Alonso, S., Rodríguez, S. & Cuevas, E. (2007b). A methodology for the quantification of the net African dust load in air quality monitoring networks. *Atmospheric Environment*. 41. p.pp. 5516–5524.

European Environment Agency (2014). *Costs of air pollution from European industrial facilities 2008–2012 — an updated assessment*. Luxembourg: Publications Office of the European Union.

Evans, D.E., Heitbrink, W. a., Slavin, T.J. & Peters, T.M. (2008). Ultrafine and Respirable Particles in an Automotive Grey Iron Foundry. *Annals of Occupational Hygiene*. 52 (1). p.pp. 9–21.

Facchini, M.C., Decesari, S., Rinaldi, M., Carbone, C., Finessi, E., Mircea, M., Fuzzi, S., Moretti, F., Tagliavini, E., Ceburnis, D. & O'Dowd, C.D. (2008). Important source of marine secondary organic aerosol from biogenic amines. *Environmental Science & Technology*. 42 (24). p.pp. 9116–21.

Falkovich, A.H. (2004). Adsorption of organic compounds pertinent to urban environments onto mineral dust particles. *Journal of Geophysical Research*. 109 (D2).

Federico, S., Pasqualoni, L., De Leo, L. & Bellecci, C. (2010). A study of the breeze circulation during summer and fall 2008 in Calabria, Italy. *Atmospheric Research*. 97 (1-2). p.pp. 1–13.

Feng, Y., Ramanathan, V. & Kotamarthi, V.R. (2013). Brown carbon: A significant

atmospheric absorber of solar radiation. *Atmospheric Chemistry and Physics*. 13 (17). p.pp. 8607–8621.

Ferge, T., Karg, E., Schröppel, a., Coffee, K.R., Tobias, H.J., Frank, M., Gard, E.E. & Zimmermann, R. (2006). Fast determination of the relative elemental and organic carbon content of aerosol samples by on-line single-particle aerosol time-of-flight mass spectrometry. *Environmental Science and Technology*. 40 (10). p.pp. 3327–3335.

Fergenson, D.P., Pitesky, M.E., Tobias, H.J., Steele, P.T., Czerwieniec, G. a., Russell, S.C., Lebrilla, C.B., Horn, J.M., Coffee, K.R., Srivastava, A., Pillai, S.P., Shih, M.T.P., Hall, H.L., Ramponi, A.J., Chang, J.T., Langlois, R.G., Estacio, P.L., Hadley, R.T., Frank, M. & Gard, E.E. (2004). Reagentless Detection and Classification of Individual Bioaerosol Particles in Seconds. *Analytical Chemistry*. 76 (2). p.pp. 373–378.

Fergenson, D.P., Song, X.H., Ramadan, Z., Allen, J.O., Hughes, L.S., Cass, G.R., Hopke, P.K. & Prather, K.A. (2001). Quantification of ATOFMS data by multivariate methods. *Analytical Chemistry*. 73 (15). p.pp. 3535–41.

Fernández Espinosa, A.J., Ternero Rodríguez, M., Barragán de la Rosa, F.J. & Jiménez Sánchez, J.C. (2001). Size distribution of metals in urban aerosols in Seville (Spain). *Atmospheric Environment*. 35 (14). p.pp. 2595–2601.

Ferretti, R., Mastrantonio, G., Argentini, S., Santoleri, R. & Viola, A. (2003). A model-aided investigation of winter thermally driven circulation on the Italian Tyrrhenian coast: A case study. *Journal of Geophysical Research: Atmospheres*. 108 (D24). p.p. 4777.

Finlayson-Pitts, B.J. & Pitts, J.N. (2000). *Chemistry of the Upper and Lower Atmosphere: Theory, Experiments, and Applications*. San Diego, USA: Academic Press.

Fitzgerald, E., Ault, A.P., Zauscher, M.D., Mayol-Bracero, O.L. & Prather, K.A. (2015). Comparison of the mixing state of long-range transported Asian and African mineral dust. *Atmospheric Environment*. 115. p.pp. 19–25.

Flament, P., Mattielli, N., Aimoz, L., Choël, M., Deboudt, K., de Jong, J., Rimetz-Planchon, J. & Weis, D. (2008). Iron isotopic fractionation in industrial emissions and urban aerosols. *Chemosphere*. 73 (11). p.pp. 1793–8.

Formenti, P., Andreae, T.W., Galani, E., Vasaras, A., Zerefos, C., Amiridis, V., Orlovsky, L., Karnieli, A., Wendisch, M., Wex, H., Holben, B.N., Maenhaut, W. & Lelieveld, J. (2001). Aerosol optical properties and large-scale transport of air masses: Observations at a coastal and a semiarid site in the eastern Mediterranean during summer 1998. *Journal of Geophysical Research*. 106. p.pp. 9807–9826.

Fortezza, F., Strocchi, V., Giovanelli, G., Bonasoni, P. & Georgiadis, T. (1993). Transport of photochemical oxidants along the northwestern adriatic coast. *Atmospheric Environment. Part A. General Topics*. 27 (15). p.pp. 2393–2402.

Fotiadi, A., Drakakis, E., Hatzianastassiou, N., Matsoukas, C., Pavlakis, K.G., Hatzidimitriou, D., Gerasopoulos, E., Mihalopoulos, N. & Vardavas, I. (2006). Aerosol physical and optical properties in the Eastern Mediterranean Basin, Crete, from Aerosol Robotic Network Data. *Atmospheric Chemistry and Physics*. 6. p.pp. 5399–5413.

de Foy, B., Smyth, A.M., Thompson, S.L., Gross, D.S., Olson, M.R., Sager, N. & Schauer, J.J. (2012). Sources of nickel, vanadium and black carbon in aerosols in

Milwaukee. *Atmospheric Environment*. 59. p.pp. 294–301.

Freney, E.J., Heal, M.R., Donovan, R.J., Mills, N.L., Donaldson, K., Newby, D.E., Fokkens, P.H.B. & Cassee, F.R. (2006). A single-particle characterization of a mobile Versatile Aerosol Concentration Enrichment System for exposure studies. *Particle and fibre toxicology*. 3. p.p. 8.

Friedman, B., Herich, H., Kammermann, L., Gross, D.S., Arneth, A., Holst, T. & Cziczo, D.J. (2009). Subarctic atmospheric aerosol composition: 1. Ambient aerosol characterization. *Journal of Geophysical Research*. 114 (D13). p.pp. 1–11.

Froyd, K.D., Murphy, S.M., Murphy, D.M., de Gouw, J. a, Eddingsaas, N.C. & Wennberg, P.O. (2010). Contribution of isoprene-derived organosulfates to free tropospheric aerosol mass. *Proceedings of the National Academy of Sciences of the United States of America*. 107 (50). p.pp. 21360–21365.

Furutani, H., Dall'Osto, M., Roberts, G. & Prather, K.A. (2008). Assessment of the relative importance of atmospheric aging on CCN activity derived from field observations. *Atmospheric Environment*. 42 (13). p.pp. 3130–3142.

Furutani, H., Jung, J., Miura, K., Takami, A., Kato, S., Kajii, Y. & Uematsu, M. (2011). Single-particle chemical characterization and source apportionment of iron-containing atmospheric aerosols in Asian outflow. *Journal of Geophysical Research*. 116 (D18). p.pp. 1–17.

Gangoiti, G., Millán, M.M., Salvador, R. & Mantilla, E. (2001). Long-range transport and re-circulation of pollutants in the western Mediterranean during the project Regional Cycles of Air Pollution in the West-Central Mediterranean. *Atmospheric Environment*. 35. p.pp. 6267–6276.

Ganor, E., Foner, H.A., Bingemer, H.G., Udisti, R. & Setter, I. (2000). Biogenic sulphate generation in the Mediterranean Sea and its contribution to the sulphate anomaly in the aerosol over Israel and the Eastern Mediterranean. *Atmospheric Environment*. 34 (20). p.pp. 3453–3462.

Garçon, G., Dagher, Z., Zerimech, F., Ledoux, F., Courcot, D., Aboukais, A., Puskaric, E. & Shirali, P. (2006). Dunkerque City air pollution particulate matter-induced cytotoxicity, oxidative stress and inflammation in human epithelial lung cells (L132) in culture. *Toxicology in Vitro*. 20 (4). p.pp. 519–528.

Gard, E., Mayer, J.E., Morrical, B.D., Dienes, T., Fergenson, D.P. & Prather, K.A. (1997). Real-Time Analysis of Individual Atmospheric Aerosol Particles: Design and Performance of a Portable ATOFMS. *Analytical Chemistry*. 69 (20). p.pp. 4083–4091.

Gard, E.E., Kleeman, M.J., Gross, D.S., Hughes, L.S., Allen, J.O., Morrical, B.D., Fergenson, D.P., Dienes, T., Galli, M.E., Johnson, R.J., Cass, G.R. & Prather, K.A. (1998a). Direct Observation of Heterogeneous Chemistry in the Atmosphere. *Science*. 279 (5354). p.pp. 1184–1187.

Gard, E.E., Kleeman, M.J., Gross, D.S., Hughes, L.S., Allen, J.O., Morrical, B.D., Fergenson, D.P., Dienes, T., Galli, M.E., Johnson, R.J., Cass, G.R. & Prather, K.A. (1998b). Direct Observation of Heterogeneous Chemistry in the Atmosphere. *Science*. 279 (5354). p.pp. 1184–1187.

Gaston, C.J., Furutani, H., Guazzotti, S.A., Coffee, K.R., Bates, T.S., Quinn, P.K., Aluwihare, L.I., Mitchell, B.G. & Prather, K.A. (2011). Unique ocean-derived particles serve as a proxy for changes in ocean chemistry. *Journal of Geophysical*

Research: Atmospheres. 116. p.pp. 1–13.

Gaston, C.J., Furutani, H., Guazzotti, S.A., Coffee, K.R., Jung, J., Uematsu, M. & Prather, K.A. (2015). Direct Night-Time Ejection of Particle-Phase Reduced Biogenic Sulfur Compounds from the Ocean to the Atmosphere. *Environmental Science & Technology*. 49 (8). p.pp. 4861–4867.

Gaston, C.J., Pratt, K.A., Qin, X. & Prather, K.A. (2010). Real-Time detection and mixing state of methanesulfonate in single particles at an inland urban location during a phytoplankton bloom. *Environmental Science & Technology*. 44 (5). p.pp. 1566–72.

Gaston, C.J., Quinn, P.K., Bates, T.S., Gilman, J.B., Bon, D.M., Kuster, W.C. & Prather, K.A. (2013). The impact of shipping, agricultural, and urban emissions on single particle chemistry observed aboard the R/V Atlantis during CalNex. *Journal of Geophysical Research: Atmospheres*. 118 (10). p.pp. 5003–5017.

Gavalas, N. a. & Clark, H.E. (1971). On the Role of Manganese in Photosynthesis. *Plant physiology*. 47 (1). p.pp. 139–143.

Georgiadis, T., Giovanelli, G. & Fortezza, F. (1994). Vertical layering of photochemical ozone during land-sea breeze transport. *Il Nuovo Cimento C*. 17 (3). p.pp. 371–375.

Gerasopoulos, E., Andreae, M.O., Zerefos, C.S., Andreae, T.W., Balis, D., Formenti, P., Merlet, P., Amiridis, V. & Papastefanou, C. (2003). Climatological aspects of aerosol optical properties in Northern Greece. *Atmospheric Chemistry and Physics*. 3. p.pp. 2025–2041.

Gerasopoulos, E., Kouvarakis, G., Babasakalis, P. & Vrekoussis, M. (2006). Origin and variability of particulate matter (PM10) mass concentrations over the Eastern Mediterranean. *Atmospheric Environment*. 40. p.pp. 4679–4690.

Gheusi, F., Durand, P., Verdier, N., Dulac, F., Attié, J.-L., Commun, P., Barret, B., Basdevant, C., Clénet, A., Derrien, S., Doerenbecher, A., El Amraoui, L., Fontaine, A., Hache, E., Jambert, C., Jaumouillé, E., Meyerfeld, Y., Roblou, L. & Tocquer, F. (2016). Adapted ECC ozone sonde for long-duration flights aboard boundary-layer pressurized balloons. *Atmos. Meas. Tech. Discuss.* 2016. p.pp. 1–41.

Ghio, A.J. & Devlin, R.B. (2001). Inflammatory Lung Injury after Bronchial Instillation of Air Pollution Particles. *American Journal of Respiratory and Critical Care Medicine*. 164 (4). p.pp. 704–708.

Ghio, A.J., Stonehuerner, J., Dailey, L. & Carter, J.D. (1999). Metals associated with both the water-soluble and insoluble fractions of an ambient air pollution particle catalyze an oxidative stress. *Inhalation Toxicology*. 11 (1). p.pp. 37–49.

Gieray, R. a., Reilly, P.T. a., Yang, M., Whitten, W.B. & Ramsey, J.M. (1997). Real-time detection of individual airborne bacteria. *Journal of Microbiological Methods*. 29 (3). p.pp. 191–199.

Gieré, R., Blackford, M. & Smith, K. (2006). TEM study of PM2.5 emitted from coal and tire combustion in a thermal power station. *Environmental science & technology*. 40 (20). p.pp. 6235–40.

Giorio, C., Tapparo, A., Dall'Osto, M., Harrison, R.M., Beddows, D.C.S., Di Marco, C. & Nemitz, E. (2012). Comparison of three techniques for analysis of data from an Aerosol Time-of-Flight Mass Spectrometer. *Atmospheric Environment*. 61. p.pp. 316–326.

Goodarzi, F. (2006). Morphology and chemistry of fine particles emitted from a Canadian

coal-fired power plant. *Fuel*. 85 (3). p.pp. 273–280.

Goss, K.U. & Eisenreich, S.J. (1997). Sorption of volatile organic compounds to particles from a combustion source at different temperatures and relative humidities. *Atmospheric Environment*. 31 (17). p.pp. 2827–2834.

Gross, D.S., Atlas, R., Rzeszotarski, J., Turetsky, E., Christensen, J., Benzaid, S., Olson, J., Smith, T., Steinberg, L. & Sulman, J. (2010). Environmental chemistry through intelligent atmospheric data analysis. *Environmental Modelling & Software*. 25 (6). p.pp. 760–769.

Gross, D.S., Barron, A.R., Sukovich, E.M., Warren, B.S., Jarvis, J.C., Suess, D.T. & Prather, K.A. (2005). Stability of single particle tracers for differentiating between heavy- and light-duty vehicle emissions. *Atmospheric Environment*. 39 (16). p.pp. 2889–2901.

Gross, D.S., Ga, M.E., Kalberer, M., Prevot, A.S.H., Dommen, J., Alfarra, M.R., Duplissy, J., Gaeggeler, K., Gascho, A. & Metzger, A. (2006). Real-Time Measurement of Oligomeric Species in Secondary Organic Aerosol with the Aerosol Time-of-Flight Mass Spectrometer. *Analytical Chemistry*. 78 (7). p.pp. 2130–2137.

Gross, D.S., Galli, M.E., Silva, P.J., Wood, S.H., Liu, D.-Y. & Prather, K.A. (2000). Single Particle Characterization of Automobile and Diesel Truck Emissions in the Caldecott Tunnel. *Aerosol Science and Technology*. 32 (2). p.pp. 152–163.

Guazzotti, S.A., Coffee, K.R. & Prather, K.A. (2001a). Continuous measurements of size-resolved particle chemistry during INDOEX-Intensive Field Phase 99. *Journal of Geophysical Research*. 106 (D22). p.pp. 28607–28627.

Guazzotti, S.A., Suess, D.T., Coffee, K.R., Quinn, P.K., Bates, T.S., Wisthaler, A., Hansel, A., Ball, P., Dickerson, R.R., Neusuß, C., Crutzen, P.J. & Prather, K.A. (2003). Characterization of carbonaceous aerosols outflow from India and Arabia: Biomass/biofuel burning and fossil fuel combustion. *Journal of Geophysical Research*. 108 (D15).

Guazzotti, S.A., Whiteaker, J.R., Suess, D.T., Coffee, K.R. & Prather, K.A. (2001b). Real-time measurements of the chemical composition of size-resolved particles during a Santa Ana wind episode, California USA. *Atmospheric Environment*. 35 (19). p.pp. 3229–3240.

Gugamsetty, B. (2012). Source Characterization and Apportionment of PM10, PM2.5 and PM0.1 by Using Positive Matrix Factorization. *Aerosol and Air Quality Research*. p.pp. 476–491.

Guzman-Morales, J., Frossard, A.A., Corrigan, A.L., Russell, L.M., Liu, S., Takahama, S., Taylor, J.W., Allan, J., Coe, H., Zhao, Y. & Goldstein, A.H. (2014). Estimated contributions of primary and secondary organic aerosol from fossil fuel combustion during the CalNex and Cal-Mex campaigns. *Atmospheric Environment*. 88. p.pp. 330–340.

El Haddad, I., Marchand, N., Temime-Roussel, B., Wortham, H., Piot, C., Besombes, J.L., Baduel, C., Voisin, D., Armengaud, a. & Jaffrezo, J.L. (2011). Insights into the secondary fraction of the organic aerosol in a Mediterranean urban area: Marseille. *Atmospheric Chemistry and Physics*. 11 (5). p.pp. 2059–2079.

Hall, B.D., Olson, M.L., Rutter, A.P., Frontiera, R.R., Krabbenhoft, D.P., Gross, D.S., Yuen, M., Rudolph, T.M. & Schauer, J.J. (2006). Atmospheric mercury speciation in Yellowstone National Park. *The Science of the Total Environment*. 367 (1). p.pp.

354–66.

Halliwell, B. & Cross, C.E. (1994). Oxygen-Derived Species: Their Relation to Human Disease and Environmental Stress. *Environmental Health Perspectives*. 102 (2). p.p. 5.

Halliwell, B. & Whiteman, M. (2004). Measuring reactive species and oxidative damage in vivo and in cell culture: how should you do it and what do the results mean? *British Journal of Pharmacology*. 142 (2). p.pp. 231–255.

Hallquist, M., Wenger, J.C., Baltensperger, U., Rudich, Y., Simpson, D., Claeys, M., Dommen, J., Donahue, N.M., George, C., Goldstein, a. H., Hamilton, J.F., Herrmann, H., Hoffmann, T., Iinuma, Y., Jang, M., Jenkin, M.E., Jimenez, J.L., Kiendler-Scharr, a., Maenhaut, W., McFiggans, G., Mentel, T.F., Monod, a., Prévôt, a. S.H., Seinfeld, J.H., Surratt, J.D., Szmigielski, R. & Wildt, J. (2009). The formation, properties and impact of secondary organic aerosol: current and emerging issues. *Atmos. Chem. Phys.* 9 (14). p.pp. 5155–5236.

Hansen, A.D.A., Rosen, H. & Novakov, T. (1984). The aethalometer — An instrument for the real-time measurement of optical absorption by aerosol particles. *Science of The Total Environment*. 36. p.pp. 191–196.

Harrison, R.M., Dall'Osto, M., Beddows, D.C.S., Thorpe, a. J., Bloss, W.J., Allan, J.D., Coe, H., Dorsey, J.R., Gallagher, M., Martin, C., Whitehead, J., Williams, P.I., Jones, R.L., Langridge, J.M., Benton, a. K., Ball, S.M., Langford, B., Hewitt, C.N., Davison, B., Martin, D., Petersson, K.F., Henshaw, S.J., White, I.R., Shallcross, D.E., Barlow, J.F., Dunbar, T., Davies, F., Nemitz, E., Phillips, G.J., Helfter, C., Di Marco, C.F. & Smith, S. (2012). Atmospheric chemistry and physics in the atmosphere of a developed megacity (London): an overview of the REPARTEE experiment and its conclusions. *Atmospheric Chemistry and Physics*. 12 (6). p.pp. 3065–3114.

Harrison, R.M. & Yin, J. (2000). Particulate matter in the atmosphere: which particle properties are important for its effects on health? *The Science of the Total Environment*. 249 (1-3). p.pp. 85–101.

Hatch, L.E., Creamean, J.M., Ault, A.P., Surratt, J.D., Chan, M.N., Seinfeld, J.H., Edgerton, E.S., Su, Y. & Prather, K.A. (2011). Measurements of Isoprene-Derived Organosulfates in Ambient Aerosols by Aerosol Time-of-Flight Mass Spectrometry - Part 1: Single Particle Atmospheric Observations in Atlanta. *Environmental Science & Technology*. 45 (12). p.pp. 5105–5111.

Hatch, L.E., Pratt, K.A., Huffman, J.A., Jimenez, J.L. & Prather, K.A. (2014). Impacts of Aerosol Aging on Laser Desorption/Ionization in Single-Particle Mass Spectrometers. *Aerosol Science and Technology*. 48 (10). p.pp. 1050–1058.

Hatzianastassiou, N., Gkikas, A., Mihalopoulos, N., Torres, O. & Katsoulis, B.D. (2009). Natural versus anthropogenic aerosols in the eastern Mediterranean basin derived from multiyear TOMS and MODIS satellite data. *Journal of Geophysical Research: Atmospheres*. 114 (24).

Hauck, H., Berner, A., Gomiscek, B., Stopper, S., Puxbaum, H., Kundi, M. & Preining, O. (2004). On the equivalence of gravimetric PM data with TEOM and beta-attenuation measurements. *Journal of Aerosol Science*. 35 (9). p.pp. 1135–1149.

Haywood, J. & Boucher, O. (2000). Estimates of the Direct and Indirect Radiative Forcing Due to Tropospheric Aerosols: A Review. *Reviews of Geophysics*. 38. p.pp. 513–543.

Heald, C.L., Ridley, D.A., Kroll, J.H., Barrett, S.R.H., Cady-Pereira, K.E., Alvarado, M.J. & Holmes, C.D. (2014). Contrasting the direct radiative effect and direct radiative forcing of aerosols. *Atmospheric Chemistry and Physics*. 14 (11). p.pp. 5513–5527.

Healy, R.M., Chen, Y., Kourtchev, I., Kalberer, M., O'Shea, D. & Wenger, J.C. (2012a). Rapid Formation of Secondary Organic Aerosol from the Photolysis of 1-Nitronaphthalene: Role of Naphthoxy Radical Self-reaction. *Environmental Science & Technology*.

Healy, R.M., Evans, G.J., Murphy, M., Sierau, B., Arndt, J., McGillicuddy, E., O'Connor, I.P., Sodeau, J.R. & Wenger, J.C. (2014). Single-particle speciation of alkylamines in ambient aerosol at five European sites. *Analytical and Bioanalytical Chemistry*.

Healy, R.M., Hellebust, S., Kourtchev, I., Allanic, A., O'Connor, I.P.P., Bell, J.M.M., Healy, D.A.A., Sodeau, J.R.R. & Wenger, J.C.C. (2010). Source apportionment of $PM_{2.5}$ in Cork Harbour, Ireland using a combination of single particle mass spectrometry and quantitative semi-continuous measurements. *Atmospheric Chemistry and Physics*. 10 (19). p.pp. 9593–9613.

Healy, R.M., O'Connor, I.P., Hellebust, S., Allanic, A., Sodeau, J.R. & Wenger, J.C. (2009). Characterisation of single particles from in-port ship emissions. *Atmospheric Environment*. 43 (40). p.pp. 6408–6414.

Healy, R.M., Sciare, J., Poulain, L., Crippa, M., Wiedensohler, a., Prévôt, a. S.H., Baltensperger, U., Sarda-Estève, R., McGuire, M.L., Jeong, C.H., McGillicuddy, E., O'Connor, I.P., Sodeau, J.R., Evans, G.J. & Wenger, J.C. (2013). Quantitative determination of carbonaceous particle mixing state in Paris using single-particle mass spectrometer and aerosol mass spectrometer measurements. *Atmospheric Chemistry and Physics*. 13 (18). p.pp. 9479–9496.

Healy, R.M., Sciare, J., Poulain, L., Kamili, K., Merkel, M., Müller, T., Wiedensohler, A., Eckhardt, S., Stohl, A., Sarda-Estève, R., McGillicuddy, E., O'Connor, I.P., Sodeau, J.R. & Wenger, J.C. (2012b). Sources and mixing state of size-resolved elemental carbon particles in a European megacity: Paris. *Atmospheric Chemistry and Physics*. 12 (4). p.pp. 1681–1700.

Healy, R.M., Wang, J.M., Jeong, C.-H., Lee, A.K.Y., Willis, M.D., Jaroudi, E., Zimmerman, N., Hilker, N., Murphy, M., Eckhardt, S., Stohl, A., Abbatt, J.P.D., Wenger, J.C. & Evans, G.J. (2015). Light-absorbing properties of ambient black carbon and brown carbon from fossil fuel and biomass burning sources. *Journal of Geophysical Research: Atmospheres*. 120 (13). p.pp. 6619–6633.

Heard, D. (2006). *Analytical Techniques for Atmospheric Measurement*. D. E. Heard (ed.). Oxford, UK: Blackwell Publishing.

Heimbürger, L.-E., Migon, C., Dufour, A., Chiffoleau, J.-F. & Cossa, D. (2010). Trace metal concentrations in the North-western Mediterranean atmospheric aerosol between 1986 and 2008: seasonal patterns and decadal trends. *Science of the Total Environment*. 408 (13). p.pp. 2629–38.

Herich, H., Kammermann, L., Friedman, B., Gross, D.S., Weingartner, E., Lohmann, U., Spichtinger, P., Gysel, M., Baltensperger, U. & Cziczo, D.J. (2009). Subarctic atmospheric aerosol composition: 2. Hygroscopic growth properties. *Journal of Geophysical Research*. 114 (D13). p.pp. 1–14.

Herich, H., Kammermann, L., Gysel, M., Weingartner, E., Baltensperger, U., Lohmann, U. & Cziczo, D.J. (2008). In situ determination of atmospheric aerosol composition as a function of hygroscopic growth. *Journal of Geophysical Research*. 113 (D16).

p.pp. 1–14.

Hering, S.V. & McMurry, P.H. (1991). Optical counter response to monodisperse atmospheric aerosols. *Atmos. Environ. A.* 25 (2). p.pp. 463–468.

Hieu, N.T. & Lee, B.-K. (2010). Characteristics of particulate matter and metals in the ambient air from a residential area in the largest industrial city in Korea. *Atmospheric Research*. 98 (2-4). p.pp. 526–537.

Hinz, K.-P., Kaufmann, R. & Spengler, B. (1994). Laser-Induced Mass Analysis of Single Particles in the Airborne State. *Analytical Chemistry*. 66 (13). p.pp. 2071–2076.

Hinz, K.-P. & Spengler, B. (2007). Instrumentation, data evaluation and quantification in on-line aerosol mass spectrometry. *Journal of Mass Spectrometry*. 42 (7). p.pp. 843–860.

Hleis, D., Fernández-Olmo, I., Ledoux, F., Kfoury, A., Courcot, L., Desmonts, T. & Courcot, D. (2013). Chemical profile identification of fugitive and confined particle emissions from an integrated iron and steelmaking plant. *Journal of Hazardous Materials*. 250-251 (August 2015). p.pp. 246–255.

Hobbs, P.V. (2000). *Introduction to Atmospheric Chemistry*. Cambridge University Press.

Hoinka, K.P. & De Castro, M. (2003). The Iberian Peninsula thermal low. *Quarterly Journal of the Royal Meteorological Society*. 129. p.pp. 1491–1511.

Holecek, J.C., Spencer, M.T. & Prather, K. a. (2007). Analysis of rainwater samples: Comparison of single particle residues with ambient particle chemistry from the northeast Pacific and Indian oceans. *Journal of Geophysical Research: Atmospheres*. 112.

Hopkins, R.J., Desyaterik, Y., Tivanski, A. V., Zaveri, R. a., Berkowitz, C.M., Tyliszczak, T., Gilles, M.K. & Laskin, A. (2008). Chemical speciation of sulfur in marine cloud droplets and particles: Analysis of individual particles from the marine boundary layer over the California current. *Journal of Geophysical Research*. 113 (D4). p.p. D04209.

Hu, D., Li, C., Chen, H., Chen, J., Ye, X., Li, L., Yang, X., Wang, X., Mellouki, A. & Hu, Z. (2014). Hygroscopicity and optical properties of alkylaminium sulfates. *Journal of Environmental Sciences (China)*. 26 (1). p.pp. 37–43.

Huang, Y., Chen, H., Wang, L., Yang, X. & Chen, J. (2012). Single particle analysis of amines in ambient aerosol in Shanghai. *Environmental Chemistry*. 9 (3). p.p. 202.

Hughes, L.S., Allen, J.O., Bhave, P., Kleeman, M.J., Cass, G.R., Liu, D.-Y., Fergenson, D.P., Morrical, B.D. & Prather, K.A. (2000). Evolution of Atmospheric Particles along Trajectories Crossing the Los Angeles Basin. *Environmental Science & Technology*. 34 (15). p.pp. 3058–3068.

Hughes, L.S., Allen, J.O., Kleeman, M.J., Johnson, R.J., Cass, G.R., Gross, D.S., Gard, E.E., Gälli, M.E., Morrical, B.D., Fergenson, D.P., Dienes, T., Noble, C.A., Liu, D.-Y., Silva, P.J. & Prather, K.A. (1999). Size and Composition Distribution of Atmospheric Particles in Southern California. *Environmental Science & Technology*. 33 (20). p.pp. 3506–3515.

Huo, J., Lu, X., Wang, X., Chen, H., Ye, X., Gao, S., Gross, D.S., Chen, J. & Yang, X. (2015). Online single particle analysis of chemical composition and mixing state of crop straw burning particles: from laboratory study to field measurement. *Frontiers*

of Environmental Science & Engineering.

Hussein, T., Karppinen, A., Kukkonen, J., Härkönen, J., Aalto, P.P., Hämeri, K., Kerminen, V.-M. & Kulmala, M. (2006). Meteorological dependence of size-fractionated number concentrations of urban aerosol particles. *Atmospheric Environment*. 40 (8). p.pp. 1427–1440.

IPCC (2007). *Contribution of Working Group I to the Fourth Assessment Report of the Intergovernmental Panel on Climate Change*. S. Solomon, D. Qin, M. Manning, Z. Chen, M. Marquis, K. B. Averyt., M. Tignor, & H. L. Miller (eds.). Cambridge, United Kingdom and New York, NY, USA.: Cambridge University Press.

IPCC (2013). Summary for Policymakers. In: T. F. Stocker, D. Qin, G.-K. Plattner, M. Tignor, S. K. Allen, J. Boschung, A. Nauels, Y. Xia, V. Bex, & P. M. Midgley (eds.). *Climate Change 2013: The Physical Science Basis. Contribution of Working Group I to the Fifth Assessment Report of the Intergovernmental Panel on Climate Change*. Cambridge, United Kingdom and New York, NY, USA.: Cambridge University Press.

Jaeglé, L., Quinn, P.K., Bates, T.S., Alexander, B. & Lin, J.T. (2011). Global distribution of sea salt aerosols: New constraints from in situ and remote sensing observations. *Atmospheric Chemistry and Physics*. 11 (2004). p.pp. 3137–3157.

Jang, H.N., Seo, Y.C., Lee, J.H., Hwang, K.W., Yoo, J.I., Sok, C.H. & Kim, S.H. (2007). Formation of fine particles enriched by V and Ni from heavy oil combustion: Anthropogenic sources and drop-tube furnace experiments. *Atmospheric Environment*. 41. p.pp. 1053–1063.

Jayne, J.T., Leard, D.C., Zhang, X., Davidovits, P., Smith, K. a., Kolb, C.E. & Worsnop, D.R. (2000a). Development of an Aerosol Mass Spectrometer for Size and Composition Analysis of Submicron Particles. *Aerosol Science and Technology*. 33 (1-2). p.pp. 49–70.

Jayne, J.T., Leard, D.C., Zhang, X., Smith, K.A., Kolb, C.E. & Worsnop, D.R. (2000b). Aerosol mass spectrometer for size and composition analysis of submicron particles. *Aerosol Science and Technology*. 33. p.pp. 49 – 70.

Jeong, C.-H., Evans, G.J., Healy, R.M., Jadidian, P., Wentzell, J., Liggio, J. & Brook, J.R. (2015). Rapid physical and chemical transformation of traffic-related atmospheric particles near a highway. *Atmospheric Pollution Research*. 6 (4). p.pp. 662–672.

Jeong, C.-H., McGuire, M.L., Godri, K.J., Slowik, J.G., Rehbein, P.J.G. & Evans, G.J. (2011). Quantification of aerosol chemical composition using continuous single particle measurements. *Atmospheric Chemistry and Physics*. 11 (14). p.pp. 7027–7044.

Jimenez, J.L., Canagaratna, M.R., Donahue, N.M., Prevot, A.S.H., Zhang, Q., Kroll, J.H., DeCarlo, P.F., Allan, J.D., Coe, H., Ng, N.L., Aiken, A.C., Docherty, K.S., Ulbrich, I.M., Grieshop, A.P., Robinson, A.L., Duplissy, J., Smith, J.D., Wilson, K.R., Lanz, V.A., Hueglin, C., Sun, Y.L., Tian, J., Laaksonen, A., Raatikainen, T., Rautiainen, J., Vaattovaara, P., Ehn, M., Kulmala, M., Tomlinson, J.M., Collins, D.R., Cubison, M.J., Dunlea, J., Huffman, J.A., Onasch, T.B.B., Alfarra, M.R.R., Williams, P.I., Bower, K., Kondo, Y., Schneider, J., Drewnick, F., Borrmann, S., Weimer, S., Demerjian, K., Salcedo, D., Cottrell, L., Griffin, R., Takami, A., Miyoshi, T., Hatakeyama, S., Shimono, A., Sun, J.Y.Y., Zhang, Y.M., Dzepina, K., Kimmel, J.R., Sueper, D., Jayne, J.T., Herndon, S.C., Trimborn, A.M., Williams, L.R., Wood, E.C.,

Middlebrook, A.M., Kolb, C.E., Baltensperger, U. & Worsnop, D.R. (2009). Evolution of Organic Aerosols in the Atmosphere. *Science*. 326 (5959). p.pp. 1525–1529.

Johnson, J.E., Webb, S.M., Thomas, K., Ono, S., Kirschvink, J.L. & Fischer, W.W. (2013). Manganese-oxidizing photosynthesis before the rise of cyanobacteria. *Proceedings of the National Academy of Sciences*. 110 (28). p.pp. 11238–11243.

Joseph, A.E. (2012). Chemical Characterization and Mass Closure of Fine Aerosol for Different Land Use Patterns in Mumbai City. *Aerosol and Air Quality Research*. (October).

Kallos, G., Kassomenos, P. & Pielke, R.A. (1993). Synoptic and mesoscale weather conditions during air pollution episodes in Athens, Greece. *Boundary-Layer Meteorology*. 62 (1-4). p.pp. 163–184.

Kamphus, M., Ettner-Mahl, M., Klimach, T., Drewnick, F., Keller, L., Cziczo, D.J., Mertes, S., Borrmann, S. & Curtius, J. (2010). Chemical composition of ambient aerosol, ice residues and cloud droplet residues in mixed-phase clouds: single particle analysis during the Cloud and Aerosol Characterization Experiment (CLACE 6). *Atmospheric Chemistry and Physics*. 10 (16). p.pp. 8077–8095.

Kanakidou, M., Mihalopoulos, N., Kindap, T., Im, U., Vrekoussis, M., Gerasopoulos, E., Dermitzaki, E., Unal, A., Koçak, M., Markakis, K., Melas, D., Kouvarakis, G., Youssef, A.F., Richter, A., Hatzianastassiou, N., Hilboll, A., Ebojie, F., Wittrock, F., von Savigny, C., Burrows, J.P., Ladstaetter-Weissenmayer, A. & Moubasher, H. (2011). Megacities as hot spots of air pollution in the East Mediterranean. *Atmospheric Environment*. 45 (6). p.pp. 1223–1235.

Kane, D.B. & Johnston, M. V. (2000). Size and Composition Biases on the Detection of Individual Ultrafine Particles by Aerosol Mass Spectrometry. *Environmental Science & Technology*. 34 (23). p.pp. 4887–4893.

Kane, D.B., Wang, J., Frost, K. & Johnston, M. V. (2002). Detection of negative ions from individual ultrafine particles. *Analytical Chemistry*. 74 (9). p.pp. 2092–2096.

Karanasiou, A., Moreno, T., Amato, F., Lumbreras, J., Narros, A., Borge, R., Tobías, A., Boldo, E., Linares, C., Pey, J., Reche, C., Alastuey, A. & Querol, X. (2011). Road dust contribution to PM levels - Evaluation of the effectiveness of street washing activities by means of Positive Matrix Factorization. *Atmospheric Environment*. 45 (13). p.pp. 2193–2201.

Karanasiou, A., Querol, X., Alastuey, A., Perez, N., Pey, J., Perrino, C., Berti, G., Gandini, M., Poluzzi, V., Ferrari, S., de la Rosa, J., Pascal, M., Samoli, E., Kelessis, A., Sunyer, J., Alessandrini, E., Stafoggia, M. & Forastiere, F. (2014). Particulate matter and gaseous pollutants in the Mediterranean Basin: results from the MED-PARTICLES project. *Science of The Total Environment*. 488-489. p.pp. 297–315.

Karanasiou, A.A., Siskos, P.A. & Eleftheriadis, K. (2009). Assessment of source apportionment by Positive Matrix Factorization analysis on fine and coarse urban aerosol size fractions. *Atmospheric Environment*. 43 (21). p.pp. 3385–3395.

Karanasiou, A.A., Sitaras, I.E., Siskos, P.A. & Eleftheriadis, K. (2007). Size distribution and sources of trace metals and n-alkanes in the Athens urban aerosol during summer. *Atmospheric Environment*. 41 (11). p.pp. 2368–2381.

Kauppinen, E.I. & Pakkanen, T. a (1990). Coal combustion aerosols: A field study. *Environmental Science and Technology*. 24 (12). p.pp. 1811–1818.

Kerminen, V.M., Aurela, M., Hillamo, R.E. & Virkkula, A. (1997). Formation of particulate MSA: Deductions from size distribution measurements in the finnish arctic. *Tellus, Series B: Chemical and Physical Meteorology*. 49 (2). p.pp. 159–171.

Klems, J.P., Zordan, C.A., Pennington, M.R. & Johnston, M.V. (2012). Chemical composition of ambient nanoparticles on a particle-by-particle basis. *Analytical chemistry*. 84 (5). p.pp. 2253–9.

Koçak, M., Kubilay, N., Herut, B. & Nimmo, M. (2005). Dry atmospheric fluxes of trace metals (Al, Fe, Mn, Pb, Cd, Zn, Cu) over the Levantine Basin: A refined assessment. *Atmospheric Environment*. 39 (38). p.pp. 7330–7341.

Koçak, M., Kubilay, N. & Mihalopoulos, N. (2004). Ionic composition of lower tropospheric aerosols at a Northeastern Mediterranean site: Implications regarding sources and long-range transport. *Atmospheric Environment*. 38 (14). p.pp. 2067–2077.

Kodavanti, U.P., Hauser, R., Christiani, D.C., Meng, Z.H., McGee, J., Ledbetter, A., Richards, J. & Costa, D.L. (1998). Pulmonary Responses to Oil Fly Ash Particles in the Rat Differ by Virtue of Their Specific Soluble Metals. *Toxicological Sciences*. 43 (2). p.pp. 204–212.

Koponen, I.K., Virkkula, A., Hillamo, R., Kerminen, V.M. & Kulmala, M. (2002). Number size distributions and concentrations of marine aerosols: Observations during a cruise between the English Channel and the coast of Antarctica. *Journal of Geophysical Research: Atmospheres*. 107 (24). p.pp. 1–8.

Koulouri, E., Saarikoski, S., Theodosi, C., Markaki, Z., Gerasopoulos, E., Kouvarakis, G., Mäkelä, T., Hillamo, R. & Mihalopoulos, N. (2008). Chemical composition and sources of fine and coarse aerosol particles in the Eastern Mediterranean. *Atmospheric Environment*. 42 (26). p.pp. 6542–6550.

Kouvarakis, G. & Mihalopoulos, N. (2002). Seasonal variation of dimethylsulfide in the gas phase and of methanesulfonate and non-sea-salt sulfate in the aerosols phase in the Eastern Mediterranean atmosphere. *Atmospheric Environment*. 36 (6). p.pp. 929–938.

Kreidenweis, S.M., Flagan, R.C., Seinfeld, J.H. & Okuyama, K. (1989). Binary nucleation of methanesulfonic acid and water. *Journal of Aerosol Science*. 20 (5). p.pp. 585–607.

Kubilay, N., Koçak, M., Çokacar, T., Oguz, T., Kouvarakis, G. & Mihalopoulos, N. (2002). Influence of Black Sea and local biogenic activity on the seasonal variation of aerosol sulfur species in the eastern Mediterranean atmosphere. *Global Biogeochemical Cycles*. 16 (4). p.pp. 27–1–27–15.

Kubilay, N. & Saydam, A.C. (1995). Trace elements in atmospheric particulates over the eastern Mediterranean; Concentrations, sources, and temporal variability. *Atmospheric Environment*. 29 (17). p.pp. 2289–2300.

Kulkarni, P., Chellam, S. & Fraser, M.P. (2006). Lanthanum and lanthanides in atmospheric fine particles and their apportionment to refinery and petrochemical operations in Houston, TX. *Atmospheric Environment*. 40. p.pp. 508–520.

Kulmala, M. & Kerminen, V.M. (2008). On the formation and growth of atmospheric nanoparticles. *Atmospheric Research*. 90 (2-4). p.pp. 132–150.

Kumar, P., Robins, A., Vardoulakis, S. & Britter, R. (2010). A review of the characteristics of nanoparticles in the urban atmosphere and the prospects for

developing regulatory controls. *Atmospheric Environment*. 44 (39). p.pp. 5035–5052.

de la Paz, D., Vedrenne, M., Borge, R., Lumbreras, J., de Andrés, J.M., Pérez, J., Rodríguez, E., Karanasiou, A., Moreno, T., Boldo, E. & Linares, C. (2013). Modelling Saharan dust transport into the Mediterranean basin with CMAQ. *Atmospheric Environment*. 70. p.pp. 337–350.

Laden, F., Neas, L.M., Dockery, D.W. & Schwartz, J. (2000). Association of fine particulate matter from different sources with daily mortality in six U.S. cities. *Environmental Health Perspectives*. 108 (10). p.pp. 941–7.

Lake, D.A., Tolocka, M.P., Johnston, M.V. & Wexler, A.S. (2004). The character of single particle sulfate in Baltimore. *Atmospheric Environment*. 38 (31). p.pp. 5311–5320.

Lambert, D., Mallet, M., Ducrocq, V., Dulac, F., Gheusi, F. & Kalthoff, N. (2011). CORSiCA: a Mediterranean atmospheric and oceanographic observatory in Corsica within the framework of HyMeX and ChArMEx. *Advances in Geosciences*. 26. p.pp. 125–131.

Lea-Langton, a. R., Baeza-Romero, M.T., Boman, G.V., Brooks, B., Wilson, a. J.M., Atika, F., Bartle, K.D., Jones, J.M. & Williams, a. (2015). A study of smoke formation from wood combustion. *Fuel Processing Technology*.

Ledoux, F., Courcot, D., Courcot, L., Aboukais, a. & Puskaric, E. (2009). Atmospheric aerosols behaviour at an industrial area in Northern France. *International Journal of Environment and Pollution*. 39 (3/4). p.p. 286.

Lee, C., Sultana, C.M., Collins, D.B., Santander, M. V., Axson, J.L., Malfatti, F., Cornwell, G.C., Grandquist, J.R., Deane, G.B., Stokes, M.D., Azam, F., Grassian, V.H. & Prather, K.A. (2015). Advancing Model Systems for Fundamental Laboratory Studies of Sea Spray Aerosol Using the Microbial Loop. *The Journal of Physical Chemistry A*. 119 (33). p.pp. 8860–8870.

Lee, G., Park, J., Jang, Y., Lee, M., Kim, K.-R., Oh, J.-R., Kim, D., Yi, H.-I. & Kim, T.-Y. (2010). Vertical variability of seawater DMS in the South Pacific Ocean and its implication for atmospheric and surface seawater DMS. *Chemosphere*. 78 (8). p.pp. 1063–70.

Lelieveld, J., Berresheim, H., Borrmann, S., Crutzen, P.J., Dentener, F.J., Fischer, H., Feichter, J., Flatau, P.J., Heland, J., Holzinger, R., Korrmann, R., Lawrence, M.G., Levin, Z., Markowicz, K.M., Mihalopoulos, N., Minikin, A., Ramanathan, V., De Reus, M., Roelofs, G.J., Scheeren, H. a, Sciare, J., Schlager, H., Schultz, M., Siegmund, P., Steil, B., Stephanou, E.G., Stier, P., Traub, M., Warneke, C., Williams, J. & Ziereis, H. (2002). Global air pollution crossroads over the Mediterranean. *Science*. 298. p.pp. 794–799.

Li, M., Dong, J.-G., Huang, Z.-X., Li, L., Gao, W., Nian, H.-Q., Fu, Z., Cheng, P. & Zhou, Z. (2012). Analysis of Cigarette Smoke Aerosol by Single Particle Aerosol Mass Spectrometer. *Chinese Journal of Analytical Chemistry*. 40 (6). p.pp. 936–939.

Li, R., Ning, Z., Majumdar, R., Cui, J., Takabe, W., Jen, N., Sioutas, C. & Hsiai, T. (2010). Ultrafine particles from diesel vehicle emissions at different driving cycles induce differential vascular pro-inflammatory responses: Implication of chemical components and NF-κB signaling. *Particle and Fibre Toxicology*. 7 (1). p.p. 6.

Li, W., Shao, L., Zhang, D., Ro, C.-U., Hu, M., Bi, X., Geng, H., Matsuki, A., Niu, H. &

Chen, J. (2015). A review of single aerosol particle studies in the atmosphere of East Asia: morphology, mixing state, source, and heterogeneous reactions. *Journal of Cleaner Production*.

Lim, J.-M., Lee, J.-H., Moon, J.-H., Chung, Y.-S. & Kim, K.-H. (2010). Airborne PM10 and metals from multifarious sources in an industrial complex area. *Atmospheric Research*. 96 (1). p.pp. 53–64.

Lin, L., Fan, Z.-H., Zhu, X., Huang, L.-H. & Bonanno, L.J. (2011). Characterization of Atmospheric Polycyclic Aromatic Hydrocarbons in a Mixed-Use Urban Community in Paterson, NJ: Concentrations and Sources. *Journal of the Air & Waste Management Association*. 61 (6). p.pp. 631–639.

Linak, W.P., Yoo, J.-I., Wasson, S.J., Zhu, W., Wendt, J.O.L., Huggins, F.E., Chen, Y., Shah, N., Huffman, G.P. & Gilmour, M.I. (2007). Ultrafine ash aerosols from coal combustion: Characterization and health effects. *Proceedings of the Combustion Institute*. 31 (2). p.pp. 1929–1937.

Lingard, J.J.N., Tomlin, a. S., Clarke, a. G., Healey, K., Hay, a. W.M., Wild, C.P. & Routledge, M.N. (2005). A study of trace metal concentration of urban airborne particulate matter and its role in free radical activity as measured by plasmid strand break assay. *Atmospheric Environment*. 39 (13). p.pp. 2377–2384.

Liu, D.-Y., Prather, K.A. & Hering, S.V. (2000). Variations in the Size and Chemical Composition of Nitrate-Containing Particles in Riverside, CA. *Aerosol Science and Technology*. 33 (1-2). p.pp. 71–86.

Liu, D.-Y., Rutherford, D., Kinsey, M. & Prather, K.A. (1997). Real-Time Monitoring of Pyrotechnically Derived Aerosol Particles in the Troposphere. *Analytical Chemistry*. 69 (10). p.pp. 1808–1814.

Liu, D.Y., Wenzel, R.J., Prather, K.A., Liu, D.Y., Edgerton, E.S. & Prather, K.A. (2003). Aerosol time-of-flight mass spectrometry during the Atlanta Supersite Experiment: 1. Measurements. *Journal of Geophysical Research*. 108 (D7). p.p. 8426.

Lohmann, U. & Feichter, J. (2005). Global indirect aerosol effects: a review. *Atmospheric Chemistry and Physics*. 5. p.pp. 715–737.

Loomis, D., Grosse, Y., Lauby-Secretan, B., Ghissassi, F. El, Bouvard, V., Benbrahim-Tallaa, L., Guha, N., Baan, R., Mattock, H. & Straif, K. (2013). *The carcinogenicity of outdoor air pollution*.

Lough, G.C., Schauer, J.J., Park, J.S., Shafer, M.M., Deminter, J.T. & Weinstein, J.P. (2005). Emissions of metals associated with motor vehicle roadways. *Environmental Science and Technology*. 39 (3). p.pp. 826–836.

Loye-Pilot, M.D. & Morelli, J. (1988). Fluctuations of ionic composition of precipitations collected in corsica related to changes in the origins of incoming aerosols. *Journal of Aerosol Science*. 19 (5). p.pp. 577–585.

Ma, L., Li, M., Zhang, H., Li, L., Huang, Z., Gao, W., Chen, D., Fu, Z., Nian, H., Zou, L., Gao, J., Chai, F. & Zhou, Z. (2015a). Comparative analysis of chemical composition and sources of aerosol particles in urban Beijing during clear, hazy, and dusty days using single particle aerosol mass spectrometry. *Journal of Cleaner Production*.

Ma, S., Ren, K., Liu, X., Chen, L., Li, M., Li, X., Yang, J., Huang, B., Zheng, M. & Xu, Z. (2015b). Production of Hydroxyl Radicals from Fe-containing Fine Particles in Guangzhou, China. *Atmospheric Environment*.

MacQueen, J. (1967). Some methods for classification and analysis of multivariate observations. *Proceedings of the Fifth Berkeley Symposium*. 1. p.pp. 281–297.

Magee Scientific Company (2005). *The Aethalometer*. Berkeley, California, USA.

Maguhn, J., Karg, E., Kettrup, A. & Zimmermann, R. (2003). On-line analysis of the size distribution of fine and ultrafine aerosol particles in flue and stack gas of a municipal waste incineration plant: effects of dynamic process control measures and emission reduction devices. *Environmental science & technology*. 37 (20). p.pp. 4761–70.

Mahajan, A.S., Plane, J.M.C., Oetjen, H., Mendes, L., Saunders, R.W., Saiz-Lopez, A., Jones, C.E., Carpenter, L.J. & McFiggans, G.B. (2010). Measurement and modelling of tropospheric reactive halogen species over the tropical Atlantic Ocean. *Atmospheric Chemistry and Physics*. 10 (10). p.pp. 4611–4624.

Majestic, B.J., Schauer, J.J. & Shafer, M.M. (2007). Development of a Manganese Speciation Method for Atmospheric Aerosols in Biologically and Environmentally Relevant Fluids. *Aerosol Science and Technology*. 41 (10). p.pp. 925–933.

Mäkelä, J., Yli-Koivisto, S. & Hiltunen, V. (2001). Chemical composition of aerosol during particle formation events in boreal forest. *Tellus B*. p.pp. 380–393.

Malan, J., Barthel, W. & Dippenaar, B. a (2004). Optimizing Manganese Ore Sinter Plants: Process Parameters and Design Implications. In: *Tenth International Ferroalloys Congress*. 2004, pp. 281–290.

Mallet, M., Dulac, F., Formenti, P., Nabat, P., Sciare, J., Roberts, G., Pelon, J., Ancellet, G., Tanré, D., Parol, F., di Sarra, A., Alados, L., Arndt, J., Auriol, F., Blarel, L., Bourrianne, T., Brogniez, G., Chazette, P., Chevaillier, S., Claeys, M., D'Anna, B., Denjean, C., Derimian, Y., Desboeufs, K., Di Iorio, T., Doussin, J.-F., Durand, P., Féron, A., Freney, E., Gaimoz, C., Goloub, P., Gómez-Amo, J.L., Granados-Muñoz, M.J., Grand, N., Hamonou, E., Jankowiak, I., Jeannot, M., Léon, J.-F., Maillé, M., Mailler, S., Meloni, D., Menut, L., Momboisse, G., Nicolas, J., Podvin, J., Pont, V., Rea, G., Renard, J.-B., Roblou, L., Schepanski, K., Schwarzenboeck, A., Sellegri, K., Sicard, M., Solmon, F., Somot, S., Torres, B., Totems, J., Triquet, S., Verdier, N., Verwaerde, C., Wenger, J. & Zapf, P. (2015). Overview of the Chemistry-Aerosol Mediterranean Experiment/Aerosol Direct Radiative Forcing on the Mediterranean Climate (ChArMEx/ADRIMED) summer 2013 campaign. *Atmospheric Chemistry and Physics Discussions*. 15 (14). p.pp. 19615–19727.

Mallet, M., Pont, V., Liousse, C., Roger, J.C. & Dubuisson, P. (2006). Simulation of aerosol radiative properties with the ORISAM-RAD model during a pollution event (ESCOMPTE 2001). *Atmospheric Environment*. 40 (40). p.pp. 7696–7705.

Mamane, Y. & Gottlieb, J. (1992). Nitrate formation on sea-salt and mineral particles—A single particle approach. *Atmospheric Environment. Part A. General Topics*. 26 (9). p.pp. 1763–1769.

Manoli, E., Voutsa, D. & Samara, C. (2002). Chemical characterization and source identification/apportionment of fine and coarse air particles in Thessaloniki, Greece. *Atmospheric Environment*. 36 (6). p.pp. 949–961.

Mao, I., Chen, C., Lin, Y. & Chen, M. (2007). Airborne particle PM2.5/PM10 mass distribution and particle-bound PAH concentrations near a medical waste incinerator. *Atmospheric Environment*. 41 (11). p.pp. 2467–2475.

Maricq, M.M. & Xu, N. (2004). The effective density and fractal dimension of soot particles from premixed flames and motor vehicle exhaust. *Journal of Aerosol*

Science. 35 (10). p.pp. 1251–1274.

Markowicz, K.M., Flatau, P.J., Ramana, M.V., Crutzen, P.J. & Ramanathan, V. (2002). Absorbing mediterranean aerosols lead to a large reduction in the solar radiation at the surface. *Geophysical Research Letters*. 29 (20). p.pp. 4–7.

Marmer, E. & Langmann, B. (2005). Impact of ship emissions on the Mediterranean summertime pollution and climate: A regional model study. *Atmospheric Environment*. 39 (August 2001). p.pp. 4659–4669.

Marris, H., Deboudt, K., Augustin, P., Flament, P., Blond, F., Fiani, E., Fourmentin, M. & Delbarre, H. (2012). Fast changes in chemical composition and size distribution of fine particles during the near-field transport of industrial plumes. *The Science of the Total Environment*. 427-428. p.pp. 126–38.

Marris, H., Deboudt, K., Flament, P., Grobéty, B. & Gieré, R. (2013). Fe and Mn Oxidation States by TEM-EELS in Fine-Particle Emissions from a Fe-Mn Alloy Making Plant. *Environmental science & technology*. (Ii).

Martin, A.N., Farquar, G.R., Frank, M., Gard, E.E. & Fergenson, D.P. (2007a). Single-Particle Aerosol Mass Spectrometry for the Detection and Identification of Chemical Warfare Agent Simulants. *Analytical Chemistry*. 79 (16). p.pp. 6368–6375.

Martin, A.N., Farquar, G.R., Gard, E.E., Frank, M. & Fergenson, D.P. (2007b). Identification of high explosives using single-particle aerosol mass spectrometry. *Analytical Chemistry*. 79 (5). p.pp. 1918–1925.

Martley, E., Gulson, B. & Pfeifer, H. (2004). Metal concentrations in soils around the copper smelter and surrounding industrial complex of Port Kembla, NSW, Australia. *Science of The Total Environment*. 325 (1-3). p.pp. 113–127.

Mason, R.P. (2009). Mercury emissions from natural processes and their importance in the global mercury cycle. In: R. Mason & N. Pirrone (eds.). *Mercury Fate and Transport in the Global Atmosphere*. Boston, MA: Springer US, pp. 173–191.

Mather, T.A., Pyle, D.M. & Oppenheimer, C. (2003). Tropospheric volcanic aerosol. In: A. Robock & C. Oppenheimer (eds.). *Volcanism and the Earth's …*. Washington, D.C.: American Geophysical Union, pp. 189–212.

Mazzei, F., D'Alessandro, a., Lucarelli, F., Marenco, F., Nava, S., Prati, P., Valli, G. & Vecchi, R. (2006). Elemental composition and source apportionment of particulate matter near a steel plant in Genoa (Italy). *Nuclear Instruments and Methods in Physics Research Section B: Beam Interactions with Materials and Atoms*. 249 (1-2). p.pp. 548–551.

Mbengue, S., Alleman, L.Y. & Flament, P. (2014). Size-distributed metallic elements in submicronic and ultrafine atmospheric particles from urban and industrial areas in northern France. *Atmospheric Research*. 135-136. p.pp. 35–47.

McGillicuddy, E.J. (2014). *Real Time Analysis of Atmospheric Single Particles in Urban Environments using Aerosol Time of Flight Mass Spectrometry*. Univesity College Cork.

McGuire, M.L., Jeong-C.-H., Slowik, J.G., Y.-W. Chang, R., Corbin, J.C., Lu, G., Mihele, C., Rehbein, P.J.G., Sills, D.M.L., Abbatt, J.P.D., Brook, J.R. & Evans, G.J. (2011). Elucidating determinants of aerosol composition through particle-type-based receptor modeling. *Atmospheric Chemistry and Physics*. 11. p.pp. 8133–8155.

McMurry, P.H. (2000). A review of atmospheric aerosol measurements. *Atmospheric*

Environment. 34 (12-14). p.pp. 1959–1999.

Meloni, D., di Sarra, a., Di Iorio, T. & Fiocco, G. (2004). Direct radiative forcing of Saharan dust in the Mediterranean from measurements at Lampedusa Island and MISR space-borne observations. *Journal of Geophysical Research D: Atmospheres*. 109 (8). p.pp. 1–15.

Meloni, D., di Sarra, A., DeLuisi, J., Di Iorio, T., Fiocco, G., Junkermann, W. & Pace, G. (2003). Tropospheric aerosols in the Mediterranean: 2. Radiative effects through model simulations and measurements. *Journal of Geophysical Research*. 108 (D10). p.pp. 1–16.

Meloni, D., di Sarra, A., Monteleone, F., Pace, G., Piacentino, S. & Sferlazzo, D.M. (2008). Seasonal transport patterns of intense Saharan dust events at the Mediterranean island of Lampedusa. *Atmospheric Research*. 88 (2). p.pp. 134–148.

Metzger, S., Mihalopoulos, N. & Lelieveld, J. (2005). Importance of mineral cations and organics in gas-aerosol partitioning of reactive nitrogen compounds: case study based on MINOS results. *Atmospheric Chemistry and Physics*. 6. p.pp. 2549–2567.

Middlebrook, A.M., Murphy, D.M., Lee, S.H., Thomson, D.S., Prather, K.A., Wenzel, R.J., Liu, D.-Y., Phares, D.J., Rhoads, K.P., Wexler, A.S., Johnston, M.V., Jimenez, J.L., Jayne, J.T., Worsnop, D.R., Yourshaw, I., Seinfeld, J.H. & Flagan, R.C. (2003). A comparison of particle mass spectrometers during the 1999 Atlanta Supersite Project. *Journal of Geophysical Research*. 108 (D7). p.p. 8424.

Middlebrook, A.M., Murphy, D.M. & Thomson, D.S. (1998). Observations of organic material in individual marine particles at Cape Grim during the First Aerosol Characterization Experiment (ACE 1). *Journal of Geophysical Research*. 103 (D13). p.p. 16475.

Millán, M., Salvador, R., Mantilla, E. & Artnano, B. (1996). Meteorology and photochemical air pollution in southern Europe: experimental results from EC research projects. *Atmospheric Environment*. 30 (12). p.pp. 1909–1924.

Millán, M.M., Mantilla, E., Salvador, R., Carratalá, A., Sanz, M.J., Alonso, L., Gangoiti, G. & Navazo, M. (2000). Ozone cycles in the western Mediterranean basin: interpretation of monitoring data in complex coastal terrain. *Journal of Applied Meteorology*. 39. p.pp. 487–508.

Millán, M.M. & Salvador, R. (1997). Photooxidant dynamics in the Mediterranean basin in summer: results from European research projects. *Journal of Geophysical Research*. 102. p.pp. 8811–8823.

Millán, M.M., Sanz, M.J., Salvador, R. & Mantilla, E. (2002). Atmospheric dynamics and ozone cycles related to nitrogen deposition in the western Mediterranean. *Environmental Pollution*. 118 (2). p.pp. 167–186.

Minguillón, M.C., Perron, N., Querol, X., Szidat, S., Fahrni, S.M., Alastuey, a., Jimenez, J.L., Mohr, C., Ortega, a. M., Day, D. a., Lanz, V. a., Wacker, L., Reche, C., Cusack, M., Amato, F., Kiss, G., Hoffer, a., Decesari, S., Moretti, F., Hillamo, R., Teinilä, K., Seco, R., Peñuelas, J., Metzger, a., Schallhart, S., Müller, M., Hansel, a., Burkhart, J.F., Baltensperger, U. & Prévót, a. S.H. (2011). Fossil versus contemporary sources of fine elemental and organic carbonaceous particulate matter during the DAURE campaign in Northeast Spain. *Atmospheric Chemistry and Physics*. 11 (23). p.pp. 12067–12084.

Minguillón, M.C., Ripoll, a., Pérez, N., Prévôt, a. S.H., Canonaco, F., Querol, X. &

Alastuey, a. (2015). Chemical characterization of submicron regional background aerosols in the western Mediterranean using an Aerosol Chemical Speciation Monitor. *Atmospheric Chemistry and Physics*. 15 (11). p.pp. 6379–6391.

Mishra, A.K., Klingmueller, K., Fredj, E., Lelieveld, J., Rudich, Y. & Koren, I. (2014). Radiative signature of absorbing aerosol over the eastern Mediterranean basin. *Atmos. Chem. Phys.* 14 (14). p.pp. 7213–7231.

Moffet, R.C., Desyaterik, Y., Hopkins, R.J., Tivanski, A.V., Gilles, M.K., Wang, Y., Shutthanandan, V., Molina, L.T., Abraham, R.G., Johnson, K.S., Mugica, V., Molina, M.J., Laskin, A. & Prather, K.A. (2008a). Characterization of Aerosols Containing Zn, Pb, and Cl from an Industrial Region of Mexico City. *Environmental Science & Technology*. 42 (19). p.pp. 7091–7097.

Moffet, R.C., de Foy, B., Molina, L.T., Molina, M.J. & Prather, K.A. (2008b). Measurement of ambient aerosols in northern Mexico City by single particle mass spectrometry. *Atmospheric Chemistry and Physics*. 8 (16). p.pp. 4499–4516.

Moffet, R.C. & Prather, K.A. (2009). In-situ measurements of the mixing state and optical properties of soot with implications for radiative forcing estimates. *Proceedings of the National Academy of Sciences of the United States of America*. 106 (29). p.pp. 11872–7.

Moffet, R.C., Qin, X., Rebotier, T., Furutani, H. & Prather, K.A. (2008c). Chemically segregated optical and microphysical properties of ambient aerosols measured in a single-particle mass spectrometer. *Journal of Geophysical Research*. 113 (D12). p.p. D12213.

Mohiuddin, K., Strezov, V., Nelson, P.F. & Stelcer, E. (2014). Characterisation of trace metals in atmospheric particles in the vicinity of iron and steelmaking industries in Australia. *Atmospheric Environment*. 83. p.pp. 72–79.

Moldanová, J., Fridell, E., Popovicheva, O., Demirdjian, B., Tishkova, V., Faccinetto, A. & Focsa, C. (2009). Characterisation of particulate matter and gaseous emissions from a large ship diesel engine. *Atmospheric Environment*. 43 (16). p.pp. 2632–2641.

Monks, P.S., Granier, C., Fuzzi, S., Stohl, a., Williams, M.L., Akimoto, H., Amann, M., Baklanov, a., Baltensperger, U., Bey, I., Blake, N., Blake, R.S., Carslaw, K., Cooper, O.R., Dentener, F., Fowler, D., Fragkou, E., Frost, G.J., Generoso, S., Ginoux, P., Grewe, V., Guenther, a., Hansson, H.C., Henne, S., Hjorth, J., Hofzumahaus, a., Huntrieser, H., Isaksen, I.S. a., Jenkin, M.E., Kaiser, J., Kanakidou, M., Klimont, Z., Kulmala, M., Laj, P., Lawrence, M.G., Lee, J.D., Liousse, C., Maione, M., McFiggans, G., Metzger, a., Mieville, a., Moussiopoulos, N., Orlando, J.J., O'Dowd, C.D., Palmer, P.I., Parrish, D.D., Petzold, a., Platt, U., Pöschl, U., Prévôt, a. S.H., Reeves, C.E., Reimann, S., Rudich, Y., Sellegri, K., Steinbrecher, R., Simpson, D., ten Brink, H., Theloke, J., van der Werf, G.R., Vautard, R., Vestreng, V., Vlachokostas, C. & von Glasow, R. (2009). Atmospheric composition change – global and regional air quality. *Atmospheric Environment*. 43 (33). p.pp. 5268–5350.

Monn, C., Braendli, O. & Schaeppi, G. (1995). Particulate matter<10 μm (PM10) and total suspended particulates (TSP) in urban, rural and alpine air in Switzerland. *Atmospheric Environment*. 29 (19). p.pp. 2565–2573.

Morawska, L. & Zhang, J. (2002). Combustion sources of particles. 1. Health relevance and source signatures. *Chemosphere*. 49 (9). p.pp. 1045–58.

Morishita, M., Keeler, G.J., Kamal, A.S., Wagner, J.G., Harkema, J.R. & Rohr, A.C. (2011a). Identification of ambient PM2.5 sources and analysis of pollution episodes in Detroit, Michigan using highly time-resolved measurements. *Atmospheric Environment*. 45 (8). p.pp. 1627–1637.

Morishita, M., Keeler, G.J., Kamal, A.S., Wagner, J.G., Harkema, J.R. & Rohr, A.C. (2011b). Source identification of ambient PM2.5 for inhalation exposure studies in Steubenville, Ohio using highly time-resolved measurements. *Atmospheric Environment*. 45 (40). p.pp. 7688–7697.

Morrical, B.D., Balaxi, M. & Fergenson, D. (2015). The on-line analysis of aerosol-delivered pharmaceuticals via single particle aerosol mass spectrometry. *International Journal of Pharmaceutics*. p.pp. 1–7.

Moulin, C., Lambert, C.E., Dayan, U., Masson, V., Ramonet, M., Bousquet, P., Legrand, M., Balkanski, Y.J., Guelle, W., Marticorena, B., Bergametti, G. & Dulac, F. (1998). Satellite climatology of African dust transport in the Mediterranean atmosphere. *Journal of Geophysical Research*. 103 (Dll). p.p. 13137.

Mühle, J., Lueker, T.J., Su, Y., Miller, B.R., Prather, K.A. & Weiss, R.F. (2007). Trace gas and particulate emissions from the 2003 southern California wildfires. *Journal of Geophysical Research*. 112 (D3). p.p. D03307.

Müller, C., Iinuma, Y., Karstensen, J., van Pinxteren, D., Lehmann, S., Gnauk, T. & Herrmann, H. (2009). Seasonal variation of aliphatic amines in marine sub-micrometer particles at the Cape Verde islands. *Atmospheric Chemistry and Physics Discussions*. 9 (4). p.pp. 14825–14855.

Murphy, D.M., Hudson, P.K., Cziczo, D.J., Gallavardin, S., Froyd, K.D., Johnston, M.V., Middlebrook, A.M., Reinard, M.S., Thomson, D.S., Thornberry, T. & Wexler, A.S. (2007). Distribution of lead in single atmospheric particles. *Atmospheric Chemistry and Physics*. 7 (2). p.pp. 3763–3804.

Murphy, D.M. & Thomson, D.S. (1995). Laser Ionization Mass Spectroscopy of Single Aerosol Particles. *Aerosol Science and Technology*. 22 (3). p.pp. 237–249.

Murphy, D.M., Thomson, D.S. & Middlebrook, a. M. (1997). Bromine, iodine, and chlorine in single aerosol particles at Cape Grim. *Geophysical Research Letters*. 24 (24). p.p. 3197.

Murphy, S.M., Agrawal, H., Sorooshian, A., Padró, L.T., Gates, H., Hersey, S., Welch, W.A., Jung, H., Miller, J.W., Cocker, D.R., Nenes, A., Jonsson, H.H., Flagan, R.C. & Seinfeld, J.H. (2009). Comprehensive Simultaneous Shipboard and Airborne Characterization of Exhaust from a Modern Container Ship at Sea. *Environmental Science & Technology*. 43 (13). p.pp. 4626–4640.

Murray, B.J., O'Sullivan, D., Atkinson, J.D. & Webb, M.E. (2012). Ice nucleation by particles immersed in supercooled cloud droplets. *Chemical Society Reviews*. 41 (19). p.pp. 6519–54.

Myhre, G., Shindell, D., Bréon, F.-M., Collins, W., Fuglestvedt, J., Huang, J., Koch, D., Lamarque, J.-F., Lee, D., Mendoza, B., Nakajima, T., Robock, A., Stephens, G., Takemura, T. & Zhan, H. (2013). Anthropogenic and Natural Radiative Forcing. In: T. F. Stocker, D. Qin, G.-K. Plattner, M. Tignor, S. K. Allen, J. Boschung, A. Nauels, Y. Xia, V. Bex, & P. M. Midgley (eds.). *Climate Change 2013: The Physical Science Basis. Contribution of Working Group I to the Fifth Assessment Report of the Intergovernmental Panel on Climate Change*. Cambridge, United Kingdom and New York, NY, USA.: Cambridge University Press, pp. 659–740.

Nabat, P., Somot, S., Mallet, M., Chiapello, I., Morcrette, J.J., Solmon, F., Szopa, S., Dulac, F., Collins, W., Ghan, S., Horowitz, L.W., Lamarque, J.F., Lee, Y.H., Naik, V., Nagashima, T., Shindell, D. & Skeie, R. (2013). A 4-D climatology (1979-2009) of the monthly tropospheric aerosol optical depth distribution over the Mediterranean region from a comparative evaluation and blending of remote sensing and model products. *Atmospheric Measurement Techniques*. 6 (5). p.pp. 1287–1314.

Neubauer, K.R., Johnston, M.V. & Wexler, A.S. (1998). Humidity effects on the mass spectra of single aerosol particles. *Atmospheric Environment*. 32 (14-15). p.pp. 2521–2529.

Neubauer, K.R., Johnston, M.V. & Wexler, A.S. (1997). On-line analysis of aqueous aerosols by laser desorption ionization. *International Journal of Mass Spectrometry and Ion Processes*. 163. p.pp. 29–37.

Neubauer, K.R., Sum, S.T., Johnston, M.V. & Wexler, A.S. (1996). Sulfur speciation in individual aerosol particles. *Journal of Geophysical Research*. 101 (D13). p.p. 18701.

Ng, N.L., Herndon, S.C., Trimborn, A., Canagaratna, M.R., Croteau, P.L., Onasch, T.B., Sueper, D., Worsnop, D.R., Zhang, Q., Sun, Y.L. & Jayne, J.T. (2011). An Aerosol Chemical Speciation Monitor (ACSM) for Routine Monitoring of the Composition and Mass Concentrations of Ambient Aerosol. *Aerosol Science and Technology*. 45 (7). p.pp. 780–794.

Nico, P.S., Kumfer, B.M., Kennedy, I.M. & Anastasio, C. (2009). Redox Dynamics of Mixed Metal (Mn, Cr, and Fe) Ultrafine Particles. *Aerosol Science and Technology*. 43 (1). p.pp. 60–70.

Niu, J., Rasmussen, P.E., Hassan, N.M. & Vincent, R. (2010). Concentration distribution and bioaccessibility of trace elements in nano and fine urban airborne particulate matter: Influence of particle size. *Water, Air, and Soil Pollution*. 213 (1-4). p.pp. 211–225.

Noble, C.A. & Prather, K.A. (1997). Real time single particle monitoring of a relative increase in marine aerosol concentration during winter rainstorms. *Geophysical Research Letters*. 24 (22). p.p. 2753.

Nordmeyer, T. & Prather, K.A. (1994). Real-Time Measurement Capabilities Using Aerosol Time-of-Flight Mass Spectrometry. *Analytical Chemistry*. 66 (20). p.pp. 3540–3542.

O'Dowd, C.D., Facchini, M.C., Cavalli, F., Ceburnis, D., Mircea, M., Decesari, S., Fuzzi, S., Yoon, Y.J. & Putaud, J.-P. (2004). Biogenically driven organic contribution to marine aerosol. *Nature*. 431. p.pp. 676–680.

O'Dowd, C.D., Jimenez, J.L., Bahreini, R., Flagan, R.C., Seinfeld, J.H., Hämeri, K., Pirjola, L., Kulmala, M., Jennings, S.G. & Hoffmann, T. (2002). Marine aerosol formation from biogenic iodine emissions. *Nature*. 417 (6889). p.pp. 632–636.

O'Dowd, C.D., Langmann, B., Varghese, S., Scannell, C., Ceburnis, D. & Facchini, M.C. (2008). A combined organic-inorganic sea-spray source function. *Geophysical Research Letters*. 35 (1). p.pp. 1–5.

O'Dowd, C.D., Smith, M.H., Consterdine, I.E. & Lowe, J. a. (1997). Marine aerosol, sea-salt, and the marine sulphur cycle: a short review. *Atmospheric Environment*. 31 (1). p.pp. 73–80.

Oberdörster, G., Elder, A., Finkelstein, J., Frampton, M., Hopke, Ph., Peters, A., Prather,

K., Wichmann, E. & Utell, M. (2010). *Assessment of Ambient UFP Health Effects:Linking Sources to Exposure and Responses in Extrapulmonary Organs*. New York.

Oberdörster, G., Oberdörster, E. & Oberdörster, J. (2005). Nanotoxicology: An Emerging Discipline Evolving from Studies of Ultrafine Particles. *Environmental Health Perspectives*. 113 (7). p.pp. 823–839.

Ohlström, M.O., Lehtinen, K.E.J., Moisio, M. & Jokiniemi, J.K. (2000). Fine-particle emissions of energy production in Finland. *Atmospheric Environment*. 34 (22). p.pp. 3701–3711.

Orsini, D. a., Ma, Y., Sullivan, A., Sierau, B., Baumann, K. & Weber, R.J. (2003). Refinements to the particle-into-liquid sampler (PILS) for ground and airborne measurements of water soluble aerosol composition. *Atmospheric Environment*. 37 (9-10). p.pp. 1243–1259.

Osornio-Vargas, Á.R., Bonner, J.C., Alfaro-Moreno, E., Martínez, L., García-Cuellar, C., Rosales, S.P.-L., Miranda, J. & Rosas, I. (2003). Proinflammatory and Cytotoxic Effects of Mexico City Air Pollution Particulate Matter in Vitro Are Dependent on Particle Size and Composition. *Environmental Health Perspectives*. 111 (10). p.pp. 1289–1293.

Pagels, J., Dutcher, D.D.D.D., Stolzenburg, M.R.M.R., Mcmurry, P.H.P.H., Gälli, M.E.M.E. & Gross, D.S.D.S. (2013). Fine-particle emissions from solid biofuel combustion studied with single-particle mass spectrometry: Identification of markers for organics, soot, and ash components. *Journal of Geophysical Research: Atmospheres*. 118 (2). p.pp. 859–870.

Pandolfi, M., Gonzalez-Castanedo, Y., Alastuey, A., de la Rosa, J.D., Mantilla, E., Sánchez de la Campa, A., Querol, X., Pey, J., Amato, F. & Moreno, T. (2011). Source apportionment of PM10 and PM2.5 at multiple sites in the strait of Gibraltar by PMF: Impact of shipping emissions. *Environmental Science and Pollution Research*. 18. p.pp. 260–269.

Pant, P. & Harrison, R.M. (2013). Estimation of the contribution of road traffic emissions to particulate matter concentrations from field measurements: A review. *Atmospheric Environment*. 77. p.pp. 78–97.

Papadimas, C.D., Hatzianastassiou, N., Matsoukas, C., Kanakidou, M., Mihalopoulos, N. & Vardavas, I. (2012). The direct effect of aerosols on solar radiation over the broader Mediterranean basin. *Atmospheric Chemistry and Physics*. 12 (15). p.pp. 7165–7185.

Pastor, S.H., Allen, J.O., Hughes, L.S., Bhave, P., Cass, G.R. & Prather, K.A. (2003). Ambient single particle analysis in Riverside, California by aerosol time-of-flight mass spectrometry during the SCOS97-NARSTO. *Atmospheric Environment*. 37 (2). p.pp. 239–258.

Patashnick, H. & Rupprecht, E.G. (1991). Continuous PM-10 Measurements Using the Tapered Element Oscillating Microbalance. *Journal of the Air & Waste Management Association*. 41 (8). p.pp. 1079–1083.

Pateraki, S., Assimakopoulos, V.D., Bougiatioti, a., Kouvarakis, G., Mihalopoulos, N. & Vasilakos, C. (2012). Carbonaceous and ionic compositional patterns of fine particles over an urban Mediterranean area. *Science of The Total Environment*. 424. p.pp. 251–263.

Pathak, R.K., Wu, W.S. & Wang, T. (2009). Summertime PM2.5 ionic species in four major cities of China: nitrate formation in an ammonia-deficient atmosphere. *Atmospheric Chemistry and Physics*. 9 (5). p.pp. 1711–1722.

Pekney, N.J., Davidson, C.I., Bein, K.J., Wexler, A.S. & Johnston, M.V. (2006). Identification of sources of atmospheric PM at the Pittsburgh Supersite, Part I: Single particle analysis and filter-based positive matrix factorization. *Atmospheric Environment*. 40. p.pp. 411–423.

Petzold, A. & Schönlinner, M. (2004). Multi-angle absorption photometry - A new method for the measurement of aerosol light absorption and atmospheric black carbon. *Journal of Aerosol Science*. 35 (4). p.pp. 421–441.

Pey, J., Querol, X., Alastuey, a., Forastiere, F. & Stafoggia, M. (2013). African dust outbreaks over the Mediterranean Basin during 2001-2011: PM10 concentrations, phenomenology and trends, and its relation with synoptic and mesoscale meteorology. *Atmospheric Chemistry and Physics*. 13. p.pp. 1395–1410.

Pey, J., Querol, X. & Alastuey, A. (2010). Discriminating the regional and urban contributions in the North-Western Mediterranean: PM levels and composition. *Atmospheric Environment*. 44 (13). p.pp. 1587–1596.

Pey, J., Querol, X., Alastuey, A., Rodríguez, S., Putaud, J.P. & Van Dingenen, R. (2009). Source apportionment of urban fine and ultra-fine particle number concentration in a Western Mediterranean city. *Atmospheric Environment*. 43 (29). p.pp. 4407–4415.

Phares, D.J.D.J., Rhoads, K.P., Johnston, M.V. & Wexler, A.S. (2003). Size-resolved ultrafine particle composition analysis 2. Houston. *Journal of Geophysical Research*. 108 (D7). p.p. 8420.

Phares, D.J.D.J., Rhoads, K.P.K.P. & Wexler, A.S.A.S. (2002). Performance of a Single Ultrafine Particle Mass Spectrometer. *Aerosol Science and Technology*. 36 (5). p.pp. 583–592.

Phinney, L., Richard Leaitch, W., Lohmann, U., Boudries, H., Worsnop, D.R., Jayne, J.T., Toom-Sauntry, D., Wadleigh, M., Sharma, S. & Shantz, N. (2006). Characterization of the aerosol over the sub-arctic north east Pacific Ocean. *Deep Sea Research Part II: Topical Studies in Oceanography*. 53 (20-22). p.pp. 2410–2433.

Pio, C.A. a., Legrand, M., Alves, C.A., Oliveira, T., Afonso, J., Caseiro, a., Puxbaum, H., Sanchez-Ochoa, A. & Gelencsér, a. (2008). Chemical composition of atmospheric aerosols during the 2003 summer intense forest fire period. *Atmospheric Environment*. 42 (32). p.pp. 7530–7543.

Pope III, C.A., Burnett, R.T., Thun, M.J., Calle, E.E., Krewski, D., Ito, K. & Thurston, G.D. (2002). Lung Cancer, Cardiopulmonary Mortality, and Long-term Exposure to Fine Particulate Air Pollution. *Journal of American Medical Association*. 287 (9). p.pp. 1132–1141.

Pope III, C.A., Burnett, R.T., Thurston, G.D., Thun, M.J., Calle, E.E., Krewski, D.J. & Godleski, J.J. (2004a). Cardiovascular mortality and long-term exposure to particulate air pollution: epidemiological evidence of general pathophysiological pathways of disease. *Circulation*. 109 (1). p.pp. 71–7.

Pope III, C.A. & Dockery, D.W. (2006). Health effects of fine particulate air pollution: lines that connect. *Journal of the Air Waste Management Association 1995*. 56 (6). p.pp. 709 – 742.

Pope III, C.A., Hansen, M.L., Long, R.W., Nielsen, K.R., Eatough, N.L., Wilson, W.E. & Eatough, D.J. (2004b). Ambient Particulate Air Pollution, Heart Rate Variability, and Blood Markers of Inflammation in a Panel of Elderly Subjects. *Environmental Health Perspectives*. 112 (3). p.pp. 339–345.

Pöschl, U. (2005). Atmospheric aerosols: composition, transformation, climate and health effects. *Angewandte Chemie (International ed. in English)*. 44 (46). p.pp. 7520–40.

Prather, K.A., Bertram, T.H., Grassian, V.H., Deane, G.B., Stokes, M.D., DeMott, P.J., Aluwihare, L.I., Palenik, B.P., Azam, F., Seinfeld, J.H., Moffet, R.C., Molina, M.J., Cappa, C.D., Geiger, F.M., Roberts, G.C., Russell, L.M., Ault, A.P., Baltrusaitis, J., Collins, D.B., Corrigan, C.E., Cuadra-Rodriguez, L.A., Ebben, C.J., Forestieri, S.D., Guasco, T.L., Hersey, S.P., Kim, M.J., Lambert, W.F., Modini, R.L., Mui, W., Pedler, B.E., Ruppel, M.J., Ryder, O.S., Schoepp, N.G., Sullivan, R.C. & Zhao, D. (2013). Bringing the ocean into the laboratory to probe the chemical complexity of sea spray aerosol. *Proceedings of the National Academy of Sciences of the United States of America*. 110 (19). p.pp. 7550–5.

Prather, K.A., Hatch, C.D. & Grassian, V.H. (2008). Analysis of Atmospheric Aerosols. *Annual Review of Analytical Chemistry (2008)*. 1 (1). p.pp. 485–514.

Prather, K.A., Nordmeyer, T. & Salt, K. (1994). Real-time characterization of individual aerosol particles using time-of-flight mass spectrometry. *Analytical Chemistry*. 66 (9). p.pp. 1403–1407.

Prati, P., Zucchiatti, A., Lucarelli, F. & Mandò, P. a. (2000). Source apportionment near a steel plant in Genoa (Italy) by continuous aerosol sampling and PIXE analysis. *Atmospheric Environment*. 34. p.pp. 3149–3157.

Pratt, K. a., Heymsfield, A.J., Twohy, C.H., Murphy, S.M., DeMott, P.J., Hudson, J.G., Subramanian, R., Wang, Z., Seinfeld, J.H. & Prather, K.A. (2010). In Situ Chemical Characterization of Aged Biomass-Burning Aerosols Impacting Cold Wave Clouds. *Journal of the Atmospheric Sciences*. 67 (8). p.pp. 2451–2468.

Pratt, K.A., DeMott, P.J., French, J.R., Wang, Z., Westphal, D.L., Heymsfield, A.J., Twohy, C.H., Prenni, A.J. & Prather, K.A. (2009a). In situ detection of biological particles in cloud ice-crystals. *Nature Geoscience*. 2 (6). p.pp. 398–401.

Pratt, K.A., DeMott, P.J., French, J.R., Wang, Z., Westphal, D.L., Heymsfield, A.J., Twohy, C.H., Prenni, A.J. & Prather, K.A. (2009b). In situ detection of biological particles in cloud ice-crystals. *Nature Geoscience*. 2. p.pp. 398–401.

Pratt, K.A., Hatch, L.E. & Prather, K.A. (2009c). Seasonal volatility dependence of ambient particle phase amines. *Environmental Science & Technology*. 43 (14). p.pp. 5276–81.

Pratt, K.A. & Prather, K.A. (2010). Aircraft measurements of vertical profiles of aerosol mixing states. *Journal of Geophysical Research*. 115.

Pratt, K.A. & Prather, K.A. (2012). Mass spectrometry of atmospheric aerosols-Recent developments and applications. Part II: On-line mass spectrometry techniques. *Mass Spectrometry Reviews*. 31 (1). p.pp. 17–48.

Pratt, K.A. & Prather, K.A. (2009). Real-Time, Single-Particle Volatility, Size, and Chemical Composition Measurements of Aged Urban Aerosols. *Environmental Science & Technology*. 43 (21). p.pp. 8276–8282.

Qin, X., Bhave, P.V. & Prather, K.A. (2006). Comparison of two methods for obtaining quantitative mass concentrations from aerosol time-of-flight mass spectrometry

measurements. *Analytical Chemistry*. 78 (17). p.pp. 6169–78.

Qin, X. & Prather, K.A. (2006). Impact of biomass emissions on particle chemistry during the California Regional Particulate Air Quality Study. *International Journal of Mass Spectrometry*. 258 (1-3). p.pp. 142–150.

Qin, X., Pratt, K. a., Shields, L.G., Toner, S.M. & Prather, K.A. (2012). Seasonal comparisons of single-particle chemical mixing state in Riverside, CA. *Atmospheric Environment*. 59. p.pp. 587–596.

Querol, X., Alastuey, A., De La Rosa, J., Sánchez-De-La-Campa, A., Plana, F. & Ruiz, C.R. (2002). Source apportionment analysis of atmospheric particulates in an industrialised urban site in southwestern Spain. *Atmospheric Environment*. 36 (19). p.pp. 3113–3125.

Querol, X., Alastuey, A., Moreno, T., Viana, M.M., Castillo, S., Pey, J., Rodríguez, S., Artiñano, B., Salvador, P., Sánchez, M., Garcia Dos Santos, S., Herce Garraleta, M.D., Fernandez-Patier, R., Moreno-Grau, S., Negral, L., Minguillón, M.C., Monfort, E., Sanz, M.J., Palomo-Marín, R., Pinilla-Gil, E., Cuevas, E., de la Rosa, J. & Sánchez de la Campa, A. (2008). Spatial and temporal variations in airborne particulate matter (PM10 and PM2.5) across Spain 1999-2005. *Atmospheric Environment*. 42. p.pp. 3964–3979.

Querol, X., Alastuey, A., Pey, J., Cusack, M., Pérez, N., Mihalopoulos, N., Theodosi, C., Gerasopoulos, E., Kubilay, N. & Koçak, M. (2009a). Variability in regional background aerosols within the Mediterranean. *Atmospheric Chemistry and Physics*. 9. p.pp. 4575–4591.

Querol, X., Alastuey, A., Puicercus, J.A., Mantilla, E., Miro, J.V., Lopez-Soler, A., Plana, F. & Artiñano, B. (1998a). Seasonal evolution of suspended particles around a large coal-fired power station: Particulate levels and sources. *Atmospheric Environment*. 32 (11). p.pp. 1963–1978.

Querol, X., Alastuey, A., Puicercus, J.A., Mantilla, E., Ruiz, C.R., Lopez-Soler, A., Plana, F. & Juan, R. (1998b). Seasonal evolution of suspended particles around a large coal-fired power station: Chemical characterization. *Atmospheric Environment*. 32 (4). p.pp. 719–731.

Querol, X., Alastuey, A., Rodriguez, S., Plana, F., Mantilla, E. & Ruiz, C.R. (2001). Monitoring of PM10 and PM2.5 around primary particulate anthropogenic emission sources. *Atmospheric Environment*. 35 (5). p.pp. 845–858.

Querol, X., Alastuey, A., Rodríguez, S., Viana, M.M., Artíñano, B., Salvador, P., Mantilla, E., Do Santos, S.G., Patier, R.F., De La Rosa, J., De La Campa, a. S., Menéndez, M. & Gil, J.J. (2004). Levels of particulate matter in rural, urban and industrial sites in Spain. *Science of the Total Environment*. 334-335 (2004). p.pp. 359–376.

Querol, X., Pey, J., Pandolfi, M., Alastuey, a., Cusack, M., Pérez, N., Moreno, T., Viana, M., Mihalopoulos, N., Kallos, G. & Kleanthous, S. (2009b). African dust contributions to mean ambient PM10 mass-levels across the Mediterranean Basin. *Atmospheric Environment*. 43 (28). p.pp. 4266–4277.

Rabbinge, R. & Van Diepen, C. a. (2000). Changes in agriculture and land use in Europe. *European Journal of Agronomy*. 13 (2-3). p.pp. 85–99.

Ramgolam, K., Chevaillier, S., Marano, F., Baeza-Squiban, a. & Martinon, L. (2008). Proinflammatory effect of fine and ultrafine particulate matter using size-resolved

urban aerosols from Paris. *Chemosphere*. 72 (9). p.pp. 1340–1346.

Ramgolam, K., Favez, O., Cachier, H., Gaudichet, A., Marano, F., Martinon, L. & Baeza-Squiban, A. (2009). Size-partitioning of an urban aerosol to identify particle determinants involved in the proinflammatory response induced in airway epithelial cells. *Particle and Fibre Toxicology*. 6 (1). p.p. 10.

Ravindra, K., Bencs, L., Wauters, E., de Hoog, J., Deutsch, F., Roekens, E., Bleux, N., Berghmans, P. & Van Grieken, R. (2006). Seasonal and site-specific variation in vapour and aerosol phase PAHs over Flanders (Belgium) and their relation with anthropogenic activities. *Atmospheric Environment*. 40 (4). p.pp. 771–785.

Reche, C., Viana, M., Moreno, T., Querol, X., Alastuey, a., Pey, J., Pandolfi, M., Prévôt, a., Mohr, C., Richard, a., Artiñano, B., Gomez-Moreno, F.J. & Cots, N. (2011). Peculiarities in atmospheric particle number and size-resolved speciation in an urban area in the western Mediterranean: Results from the DAURE campaign. *Atmospheric Environment*. 45 (30). p.pp. 5282–5293.

Rehbein, P.J.G., Jeong, C.H., McGuire, M.L., Yao, X., Corbin, J.C. & Evans, G.J. (2011). Cloud and fog processing enhanced gas-to-particle partitioning of trimethylamine. *Environmental Science and Technology*. 45 (10). p.pp. 4346–4352.

Reid, J.S., Eck, T.F., Christopher, S.A., Koppmann, R., Dubovik, O., Eleuterio, D.P., Holben, B.N., Reid, E.A. & Zhang, J. (2005). A review of biomass burning emissions part III: intensive optical properties of biomass burning particles. *Atmospheric Chemistry and Physics*. 5 (3). p.pp. 827–849.

Reilly, T.A.P., Lazar, A.C., Gieray, R.A., Whitten, W.B., Ramsey, J.M., Reilly, P.T.A., Lazar, A.C., Gieray, R.A., Whitten, W.B. & Ramsey, J.M. (2000). The Elucidation of Charge-Transfer-Induced Matrix Effects in Environmental Aerosols Via Real-Time Aerosol Mass Spectral Analysis of Individual Airborne Particles. *Aerosol Science & Technology*. 33 (1-2). p.pp. 135–152.

Reinard, M.. & Johnston, M.. (2008). Ion formation mechanism in laser desorption ionization of individual nanoparticles. *Journal of the American Society for Mass Spectrometry*. 19 (3). p.pp. 389–99.

Reinard, M.S., Adou, K., Martini, J.M. & Johnston, M.V. (2007). Source characterization and identification by real-time single particle mass spectrometry. *Atmospheric Environment*. 41 (40). p.pp. 9397–9409.

Renard, J.-B., Dulac, F., Berthet, G., Lurton, T., Vignelle, D., Jégou, F., Tonnelier, T., Thaury, C., Jeannot, M., Couté, B., Akiki, R., Mineau, J.-L., Verdier, N., Mallet, M., Gensdarmes, F., Charpentier, P., Mesmin, S., Duverger, V., Dupont, J.-C.C., Elias, T., Crenn, V., Sciare, J., Giacomoni, J., Gobbi, M., Hamonou, E., Olafsson, H., Dagsson-Waldhauserova, P., Camy-Peyret, C., Mazel, C., Décamps, T., Piringer, M., Surcin, J., Daugeron, D., Vignelles, D., Jégou, F., Tonnelier, T., Thaury, C., Jeannot, M., Couté, B., Akiki, R., Verdier, N., Mallet, M., Gensdarmes, F., Charpentier, P., Mesmin, S., Duverger, V., Dupont, J.-C.C., Elias, T., Crenn, V., Sciare, J., Giacomoni, J., Gobbi, M., Hamonou, E., Olafsson, H., Dagsson-Waldhauserova, P., Camy-Peyret, C., Mazel, C., Décamps, T., Piringer, M., Surcin, J. & Daugeron, D. (2015). LOAC: a small aerosol optical counter/sizer for ground-based and balloon measurements of the size distribution and nature of atmospheric particles – Part 2: First results from balloon and unmanned aerial vehicle flights. *Atmos. Meas. Tech. Discuss.* 2015. p.pp. 1261–1299.

Riffault, V., Arndt, J., Marris, H., Mbengue, S., Setyan, A., Alleman, L.Y., Deboudt, K.,

Flament, P., Augustin, P., Delbarre, H. & Wenger, J. (2015). Fine and Ultrafine Particles in the Vicinity of Industrial Activities: A Review. *Critical Reviews in Environmental Science and Technology*. 45 (21). p.pp. 2305–2356.

Rijkenberg, M.J., Powell, C.F., Dall'Osto, M., Nielsdottir, M.C., Patey, M.D., Hill, P.G., Baker, A.R., Jickells, T.D., Harrison, R.M. & Achterberg, E.P. (2008). Changes in iron speciation following a Saharan dust event in the tropical North Atlantic Ocean. *Marine Chemistry*. 110 (1-2). p.pp. 56–67.

Rimetz-Planchon, J., Perdrix, E., Sobanska, S. & Brémard, C. (2008). PM10 air quality variations in an urbanized and industrialized harbor. *Atmospheric Environment*. 42 (31). p.pp. 7274–7283.

Riva, M., Healy, R.M., Flaud, P.-M., Perraudin, E., Wenger, J.C. & Villenave, E. (2015). *Gas- and Particle-phase Products from the Chlorine-initiated Oxidation of Polycyclic Aromatic Hydrocarbons (PAHs)*.

Rodríguez, S., Querol, X. & Alastuey, A. (2001). Saharan dust contributions to PM10 and TSP levels in Southern and Eastern Spain. *Atmospheric Environment*. 35. p.pp. 2433–2447.

Rodríguez, S., Querol, X., Alastuey, A. & de la Rosa, J. (2007). Atmospheric particulate matter and air quality in the Mediterranean: A review. *Environmental Chemistry Letters*. 5 (1). p.pp. 1–7.

Rodríguez, S., Querol, X., Alastuey, A. & Mantilla, E. (2002). Origin of high summer PM10 and TSP concentrations at rural sites in Eastern Spain. *Atmospheric Environment*. 36. p.pp. 3101–3112.

Rodríguez, S., Querol, X., Alastuey, A. & Plana, F. (2002). Sources and processes affecting levels and composition of atmospheric aerosol in the western Mediterranean. *Journal of Geophysical Research: Atmospheres*. 107 (24). p.pp. 1–14.

Roelofs, G.J. (2007). A GCM study of organic matter in marine aerosol and its potential contribution to cloud drop activation. *Atmospheric Chemistry and Physics Discussions*. 7. p.pp. 5675–5700.

Roger, J.C., Mallet, M., Dubuisson, P., Cachier, H., Vermote, E., Dubovik, O. & Despiau, S. (2006). A synergetic approach for estimating the local direct aerosol forcing: Application to an urban zone during the Expérience sur Site pour Contraindre les Modèles de Pollution et de Transport d'Emission (ESCOMPTE) experiment. *Journal of Geophysical Research: Atmospheres*. 111 (13). p.pp. 1–9.

Röösli, M., Theis, G., Künzli, N., Staehelin, J., Mathys, P., Oglesby, L., Camenzind, M. & Braun-Fahrländer, C. (2001). Temporal and spatial variation of the chemical composition of PM10 at urban and rural sites in the Basel area, Switzerland. *Atmospheric Environment*. 35 (21). p.pp. 3701–3713.

Roscoe, H.K., Jones, A.E., Brough, N., Weller, R., Saiz-Lopez, A., Mahajan, A.S., Schoenhardt, A., Burrows, J.P. & Fleming, Z.L. (2015). Particles and iodine compounds in coastal Antarctica. *Journal of Geophysical Research: Atmospheres*. (June). p.p. n/a–n/a.

Roukos, J., Riffault, V., Locoge, N. & Plaisance, H. (2009). VOC in an urban and industrial harbor on the French North Sea coast during two contrasted meteorological situations. *Environmental Pollution*. 157 (11). p.pp. 3001–3009.

Royer, P., Raut, J.C., Ajello, G., Berthier, S. & Chazette, P. (2010). Synergy between

CALIOP and MODIS instruments for aerosol monitoring: Application to the Po Valley. *Atmospheric Measurement Techniques*. 3 (4). p.pp. 893–907.

Saffari, A., Daher, N., Shafer, M.M., Schauer, J.J. & Sioutas, C. (2013). Seasonal and spatial variation of trace elements and metals in quasi-ultrafine (PM0.25) particles in the Los Angeles metropolitan area and characterization of their sources. *Environmental Pollution*. 181. p.pp. 14–23.

Salvador, P., Alonso-Pérez, S., Pey, J., Artíñano, B., de Bustos, J.J.J., Alastuey, A. & Querol, X. (2014). African dust outbreaks over the western Mediterranean Basin: 11-year characterization of atmospheric circulation patterns and dust source areas. *Atmospheric Chemistry and Physics*. 14 (13). p.pp. 6759–6775.

Salvador, P., Artíñano, B., Molero, F., Viana, M., Pey, J., Alastuey, A. & Querol, X. (2013). African dust contribution to ambient aerosol levels across central Spain: Characterization of long-range transport episodes of desert dust. *Atmospheric Research*. 127. p.pp. 117–129.

Salvador, R., Calbó, J. & Millán, M.M. (1999). Horizontal grid size selection and its influence on mesoscale model simulations. *Journal of Applied Meteorology*. 38. p.pp. 1311–1329.

Salvi, S. & Holgate, S.T. (1999). Mechanisms of particulate matter toxicity. *Clinical and Experimental Allergy*. 29. p.pp. 1187–1194.

Samet, J.M., Rappold, A., Graff, D., Cascio, W.E., Berntsen, J.H., Huang, Y.-C.T., Herbst, M., Bassett, M., Montilla, T., Hazucha, M.J., Bromberg, P. a. & Devlin, R.B. (2009). Concentrated Ambient Ultrafine Particle Exposure Induces Cardiac Changes in Young Healthy Volunteers. *American Journal of Respiratory and Critical Care Medicine*. 179 (11). p.pp. 1034–1042.

Sánchez de la Campa, a. M., de la Rosa, J., González-Castanedo, Y., Fernández-Camacho, R., Alastuey, a., Querol, X., Stein, a. F., Ramos, J.L., Rodríguez, S., Orellana, I.G. & Nava, S. (2011). Levels and chemical composition of PM in a city near a large Cu-smelter in Spain. *Journal of Environmental Monitoring*. 13 (5). p.p. 1276.

Sánchez de la Campa, A.M., de la Rosa, J.D., González-Castanedo, Y., Fernández-Camacho, R., Alastuey, A., Querol, X. & Pio, C. (2010). High concentrations of heavy metals in PM from ceramic factories of Southern Spain. *Atmospheric Research*. 96 (4). p.pp. 633–644.

Sánchez-Soberón, F., Rovira, J., Mari, M., Sierra, J., Nadal, M., Domingo, J.L. & Schuhmacher, M. (2015). Main components and human health risks assessment of PM10, PM2.5, and PM1 in two areas influenced by cement plants. *Atmospheric Environment*. 120. p.pp. 109–116.

Sanderson, P., Delgado-Saborit, J.M. & Harrison, R.M. (2014). A review of chemical and physical characterisation of atmospheric metallic nanoparticles. *Atmospheric Environment*. 94. p.pp. 353–365.

Sandroni, V. & Migon, C. (1997). Significance of trace metal medium-range transport in the western Mediterranean. *Science of the Total Environment*. 196. p.pp. 83–89.

Di Sarra, a., Cacciani, M., Chamard, P., Cornwall, C., DeLuisi, J.J., Di Iorio, T., Disterhoft, P., Fiocco, G., Fuà, D. & Monteleone, F. (2002). Effects of desert dust and ozone on the ultraviolet irradiance at the Mediterranean island of Lampedusa during PAUR II. *Journal of Geophysical Research: Atmospheres*. 107 (18). p.pp. 1–

14.

di Sarra, A., Di Biagio, C., Meloni, D., Monteleone, F., Pace, G., Pugnaghi, S. & Sferlazzo, D. (2011). Shortwave and longwave radiative effects of the intense Saharan dust event of 25-26 March 2010 at Lampedusa (Mediterranean Sea). *Journal of Geophysical Research: Atmospheres*. 116 (23). p.pp. 1–11.

di Sarra, A., Di Iorio, T., Cacciani, M., Fiocco, G. & Fuà, D. (2001). Saharan dust profiles measured by lidar at Lampedusa. *Journal of Geophysical Research*. 106 (D10). p.p. 10335.

Sartelet, K.N., Couvidat, F., Seigneur, C. & Roustan, Y. (2012). Impact of biogenic emissions on air quality over Europe and North America. *Atmospheric Environment*. 53 (July 1995). p.pp. 131–141.

Sauvage, S., Plaisance, H., Locoge, N., Wroblewski, a., Coddeville, P. & Galloo, J.C. (2009). Long term measurement and source apportionment of non-methane hydrocarbons in three French rural areas. *Atmospheric Environment*. 43 (15). p.pp. 2430–2441.

Saxe, H. & Larsen, T. (2004). Air pollution from ships in three Danish ports. *Atmospheric Environment*. 38. p.pp. 4057–4067.

Schaumann, F., Borm, P.J. a., Herbrich, A., Knoch, J., Pitz, M., Schins, R.P.F., Luettig, B., Hohlfeld, J.M., Heinrich, J. & Krug, N. (2004). Metal-rich Ambient Particles (Particulate Matter $_{2.5}$) Cause Airway Inflammation in Healthy Subjects. *American Journal of Respiratory and Critical Care Medicine*. 170 (8). p.pp. 898–903.

Scheeren, H.A., Lelieveld, J., Roelofs, G.J., Williams, J., Fischer, H., de Reus, M., de Gouw, J.A., Warneke, C., Holzinger, R., Schlager, H., Klüpfel, T., Bolder, M., van der Veen, C. & Lawrence, M. (2003). The impact of monsoon outflow from India and Southeast Asia in the upper troposphere over the eastern Mediterranean. *Atmos. Chem. Phys.* 3 (5). p.pp. 1589–1608.

Schembari, C., Bove, M.C., Cuccia, E., Cavalli, F., Hjorth, J., Massabò, D., Nava, S., Udisti, R. & Prati, P. (2014). Source apportionment of PM10 in the Western Mediterranean based on observations from a cruise ship. *Atmospheric Environment*. 98. p.pp. 510–518.

Schembari, C., Cavalli, F., Cuccia, E., Hjorth, J., Calzolai, G., Pérez, N., Pey, J., Prati, P. & Raes, F. (2012). Impact of a European directive on ship emissions on air quality in Mediterranean harbours. *Atmospheric Environment*. 61. p.pp. 661–669.

Schumann, U. & Huntrieser, H. (2007). The global lightning-induced nitrogen oxides source. *Atmospheric Chemistry and Physics Discussions*. 7 (1). p.pp. 2623–2818.

Schwartz, J. & Neas, L.M. (2000). Fine particles are more strongly associated than coarse particles with acute respiratory health effects in schoolchildren. *Epidemiology (Cambridge, Mass.)*. 11 (1). p.pp. 6–10.

Schwarze, P.E., Ovrevik, J., Lag, M., Refsnes, M., Nafstad, P., Hetland, R.B. & Dybing, E. (2006). Particulate matter properties and health effects: consistency of epidemiological and toxicological studies. *Human & Experimental Toxicology*. 25 (10). p.pp. 559–579.

Sciare, J., Cachier, H., Oikonomou, K., Ausset, P., Sarda-Estève, R. & Mihalopoulos, N. (2003). Characterization of carbonaceous aerosols during the MINOS campaign in Crete, July–August 2001: a multi-analytical approach. *Atmos. Chem. Phys.* 3 (5). p.pp. 1743–1757.

Sciare, J., Oikonomou, K., Favez, O., Markaki, Z., Liakakou, E., Cachier, H. & Mihalopoulos, N. (2008). Long-term measurements of carbonaceous aerosols in the eastern Mediterranean: evidence of long-range transport of biomass burning. *Atmospheric Chemistry and Physics*. 8. p.pp. 5551–5563.

See, S.W., Wang, Y.H. & Balasubramanian, R. (2007). Contrasting reactive oxygen species and transition metal concentrations in combustion aerosols. *Environmental Research*. 103 (3). p.pp. 317–324.

Seinfeld, J.H. & Pandis, S.N. (2006). *Atmospheric Chemistry and Physics: From Air Pollution to Climate Change*. Wiley.

Sellegri, K., Gourdeau, J., Putaud, J.-P. & Despiau, S. (2001). Chemical composition of marine aerosol in a Mediterranean coastal zone during the FETCH experiment. *Journal of Geophysical Research*. 106 (D11). p.p. 12023.

Service, N.M. & Prezerakos, N.G. (1984). *Does the Extension of the Azores ' Anticyclone Towards the Balkans Really Exist ?* 227. p.pp. 217–227.

Shields, L.G. (2008). *Single Particle Characterization, Source Apportionment, and Aging Effects of Ambient Aerosols in Southern California*. ProQuest.

Shields, L.G., Qin, X., Toner, S.M. & Prather, K.A. (2008). Detection of Ambient Ultrafine Aerosols by Single Particle Techniques During the SOAR 2005 Campaign. *Aerosol Science and Technology*. 42 (8). p.pp. 674–684.

Shields, L.G., Suess, D.T. & Prather, K.A. (2007). Determination of single particle mass spectral signatures from heavy-duty diesel vehicle emissions for PM2.5 source apportionment. *Atmospheric Environment*. 41 (18). p.pp. 3841–3852.

Shinyashiki, M., Eiguren-Fernandez, A., Schmitz, D. a., Di Stefano, E., Li, N., Linak, W.P., Cho, S.H., Froines, J.R. & Cho, A.K. (2009). Electrophilic and redox properties of diesel exhaust particles. *Environmental Research*. 109 (3). p.pp. 239–244.

Sicard, M., Barragan, R., Dulac, F., Alados-Arboledas, L. & Mallet, M. (2016). Aerosol optical, microphysical and radiative properties at three regional background insular sites in the western Mediterranean Basin. *Atmos. Chem. Phys. Discuss.* 2016. p.pp. 1–66.

Sicard, P., De Marco, A., Troussier, F., Renou, C., Vas, N. & Paoletti, E. (2013). Decrease in surface ozone concentrations at Mediterranean remote sites and increase in the cities. *Atmospheric Environment*. 79. p.pp. 705–715.

Sillanpää, M., Hillamo, R., Saarikoski, S., Frey, A., Pennanen, A., Makkonen, U., Spolnik, Z., Van Grieken, R., Braniš, M. & Brunekreef, B. (2006). Chemical composition and mass closure of particulate matter at six urban sites in Europe. *Atmospheric Environment*. 40. p.pp. 212–223.

Silva, P.J., Carlin, R.A. & Prather, K.A. (2000). Single particle analysis of suspended soil dust from Southern California. *Atmospheric Environment*. 34 (11). p.pp. 1811–1820.

Silva, P.J., Liu, D.-Y.D.-Y., Noble, C.A. & Prather, K.A. (1999). Size and Chemical Characterization of Individual Particles Resulting from Biomass Burning of Local Southern California Species. *Environmental Science & Technology*. 33 (18). p.pp. 3068–3076.

Silva, P.J. & Prather, K.A. (2000). Interpretation of mass spectra from organic compounds in aerosol time-of-flight mass spectrometry. *Analytical Chemistry*. 72 (15). p.pp.

3553–62.

Silva, P.J. & Prather, K.A. (1997). On-Line Characterization of Individual Particles from Automobile Emissions. *Environmental Science & Technology*. 31 (11). p.pp. 3074–3080.

Sinha, M.P., Platz, R.M., Vilker, V.L. & Friedlander, S.K. (1984). Analysis of individual biological particles by mass spectrometry. *International Journal of Mass Spectrometry and Ion Processes*. 57 (1). p.pp. 125–133.

Smith, S., Ward, M., Lin, R., Brydson, R., Dall'Osto, M. & Harrison, R.M. (2012). Comparative study of single particle characterisation by Transmission Electron Microscopy and time-of-flight aerosol mass spectrometry in the London atmosphere. *Atmospheric Environment*. 62. p.pp. 400–407.

Snyder, D.C., Schauer, J.J., Gross, D.S. & Turner, J.R. (2009). Estimating the contribution of point sources to atmospheric metals using single-particle mass spectrometry. *Atmospheric Environment*. 43 (26). p.pp. 4033–4042.

Sodeman, D.A., Toner, S.M. & Prather, K.A. (2005). Determination of single particle mass spectral signatures from light-duty vehicle emissions. *Environmental Science & Technology*. 39 (12). p.pp. 4569–80.

Song, X.H., Hopke, P.K., Fergenson, D.P. & Prather, K.A. (1999). Classification of Single Particles Analyzed by ATOFMS Using an Artificial Neural Network, ART-2A. *Analytical Chemistry*. 71 (4). p.pp. 860–865.

Song, X.H., Klaas, N., Faber, M., Hopke, P.K., Suess, D.T., Prather, K.A., Schauer, J.J. & Cass, G.R. (2001). Source apportionment of gasoline and diesel by multivariate calibration based on single particle mass spectral data. *Analytica Chimica Acta*. 446. p.pp. 329–343.

Soriano, C., Baldasano, J.M., Buttler, W.T. & Moore, K.R. (2001). Circulatory patterns of air pollutants within the Barcelona air basin in a summertime situation: lidar and numerical approaches. *Boundary-Layer Meteorology*. 98. p.pp. 33–55.

Sorooshian, A., Padro, L.T., Nenes, A., Feingold, G., McComiskey, A., Hersey, S.P., Gates, H., Jonsson, H.H., Miller, S.D., Stephens, G.L., Flagan, R.C. & Seinfeld, J.H. (2009). On the link between ocean biota emissions, aerosol, and maritime clouds: Airborne, ground, and satellite measurements off the coast of California. *Global Biogeochemical Cycles*. 23. p.pp. 1–15.

Spencer, M. & Prather, K.A. (2006). Using ATOFMS to Determine OC/EC Mass Fractions in Particles. *Aerosol Science & Technology*. 40 (8). p.pp. 585–594.

Spencer, M.., Holecek, J.C., Corrigan, C.E., Ramanathan, V. & Prather, K.A. (2008). Size-resolved chemical composition of aerosol particles during a monsoonal transition period over the Indian Ocean. *Journal of Geophysical Research*. 113 (D16). p.pp. 1–14.

Spencer, M.T., Shields, L.G., Sodeman, D.A., Toner, S.M. & Prather, K.A. (2006). Comparison of oil and fuel particle chemical signatures with particle emissions from heavy and light duty vehicles. *Atmospheric Environment*. 40 (27). p.pp. 5224–5235.

Steele, P.T., Srivastava, A., Pitesky, M.E., Fergenson, D.P., Tobias, H.J., Gard, E.E. & Frank, M. (2005). Desorption/ionization fluence thresholds and improved mass spectral consistency measured using a flattop laser profile in the bioaerosol mass spectrometry of single Bacillus endospores. *Analytical Chemistry*. 77 (22). p.pp. 7448–7454.

Steele, P.T., Tobias, H.J., Fergenson, D.P., Pitesky, M.E., Horn, J.M., Czerwieniec, G. a, Russell, S.C., Lebrilla, C.B., Gard, E.E. & Frank, M. (2003). Laser power dependence of mass spectral signatures from individual bacterial spores in bioaerosol mass spectrometry. *Analytical Chemistry*. 75 (20). p.pp. 5480–5487.

Sternbeck, J., Sjödin, Å. & Andréasson, K. (2002). Metal emissions from road traffic and the influence of resuspension - Results from two tunnel studies. *Atmospheric Environment*. 36 (30). p.pp. 4735–4744.

Stevens, R.G., Pierce, J.R., Brock, C.A., Reed, M.K., Crawford, J.H., Holloway, J.S., Ryerson, T.B., Huey, L.G. & Nowak, J.B. (2012). Nucleation and growth of sulfate aerosol in coal-fired power plant plumes: sensitivity to background aerosol and meteorology. *Atmospheric Chemistry and Physics*. 12 (1). p.pp. 189–206.

Stier, P., Seinfeld, J.H., Kinne, S. & Boucher, O. (2007). Aerosol absorption and radiative forcing. *Atmospheric Chemistry and Physics*. 7. p.pp. 5237–5261.

Stolzenburg, M., Kreisberg, N. & Hering, S. (1998). Atmospheric Size Distributions Measured by Differential Mobility Optical Particle Size Spectrometry. *Aerosol Science and Technology*. 29 (5). p.pp. 402–418.

Straif, K., Cohen, A. & Samet, J. (2013). *Air pollution and cancer*. Lyon, France.

Strawbridge, K.B. (2006). Scanning lidar: a means of characterizing the Noranda-Horne smelter plume. *Geochemistry-Exploration Environment Analysis*. 6. p.pp. 121–129.

Su, Y., Sipin, M., Spencer, M., Qin, X., Moffet, R., Shields, L., Prather, K.A., Venkatachari, P., Jeong, C.-H., Kim, E., Hopke, P., Gelein, R., Utell, M., Oberdörster, G., Berntsen, J., Devlin, R. & Chen, L. (2006). Real-Time Characterization of the Composition of Individual Particles Emitted From Ultrafine Particle Concentrators. *Aerosol Science and Technology*. 40 (6). p.pp. 437–455.

Su, Y., Sipin, M.F., Furutani, H. & Prather, K.A. (2004). Development and Characterization of an Aerosol Time-of-Flight Mass Spectrometer with Increased Detection Efficiency. *Analytical Chemistry*. 76 (3). p.pp. 712–719.

Su, Y., Sipin, M.F., Prather, K.A., Gelein, R.M., Lunts, A. & Oberdorster, G. (2005). ATOFMS Characterization of Individual Model Aerosol Particles Used for Exposure Studies. *Aerosol Science and Technology*. 39. p.pp. 400 – 407.

Suess, D.T. & Prather, K.A. (2002). Reproducibility of Single Particle Chemical Composition during a Heavy Duty Diesel Truck Dynamometer Study. *Aerosol Science and Technology*. 1141. p.pp. 1139–1141.

Sullivan, R.C., Guazzotti, S.A., Sodeman, D.A. & Prather, K.A. (2007). Direct observations of the atmospheric processing of Asian mineral dust. *Atmospheric Chemistry and Physics*. 7 (5). p.pp. 1213–1236.

Sullivan, R.C. & Prather, K.A. (2007). Investigations of the diurnal cycle and mixing state of oxalic acid in individual particles in Asian aerosol outflow. *Environmental Science & Technology*. 41 (23). p.pp. 8062–9.

Sullivan, R.C. & Prather, K.A. (2005). Recent Advances in Our Understanding of Atmospheric Chemistry and Climate Made Possible by On-Line Aerosol Analysis Instrumentation. *Analytical Chemistry*. 77. p.pp. 3861 – 3886.

Tafuro, A.M., Kinne, S., De Tomasi, F. & Perrone, M.R. (2007). Annual cycle of aerosol direct radiative effect over southeast Italy and sensitivity studies. *Journal of Geophysical Research: Atmospheres*. 112 (20). p.pp. 1–13.

Taiwo, A.M., Beddows, D.C.S., Calzolai, G., Harrison, R.M., Lucarelli, F., Nava, S., Shi, Z., Valli, G. & Vecchi, R. (2014a). Receptor modelling of airborne particulate matter in the vicinity of a major steelworks site. *Science of The Total Environment*. 490. p.pp. 488–500.

Taiwo, A.M., Harrison, R.M., Beddows, D.C.S. & Shi, Z. (2014b). Source apportionment of single particles sampled at the industrially polluted town of Port Talbot, United Kingdom by ATOFMS. *Atmospheric Environment*. 97 (September 2015). p.pp. 155–165.

Tan, P. V., Evans, G.J., Tsai, J., Owega, S., Fila, M.S., Malpica, O. & Brook, J.R. (2002a). On-line Analysis of Urban Particulate Matter Focusing on Elevated Wintertime Aerosol Concentrations. *Environmental Science & Technology*. 36 (16). p.pp. 3512–3518.

Tan, P. V., Fila, M.S., Evans, G.J. & Jervis, R.E. (2002b). Aerosol Laser Ablation Mass Spectrometry of Suspended Powders from PM Sources and Its Implications to Receptor Modeling. *Journal of the Air & Waste Management Association*. 52 (1). p.pp. 27–40.

Tao, F., Gonzalez-Flecha, B. & Kobzik, L. (2003). Reactive oxygen species in pulmonary inflammation by ambient particulates. *Free Radical Biology and Medicine*. 35 (4). p.pp. 327–340.

Tao, S., Wang, X., Chen, H., Yang, X., Li, M., Li, L. & Zhou, Z. (2011). Single particle analysis of ambient aerosols in Shanghai during the World Exposition, 2010: two case studies. *Frontiers of Environmental Science & Engineering in China*. 5 (3). p.pp. 391–401.

Thomassen, Y., Koch, W., Dunkhorst, W., Ellingsen, D.G., Skaugset, N.-P., Jordbekken, L., Arne Drabløs, P. & Weinbruch, S. (2006). Ultrafine particles at workplaces of a primary aluminium smelter. *J. Environ. Monit.* 8 (1). p.pp. 127–133.

Thomson, D., Schein, M. & Murphy, D. (2000). Particle Analysis by Laser Mass Spectrometry WB-57F Instrument Overview. *Aerosol Science and Technology*. 33 (1). p.pp. 153–169.

Thomson, D.S., Middlebrook, A.M. & Murphy, D.M. (1997). Thresholds for Laser-Induced Ion Formation from Aerosols in a Vacuum Using Ultraviolet and Vacuum-Ultraviolet Laser Wavelengths. *Aerosol Science and Technology*. 26 (February 2015). p.pp. 544–559.

Tobias, H.J., Schafer, M.P., Pitesky, M., Fergenson, P., Horn, J., Frank, M., Eric, E., Fergenson, D.P. & Gard, E.E. (2005). *Bioaerosol Mass Spectrometry for Rapid Detection of Individual Airborne Mycobacterium tuberculosis H37Ra Particles Bioaerosol Mass Spectrometry for Rapid Detection of Individual Airborne Mycobacterium tuberculosis H37Ra Particles*. 71 (10). p.pp. 6086–6095.

Toner, S.M., Shields, L.G., Sodeman, D.A. & Prather, K.A. (2008). Using mass spectral source signatures to apportion exhaust particles from gasoline and diesel powered vehicles in a freeway study using UF-ATOFMS. *Atmospheric Environment*. 42 (3). p.pp. 568–581.

Toner, S.M., Sodeman, D.A. & Prather, K.A. (2006). Single Particle Characterization of Ultrafine and Accumulation Mode Particles from Heavy Duty Diesel Vehicles Using Aerosol Time-of-Flight Mass Spectrometry. *Environmental Science & Technology*. 40 (12). p.pp. 3912–3921.

Tsai, J., Lin, K., Chen, C., Ding, J., Choa, C. & Chiang, H. (2007). Chemical constituents in particulate emissions from an integrated iron and steel facility. *Journal of Hazardous Materials*. 147 (1-2). p.pp. 111–119.

TSI (2007). *Series 3800 Aerosol Time-of-Flight Mass Spectrometers (ATOFMS) with Aerodynamic Focusing Lens*.

Turnbull, A.B. & Harrison, R.M. (2000). Major component contributions to PM10 composition in the UK atmosphere. *Atmospheric Environment*. 34 (19). p.pp. 3129–3137.

Tyrlis, E. & Lelieveld, J. (2013). Climatology and Dynamics of the Summer Etesian Winds over the Eastern Mediterranean*. *Journal of the Atmospheric Sciences*. 70 (11). p.pp. 3374–3396.

UNEP/MAP (2015). *United Nations Environment Programme - Mediterranean Action Plan*. [Online]. 2015. Available from: http://www.unepmap.org/index.php?module=content2&catid=001003002. [Accessed: 20 January 2015].

United Nations Environment Programme/Mediterranean Action Plan (UNEP/MAP) (2012). *State of the Marine and Coastal Mediterranean*. Barcelona Convention, Athens.

Utsunomiya, S., Jensen, K., Keeler, G.J. & Ewing, R.C. (2004). Direct identification of trace metals in fine and ultrafine particles in the Detroit urban atmosphere. *Environmental Science & Technology*. 38 (8). p.pp. 2289–97.

Vega, E., Reyes, E., Ruiz, H., García, J., Sánchez, G., Martínez-Villa, G., González, U., Chow, J.C. & Watson, J.G. (2004). Analysis of $PM_{2.5}$ and PM_{10} in the Atmosphere of Mexico City during 2000-2002. *Journal of the Air & Waste Management Association*. 54 (7). p.pp. 786–798.

Velchev, K., Cavalli, F., Hjorth, J., Marmer, E., Vignati, E., Dentener, F. & Raes, F. (2011). Ozone over the Western Mediterranean Sea – results from two years of shipborne measurements. *Atmospheric Chemistry and Physics*. 11 (2). p.pp. 675–688.

Viana, M., Amato, F., Alastuey, A., Querol, X., Moreno, T., Dos Santos, S.G., Herce, M.D. & Fernández-Patier, R. (2009). Chemical tracers of particulate emissions from commercial shipping. *Environmental Science and Technology*. 43 (19). p.pp. 7472–7477.

Viana, M., Salvador, P., Artíñano, B., Querol, X., Alastuey, A., Pey, J., Latz, A.J., Cabañas, M., Moreno, T., García Dos Santos, S., Herce, M.D., Diez Hernández, P., Romero García, D. & Fernández-Patier, R. (2010). Assessing the performance of methods to detect and quantify African dust in airborne particulates. *Environmental Science and Technology*. 44 (23). p.pp. 8814–8820.

Vincent, J., Laurent, B., Losno, R., Bon Nguyen, E., Roullet, P., Sauvage, S., Chevaillier, S., Coddeville, P., Ouboulmane, N., di Sarra, A.G., Tovar-Sánchez, A., Sferlazzo, D., Massanet, A., Triquet, S., Morales Baquero, R., Fornier, M., Coursier, C., Desboeufs, K., Dulac, F. & Bergametti, G. (2015). Variability of mineral dust deposition in the western Mediterranean basin and South-East of France. *Atmos. Chem. Phys. Discuss.* 2015 (23). p.pp. 34673–34717.

Voutsa, D. & Samara, C. (2002). Labile and bioaccessible fractions of heavy metals in the airborne particulate matter from urban and industrial areas. *Atmospheric*

Environment. 36 (22). p.pp. 3583–3590.

Voutsa, D., Samara, C., Kouimtzis, T. & Ochsenkühn, K. (2002). Elemental composition of airborne particulate matter in the multi-impacted urban area of Thessaloniki, Greece. *Atmospheric Environment*. 36 (28). p.pp. 4453–4462.

Vu, T. V., Delgado-Saborit, J.M. & Harrison, R.M. (2015). Review: Particle number size distributions from seven major sources and implications for source apportionment studies. *Atmospheric Environment*. 122. p.pp. 114–132.

Wang, X. & McMurry, P.H. (2006). A Design Tool for Aerodynamic Lens Systems. *Aerosol Science and Technology*. 40 (5). p.pp. 320–334.

Wang, X., Williams, B.J., Wang, X., Tang, Y., Huang, Y., Kong, L., Yang, X. & Biswas, P. (2013). Characterization of organic aerosol produced during pulverized coal combustion in a drop tube furnace. *Atmospheric Chemistry and Physics*. 13 (21). p.pp. 10919–10932.

Wang, X., Ye, X., Chen, H., Chen, J., Yang, X. & Gross, D.S. (2014). Online hygroscopicity and chemical measurement of urban aerosol in Shanghai, China. *Atmospheric Environment*. 95. p.pp. 318–326.

Wang, X., Zhang, Y., Chen, H., Yang, X., Chen, J. & Geng, F. (2009). Particulate Nitrate Formation in a Highly Polluted Urban Area: A Case Study by Single-Particle Mass Spectrometry in Shanghai. *Environmental Science & Technology*. 43 (9). p.pp. 3061–3066.

Watson, J.G., Chow, J.C. & Chen, L.A. (2005). Summary of Organic and Elemental Carbon/Black Carbon Analysis Methods and Intercomparisons. *Aerosol and Air Quality Research*. 5 (1). p.pp. 65–102.

Wei, S., Huang, B., Liu, M., Bi, X., Ren, Z., Sheng, G. & Fu, J. (2012). Characterization of PM2.5-bound nitrated and oxygenated PAHs in two industrial sites of South China. *Atmospheric Research*. 109-110. p.pp. 76–83.

Weitkamp, E. a., Lipsky, E.M., Pancras, P.J., Ondov, J.M., Polidori, A., Turpin, B.J. & Robinson, A.L. (2005). Fine particle emission profile for a large coke production facility based on highly time-resolved fence line measurements. *Atmospheric Environment*. 39 (36). p.pp. 6719–6733.

Wenzel, R.J. (2003). Aerosol time-of-flight mass spectrometry during the Atlanta Supersite Experiment: 2. Scaling procedures. *Journal of Geophysical Research*. 108 (D7). p.p. 8427.

Wenzel, R.J. & Prather, K.A. (2004). Improvements in ion signal reproducibility obtained using a homogeneous laser beam for on-line laser desorption/ionization of single particles. *Rapid Communications in Mass Spectrometry*. 18 (13). p.pp. 1525–1533.

Wexler, A.S. & Seinfeld, J.H. (1990). The Distribution of Ammonium-Salts Among a Size and Composition Dispersed Aerosol. *Atmospheric Environment*. 24A (5). p.pp. 1231–1246.

Whiteaker, J.R. & Prather, K.A. (2003a). Detection of Pesticide Residues on Individual Particles. *Analytical Chemistry*. 75 (1). p.pp. 49–56.

Whiteaker, J.R. & Prather, K.A. (2003b). Hydroxymethanesulfonate as a tracer for fog processing of individual aerosol particles. *Atmospheric Environment*. 37 (8). p.pp. 1033–1043.

Whiteaker, J.R., Suess, D.T. & Prather, K.A. (2002). Effects of meteorological conditions

on aerosol composition and mixing state in Bakersfield, CA. *Environmental Science & Technology*. 36 (11). p.pp. 2345–53.

WHO (2006). *Air Quality Guidelines - Global Update 2005*.

Wu, Y.-S., Fang, G.-C., Lee, W.-J., Lee, J.-F., Chang, C.-C. & Lee, C.-Z. (2007). A review of atmospheric fine particulate matter and its associated trace metal pollutants in Asian countries during the period 1995–2005. *Journal of Hazardous Materials*. 143 (1-2). p.pp. 511–515.

Wyslouzil, B.E., Seinfeld, J.H., Flagan, R.C. & Okuyama, K. (1991a). Binary nucleation in acid–water systems. I. Methanesulfonic acid–water. *The Journal of Chemical Physics*. 94 (10). p.p. 6827.

Wyslouzil, B.E., Seinfeld, J.H., Flagan, R.C. & Okuyama, K. (1991b). Binary nucleation in acid–water systems. II. Sulfuric acid–water and a comparison with methanesulfonic acid–water. *The Journal of Chemical Physics*. 94 (10). p.p. 6842.

Yang, F., Chen, H., Du, J., Yang, X., Gao, S., Chen, J. & Geng, F. (2012). Evolution of the mixing state of fine aerosols during haze events in Shanghai. *Atmospheric Research*. 104-105. p.pp. 193–201.

Yang, F., Chen, H., Wang, X., Yang, X., Du, J. & Chen, J. (2009). Single particle mass spectrometry of oxalic acid in ambient aerosols in Shanghai: Mixing state and formation mechanism. *Atmospheric Environment*. 43 (25). p.pp. 3876–3882.

Yang, H.H., Lai, S.O., Hsieh, L.T., Hsueh, H.J. & Chi, T.W. (2002). Profiles of PAH emission from steel and iron industries. *Chemosphere*. 48 (10). p.pp. 1061–1074.

Yao, X., Fang, M. & Chan, C.K. (2002). Size distributions and formation of dicarboxylic acids in atmospheric particles. *Atmospheric Environment*. 36 (13). p.pp. 2099–2107.

Yao, X., Rehbein, P.J.G., Lee, C.J., Evans, G.J., Corbin, J. & Jeong, C.-H. (2011). A study on the extent of neutralization of sulphate aerosol through laboratory and field experiments using an ATOFMS and a GPIC. *Atmospheric Environment*. 45 (34). p.pp. 6251–6256.

Yu, J.Z., Huang, X.-F., Xu, J. & Hu, M. (2005). When aerosol sulfate goes up, so does oxalate: implication for the formation mechanisms of oxalate. *Environmental science & technology*. 39 (1). p.pp. 128–133.

Yuan, T., Remer, L. a., Pickering, K.E. & Yu, H. (2011). Observational evidence of aerosol enhancement of lightning activity and convective invigoration. *Geophysical Research Letters*. 38 (4). p.pp. 1–5.

Zauscher, M.D., Moore, M.J.K., Lewis, G.S., Hering, S.V. & Prather, K.A. (2011). Approach for Measuring the Chemistry of Individual Particles in the Size Range Critical for Cloud Formation. *Analytical Chemistry*. 83. p.pp. 2271–2278.

Zelenyuk, A., Juan, Y., Chen, S., Zaveri, R.A. & Imre, D. (2008). 'Depth-profiling' and quantitative characterization of the size, composition, shape, density, and morphology of fine particles with SPLAT, a single-particle mass spectrometer. *Journal of Physical Chemistry A*. 112. p.pp. 669–671.

Zhai, J., Wang, X., Li, J., Xu, T., Chen, H., Yang, X. & Chen, J. (2015). Thermal desorption single particle mass spectrometry of ambient aerosol in Shanghai. *Atmospheric Environment*. p.pp. 1–8.

Zhang, F., Zhao, J., Chen, J., Xu, Y. & Xu, L. (2011a). Pollution characteristics of organic and elemental carbon in PM2.5 in Xiamen, China. *Journal of Environmental*

Sciences. 23 (8). p.pp. 1342–1349.

Zhang, G., Bi, X., Chan, L.Y., Li, L., Wang, X., Feng, J., Sheng, G., Fu, J., Li, M. & Zhou, Z. (2012). Enhanced trimethylamine-containing particles during fog events detected by single particle aerosol mass spectrometry in urban Guangzhou, China. *Atmospheric Environment*. 55. p.pp. 121–126.

Zhang, G., Bi, X., Han, B., Qiu, N., Dai, S., Wang, X., Sheng, G. & Fu, J. (2015). Measurement of aerosol effective density by single particle mass spectrometry. *Science China Earth Sciences*.

Zhang, J., McCreanor, J.E., Cullinan, P., Chung, K.F., Ohman-Strickland, P., Han, I.-K., Järup, L. & Nieuwenhuijsen, M.J. (2009a). *Health effects of real-world exposure to diesel exhaust in persons with asthma.* Boston, USA.

Zhang, Q., Jimenez, J.L., Canagaratna, M.R., Ulbrich, I.M., Ng, N.L., Worsnop, D.R. & Sun, Y. (2011b). Understanding atmospheric organic aerosols via factor analysis of aerosol mass spectrometry: A review. *Analytical and Bioanalytical Chemistry*. 401 (10). p.pp. 3045–3067.

Zhang, X., Wu, G., Yao, T., Zhang, C. & Yue, Y. (2011c). Characterization of individual fly ash particles in surface snow at Urumqi Glacier No. 1, Eastern Tianshan. *Chinese Science Bulletin*. 56 (32). p.pp. 3464–3473.

Zhang, Y., Wang, X., Chen, H., Yang, X., Chen, J. & Allen, J.O. (2009b). Source apportionment of lead-containing aerosol particles in Shanghai using single particle mass spectrometry. *Chemosphere*. 74 (4). p.pp. 501–7.

Zimmer, A.T. (2002). The influence of metallurgy on the formation of welding aerosols. *Journal of Environmental Monitoring*. 4 (5). p.pp. 628–632.

Zimmer, A.T. & Biswas, P. (2001). Characterization of the aerosols resulting from arc welding processes. *Journal of Aerosol Science*. 32 (8). p.pp. 993–1008.

Zimmermann, R., Ferge, T., Gälli, M. & Karlsson, R. (2003). Application of single-particle laser desorption/ionization time-of-flight mass spectrometry for detection of polycyclic aromatic hydrocarbons from soot particles originating from an industrial combustion process. *Rapid Communications in Mass Spectrometry*. 17 (8). p.pp. 851–859.

Zorn, S.R., Drewnick, F., Schott, M., Hoffmann, T. & Borrmann, S. (2008). Characterization of the South Atlantic marine boundary layer aerosol using an Aerodyne Aerosol Mass Spectrometer. *Atmospheric Chemistry and Physics*. 8. p.pp. 4711–4728.

7. APPENDIX I – SCALING

7.1 THE SCALING PROCESS

As established in Section 2.2.1, the electrical mobility, D_m, and optical diameters, D_o, employed by the SMPS and OPS/OPC need to be converted to aerodynamic diameter, D_{va}, according to:

$$d_{va} = \frac{\rho_p}{\rho_0}\frac{d_{ve}}{\chi}$$

Where D_{ve} is the volume equivalent diameter and represents D_m and D_o. We assume that particles are spherical, so the shape factor $\chi = 1$. The standard density, ρ_0, is 1 g cm^{-3} so D_{ve} can be multiplied by an assumed density to equate to D_{va}.

For both NANO-INDUS and ADRIMED/SAF-MED measurements a density of 1.7 was chosen. The density informs which SMPS and OPS/OPC size bins are chosen to scale the ATOFMS particle numbers with. The ATOFMS size range, in aerodynamic diameter, is 100-3000 nm. With a density of 1.7 this equates to a size range of 58.8-1764.7 nm in D_m/D_o.

The SMPS and OPS/OPC often have overlapping size ranges; the SMPS for both measurements detected particles up to ~500 nm in diameter, while the smallest particles the OPS/OPC measured were 300 nm in diameter. It is therefore necessary to compare particle numbers in the overlapping size bins from the instruments and decide which data should be used for scaling the ATOFMS numbers. An example of such a comparison is shown in Figure 7.1. Based on this, the SMPS data in the 300-400 nm size range was chosen and the OPC was used for particles larger than 400 nm.

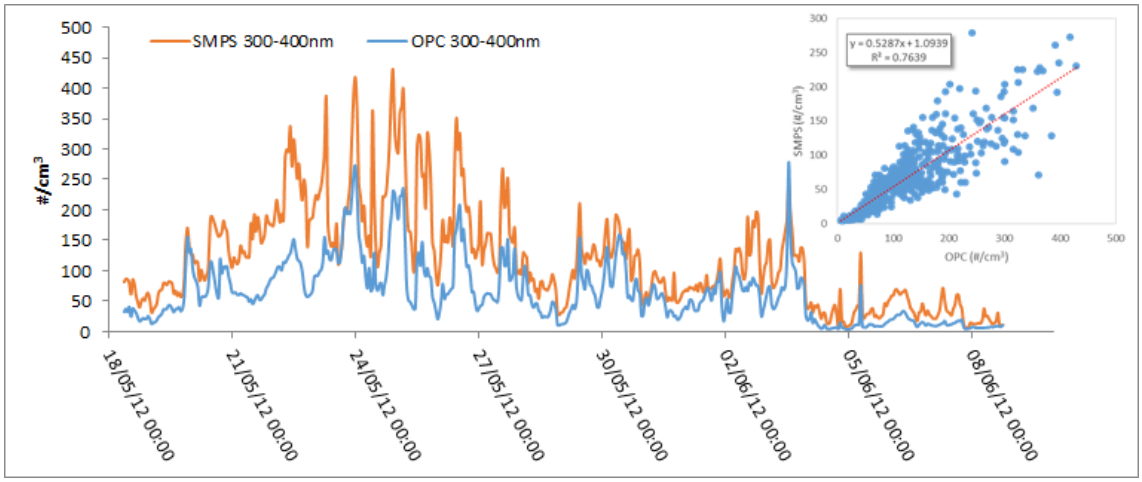


Figure 7.1. Comparison of SMPS and OPC number concentrations for particles between 300-400 nm in diameter.

Once the limits of the SMPS and OPS/OPC size ranges have been determines, it may then be necessary to merge some of the size bins produced by each instrument. The ATOFMS usually detects only low numbers of small and large particles (<300 nm and >1000 nm D_{va}) so dividing these into narrow size bins, such as those used by the SMPS, can result in poor scaling factors. The number of SMPS and OPS/OPC bins merged will depend on the ATOFMS data and will become apparent after some trial and error – the error usually manifests itself as scaling factors of zero, and a size bin full of these is probably too narrow and needs to be merged with others to widen the size range the ATOFMS particles fall into. Merging is simply a matter of summing the particle numbers for several SMPS and OPS/OPC size bins. An example of a finalised set of SMPS and OPS/OPC size bins ready for scaling is shown in Figure 7.2.

	SMPS Counts divided by channels per decade (64)			OPC Bins & Counts (converted to #/cm3)					
Timestamp	UCC SMPS 100-200nm	UCC SMPS 200-300nm	UCC SMPS 300-400nm	OPC 400-500nm	OPC 500-650nm	OPC 650-800nm	OPC 800-1000nm	OPC 1000-1600nm	OPC 1600-2000nm
18/05/2012 09:00	658.534566	302.2123438	69.00392969	5.29	1.64	0.56	0.39	0.22	0.11
18/05/2012 10:00	673.4140214	298.6061694	74.29145123	6.21	1.82	0.55	0.35	0.16	0.09
18/05/2012 11:00	636.5803656	287.9137703	72.96327539	5.90	1.90	0.58	0.37	0.16	0.09
18/05/2012 12:00	597.0733409	325.5315979	66.26818676	7.52	2.95	1.31	1.10	0.57	0.34
18/05/2012 13:00	428.8144	250.4820345	51.29878158	4.62	1.51	0.59	0.41	0.18	0.09
18/05/2012 14:00	365.4194827	276.3481003	73.46256497	7.40	3.11	1.37	0.94	0.43	0.23
18/05/2012 15:00	315.2017813	237.6638084	68.10857574	7.29	3.19	1.35	0.94	0.43	0.23
18/05/2012 16:00	323.2597567	218.8217393	49.47188618	6.31	3.08	1.36	0.96	0.43	0.24
18/05/2012 17:00	299.1965321	199.7718512	40.17284301	4.77	2.48	1.06	0.73	0.33	0.18
18/05/2012 18:00	296.1143722	184.1446836	34.11157656	3.88	1.72	0.54	0.27	0.07	0.03
18/05/2012 19:00	337.9951842	203.0095946	42.18140074	4.02	1.78	0.63	0.35	0.11	0.06
18/05/2012 20:00	376.0752763	225.4352171	44.8659236	4.90	2.11	0.69	0.35	0.11	0.05
18/05/2012 21:00	364.710171	230.9302274	43.13500269	4.23	1.74	0.59	0.31	0.09	0.04
18/05/2012 22:00	376.0632936	246.3183367	49.91588227	4.29	1.70	0.56	0.29	0.09	0.04
18/05/2012 23:00	438.0191974	261.1979408	53.29142648	5.11	1.93	0.63	0.32	0.09	0.04
19/05/2012 00:00	429.7360898	235.5116016	43.90884867	4.37	1.75	0.59	0.31	0.09	0.03

Figure 7.2. Example of SMPS and OPC size bins ready for scaling. The diameters given are electrical mobility/optical. The size ranges were chosen based on the smallest and largest ATOFMS particles detected, with a density of 1.7 for diameter conversion (i.e. the SMPS bin 100-200 nm corresponds to 170-340 nm in D_{va}).

The total ATOFMS particles now need to be sorted into the chosen SMPS and OPS/OPC size bins. An example of this is shown in Figure 7.3. We have a MATLAB script which takes a file comprised of a list of the ATOFMS particles and their diameters and timestamps and sorts the particles into the specified size bins per hour. A file with a list of particles needs to be generated for the total ATOFMS particles in the dataset and for each particle class.

		ATOFMS particles, aerodynamic diameter								
		SMPS Bins			OPC Bins					
		100-170 nm	170-340 nm	340-510 nm	510-680 nm	680-850 nm	850-1105 nm	1105-1360 nm	1360-1700 nm	1700-2720 nm
18/05/12	09:00	3	22	366	378	170	102	48	56	41
18/05/12	10:00	1	22	399	408	159	89	45	50	27
18/05/12	11:00	1	44	380	441	203	110	46	67	49

Figure 7.3. Example of total ATOFMS particle numbers per SMPS/OPS/OPC size bin, in corresponding D_{va}.

Dividing the SMPS/OPS/OPC particle numbers in a given size bin by the ATOFMS particle numbers in the same bin produces a scaling factor for each bin, per hour, as shown in Figure 7.4.

	Scaling Factor (density=1.7 to convert SMPS/OPC bins to aerodynamic)								
	SMPS Bins			OPC Bins					
Timestamp (CEST)	100-170 nı	170-340 nı	340-510 nı	510-680 nı	680-850 nı	850-1105 r	1105-1360	1360-1700	1700-2720 nm
18/05/12 09:00	=B5/O5	29.93339	0.825717	0.085812	0.031094	0.016029	0.011583	0.006893	0.005439
18/05/12 10:00	742.6702	30.60973	0.748386	0.091703	0.039043	0.020464	0.012257	0.006953	0.005775
18/05/12 11:00	761.5452	14.46774	0.757668	0.073287	0.029052	0.017286	0.012556	0.005448	0.00323
18/05/12 12:00	110.1843	13.56985	0.606204	0.072803	0.030214	0.016591	0.012558	0.00956	0.00563
18/05/12 13:00	139.1138	9.972428	0.548101	0.045231	0.020635	0.00763	0.004125	0.003596	0.002382
18/05/12 14:00	132.0208	8.498128	0.839964	0.084445	0.028664	0.01125	0.006802	0.006036	0.005063
18/05/12 15:00	186.181	7.880045	0.784369	0.08109	0.026721	0.011876	0.007853	0.005994	0.005759

Figure 7.4. Example of scaling factors produced by dividing SMPS/OPS/OPC particle numbers by ATOFMS numbers in the same size bin. In the highlighted cell B5 represents the SMPS/OPS/OPC particle number and O5 represents the number of ATOFMS particles.

This scaling factor can then be applied to the particle numbers of each ATOFMS particle class, which have been also been sorted into the chosen size bins, by multiplying the ATOFMS particle numbers by the scaling factor. This results in scaled particle numbers for each ATOFMS particle class; an example of scaled ATOFMS *Sea salt* particles is shown in Figure 7.5.

Scaled Counts		Sea salt								
		SMPS Bins			OPC Bins					
		100-170 nm	170-340 nm	340-510 nm	510-680 nm	680-850 nm	850-1105 nm	1105-1360 nm	1360-1700 nm	1700-2720 nm
18/05/12	09:00	=CC5*$BH5	29.9333894	3.30286714	0.34324868	0.18656471	0.304558824	0.24325	0.255035714	0.08702439
18/05/12	10:00	0	0	0.74838639	0.64192259	0.54660168	0.204644195	0.232890741	0.257273333	0.092395062
18/05/12	11:00	0	0	3.03067127	0.36643424	0.17431034	0.3803	0.288791667	0.234253731	0.074280612
18/05/12	12:00	110.18431	13.5698487	1.21240819	0.29121348	0.57405689	0.846132022	0.703230769	0.707450725	0.230844884

Figure 7.5. Example of scaled ATOFMS Sea salt particle numbers.

The scaled ATOFMS numbers, in each size bin per hour, for each class can be converted to volume and mass according to:

$$Mass\ concentration = Scaled\ ATOFMS\ particle\ numbers\ * \frac{\pi}{6} * \left(\frac{D_{ve}\ (midpoint)}{1000}\right)^3 * \rho_p$$

An example of this is shown in Figure 7.6. Summing the mass concentrations in each size bin provides the total mass concentration per hour for an ATOFMS particle class. Summing the mass concentrations for each particle class then provides the total ATOFMS mass concentrations, or the same volume and mass conversion can be applied to the total scaled ATOFMS particle numbers. However, since the mass concentrations for each particle class are always of interest, summing these to provide a total ATOFMS mass is my preferred method. While a single density at the diameter conversion stage is the most efficient in terms of data analysis, different densities can be easily applied at this mass conversion stage.

=(NZ5*3.141/6*(ZM$4/1000)^3)*2.2

	ZL	ZM	ZN	ZO	ZP	ZQ	ZR	ZS	ZT	ZU
		Sea salt [density=2.2]								
Volume & Mass		SMPS Bins			OPC Bins					
Timestamp (CEST)		77.07139547	141.4213562	244.9489743	346.4101615	447.2135955	570.0877125	721.1102551	894.427191	1264.911064
18/05/12 09:00		00)^3)*2.2	0.097508001	0.055905862	0.016433123	0.01921825	0.064988363	0.105050284	0.21017224	0.202843142
18/05/12 10:00		0	0	0.012667535	0.030732217	0.056306084	0.043668054	0.10057652	0.21201624	0.215361517
18/05/12 11:00		0	0	0.051298548	0.017543138	0.017955914	0.081150413	0.124717972	0.19304603	0.173138964
18/05/12 12:00		0.058095005	0.044203775	0.020521784	0.013941924	0.059134278	0.180552098	0.30369822	0.58300267	0.538071012
18/05/12 13:00		0	0	0.018554815	0.012992679	0.038261525	0.144904485	0.154984258	0.21932345	0.111044591
18/05/12 14:00		0	0	0.028435235	0.064685474	0.129919723	0.355295987	0.42008028	0.57206422	0.436602382
18/05/12 15:00		0	0.025669241	0.026553187	0.054350697	0.079825206	0.387729736	0.417153626	0.59764973	0.483247482
18/05/12 16:00		0	0	0	0.073060875	0.173942697	0.43126994	0.471187494	0.64050783	0.517843155

Figure 7.6. Example of conversion of scaled ATOFMS particle numbers to mass concentration using volume and density. In the formula bar at the top of the image NZ5 represents the scaled ATOFMS numbers and ZM4 represents the midpoint of the SMPS/OPS/OPC size bin, in electrical mobility/optical diameter.

The midpoint of each size bin, in electrical mobility/optical diameter, is required for calculating the volume of the particles per hour. This was calculated as per Figure 7.7.

Original	Final Bin Limits (nm)	Midpoint (nm)		
	59.4	(LOG(B4)+LOG(B3))/2	10^(E3)	F3/1000
SMPS Bins Combined	100	2.150514998	141	0.141421
	200	2.389075625	245	0.244949
	300	2.539590623	346	0.346410
	400	2.650514998	447	0.447214
	500	2.75594168	570	0.570088
OPS Bins (some combined)	650	2.858001672	721	0.721110
	800	2.951544993	894	0.894427
	1000	3.102059991	1265	1.264911
	1600	3.252574989	1789	1.788854
	2000		1	

Figure 7.7. Calculations for midpoints of SMPS/OPS/OPC size bins. Cell B4 represents 100 nm and B3 represents 59.4 nm.

7.2 SCALING FACTORS

A comparison of the resulting scaling factors is shown in Figure 7.8. The scaling factors for the ADRIMED/SAF-MED 510-984 nm and 984-3000 nm size bins are similar to those in the equivalent size bins for NANO-INDUS. The scaling factors for the ADRIMED/SAF-MED 292-510 nm size lie between those of the NANO-INDUS 170-340 nm and 340-510 bins. No scaling factors were obtained for ADRIMED/SAF-MED particles less than 300 nm in diameter, due to the particle sizing issues experienced during those campaigns (discussed in Section 4.2.2.). The scaling factors for particles in the 100-170 nm size bin during NANO-INDUS are approximately two orders of magnitude less than those found by Healy et al. in Paris (2012) for their smallest size bin, 150-191 nm. This can be explained by lower particle number concentrations measured by the SMPS in Dunkirk as compared to the heavily urbanised megacity of Paris. The more particles

counted by the SMPS in these small size ranges, the greater the scaling factors will be, as the ATOFMS is limited in the detection of these particles.

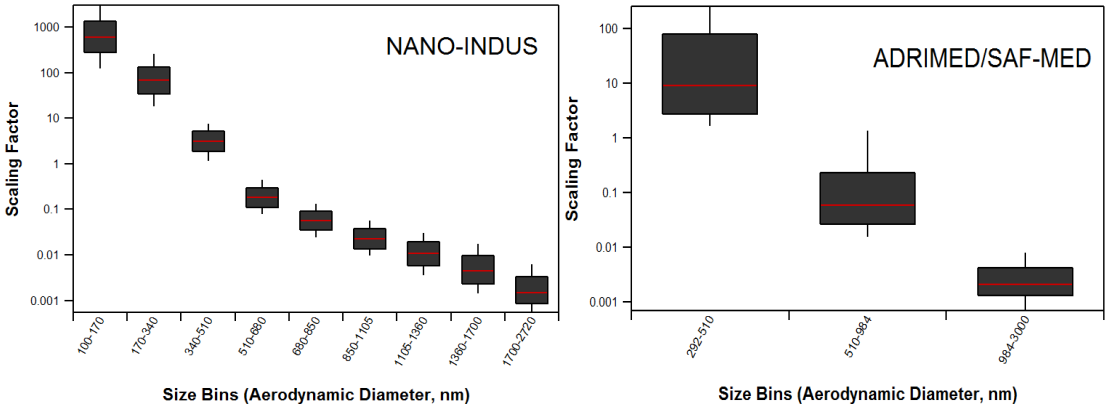


Figure 7.8. Box-plot of hourly size-dependent scaling factors for each sampling campaign (NANO-INDUS: n = 511, ADRIMED/SAF-MED: n = 784). Median, 75th percentile and 90th percentile are denoted by the solid red line, box and whisker respectively.

8. APPENDIX II – NANO-INDUS

8.1 ANALYSIS OF GMF ORES AND CHIMNEY FILTERS

The ATOFMS was used to analyse samples of the main manganese ores used by the ferromanganese alloy facility from May-September 2012; two ores from Brazil (MF13 and MF15) and one from South Africa (SA). The instrument also analysed samples of PM deposited on the industrial filters of the three chimneys; firing area (Chimney A), cooling area (Chimney B) and smelting unit (Chimney C). These samples were collected in 2010 and analysed by ULCO-LPCA with the same SEM-EDX used for the field campaign samples.

For ATOFMS characterisation, PM samples were suspended in deionized water, shaken and sonicated for 10 minutes. The suspended samples were then aerosolized using an aerosol generator (TSI Model 3076), passed through a diffusion dryer, a charge neutralizer and into the sampling inlet of the ATOFMS. Several thousand spectra were collected for each sample over 1-2 hours and analysed with ENCHILADA as outlined in Chapter 2.

SEM-EDX characterization of the particles collected on the industrial filters was performed by colleagues at ULCO-LPCA. A small amount of each industrial filter sample was added to a vacuum flask held in an ultrasonic water bath and the flask was connected to a nitrogen gas jet to transfer particles to a polyethylene bag. The particles were then collected on boron substrates by cascade impaction. The individual particle analysis was carried out using a Scanning Electron Microscope FEI Quanta 200 equipped with an EDAX energy dispersive detector. Particles were classified according to their elemental composition. Only elements with concentration higher than 5 at.% were considered for this classification, except for carbon associated with a threshold of 15 at.% (due to its higher detection limit). Particles were then classified by composition. For example, the class named C/O/Al/Si/Ca contains particles with an atomic C concentration higher than 15% and O, Al, Si, Ca atomic concentrations all higher than 5%. All SEM-EDX compositional data below refer to atomic percentage composition.

A third set of PM samples was collected (May to September 2012) in the flues of each chimney (downstream of the industrial filters) to enable comparison of the emitted particles with those collected on the industrial filters. This was achieved by locating a 3 stage-cascade impactor (Dekati Ltd) inside the chimney flues just before the point where

particles are released to the atmosphere. The impactor was fitted with a home-made boron substrate suitable for use in SEM-EDX characterization (Choël et al., 2005). As it was not possible to connect the ATOFMS sampling line directly to the chimneys, the particles present in the chimney flues downstream of the filters have only been characterized by SEM-EDX.

8.2 RESULTS: GMF ORES AND CHIMNEY FILTERS

Average mass spectra for major and minor particle classes produced by ATOFMS analysis of chimney filters and ores are shown in Figure 8.2, Figure 8.3 and Figure 8.4.

8.2.1 ORES

Figure 8.1 shows the composition of the three ores analysed by ATOFMS. The majority of particles produced from the ore samples contain $^{55}Mn^+$, $^{56}Fe^+$, $^{27}Al^+$, $^{39}K^+$ and aluminosilicates ($^{60}SiO_2^-$, $^{76}SiO_3^-$, $^{77}HSiO_3^-$, $^{103}AlSiO_3^-$) but the combination of these varies more for MF15, resulting in more particle classes (Figure 8.2 and Figure 8.4). Three particle classes were common to all ore samples and account for the majority of the particles analysed: *K-Mn*, *Al-Mn-K* and *Mn-K-Al* particles. Together they account for 85-97% of the total ore particles.

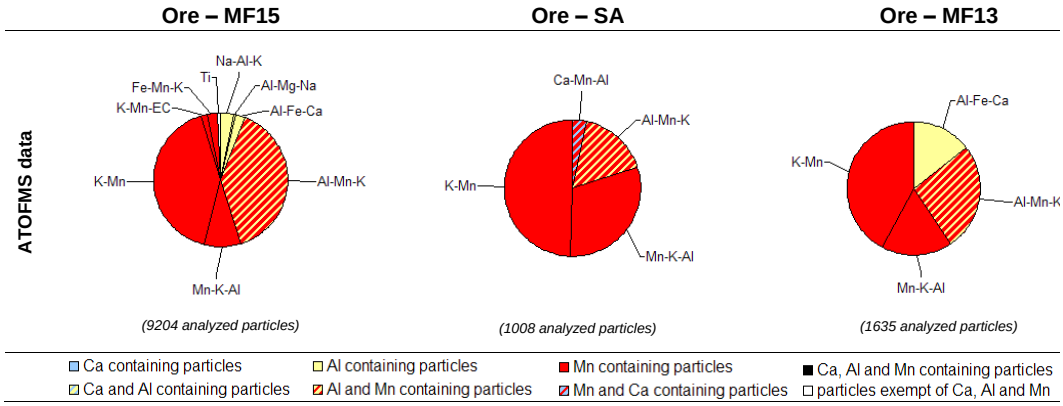


Figure 8.1. Composition of ore samples analysed by ATOFMS. Wedge size corresponds to the relative abundance of each particle class by number.

All three classes are characterised by $^{16}O^-$, $^{35}Cl^-$, aluminium oxide ($^{43}AlO^-$, $^{59}AlO_2^-$), silicate ($^{60}SiO_2^-$, $^{76}SiO_3^-$, $^{77}HSiO_3^-$), aluminosilicate ($^{103}AlSiO_3^-$) and phosphate ($^{63}PO_2^-$, $^{79}PO_3^-$) fragments in their negative mass spectra. $^{16}O^-$ produced the strongest negative ion signal in most ore particles, consistent with their mineral origins. Nitrate ($^{46}NO_2^-$) was found in almost all ore particles and infrequently in the chimney filter samples; its presence in *K-Mn* and *Al-Mn-K* particles as shown in Figure 8.2 is a result of averaging all mass spectra from ore and chimney samples for those particle classes. Samples were taken from the surface of the storage piles, which are stored outdoors.

The three classes were distinguished by their positive mass spectra: *K-Mn* particles were dominated by $^{39}K^+$ and also contained $^{55}Mn^+$; *Al-Mn-K* particles were characterised by a strong signal for Al, as well as ones for $^{55}Mn^+$ and $^{39,41}K^+$; *Mn-K-Al* particles produced a strong signal for as well as $^{39}K^+$, $^{27}Al^+$, $^{56}Fe^+$ and $^{23}Na^+$.

Minor particle classes obtained from the ores include *Al-Fe-Ca, Al-Mg-Na, Ca-Mn-Al, Fe-Mn-K, Na-Al-K, K-Mn-EC* and *Ti*. Some of these produced signals for $^{24}Mg^+$, $^{48}Ti^+$ and $^{64}TiO^+$ ions, not found in the major ore classes, while the negative mass spectra were largely similar.

8.2.2 Sintering unit – Firing Area (Chimney filter A)

Most of the ATOFMS particle classes found in the chimney filter in the firing area were internal mixtures of $^{40}Ca^+$ (and associated oxides; $^{56}CaO^+$, $^{96}Ca_2O^+$), $^{39}K^+$, $^{27}Al^+$, aluminium oxides ($^{43}AlO^-$), aluminosilicates ($^{60}SiO_2^-$, $^{76}SiO_3^-$, $^{77}HSiO_3^-$), phosphates ($^{79}PO_3^-$) and oxygen ($^{16}O^-$). Mass spectra for major ATOFMS particle classes in the chimney filters are shown in Figure 8.2, the remaining mass spectra can be found in Figure 8.4. The *Ca-K* particle class constituted most (45%) of the firing chimney sample and calcium dominated most of the firing chimney particles (*K-Al* class only one not to contain any). This class cannot be considered a unique marker for emissions from the GMF facility as calcite and aluminosilicates are also usually emitted by the sintering units of iron and steel making plants, as well as potassium chloride (Dall'Osto et al., 2008; Ebert et al., 2012; Hleis et al., 2013).

The following chemical species are unique to the firing chimney particles; $^{19}F^-$, $^{59}CaF^+$ and $^{208}Pb^+$ and could be useful markers. Most firing chimney particles produced stronger EC signals ($^{12,24,36,..}C_n^-$) than the other chimney or ore particles, probably indicative of the use of anthracite as a reducing agent in this process. $^{26}CN^-$, a marker for organic nitrogen compounds in biomass burning (Silva et al., 1999) or biogenic emissions (Pratt et al., 2009a), dominated the negative mass spectra of most firing chimney particles.

Fe-Ca-K particles, while only making up a small fraction of each sample, are the only class present in all three chimneys. Minor particle classes unique to the firing chimney sample include *K-Ca-Na, Ca, Ca-Mg-Al, CaF-K-Ca, Ca-K-Al* and *Mn-Ca-Pb*.

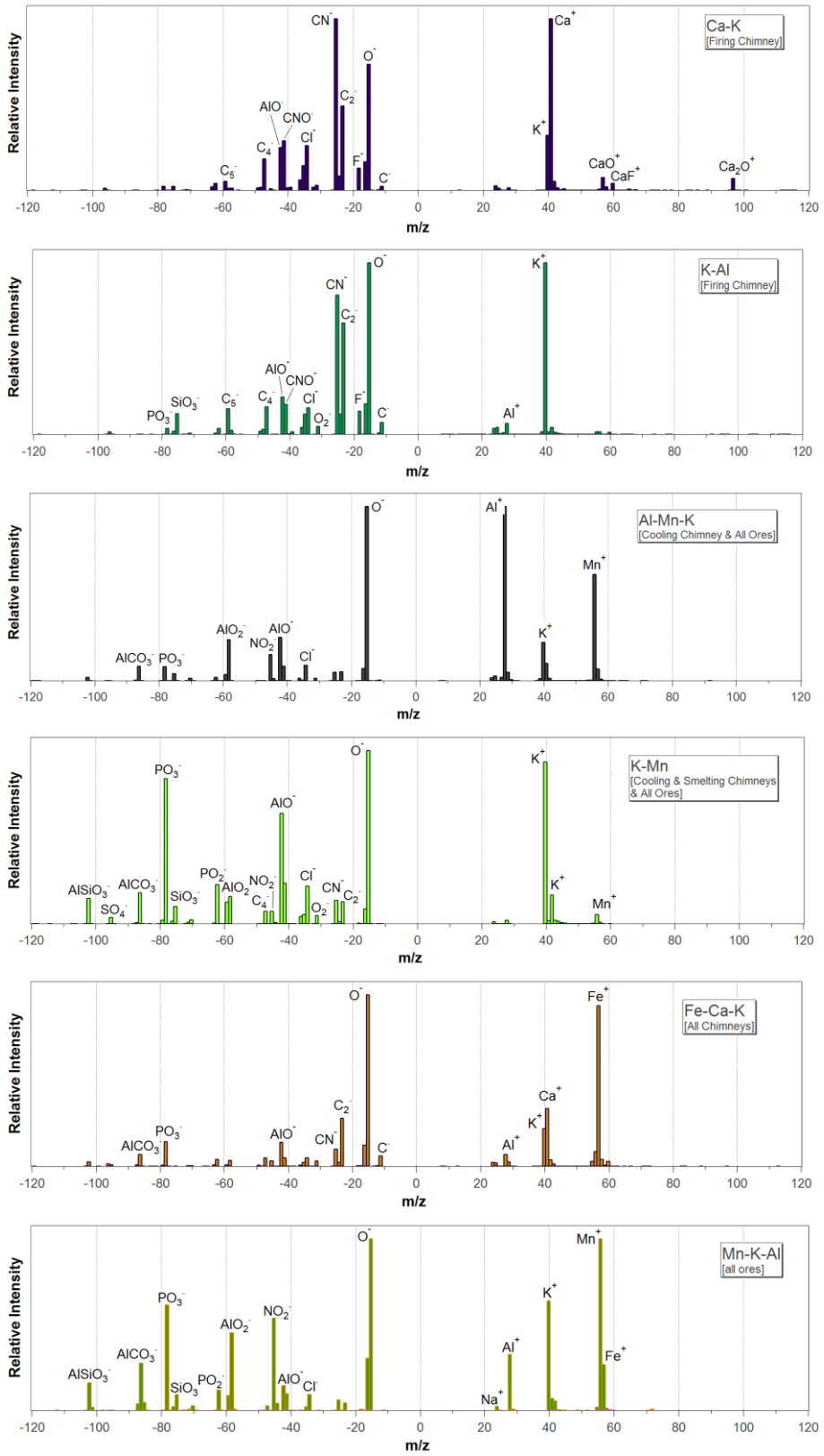


Figure 8.2. Average mass spectra of major ATOFMS particle classes detected in chimney filter and ore samples.

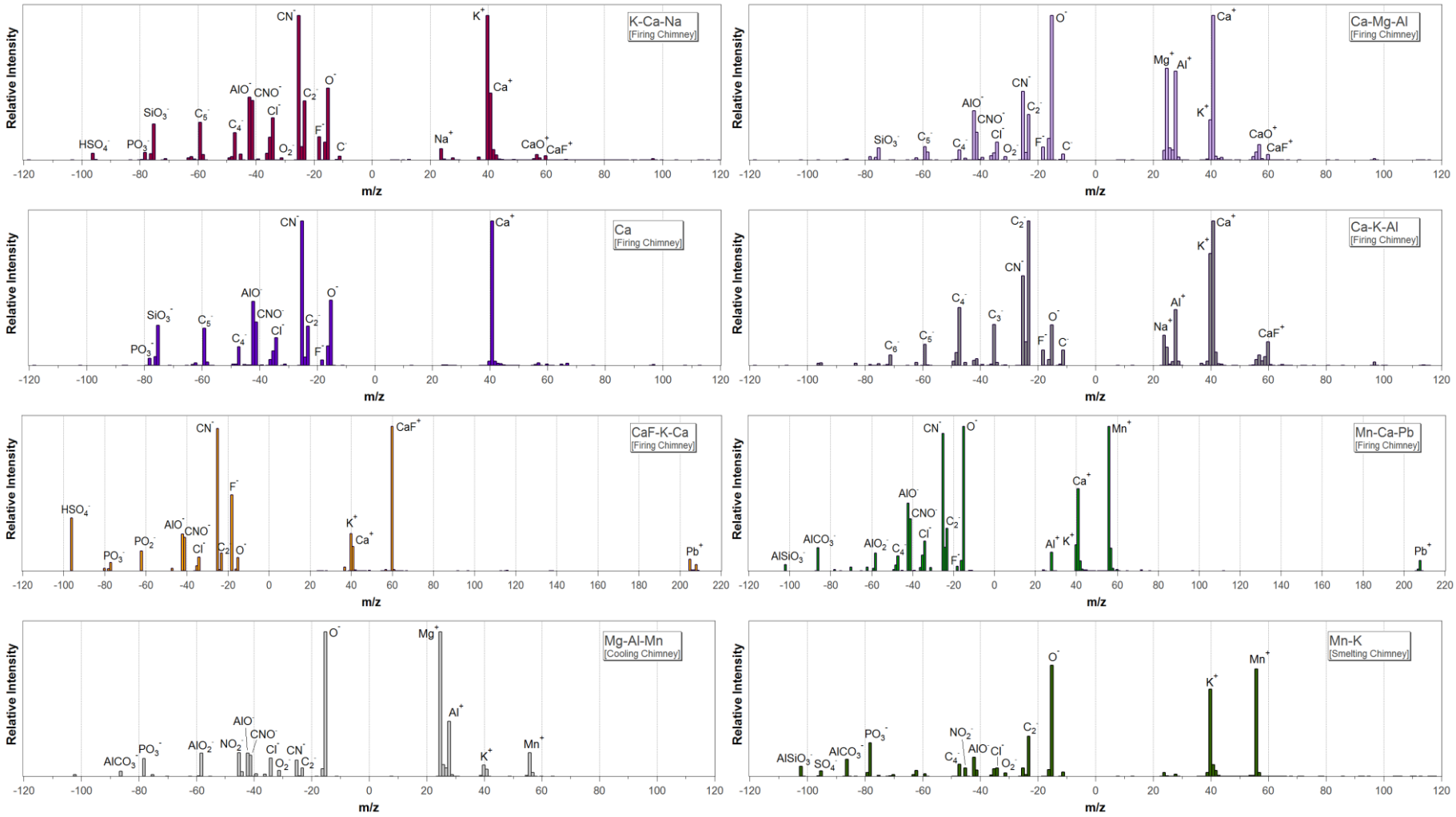


Figure 8.3. Average mass spectra of minor ATOFMS particle classes (except Mn-K) in chimney filter samples.

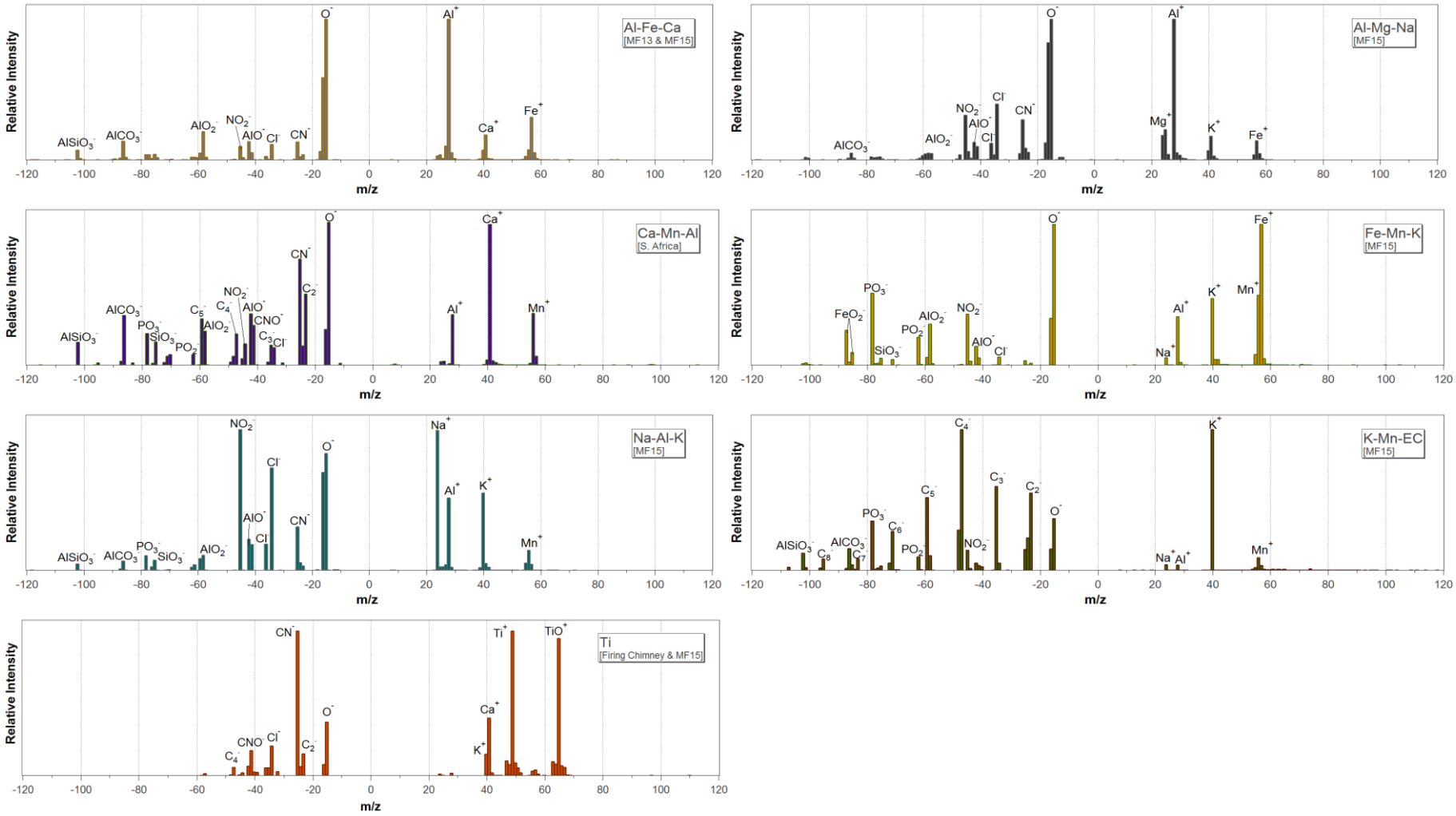


Figure 8.4. Average mass spectra of minor ATOFMS particle classes in ore samples.

8.2.3 Sintering unit – Cooling Area (Chimney filter B)

ATOFMS analysis of the chimney filter sample from the cooling area indicates that *Al-Mn-K* and *K-Mn* are the dominant particle classes. *Al-Mn-K* particles account for 64% of the total number of particles analysed and are specific to this chimney (Figure 8.5). Although *Al-Mn-K* particles were also observed in ore samples, the size information for particles observed in the ambient atmosphere should enable the larger particles coming from stock piles of ores to be distinguished from the smaller particles emitted by chimneys. The composition of *K-Mn* particles was virtually identical in both the cooling and smelting chimney filters. $^{96}SO_4^-$ and $^{46}NO_2^-$, not observed in firing chimney particles, were present in *K-Mn* particles and the signal for $^{79}PO_3^-$ was the largest in all the average spectra.

A minor particle class unique to the cooling chimney sample was *Mg-Al-Mn*, but only contributed 0.3% to the total particles from this sample.

8.2.4 Smelting Unit (Chimney filter C)

Mn-K is the most dominant particle class detected by ATOFMS in the sample from the smelting chimney. This class is very similar to *K-Mn* in terms of core composition, but with different relative intensities for Mn and K. It should be noted that K was prevalent in most of the ATOFMS classes, however this probably reflects the high level of sensitivity of the instrument to this element (Gross et al., 2010). As a result, in mass spectra that contain K but are dominated by other species, for example in *Mn-K* particles, it is reasonable to assume that the K content is less than that of Mn.

8.2.5 Comparison of ores and industrial filter samples

Several particle classes identified from ATOFMS data were common to both chimney-filter and ore samples; *K-Mn* is observed in the cooling and smelting chimneys and in all three ores, while *Al-Mn-K* was found in the cooling chimney and in all three ores.

Additionally, several particle classes were observed only in the ores and not in the chimney filters, which may prove useful in distinguishing between ambient particles coming from the raw materials or from the process. *Mn-K-Al* particles were found in all three ore samples. *Al-Fe-Ca* particles were found in two of the ore samples, and were very similar in composition to *Fe-Ca-K* particles found in all chimneys; both classes contain Al, K, Ca and Fe, but the signal for Al is larger relative to Fe in the *Al-Fe-Ca* class. This may be indicative of *Al-Fe-Ca* particles containing more Al before the ores go

through the processes. They are also the only Fe-containing particles found in the chimney samples, which should aid significantly in ambient particle source identification.

8.2.6 Comparison of ATOFMS and SEM-EDX techniques

The composition of the three industrial chimney filters as analysed by ATOFMS and SEM-EDX is shown in Figure 8.5. The SEM-EDX data are in good agreement with the ATOFMS observations. The composition of the flue samples as analysed by SEM-EDX was generally similar to that of the industrial filters, suggesting that the filter samples can be considered representative of emissions from the chimneys.

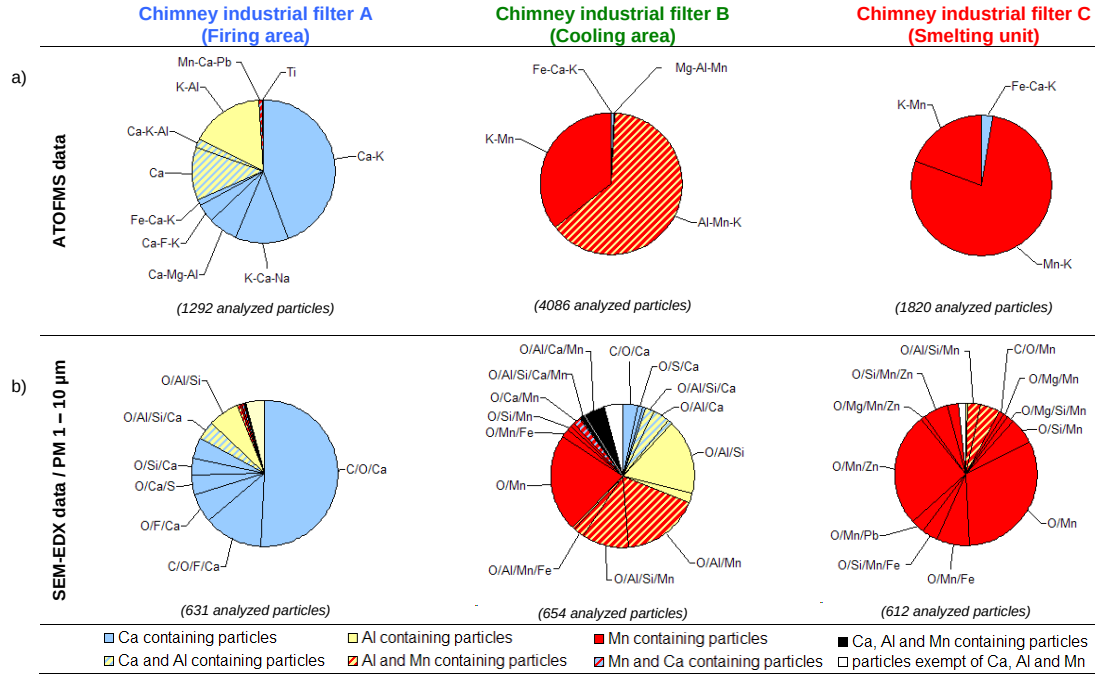


Figure 8.5. Composition of samples collected in the industrial chimney filters (particle classes & relative abundances as percentage of total analysed particles) by a) ATOFMS and b) SEM-EDX.

51% of particles collected by the industrial filter of the firing area are composed on average of 20, 68 and 17% of C, O and Ca, respectively (C/O/Ca particle class) and are identified as calcite particles ($CaCO_3$). The O/F/Ca and C/O/F/Ca particle classes account for 19.5% of analysed particles and were identified as CaF_2 and an internal mixture of CaF_2 with calcite, respectively. In agreement with the ATOFMS analysis, SEM-EDX also indicates that F-containing particles are unique to the firing chimney. Finally, a significant contribution (11%) from aluminosilicate particles was observed in the firing chimney (O/Al/Si and O/Al/Si/Ca classes). 34% of the particles in these two classes contain K as a minor element. This helps explain the relatively high proportion of K-rich particles identified by ATOFMS, which is sensitive to alkali metals (Gross et al., 2000). SEM-EDX analysis of samples collected in the chimney flue showed 35% of particles did not contain Ca, Al or Mn. Instead they were dominated by K, which was not observed by

Marris et al. (2012). A recent change from lime to potash as a neutralising agent in the gaseous washer of the sintering unit (for SO_2 reduction) is the most likely reason for the high proportion of K-containing particles observed in the flue.

The major particle classes from the cooling chimney were identified by SEM-EDX as aluminosilicates (O/Al/Si, 19%), manganese oxide (O/Mn, 26%) and internal mixtures of aluminosilicates and manganese oxides (O/Al/Mn, O/Al/Si/Mn and O/Al/Mn/Fe classes, 31%). Mn is a major element in the Al and Mn-containing particles, but also a minor element in the Al-containing particles, which agrees with ATOFMS analysis. Most of the particle classes identified by SEM-EDX are aluminosilicates and cannot be considered as unique to this sintering process because they can originate from a number of other industrial sources, as well as wind-blown dust. Nevertheless they can be distinguished from the emissions of iron and steel making plants as this elemental association (Al, Si and Mn as major elements) is very unusual in single particles from these sources (Mazzei et al., 2006; Taiwo et al., 2014a). Furthermore, particle emissions from steelworks are known to have a considerably higher Fe content than those detected in this work (Ebert et al., 2012; Hleis et al., 2013).

For the smelting chimney filter, the SEM-EDX data agree with the ATOFMS observations since the majority of analysed particles contain Mn. They are essentially pure manganese oxides (O/Mn class, 31%) or manganese oxides enriched in Fe (O/Mn/Fe and O/Si/Mn/Fe classes, 11%) or Zn (O/Mn/Zn, O/Mg/Mn/Zn and O/Si/Mn/Zn classes, 33%). A small proportion of particles (3.0%) contains on average 7.7 % of Pb (O/Mn/Pb class), although $^{208}Pb^{+}$ is not detected by ATOFMS for this sample. This is somewhat surprising given the ability of the ATOFMS to detect lead (Snyder et al., 2009; Zhang et al., 2009b), but may be due to a matrix effect limiting the desorption/ionisation efficiency for lead in this instance. Zn- and Pb-containing particles are unique to the smelting unit and are not observed for the two other chimneys. This can be explained by the high operating temperature of the smelting process (1400°C) which promotes volatilisation of heavy elements such as Zn and Pb. Zn and Pb have also been associated with steelworks emissions (Reinard et al., 2007; Corbin et al., 2012), however the combination of these two elements with Mn has not been seen for these sources, as it is a trace element with a considerably lower concentration than Fe or Zn (Tsai et al., 2007; Ebert et al., 2012; Hleis et al., 2013). O/Mn/Zn particles can then be considered a unique tracer for ferromanganese smelting emissions.

8.3 ATOFMS DATA CAPTURE

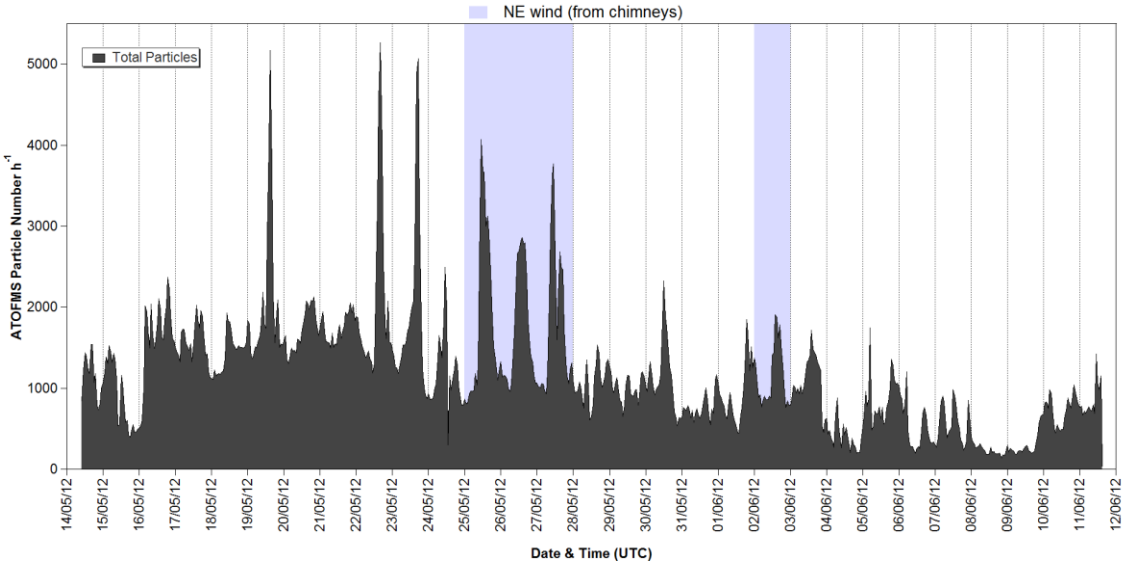


Figure 8.6. Hourly summed counts for full ATOFMS dataset collected from 10th May 10:00 - 11th June 15:00 UTC.

8.4 HYSPLIT

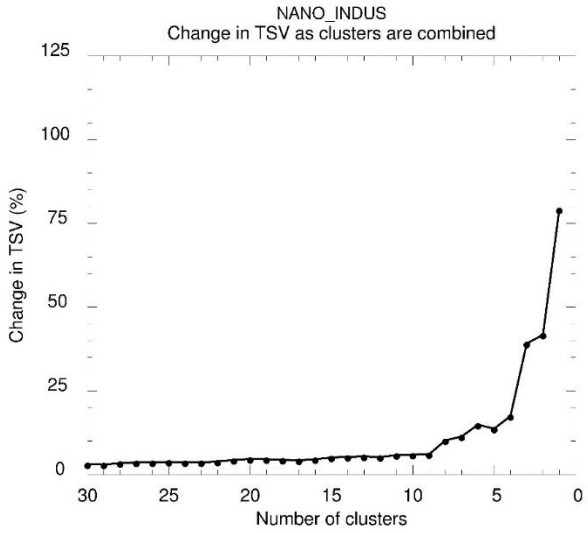


Figure 8.7. Change of the total spatial variance (TSV) as a function of the number of clusters for the HYSPLIT 120-hour back trajectory cluster analysis. Trajectories for 500 m above ground level (AGL) were produced every hour for NANO-INDUS.

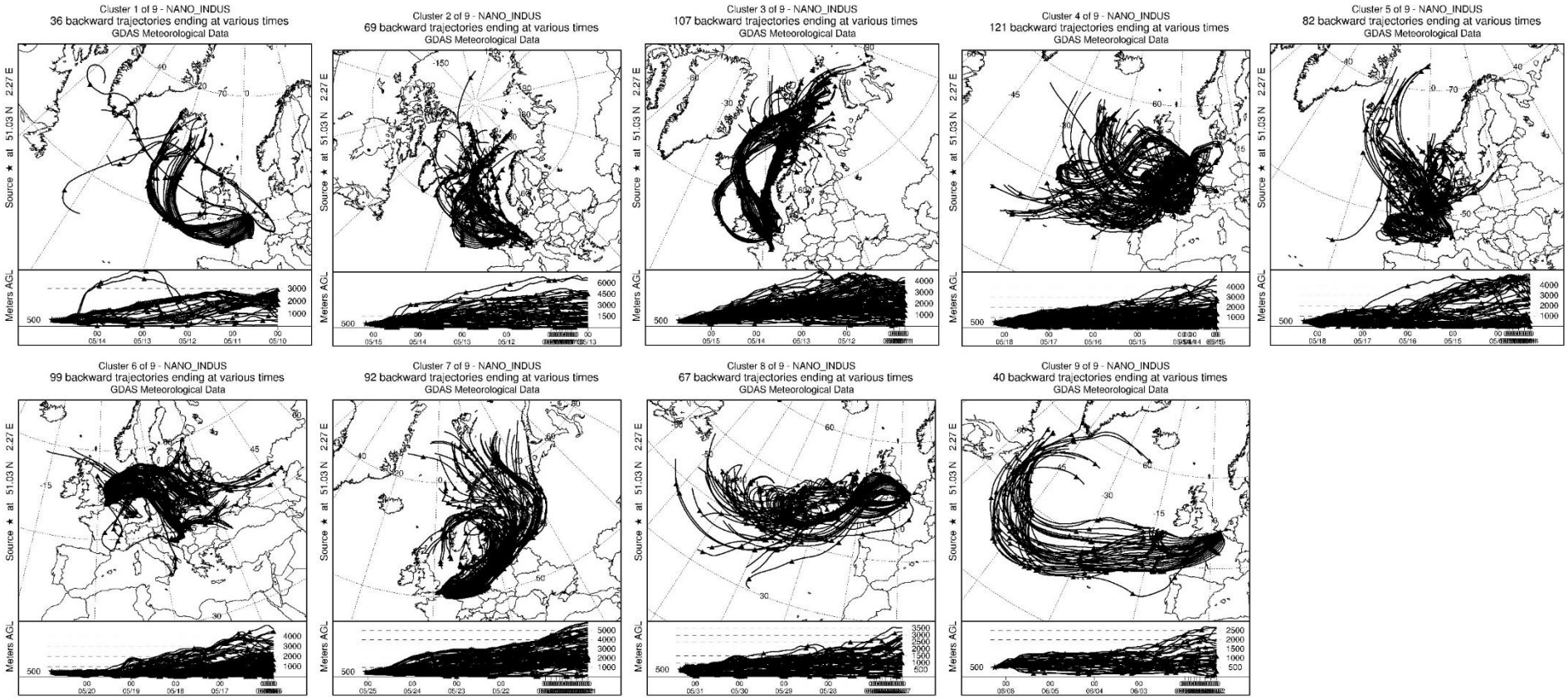


Figure 8.8. Individual HYSPLIT 120-hour back trajectories for each cluster for NANO-INDUS.

8.5 SIZE DISTRIBUTIONS

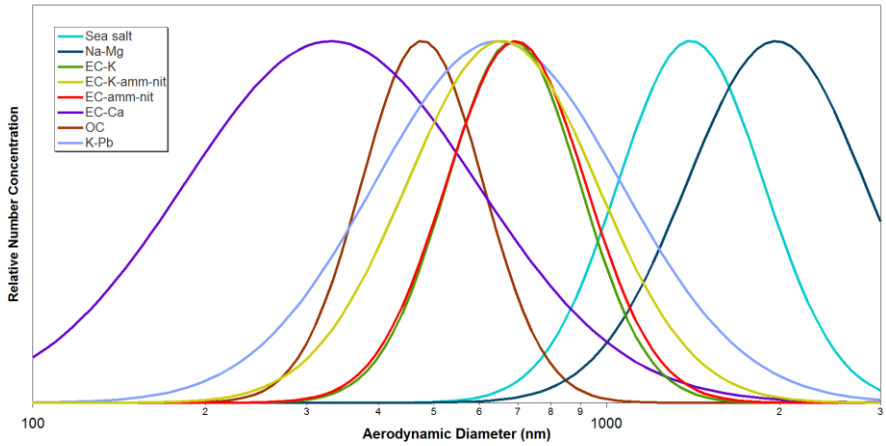


Figure 8.9. Normalised lognormal size distributions for particle classes with little variation in size throughout NANO-INDUS.

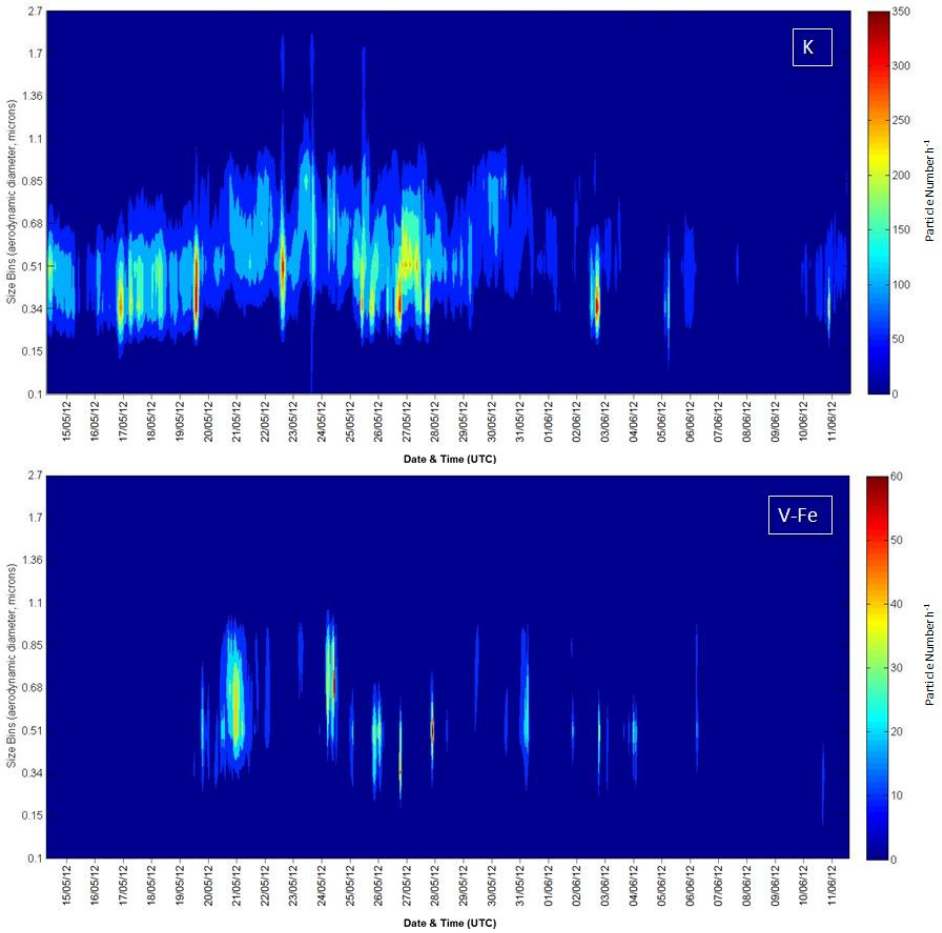


Figure 8.10. Hourly size distribution for unscaled ATOFMS particles from transported/urban and transported industrial sources observed during NANO-INDUS. V-Fe distirbution is representative of Fe, Mn, Fe-EC and Na-V classes.

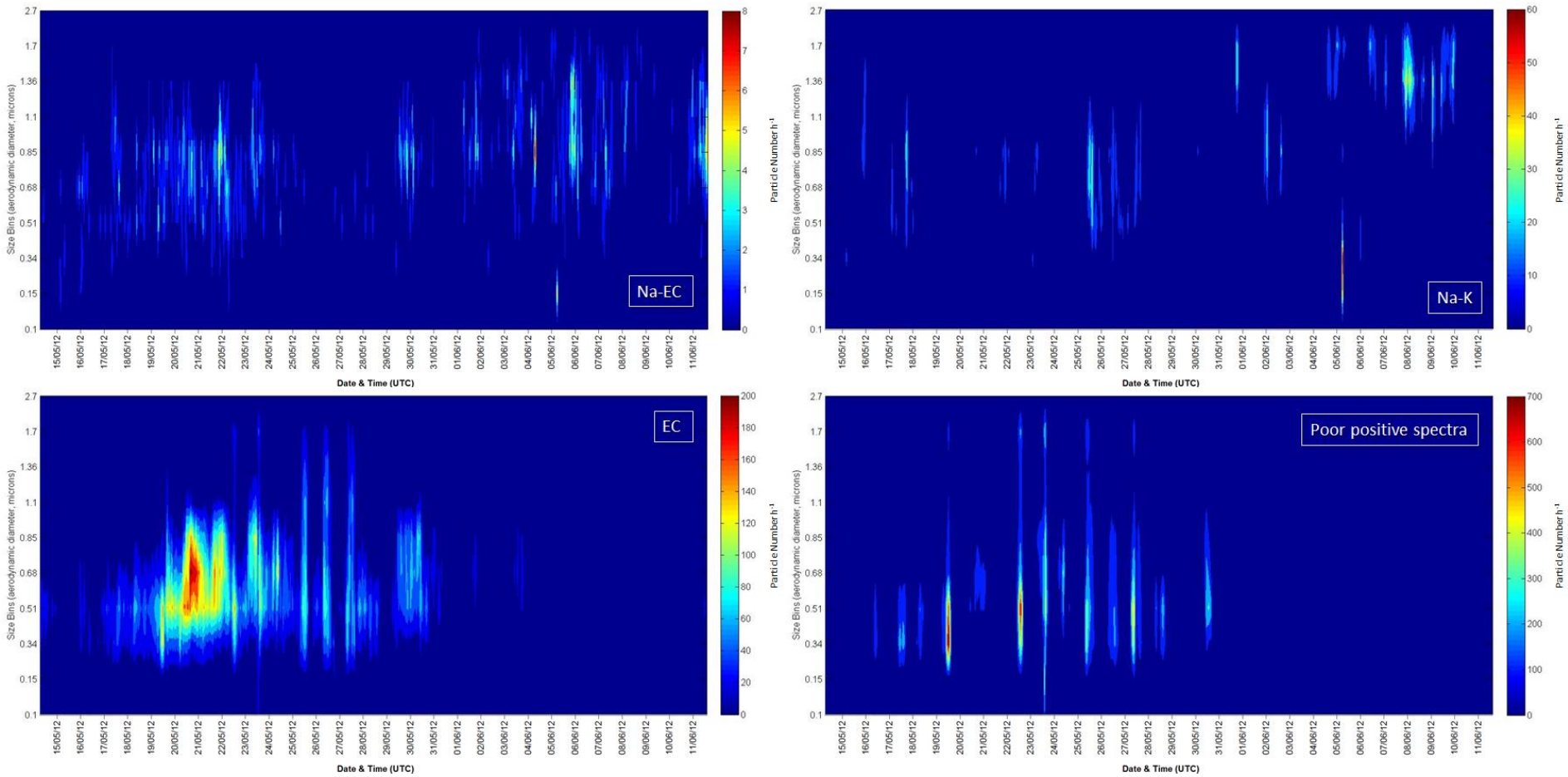


Figure 8.11. Hourly size distribution for unscaled ATOFMS particles from marine and transported/local industrial sources observed during NANO-INDUS.

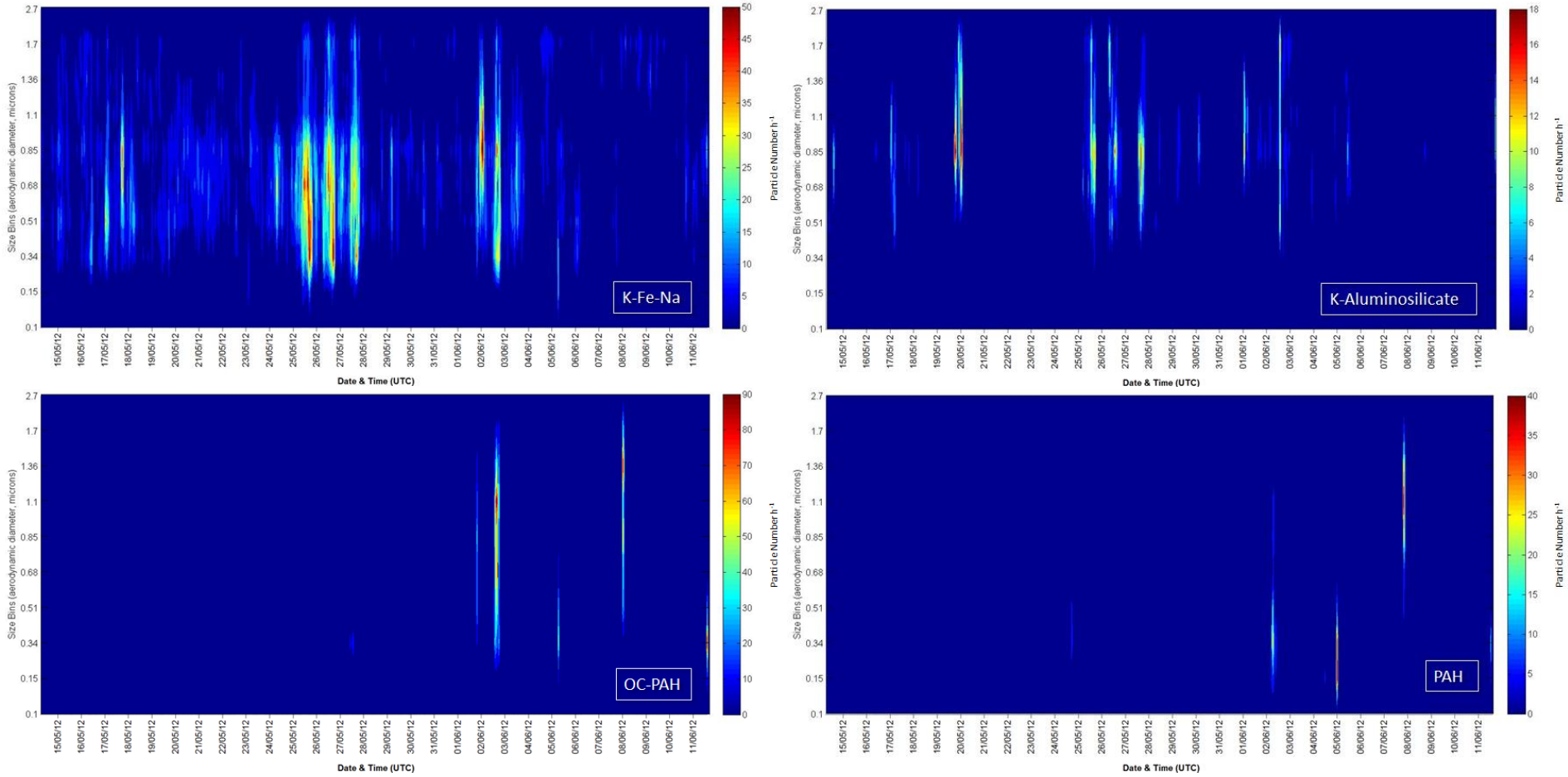


Figure 8.12. Hourly size distribution for unscaled ATOFMS particles from industrial sources observed during NANO-INDUS. K-Fe-Na size distribution is representative of Fe-K-Ca, K-Mn, Al-K-Mn, Mn-K-Fe, K-Cl, K-Al, Li-Zn, Ca and Ca-K.

9. APPENDIX III – ADRIMED/SAF-MED

9.1 ATOFMS DATA CAPTURE

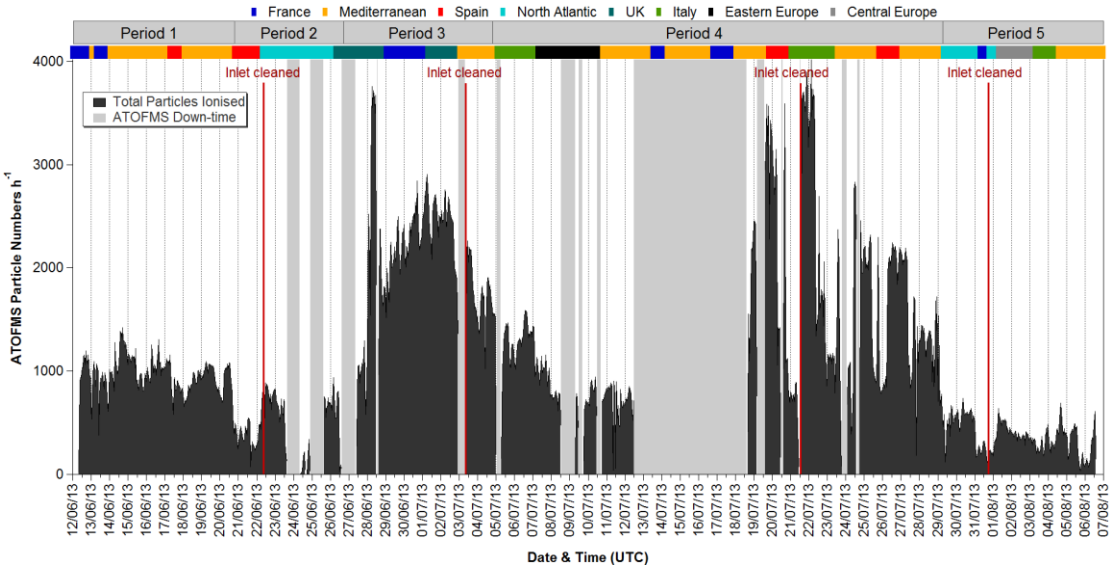


Figure 9.1. Hourly summed counts for full ATOFMS dataset collected from 12th June 08:00 - 6th August 14:00 UTC, including periods where instrument was not collecting data and points where the critical orifice (inlet) was cleaned. A partially blocked inlet can result in lower particle numbers.

9.2 OC COMPARISON

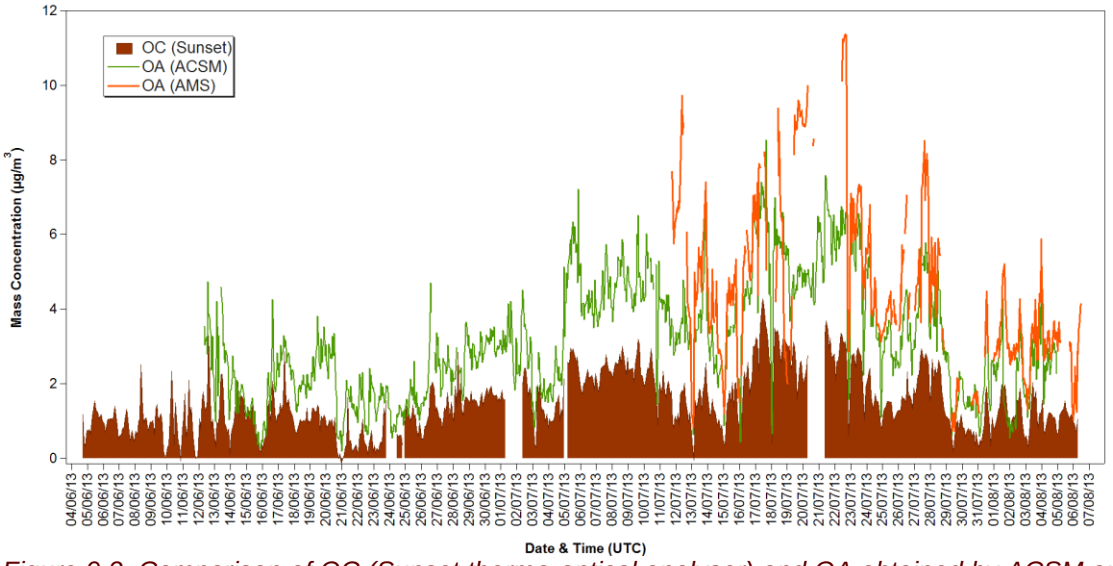


Figure 9.2. Comparison of OC (Sunset thermo-optical analyser) and OA obtained by ACSM and AMS.

9.3 HYSPLIT

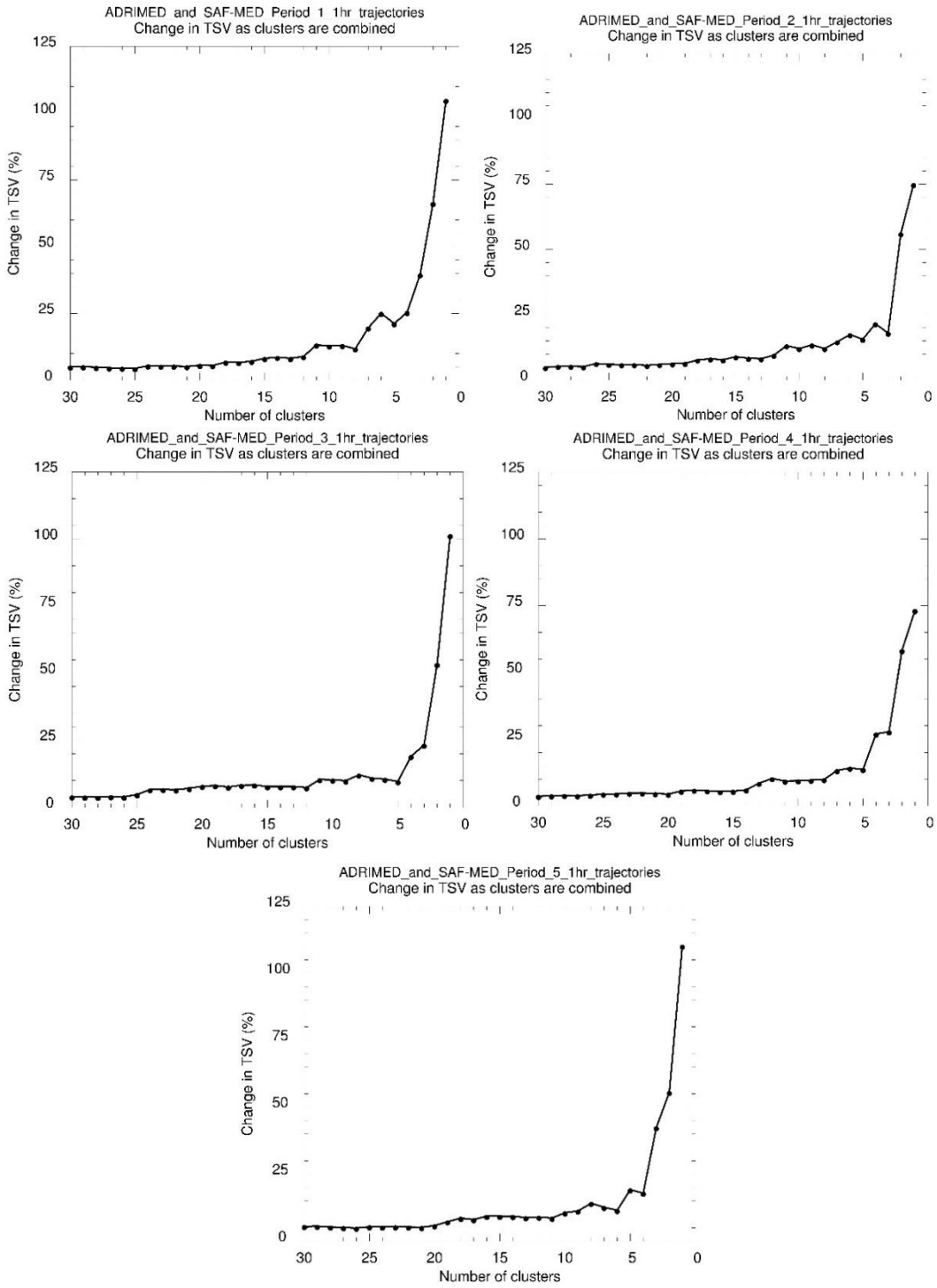


Figure 9.3. Change of the total spatial variance (TSV) as a function of the number of clusters for the HYSPLIT 120-hour back trajectory cluster analysis. Trajectories for 500 m above ground level (AGL) were produced every hour for each period of ADRIMED/SAF-MED and grouped into five periods.

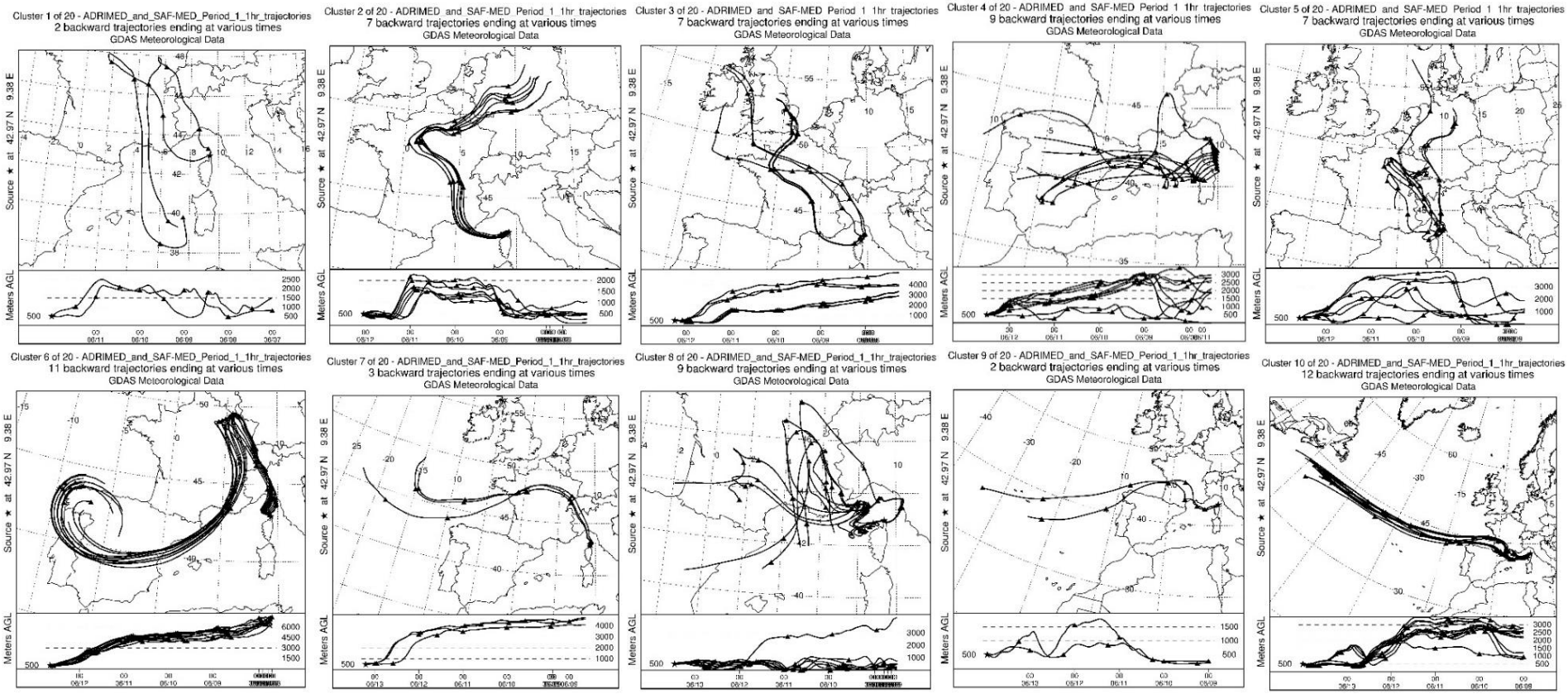


Figure 9.4. Individual HYSPLIT 120-hour back trajectories for each cluster for Period 1 during ADRIMED/SAF-MED.

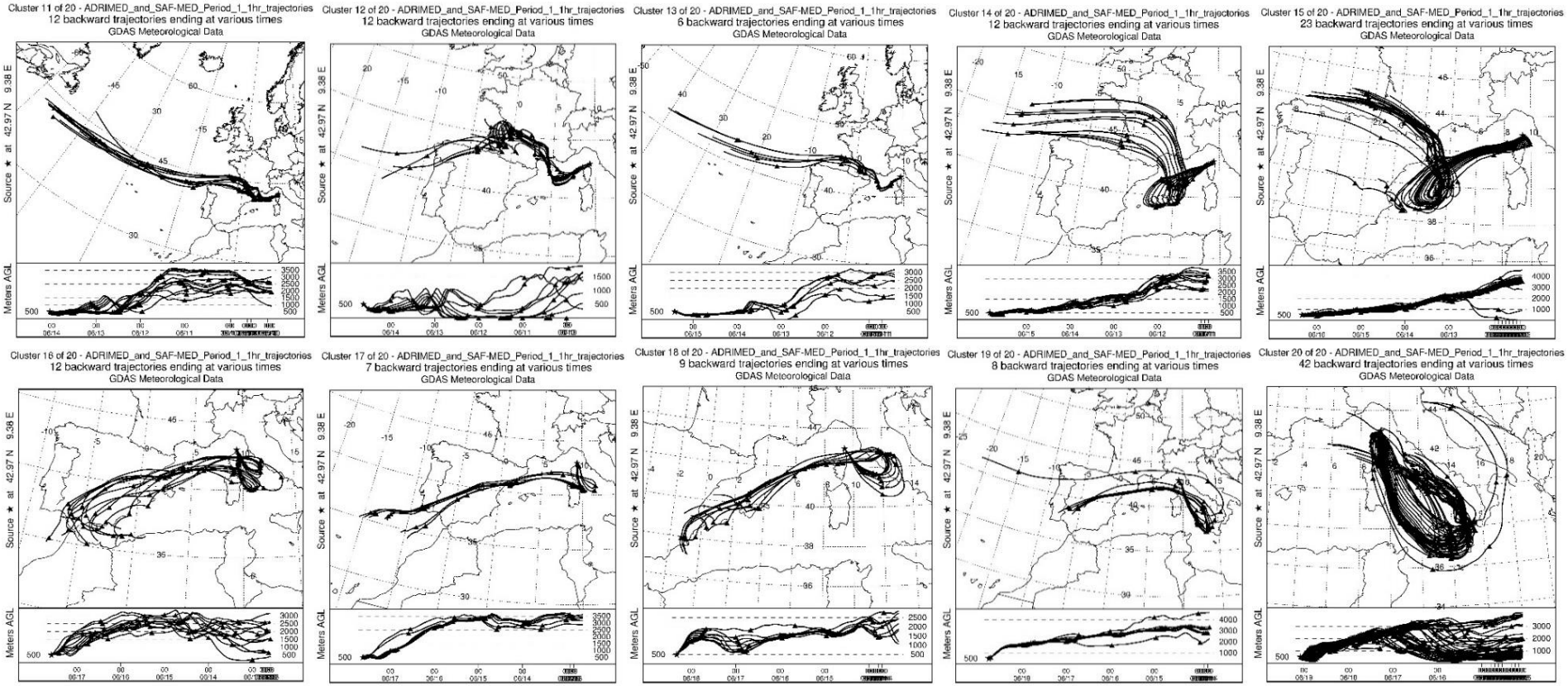


Figure 9.5. Individual HYSPLIT 120-hour back trajectories for each cluster for Period 1 during ADRIMED/SAF-MED (continued).

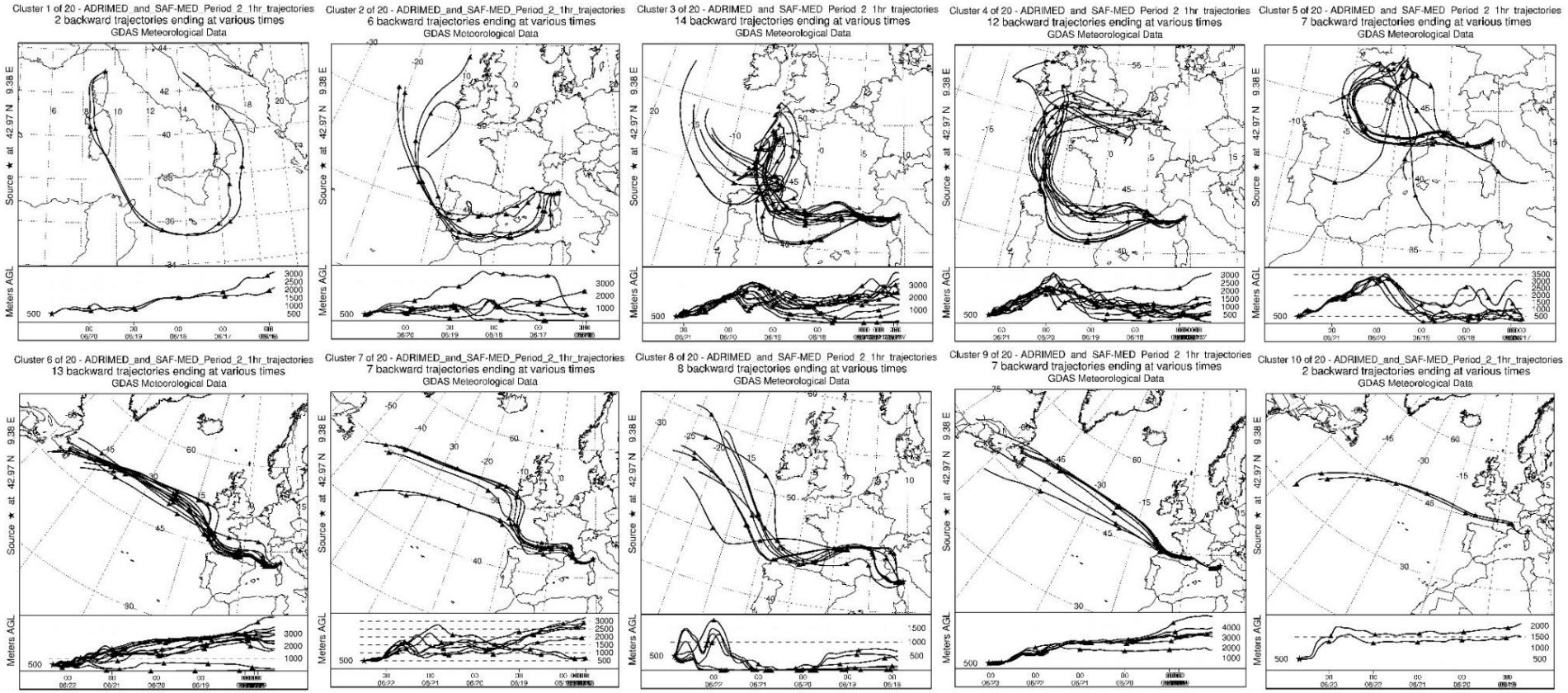


Figure 9.6. Individual HYSPLIT 120-hour back trajectories for each cluster for Period 2 during ADRIMED/SAF-MED.

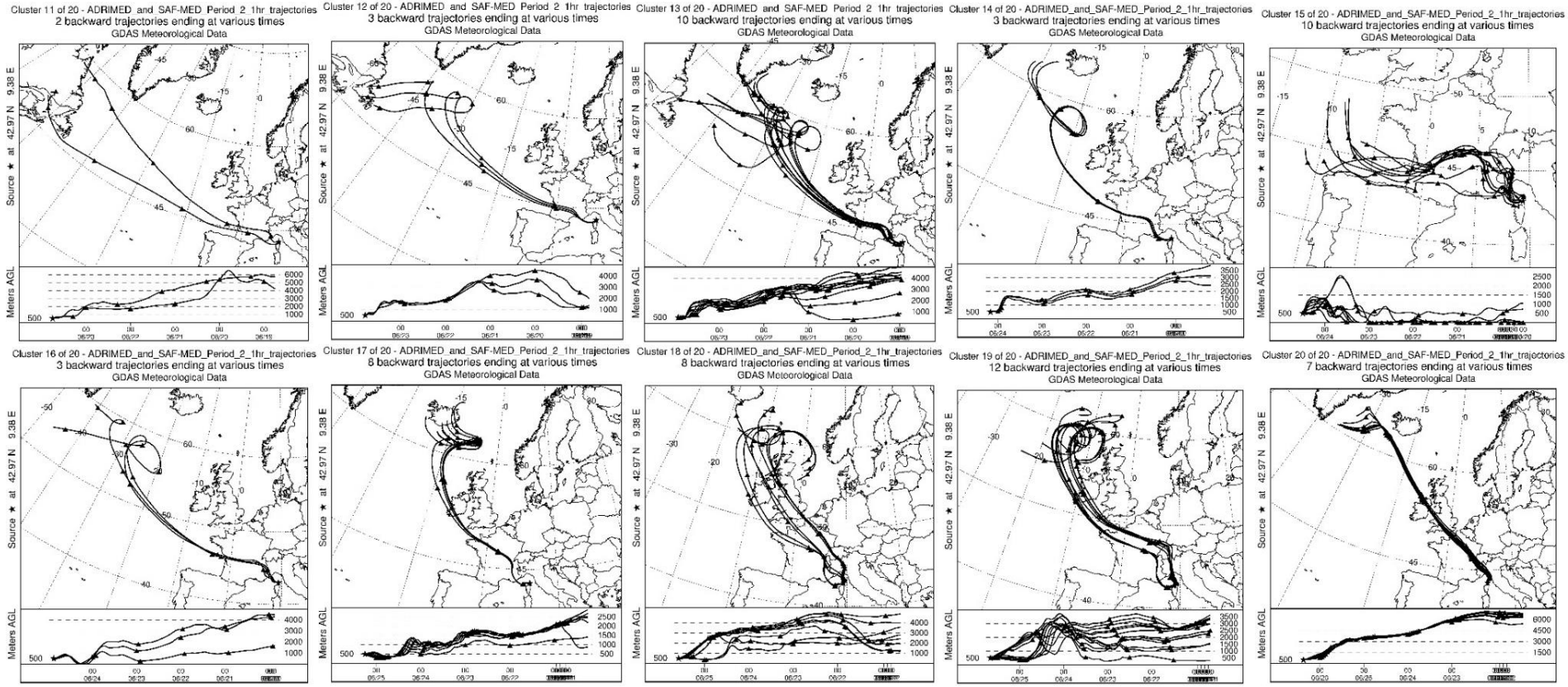


Figure 9.7. Individual HYSPLIT 120-hour back trajectories for each cluster for Period 2 during ADRIMED/SAF-MED (continued).

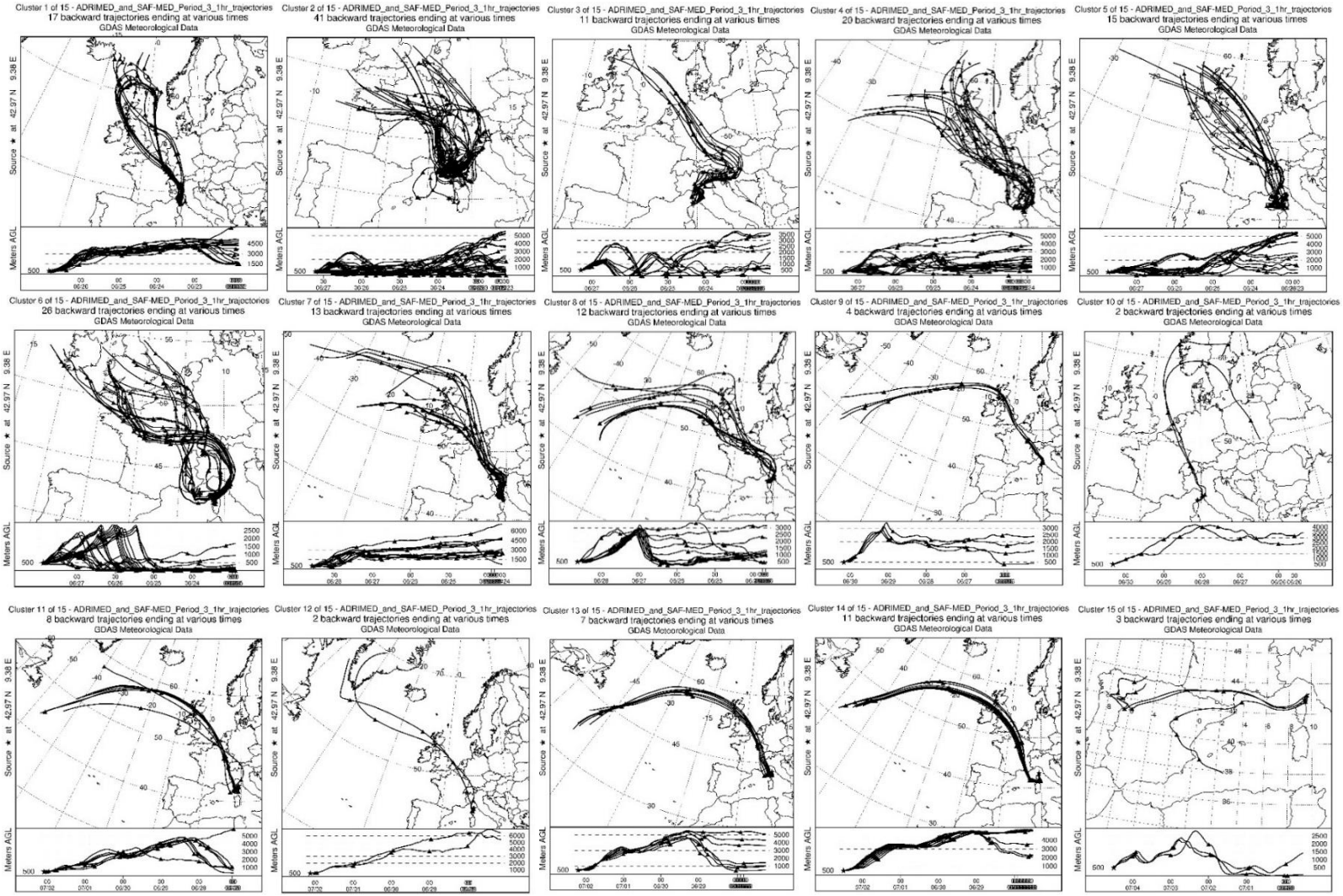


Figure 9.8. Individual HYSPLIT 120-hour back trajectories for each cluster for Period 3 during ADRIMED & SAF-MED.

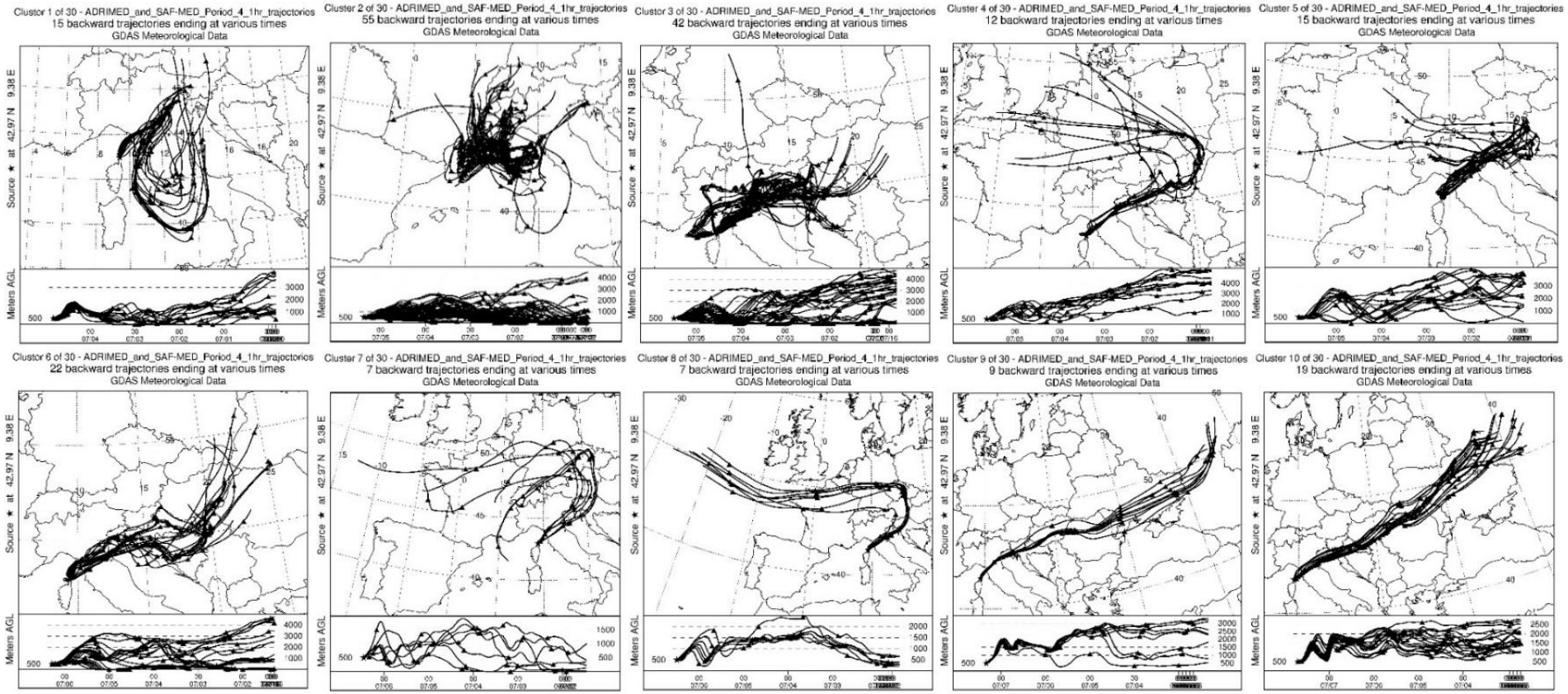


Figure 9.9. Individual HYSPLIT 120-hour back trajectories for each cluster for Period 4 during ADRIMED/SAF-MED.

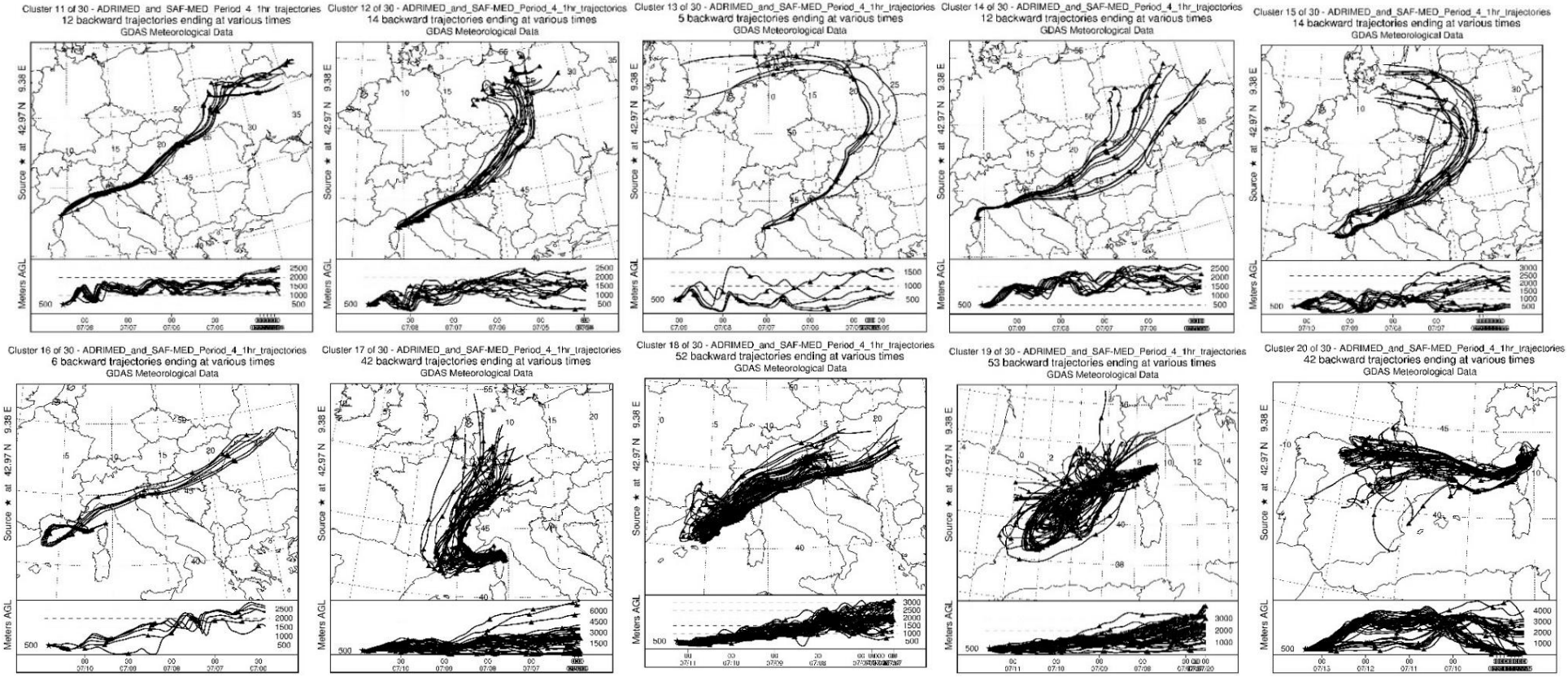


Figure 9.10. Individual HYSPLIT 120-hour back trajectories for each cluster for Period 4 during ADRIMED/SAF-MED (continued).

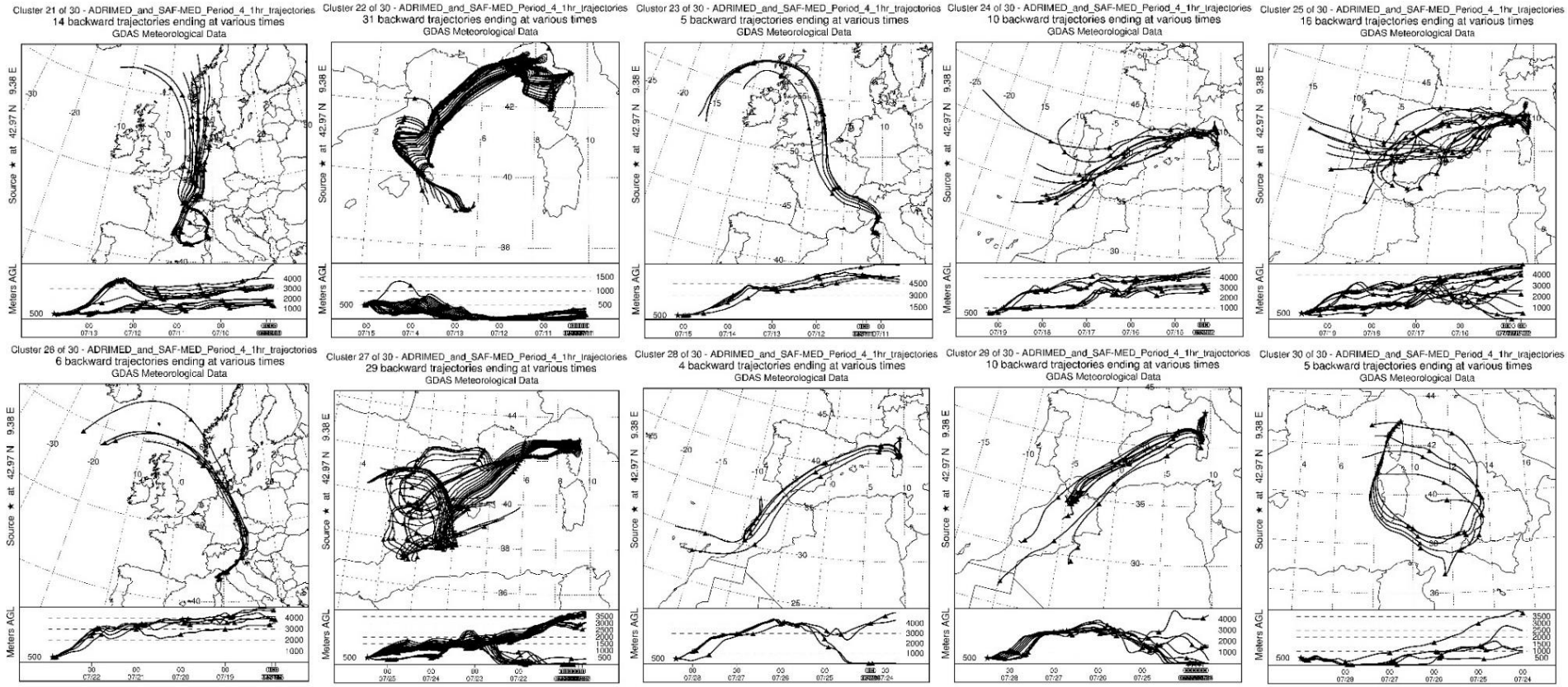


Figure 9.11. Individual HYSPLIT 120-hour back trajectories for each cluster for Period 4 during ADRIMED/SAF-MED (continued).

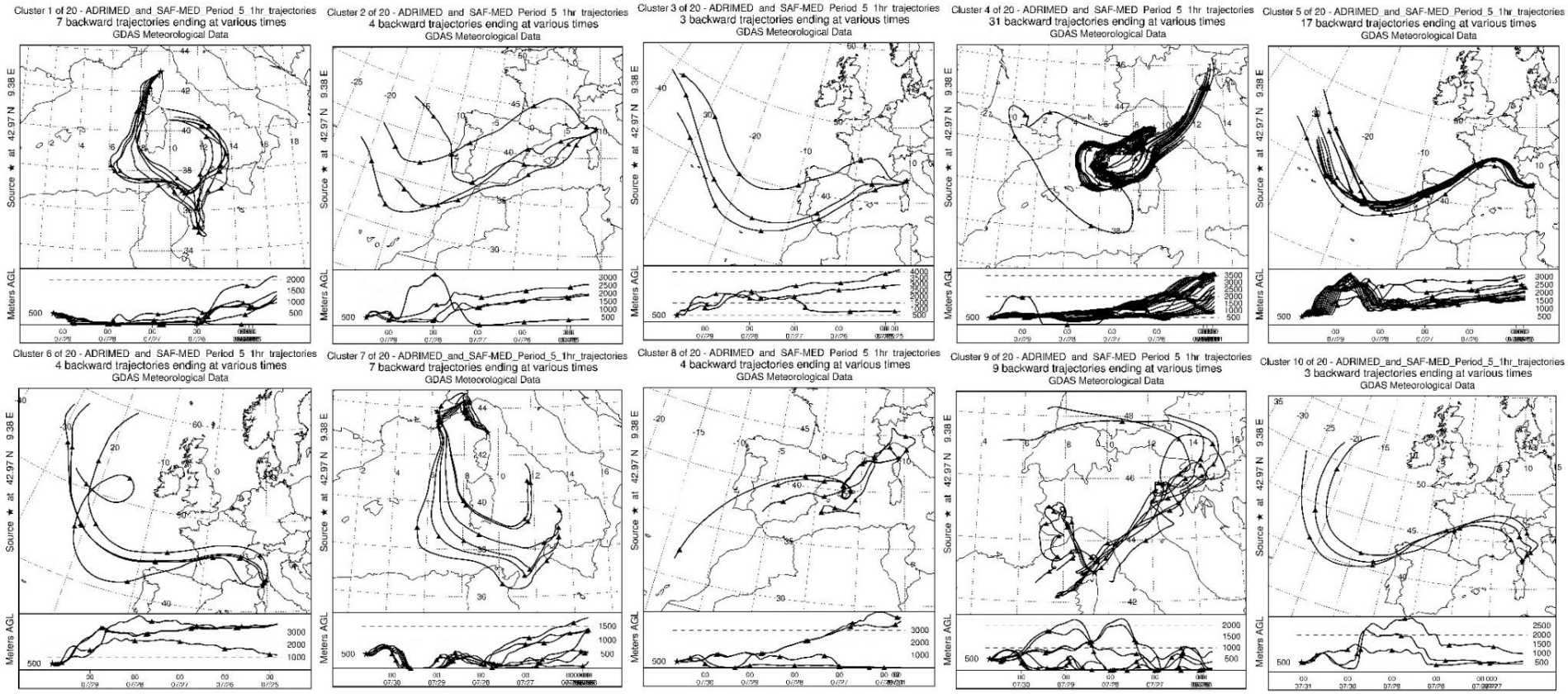


Figure 9.12. Individual HYSPLIT 120-hour back trajectories for each cluster for Period 5 during ADRIMED/SAF-MED.

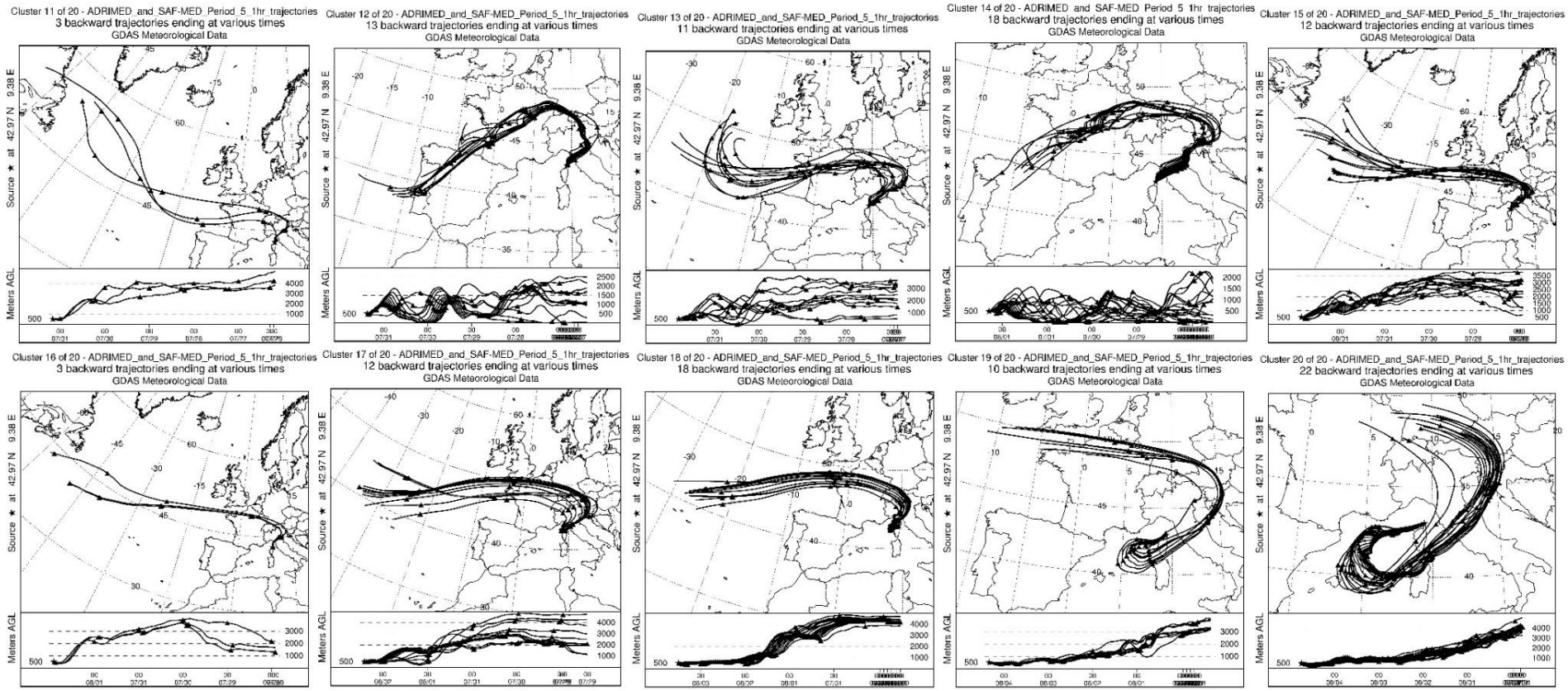


Figure 9.13. Individual HYSPLIT 120-hour back trajectories for each cluster for Period 5 during ADRIMED/SAF-MED (continued).

9.4 SIZE DISTRIBUTIONS

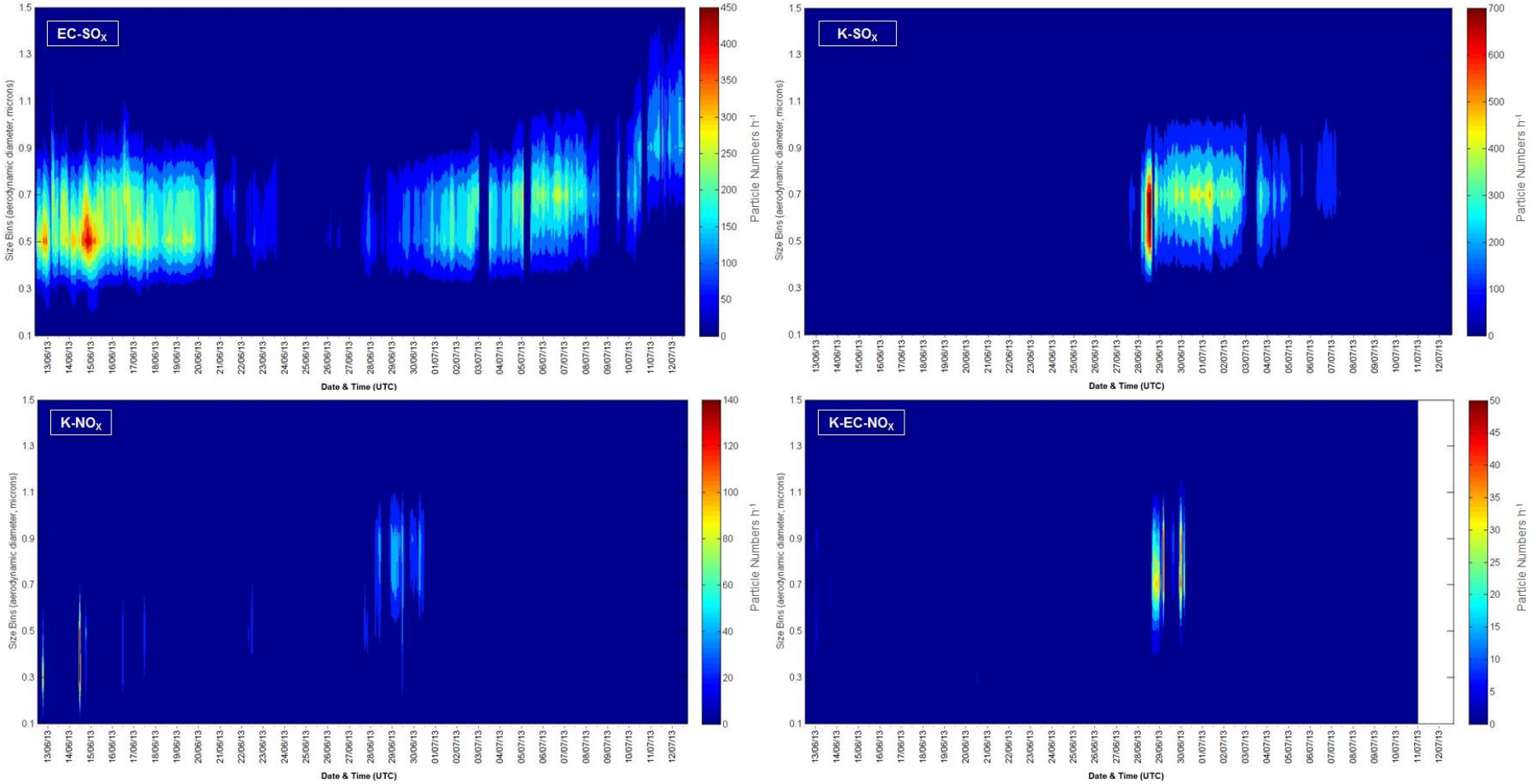


Figure 9.14. Hourly size distributions for regional combustion and local combustion particle classes observed during ADRIMED. EC-SO_X is representative of EC-K and EC-Oxalate. K-SO_X is representative of K-CN, K-EC-Oxalate and EC-K-Oxalate, with the exception of 28th June peak. K-NO_X is representative of OC-SO_X and OC-NO_X.

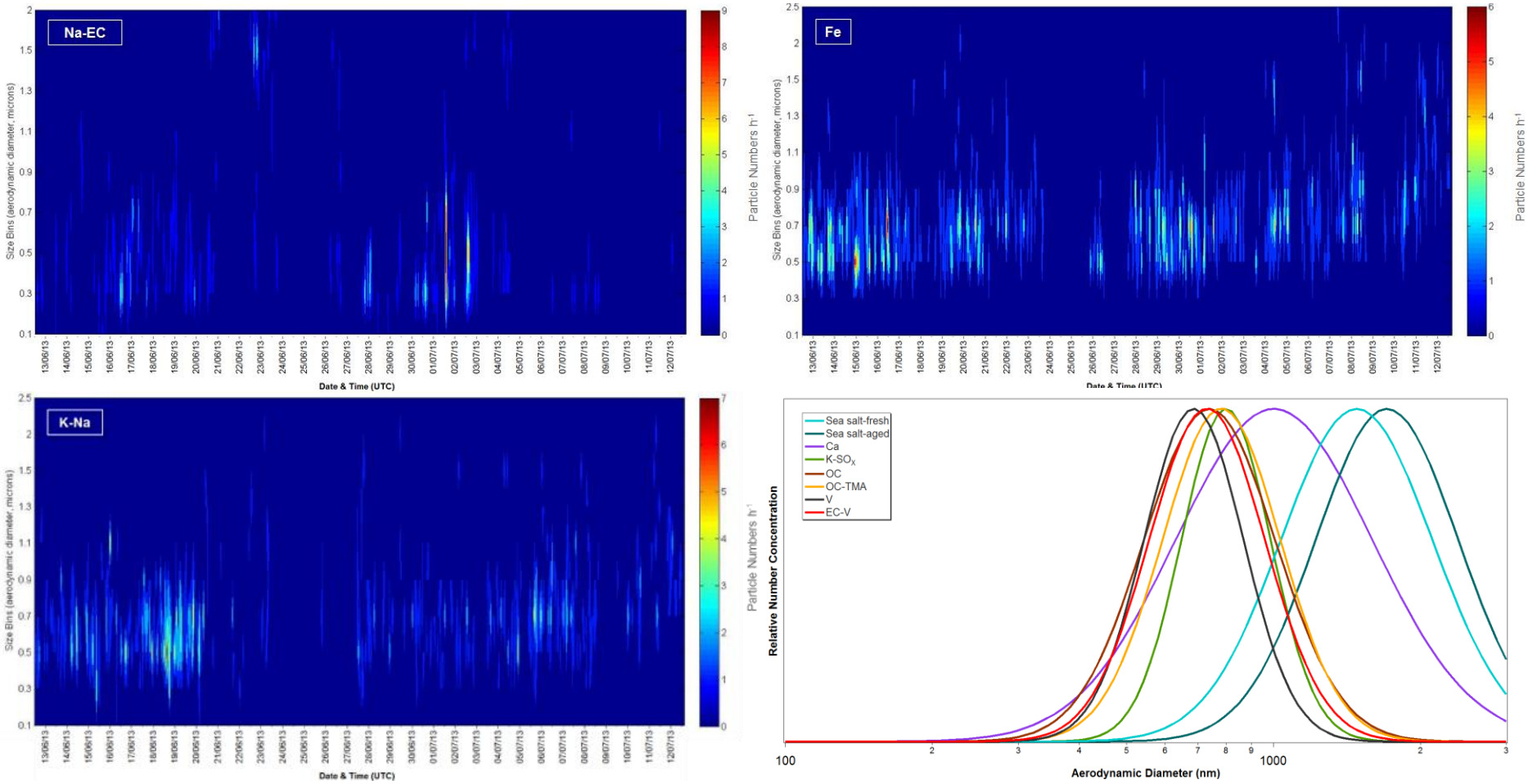


Figure 9.15. Hourly size distributions for local combustion and possible dust particles, and normalised lognormal size distributions (bottom right) for particle classes with little variation in size during ADRIMED.

9.5 CORRELATIONS

Table 9.1. Correlations between ATOFMS sea salt particle numbers and mass concentrations and OPS, PILS and ACSM measurements.

		ATOFMS Particle Numbers		*ATOFMS Mass Concentration*	
		Sea salt-fresh	Sea salt-aged	Sea salt-fresh	Sea salt-aged
Full sampling	OPS 0.579-2.156 µm (#/cm³)	0.30	0.05	0.50	0.12
	SSA (PILS) µg/m³	0.36	0.09	0.67	0.09
	Na^+ (PILS) µg/m³	0.42	0.11	0.64	0.10
	Cl^- (PILS) µg/m³	0.51	0.09	0.80	0.07
	Mg^+ (PILS) µg/m³	0.38	0.12	0.64	0.10
Period 1	OPS 0.579-2.156 µm (#/cm³)	0.20	0.37	0.46	0.65
	SSA (PILS) µg/m³	0.33	0.46	0.61	0.65
	Na^+ (PILS) µg/m³	0.28	0.50	0.55	0.69
	Cl^- (PILS) µg/m³	0.44	0.27	0.74	0.40
	Mg^+ (PILS) µg/m³	0.29	0.49	0.51	0.64
	SO_4^{2-} (ACSM)	0.09	0.27	0.20	0.53
	NH_4^+ (ACSM)	0.06	0.20	0.15	0.45
	Chl (ACSM)	0.25	0.28	0.51	0.46
Period 2	OPS 0.579-2.156 µm (#/cm³)	0.19	0.03	0.81	0.08
	SSA (PILS) µg/m³	0.15	0.06	0.81	0.02
	Na^+ (PILS) µg/m³	0.14	0.03	0.75	0.05
	Cl^- (PILS) µg/m³	0.14	0.13	0.84	0.00
	Mg^+ (PILS) µg/m³	0.11	0.03	0.69	0.07
	Ca^{2+} (PILS)	0.02	0.03	0.50	0.03
	K^+ (PILS)	0.04	0.02	0.47	0.08
	Total PILS Mass	0.09	0.02	0.64	0.11
Period 5	OPS 0.579-2.156 µm (#/cm³)	0.64	0.25	0.22	0.16
	SSA (PILS) µg/m³	0.62	0.43	0.09	0.08
	Na^+ (PILS) µg/m³	0.85	0.50	0.04	0.07
	Cl^- (PILS) µg/m³	0.85	0.17	0.39	0.12
	Mg^+ (PILS) µg/m³	0.69	0.49	0.01	0.06
	NO_3^- (PILS)	0.63	0.49	0.15	0.15